

UNITED STATES AIR FORCE
SUMMER RESEARCH PROGRAM -- 1997
SUMMER RESEARCH EXTENSION PROGRAM FINAL REPORTS

VOLUME 2
PHILLIPS LABORATORY

RESEARCH & DEVELOPMENT LABORATORIES
5800 Uplander Way
Culver City, CA 90220-6608

Program Director, RDL
Gary Moore

Program Manager, AFOSR
Major Linda Steel-Goodwin

Program Manager, RDL
Scott Licoscas

Program Administrator, RDL
Johnetta Thompson

Program Administrator, RDL
Rebecca Kelly-Clemmons

Submitted to:

AIR FORCE OFFICE OF SCIENTIFIC RESEARCH
Bolling Air Force Base
Washington, D.C.
December 1997

20010319 032

REPORT DOCUMENTATION PAGE

AFRL-SR-BL-TR-00-

Public reporting burden for this collection of information is estimated to average 1 hour per response, including the time for reviewing instructions, searching existing data sources, gathering the required data, reviewing and collecting the information, and completing and reviewing the collection of information. Send comments regarding this burden estimate or any other aspect of this collection of information, including suggestions for reducing the burden, to Washington Headquarters Services, Directorate for Information Operations and Reports, 1215 Jefferson Davis Highway, Suite 1204, Arlington, VA 22202-4302, and to the Office of Management and Budget, Paperwork Project, Washington, DC 20503.

I reviewing
information

0709

1. AGENCY USE ONLY (Leave blank)		2. REPORT DATE December, 1997		3. REPORT NUMBER	
4. TITLE AND SUBTITLE 1997 Summer Research Program (SRP), Summer Research Extension Program (SREP), Final Report, Volume 2, Phillips Laboratory				5. FUNDING NUMBERS F49620-93-C-0063	
6. AUTHOR(S) Gary Moore					
7. PERFORMING ORGANIZATION NAME(S) AND ADDRESS(ES) Research & Development Laboratories (RDL) 5800 Uplander Way Culver City, CA 90230-6608				8. PERFORMING ORGANIZATION REPORT NUMBER	
9. SPONSORING/MONITORING AGENCY NAME(S) AND ADDRESS(ES) Air Force Office of Scientific Research (AFOSR) 801 N. Randolph St. Arlington, VA 22203-1977				10. SPONSORING/MONITORING AGENCY REPORT NUMBER	
11. SUPPLEMENTARY NOTES					
12a. DISTRIBUTION AVAILABILITY STATEMENT Approved for Public Release				12b. DISTRIBUTION CODE	
13. ABSTRACT (Maximum 200 words) The United States Air Force Summer Research Program (SRP) is designed to introduce university, college, and technical institute faculty members to Air Force research. This is accomplished by the faculty members, graduate students, and high school students being selected on a nationally advertised competitive basis during the summer intersession period to perform research at Air Force Research Laboratory (AFRL) Technical Directorates and Air Force Air Logistics Centers (ALC). AFOSR also offers its research associates (faculty only) an opportunity, under the Summer Research Extension Program (SREP), to continue their AFOSR-sponsored research at their home institutions through the award of research grants. This volume consists of a listing of the participants for the SREP and the technical report from each participant working at the AF Phillips Laboratory.					
14. SUBJECT TERMS Air Force Research, Air Force, Engineering, Laboratories, Reports, Summer, Universities, Faculty, Graduate Student, High School Student				15. NUMBER OF PAGES	
				16. PRICE CODE	
17. SECURITY CLASSIFICATION OF REPORT Unclassified	18. SECURITY CLASSIFICATION OF THIS PAGE Unclassified	19. SECURITY CLASSIFICATION OF ABSTRACT Unclassified	20. LIMITATION OF ABSTRACT UL		

GENERAL INSTRUCTIONS FOR COMPLETING SF 298

The Report Documentation Page (RDP) is used in announcing and cataloging reports. It is important that this information be consistent with the rest of the report, particularly the cover and title page. Instructions for filling in each block of the form follow. It is important to **stay within the lines** to meet **optical scanning requirements**.

Block 1. Agency Use Only (Leave blank).

Block 2. Report Date. Full publication date including day, month, and year, if available (e.g. 1 Jan 88). Must cite at least the year.

Block 3. Type of Report and Dates Covered. State whether report is interim, final, etc. If applicable, enter inclusive report dates (e.g. 10 Jun 87 - 30 Jun 88).

Block 4. Title and Subtitle. A title is taken from the part of the report that provides the most meaningful and complete information. When a report is prepared in more than one volume, repeat the primary title, add volume number, and include subtitle for the specific volume. On classified documents enter the title classification in parentheses.

Block 5. Funding Numbers. To include contract and grant numbers; may include program element number(s), project number(s), task number(s), and work unit number(s). Use the following labels:

C - Contract
G - Grant
PE - Program
Element

PR - Project
TA - Task
WU - Work Unit
Accession No.

Block 6. Author(s). Name(s) of person(s) responsible for writing the report, performing the research, or credited with the content of the report. If editor or compiler, this should follow the name(s).

Block 7. Performing Organization Name(s) and Address(es). Self-explanatory.

Block 8. Performing Organization Report Number. Enter the unique alphanumeric report number(s) assigned by the organization performing the report.

Block 9. Sponsoring/Monitoring Agency Name(s) and Address(es). Self-explanatory.

Block 10. Sponsoring/Monitoring Agency Report Number. (If known)

Block 11. Supplementary Notes. Enter information not included elsewhere such as: Prepared in cooperation with....; Trans. of....; To be published in.... When a report is revised, include a statement whether the new report supersedes or supplements the older report.

Block 12a. Distribution/Availability Statement. Denotes public availability or limitations. Cite any availability to the public. Enter additional limitations or special markings in all capitals (e.g. NOFORN, REL, ITAR).

DOD - See DoDD 5230.24, "Distribution Statements on Technical Documents."

DOE - See authorities.

NASA - See Handbook NHB 2200.2.

NTIS - Leave blank.

Block 12b. Distribution Code.

DOD - Leave blank.

DOE - Enter DOE distribution categories from the Standard Distribution for Unclassified Scientific and Technical Reports.

Leave blank.

NASA - Leave blank.

NTIS -

Block 13. Abstract. Include a brief (*Maximum 200 words*) factual summary of the most significant information contained in the report.

Block 14. Subject Terms. Keywords or phrases identifying major subjects in the report.

Block 15. Number of Pages. Enter the total number of pages.

Block 16. Price Code. Enter appropriate price code (*NTIS only*).

Blocks 17. - 19. Security Classifications. Self-explanatory. Enter U.S. Security Classification in accordance with U.S. Security Regulations (i.e., UNCLASSIFIED). If form contains classified information, stamp classification on the top and bottom of the page.

Block 20. Limitation of Abstract. This block must be completed to assign a limitation to the abstract. Enter either UL (unlimited) or SAR (same as report). An entry in this block is necessary if the abstract is to be limited. If blank, the abstract is assumed to be unlimited.

PREFACE

This volume is part of a five-volume set that summarizes the research of participants in the 1997 AFOSR Summer Research Extension Program (SREP.)

Reports presented in this volume are arranged alphabetically by author and are numbered consecutively – e.g., 1-1, 1-2, 1-3; 2-1, 2-2, 2-3. Reports in the five-volume set are organized as follows:

VOLUME

TITLE

1

Armstrong Laboratory

2

Phillips Laboratory

3

Rome Laboratory

4A

Wright Laboratory

4B

Wright Laboratory

5

Arnold Engineering Development Center
Air Logistics Centers
United States Air Force Academy
Wilford Hall Medical Center

1997 SREP Final Technical Report Table of Contents

Armstrong Laboratory

Volume 1

	Principle Investigator	Report Title University/Institution	Laboratory & Directorate
1	Dr. Richelle M. Allen-King	Trans-1,2-Dichloroethene Transformation Rate in a Metallic Iron/Water System: Effects of Concentration and Temperature Washington State University	AL/EQC
2	Dr. Anthony R. Andrews	Development of Multianalyte Electrochemiluminescence Sensors & Biosensors Ohio University	AL/EQC
3	Dr. Jer-Sen Chen	Development of Perception Based Video Compression Algorithms Using Reconfigurable Hardware Wright State University	AL/CFHV
4	Dr. Cheng Cheng	Investigation & Eval of Optimization Algorithms Guiding the Assignment of Recruits to Training School Seats John Hopkins University	AL/HRM
5	Dr. Randolph D. Glickman	Optical Detection of Intracellular Photooxidative Reactions University of Texas Health Science Center	AL/OEO
6	Dr. Nandini Kannan	Predicting Altitude Decompression sickness Using Survival Models University of Texas at San Antonio	AL/CFTS
7	Dr. Antti J. Koivo	Skill Improvements Via Reflected Force Feedback Purdue Research Foundation	AL/CFBA
8	Dr. Suk B. Kong	Degradation & Toxicology Studies of JP-8 Fuel in Air, Soil & Drinking Water Incarnate Word College	AL/OEA
9	Dr. Audrey D. Levine	Biogeochemical Assessment of Natl Attenuation of JP-4 Contaminated Ground in the Presence of Fluorinated Surfactants Utah State University	AL/EQC
10	Dr. Robert G. Main	The Effect of Video Image Size & Screen Refresher Rate On Mess Retention Cal State University, Chico	AL/HRT
11	Dr. Phillip H. Marshall	On the Resilience of Time-to-Contact Judgements: The Determination of Inhibitory and Facilitory Influences, and Factor Structure Texas Tech University	AL/HRM
12	Dr. Bruce V. Mutter	Environmental cost Analysis: Calculating Return on Investment for Emerging Technologies Bluefield State College	AL/EQP

1997 SREP Final Technical Report Table of Contents

Armstrong Laboratory

Volume 1 (cont.)

	Principle Investigator	Report Title University/Institution	Laboratory & Directorate
13	Dr. Sundaram Narayanan	Java-Based Interactive Simulation Architecture for Airbase Logistics Modeling Wright State University	AL/HRT
14	Dr. Barth F. Smets	Coupling of 2, 4-&2, 6-Dinitrotoluene Mineralization W/NO ₂ Removal by University of Cincinnati	AL/EQC
15	Dr. Mary Alice Smith	In Vitro Detection of Apoptosis in Differentiating Mesenchymal Cells Using Immunohistochemistry and Image Analysis University of Georgia	AL/OET
16	Dr. William A. Stock	Application of Meta-Analysis to Research on Pilot Training: Extensions to Flight Simulator Visual System Research Arizona State University	AL/HRA
17	Dr. Nancy J. Stone	Evaluation of a Scale Designed to Measure the Underlying Constructs of Engagement, Involvement, & Self-Regulated Learning Creighton University	AL/HRT
18	Dr. Mariusz Ziejewski	Characterization of Human Head/Neck Response in Z-Direction in Terms of Significant Anthropomorphic Parameters, Gender, Helmet Weight and Helmet Center North Dakota State University	AL/CFBV
19	Dr. Kevin M. Lambert	Magnetic Effects on the Deposition & Dissolution of Calcium Carbonate Scale Brigham Young University	AL/EQS
20	Dr. Jacqueline C. Shin	Coordination of Cognitive & Perceptual-Motor Activities Pennsylvania State University	AL/HRM
21	Dr. Travis C. Tubre	The Development of a General Measure of Performance Texas A&M University-College Station	AL/HRT
22	Dr. Robert B. Trelease	Development of Qualitative Process Modeling Systems for Cytokines, Cell Adhesion Molecules, and Gene Regulation University of California - Los Angeles	AL/AOH

1997 SREP Final Technical Report Table of Contents

Phillips Laboratory

Volume 2

	Principle Investigator	Report Title University/Institution	Laboratory & Directorate
1	Dr. Graham R. Allan	Temporal & Spatial Characterization of a Synchronously-Pumped New Mexico Highlands University	PL/LIDN
2	Dr. Joseph M. Calo	Transient Studies of the Effects of Fire Suppressants in a Well-Stirred Combustor Brown University	PL/GPID
3	Dr. James J. Carroll	Examination of Critical Issues in the Triggering of Gamma Rays from 178Hfm2 Youngstown State University	PL/WSQ
4	Dr. Soyoung S. Cha	Gradient-Data Tomography for Hartman Sensor Application to Aero-Optical Field Reconstruction University of Illinois at Chicago	PL/LIMS
5	Dr. Judith E. Dayhoff	Dynamic Neural Networks: Towards Control of Optical Air Flow Distortions University of Maryland	PL/LIMS
6	Dr. Ronald R. DeLyser	Computational Evaluation of Optical Sensors University of Denver	PL/WSTS
7	Dr. Andrew G. Detwiler	Analysis & Interpretation of Contrail Formation Theory & Observations South Dakota School of Mines – Technology	PL/GPAB
8	Dr. Itzhak Dotan	Measurements of Ion-Molecule Reactions at Very High Temperature The Open University of Israel	PL/GPID
9	Dr. George W. Hanson	Electromagnetic Modeling of Complex Dielectric/Metallic Mines In A Layered University of Wisconsin – Milwaukee	PL/WSQ
10	Dr. Mayer Humi	Optical & Clear Air Turbulence Worcester Polytechnic Inst.	PL/GPAA
11	Dr. Christopher H. Jenkins	Shape Control of an Inflated Circular Disk Experimental Investigation South Dakota School of Mines – Technology	PL/VT
12	Dr. Dikshitulu K. Kalluri	Numerical Simulation of Electromagnetic Wave Transformation in a Dynamic Magnetized Plasma University of Lowell	PL/GPIA
13	Dr. Aravinda Kar	Improved Chemical Oxygen-Iodine Laser (COIL) Cutting Models to Optimize Laser Parameters University of Central Florida	PL/LIDB

1997 SREP Final Technical Report Table of Contents

Phillips Laboratory

Volume 2 (cont.)

	Principle Investigator	Report Title University/Institution	Laboratory & Directorate
14	Dr. Andre Y. Lee	Characterization of Thermoplastic Inorganic-Organic Hybrid Polymers Michigan State University	PL/RKS
15	Dr. Feng-Bao Lin	Improvement in Fracture Propagation Modeling for Structural Ballistic Risk Assessment Polytechnic University of New York	PL/RKEM
16	Dr. Ronald A. Madler	Cross Sectional Area Estimation of Orbital Debris Embry-Riddle Aeronautical University	PL/WSAT
17	Dr. Carlos A. Ordonez	Incorporation of Boundary condition Models into the AF Computer Simulation University of North Texas	PL/WSQA
18	Dr. James M. Stiles	Wide Swath, High Resolution, Low Ambiguity SAR Using Digital Beamforming Arrays University of Kansas	PL/VTRA
19	Dr. Charles M. Swenson	Balloon Retromodulator Experiment Post- flight Analysis Utah State University	PL/VTRA
20	Dr. Miguel Velez-Reyes	Development of Algorithms for Linear & Nonlinear Retrieval Problems in Atmospheric Remote Sensing University of Puerto Rico	PL/GPAS
21	Dr. John D. Holtzclaw	Experimental Investigation of Ipinging Jets University of Cincinnati	PL/RKS
22	Dr. Jeffrey W. Nicholson	Radar Waves with Optical Carriers University of New Mexico	PL/LIDB

1997 SREP Final Technical Report Table of Contents

Rome Laboratory

Volume 3

Principle Investigator	Report Title University/Institution	Laboratory & Directorate
1 Dr. A. F. Anwar	Deep Quantum Well Channels for Ultra Low Noise HEMTs for Millimeter and Sub-millimeter Wave Applications University of Connecticut	AFRL/SNH
2 Dr. Ahmed E. Barbour	Investigating the Algorithmic Nature of the Proof Structure of ORA Larch/VHDL Georgia Southern University	RL/ERDD
3 Dr. Milica Barjaktarovic	Specification & Verification of MISSI Architecture Using SPIN Wilkes University	RL/C3AB
4 Dr. Daniel C. Bukofzer	Analysis, Performance Evaluations, & Computer Simulations of Receivers Processing Low Probability of Intercept Signals Cal State Univ. Fresno	RL/C3BA
5 Dr. Xuesheng Chen	Non-Destructive Optical Characterization of Composition & Its Uniformity in Multilayer Ternary Semiconductor Stacks Wheaton College	RL/ERX
6 Dr. Jun Chen	Amplitude Modulation Using Feedback Sustained Pulsation as Sub-Carrier in Rochester Inst of Technol	RL/OCPA
7 Dr. Everett E. Crisman	Development of Anti-Reflection Thin Films for Improved Coupling of Laser Energy into Light Activated, Semiconductor Re-Configurable, Microwave Source/Antenna Brown University	RL/ERAC
8 Dr. Digendra K. Das	Development of a Stimulation Model for Determining the Precision Of Reliability SUNYIT	RL/ERSR
9 Dr. Matthew E. Edwards	An Application of PROFILER for Modeling the Diffusion of Of Aluminum-Copper on a Silicon Substrate Spelman College	RL/ERDR
10 Dr. Kaliappan Gopalan	Analysis of Stressed Speech Using Cepstral Domain Features Purdue University – Calumet	RL/IRAA
11 Dr. James P. LeBlanc	Multichannel Autoregressive Modeling & Multichannel Innovations Based New Mexico State University	RL/OCSS
12 Dr. Hrushikesh N. Mhaskar	Multi-Source Direction Finding Cal State University, Los Angeles	RL/ERAA
13 Dr. Ronald W. Noel	An Evolutionary Sys for Machine Recognition of Software Source Code Rensselaer Polytechnic Inst	RL/C3CA

1997 SREP Final Technical Report Table of Contents

Rome Laboratory

Volume 3 (cont.)

Principle Investigator	Report Title University/Institution	Laboratory & Directorate
14 Dr. Glenn E. Prescott	Rapid Prototyping of Software Radio Sys Using Field Programmable Gate Arrays University of Kansas Center for Research	RL/C3BB
15 Dr. Mysore R. Rao	Wavelet Transform Techniques for Isolation, Detection & Classification of Concealed Objects in Images Rochester Institute of Technology	RL/OCSM
16 Dr. Scott E. Spetka	IPL HTML Interface Performance Evaluation SUNY of Tech Utica	RL/IRD
17 Dr. Gang Sun	Investigation of Si/ZnS Near Infrared Intersubband Lasers University of Massachusetts-Boston	RL/ERO
18 Mr. Parker E. Bradley	Development of a User-Friendly Computer Environment for Blind Source Syracuse University	RL/C3BB

1997 SREP Final Technical Report Table of Contents

Wright Laboratory

Volume 4A

Principle Investigator	Report Title University/Institution	Laboratory & Directorate
1	Dr. Mohammad S. Alam Infrared Image Registration & High Resolution Reconstruction Using Rotationally Translated Video Sequences* Purdue University	WL/AAJT
2	Dr. Pnina Ari-Gur Optimizing Microstructure, Texture & Orientation Image Microscopy of Hot Rolled Ti-6Al-4V Western Michigan University	WL/MLLN
3	Dr. James D. Baldwin Multi-Site & Widespread Fatigue Damage in Aircraft Structure in the Presence of Prior Corrosion University of Oklahoma	WL/FIB
4	Dr. Armando R. Barreto Deconvolution of the Space-Time Radar Spectrum Florida International University	WL/AAMR
5	Dr. Marc M. Cahay Improved Modeling of Space-Charge Effects in a New Cold Cathode Emitter University of Cincinnati	WL/AADM
6	Dr. Reaz A. Chaudhuri Interfacing of Local Asymptotic Singular & Global Axisymmetric Micromechanical University of Utah	WL/MLBM
7	Dr. Robert J. DeAngelis Texture Formation During the Thermo-Mechanical Processing of Copper Plate University of Nebraska – Lincoln	WL/MNMW
8	Dr. Gregory S. Elliott The Study of a Transverse Jet in a Supersonic Cross-Flow Using Advanced Laser Rutgers: State University of New Jersey	WL/POPT
9	Dr. Altan M. Ferendeci Development of Multiple Metal-Dielectric Layers for 3-D MMIC University of Cincinnati	WL/AADI
10	Dr. Allen G. Greenwood Development of a Prototype to Test & Demonstrate the MODDCE Framework Mississippi State University	WL/MTI
11	Dr. Michael A. Grinfeld Mismatch Stresses & Lamellar Microstructure of TiAl-Alloys Rutgers University- Piscataway	WL/MLLM
12	Dr. Michael C. Larson Interfacial Sliding in Brittle Fibrous Composites Tulane University	WL/MLLM
13	Dr. Douglas A. Lawrence Tools for the Analysis & Design of Gain Scheduled Missile Autopilots Ohio University	WL/MNAG

1997 SREP Final Technical Report Table of Contents

Wright Laboratory (cont.)

Volume 4A

	Principle Investigator	Report Title University/Institution	Laboratory & Directorate
14	Dr. Junghsen Lieh	Determination of 3D Deformations, Forces & Moments of Aircraft Wright State University	WL/FIVM
15	Dr. Zongli Lin	Control of Linear Sys w/Rate Limited Actuators & Its Applications to Flight Control Systems SUNY Stony Brook	WL/FI
16	Dr. Paul Marshall	Experimental & Computational Investigations of Bromine & Iodine Chemistry in Flame Suppression University of North Texas	WL/MLBT
17	Dr. Hui Meng	Development of Holographic Visualization & Holographic Velocimetry Techniques Kansas State University	WL/POSC
18	Dr. Douglas J. Miller	Band Gap Calculations on Squarate-Containing Conjugated Oligomers for the Prediction of Conductive and Non-Linear Optical Properties of Polymeric Materials Cedarville College	WL/MLBP
19	Dr. Timothy S. Newman	Classification & Visualization of Tissue in Multiple Modalities of Brain MR University of Alabama at Huntsville	WL/AACR
20	Dr. Mohammed Y. Niamat	FPGA Implementation of the Xpatch Ray Tracer University of Toledo	WL/AAST
21	Dr. Anthony C. Okafor	Development of Optimum Drilling Process for Advanced Composites University of Missouri – Rolla	WL/MTI
22	Dr. George A. Petersson	Absolute Rates for Chemical Reactions Wesleyan University	WL/MLBT
23	Dr. Mohamed N. Rahaman	Process Modeling of the Densification of Granular Ceramics Interaction Between Densification and Creep University of Missouri – Rolla	WL/MLLN

1997 SREP Final Technical Report Table of Contents

Wright Laboratory (cont.)

Volume 4B

	Principle Investigator	Report Title University/Institution	Laboratory & Directorate
24	Dr. Martin Schwartz	Quantum Mechanical Modeling of the Thermochemistry of Halogenated Fire Suppressants University of North Texas	WL/MLBT
25	Dr. Marek Skowronski	Investigation of Slip Boundaries in 4H-SiC Crystals Carnegie Melon University	WL/MLPO
26	Dr. Yong D. Song	Guidance & Control of Missile Sys Under Uncertain Flight Conditions North Carolina A&T State University	WL/MNAG
27	Dr. Raghavan Srinivasan	Models for Microstructural Evolution During Dynamic Recovery Wright State University	WL/MLIM
28	Dr. Scott K. Thomas	The Effects of Transient Acceleration Loadings on the Performance of a Copper-Ethanol Heat Pipe with Spiral Grooves Wright State University	WL/POOS
29	Dr. James P. Thomas	The Effect of Temperature on Fatigue Crack Growth of TI-6AL-4V in the Ripple University of Notre Dame	WL/MLLN
30	Dr. Karen A. Tomko	Scalable Parallel Solution of the 3D Navier-Stokes Equations Wright State University	WL/FIM
31	Dr. J. M. Wolff	Off Design Inviscid/Viscous Forced Response Prediction Model for High Cycle Wright State University	WL/POTF
32	Mr. Todd C. Hathaway	Experiments on Consolidation of Aluminum Powders Using Simple Shear University of North Texas	WL/MLLN
33	Ms. Diana M. Hayes	Error Correction & Compensation for Mueller Matrices Accounting for Imperfect Polarizers University of North Texas	WL/MNGA

1997 SREP Final Technical Report Table of Contents

Volume 5

	Principle Investigator	Report Title University/Institution	Laboratory & Directorate
		Arnold Engineering Development Center	
1	Dr. Frank G. Collins	Development of Laser Vapor Screen Flow Visualization Sys Tennessee University Space Institute	AEDC
		United States Air Force Academy	
2	Mr. Derek E. Lang	Experimental Investigation of Liquid Crystal Applications for Boundary Layer Characterization University of Washington	USAFA/DFA
		Air Logistics Centers	
3	Dr. Sandra A. Ashford	Development of Jet Engine Test Facility Vibration Signature & Diagnostic System University of Detroit Mercy	OCALC/TIE
4	Dr. Roger G. Ford	Use of Statistical Process Control in a Repair/Refurbish/ Remanufactureg Environment St. Mary's University	SAALC
		Wilford Hall Medical Center	
5	Dr. Stedra L. Stillmana	Metabolite Profile Following the Administration of Fenproporex University of Alabama at Birmingham	WHMC

Graham R. Allan
Report not available at time of publication.

TRANSIENT STUDIES OF THE EFFECTS OF FIRE SUPPRESSANTS
IN A WELL-STIRRED COMBUSTOR

J.M. Calo
Professor
Division of Engineering

BROWN UNIVERSITY
Providence, RI 02912

Final Report for
Summer Research Extension Program

Sponsored by:
Air Force Office of Scientific Research
Bolling Air Force Base, DC

and

Phillips Laboratory

December 1998

TRANSIENT STUDIES OF THE EFFECTS OF FIRE SUPPRESSANTS IN A WELL-STIRRED COMBUSTOR

J.M. Calo
Professor
Division of Engineering
BROWN UNIVERSITY
Providence, RI 02912

Abstract

The effects of three different fire suppressants on the transient behavior of the composition of the effluent gas from a combustor were investigated in an experimental program conducted at the Well Stirred Reactor (WSR) facility at Wright-Patterson Air Force Base during the months of July and August 1996. A quadrupole mass spectrometer, that was originally designed and constructed to sample rocket exhaust gases, was used to sample the effluent gas composition from the WSR. These experiments employed premixed propane/air and methane/air gas mixtures at near-atmospheric pressure in the WSR. Transient measurements were performed on the effects of injecting the fire suppressants Halon 1301 (CF_3Br), pentafluoroethane (C_2HF_5 , HFC-125), and trifluoroiodomethane (CF_3I) into air/fuel mixtures at various concentration levels using a fast, pulsed valve system. Selected results from the experimental program are presented and discussed. It was concluded that the three fire suppressants exhibit some similarities in their behavior in combustion environments, as well as some distinct differences.

Results are presented from a numerical model of the WSR combustor system. This model was developed to interpret the resultant transient responses of gas phase species measured mass spectrometrically. The model includes the effects of the residence time distribution of the jet ring distributor, as determined from a fluid mechanical model developed for this purpose, and the detailed kinetics in the well-mixed combustor and the sampling line to the mass spectrometer. The latter two components of the model are based on the CHEMKIN II package of codes, especially the perfectly-stirred reactor (PSR) and SENKIN modules. Work has also been done on transforming the mole fractions reported by the model into corresponding mass spectrometric signals. Direct comparison of model results with the combustion data has been initiated.

The transient method, coupled with model analysis, as developed here, can be quite useful for the identification of key reactions in mechanisms of the behavior of fire suppressants in combustion systems. This approach can also be extended to determine kinetic rates for certain reactions. This effort is expected to improve the understanding of fire suppression mechanisms.

The unique capabilities of the REMS/WSR apparatus could be used to identify and measure in a definitive, quantitative manner the efficacy of candidate fire suppressants using only minimal pulsed amounts, as well as aid in the assessment of the important environmental effects of using fire suppressants in combustion systems relevant to Air Force operations.

TRANSIENT STUDIES OF THE EFFECTS OF FIRE SUPPRESSANTS IN A WELL-STIRRED COMBUSTOR

J.M. Calo

Background

The ban on the use of Halon 1301 in fire suppression systems for Air Force gas turbine engines, requires the identification of effective replacements. However, thus far the search for more environmentally benign replacement agents has identified only less effective substitutes. The interactions of chemical agents, such as Halon 1301, in combustion environments is a complex thermo- and physicochemical process which is still not completely understood [1,2,3]. In fact, it has been shown that even Halon 1301 can actually *enhance* combustion under certain conditions [3]. Consequently, the search for safe, effective substitute fire suppressant agents would benefit considerably from advancing the fundamental understanding of the interaction of fire suppressants with the complex combustion gas milieu. This is the primary objective of the work reported here.

The effects of three different fire suppressant agents on the transient behavior and composition of the effluent gas from a combustor were investigated in an experimental program conducted at the Well Stirred Reactor (WSR) facility at Wright-Patterson Air Force Base during the months of July and August 1996. A quadrupole mass spectrometer, that was originally designed and constructed to sample rocket exhaust gases, was used to sample the effluent gas composition from the WSR. These experiments employed premixed propane/air and methane/air gas mixtures at near-atmospheric pressure in the WSR. The parameter values for the three principal sets of operating conditions of the WSR system for methane combustion are presented below in Table I.

Transient measurements were performed on the effects of injecting the fire suppressants Halon 1301 (CF_3Br), pentafluoroethane (C_2HF_5 , HFC-125), and trifluoriodomethane (CF_3I) into air/fuel mixtures at various concentration levels using a fast, pulsed valve system.

In order to analyze the resultant transient data, a numerical model of the WSR and mass spectrometer sampling line have been formulated.

Table I. Nominal (average) WSR methane combustion run conditions.

Air (slm)	Methane (slm)	Ring T (K)	Ring P (kPa)	WSR T (K)	WSR P (kPa)	WSR τ (ms)	ϕ (equivalence ratio)
148	5.5	600	137.2 (128)	1500	100.5	17.8	0.56
200	14.8	580	148.5 (139.5)	1790	100.5	11.1	0.7
390	28.5	573	223.8 (230)	1770	101.3	5.7	0.7

Experimental

The Well Stirred Reactor (WSR) facility, located in the Fuels and Lubricants Group of Wright Laboratories at Wright-Patterson Air Force Base, Ohio, has been well described elsewhere [4,5]. The reactor is cast from alumina insulating cement in two halves which together form a toroidal shape, 250 ml in volume. Gas is admitted into the WSR *via* 32, 1.0 mm I.D. jets, made from alumina tubes, located 20° off radius and held in place in the a jet ring assembly which serves as the gas distributor for the reactor. The jets intensely mix the reactor contents and are responsible for its well-mixed behavior. The gas outlet is located in the center of the top half of the reactor, 90° to the feed gas flow, and exhausts into a large diameter plug flow reactor (PFR) section. Nominal reactor operating parameters include residence times on the order of 6 - 18 ms, operation up to 5 atm pressure and 2300K due to the use of zirconia-coated refractory materials. The three principal sets of operating conditions used in the current work

The three different fire suppressants were introduced into the WSR *via* a fast, pulsed solenoid valve manufactured by the General Valve Corporation. These valves were originally developed for molecular beam laser spectroscopy experiments. The valves are set for 2 ms at rated voltage, but can achieve even shorter pulse widths by overdriving with a 300V pulse for 165 μ s. The valve on and off times were controlled with the mass spectrometer microcomputer. The minimum “open” time used in the current experiments was 5 ms, which was the same as the

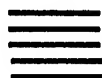
resolution of the mass spectrometer data collection system.

The effluent gas from the reactor was sampled into the mass spectrometer *via* an air-cooled quartz probe, which was connected to the bottom of the WSR through a drilled-out stainless steel Swagelok™ fitting with a graphite ferrule. The opening of the probe was positioned 1-2 mm away from the toroidal combustion volume. The flow rate through the probe was controlled by a pump which was throttled to approximately 8-10 slm. The probe was about 35.5 cm in length, with an I.D. of 0.28 cm. Under typical sampling conditions, the probe was operated at temperatures greater than 100°C in order to prevent water vapor condensation.

The quadrupole mass spectrometer was designed and constructed by the GPID Branch of the Ionospheric Effects Division, Geophysics Directorate of the Phillips Laboratory. The gas from the sampling probe flowed through a stainless steel cap which was maintained at temperatures greater than 100°C. Part of the gas was sampled through a 100 μm orifice into a two-stage, differential vacuum system, pumped by three turbomolecular pumps. The volume between the inlet orifice and the skimmer element was maintained at about 10^{-4} torr. The flow sampled through the skimmer was admitted to the mass spectrometer stage which typically operated at about 10^{-6} - 10^{-7} torr.

The mass spectrometer was controlled *via* a digital interface with a laptop computer. Other than for diagnostic scans over a selected mass range, the mass spectrometer was run in a "mass programming" mode. That is, while the fast solenoid valve was pulsing a particular fire suppressant into the WSR, certain selected mass peaks were monitored for a preset sampling time in a sequential fashion. The signal intensities of these selected mass peaks were recorded as a function of time. The final transient response is actually the averaged sum of the responses for a large number of fire suppressant pulses.

Krypton gas was used as an inert tracer to determine the time response of the reactor system. Figure 1 presents some typical data obtained for the ignited reactor operating with methane as the fuel. As shown, the krypton pulses reflect the varying duration of the valve "open" time. Also, as indicated in the figure caption, the apparent characteristic time constant for the pulse rise is on the order of 45 ms and that for the pulse decay is 22 ms. These are both significantly longer than the WSR residence time which was about 12 ms. Analysis of the transient response of the entire reactor system indicates that the longer time constants observed are caused by a combination of dispersion of the tracer upstream of the jet ring where the pulsed gas mixes with the feed flow, as well as dispersion caused by the time delay of the gas feed to all the jets in the jet ring distributor,



as subsequently analyzed below.

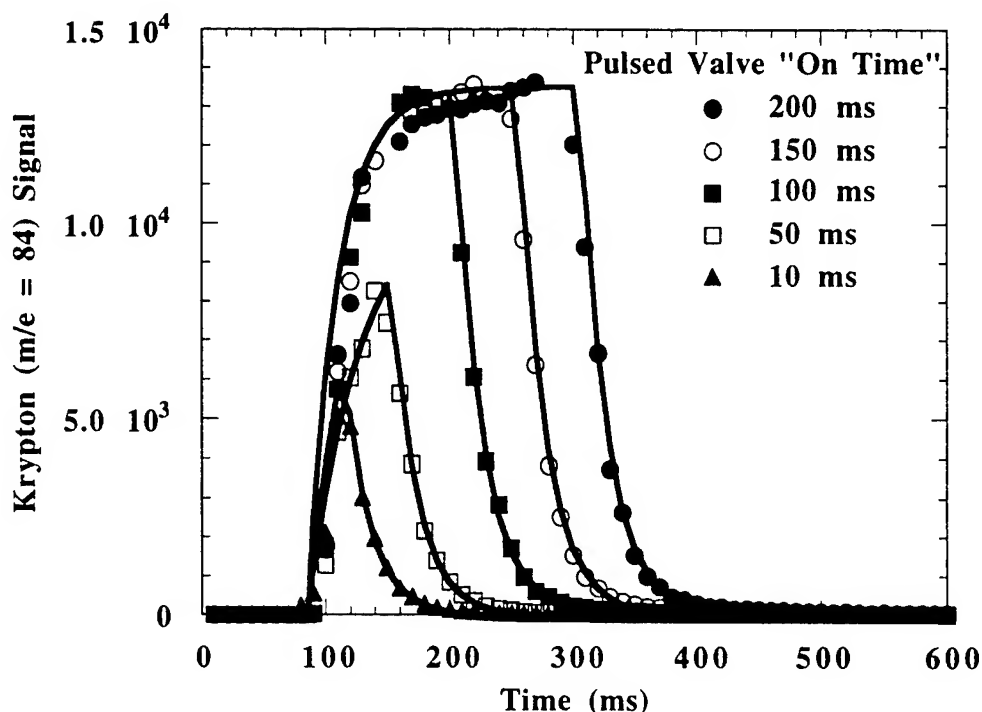


Figure 1. Krypton signal response data for variable duration pulses and the corresponding exponential fits to the data for the ignited WSR operating with 200 slm air and 14.7 slm methane ($\tau \approx 12$ ms). The characteristic time constant for the pulse rise is ~ 45 ms, and 22 ms for the pulse decay, which differs significantly from τ .

Experimental Results and Discussion

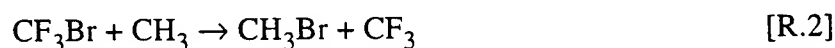
Halon 1301

The principal ion fragments which have been reported for electron impact ionization of CF_3Br are: 69 - CF_3^+ (100%); 148 and 150 - CF_3Br^+ (11.2%); 129 and 131 - CF_2Br^+ (8.9%); 50 - CF_2^+ (5.8%); 79 and 81 - Br^+ (5.8%); 41 - $(\text{CF})^+$ (4.3%); and 12 - C^+ (1.8%) [6]. Since this pattern is never observed in the current work, it is concluded that, in general, little Halon 1301 survives the WSR under the current experimental conditions; i.e., it is primarily converted to other species. This is entirely consistent with the anticipated behavior of CF_3Br in combustion environments. Since the C-F bond energy is much greater than that of C-Br ($\sim 500\text{kJ/mol}$ vs. 295.4 kJ/mol , respectively) [7], Halon 1301 readily decomposes *via*:

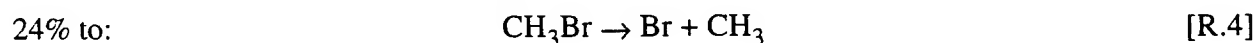
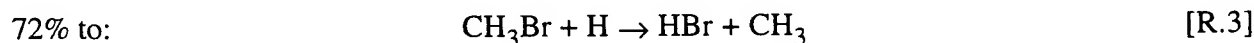


Indeed, the fire retardant properties of Halon 1301 have been attributed to the reaction of the Br and CF₃ radicals liberated in this manner with other species in the flame such as to remove chain carriers from the reaction mechanism [1,3].

Recent work suggests that at short residence times (~0.1 s) under steady-state conditions only a small fraction (~8%) of Halon 1301 decomposes *via* [R.1], with the majority (92%) reacting with methyl radicals to form CH₃Br *via* [3]:



The product of this reaction, methyl bromide, is an important species in the decomposition mechanism of Halon 1301 in combustion environments. Indeed, this species has been detected by GC-MS [3]. However, the parent peaks for this species (masses 94 and 96) were generally not observed in the current work. This is undoubtedly because of the weak C-Br bond (292.9 kJ/mol) [7] and the fact that methyl bromide is rapidly consumed to produce HBr. Battin-Leclerc *et al.* [3] computed that at a residence time of 0.5 s the consumption of CH₃Br is primarily *via*:



In addition to [R.3], HBr is generally produced by abstraction of H by Br radicals from fuel-related hydrocarbons, as well as by direct abstraction of Br by H from CF₃Br:



Due to all the various sources, HBr is the major stable species produced by the decomposition of CF₃Br in combustion environments. Indeed, this is the prevalent species that was observed in the spectra whenever Halon 1301 was introduced in the WSR.

It was previously established that the major stable products from the addition of Halon 1301 to the combustor were HF and HBr [8]. Figure 2 presents the transient response of HF⁺ (m/e = 20) and masses, m/e = 79 (⁷⁹Br⁺), 80 (H⁷⁹Br⁺), 81 (⁸¹Br⁺), and 82 (H⁸¹Br⁺). As shown, The

79/81 ratio was typically close to unity, consistent with the natural bromine isotopic abundance of 0.507/0.493 [7]. As shown, however, the 82 signal was significantly less than that for 80, so there are probably additional contributions to 80 than from H^{79}Br^+ . Electron impact fragmentation of HBr is known to produce Br^+ at a little less than half the the intensity of the HBr^+ signal. Battin-Leclerc *et al.* [3] noted that the Br radical concentration should closely follow that of HBr in the reactor, except at very long residence times, although it is less by almost two orders of magnitude. With the sampling configuration that was used in the current experiments, Br radicals probably do not survive the gas sampling system as such, and, therefore, there must also be some contribution to the Br^+ signal as ion fragments from more stable brominated species in addition to HBr, such as CH_3Br , and Br_2 . The parent ion peaks for Br_2^+ , 158 and 162, were not observed. However, due to the weak Br-Br bond (192.8 kJ/mol) [7], it is expected that Br^+ would be the predominant ion produced from Br_2 .

As shown in Figure 2, although the rise of mass 20 is quite similar to that of the inert krypton tracer, its decay is much longer. This is interpreted as being indicative of the flame chemistry which produces HF as a terminal stable product *via* a number of different reactions. The HBr^+/Br^+ signals also seem to follow the HF^+ rise and decay as well, consistent with the hypothesis that these mass peaks too are indicative of stable product species.

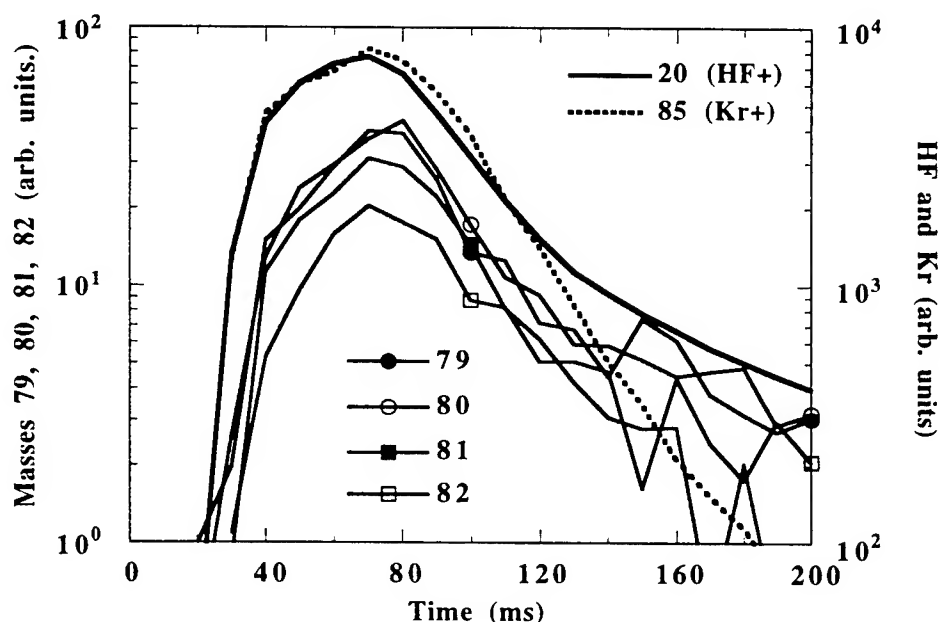


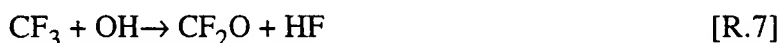
Figure 2. HBr^+/Br^+ and HF^+ signal responses to 1% Halon 1301 pulses of 50 ms duration into the ignited WSR operating with 200 slm air and 5.9 slm propane ($\tau \approx 12$ ms). The Kr^+ response is plotted as a reference.

The other series of major ion peaks associated with the CF_3Br pulses are masses 47, 66, and 85, as discussed above, which are attributed to the ions CFO^+ , CF_2O^+ , and CF_3O^+ , respectively. As shown in Figure 3, unlike the behavior of mass 20 (HF^+), which exhibits a longer characteristic decay time, the response of masses 47 and 66 are significantly shorter, following the inert krypton tracer response quite closely. This is the type of response that would be expected as being indicative of intermediate product species in the flame chemistry, that react further to form more stable terminal product species. As shown in Figure 4, the responses of masses 47 and 66 are approximately proportional to the concentration level of the Halon 1301 pulses. Their responses also exhibit a distinct "double-peaked" behavior under these conditions.

As shown in Figure 5, the behavior of mass 85 is decidedly different than that of masses 47 and 66 (as shown in Figure 4). Although it also varies monotonically with the concentration level of the Halon 1301 pulses, it does not exhibit the same "double-peaked" behavior, and definitely lags the responses for the other two masses.

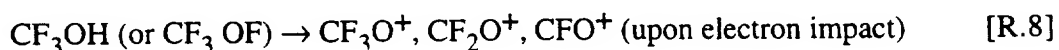
Figure 6 presents an example of the behavior of these three mass peaks with WSR residence time. It is quite evident that both the relative and absolute magnitudes of the three peaks are sensitive to the WSR residence time on the time-scales involved. For example, while mass 85 is the smallest signal by far for a residence time of 19 ms, it becomes the largest signal for residence times of 12 ms and 6 ms. Thus mass 85 reflects characteristics of a species which forms early in the interactions of Halon 1301 with the combustion environment, and is then consumed in subsequent reactions.

Reaction mechanisms that have been developed to describe the behavior of CF_3Br in combustion environments, all include FCO (mass 47) and CF_2O (mass 66), carbonyl fluoride [1,2,3]. The latter is a stable, colorless, pungent, toxic gas [9] which can certainly survive the gas sampling system. CF_2O is produced in the WSR primarily by the reactions:

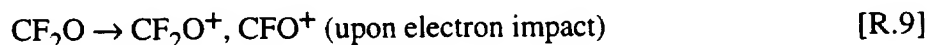


Since these two reactions are both much faster than the bond scission reaction for the decomposition of CF_3Br , [R.1], it is logical that the mass 66 (CF_2O^+) signal would parallel the

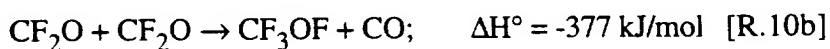
behavior of the Br^+/HBr^+ mass numbers, at least early in the reaction mechanism, and that it would increase with increasing levels of CF_3Br (i.e., CF_3). This is consistent with the data presented in Figures 2 and 3. FCO , on the other hand, is a radical species which cannot survive the gas sampling tube to the inlet of the mass spectrometer. However, FCO^+ can be produced as an ion fragment of stable species such as CF_2O , or CF_3OF (see below). In Figure 4, it is noted that mass 47 signal is consistently less than that of mass 66, which is consistent with mass 47 being a fragment ion. It is also noted that the "double-peaked" responses of masses 47 and 66 become notable only when the mass 85 signal is high (e.g., at lower residence times), and that the mass 85 response coincides quite well with the second peak of the "double-peaked" responses. This is consistent with some contribution to masses 47 and 66 due to fragmentation of the parent species of mass 85 caused by electron impact in the ion source of the mass spectrometer; i.e.:



as well as:



Mass 85 must arise from a parent species of at least molecular weight 85 or higher. It is noted that the species CF_3OF has been reported in the literature [10], although it is not currently included in the Halon 1301 combustion codes [1,2,3]. However, from the various Halon-associated radicals that are present in the combustion system, it is certainly plausible that CF_3OF can be produced from a number of radical termination reactions, such as:



which are all exothermic, as calculated from enthalpy of formation data [7]. Ionization of CF_3OF would almost certainly result primarily in the production of the fragment ion CF_3O^+ , since the O-F bond is the weakest in the molecule by far at 182 kJ/mol [7]. Moreover, the parent ion peak would be mass 104. It is noted that a very small, but measurable amount of mass 104 was typically detected whenever mass 85 was most intense.

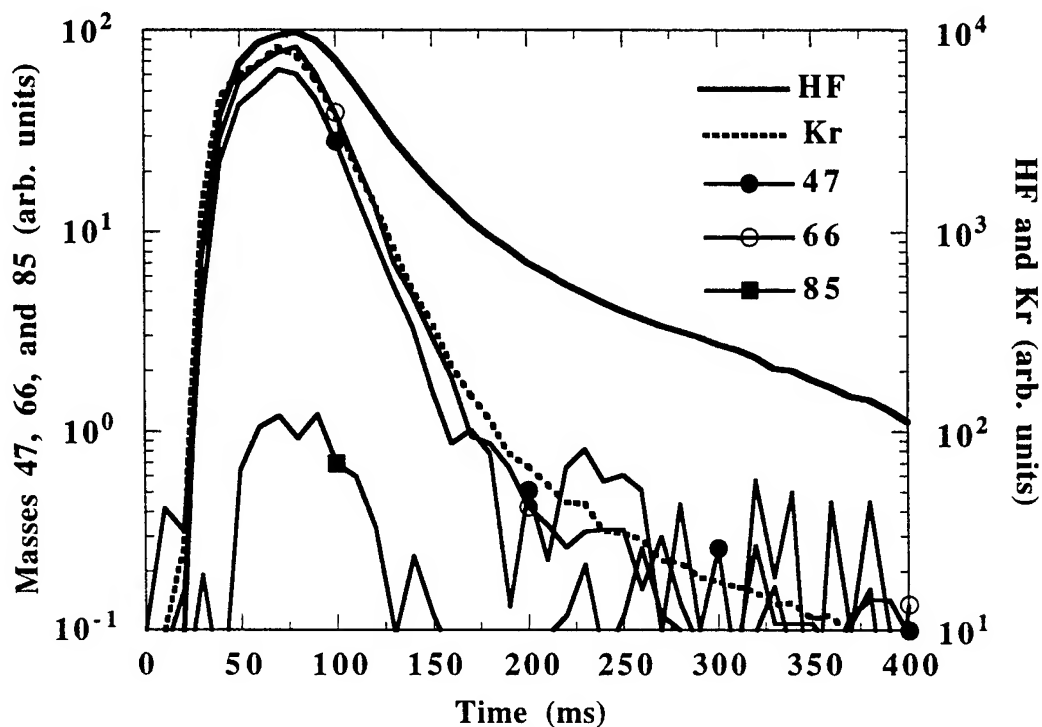


Figure 3. Mass 47, 66 and 85 signal responses for 0.75% Halon 1301 pulses of 50 ms duration into the ignited WSR operating with 150 slm air and 3.5 slm propane ($\tau \approx 19$ ms). The Kr^+ inert tracer response is plotted as a reference.

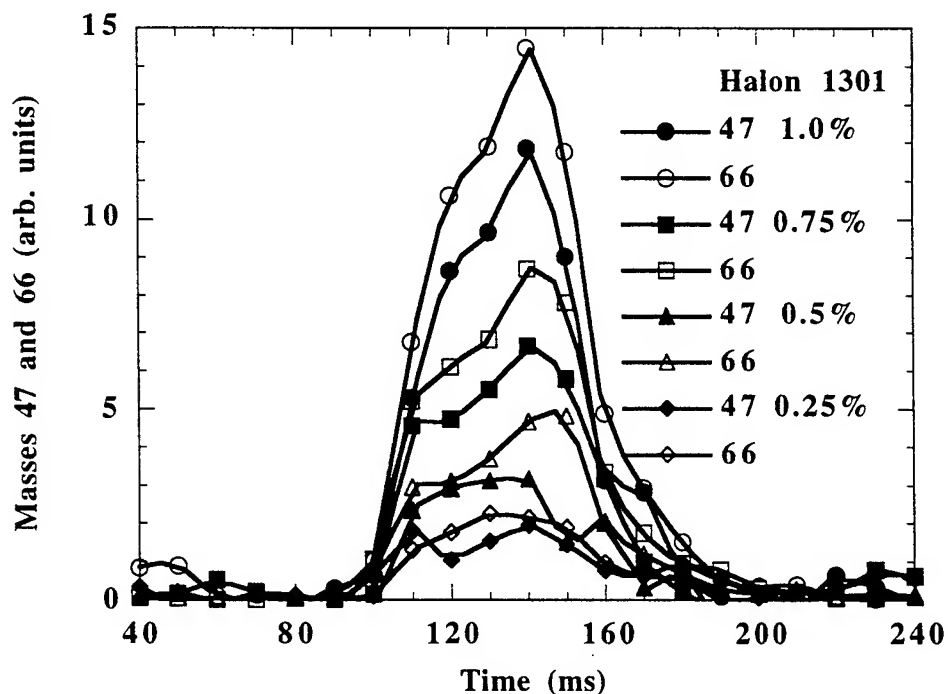


Figure 4. Mass 47 and 66 signal responses as a function of Halon 1301 concentration level of 50 ms pulses into the ignited WSR operating with 200 slm air and 5.9 slm propane ($\tau \approx 12$ ms).

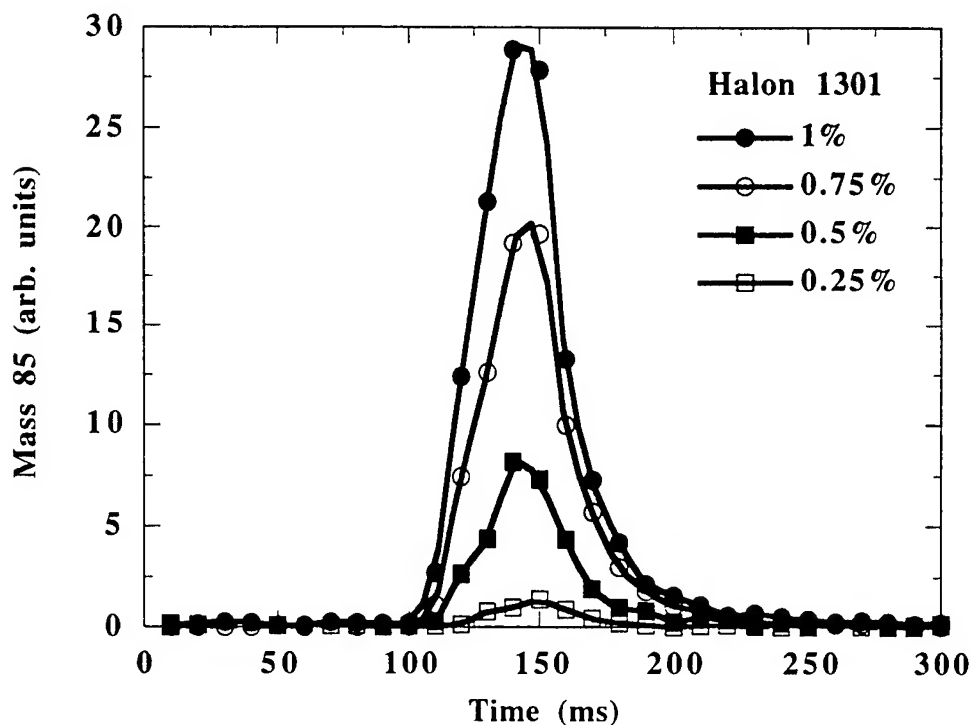


Figure 5. Mass 85 signal response as a function of Halon 1301 concentration level of 50 ms pulses into the ignited WSR operating with 200 slm air and 5.9 slm propane ($\tau \approx 12$ ms).

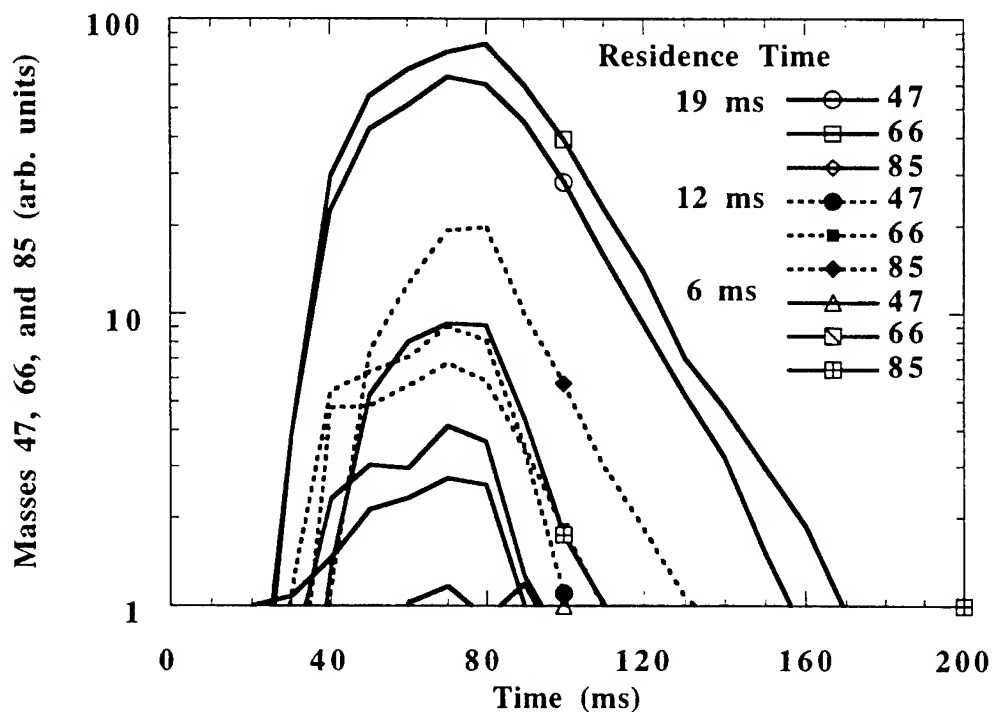


Figure 6. Mass 47, 66, and 85 signal responses for 0.75% Halon 1301 50 ms pulses as a function of WSR residence time.

CF_3I

Due to its chemical similarity to Halon 1301, the behavior of CF_3I in the combustor was expected to be quite similar as well. The products of the interaction of CF_3I with the combustion environment were primarily HF and HI, which were observed as mass peaks 127 (which includes contributions from all iodine-containing species) and 128. In addition, molecular iodine, I_2 , was evident as a purplish gas in the effluent from the combustor. Mass peaks 47, 66, and 85 are also present, as shown in Figure 7, at intensities that are quite similar to those in Figure 6 (although mass 85 is somewhat larger for CF_3I , under similar conditions). The major difference that is apparent in Figure 7 is that mass 85 has a longer characteristic decay time than for masses 47 and 66, unlike for Halon 1301. Also, the "double-peaked" behavior of masses 47 and 66 is not apparent, and the three signals seem to superimpose more than was noted for Halon 1301. These are all indicators that there may be some differences in the combustion reaction mechanism for these two species. It was also noted that for similar concentration levels, CF_3I seemed to be slightly more effective insofar as bring the reactor to "near-blowout" conditions.

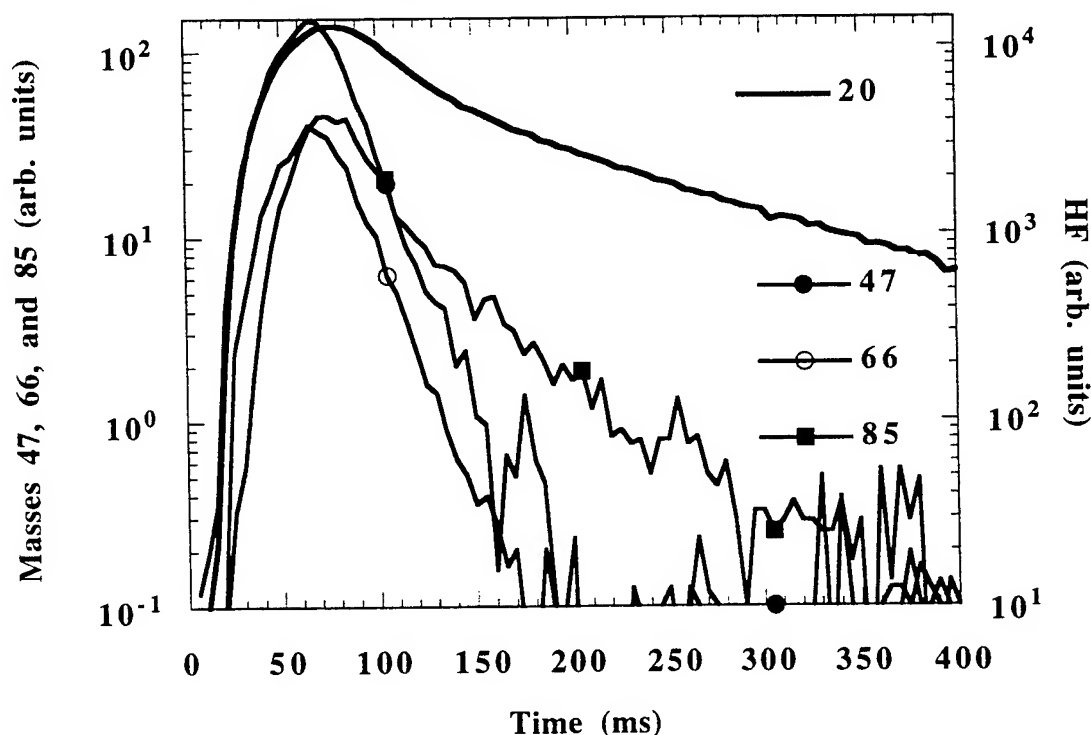


Figure 7. Mass 47, 66 and 85 signal responses for 0.75% CF_3I pulses of 50 ms duration into the ignited WSR operating with 200 slm air and 14.8 slm methane ($\tau \approx 12$ ms).

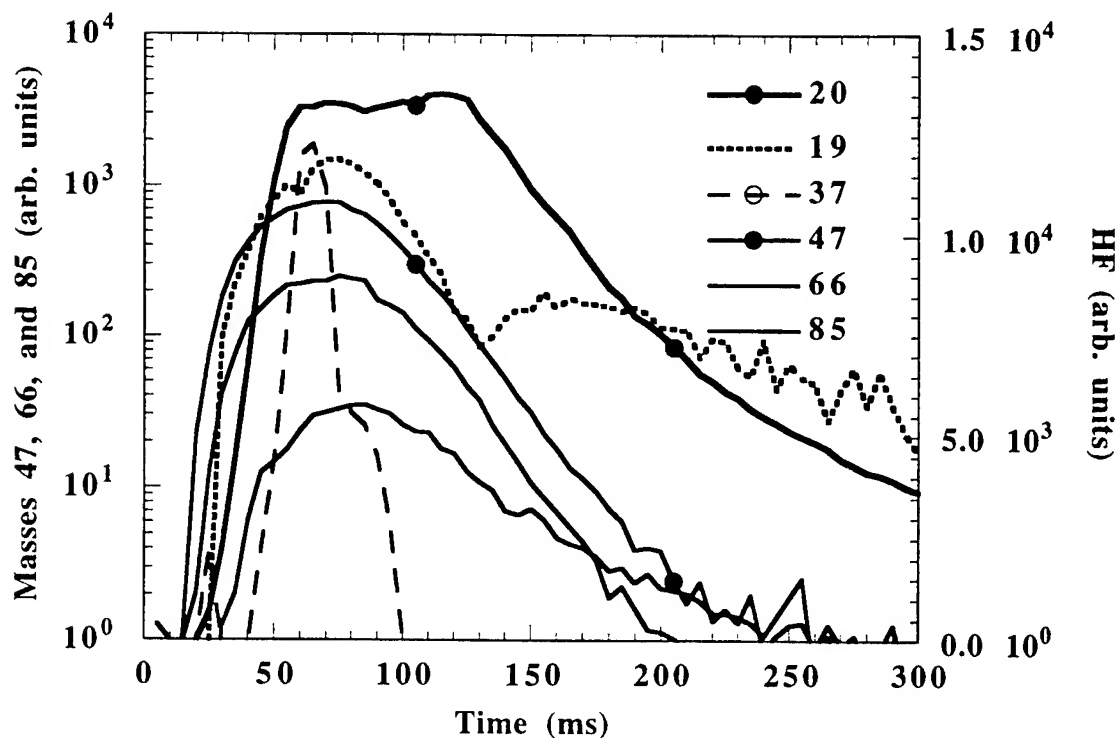


Figure 8. Mass 19, 20, 37, 47, 66 and 85 signal responses for 0.75% HFC-125 pulses of 50 ms duration into the ignited WSR operating with 150 slm air and 5.25 slm methane ($\tau \cong 19$ ms).

HFC-125

HFC-125 (C_2HF_5) exhibited somewhat different behavior than the other two fire suppressants used in the current investigation. Its fire suppressant action is generally believed to be more physical than chemical. This was substantiated by the observation that it took about an order of magnitude more HFC-125 than the other two agents to bring the reactor to “near-blowout” conditions. In addition, HFC-125 behaved as fuel in that the reactor temperature pulsed by as much as 50K in synchronization with the HF-125 pulses. Neither CF_3Br or CF_3I exhibited this behavior; i.e., the reactor temperature always remained constant during pulsing.

Figure 8 presents the behavior of masses 20, 47, 66, and 85. As shown, the latter three exhibit behavior similar to that observed for CF_3I . In this figure mass 85 is the smallest of the three, but this is primarily due to the longer residence time of the WSR, as is evident in the data in Figure 6. In addition, the decay of the mass 85 response appears to be longer than that for mass 47 and 66, just as was observed in Figure 7 for CF_3I .

In Figure 8, the mass 20 (HF) response is plotted on a linear scale to accentuate the fact that

the pulse peak exhibits a minimum. This behavior is preceded by a large increase in the mass 19 (F^+) signal, accompanied by a similar increase in the mass 37 ($H_2O \cdot H_3O^+$) water cluster signal, which was used to monitor water indirectly due to the very large mass 18 parent water peak which saturated the mass spectrometer. This appears to be related to the apparent behavior of HFC-125 as a fuel. That is, initially it decomposes and combusts to form water and various fluorine-containing species, and then it begins to participate in the reaction chemistry in a fashion more similar to that of CF_3Br and CF_3I . If this is indeed the case, transient data such as these for HFC-125 and similar species, may eventually provide improved insight concerning fire suppression mechanisms in general.

Model Formulation

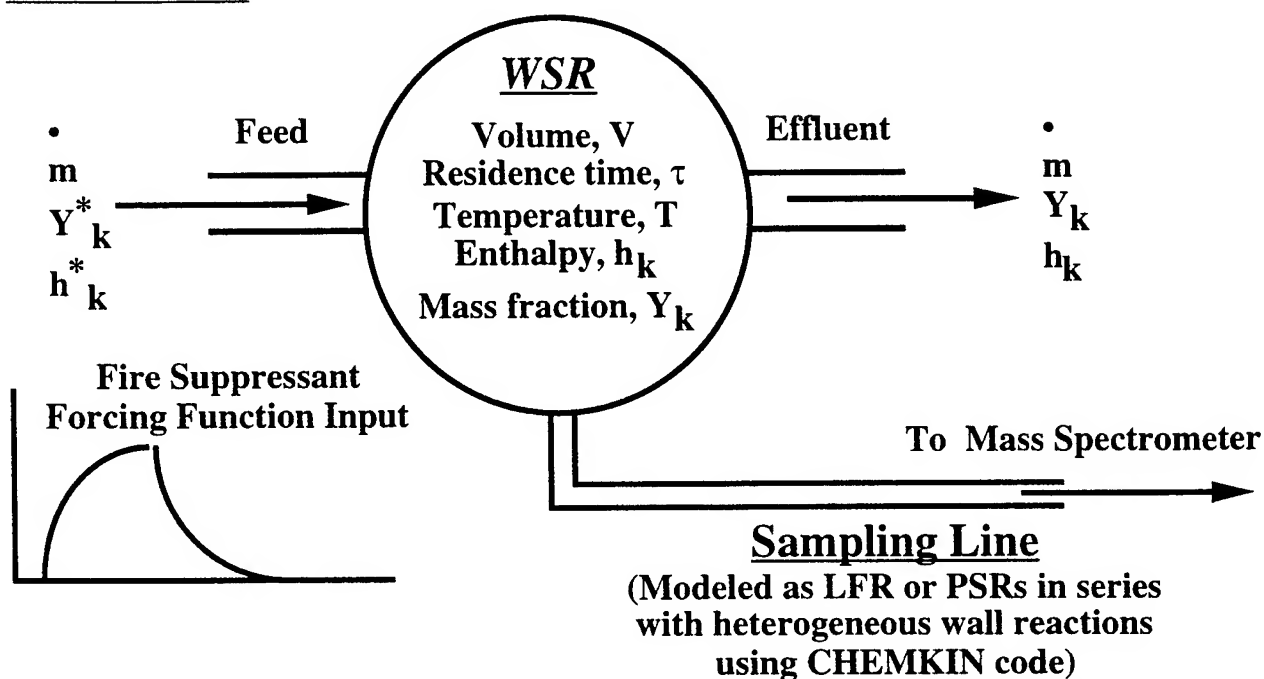


Figure 9. Schematic of the overall transient model for pulse injections of fire suppressants.

A numerical model has been developed in order to analyze the transient measurements. The overall model consists of three parts, each corresponding to one of the three physical elements of the combustor apparatus: (1) the jet ring distributor; (2) the well mixed combustor; and (3) the mass spectrometer sampling line. The basis of the jet ring distributor model is presented immediately below. The combustor and sampling line models are based on a package of FORTRAN codes known as CHEMKIN II [11]. In particular, the PSR (perfectly stirred reactor)

module from this code [12] was used to model the behavior of the WSR, while the SENKIN module [13] was used to model the constant-pressure reactions and radical wall-terminations within the sampling tube. A conceptual schematic of the model is presented in Figure 9.

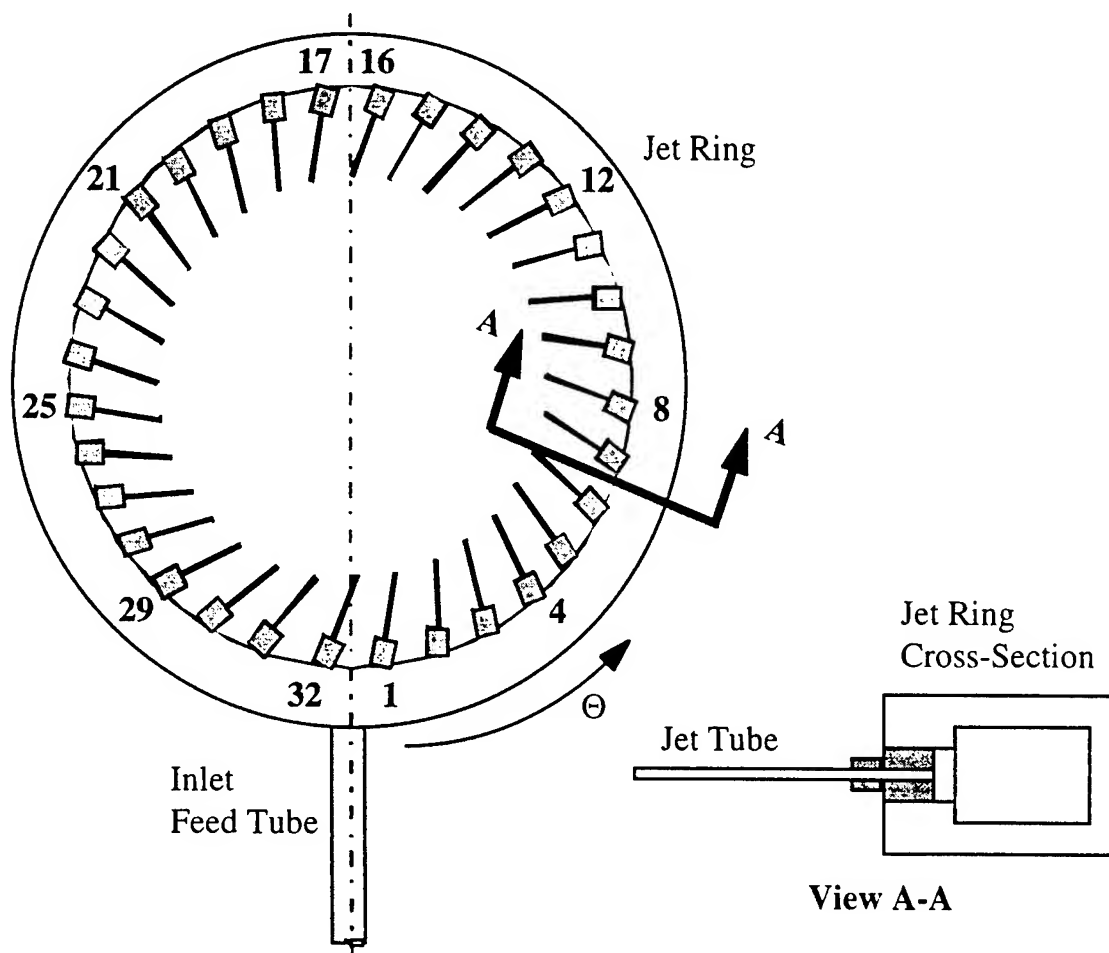


Figure 10. Schematic of the WSR jet ring gas distributor.

Jet Ring Gas Distributor Model - Residence Time Distribution (RTD) of the Jet Ring

In order to properly analyze the transient data, it is necessary to know the time response of the entire system consisting of the pulsed valve/jet ring/reactor combination. The residence time distribution (RTD) of the WSR is known to be exponential, characterized by a time constant equal to the reactor residence time. However, the RTD of the jet ring gas distributor which feeds the reactor was not known, and thus had to be determined for the development of the model.

A schematic of the jet ring gas distributor is presented in Figure 10. as shown, the WSR jet

ring is annular with an O.D. of 11.8 cm and I.D. of 10.8 cm. The annular ring has a rectangular cross section, 1 cm wide x 0.635 cm in height. The jet ring holds the 32 jet tubes of the WSR in place at its I.D., and serves as a manifold/distributor for the air/fuel mixture through the jet tubes into the reactor volume. The following analysis was conducted to characterize the behavior of the jet ring distributor.

Velocity and Pressure Distributions in the Jet Ring. The jet ring serves as a manifold distributor for the WSR. Its behavior can be described using the energy balance and the continuity equation. Using cylindrical coordinates, it is assumed that the gas velocity, density, and pressure in the jet ring are uniform in the z direction.

The integrated form of the steady-state energy balance on a control volume (c.v.) is given by:

$$\iint_{c.s.} \rho \mathbf{v} \cdot (\mathbf{v}^2/2 + w^2/2 + P/\rho) \cdot d\mathbf{S} = -\Phi \quad [1]$$

where the bold symbols represent the velocity vector, \mathbf{v} , and the normal surface area vector, $d\mathbf{S}$, for points on the control surface (c.s.) through which fluid flows into and out of the control volume, and Φ is the energy loss due to friction within the control volume. In this expression, the scalar components of the velocity vector are denoted as $v = v_r$, and $w = v_\theta$. Within the jet ring distributor, the gas velocity is well below sonic such that the fluid may be treated as incompressible and the density will be approximately constant. With these assumptions, application of Eq. [1] to a control volume *between jets* in the jet ring of rectangular cross section of height h ($h = 0.25$ in. = 0.635 cm), as shown in Figure 10, yields:

$$-\rho wh (R_2 - R_1) (w^2/2 + P/\rho) \Big|_\theta + \rho wh (R_2 - R_1) (w^2/2 + P/\rho) \Big|_{\theta+d\theta} = -[pf(w^2/2)/4] w dA, \quad [2]$$

where R_1 and R_2 are the inner and outer diameters of the jet ring, respectively, f is the friction factor, and dA is the total differential wall surface area of the rectangular duct. The friction factor, f , was determined from the empirical expression [18]:

$$f = 0.25/[\log(\epsilon/(3.7 \times 4R_h) + 5.74/Re^{0.9})]^2 \quad [3]$$

where ϵ is the roughness (assumed as 6×10^{-5} in. for stainless steel), and R_h is the hydraulic

radius of the rectangular duct:

$$R_h = (R_2 - R_1) h / [2 / (h + R_2 - R_1)] \quad [4]$$

and Re is the corresponding Reynolds number:

$$Re = 4 R_h w \rho / \nu, \quad [5]$$

where ν is the kinematic viscosity of the gas. For air [19],

$$\nu = 1.458 \times 10^{-6} T^{1.5} / (T + 110.4) / (P / (287 T)), \text{ m}^2/\text{s}$$

where T is the temperature in K, and P is the pressure in Pa.

For the jet ring duct of rectangular cross section, the total wall surface area for a differential volume element of angular arc $d\theta$ is:

$$dA = [(R_2 + R_1)(R_2 - R_1) + 2R_2 h] d\theta \quad [6]$$

Taking the limit of Eq. [2] as $d\theta \rightarrow 0$:

$$w dw/d\theta + (1/\rho) dP/d\theta = - (f w^3/8) \phi, \quad [7]$$

where the geometric factor,

$$\phi = (R_2 + R_1)/h + 2R_2/(R_2 - R_1) \quad [8]$$

The integrated form of the steady-state continuity equation for the control volume is:

$$\rho \iint_{C.S.} \mathbf{v} \cdot d\mathbf{S} = 0 \quad [9]$$

For the same differential control volume of rectangular cross section, this expression becomes:

$$d[\rho w h (R_2 - R_1)]/d\theta = 0, \text{ or } dw/d\theta = 0, \quad [10]$$

and Eq. [7] becomes:

$$dP/d\theta = - (\rho f w^2/8) \phi \quad [11]$$

Eq. [11] was used to calculate the pressure drop in the control volumes between jets in the jet ring distributor.

The pressure change due to removal of gas from the jet ring *via* the jet tubes is determined by integrating the energy balance, Eq. [1]:

$$\rho w_2 (w_2^2/2 + P_2/\rho) - \rho w_1 (w_1^2/2 + P_1/\rho) + \rho_j u_j (\pi/4) d^2 (u_j^2/2 + P_j/\rho_j) = 0 \quad [12]$$

where, for example, P_1 is the pressure upstream of the jet tube, and P_2 downstream of the jet tube, and the subscript "j" denotes flow conditions in the jet tube, and d is its diameter. Frictional losses were ignored in this expression since they have a negligible effect on the pressure in comparison to the relatively large pressure increase due to the removal of a fraction of the gas from the jet ring, as well as the fact that the spatial extent of the region is small in comparison to the control volumes between jet tubes.

The continuity equation yields:

$$\rho w_2 h (R_2 - R_1) - \rho w_1 h (R_2 - R_1) + \rho_j u_j (\pi/4) d^2 = 0 \quad [13]$$

Substituting this expression into Eq. [12] yields:

$$\rho w_2 (w_2^2/2 + P_2/\rho) - \rho w_1 (w_1^2/2 + P_1/\rho) + (w_1 - w_2) P_1 = 0 \quad [14]$$

In this expression, the total specific energy of the fluid in the jet, $(u_j^2/2 + P_j/\rho_j)$, was equated to P_1/ρ , since this represents the stagnation conditions for the jet flow, which is assumed to be adiabatic (see below). Solving Eq. [14] for P_2 :

$$P_2 = P_1 + \rho (w_1^3 - w_2^3)/(2w_2) \quad [15]$$

The jets are all positioned at an angle of 20° with respect to the normal to the tangent of the jet ring circle. Therefore, the gas velocity in the ring has a component along the jet tube axis of $w \cos(70^\circ)$, directed towards the jet tube opening in one-half of the ring, and away from the opening in the other half. However, in comparison to the static pressure in the jet ring, this velocity head is quite small, and, therefore, was neglected.

Mass Flowrate in the Jet Tubes. It was assumed that the flow in the jet tubes is adiabatic and compressible since they are well insulated from their surroundings and the reactor, and the thermal conductivity of alumina is quite low. In order to calculate the mass flowrate through each tube, it was first assumed that choked (sonic) flow was attained at the tube exit ($M_e = 1$). In this case, the Mach number at the tube inlet, M , is given by the expression [20]:

$$(1 - M^2)/kM^2 + [(k+1)/2k] \ln[(k+1)M^2/(2 + (k-1)M^2)] + (1 - kM^2)/(kM^2) = f_j L/d, \quad [16]$$

where k is the heat capacity ratio of the gas, L is the jet tube length, d is its diameter, and f_j is the average friction factor for flow in the jet tubes. The latter was determined from [21]:

$$f_j = 0.0264 (T_0/P_0)^{0.23} + 0.45 d/(2L), \quad [17]$$

where T_0 and P_0 are the temperature and pressure in the jet ring. This correlation for the friction factor has been experimentally verified for the jets used in the jet ring distributor [22].

Eq. [16] was solved using Newton's method updating the average friction factor, f , at each iteration. The ratio of the pressure at this point in the tube, P , to the exit pressure, P_e , was then determined from [23]:

$$P/P_e = (1/M) [(k+1)/(2 + (k-1)M^2)]^{1/2} \quad [18]$$

This ratio was then compared to the ratio P/P_0 , where P_0 is the reactor pressure, which was approximately atmospheric. Choked flow at the jet tube exit was confirmed by checking for

$$P_e \geq P_o.$$

If $P_e < P_o$, then the flow at the jet tube exit is subsonic. In this case, the correct Mach numbers at the tube inlet and exit must be found. This was done in an iterative fashion by first assuming sonic flow at the jet tube exit ($M_e = 1$) and the Mach number, M , at the inlet determined from the original choked flow calculation. These values were used to determine the Mach number at the jet tube exit by solving the following transcendental expression using Newton's method [20]:

$$P/P_e = (M_e/M) [(2 + (k-1)M_e^2)/(2 + (k-1)M^2)]^{1/2} \quad [19]$$

The resultant value of M_e was then used in the following expression for isentropic, compressible flow in a duct of constant cross section [20] to yield an updated value for the Mach number at the jet tube inlet, M :

$$1/(2M^2) - [(k+1)/2] \ln(M) + [(k+1)/4] \ln[1 + (k-1)M^2/2] = kf_j x/d + C, \quad [20]$$

where C is a constant of integration evaluated at the jet tube exit ($M = M_e$, $x = L$). The resultant value of M ($x = 0$) was then compared to the initially assumed value and the entire process involving Eqns. [19] and [20] was iterated until the assumed and calculated values of the Mach number at the jet tube inlet, M , agreed. This calculation procedure also yielded the corresponding value of the exit Mach number which is updated during the calculation, as well as the average friction factor, f , which is also updated during the course of the iterative calculation.

The resultant Mach number at the jet tube inlet was used to determine the gas density at this point from the isentropic flow relations. The jet tube mass flowrate is then given by:

$$(dm/dt)_j = \rho M (k R T_o)^{1/2} (\pi/4) d^2, \quad [21]$$

Calculation Procedure. Application of the preceding formulations was performed in the following manner to obtain the pressure and velocity distributions in the jet ring.

(1) From the gas flowrate in the inlet feed tube, the value of the inlet velocity in one-half of the jet ring, w_{in} , is determined from continuity:

$$A_f v_f = 2 A_{ring} w_{in} \quad [22]$$

where A_f and A_{ring} are the cross sectional areas of the inlet feed tube and jet ring, respectively, and v_f is the gas velocity in the inlet feed tube. The pressure at the entrance to either half of the jet ring is given by the Bernoulli equation:

$$P_{in} = P_f + \rho (v_f^2 - w_{in}^2)/2, \quad [23]$$

where P_f is the pressure in the feed tube (5/16 in. I.D.).

(2) The calculation then proceeds around the ring in one direction using Eq. [11] to determine the pressure at the end of each control volume without a jet tube, and Eq. [15] for the pressure change across each jet tube inlet.

(3) The flow rate through each jet tube, $(dm/dt)_j$, is then calculated from Eq. [21] as described above.

(4) For each of the control volumes containing a single jet tube, the exit velocity from this control volume in the jet ring, w_2 , is determined from the continuity equation, Eq. [13]:

$$w_2 = w_1 - (dm/dt)_j / [\rho h (R_2 - R_1)] \quad [24]$$

(5) The sum of the flow rates through all the jet tubes is compared to the total flow rate, and the pressure in the feed inlet tube is adjusted until these agree. At this point the velocity and pressure at the inlet of the jet ring will also agree.

The preceding calculation procedure was implemented on an EXCEL™ spreadsheet using a MACRO.function for the flow through the jet tubes (sonic or subsonic).

Jet Ring Distribution Results. Figure 11 presents the resultant pressure and velocity distributions for the case of 390 slm of air and 28.7 slm of methane ($\phi = 0.7$), characteristic of the 5 ms residence time combustion runs that were conducted in the WSR. For these conditions, sonic flow was attained at the exits of the jet tubes. (For the 200 slm and 150 slm runs, the flow was subsonic in the jet tubes.) As shown, the gas velocity in the jet ring decreases discretely at each jet tube, corresponding to the amount of gas which flows into the reactor at that point, as determined by continuity. The pressure in the jet ring decreases due to wall friction, and increases due to the momentum loss at each jet tube.

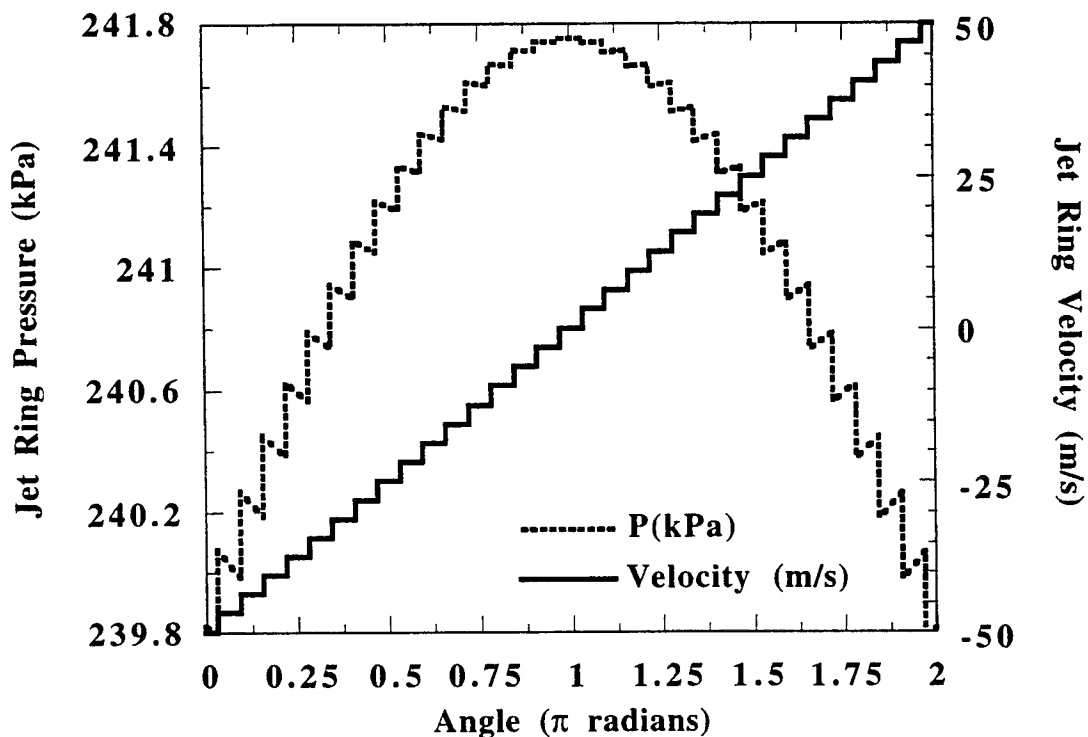


Figure 11. Pressure and velocity distributions in the jet ring for a flowrate of 390 slm air and 28.7 slm methane ($\phi = 0.7$). The jet ring temperature was assumed constant at 300°C. Sonic flow conditions occurred in all the jet tubes.

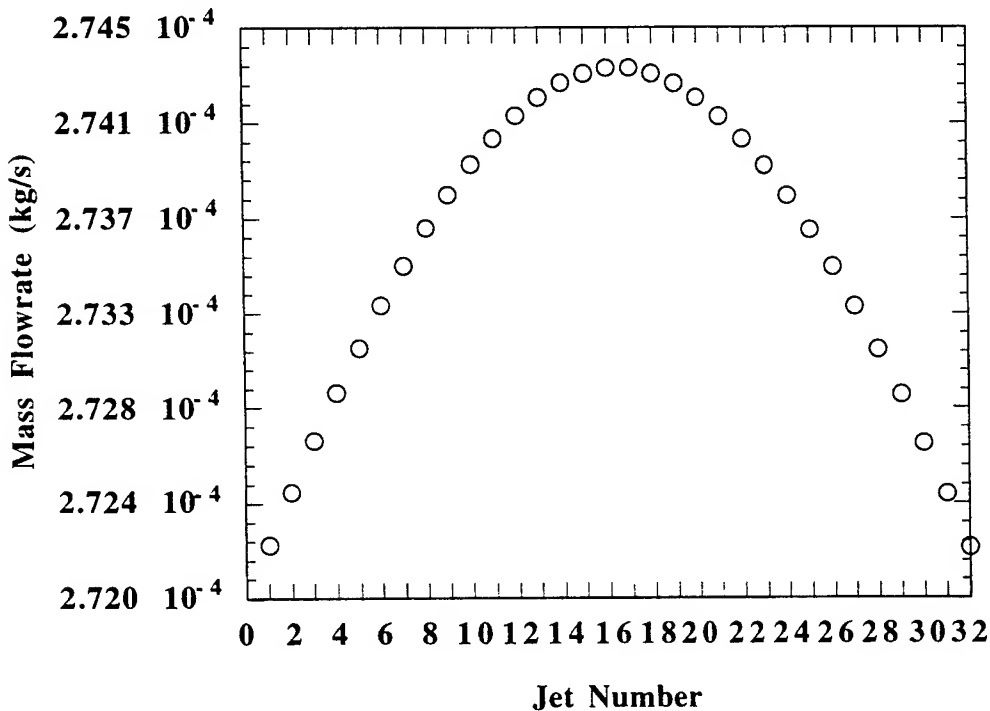


Figure 12. Mass flowrate distribution corresponding to the calculation presented in Figure 11.

The overall effect is to progressively increase the jet ring pressure until about one-half of the way around the ring, whereupon it then begins to decrease to match the inlet pressure at the end of the ring. As shown in Figure 11, the pressure distribution is symmetric with respect to the two halves of the jet ring. This is also reflected in the flow distribution through the jet tubes, as shown in Figure 12. Although the flowrate increases progressively to the midpoint of the jet ring, it is noted that there is negligible flow *maldistribution*, with the flowrate differing by less than 1% from the minimum to the maximum; i.e., practically equal amounts of gas flow through each jet tube.

The corresponding results for the other two principal flow conditions that were used in the current work are qualitatively similar, with the model calculation agreeing quite well with the experimental conditions. The largest deviation between the model and the data occurred for the 150 slm case. There are a number of possible reasons for the minor discrepancies noted. First of all, the pressure in the jet ring was not measured directly; it was estimated from the pressure just upstream of the feed inlet tube at the “vaporizer.” Another problem was that the average temperatures of the jet tubes were probably greater than the measured jet ring temperature. Also, the latter temperature generally tended to increase steadily during a run. The value cited was simply an average over a period of time.

Contrary to the results of the preceding calculations, tracer tests conducted on a room temperature jet ring that had been removed from the reactor, revealed significant fluid maldistribution. An example of these data are presented in Figure 13, which is a compilation of tracer responses from selected individual jets. For perfect distribution, the response of “mirror image” jet pairs from each half of the jet ring should be exactly the same. As shown, however, although the responses of the jet pairs superimpose quite well near the feed tube inlet (e.g., #1-32), they progressively separate as the flow proceeds through the ring, such that the response for #20 is much slower than for #12, and it is even slower than for #16. This indicates that the flow is quite asymmetric, with the zero velocity point occurring beyond π radians, and with more gas flowing through the jets located from π to 2π , than for those between 0 and π . However, this jet ring differed from the one that was used in the combustor for all the current experiments. It was an older one fitted with all stainless steel jet tubes, that had already experienced significant service in the combustor. Some of the tubes were obviously worn, and some were noncircular and partially “crimped” at the exit. Nine of the jet tubes (#1, 4, 8, 12, 16, 20, 24, 28, and 32) were replaced

with alumina tubes of the same type used in the reactor for the combustion runs, but the remaining 23 were the original stainless steel tubes. Consequently, it is hypothesized that the fluid maldistribution resulted from jet tubes which had considerably lower conductances than the others.

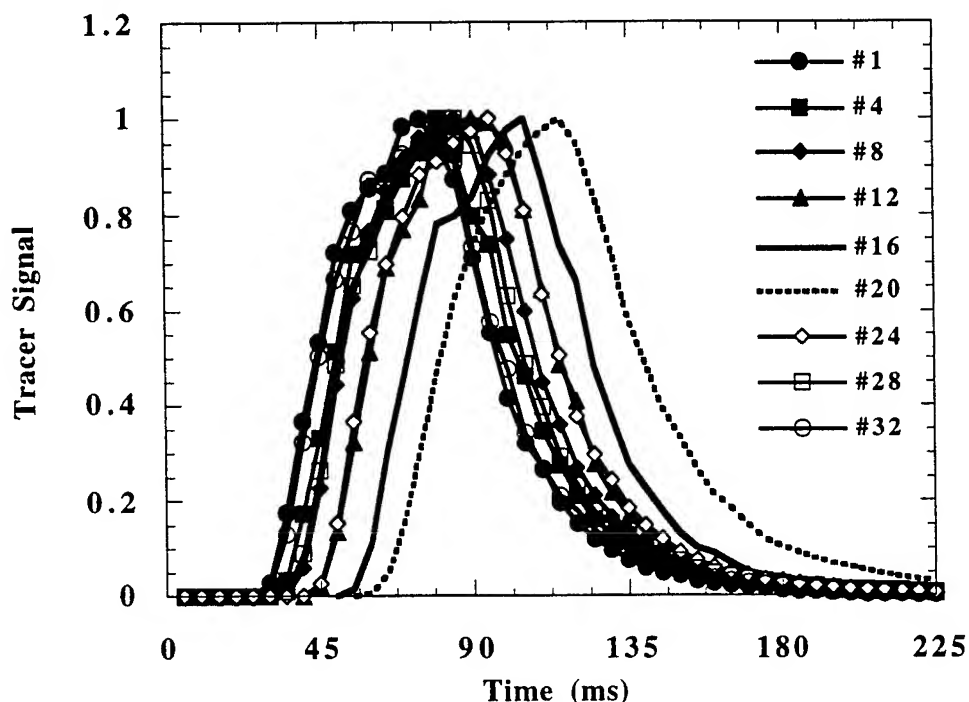


Figure 13. Tracer (50 ms CF_3Br pulses at room temperature) response of selected jets in the jet ring at a flowrate of 200 slm of air. The jets are counted counterclockwise from the inlet feed tube. "Mirror-image" jet pairs: 1-32, 4-28, 8-24, 12-20; 16 is located at $\theta = 31\pi/32$.

In order to demonstrate the effect of variations in jet tube conductance, the conductance of tubes 1-16 were arbitrarily reduced to 75% of capacity in the model for the 390 slm case. The results of this calculation are presented in Figures 14 and 15. As shown in Figure 14, the pressure and velocity distributions are clearly asymmetric, and the pressure in the feed tube had to be increased in order to maintain the measured flowrate. Figure 15 shows the reduction in flow through tubes 1-16, and the considerably larger flow that was forced to occur through tubes 17-32.

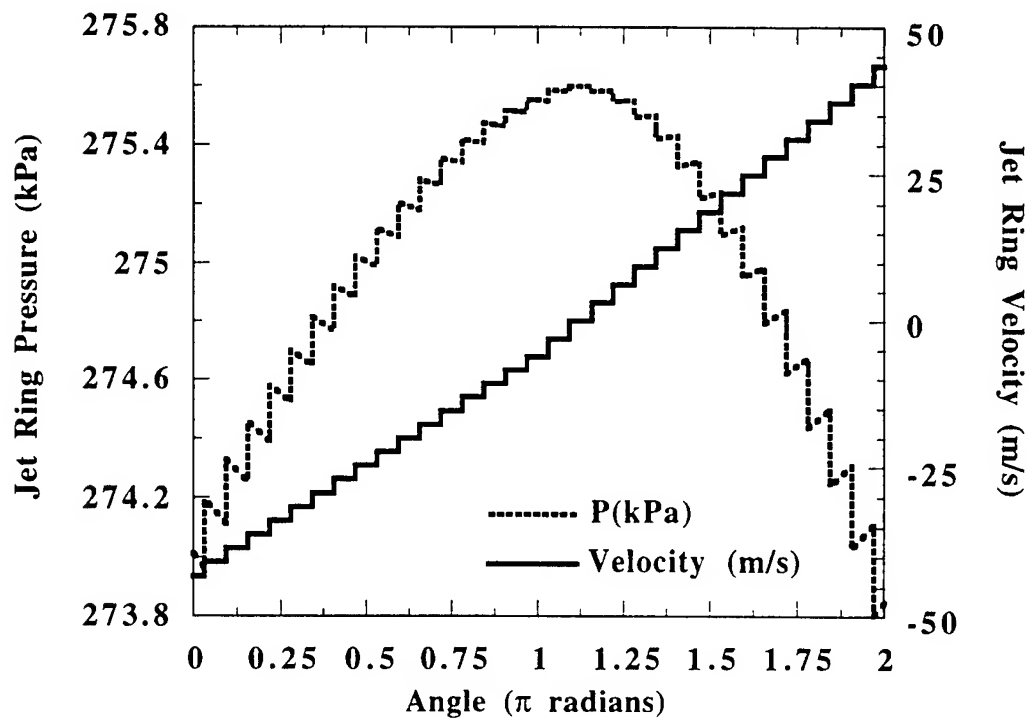


Figure 14. Pressure and velocity distributions in the jet ring for a flowrate of 390 slm air and 28.7 slm methane ($\phi = 0.7$), with jets 1-16 operating at 75% of capacity.. The resultant inlet feed tube pressure is 265.5 kPa.

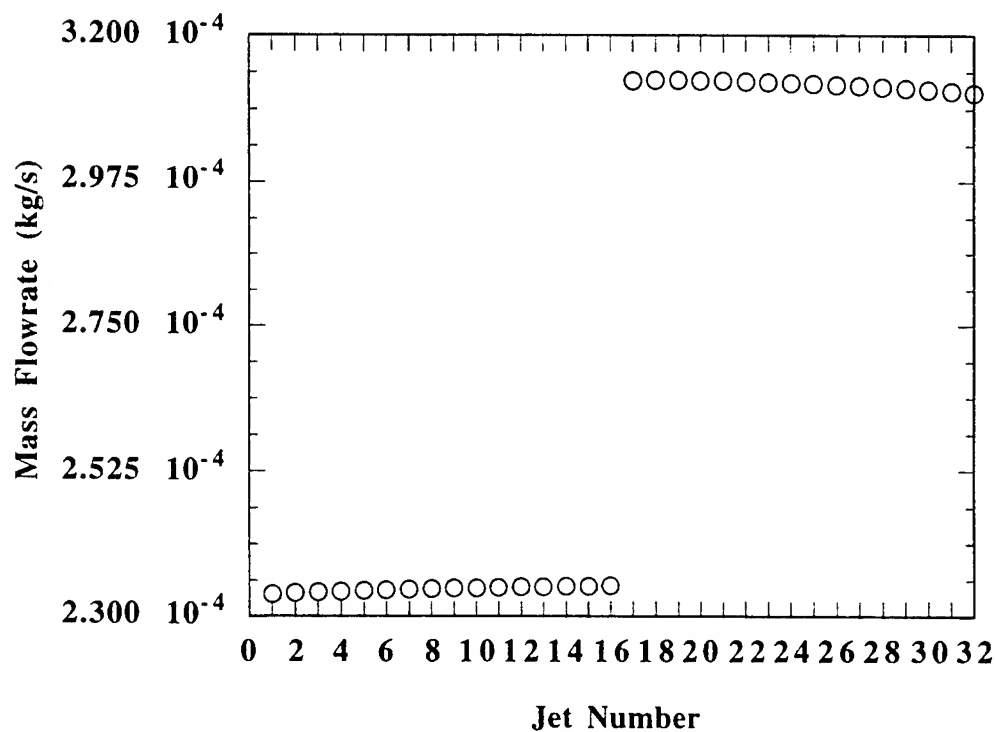


Figure 15. Mass flowrate distribution corresponding to the calculation presented in Figure 14.

Response to an Inert Tracer. A tracer mass balance on a jet ring control volume including a single jet of length $R_2 \Delta\theta$, (assuming it is sufficiently small to be approximated as well-mixed), is given by:

$$dC/dt = [w_{in} C_{in} - w_{out} C - (dm/dt)_j C/\rho]/R_2 \Delta\theta \quad [25]$$

Substituting for $(dm/dt)_j/\rho$ from Eq. [24]:

$$dC/dt = [w_{in} (C_{in} - C)]/R_2 \Delta\theta, \quad [26]$$

or, in finite difference form:

$$C_{t+\Delta t} = [C_t + (\Delta t/R_2 \Delta\theta) w_{in} C_{in}]/[1 + (\Delta t/R_2 \Delta\theta) w_{in}] \quad [27]$$

The solution to Eq. [27] will give the transient tracer response for each of the 32 jets. Although this solution inherently assumes well-mixed regions between jets, overall the 32 regions in series will behave quite close to a plug flow system.

The concentration of tracer in the total effluent from the WSR, $C(t)$, is then given by:

$$V_{WSR} dC/dt = \Sigma\{(dm/dt)_j C_j / \rho\} - C Q_{WSR} \quad [28]$$

where the summation is over all (32) jets, C_j is the tracer concentration as a function of time at the source point in the jet ring for each jet tube, determined from Eq. [26], and V_{WSR} and Q_{WSR} are the volume and total effluent volumetric flowrate of the WSR. In finite difference form, Eq. [28] becomes:

$$C_{t+\Delta t} = [\Delta t \Sigma\{(dm/dt)_j C_j / \rho\}/V_{WSR} + C_t]/[1 + \Delta t (Q/V)_{WSR}] \quad [29]$$

A numerical scheme to calculate the transient response of the jet ring according to Eqns. [27] and [29] was implemented in the form of an EXCELTM spreadsheet. Figure 16 presents tracer

responses calculated with this model for the 200 slm case. Since the pulsed valve has a response time of ~ 0.5 ms, the input to the jet ring is the square pulse depicted in this figure. Although the jet ring distributor does not mix the gas *per se*, it does introduce increasing time delays to the gas emanating from each jet as the gas flows around the ring from the feed tube connection to the jets progressively further away. Consequently, the effect of gas distribution through the 32 jets in this manner causes a broadening of the distribution of residence times. This can be clearly seen from the curve of the tracer flowrate from the jet ring into the WSR (dashed curve), which is already considerably broadened in comparison to the square pulse input introduced in the feed tube. This already broadened distribution is then broadened further due to the mixing in the WSR to the final pulse in the effluent from the WSR presented in Figure 16. However, from this figure it is quite evident that the jet ring distributor causes most of the resultant broadening in comparison to the contribution of the WSR.

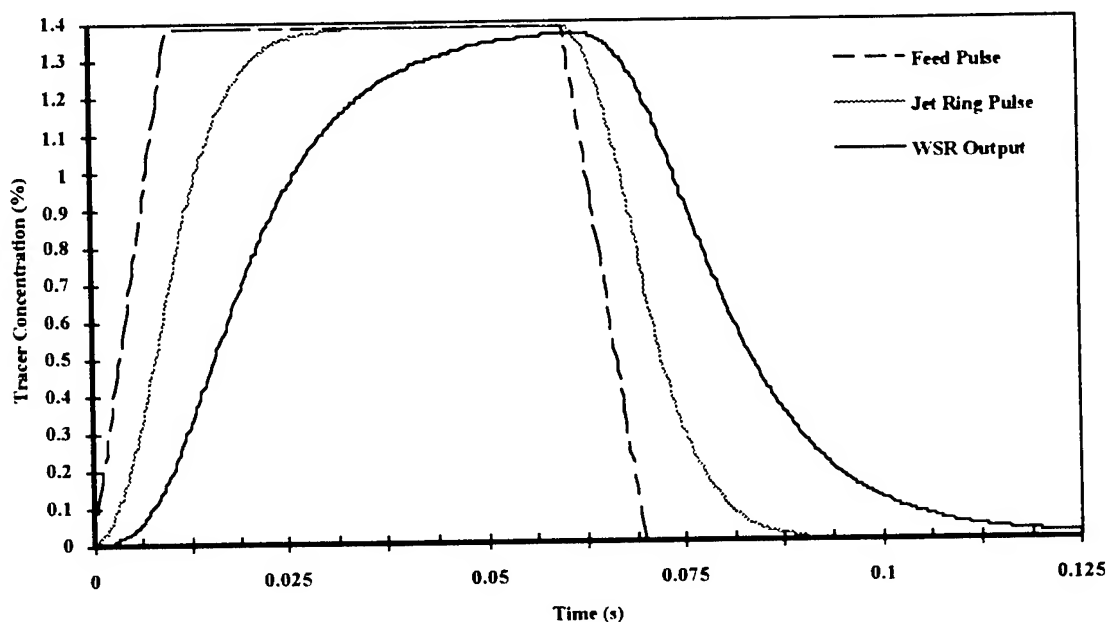


Figure 16. Calculated tracer response from the model for a total flowrate of 200 slm air and 14.7 slm methane ($\phi = 0.7$) and a pulse of 50 ms duration.

Figure 17 presents the calculated tracer responses at selected individual jet tubes corresponding to the same conditions depicted in Figure 16. In this figure the solid curves are the responses from jet numbers 1,4,8,12, and 16, and the dashed curves are the corresponding responses from jets 20,24,28, and 32. The effect of increasing time delay as the gas proceeds

around the ring to jets progressively further away is clearly shown. In addition, since the responses for the “mirror image jet pairs, 1:32, 4:28, 8:24, and 12:20, are coincident, this demonstrates that the distribution for one-half of the ring is perfectly symmetric with respect to the other half of the ring.

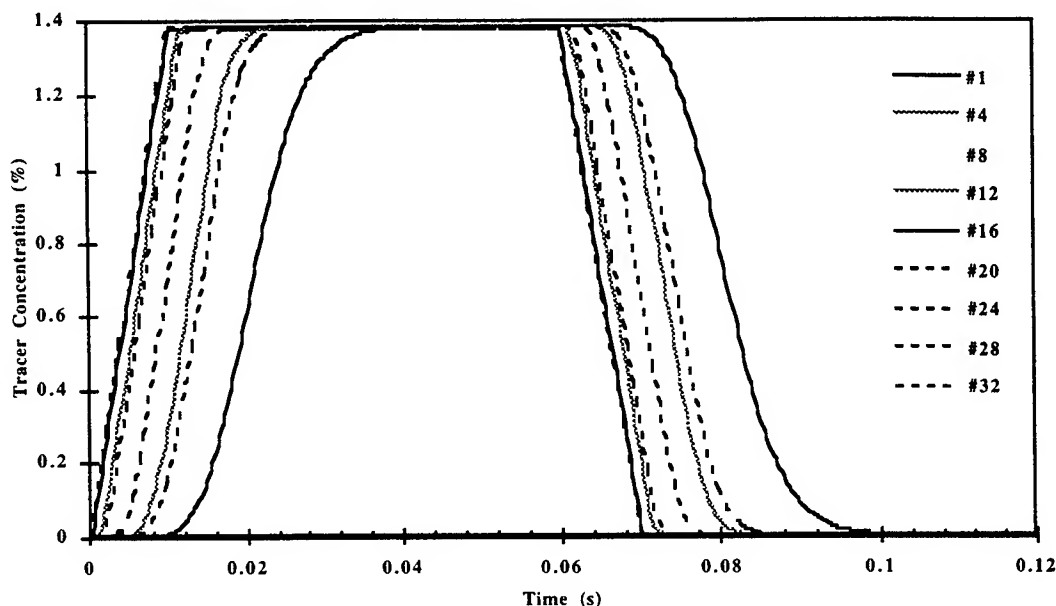


Figure 17. Calculated tracer response from the jet ring distributor model for individual jet tubes for a total flowrate of 200 slm air and 14.7 slm methane ($\phi = 0.7$) and a pulse of 50 ms duration.

Figure 18 presents inert tracer response predictions calculated with the jet ring distributor model compared to actual krypton tracer data of varying pulse duration from 10 to 200 ms. As can be seen from the figure, the actual data exhibit a somewhat more “sluggish” response than predicted by the model; i.e., the model rises and falls at a somewhat faster rate than the experimental data. This is most noticeable with the 50 ms pulse, for which the model predicts that the pulse attains its maximum krypton concentration, while the data indicates that it does not. Apparently, the nominal time response characteristics that were assumed for the pulsed valve did not correspond to the actual time response of the valve for the manner in which it was operated. For the 10, 100, 150, and 200 ms pulses, however, there is reasonable agreement between the model and the data. In any case, this does not represent a significant problem, since the pulsed valve time response characteristics can be modified to match the experimental data, thereby fixing the actual valve behavior.

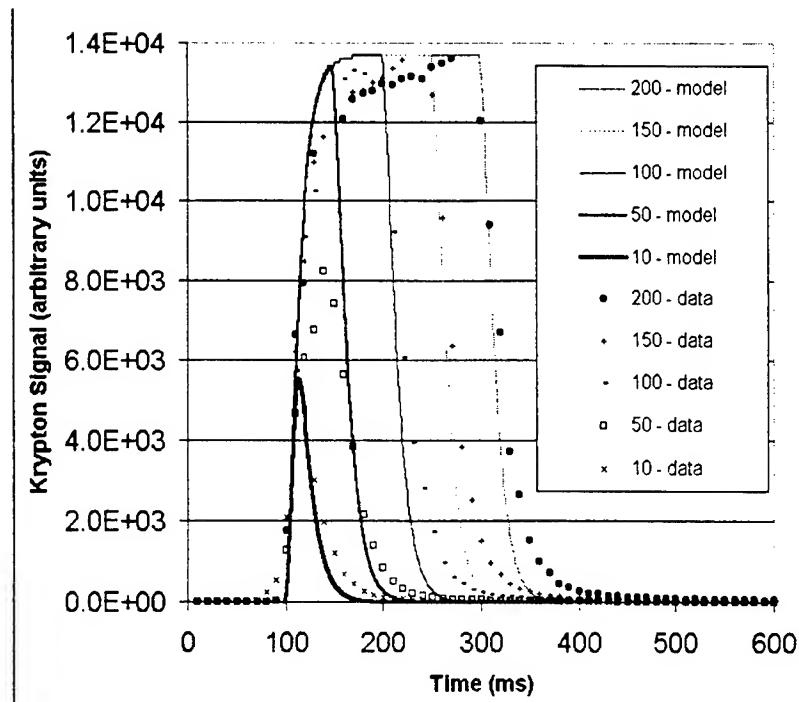


Figure 18. Krypton signal responses for variable duration pulses (in milliseconds) and the corresponding jet ring model predictions for the ignited WSR operating with 200 slm air and 14.7 slm methane.

CHEMKIN-Based Model Elements

The first step in formulating a model of the combustor system was to develop a complete chemical kinetics input file from published chemical reaction mechanisms. Specifically, the combustion mechanism of the reactions of methane in air, plus all the additional reactions required from the interaction of Halon 1301 with the gas milieu. This was accomplished with a combination of Konnov's methane combustion mechanism [14], NIST's CKMech hydrofluorocarbon and Halon 1301 mechanisms [15], and the Halon 1301 mechanism of Battin-Leclerc *et al.* [3]. In addition, species identified from the mass spectrometric data (e.g. CF_3OF , CF_3OH , etc.), which were not included in any of the published mechanisms, were added to the mechanism. Thermodynamic data and rate constants for these species were found in the literature [16].

The resultant chemical kinetic mechanism is the input to the PSR module of the CHEMKIN II code. However, the PSR module, as originally written, employs Newton's method to solve the steady-state species mass balances and the energy equation. Furthermore, the equilibrium composition of the species at the reactor temperature is used as a starting estimate for the iteration [13]. Thus, in order for the program to serve the requirements of the current model, these aspects

of the PSR module had to be modified.

One modification involved replacing the Newton's method solution of the steady-state species mass balances with a solution of the time-dependent differential equation mass balances, which describe the evolution to the steady-state solution. This was accomplished by bypassing the solver call to the Newton's method subroutine, and replacing it with a call to TWOPNT, which is a subroutine that time-steps using the backward-Euler method. In this method, the time derivatives are approximated by finite differences. Once this was accomplished, a readable output file was created in spreadsheet form to report the result of each time-step.

The transient Halon 1301 pulses were introduced by recalculating the input composition after each time- step. In order to accurately model the input pulse of fire suppressant, a jet ring distributor model (described below) was developed. The pulse shapes determined with this jet ring model were fit to rising and falling exponentials using Microsoft's Curve Expert software, and it was these fits which are used as inputs to the PSR code. When the program is run, an updated input percentage of the fire suppressant is calculated after each time step using the pulse shape fits, and the input concentrations of all other species are adjusted accordingly.

The final necessary modification was to allow for a starting estimate of the solutions other than thermodynamic equilibrium. Ideally, the model would run by starting the time stepping with a reactor composition equal to the results of steady-state methane combustion at the reactor conditions. This modification was achieved by running the PSR program in its original unmodified form using the methane combustion mechanism with no input Halon 101 pulse, and retaining the steady-state solution calculated by the program. This steady-state solution was then used as a starting estimate for the modified transient PSR calculation by utilizing the XEST command, which allows for user- supplied starting estimates.

A listing of the principal subroutines and their relationships is presented in the Appendix.

Implementation all the preceding modifications results in a robust method for the calculation of the WSR composition as a function of time for virtually any set of reactor conditions. The model was run with Halon 1301 input pulses at a variety of fuel-to-air ratios, reactor temperatures, pulse intensities, and flow rates. The results appeared to be qualitatively consistent with the corresponding data, and showed no signs of spurious or chaotic behavior as the variables were varied. Sample characteristic output data for Br_2 , O_2 , HF, and CH_4 are presented in Figures 19-23. In particular, it is noted that the model results for the behavior of methane are in agreement

with the findings of Battin-Leclerc *et al.* [3]. For example, in these latter studies it was found that at a temperature of 1070K, for space times (τ = WSR Volume/Feed Flow Rate) less than 1.5 s, Halon 1301 actually increased methane conversion. The transient data in Figure 23 support this behavior by showing a net increase in methane conversion from the steady-state value at 1773.15K when Halon 1301 is pulsed in at a WSR space time of τ = 0.07s. In Figure 22, transient model results for τ = 10.5 ms show that the net methane conversion at 1773.15K does actually decrease after an initial 9 seconds of increased methane conversion. These results demonstrate that the resultant model is consistent with others found in the literature.

The model results have still not been exhaustively compared to the mass spectrometric data; this effort is currently ongoing. Calibration and fragmentation data are available to facilitate this direct comparison. For example, mass spectra for most of the species have been obtained from the NIST Chemistry Web book [16]. Examples of mass spectrometric results predicted by the PSR model are presented in Figures 24 and 25.

However, the PSR model results *per se* do not include the effects of the sampling line from the WSR combustor to the mass spectrometer. The effects of any additional reactions and radical terminations on the tube walls on the resultant gas phase composition are not taken into account. In order to model the processes which occur in the sampling line, the constant pressure version of the SENKIN module was applied by adapting an approach that has previously been used to model the variation in stratospheric gas composition caused by sampling through a tube in laminar flow [17]. The gas sampling rate, at 8-10 slm, was calculated to be well within the laminar flow regime, with an average Reynolds number of about 260. The residence time in the sampling tube was approximately 15 ms, which is of the same order of magnitude as the duration of the Halon 1301 pulses. The gas composition from the WSR, determined from the transient PSR module calculations, along with the diffusion coefficients for the radical species (estimated using a technique given by Fuller [18]), and the sampling line temperature and pressure, are the inputs to the sampling line model.

The SENKIN module was modified to enable it to read input data directly from the PSR program, thereby eliminating the necessity of manually transferring composition data. The SENKIN module then time-steps through the entire length of the sampling tube (~15 ms) for each time-step composition that is reported by the PSR program. This final element of the overall transient model has been completed and is currently being interfaced to the PSR module.

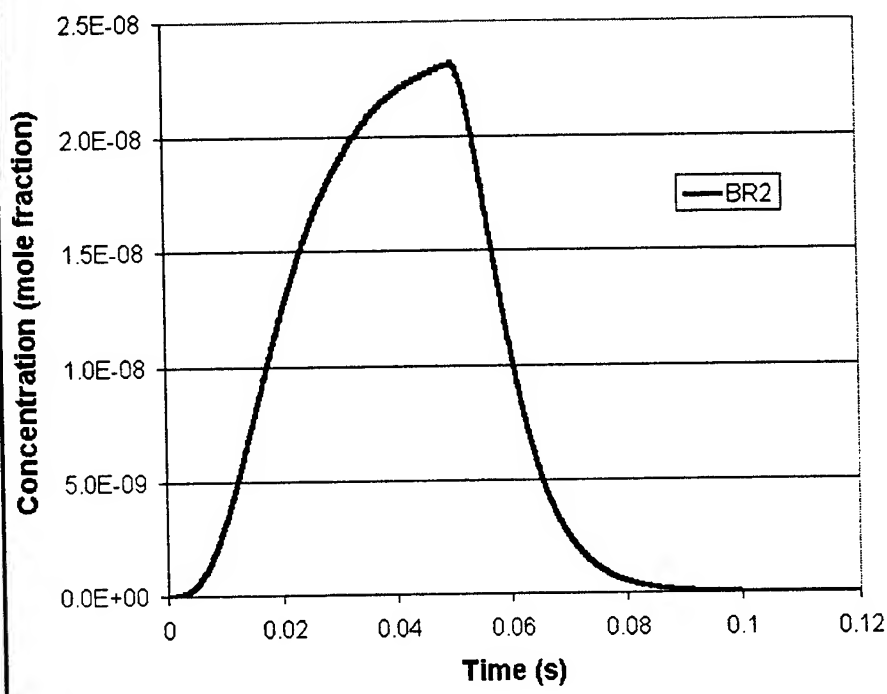


Figure 19. Transient behavior of Br_2 calculated from the PSR model for a 1.38% Halon 1301 pulse of 50 ms duration into an ignited WSR operating at 1773.15K with 200 slm air and 14.7 slm methane.

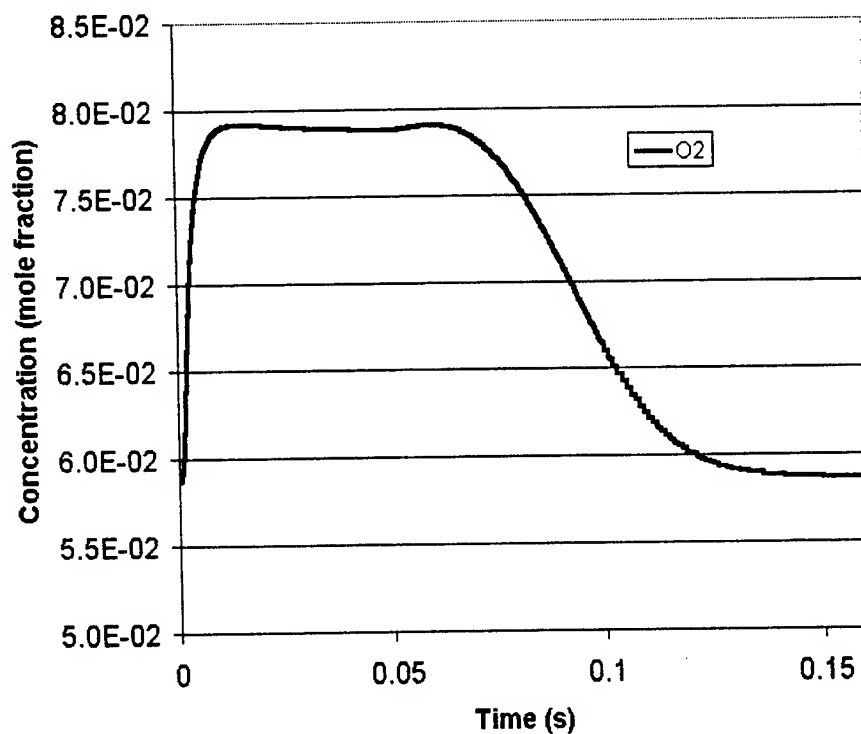


Figure 20. Transient behavior of O_2 calculated from the PSR model for a 1.38% Halon 1301 pulse of 50 ms duration into an ignited WSR operating at 1773.15K with 200 slm air and 14.7 slm methane.

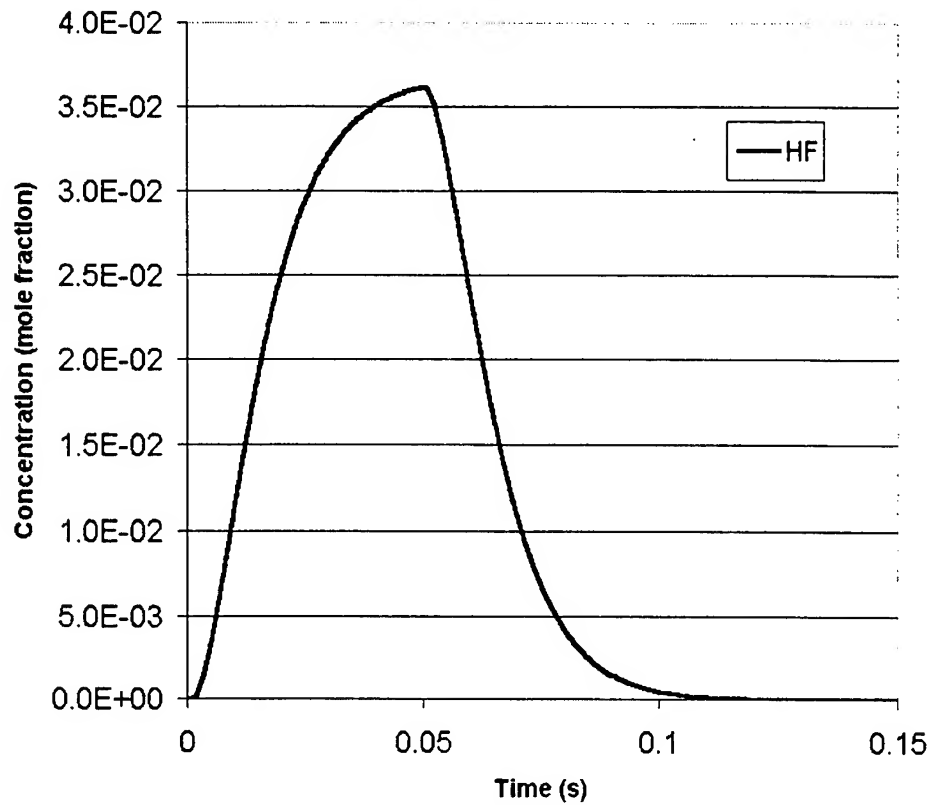


Figure 21. Transient behavior of HF calculated from the PSR model for a 1.38% Halon 1301 pulse of 50 ms duration into an ignited WSR operating at 1773.15K with 200 slm air and 14.7 slm methane.

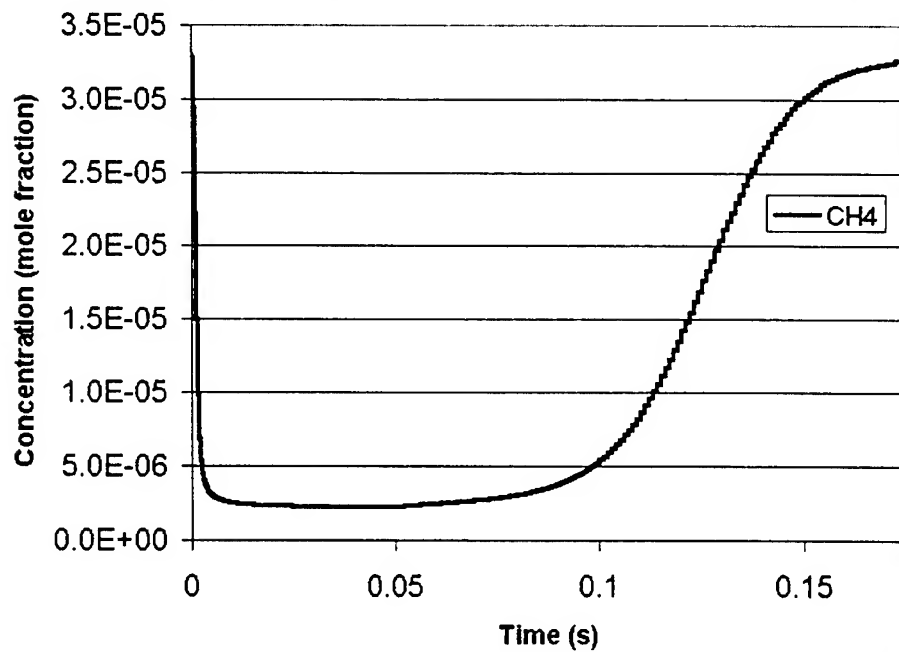


Figure 22. Transient behavior of CH₄ calculated from the PSR model for a 1.38% Halon 1301 pulse of 50 ms duration into an ignited WSR operating at 1773.15K with 200 slm air and 14.7 slm methane.

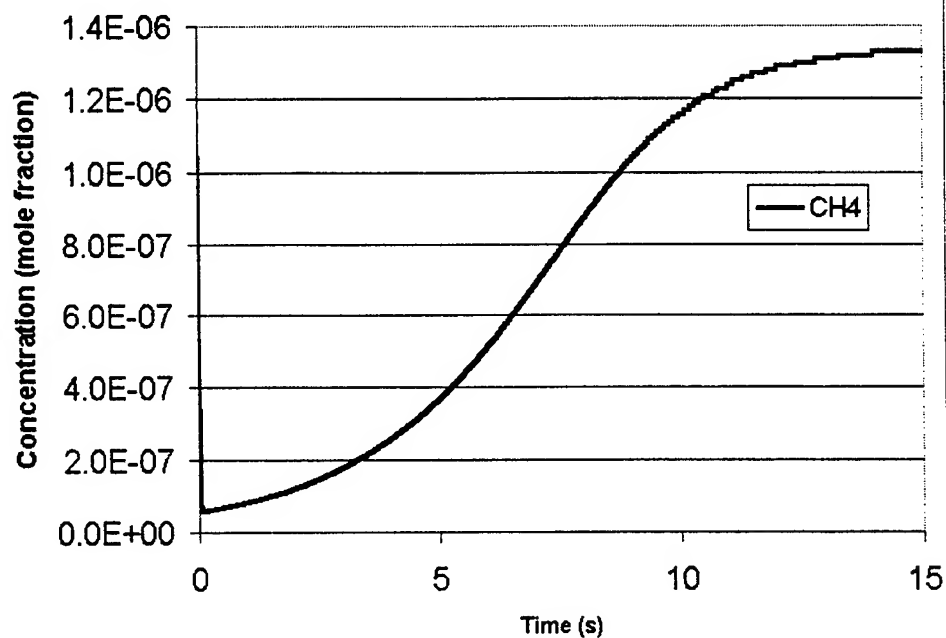


Figure 23. Transient behavior of CH_4 calculated from the PSR model for a 1.38% Halon 1301 pulse of 50 ms duration into an ignited WSR operating at 1773.15K with 1.35 slm air and 0.1 slm methane.

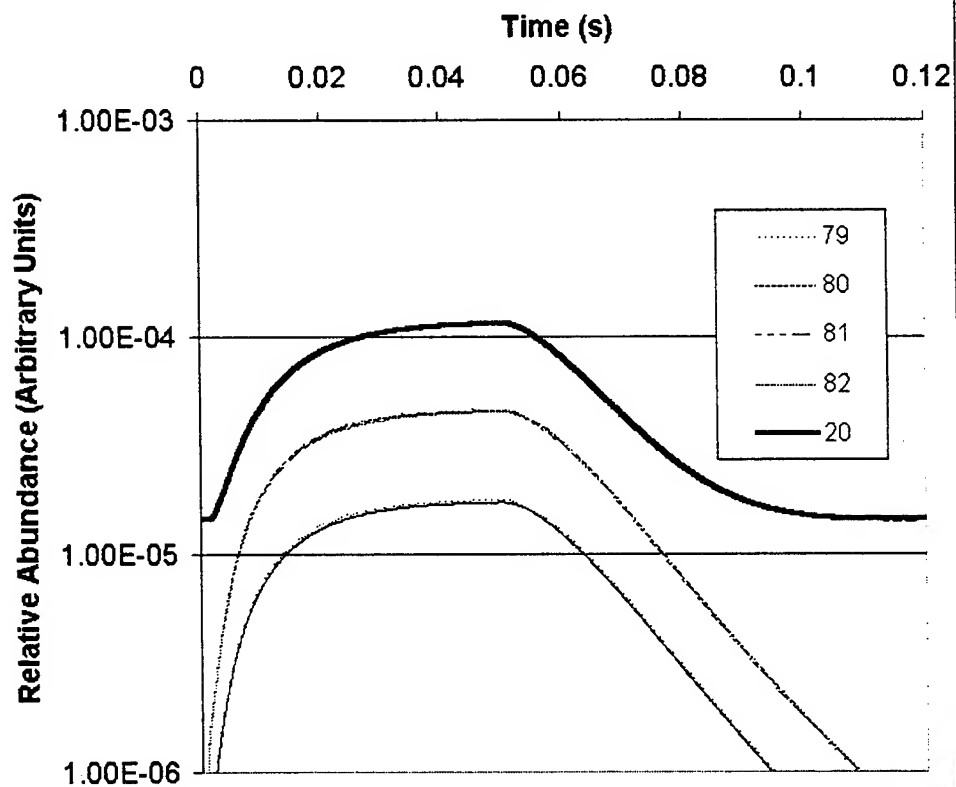


Figure 24. Calculated signal responses to a 1.38% Halon 1301 pulse of 50 ms duration into an ignited WSR operating at 1773.15K with 200 slm air and 14.7 slm methane.

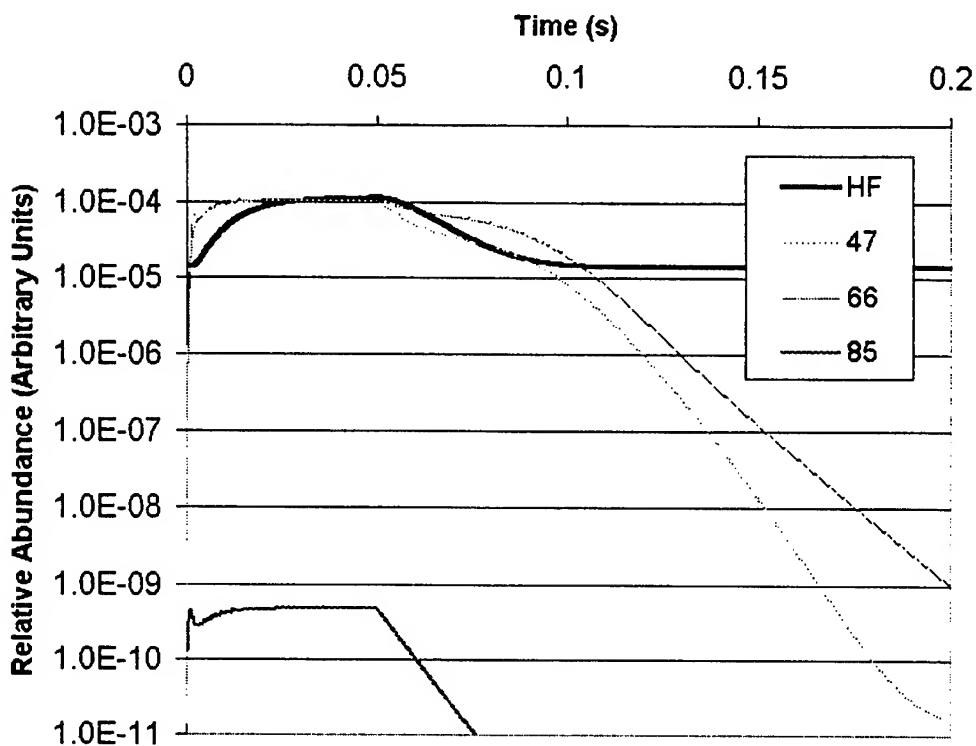


Figure 25: Modeled and calculated signal responses to a 1.38% Halon 1301 pulse of 50 ms duration into an ignited WSR operating at 1773.15*K with 200 slm air and 14.7 slm methane.

Summary and Conclusions

The WSR/REMS apparatus has been demonstrated to be capable of monitoring both the steady-state and dynamic behavior of the WSR combustor.

It was concluded that the three fire suppressants exhibit certain similarities in their behavior in combustion environments, as well as some distinct differences. The major product species produced by their injection into the WSR combustor are HF (for all three), HBr (for CF_3Br), and HI (for CF_3I). All three fire suppressant agents also produced significant mass peaks at 47, 66, and 85, which are attributed to the ion series CFO^+ , CF_2O^+ , and CF_3O^+ , respectively. CF_2O^+ is most probably the parent ion peak of the stable species, carbonyl fluoride. High levels of this very toxic gas were produced at short reactor residence times. Masses 47 and 85, CFO^+ and CF_3O^+ , are most probably fragment ions from stable neutral species such as CF_3OF and CF_3OH . These latter species should be included in fire suppressant reaction mechanisms.

A numerical model of the WSR combustor system has been developed to interpret the

resultant transient responses of gas phase species measured mass spectrometrically. This model includes the effects of the residence time distribution of the jet ring distributor, as determined from a fluid mechanical model developed for this purpose, and the detailed kinetics in the well-mixed combustor and the sampling line to the mass spectrometer. The latter two components of the model are based on the CHEMKIN II package of codes, especially the perfectly-stirred reactor (PSR) and SENKIN modules. Work has also been done on transforming the mole fractions reported by the model into corresponding mass spectrometric signals. Direct comparison of model results with the combustion data has been initiated.

It is anticipated that the transient data coupled with the model analysis will result in the identification of the key reactions in the mechanisms responsible for the behavior of fire suppressants in combustion systems. This approach will also be used to determine kinetic rates for the reactions involved. This effort is expected to improve the understanding of fire suppression mechanisms.

The unique capabilities of the REMS/WSR apparatus could be used to identify and measure in a definitive, quantitative manner the efficacy of candidate fire suppressants using only minimal pulsed amounts, as well as aid in the assessment of the important environmental effects of using fire suppressants in combustion systems relevant to Air Force operations.

References

- [1] P.R. Westmoreland, D.R.F. Burgess, Jr., W. Tsang, and M.R. Zachariah, paper presented at Eastern States Section, The Combustion Institute, October, 1993.
- [2] C.K. Westbrook, *Comb. Sci. Tech.* **34**, 201 (1983).
- [3] F. Battin-Leclerc, G.M. Côme, and F. Baronnet, *Comb. Flame* **99**, 644 (1994).
- [4] J. Zelina and D.R. Ballal, "Combustion Studies in a Well Stirred Reactor," AIAA 94-0114, presented at the 32nd Aerospace Sciences Meeting, January, 1994, Reno, NV.
- [5] J. Zelina and D.R. Ballal, "Combustion and Emission Studies Using a Well Stirred Reactor," AIAA 94-2903, presented at the 30th AIAA/ASME/SAE/ASEE Joint Propulsion Conference, June, 1994, Indianapolis, IN.
- [6] V.H. Diebler, R.M. Reese, and F.L. Mohler, *J. Res. N.B.S.* **57**, 113 (1956).
- [7] Handbook of Chemistry and Physics, 75th, D.R. Lide, ed., CRC Press, Boca Raton, 1994.

- [8] J.M. Calo, Final Report for AFOSR Summer Faculty Research Program, September 1995.
- [9] W. Braker and A.L. Mossman, Matheson Gas Data Book, 6th ed., Matheson Co., Lyndhurst NJ, 1980, p. 144.
- [10] J. Czarnarski, E. Castellano, and H.J. Schumacher, *Chem. Comm.* 1255 (1968).
- [11] R.J. Kee, F.M. Rupley, and J.A. Miller, "CHEMKIN II: A FORTRAN Chemical Kinetics Package for the Analysis of Gas-Phase Chemical Kinetics," SAND89-8009B, November, 1991, Sandia National Laboratories, Livermore, CA.
- [12] P. Glarborg, R.J. Kee, J.F. Grcar, and J.A. Miller, "PSR: A FORTRAN Program for Modeling Well-Stirred Reactors," SAND86-8209, February, 1986, Sandia National Laboratories, Livermore, CA.
- [13] A.E. Lutz, R.J. Kee, and J.A. Miller, "SENKIN: A FORTRAN Program for Predicting Homogeneous Gas Phase Chemical Kinetics with Sensitivity Analysis," SAND87-8248, February, 1988, Sandia National Laboratories, Livermore, CA.
- [14] A.A. Konnov, "Detailed reaction mechanism for small hydrocarbons combustion," Release 0.3, <http://homepages.vub.ac.be/~akonnov/>, 1997.
- [15] D.R.F. Burgess, Jr., M.R. Zachariah, W. Tsang, and P.R. Westmoreland, NIST WWW CKMech, <http://www.nist.gov/csl/div836/ckmech/Mechanisms.html> , 1998.
- [16] W.G. Mallard, NIST Chemistry Web Book, <http://webbook.nist.gov/chemistry/>, 1998.
- [17] J.M. Calo, "Composition Alteration of Stratospheric Air Due to Sampling Through a Flow Tube," AFGL-TR-84-0045, Ionospheric Physics Division, Air Force Geophysics Laboratory, Hanscom AFB, MA, 1984.
- [18] J.A. Roberson and C.T. Crowe, *Engineering Fluid Mechanics*, Houghton Mifflin Co., Boston, 1990, p. 424.
- [19] Handbook of Geophysics and the Space Environment, A.S. Jursa, ed., Air Force Geophysics Laboratory, U.S. Air Force, 1985, p. 14-5.
- [20] Roberson and Crowe, *Ibid.*, p. 550.
- [21] J.E. Nenniger, "Polycyclic Aromatic Hydrocarbon Production in a Jet-Stirred Combustor," Doctor of Science Thesis, Massachusetts Institute of Technology, 1983, pp. 153-164.
- [22] J. Blust, Fuels and Lubricants Group, Wright Laboratories, Wright-Patterson Air Force Base, Ohio, *Private Communication*, 1996.
- [23] Roberson and Crowe, *Ibid.*, p. 554.

Appendix

Description of Files Comprising the Model

FORTTRAN Code:

<i>CKInterp39.for</i> –	CHEMKIN code that reads input mechanisms and formats them to be used for further computations.
<i>LatestPSR24.for</i> –	Code that reads in the parameters of the reactor and feed stream, and calculates the composition within the PSR as a function of time.
<i>LatestTwopnt22D.for</i> –	Computes the time-stepped solutions to the differential equations formulated by the PSR model.
<i>PSRDriver.for</i> –	Apportions the work spaces for the PSR model and opens all necessary PSR Input/Output files.
<i>Senkin.for</i> –	Apportions the work spaces for the sampling line model and calculates the composition at the end of the sampling line, from the output from the PSR model.
<i>CKStrt.h</i> –	File required for <i>CKLib43</i> .
<i>CKLib43.for</i> –	Subroutine library.
<i>Dasac.for</i> –	Subroutine library.
<i>Eqlib.for</i> –	Subroutine library.
<i>Math.for</i> –	Subroutine library.
<i>Stanlib.for</i> –	Subroutine library.
<i>Vode.for</i> –	Subroutine library.

Input/Output Files:

CHEMKIN Interpreter (PSR):

<i>chem.inp</i> –	User-supplied input file containing the necessary elements, species, thermodynamic data, and chemical reactions for the PSR model.
<i>chem.out</i> –	CHEMKIN output file, displaying the input and reporting any error messages.
<i>therm.dat</i> –	Input file containing the thermodynamic properties of all the species included in the reaction mechanism.
<i>PSRchem.bin</i> –	Output file opened and read by the PSR module.

CHEMKIN Interpreter (SENKIN):

<i>SENchem.inp</i> –	User-supplied input file containing the necessary elements, species, thermodynamic data, and chemical reactions for the sampling line model.
<i>SENchem.out</i> –	CHEMKIN output file, displaying the input and reporting any error messages.
<i>therm.dat</i> –	Input file containing the thermodynamic species of all the species included in the reaction mechanism.
<i>SENchem.bin</i> –	Output file opened and read by the SENKIN module.

PSR Module:

<i>PSR.inp</i> -	User-supplied input file containing the reactor parameters.
<i>PSR.out</i> -	PSR output file, containing the results of the PSR computations.
<i>PSRrest.bin</i> -	PSR output file, containing the final solution for use as a starting point for further computations.
<i>PSRrecov.bin</i> -	PSR output file, which is rewound and rewritten after each successful series of time steps.
<i>PSRsave.bin</i> -	PSR output file, written after the successful completion of the entire simulation.
<i>PSRInputStream</i> -	Spreadsheet format file which displays the composition of the reactor feed stream as a function of time.
<i>PSRExcelresults</i> -	Spreadsheet format file which displays the composition in the PSR as a function of time.
<i>SENKINtransfer.bin</i> -	PSR output file which serves as an input to the SENKIN module.

SENKIN Module:

<i>SENKIN.inp</i> -	User-supplied input file containing sampling line parameter values.
<i>SENKIN.out</i> -	SENKIN output file, containing the results of the sampling line computations.
<i>SENrest-.bin</i> -	SENKIN output file, containing the final solution for use as a starting point for further computations.
<i>SENsave.bin</i> -	SENKIN output file, written after the successful completion of the entire problem.
<i>SENKINExcelresults</i> -	Spreadsheet format file which displays the composition at the end of the sampling line as a function of time.

James Carroll
Report not available at time of publication.

**GRADIENT-DATA TOMOGRAPHY FOR HARTMANN SENSOR APPLICATION
TO
AERO-OPTICAL FIELD RECONSTRUCTION**

Soyoung Stephen Cha
Associate Professor
Department of Mechanical Engineering

University of Illinois at Chicago
2939 ERF, 842 west Taylor Street
Chicago, IL 60607-7022

Final Report for:
Research Initiation Program
Phillips Laboratory

Sponsored by:
Air Force Office of Scientific Research
Bolling Air Force Base, Washington, D.C.

and

University of Illinois at Chicago

January 1998

GRADIENT-DATA TOMOGRAPHY FOR HARTMANN SENSOR APPLICATION TO AERO-OPTICAL FIELD RECONSTRUCTION

Soyoung Stephen Cha
Associate Professor
Department of Mechanical Engineering
University of Illinois at Chicago

Abstract

Optical tomography based on the Hartmann sensor can be a very useful diagnostic tool for aero-optics and aero-dynamic measurements. It has strengths in remote sensing and gross-field capture with high data-acquisition rate for fast transient phenomena. For expanding its practical applicability, however, some problems need to be resolved. First, the Hartmann sensor provides field-gradient projections. Conventional tomographic algorithms require field projections instead of gradients, thus requiring integration of gradient data. They also limit the application scope to those with zero boundaries for definite integration. Second, the fields to be reconstructed have been assumed to be square or circular. If the boundary is irregular, some reconstruction errors arise under these simplifying assumptions. The reflection of accurate field shapes can result in much better accuracy. To simplify the Hartmann sensor optical setup or its application scope, we also need accurate reconstruction with a less number of projections, that is, reconstruction from limited data with restricted scanning and incomplete projections. The goal proposed here is twofold. The primary objective is to develop tomographic algorithms, which can utilize both integrated and gradient data for arbitrary field shapes. The method can provide us with flexibility and allow us to test the accuracy of two modes of reconstruction. The secondary goal is to develop a hybrid technique to further enhance the reconstruction accuracy by incorporating *a priori* information. In these efforts, a new algorithm, termed Curvilinear Nonlocal Basis Function Method, has been developed and combined with the Complementary Field Method to produce a hybrid approach. The combined method is tested especially for ill-posed conditions but only for integrated data, due to the limited funding. The performance of the hybrid method is better than a single method. The combined method is powerful to deal with arbitrary boundaries and ill-posed problems of limited data especially for the Hartmann sensor.

GRADIENT-DATA TOMOGRAPHY FOR HARTMANN SENSOR APPLICATION TO AERO-OPTICAL FIELD RECONSTRUCTION

Soyoung Stephen Cha

1. Introduction

Reconstruction of refractive-index fields from projection data, that is, optical tomography, can be a very useful diagnostic tool for flow field imaging especially in aero-optics or aero-dynamics. It can provide merits in nonintrusive remote sensing, gross-field capture, high measurement accuracy, and good spatial resolution as compared to conventional techniques. Currently, the aero-optics research group of the Lasers and Imaging Directorate at the Air Force Phillips Laboratory conducts tomographic reconstruction for imaging three-dimensional (3-D) flow fields. The optical tomographic system at the Phillips Laboratory consists of two parts: that is, the Hartmann-sensor hardware for obtaining projection data of test fields and computational software for reconstructing the fields from projections. Optical tomography based on the Hartmann system provides an additional merit, that is, rapid sampling of two-dimensional (2-D) projections of a field. It can thus allow continuous real-time monitoring for reconstructing 3-D fast transient phenomena. For expanding the practical applicability of the Hartmann sensor, however, some problems need to be resolved.

The Hartmann sensor provides integrated gradient data of refractive-index along an optical ray unlike integrated optical pathlength data in interferometric tomography. Conventional computational tomographic algorithms require projection pathlength data. The

present practice thus resorts to additional data processing of integrating gradient data for obtaining optical pathlength data. Hence, it is very desirable to develop a new approach that allows an additional capability for reconstructing refractive-index fields directly from gradient projections. The approach solely based on the integrated data may limit the application scope to a special type of problems: i.e., free jets with zero projection values at the boundary. Second, the fields to reconstructed have been assumed to be square or circular. If the field boundary is irregular, some reconstruction errors arise under these simplifying assumptions of the field shape. The reflection of accurate field shapes can results in much better accuracy especially under limited data points with restricted angular scanning and incomplete projections whose capability is much needed as explained later. The proposed research goal is twofold.

- The primary objective of the proposed research is to develop and test computational tomographic algorithms for reconstructing refractive-index fields, which can utilize both integrated and gradient data obtained by Hartmann sensors for arbitrary boundary shapes. The method can provide us with flexibility and allow us to test the accuracy of two modes of reconstruction.

Tomographic hardware collects projection information. Hartmann sensors, being based on micro-fabrication binary-optics, can provide only a small sensing area. Currently, experiments at the Phillips Laboratory employ a parallel-beam configuration to obtain projection data. If so, beam-collimation and collection lenses, which are greater in size than the field to be scanned, are needed. For large-field scanning, this approach becomes impractical, resulting in a

bulky system that consists of many beam projection-collection pairs of comparable aperture, that is, many large and expensive lenses. It is thus necessary to produce efficient hardware and software to reconstruct fields with limited data points restricted in scanning and incomplete in projection. This allow us to provide a much simpler setup at a reduced cost in conducting experiments.

- The secondary goal of the proposed research is to develop a hybrid technique which we believe to further enhance the reconstruction accuracy by incorporating *a priori* information.

In these efforts, a new reconstruction algorithm, termed Curvilinear Nonlocal Basis Function Method (CNBFM), has been developed and combined with the Complementary Field Method (CFM) to produce a hybrid approach. The combined method is tested with numerically generated fields especially under ill-posed conditions but only for integrated dada, due to the time limitation in the funding. The complete accomplishment of the research to fully understand the nature of the proposed goals is very extensive and requires a long-term commitment. The summary of the investigation, including approaches, methodology, and analyses are presented hereafter

2. Curvilinear Nonlocal Basis Function Method (CNBFM)

Mathematically, any 2-D field $f(x,y)$ can be expressed by an infinite series. Series

expansion methods are suitable for ill-posed reconstruction. The bases in series expansion can be local or nonlocal. Some example of local basis function methods are the fixed grid method, cubic-spline method, variable grid method [1,2], etc. Nonlocal basis function methods include the sinc function method and orthogonal series method [3,4]. Practically all the previous efforts were made on the fields with regular field boundaries and without opaque objects [5,6,7], i.e., circular or rectangular. In the CNBFM, fields are represented by

$$f(r,\phi)=\sum_{i=0}^{\infty} C_i S_i(r,\phi). \quad (1)$$

Here $S_i(r,\phi)$ is the series term in polar coordinates and C_i is the correspondent coefficient. With a reasonable accuracy, the infinite series can be approximated by a finite terms of

$$f(r,\phi)=\sum_{i=1}^M C_i S_i(r,\phi) \quad (2)$$

where M is the number of basis functions. Various basis function can be chosen for series expansion. Here Legendre polynomials in r and the harmonic functions in ϕ , i.e., sine and cosine functions, were adopted as basis functions. If so, equation (2) becomes

$$\begin{aligned} f(r,\phi) &= \sum_{m=0}^M \sum_{n=0}^N C_{mn} P_m(r) \Phi_n(\phi) \\ &= \sum_{m=0}^M \sum_{n=0}^N [A_{mn} P_m(r) \cos(n\phi) + B_{mn} P_m(r) \sin(n\phi)] \end{aligned} \quad (3)$$

where $\Phi_n(\phi)$ is a circular harmonic of order n , $P_m(r)$ is the Legendre polynomial of order of m , M and N are the highest order of polynomials and harmonic functions, respectively. C_{mn} are the coefficients to be determined for a field reconstruction. If these coefficients are known, the distribution of the physical property of the field can be found. The primary goal of reconstruction

is thus to find the coefficients in Equation (3).

The optical pathlength data can be expressed by

$$\begin{aligned}
 g(\rho, \theta) &= \int_{\text{ray}} f(r, \phi) \delta(\rho - x \cos \phi - y \sin \phi) ds \\
 &= \int_{\text{ray}} \sum_{m=1}^M \sum_{n=1}^N [A_{mn} P_m(r) \cos(n\phi) + B_{mn} P_m(r) \sin(n\phi)] ds \\
 &= \sum_{m=1}^M \sum_{n=1}^N [A_{mn} \int_{\text{ray}} P_m(r) \cos(n\phi) ds + B_{mn} \int_{\text{ray}} P_m(r) \sin(n\phi) ds] \quad (4)
 \end{aligned}$$

The total number of unknowns in Equation (4) is $M(2N-1)$. Depending on the view angle and number of data points in each projection, that is, step sizes of ρ and θ in sampling, which are denoted by $\Delta\rho$ and $\Delta\theta$, the total number of equations can vary significantly. Practically, the number of equations can always be greater than that of unknowns to make the system of linear algebraic equations over-determined. The redundancy is very important in calculating the unknowns when higher accuracy is required. A convenient and also effective method for solving this redundant system is the least square method.

Assume that Equation (4) is expressed by a matrix notation of $A\underline{X}=\underline{B}$ where A , \underline{X} , and \underline{B} represent Radon transform values of individual series terms for rays (ρ, θ) , series expansion coefficient, and measured data, respectively. In a system of linear equations, if there exist errors in some elements in the coefficients matrix A or the constant vector \underline{B} in $A\underline{X}=\underline{B}$, a large amount of distortions may arise in the estimated result of \underline{X} . There always exist some errors in measurements of optical pathlength data. To reduce the effect of measurement errors and ill-posed data collection as much as possible, suitable redundancy is necessary. There should be a trade-off in selecting the optimal numbers of $(\Delta\rho, \Delta\theta)$ and (M, N) . These values differ for

individual problems.

When tomographic reconstruction is performed upon a field with an opaque object inside the field, the polynomial $P_m(r)$ in Equation (3.5) changes to $P_m(2 \frac{r - R_{min}}{R_{max} - R_{min}} - 1)$, where R_{min} and R_{max} are shown in Figure 1. This will guarantee the argument of P_m ranges in $[-1,1]$ where the orthogonal Legendre polynomials are defined.

The above algorithm implemented into a computer code can be described step by step as follows:

1. Assume a field $f(r,\phi)$, or in the Cartesian coordinates $f(x,y)$, boundaries of the field, and an opaque object together with the sets of $(\Delta\rho,\Delta\theta)$ and (M,N) .
2. Integrate $f(x,y)$ along each probing ray (ρ,θ) to obtain $g(\rho,\theta)$.
3. Integrate the $M(2N-1)$ basis functions along the same ray (ρ,θ) according to right-hand side of Equation (4).
4. Set up a system of linear algebraic equations for each ray (ρ,θ) based on Equation (4).
5. Apply the least square method to solve the over-determined system of equations obtained from step 4 to find the coefficients A_{mn} and B_{mn} .
6. Reconstruct the field by substituting A_{mn} and B_{mn} back into Equation (3). Compare the original values of $f(x,y)$ with the reconstructed values with a set of sampling points by finding the average and maximum errors.

2.1. Computer Simulation

In order to test the reconstruction accuracy by the algorithm presented in Section 2, we used computer- simulated data for refractive-index fields. Two different fields were tested, field $f_1(x,y)$ with a single-hump and field $f_2(x,y)$ with double-humps. The mathematical expressions

for $f_1(x,y)$ and $f_2(x,y)$ are as follows:

$$f_1(x,y)=0.7\exp\{-5[(x-0.1)^2 + (y-0.2)^2]\} \quad (5)$$

$$f_2(x,y)=0.8\exp\left[-20\frac{(x-0.15)^2 + (y-0.4)^2}{2.1-x^2-y^2}\right] + 0.6\exp\left[-25\frac{(x+0.25)^2 + (y+0.35)^2}{2.1-x^2-y^2}\right] \quad (6)$$

An opaque object was selected in testing the reconstruction algorithm for incomplete projection data, that is ,

$$5(x+0.1)^2+4(y-0.1)^2=1 \quad (7)$$

For the purpose of comparison, we defined two types of errors as follows:

$$\sigma_{\max} = \frac{\text{Max}(|f(x_i, y_i) - f_r(x_i, y_i)|)}{\text{Max}(|f(x_i, y_i)|)} \cdot 100 \quad (8)$$

$$\sigma_{\text{ave}} = \frac{\sum_{i=1}^{N_d} |f(x_i, y_i) - f_r(x_i, y_i)|}{N_d \cdot \text{Max}(|f(x_i, y_i)|)} \cdot 100 \quad (9)$$

where σ_{\max} and σ_{ave} denote maximum error and average error, respectively. N_d is the total number of nodes (x_i, y_i) inside the field boundary but outside of the opaque object when an opaque object is present.

To investigate the behavior of the algorithms under incomplete projection, various view angles were tested for each of the six different test cases, that is, full angle 180° , 160° , 120° , 90° , 60° , and 40° , respectively. For each test case, there were many combination of M and N as the highest order of polynomials and harmonic functions. Different combinations of (M,N) result in different reconstruction accuracies. There must be an optimal (M,N) corresponding to the best accuracy in each different case. Tables 1 and Table 2 show the minimum value of the maximum and average errors and the corresponding (M,N) . Figures 2 and 3 graphically show the results.

Obviously for all the cases, the maximum and average errors decreased considerably as the view angle increased. Some plots of the reconstructed fields are presented in Figures 4 and 5. Figure 4 shows the reconstruction result for the one-hump field with an opaque object under the full view angle. There was no visible distortion as seen in the plot. Quantitatively, the maximum and average errors were as low as 0.086% and 0.001%, respectively. When the view angle becomes the lowest value of 40° as seen in Figure 5, there is still no visible distortion of the field with the maximum and average errors of 0.39% and 0.036%, respectively. For the cases with two humps as shown in Figure 6, visible distortions appear with the small view angle of 40° in the reconstructed fields especially in the area blocked by the opaque object. This is the direct effects of ill-posed data sampling.

2.2. Conclusion

A new tomographic algorithm has been developed by employing a series expansion method based on nonlocal basis functions, termed Curvilinear Nonlocal Basis Function Method (CNBFM). Unlike local base function methods, it represents the entire field with an orthogonal series. By finding the coefficients of all the basis functions with the measured data, the field can be reconstructed. Computer simulation results show that the CNBFM provided high reconstruction accuracy after optimization of the highest order of polynomials and harmonic functions. The results indicate the developed algorithms are reliable and applicable in reconstructing 3-D flow fields.

3. Complementary Field Method (CFM)

The Complementary Field Method (CFM) is iterative and was developed by Sun and Cha

[7, 8] as a unified approach for reconstructing fields under various ill-posed conditions. It utilizes the field estimation as *a priori* information. The step-by-step procedure is as follows:

1. Assume an initial estimate $f_e(x,y)$ of the original field $f(x,y)$ to be reconstructed.
2. Calculate the projection data $g_e(\rho,\theta)$ of the field estimate $f_e(x,y)$ only at the points where the measured $g(\rho,\theta)$ are available:

$$g_e(\rho,\theta)=L\{f_e(x,y)\}$$

where L is the line integral transform operator.

3. Calculate the difference in the projection domain for the projection data of the complementary field $f_c(x,y)$ which is the difference between $f(x,y)$ and $f_e(x,y)$:

$$g_c(\rho,\theta)=C_1\{g(\rho,\theta)-g_e(\rho,\theta)\}$$

where C_1 is the constraint operator about the Radon transform of the complementary field.

4. Reconstruct the complementary field:

$$f_c(x,y)=R\{g_c(\rho,\theta)\}$$

where R is the reconstruction operator.

5. Improve the estimate of the original field by

$$f_i(x,y)=f_e(x,y)+f_c(x,y)$$

Now physical constraints can be incorporated to make the estimate more meaningful.

$$f_e^{new}(x,y)=C_2\{f_i(x,y)\}$$

where C_2 is the constraint operator on the reconstructed field.

6. Return to step 2 with the new estimate $f_e^{new}(x,y)$ unless some suitable termination criteria are satisfied.

Based on *a priori* information, the two important types of constraints C_1 and C_2 can be formulated. Possible *a priori* information can be: (1) the Radon transform of the original field such as positiveness of the line integrals, periodicity of measured data with respect to the projection angle; (2) physical configuration information of the field such as the range of field values and local maximum value locations. Operators R and L in the step 2 and 4 may bring some inherent errors because they operate with approximate discrete numerical processing and a finite number of ill-posed data. All reconstruction algorithms practically produce a null field

from null projection data. This implies that the closer the $f_c(x,y)$ is to $f(x,y)$, the nearer $f_c(x,y)$ is to a null field to achieve a more accurate reconstruction. This can be easily seen in the above iterative steps. One advantage of the CFM is the ease in using *a priori* information. Even slight knowledge of the field can be incorporated very easily into the procedure. Compared with conventional iteration methods that directly work with limited data, the CFM works with the complementary field.

3.1. Computer Simulation

In the computer simulation of experiments, the results from the reconstruction were compared with the originally-known test fields, that is, single-hump field $f_1(x,y)$ and double-hump field $f_2(x,y)$ as in Section 2. In numerical simulations, the boundaries of the fields were defined as

$$2x^2+y^2=1 \quad (10)$$

In defining the opaque objects, consideration was given to generate asymmetric configurations. Two different opaque objects were selected to test the reconstruction algorithm. That is,

$$\text{opaque object \#1: } 4(x+0.1)^2+3(y-0.1)^2=1; \quad (11)$$

$$\text{opaque object \#2: } 5(x+0.1)^2+4(y-0.1)^2=1. \quad (12)$$

In this manner, six different test cases were generated for testing; more specifically, one-hump field and two-hump field with and without opaque objects #1 and #2, respectively. To investigate the behavior of the algorithms under incomplete projection, various view angles were tested for each of the six different test cases: that is, full angle 180° , 160° , 120° , 90° , 60° , and 40° , respectively.

Figures 7 to 10 show the results from computer simulation of experiments. The general trends are similar to the cases of the CNBFM. For all the cases, the maximum and average errors decreased considerably with the increase of view angle. For the cases with two humps, visible distortions appears with the small view angles of 40° and 60° in the reconstructed fields especially in the area blocked by the opaque object. This is the direct effects of ill-posed data sampling. But the reconstruction of the areas, which were scanned by the probing beams, were fairly reliable. Since the CFM was developed to deal with ill-posed problems and also the CNBFM showed good reconstruction accuracy under well-posed conditions, the CFM was mainly tested for the reconstruction of ill-posed problems, i.e., with an opaque object in a field

and a view angle smaller than 90° . Tables 3, 4 and 5 show the maximum and average errors for the cases of: (1) no opaque object in the two-hump field; (2) opaque object #1 in the two-hump field; and (3) opaque object #2 in the two-hump field, respectively.

It can be clearly seen that under a limited view angle and with an opaque object inside the field, the CFM increased the accuracy in reconstruction. The relatively small reduction improvement when the CFM was incorporated is believed to be due to the good performance of the CNBFM. The good reconstruction by the CNBFM left a minimal improvement by the CFM.

Since the field boundaries and opaque object shapes were specified in the CNBFM, it practically utilized *a priori* information. This can be one of the reasons why the CNBFM provided good reconstruction. The *a priori* information, however, could have been incorporated in the CFM.

3.2. Conclusion

In the research, a few different computer-generated fields were used to test the performances of the CNBFM combined with the CFM. The combination of the CNBFM and the CFM provided satisfactory accuracy especially under severely ill-posed conditions, i.e., limited view angle and/or with opaque object inside a field which blocked part of the probing rays. The performance of the hybrid method is apparently better than using a single method. The result shows that the combined method can be powerful to deal with ill-posed conditions with limited data especially for the Hartmann sensor.

4. References

1. Cha, D. J. and Cha, S. S.: Three-dimensional natural convection flow around two interacting isothermal cubes. *Int. J. Mass Transfer.* 38: 2343-2352, 1995.
2. Cha, D. J.: Interferometric tomography: reconstruction algorithm, experiment, and comparison with a numerical study. Ph.D thesis, University of Illinois at Chicago, 1993.
3. Deans, S. R.: The Radon transform and some of its applications. New York, John Wiley & Sons, 1983.
4. Ramachandram, F. N. and Lakshminarayanan, A. V.: Three-dimensional reconstruction from radiographs & electron micrographs: Part III-Description & Application of the convolution method. *Indian J. of Pure & Appl. Phys.* 9:997-1003, 1971.

5. Cormack, A. M.: Representation of a function by its line integrals, with some radiological applications. II. J. Appl. Phys. 35: 2908-2913, 1964.
6. Cha, S. S. and Sun, H.: Tomography for reconstructing continuous fields from ill-posed multidirectional interferometric data. Appl. Opt. 29: 251-258, 1990.
7. Sun, H. and Cha, S. S.: Computational tomographic reconstruction for limited ill-posed interferometric data. Opt. Lasers Eng. 17: 167-178, 1992.
8. Sun, H.: Interferometric tomography for reconstructing three-dimensional flow fields. Ph.D thesis, Univesity of Illinois at Chicago, 1991.

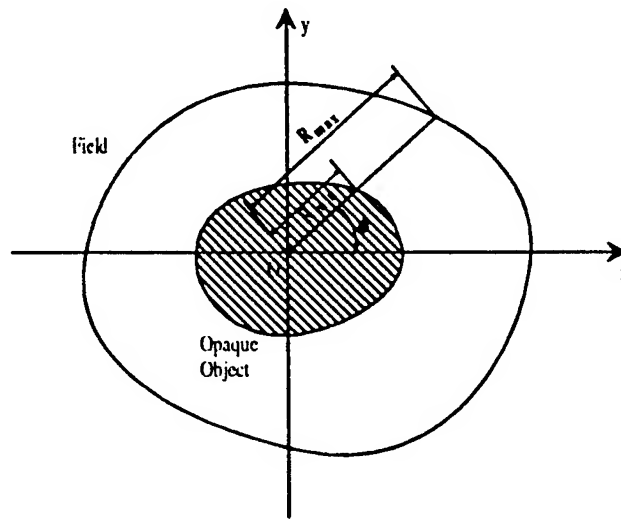


Figure 1. Definition of the R_{min} and R_{max} .

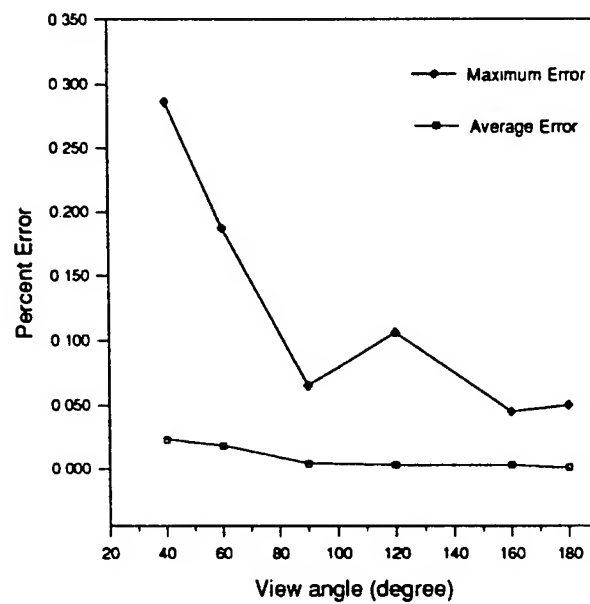


Figure 2. Reconstruction errors: one-hump field with opaque object.

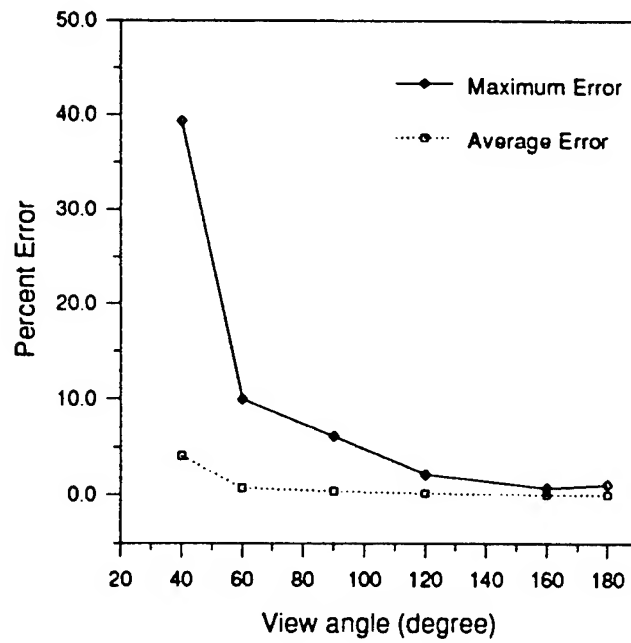


Figure 3. Reconstruction errors: 2-hump-field, opaque object.

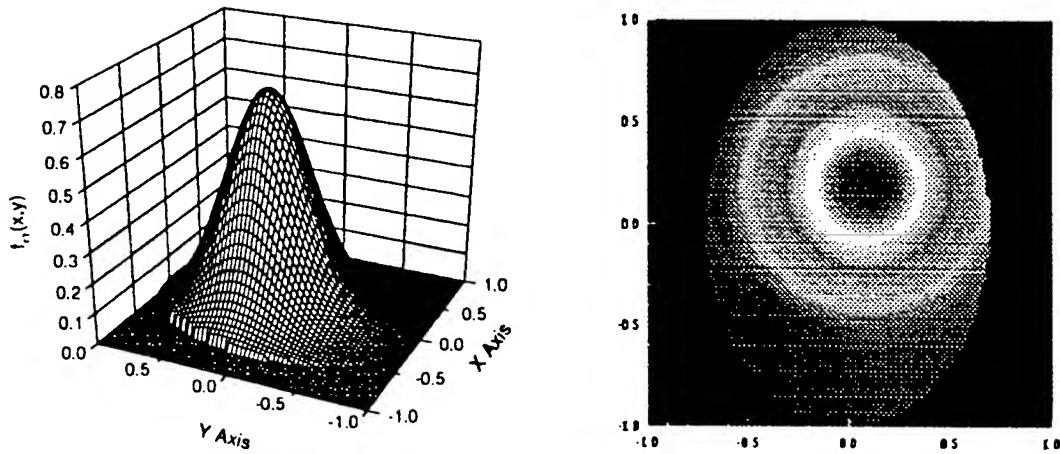


Figure 4. Reconstruction result: one-hump field with no opaque object and the full view angle of 180° .

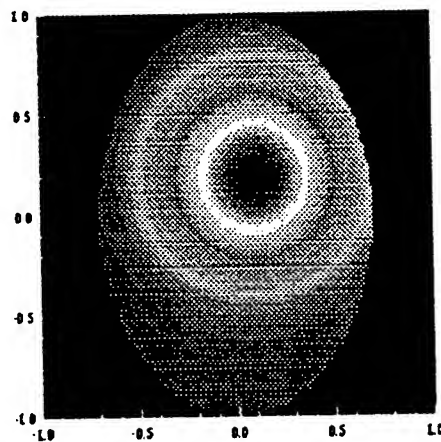
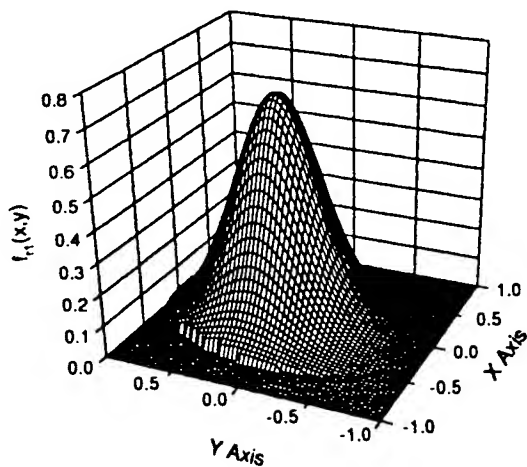


Figure 5. Reconstruction result: one-hump field with no opaque object and a view angle of 40° .

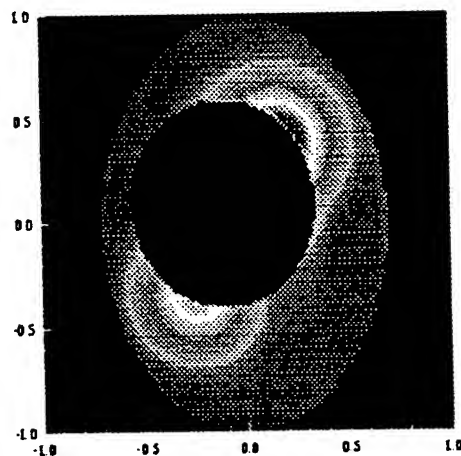
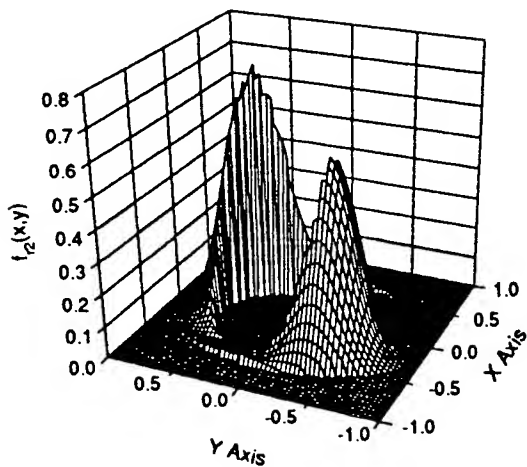


Figure 6. Reconstruction result: two-hump field with opaque object and a view angle of 60° .

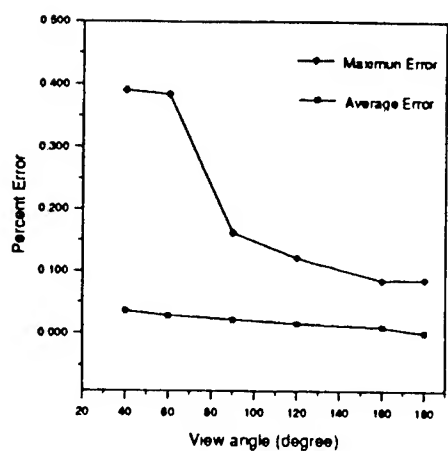


Figure 7. Reconstruction errors: one-hump field with no opaque object.

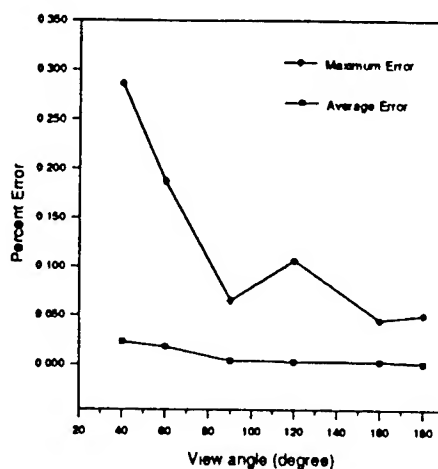


Figure 8. Reconstruction errors: one-hump field with opaque object #2.

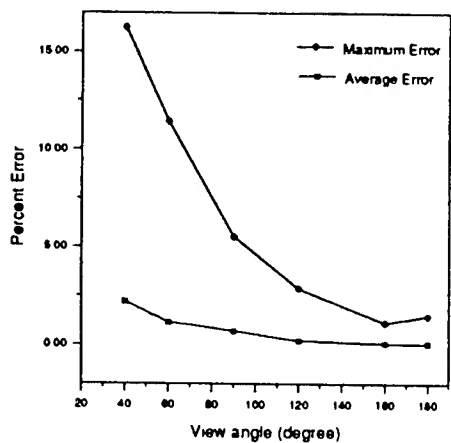


Figure 9. Reconstruction errors: two-hump.

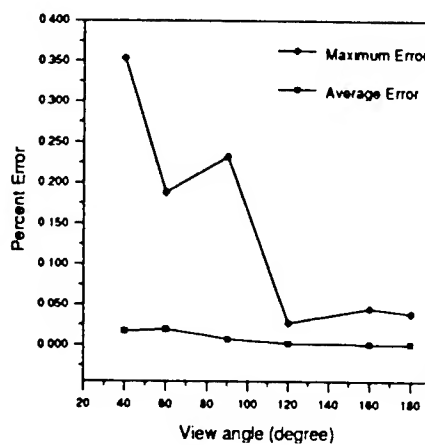


Figure 10. Reconstruction errors: one-hump.

TABLE 1. Reconstruction errors: one hump field with opaque object #2.

View Angle	40°	60°	90°	120°	160°	180°
Max. error (%)	0.286	0.187	0.065	0.106	0.045	0.050
Av. error (%)	0.023	0.018	0.004	0.003	0.003	0.001
(M, N)	(11, 5)	(10, 5)	(11, 6)	(11, 6)	(9, 6)	(10, 8)

TABLE 2. Reconstruction errors: two-hump field with opaque object #2.

View Angle	40°	60°	90°	120°	160°	180°
Max. error (%)	39.304	9.891	6.107	2.133	0.726	1.083
Av. error (%)	4.080	0.737	0.414	0.166	0.036	0.028
(M, N)	(4, 4)	(12, 8)	(12, 8)	(11, 9)	(12, 11)	(12, 12)

TABLE 3. Reconstruction error comparison between the CNBFM and CNBFM+CFM:
two-hump field with opaque object #1.

Max. error (%) Av. error (%)	CNBFM	CNBFM + CFM	Error decreases
90°	8.550	7.003	1.547
	0.956	0.793	0.163
60°	18.294	14.326	3.968
	1.157	1.010	0.147
40°	27.544	22.358	5.186
	3.169	2.085	1.084

TABLE 4. Reconstruction error comparison between the CNBFM and CNBFM+CFM:
two-hump field with no opaque object.

Max. error (%) Av. error (%)	CNBFM	CNBFM + CFM	Error decreases
90°	9.416	7.983	1.433
	1.339	1.457	-0.118
60°	16.550	12.459	4.091
	1.961	1.704	0.257
40°	27.635	22.162	5.473
	3.427	2.975	0.452

TABLE 5. Reconstruction error comparison between the CNBFM and CNBFM+CFM:
two-hump field with opaque object #2.

Max. error (%) Av. error (%)	CNBFM	CNBFM + CFM	Error decreases
90°	6.107	5.050	1.057
	0.414	0.428	-0.014
60°	9.891	7.134	2.757
	0.737	0.640	0.097
40°	39.304	29.796	9.580
	4.080	3.263	0.817

**DYNAMIC NEURAL NETWORKS: TOWARDS CONTROL OF OPTICAL
AIR FLOW DISTORTIONS**

PRINCIPAL INVESTIGATOR: Dr. Judith E. Dayhoff
Institute for Systems Research
University of Maryland
College Park, MD 20742
(w) 301-405-6556
(FAX) 301-314-9920
Email: dayhoff@isr.umd.edu

**Final Report for: AFOSR SUMMER RESEARCH EXTENSION
PROGRAM**

Supported by Air Force Office of Scientific Research, Bolling AFB

March 1999

DYNAMIC NEURAL NETWORKS: TOWARDS CONTROL OF OPTICAL AIR FLOW DISTORTIONS

PRINCIPAL INVESTIGATOR: Dr. Judith E. Dayhoff

Institute for Systems Research

University of Maryland

College Park, MD 20742

Abstract

A neural network with time-delay elements has been shown to be a promising approach to the prediction of optical distortion due to air flow perturbations. Preliminary experiments accomplished during the AFOSR summer research program have indicated that the neural network shows potential for extracting patterns, and could lead to new methods that could be effective for these predictions. If carefully timed with appropriate feedback sensors, neural network output could potentially be used to control an array of tiny mirrors to provide ongoing corrections to distortions caused by turbulent air flows. In experiments performed at the Phillips Laboratory, a jet flow of hot air was produced and measured at multiple downstream positions to determine the amount of optical refraction produced at the interface between the hot air flow and the surrounding cooler air ([MVF95] [MMC⁺95]). A series of measurements were taken over time, to measure the time-dynamic structure of the air jet flow from varying distances from the flow nozzle. Preliminary experiments were based on this data. In this report, we extend our work to include further computations on air flow prediction, increased capabilities of the neural network implementations for prediction, and consideration of a comparison between the statistical method of linear stochastic estimation and neural networks. We also report some intriguing properties of dynamic neural networks, which show promise for future research but are not immediately ready for application. We describe work currently in progress.

1 Overview and Significance

Dynamic neural networks include architectures that imbue the network with properties that are dynamic over time, such as the ability to model and predict time series that are complex or chaotic, the ability to evoke oscillations in the network, and the capability of training the network on oscillations, including complicated oscillations that do not appear to repeat exactly over any observed length of time. Networks that are promising for time series predictions include feed-forward architectures with time-delay elements, such as the time-delay neural network (TDNN) and the adaptive time-delay neural network (ATNN). These networks adapt weights and sometimes time-delays, and have proven highly effective in being trained to produce limit cycle oscillations and chaotic time series ([LDL94], [LDL95]).

We have researched the possibility that neural networks can be used to predict optical wave front distortions in a flow field, where dynamically changing air flows can distort optical signals. The refraction of an optical signal changes dynamically over time because of the continuous motion and turbulence in a warm air flow. Whereas individual points of laser light are refracted by the air flow, which has been experimentally measured, entire images would also be distorted. Our long-term goal is to be able to restore an optical image at a high resolution, by compensating for the distortion in a timely fashion, utilizing the neural network's prediction. In this study, we are predicting refraction of an individual laser light signal with a neural network, so that the neural network prediction can later be used to compensate for the refraction and to stabilize and clarify the reception of the light signal.

An experiment was previously devised and implemented at the Phillips Laboratory to measure the optical refraction of the boundary between a hot air flow and the surrounding cooler air ([MMC+95]). Sensors were configured to detect the change in position of a laser light after it passes through a warm jet air flow. The sensor consisted of a lateral effects detector (LED), which is a dual-axis photodiode that can measure the centroid location of an incident laser beam. The LED works similar to typical photodiodes in that it induces a current proportional to the intensity of the beam. The current is divided among four strip terminals, where current is measured, and the position of the beam is then calculated.

With the LED sensors, data measurements were taken at varied distances and from different orientations. Each data channel reports refraction over a series of time steps. Measurements included data taken at different distances from the origin of the jet flow, in x and y directions, and under varying conditions of forced flow, non-forced flow, and background.

Preliminary experiments were performed in which a neural network was applied to the air flow data. A time history of measurements was used to train the neural network to predict the next measurement in the sequence. A series of preliminary computational training runs were performed in which networks were trained on the first 500 data points and tested on the next 1000 data points. A high performance was attained, with the neural network predictions usually explaining 80-93 % of the variation. These results are highly promising and motivate further studies on neural network prediction of air flow data.

The neural networks used for air flow prediction were feed-forward configurations with three layers. Time-delay elements were included on both layers of weights, causing

inputs to the network to include a time history of data. In addition, time-delays on the hidden-to-output layer allowed the output layer to receive a time history of hidden unit activations. Adaptive training was performed on the weights, and, in some cases, on the time-delays as well. A new training run was done on each data signal. For each data signal, the network configuration was left the same but a different set of initial starting weights was used. Training converged successfully in almost all cases where the data was collected with forced or non-forced air. For background measurements, the neural network often did not converge, as the measurements were extremely small. In a few cases, background recordings were predicted by the neural network, presumably because of ambient perturbations present in the air flow.

This SREP project extends the preliminary experiments to research more situations appropriate to controlling and correcting for realistic optical distortions. The preliminary experiments were limited in the length of data analyzed, the amount of pre-processing, and the timing of data measurements used for analysis. We are addressing these limitations. We also consider here a comparison between traditional statistical methods for time series prediction and the neural network. Lastly, we explore the computational abilities of a neural network that is similar to the time-delay neural network used in our air flow studies, but extends its dynamic properties.

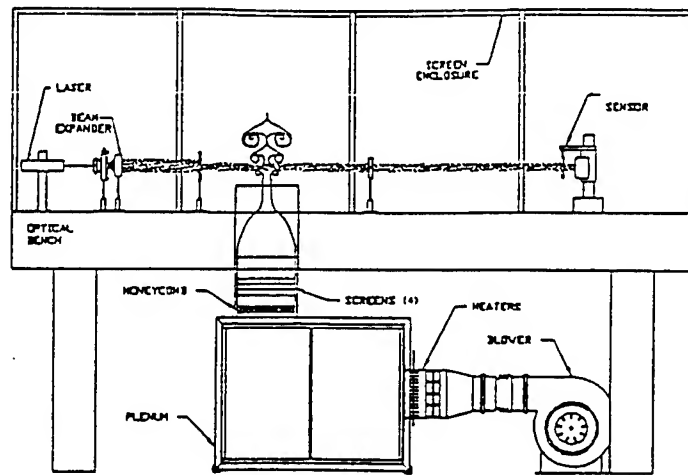


Figure 1: Air jet flow apparatus. Reprinted with permission.

2 Methodology

2.1 Wave Front Sensing

Figure 1 shows the heated air-jet flow generation system. A blower pumps air across a heater and into a plenum chamber, which becomes a source for heated air to flow upwards into a nozzle to form a jet of heated air from a 2.5-cm opening. The air-jet flow then rises vertically, and a laser beam is passed through the heated air as it moves upwards. The sensor receives the laser light and measures the focal spot intensity on a plane, placed perpendicular to the laser light beam. The velocity of the flow center is 4.5 m/s on average, and the average temperature of the air in the jet is approximately 10 degrees C above ambient.

The distance of the sensor above the nozzle can be varied, and a spectrum of data was taken at different distances. Measurements were taken above the nozzle and perpendicular to the air flow. These measurements were taken in the x and y directions in the plane perpendicular to the air flow. The experimental conditions included (1) forced air flow,

(2) non-forced air flow, and (3) background. Thus, for each height above the nozzle, 6 data streams were taken, consisting of two different directions under each of the three air flow conditions.

The sensor was a lateral effects detector (LED), which is comprised of a dual-axis photodiode. The LED induces a current from which the centroid location of an incident laser beam can be calculated. The current is proportional to the intensity of the beam, and is divided among four strip terminals, where current is measured, so that the position of the beam can be calculated [Lun96].

2.2 Neural Networks with Embedded Time-Delays

The time-delay neural network (TDNN) originally proposed by Waibel ([Wai89], [WHH⁺89], [HW92]) employs time-delays on connections and has been successfully applied to phoneme recognition, classification of spatiotemporal patterns ([LDL92c]), and missile discrimination ([LDR95]). In the TDNN architecture, each neuron takes into account not only the current information from its input neurons of the previous layer, but also a certain amount of past information from those neurons due to delays on interconnections. Typically the time delays are evenly spaced over a time interval called the frame window, although arbitrary time delays may be used. Training is done with spatiotemporal patterns, one or more signal channels over time, and the classification of those patterns is reported at each time step by the output layer. After training, the weights are strengthened along those interconnections whose time delays are important to recognition.

The adaptive time-delay neural network (ATNN), which adapts time delays as well

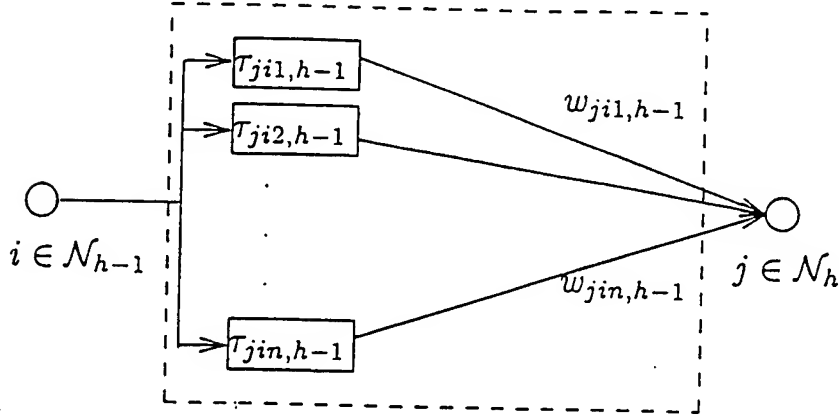


Figure 2: Delay block in a time-delay neural network.

as weights during training, is a more advanced version of the TDNN. The result is a dynamic learning technique for spatiotemporal classification and for time series prediction ([LDL92a]). The ATNN model employs multiple interconnections between each pair of neurons in a feed-forward configuration, with each interconnection having its own weight and time-delay. Both time delays and weights are adjusted according to system dynamics in an attempt to achieve the desired optimization. The adaptation of the delays and weights are derived based on the gradient descent method to minimize the error during training. Processing units do not receive data through a fixed time window, but gather important information from various time delays which are adapted via the learning procedure.

The schematic architecture of the connections from one processing unit to another processing unit of the ATNN is depicted in Figure 2. The configuration of multiple interconnections between a single pair of units, each with its own delay, is called a delay block. Node i of layer $h-1$ is connected to node j of the next layer h , with the connection line k having an independent time delay $\tau_{jik,h-1}$ and synaptic weight $w_{jik,h-1}$.

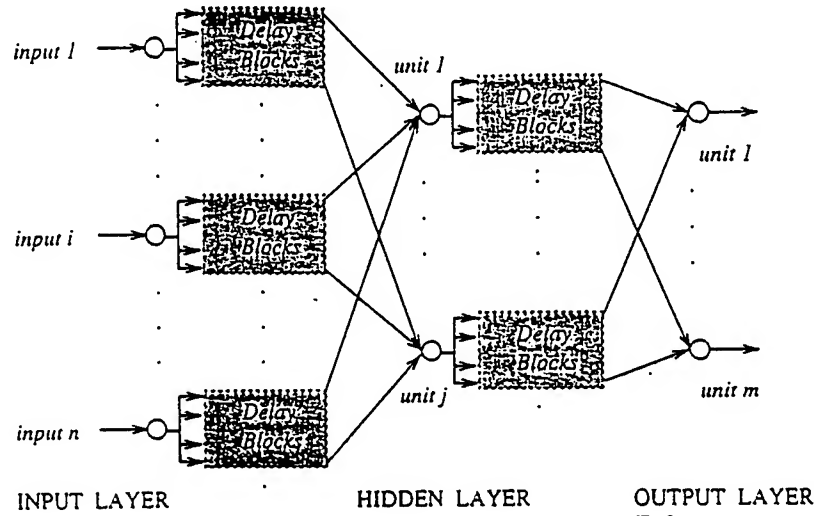


Figure 3: Time-delay neural network depicted as built from delay blocks.

The entire network is constructed by the delay blocks that connect neurons layer by layer, as illustrated in Figure 3. It is not necessary to have the same number of delays for different units in the same layer or the same delay values from different units, because the computation is local for each interconnection. Each connection can have an arbitrary delay value and each pair of neurons can have any number of delayed interconnections.

In the TDNN, the adaptation variables are the weights, and in the ATNN, the adaptation variables are time-delays and weights. Each node sums up the net inputs from the activation values of the previous neurons, through the corresponding time delays on each connection line, that is, at time t_n (e.g., time step n) unit j on layer h receives a weighted sum

$$S_{j,n} = \sum_i \sum_k w_{jik,h-1} a_{i,h-1}(t_n - \tau_{jik,h-1}) \quad (1)$$

where $a_{i,h-1}(t)$ is the activation of unit i in layer $h-1$ at time t . Then the output of node j is governed by a nondecreasing sigmoid function as follows

$$f(S) = 2/(1 - e^{-S}) - 1 \quad (2)$$

where S is the incoming sum, as in (1).

The adaptation of the delays and weights are derived based on the gradient descent method to minimize the error function E during training, where

$$E(t_n) = 1/2[\sum_j (d_j(t_n) - a_{j,h}(t_n))^2] \quad (3)$$

where $d_j(t_n)$ is the target value for output unit j at time t_n .

The weights and time delays are updated step by step proportional to the opposite direction of the error gradient, respectively,

$$\Delta w_{jik,h} = -\eta_1 \delta E(t_n) / \delta w_{jik,h} \quad (4)$$

$$\Delta \tau_{jik,h} = -\eta_2 \delta E(t_n) / \delta \tau_{jik,h} \quad (5)$$

where η_1 and η_2 are the learning rates.

The derivation of this algorithm has been previously addressed ([DD91], [DD93], [LDL92b], [LDL92a]). The learning rules may be summarized as follows

$$\Delta w_{jik,h-1} = \eta_1 \delta_{j,h}(t_n) a_{i,h-1}(t_n - \tau_{jik,h-1}) \quad (6)$$

$$\Delta \tau_{jik,h-1} = -\eta_2 \delta_{j,h}(t_n) w_{jik,h-1} a'_{i,h-1}(t_n - \tau_{jik,h-1}) \quad (7)$$

where

$$\delta_{j,h}(t_n) = (d_j(t_n) - a_{j,h}(t_n)) f'(S_{j,h}(t_n)) \text{ if } j \text{ is an output unit, and}$$

$$\delta_{j,h}(t_n) = \sum_p \sum_q \delta_{p,h+1}(t_n) w_{pqh}(t_n) f'(S_{j,h}(t_n)) \text{ if } j \text{ is a hidden unit.}$$

Characterization and application of the ATNN network has been addressed previously ([LDL95]).

2.3 Dynamic Neural Networks

Neural networks with time-delay elements can learn dynamic behavior by training to produce complex oscillations or limit cycles. Previous research has demonstrated training of TDNN and ATNN networks on a chaotic sequence ([LDL94]) and on limit cycle attractors ([LDL95]). The type of air flow data analyzed in this report has previously been shown to contain similar dynamic fluctuations ([MVF95]). Thus the TDNN and ATNN approach is highly promising. We have also examined an extension to this approach through researching a single-layer recurrent network with random weights which can be altered to evoke chaotic behavior spontaneously without training. Specific patterns applied to this network evoke specific oscillations. Thus, a pattern-to-oscillation map could be used for recognition.

2.4 Preliminary Results

TDNN neural networks were trained on a series of recorded air jet flows. The configuration used was 1 input unit, 3 hidden units, and one output unit. There were two interconnections connecting each pair of neurons in a feed-forward direction. For each pair, one interconnection had no time-delay (e.g., a time-delay of zero), and the other interconnection had a time-delay of one time step. In our initial set of training runs, reported here, the weights were trained and the time-delays were held fixed. The learning rate parameter, η , was started at 0.2, its highest value, and then relaxed linearly to take on lower and lower values over 20,000 iterations of training. The final learning rate value was 0.08. Training was terminated automatically after 20,000 iterations.

The data sets were prepared from more than fifty recordings of air jet flows, taken at varying distances from the flow nozzle. Distances varied from 0.5 diameters to 8.0 nozzle diameters were covered. Conditions of air jet flow included forced air and non-forced air flow, and background noise recordings. Angles at which optical distortion were taken included an x-direction and a y-direction, both perpendicular to the flow of the air.

Each data recording constituted one time series to be learned and predicted by one neural network. The neural network was initialized, by generating small random weights, before training began on each time series. The first 500 data measurements were used as the training set, and the next 1000 measurements were a testing performance set. A verification set was not needed to provide a stopping criterion for the neural network, because the network training was terminated after 20,000 iterations automatically. Future experiments are planned in which a verification set will be used for a stopping criterion, to possibly boost performance. Training was quite successful nevertheless because the relaxation of the η parameter effectively stopped training at relatively favorable times.

Table 1 summarizes the performance attained by the trained neural networks. The performance reported is a computation that reflects the percent variation in the data that is explained by network predictions. First a ratio is computed. The numerator of the ratio is the root-mean-square of the network's error compared to its target values, as follows.

$$R = \sqrt{(1/n) \sum_k (d(t_k) - a(t_k))^2} \quad (8)$$

where $d(t_k)$ is the target value at time t_k , and $a(t_k)$ is the output value at time t_k . The denominator of the ratio is the standard deviation of the target values (e.g., the data

Dist	x/y	1st 500	2nd 500	3rd 500
----	---	---	---	---

Forced:

05	x	75	76	72
05	y	88	88	88
20	x	92	93	92
20	y	87	86	85
30	x	90	88	92
30	y	89	88	89
35	x	92	78	81
35	y	90	91	86
40	x	93	89	90
40	y	89	89	90
50	x	92	88	60
50	y	99	81	82
60	x	92	86	93
60	y	89	88	87
70	x	91	90	92
70	y	0	0	0
80	x	93	79	91
80	y	92	87	87

Non-forced:

35	x	91	84	75
35	y	83	81	86
40	x	93	88	90
40	y	91	84	87
50	x	90	82	80
50	y	87	84	78
60	x	93	66	85
60	y	85	85	86
70	x	0	0	0
70	y	11	0	0
80	x	94	79	86
80	y	92	83	76

Background:

35	x	0	0	0
35	y	0	0	0
40	x	0	0	0
40	y	40	43	46
50	x	93	94	92
50	y	0	0	0
60	x	95	94	94
60	y	43	41	30
70	x	0	0	0
70	y	30	14	41
80	x	79	81	82
80	y	19	15	98

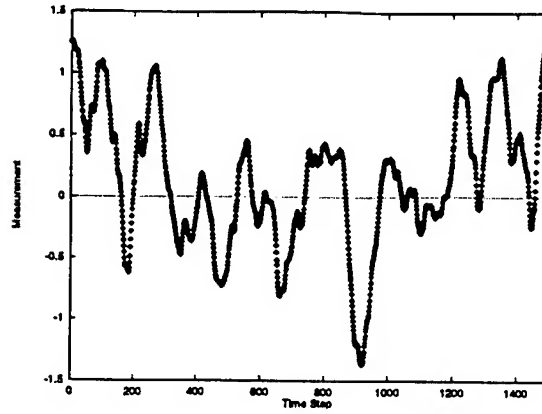
Table 1: Performances of trained neural networks.

measurements).

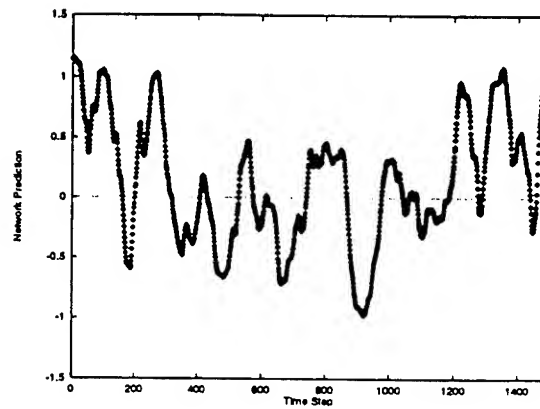
$$S = \sqrt{(1/n) \sum_k (d(t_k) - d_{mean})^2} \quad (9)$$

where d_{mean} is the average target (measurement) value. The ratio is then R/S , and the value $F = 1 - R/S$ reflects the fraction of variation in the data that the network explained through its predictions.

Performance varied between 72% and 93% for forced and non-forced air experiments.



(a)

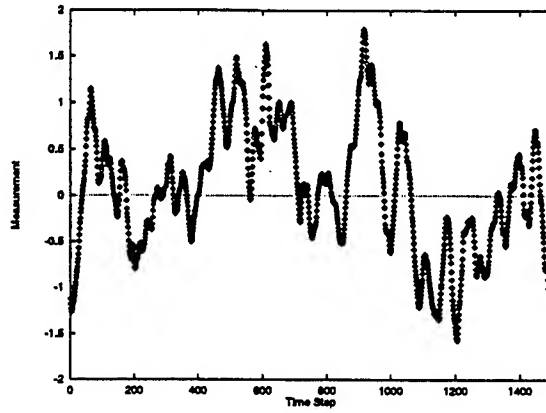


(b)

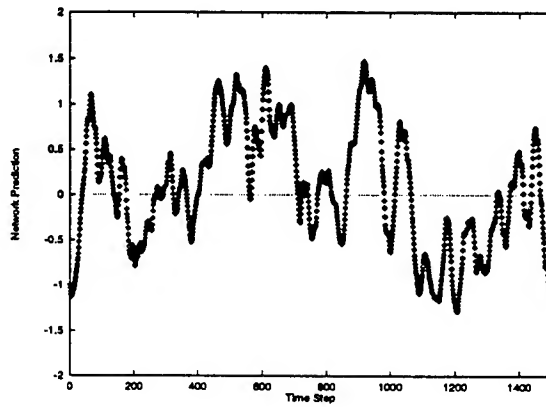
Figure 4: Optical distortion due to hot air flow, forced air measured at 8.0 diameters from nozzle. (a) Measurements. (b) Prediction by trained neural network. 1500 data points in each graph. Orientation: x direction.

The background measurements were typically of much smaller magnitude compared with the air flow experimental data. For most of the background trials, the neural network did not converge to be able to predict the noise. However, the background tends to oscillate irregularly, and in some cases the neural network converged to a prediction of a substantial portion of the measurement variations.

Figure 4 shows results for forced air flow measurements taken at 8.0 diameters from the flow nozzle. Figure 4 (a) shows the first 1500 measurements taken, from the x direction



(a)

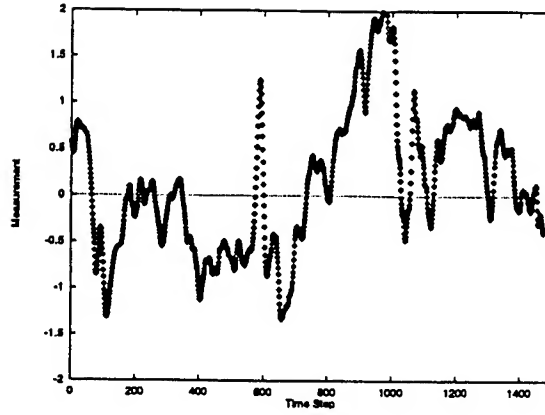


(b)

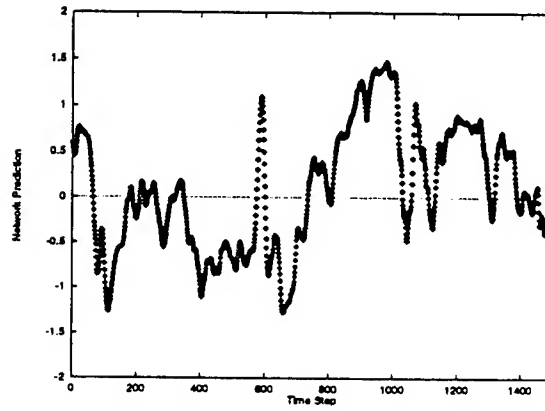
Figure 5: Optical distortion due to hot air flow, forced air measured at 8.0 diameters from nozzle. (a) Measurements. (b) Prediction by trained neural network. 1500 data points in each graph. Orientation: y direction.

orientation, and Figure 4(b) shows the predictions for those measurements provided by the trained neural network. The first 500 of the time steps shown were the training set, and the remainder were the performance testing set. The prediction follows the data extremely well, with the exception that at some of the peaks the prediction does not reach the magnitude of the data. Figure 5 is analogous but for the y direction orientation.

Figure 6 shows results for non-forced air flow measurements taken at 8.0 diameters from the flow nozzle. Figure 6 (a) shows the first 1500 measurements taken, from the



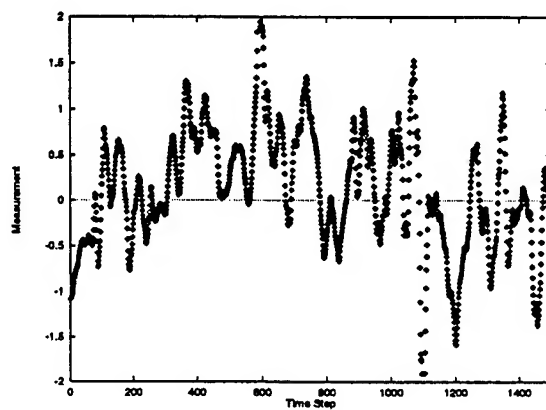
(a)



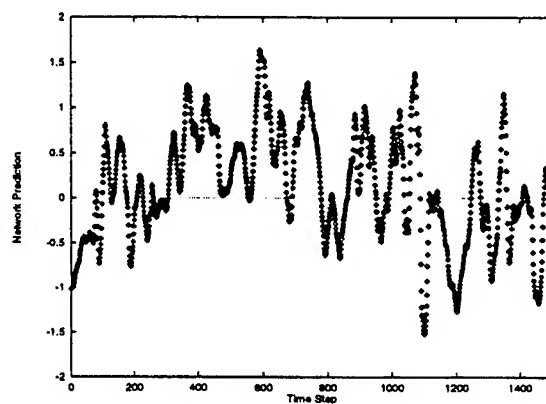
(b)

Figure 6: Optical distortion due to hot air flow, non-forced air measured at 8.0 diameters from nozzle. (a) Measurements. (b) Prediction by trained neural network. 1500 data points in each graph. Orientation: x direction.

x direction orientation, and Figure 6(b) shows the predictions for those measurements provided by the trained neural network. The first 500 of the time steps shown were the training set, and the remainder were the performance testing set. The prediction follows the data extremely well, with the exception that at some of the peaks the prediction does not reach the magnitude of the data. Figure 7 is analogous but for the y direction orientation.



(a)



(b)

Figure 7: Optical distortion due to hot air flow, non-forced air measured at 8.0 diameters from nozzle. (a) Measurements. (b) Prediction by trained neural network. 1500 data points in each graph. Orientation: y direction.

3 Research Results

The primary focus of this research is to predict air flow distortions in as realistic a fashion as possible. To this end, we wish to extend our experiments to deal with new considerations that will arise when distortions are corrected by an array of tiny mirrors (MEM). Extension of previous experiments is thus underway, and includes the use of larger data sets and varied timing schedules, a comparison of the performance of the neural networks to other statistical methods, and additional research on alternative dynamic network architectures and their computational capabilities.

Initial neural network runs were performed on data with 500 successive points. Experiments on longer data sets are underway, to test the performance observed in the preliminary runs. The longer data sets consist of up to 45,000 points. Each data set will be divided into a training set, a test set, and a verification set. The test set will be used to decide when to stop training the neural network, and the verification set will be used for a performance report.

The rate of data-taking is 10 kiloHertz. Thus the 45,000 data points take 4.5 seconds. The ultimate application for this work is in the control of an array of tiny mirrors. We estimate that the mirrors can be adjusted at a rate of about 2 kiloHertz, or once for every 5 data points measured. Thus a time-series prediction scheme must be devised and tested so that the maximum rate of data is exploited, but there can be no new data used after the command to adjust a mirror is issued. Thus, the time series prediction should be tested at 5 steps ahead.

We have completed software that provides pre-processing of the data to set up ex-

periments with n -step-ahead predictions. The user can choose how many steps ahead to train the neural network to predict. Previous experiments were limited to one-step-ahead prediction. Additional runs have been done at a 5-step-ahead interval, and performance was still surprisingly good. For example, a training run was done in which trained networks explained 81 % of the variance in the training set, and 74 % of the variance in the performance set. The data for this run was taken at 8 diameters from the nozzle, the longest distance and thus likely the hardest to predict.

Other timing considerations can impact on how a neural network should be trained to fit into a controller structure for an array of tiny mirrors. For example, it may be beneficial to have sparse sampling of the data for n -step ahead predictions, where $n > 1$. For example, a network could be trained on data that is sampled every 5 time steps if a 5-step ahead prediction is to be done. We aim to perform experiments to find out what is the best timing of the data to be used in training the needed predictors. The adaptive time-delay neural network (ATNN) developed in software by the P.I. is an auspicious technique for using past data samples in prediction. The ATNN allows time delays to be incorporated in the neural network, so that past values of the time series data can be used during prediction. Furthermore, the ATNN automatically evaluates whether the particular time delays for the past values are the best, or whether the time delays should be shifted to optimize performance.

New software has been developed to consider the difference between two different components of the prediction - the value of the previous data sample, and the difference between the previous data sample and the next data sample. Thus, we can test the neural network's predictive power of the two components separately. When the neural network

was trained to predict the next air flow distortion value in a time series of data, the network first captured the value of the previous data sample in its prediction of the next data sample. Since the previous data sample may be available in a real-life situation, we can subtract that away and train the neural network on the difference between the previous sample and the upcoming sample. Then, the neural network's predictive power will be most challenged. Our new software reports the predictive power of using the previous data sample as the prediction, and allows us to compare this to the neural network's prediction. Additional pre-processing software prepares the data so that the neural network can be trained on the difference between previous and upcoming values alone.

Additional experiments that include different training criteria and schedules are desirable and will be done in the future if time permits. These experiments would include variations in performance and training criteria, such as training to minimize the absolute error, varying the stopping criteria, varying the lengths of the training and verification sets, and varying the neural network configurations.

3.1 Comparison of neural networks to traditional statistical methods for time series prediction.

It is important to compare the performance of the neural network with traditional statistical methods for time series. Our aim is to find the best method(s) for prediction rather than to insist that a particular pre-specified approach be followed. Ideally, the best time series prediction method that is not a neural network would be used in the comparison,

and then its performance could be benchmarked against a neural network approach.

Other investigations have explored the approach of linear stochastic estimation (LSE) to air flow predictions. This technique relies on several additional measurements being done in the air flow simultaneously to the prediction that is performed. Results have been reported to be very good ([Lun96], [LTM97], [TMP⁺98]). It is important to note that this technique relies on additional information that was not available to the neural networks trained in this project. The additional data consists of several time series of temperature measurements in the turbulent air flow. A new experiment could be tailored to compare the neural network more directly to the LSE approach by giving the neural network the same additional temperature measurements. We could then test whether the neural network can increase the performance of the current LSE method, or whether adding a neural network to the LSE method would increase performance.

In a realistic real-life situation, however, these additional temperature measurements may not be possible to get. Then, the neural network could be the best technique for prediction because it does not require additional data channels before a prediction can be made. However, in a real application, any data that is possible to obtain should be made available to the neural network.

3.2 Alternative dynamic network architectures and their computational capabilities.

Neural networks with time-delay elements are used in this study to do time series prediction. Previously, these networks have been shown to learn dynamic behavior by training

to produce complex oscillations or limit cycles. Training of TDNN and ATNN networks has been demonstrated on a chaotic sequence ([LDL94]) and on limit cycle attractors ([LDL95]). The type of air flow data analyzed in this report has previously been shown to contain similar dynamic fluctuations ([MVF95]). Thus the TDNN and ATNN approach is highly promising.

We would like to explore the possibility that other architectures for dynamic neural networks would be promising for selected applications. We are currently researching a single-layer recurrent network with random weights which can be altered to evoke chaotic behavior spontaneously without training. We are considering the problem of how to utilize the attractors (oscillations) in this dynamic neural network to perform pattern recognition and other computational tasks ([PD95]).

The network is set up as follows. A random network is constructed with sparse interconnections in a single layer of neurons. A multiplier g can be applied to all of the weights at the same time and, when g is increased, chaotic behavior occurs. An external pattern is then applied to the network as a fixed bias, and a pattern-to-oscillation map can be constructed. Figure 8 illustrates an oscillation from a 64-neuron network after an external pattern is applied. The network is chaotic in the absence of the external pattern.

The neural units are simple biologically-inspired nodes, performing a weighted sum followed by a nonlinear squashing function f .

$$a_j(t+1) = f(\sum_{i=1}^N g w_{ji} a_i(t)) + \alpha e_i \quad (10)$$

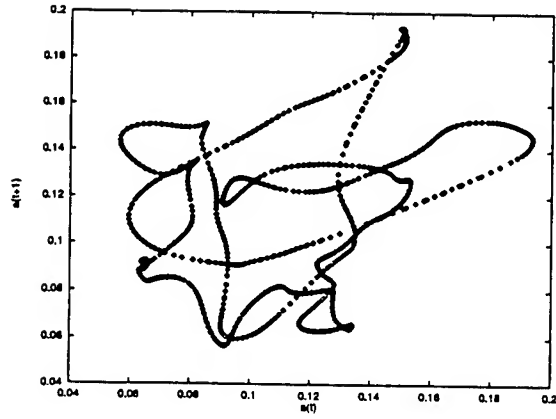
where g in (11) is the multiplier for all weights in the network, and the weights are

randomly assigned with variation $1/k$ where k is the number of randomly selected inputs to each node. E is the fixed external pattern applied as a bias to the network, and α_i is the strength with which the external pattern is applied. This network has previously been studied and theoretically considered ([DCQS93], [DCQS95], [QDS95], [CDQS94], [SCS88]).

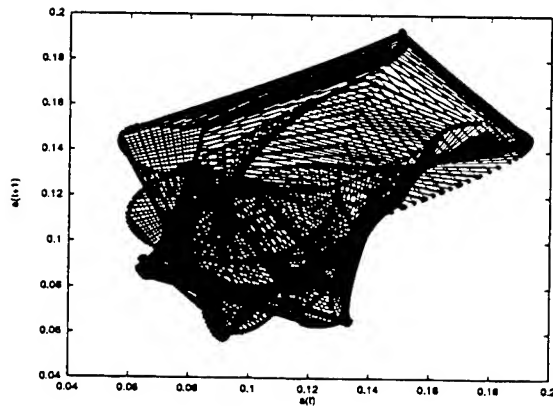
The P.I. has developed a method for evoking a pattern - to - oscillation map for this network, where the oscillations are constricted to be either a finite-state (n -state) oscillation or a limit cycle. First, a network with no external pattern ($E=0$) is applied, and g is increased to produce chaotic behavior. Then an external pattern E is applied. Transients are passed by iterating the network through (11) above. If the evoked attractor satisfies the oscillation criterion, then the evoked oscillation is the result of the pattern-to-oscillation map for pattern E . If the evoked attractor is too chaotic, then the strength α must be increased for pattern E . If the evoked attractor is a fixed point, then the strength α must be decreased to produce more complex dynamics. Through an algorithm for making successive adjustments to α , the pattern-to-oscillation map can be constructed uniquely for all patterns, given the initial chaotic network. This algorithm has been proposed by the P.I. and constitutes an advance in the development of new dynamic neural networks.

4 Impact and Future Directions

A set of preliminary runs were performed on neural network modeling of turbulent air flow phenomena. Neural networks with time-delay elements were trained to predict the amount of optical distortion caused by the flow of warm air out of a nozzle, in an environ-



(a)



(b)

Figure 8: Map of a neural network oscillation. The network had 64 neural units, with 16 randomly assigned inputs to each unit. (a) Plot of average activation $a(t)$ versus $a(t+1)$, at successive time steps. (b) The same points are plotted as in (a), but successive points are connected to illustrate that the limit cycle is comprised of a dense set of points along a closed curve. One thousand transient steps were skipped before the pattern was applied, then another thousand transient steps were skipped after the pattern was applied. The graphs show the next thousand points.

ment where the air is cooler and optical distortion arises from refraction at the boundary between warm and cooler air. Neural network experiments show that the networks converged to attain considerable predictive power.

Closer examination of the results indicated that some traditional statistical time series methods may perform well on the predictive task attempted by the neural networks. LSE methods performed well, but required additional data to be taken during the experiment.

The ultimate aim of this type of research is to use neural networks and time series predictions to control an array of tiny mirrors that will correct for optical distortion from the atmosphere. A key part of such a controller is a model that predicts upcoming distortion values, so that a command can be issued to individual mirrors to compensate for the movement of optical signals across the grid, due to air distortion.

We also extend our research on dynamic neural networks. The neural networks used in this study contain time- delay elements and can be trained on dynamically changing data. They adapt time-delays to optimize the information used from the past for the neural network prediction.

Alternative architectures for dynamic neural networks show flexibility in a pattern-to-oscillation map and will have increased capacity compared to static neural networks. These results provide insight into the potential computational capabilities of dynamic neural network computations.

References

- [CDQS94] B. Cessac, B. Doyon, M. Quoy, and M. Samuelides. Mean-field equations, bifurcation map and chaos in discrete time neural networks. *Physica D*, 74:24–

44, 1994.

- [DCQS93] B. Doyon, B. Cessac, M. Quoy, and M. Samuelides. Control of the transition of chaos in neural networks with random connectivity. *International Journal Bifurcation and Chaos*, 3(2):279–291, 1993.
- [DCQS95] B. Doyon, B. Cessac, M. Quoy, and M. Samuelides. Mean-field equations, bifurcation map and chaos in discrete time, continuous state, random neural networks. *Acta Biotheoretica*, 43:169–175, 1995.
- [DD91] S. P. Day and M. Davenport. Continuous-time temporal back-propagation with adaptive time delays. Neuroprose archive, Ohio State University. Accessible on Internet via anonymous ftp on archive.cis.ohio-state.edu, in pub/neuroprose/day.tempora.ps August, 1991., 1991.
- [DD93] S. P. Day and M. R. Davenport. Continuous-time temporal back-propagation with adaptive time delays. *IEEE Trans. on Neural Networks*, 4(2):348–354, March 1993.
- [HW92] P. Haffner and A. Waibel. Multi-state time delay neural networks for continuous speech recognition. In S. J. Hanson J. E. Moody and R. P. Lippmann, editors, *Advances in Neural Information Processing Systems*, volume 4, pages 135–142, Denver 1992, 1992. Morgan Kaufmann, San Mateo.
- [LDL92a] D.-T. Lin, J. E. Dayhoff, and P. A. Ligomenides. Adaptive time-delay neural network for temporal correlation and prediction. In *Intelligent Robots and*

Computer Vision XI: Biological, Neural Net, and 3-D Methods, Proc. SPIE, volume 1826, pages 170–181, Boston, November, 1992.

- [LDL92b] D.-T. Lin, J. E. Dayhoff, and P. A. Ligomenides. A learning algorithm for adaptive time-delays in a temporal neural network. Technical Report SRC-TR-92-59, Systems Research Center, University of Maryland, College Park, Md 20742, May 15 1992.
- [LDL92c] D.-T. Lin, J. E. Dayhoff, and P. A. Ligomenides. Trajectory recognition with a time-delay neural network. In *International Joint Conference on Neural Networks*, volume 3, pages 197–202, Baltimore, 1992. IEEE, New York.
- [LDL94] D.-T. Lin, J. E. Dayhoff, and Panos A. Ligomenides. Prediction of chaotic time series and resolution of embedding dynamics with the ATNN. In *World Congress on Neural Networks*, volume 2, pages 231–236, San Diego, CA, 1994. INNS Press, New York.
- [LDL95] D.-T. Lin, J. E. Dayhoff, and Panos A. Ligomenides. Trajectory production with the adaptive time-delay neural network. *nn*, 8(3):447–461, 1995.
- [LDR95] D.-T. Lin, J. E. Dayhoff, and C. L. Resch. Target discrimination with neural networks. Technical Report ISR-TR-95-54, Institute for Systems Research, University of Maryland, College Park, MD 20742, 1995.
- [LTM97] T. Luna, C. R. Truman, and B. S. Masson. Linear stochastic estimation of optical beam deflection through a heated jet. Technical Report AIAA 97-

0072, American Institute of Aeronautics and Astronautics, 1801 Alexander Bell Dr., Suite 500, Reston, VA 20191, 1997.

- [Lun96] T. G. Luna. Linear stochastic estimation of optical beam deflection through a heated round turbulent jet. Master's thesis, University of New Mexico, Department of Mechanical Engineering, Albuquerque, NM, 1996.
- [MMC⁺95] L. McMackin, B. Masson, N. Clark, K. Bishop, R. Pierson, and E. Chen. Hartmann wave front sensor studies of dynamic organized structure in flow-fields. *AIAA Journal (American Institute of Aeronautics and Astronautics)*, 33(11):2158–2164, 1995.
- [MVF95] L. McMackin, D. G. Voetz, and J. S. Fender. Chaotic attractors in the transition region of an air-jet flow. ., 1995.
- [PD95] P. J. Palmadesso and J. E. Dayhoff. Attractor locking in a chaotic network: stimulus patterns evoke limit cycles. *Proceedings of World Congress on Neural Networks (WCNN)*, 1:254–257, 1995.
- [QDS95] M. Quoy, B. Doyon, and M. Samuelides. Dimension reduction by learning in a discrete time chaotic neural network. *Proceedings of World Congress on Neural Networks (WCNN)*, 1:300–303, 1995.
- [SCS88] H. Sompolinsky, A. Crisanti, and H. J. Sommers. Chaos in random neural networks. *Phys. Rev. Let.*, 61(3):259–262, 1988.
- [TMP⁺98] C. R. Truman, L. McMackin, R. E. Pierson, K. P. Bishop, and E. Y. Chen. Open-loop control of compensation for optical propagation through a tur-

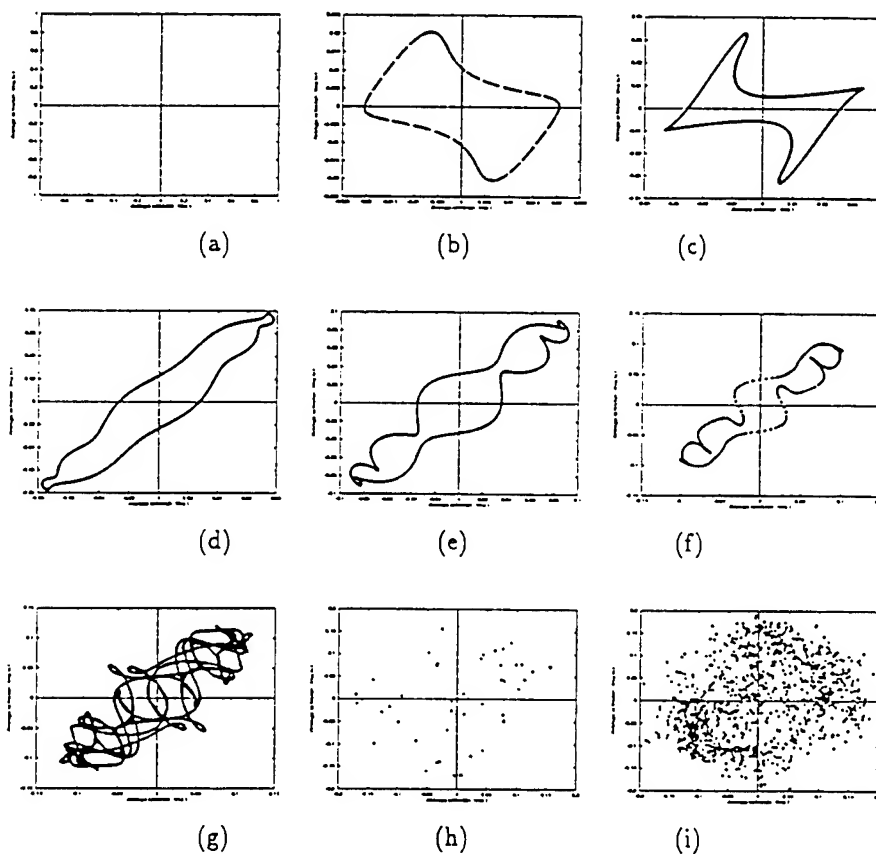
bulent shear flow. Technical Report AIAA 98-2932, American Institute of Aeronautics and Astronautics, 1801 Alexander Bell Dr., Suite 500, Reston, VA 20191, 1998.

[Wai89] A. Waibel. Modular construction of time-delay neural networks for speech recognition. *Neural Computation*, 1:39-46, 1989.

[WHH⁺89] A. Waibel, T. Hanazawa, G. Hinton, K. Shikano, and K. Lang. Phoneme recognition using time-delay neural networks. *IEEE Trans. on Acoust., Speech, Signal Processing*, 37(3):328-339, 1989.

Appendix

Figures 9-13 show some example calculations resulting from the dynamic network described in Section 3.2.



Progression from fixed point to chaos in a random (64,16) network. The horizontal axis is average activation at time $t + 1$, $a(t + 1)$, and the vertical axis is average activation at time t , $a(t)$. (a) $g = 0.9$ (b) $g = 1.0$ (c) $g = 1.1$ (d) $g = 1.2$ (e) $g = 1.3$ (f) $g = 1.4$ (g) $g = 1.5$ (h) $g = 1.6$ (i) $g = 1.7$

Figure 9

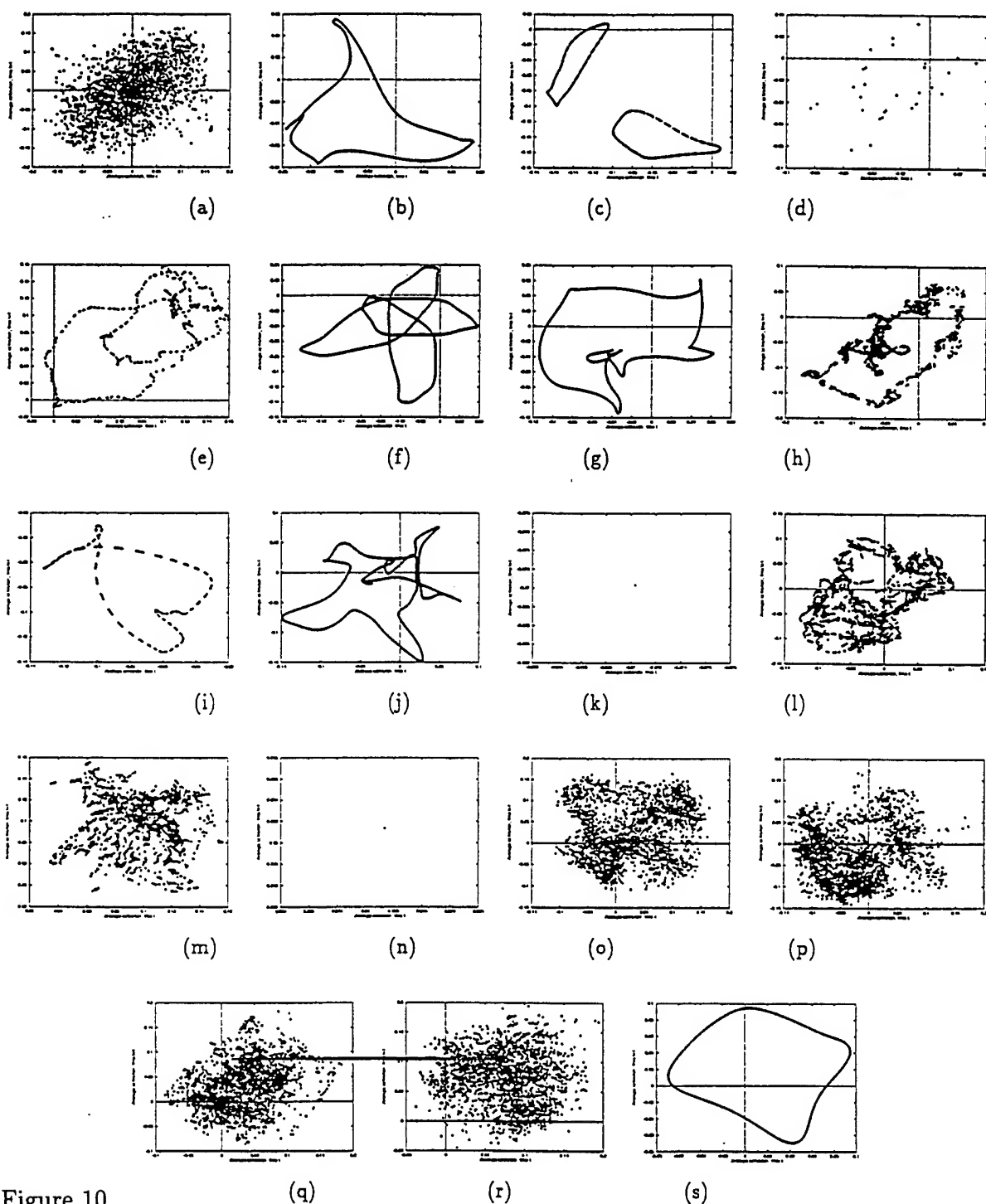


Figure 10

A chaotic network has 18 different patterns applied, with different results on the dynamics. (a) Activity of the chaotic network, before an external pattern is applied. Multiplier g is set just above the value where chaotic activity occurs. (Here, $g = \dots$) (b-s) Activity of the network after 18 different patterns were applied. Evoked dynamics is highly unique. Most graphs show recognizable low-order dynamics - limit cycles and n-state oscillations - but some show chaotic (irregular) behavior and others show fixed points only. Graphs have the horizontal axis as average activation at time $t+1$, $a(t-1)$, and the vertical axis as average activation at time t , $a(t)$. The 18 patterns were generated from a uniform random distribution $[-1, 1]$.

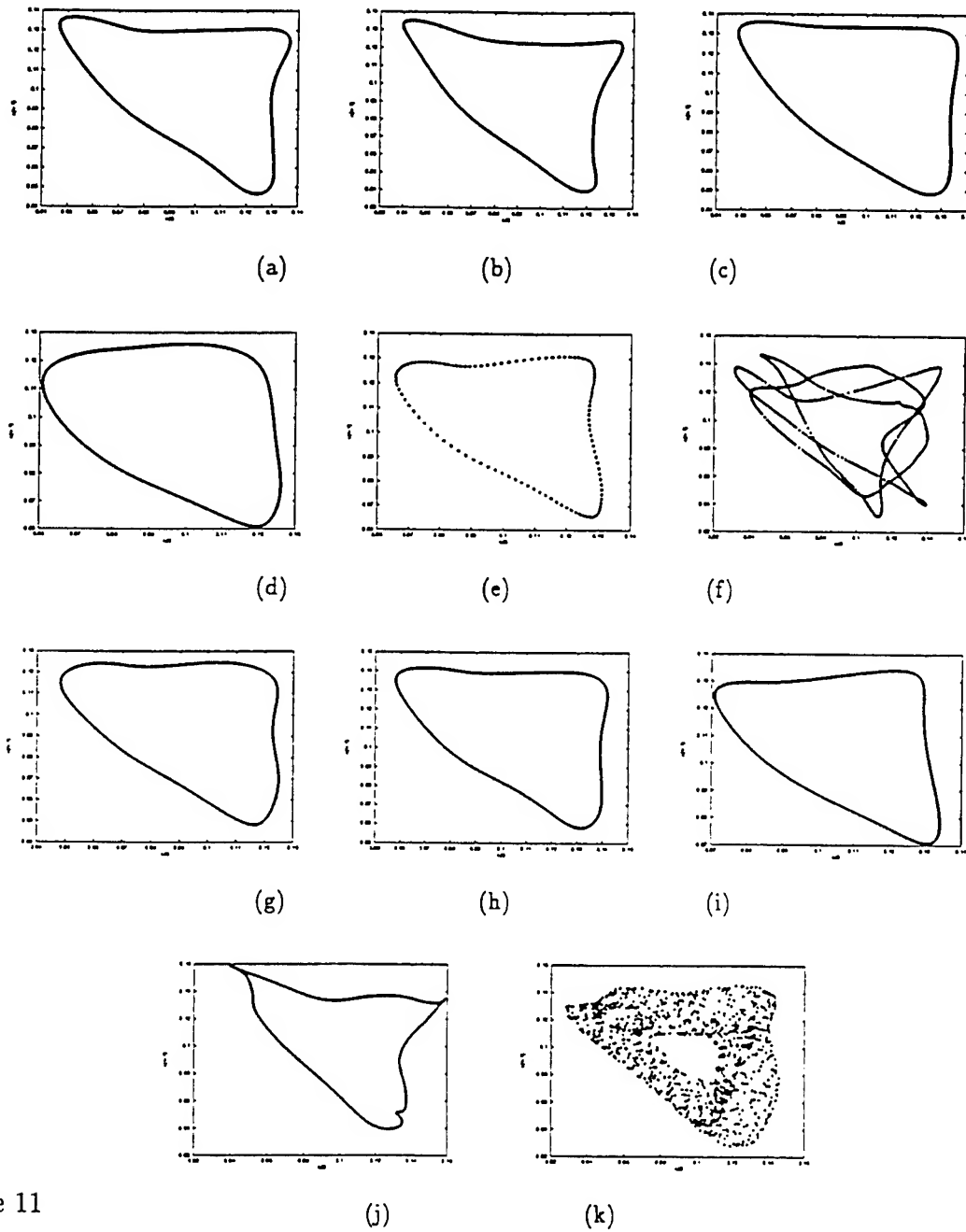


Figure 11

A chaotic network has different external patterns applied, each at strength $\alpha = 1.6$. (a) The base pattern, with 64 entries, each from a uniform random distribution (-1:1). (b-k) The base pattern with 5 % noise added, to make 10 different variations of the pattern.

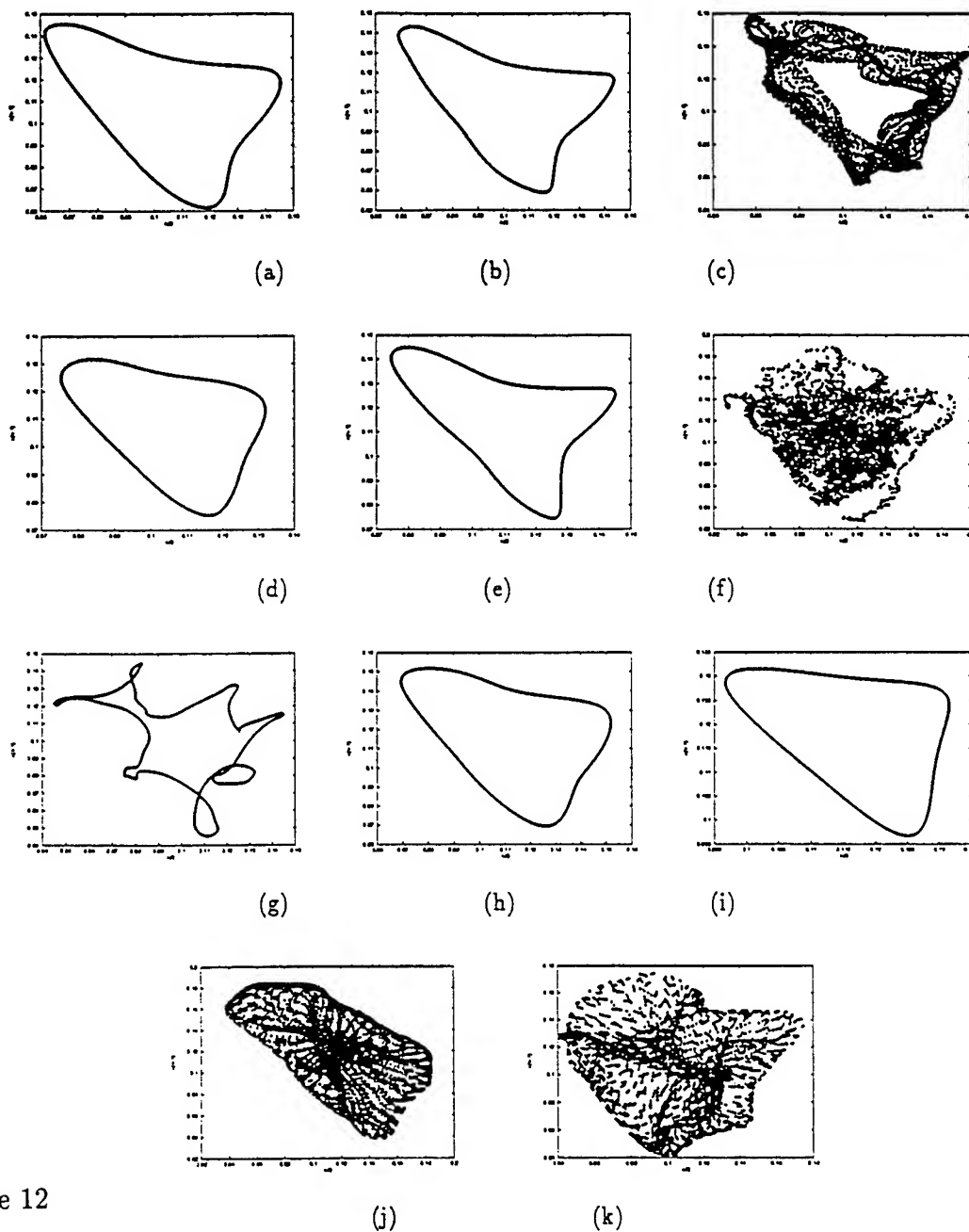


Figure 12

The base pattern (a) and its ten variations (b-k). Here the pattern strength (α was 1.4, a decrease compared with Figure 14).

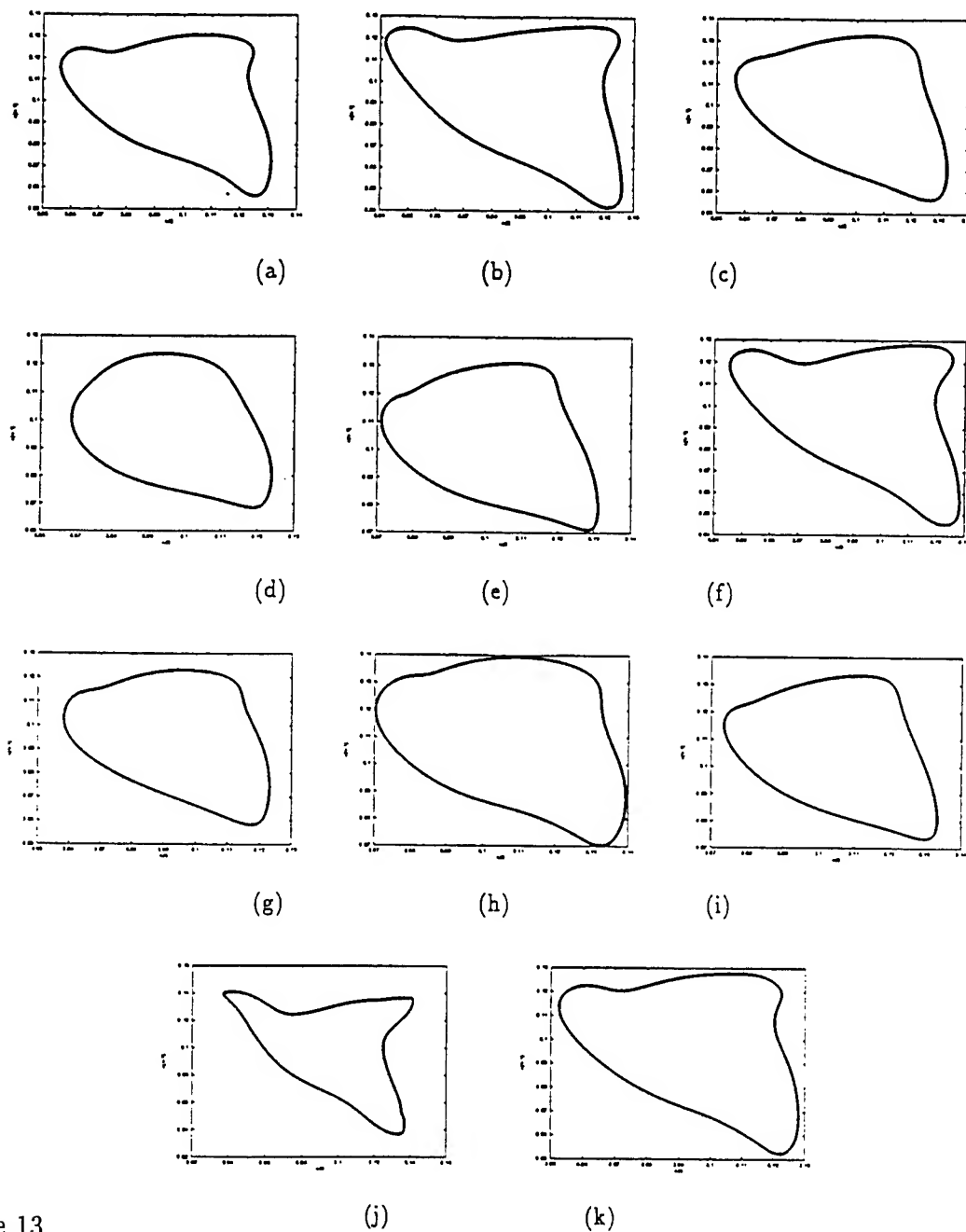


Figure 13

The base pattern (a) and its ten variations (b-k). Here the pattern strength α was 1.8, an increase compared with Figure 14. The variation between the evoked attractors is less compared with Figure 14, where α was 1.6.

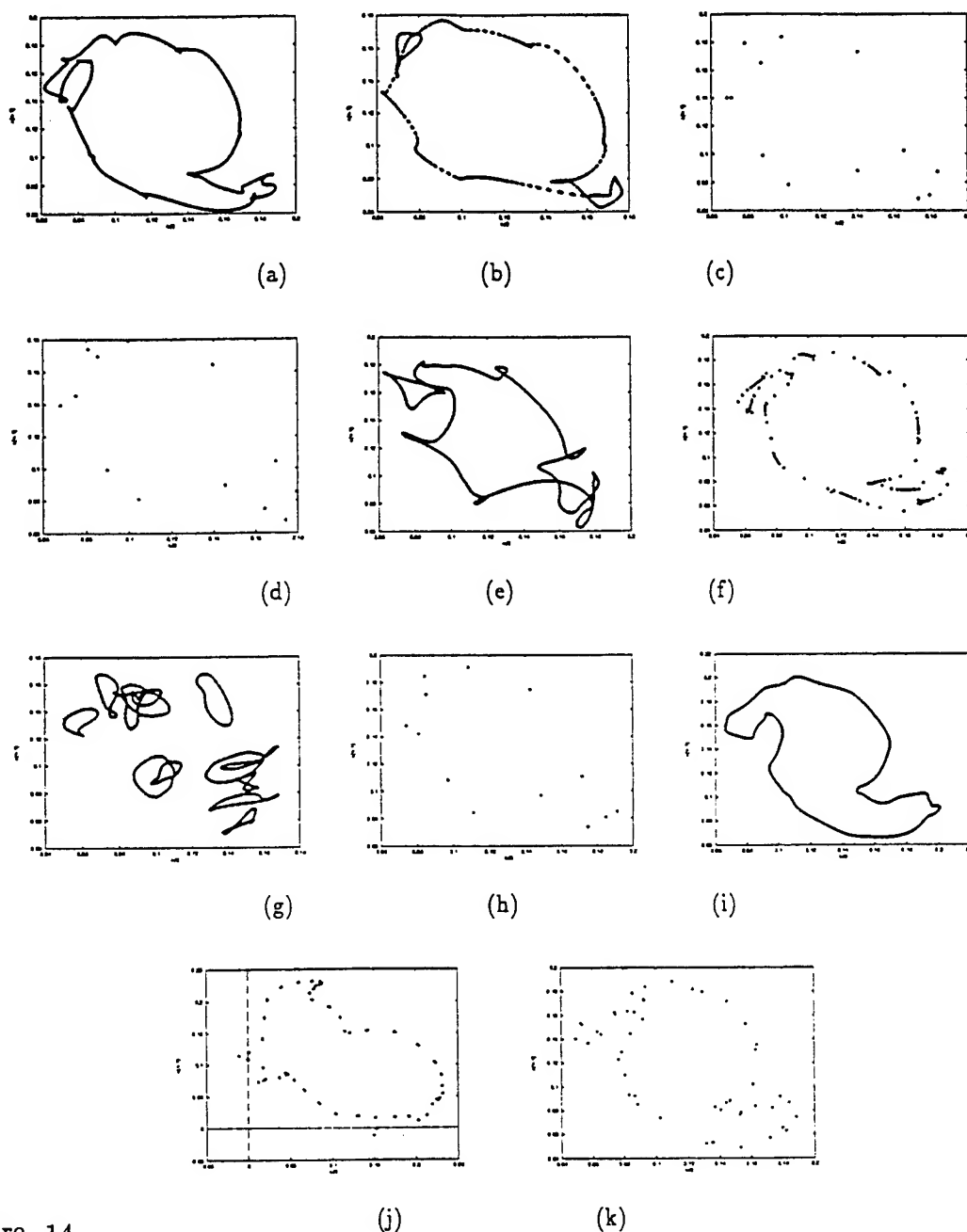


Figure 14

The base pattern (a) and its ten variations (b-k). Here the pattern strength α was 1.2, a large decrease compared with Figure 14. The variation between the evoked attractors is considerably higher compared with Figure 14, where α was 1.6.

COMPUTATIONAL EVALUATION OF OPTICAL SENSORS

Ronald R. DeLyser
Associate Professor of Electrical Engineering
Department of Engineering

University of Denver
2390 S. York St.
Denver, CO 80241

Final Report for:
Summer Research Extension Program
Phillips Laboratory

Sponsored by:
Air Force Office of Scientific Research
Bolling Air Force Base, DC

December, 1997

COMPUTATIONAL EVALUATION OF OPTICAL SENSORS

Ronald R. DeLyser
Associate Professor of Electrical Engineering
Department of Engineering
University of Denver

Abstract

The Temporal Electromagnetic Analysis Code (TEMAC3D) and the Temporal Scattering and Response (TSAR) code, two Finite Difference Time Domain (FDTD) codes; and, Ansoft μ WaveLab, a Finite Element Method (FEM) code are compared using models of the Celestron-8 telescope and a satellite optical sensor. Each code has attractive features which are suited to large, open cavity problems. They also have requirements that limit the type and amount of output data or increase the computational expense of solving these types of problems. This report will show the relative merits and disadvantages of these software packages.

The TSAR FDTD solver was installed at the University of Denver on an IBM RS6000, however, the rest of the TSAR suite consisting of Anastasia (the mesh generator), Image (the mesh viewer) and all of the post processing packages were not installed due to incompatibility of the installation package with the IBM RS6000, and subsequent lack of support from Lawrence Livermore National Laboratory (LLNL).

COMPUTATIONAL EVALUATION OF OPTICAL SENSORS

Ronald R. DeLyser

Introduction

This report documents a continuation of other projects reported in [1], [2] and [3]. It is also complimentary to another study funded by Phillips Laboratory and reported in [4]. The objective of those studies was to determine the electromagnetic response of a Celestron-8 telescope and a satellite optical sensor using numerical analyses. The analyses used the Method of Moments (MoM), the Finite Element Method (FEM), and the Finite Difference Time Domain (FDTD) method. The programs used were CARLOS-3D [5] (MoM), the Hewlett Packard High Frequency Structure Simulator (HFSS), a commercially available FEM program, and the Temporal Electromagnetic Analysis Code (TEMAC3D) [6] an FDTD code. The inherent problems with CARLOS-3D [3] [7] and the computational expense of HP HFSS [3] [8] suggested that the FDTD method [9] may be more suited to these studies. TEMAC3D, a FORTRAN program that is based on the three dimensional implementation of the FDTD method used for open problems (structures that are surrounded with open space), was used to analyze models of the Celestron-8 telescope and the optical satellite sensor.

From the experience gained solving large problems with all of these codes, some of the conclusions that were reported in [1] and in [10] were: (1) The FEM in general is not an efficient method for evaluating frequency response of large complex cavities. It can, however, be used to verify testing and other calculations for radiation problems at specified frequencies. Still, large computational resources are necessary for HP HFSS. Models of reasonable fidelity are limited to relatively low frequencies. (2) Another commercially available FEM package was identified, Ansoft Corporation's μ WaveLab, which can take advantage of symmetry, has the capability of using second order elements, seeded meshing and can do the radiation problem with symmetry. (3) An FDTD code with the capabilities of perfect magnetic and perfect electric boundaries would allow the user to specify ground planes or apply symmetry to problems, thus reducing computational requirements. This capability would also allow the modeling of the sensor on a ground plane.

While modifications of TEMAC3D to achieve the capabilities of the desired FDTD code were beyond the scope of the present study, evaluation and minor modifications of the Temporal Scattering and Response (TSAR) code, another FDTD program for open problems from Lawrence Livermore National Laboratory (LLNL) were done. The capabilities that TSAR had beyond those contained in TEMEC3D were implementation of perfect magnetic and perfect electric boundaries. Results of scattering problems using these

capabilities in TSAR are reported here and compared to the TEMAC3D results. Unfortunately, there were problems with TSAR for radiation simulations so that no results can be presented.

Installation of Software at The University of Denver

Prior to doing the analysis of the Celestron-8 and the optical sensor, certain pieces of software were identified for installation at The University of Denver. These were BRL-CAD, the TSAR software suite (the TSAR FDTD solver, Anastasia and Image) and Ansoft's μ WaveLab.

Problems with installation of BRL-CAD and the TSAR suite on the AIX based IBM RS6000s came quickly. Installation of BRL-CAD was eventually accomplished by Bob Strausser of the SURVICE Engineering Company. The installation of the TSAR suite was abandoned because of installation problems and the lack of support from LLNL. The personnel who were once at LLNL and who created and supported TSAR are no longer there. Therefore, a modified version of the TSAR FDTD solver was acquired from Ernie Baca and Jeff MacGillivray at Sandia Labs. The installation of that version was successful. However, use of Anastasia (the mesh generator) and Image (the mesh viewer) on a Sun workstation located at Phillips Laboratory must continue.

There were no problems installing or running μ WaveLab. It was leased from Ansoft with allocated funds from this contract. This purchase also made it possible to switch from HP HFSS to Ansoft HFSS at no cost. In the future all of the features of μ WaveLab will be incorporated into Ansoft HFSS.

Software Capabilities

TEMAC3D requires a suite of peripheral software to generate solid models, generate the Finite Difference (FD) mesh, view the mesh for consistency, generate the problem namelist and header files, and view the results of the analysis. The solid model geometry file is generated by BRL-CAD, available from Ballistics Research Laboratory, Aberdeen Proving Ground, MD. The geometry file is then input to ANASTASIA which generates a mesh given the number of "pad" cells¹ and the size of the cell. IMAGE is used to view the mesh to be sure that the FD mesh is really the desired mesh. This mesh file is then an input for XTEAR (X-window Temporal Electromagnetic Analysis and Response) [6] which is a graphical user interface designed for input of all relevant parameters for the FDTD simulations using TEMAC3D. Finally, software is needed to view output fields as a function of time, frequency and/or position, to generate far-field scattering and/or radiation plots, and to do Fast Fourier Transforms (FFTs) in order to determine the frequency response. FORTRAN programs were provided by Dr. John Beggs for far zone processing and radiation plots.

¹Pad cells occupy the space between the outermost cells of the modeled object and the outermost cells of the problem space which implement the absorbing boundary conditions.

A Gaussian pulse with plane wave excitation is used for scattering simulations of the sensor and the Celestron-8. Point sensors are located inside the cavity to determine the time domain response for a time believed to be long enough to reach steady state. Mathcad is then used to FFT the data to the frequency domain. Presentation of the data can be in the form of graphs taken directly from Mathcad or the data can be further processed using MathSoft Axum.

For radiation simulations, the excitation is point source with a ramped sinusoidal signal. Equivalent surface currents are calculated at a surface surrounding the radiator. These equivalent surface currents are then written to a file for post processing by another program called "patterns". With patterns, desired cut planes are specified either in elevation or azimuth. For this study, angular sweeps are specified in the θ direction (angle measured from the z-axis - elevation) at constant values of ϕ (angle measured from the x-axis - azimuth). If another cut plane is needed, "patterns" is run again using the surface current data to generate the far field pattern on the specified cut plane. If the far field pattern for another frequency is needed, TEMAC3D must be run again with the ramped sinusoid at the new frequency. The radiation data is plotted using Axum.

Fields along slices internal to the cavity are used to determine resonance modes. Field and/or current slice sensors can be placed in any plane. Any total or scattered field or current quantity can be defined for the slice sensor. The only disadvantage to this capability is that some "intuitive guessing" is required for placement and type of sensors.

The TSAR electromagnetic modeling system consists of a family of related codes which have been designed to work together to provide the user with a practical way to set up, run, and interpret the results from a 3-D electromagnetic simulation. The various codes in the TSAR system have been in development at LLNL since 1987 and in active use since 1988. TSAR uses FDTD to solve Maxwell's equations in 3-D on a rectangular, Cartesian grid. As with TEMAC3D, BRL-CAD is used to generate the solid model; Anastasia and Image are used to create and view the mesh; the FDTD solver is used to do the analysis. A number of post-processing tools are also available. An interactive signal processing code developed at LLNL is used to plot field values at a point vs. time. The package allows data to be scaled, shifted and Fourier transformed. Contour and surface plotters based on the commercial graphics package CA-DISSPLA can be used to plot a slice of data through the 3-D simulation volume in either a contour or surface format. These codes are primarily used to provide snapshots in time of field patterns. There is also a group of workstation-based codes that can be used to interactively examine a time sequence of 2-D field data and to plot this data on videotape. Unfortunately, none of these post-processing codes could be evaluated because of the problems

encountered during installation of the LLNL release of TSAR.

The differences in capabilities between TEMAC3D and TSAR are few but significant. TSAR has first and second order MUR absorbing boundaries (TEMAC3D uses second order Liao) and is also capable of using perfect electric and perfect magnetic boundaries. The same procedure for the scattering problem that was used for TEMAC3D is used for TSAR. For the radiation problem, the input can be any of the excitations used for scattering problems which includes a ramped sinusoid. Use of the time domain excitations allow the user the capability of specifying a number of frequencies. A virtual surface is defined over which equivalent currents are calculated. These equivalent surface currents are then used as sources for calculated time domain near and far fields at specified locations or Fast Fourier Transformed far fields to produce frequency domain responses for cut planes or points. All of these calculation are done within the TSAR code itself. Outputs for radiation problems are in three forms: (1) frequency domain far field ϕ and θ components of the electric fields at specific points, (2) time domain near field ϕ and θ components of the electric fields at specific points, and (3) frequency domain far field ϕ and θ components of the electric fields at specific points designated by a sweep through specified values of ϕ at a constant value of θ .

Radiation plots are usually generated for aperture antennas with the normal vector of the aperture in the z direction. Angular sweeps of the field quantities or the power radiated are then done in the θ direction at constant values of ϕ . This inconsistency with what TSAR does was overcome by reprogramming the relevant subroutines so that the patterns produced are a function of θ at constant values of ϕ . However, the outputs for a particular run are specified far field points in the time domain, or radiation patterns for specified frequencies. If a different pattern or far field point is needed, the problem has to be run again. To plot the radiation data, a separate commercial graphing program is necessary. Unfortunately, this version of TSAR had difficulties with the radiation problem so those simulations gave incorrect or no results.

As it is for TEMAC3D, slice sensors can be placed in any plane. Any total or scattered field or current quantity can be defined for the slice sensor. The same "intuitive guess work" as for TEMAC3D must be accomplished for placement and selection of type of these slice sensors.

μ WaveLab is a comprehensive, full-wave, 3D electromagnetic simulation and analysis system that addresses arbitrary structures providing all field information. A comprehensive set of 3-D elements is available in linear and quadratic accuracy. Fast, efficient, absorbing boundaries emulate infinity to accommodate unbounded models. Solid modeling, auto-meshing, and push-button calculations are provided.

With the time domain codes, generating a frequency response to an external stimulus identifies frequencies of interest for further investigation by solving the radiation problem. With μ WaveLab, the capability of doing

the scattering problem with an incoming plane wave does not exist. Instead, the radiation problem is done by exciting the structure as an antenna and the port scattering parameter, S_{11} , is calculated at a number of frequencies. This gives us the desired response needed to identify frequencies of interest.

All radiation data at all angles for all frequencies of the frequency sweep can be generated. This takes an enormous amount of time (compared to turning off the radiation data production) and generates an enormous amount of data, most of which is not of interest. A two step process of identifying frequencies via S_{11} followed by doing the problem at the frequencies of interest with the radiation data production on is accomplished. Post processing produces radiation data at any angle of interest for each of the frequencies selected for the analysis. Since μ WaveLab is a frequency domain simulator, a run for each frequency is necessary. The plots of the radiation pattern can be done within μ WaveLab. Since there is no easy way to format the data for commercial graphing programs, the plots are captured with a screen capture utility and saved for inclusion in reports. Field and current quantities on surfaces that are defined during the geometric modeling are stored and can be viewed with the post processing capabilities of μ WaveLab. As with the codes presented above, a certain amount of "engineering intuition" is needed for placement of these surfaces.

TEMAC3D Baseline Results²

Larger models for the Celestron-8 and the optical sensor than were reported in [1] and [2] were generated and simulated using TEMAC3D. These, along with radiation calculations for the optical sensor reported in [1] [2] and measurements on the Celestron-8 reported in [3] were the baseline results with which the results from the other simulators are compared. A drawing of the Celestron-8 is shown in Figure 1. A large model of the Celestron-8 which incorporates the loss in the Plexiglass window (dielectric constant, $\epsilon_R = 2.6$ and conductivity, $\sigma = .002$ S/m) and includes the glass ($\epsilon_R = 4.25$ and $\sigma = .002$ S/m) behind the primary mirror was created. The resulting mesh is shown in Figure 2. The scattering problem was done with an x-polarized, Gaussian shaped pulse plane wave incident on boresight. Field point sensors are located at various points inside the telescope model. Figure 3 shows a comparison of the normalized magnitudes of the electric fields at the eye-piece location, the probe location, and the measured data reported in [3]. In the low frequency range, the measured data track the probe location data fairly well, even though the measured data are taken at the location of the eye piece. The Phillips lab testers believe that this can be explained by poor isolation between the large cavity region and the location of the test sensor at the eye piece. The resonances at 1.02 GHz, 1.45 GHz, 1.61 GHz and 1.76 GHz were investigated with an x directed point source

²Results that correspond to μ WaveLab and TSAR results are presented here. Other results are reported in [4].

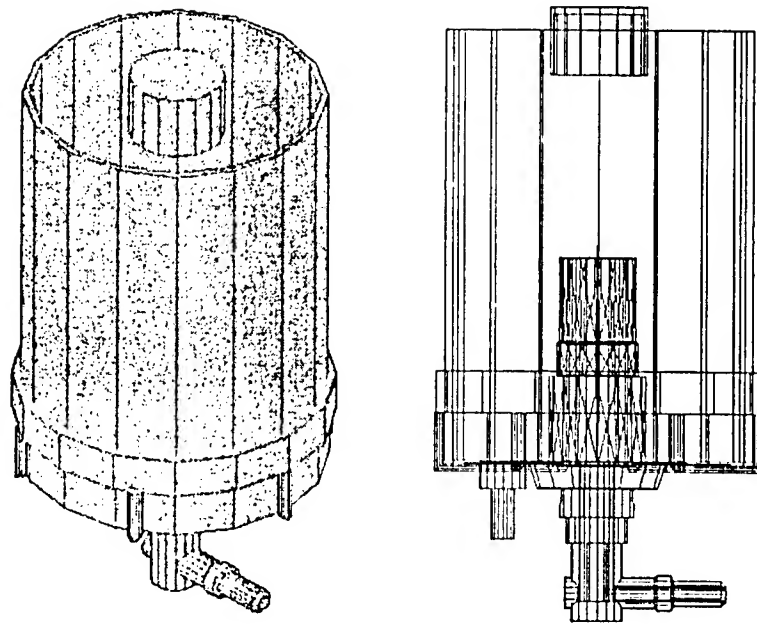


Figure 1: The Celestron-8 telescope.

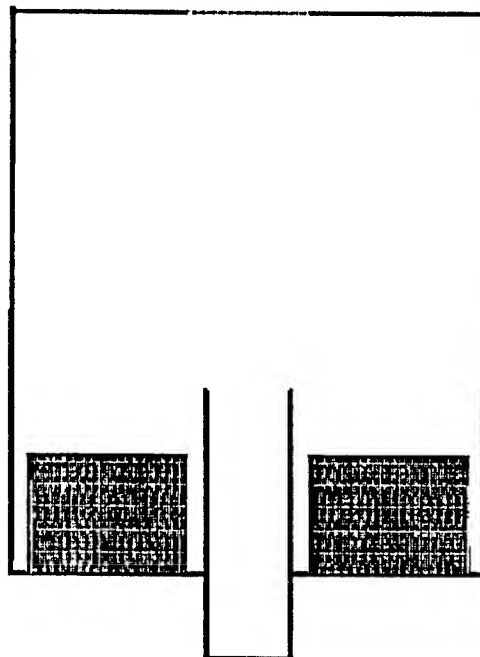


Figure 2: Cross-section of the mesh for the Celestron-8.

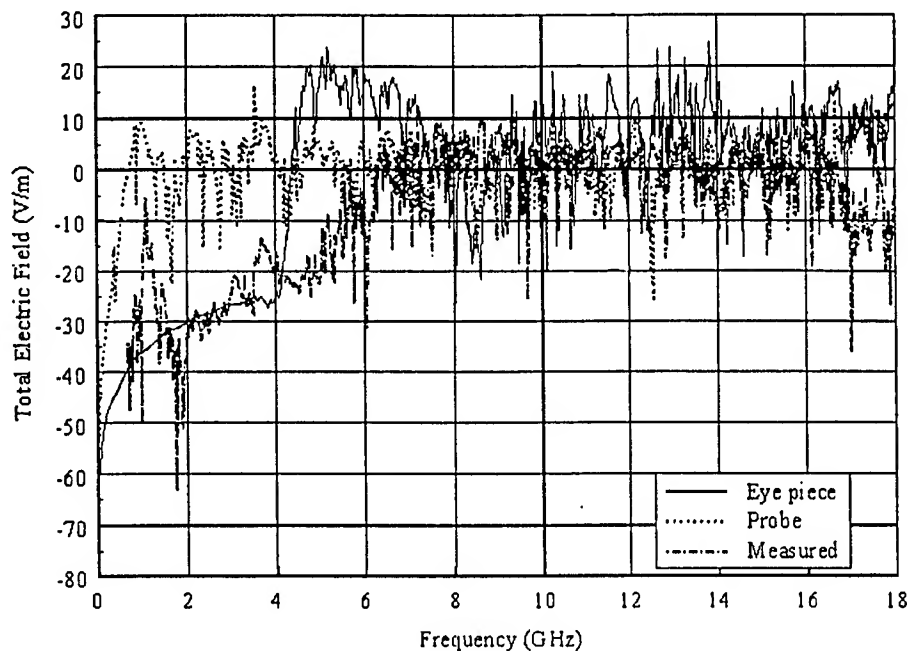


Figure 3: Comparisons of numerical and measured results.

at the probe location specified for the measurements reported in [3]. The radiation patterns for 1.02 GHz and 1.45 GHz in the xz ($\phi = 0$) and yz ($\phi = 90$) planes are shown in Figure 4.

The model³ of the sensor was generated with cell sides of 0.66 mm (see Figure 5). The scattering problem was done with a Gaussian pulse type, that was a y-polarized plane wave incident on boresight. Field sensors were placed at five different locations in the sensor model. The time domain information for all of these locations showed the characteristic exponential decay indicative of a valid simulation. The frequency domain plots for the detector and cavity center locations are shown in Figures 6 and 7. The results from this large model compare favorably with the results reported in [1] for the smaller model.

The radiation problem for frequencies of 3.58 GHz and 6.47 GHz are reported in [1] and [10]. Since the smaller model of that report was of sufficient detail for accurate results, those results are reproduced here (Figures 8 and 9) for completeness and comparisons with results from the other software packages. Even though the model of the sensor was analyzed and reported in [1], the fields internal to the sensor were not recorded. Figures 10 and 11 show field magnitudes for slice sensors in the xy plane in the center of the large cavity.

³Details of the evolution of this model are given in [1].

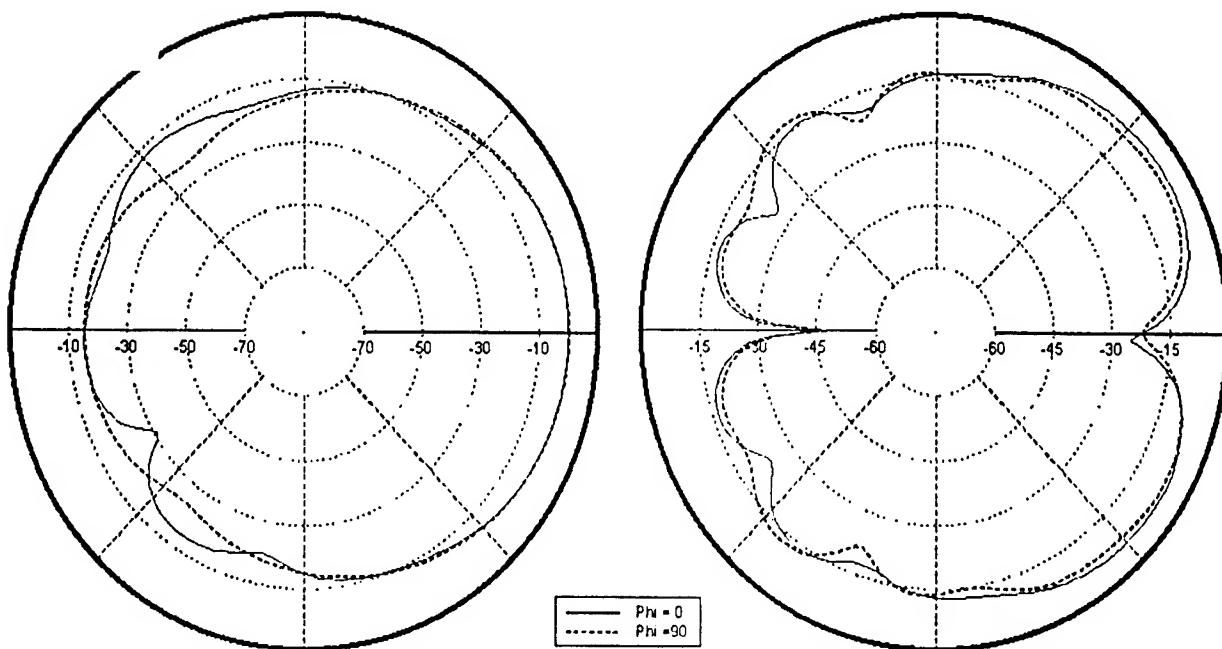


Figure 4: Celestron-8 radiation 1.02 GHz and 1.45 GHz.

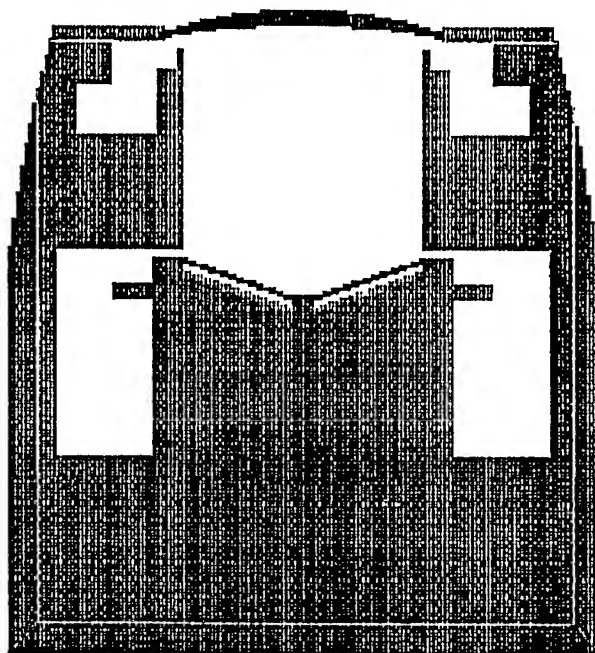


Figure 5: Cross-section of the large model mesh for the sensor.

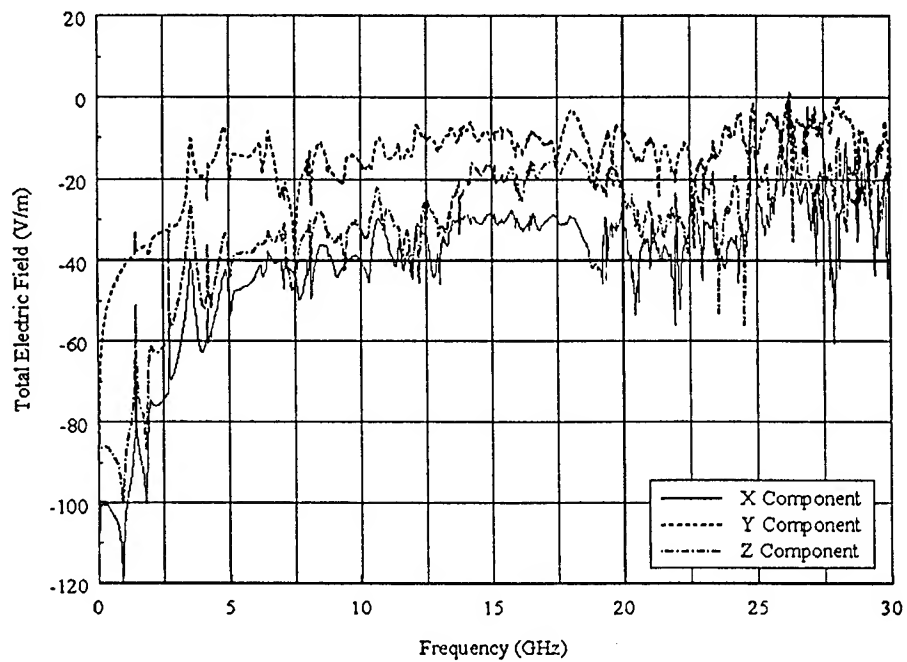


Figure 6: Normalized total electric fields for the detector location.

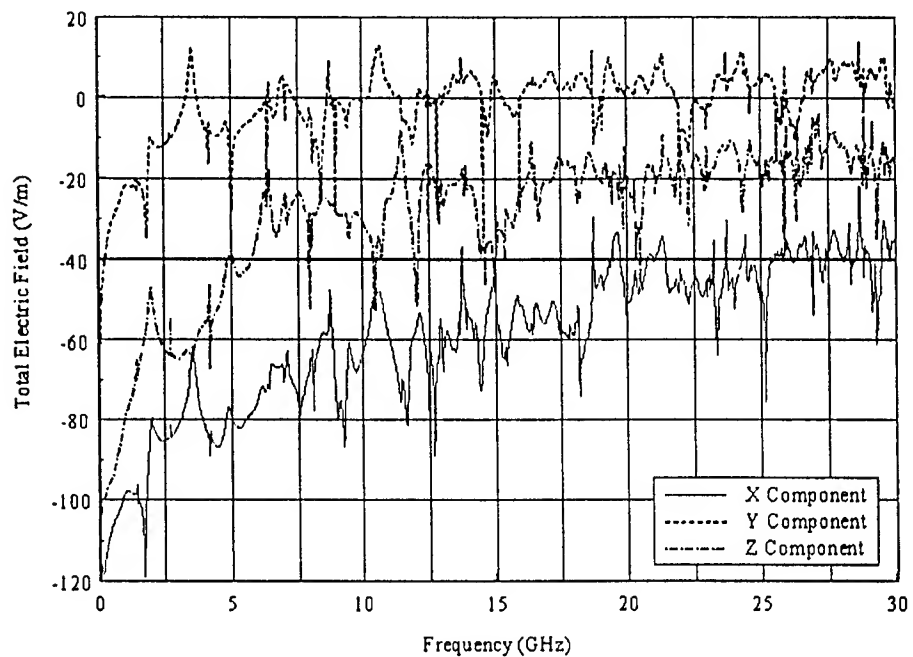


Figure 7: Normalized total electric fields for the cavity center location.

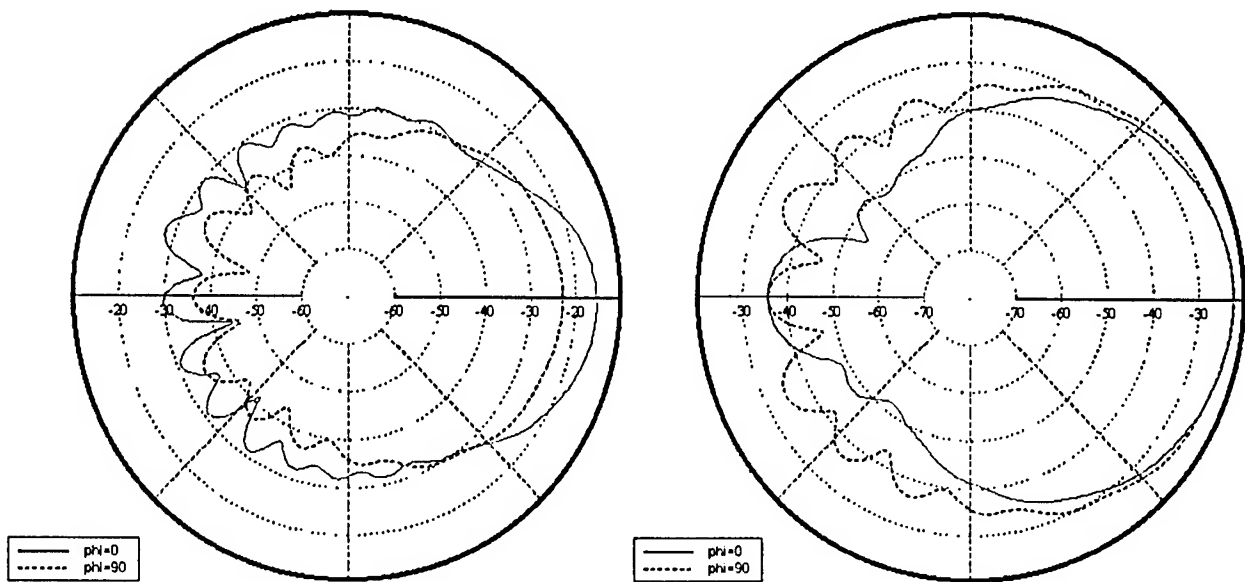


Figure 8: Radiation for x and y polarized sources - 3.58 GHz.

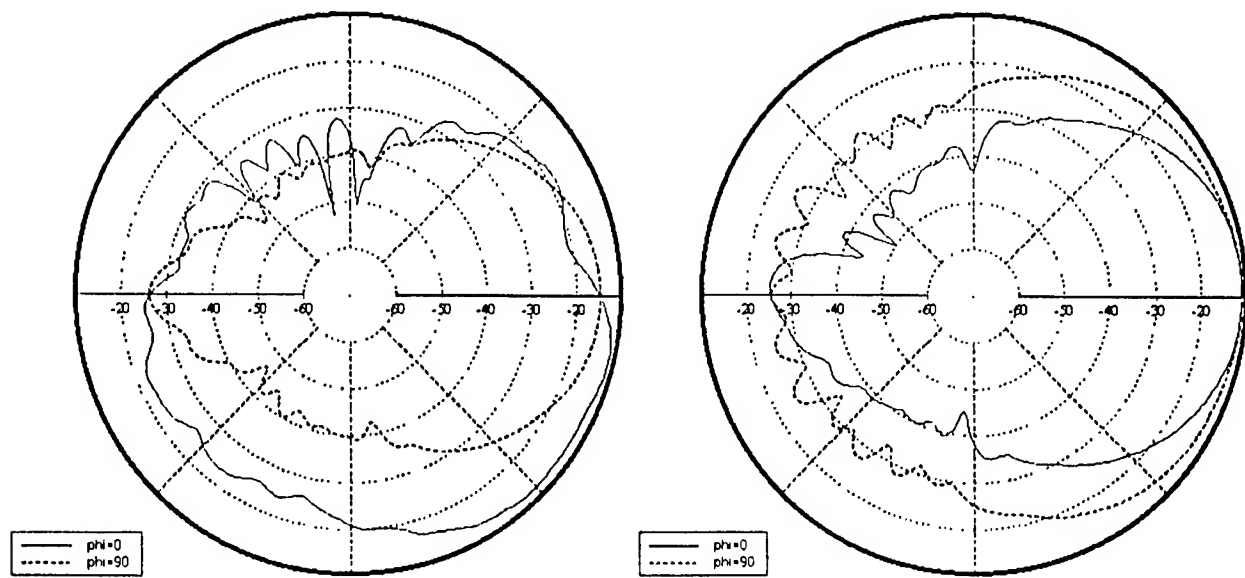


Figure 9: Radiation for x and y polarized sources - 6.47 GHz.

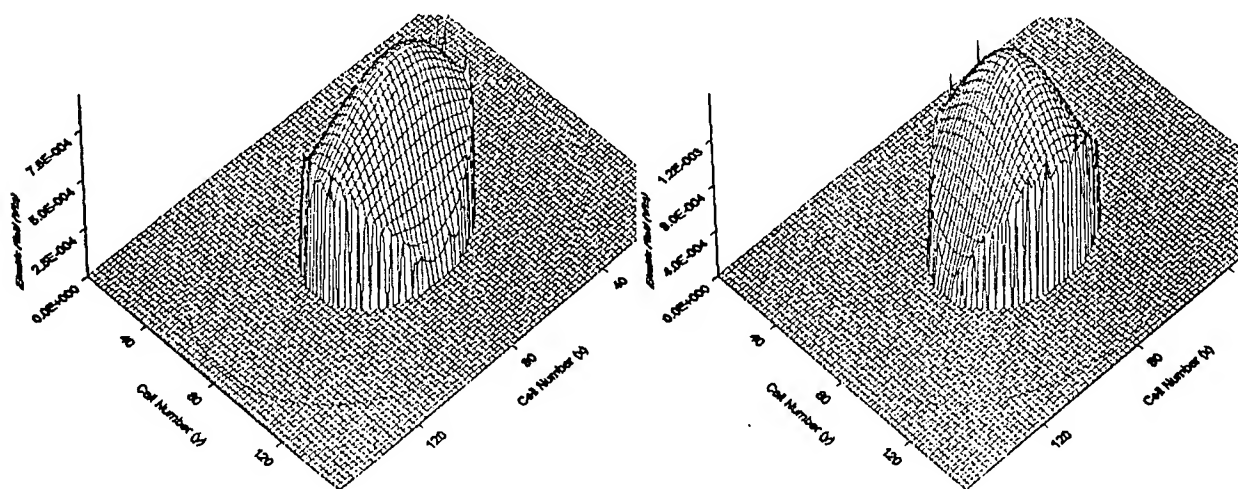


Figure 10: Electric field in the center for x and y polarizations - 3.58 GHz.

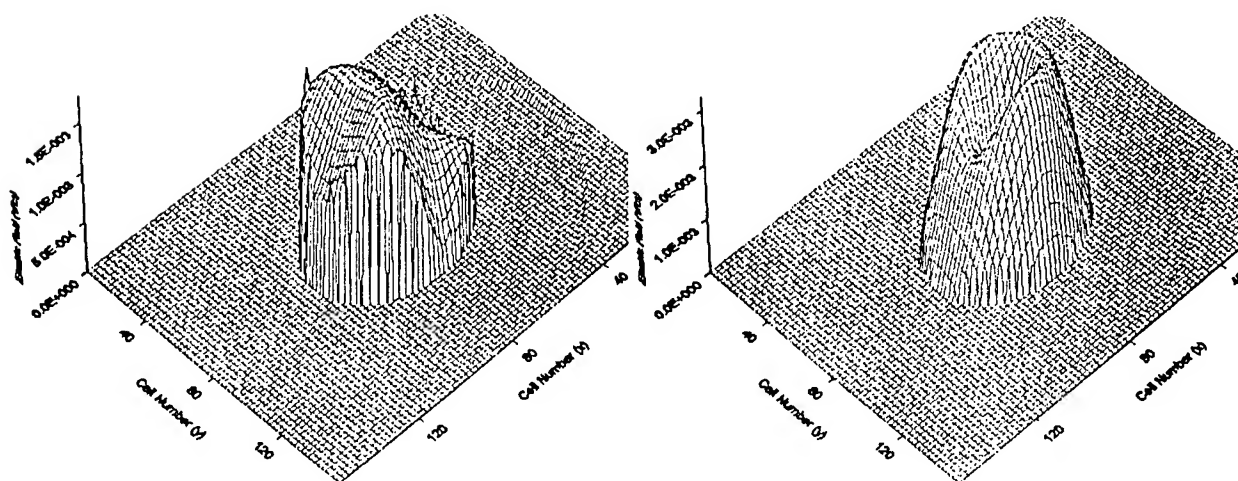


Figure 11: Electric field in the center for x and y polarizations - 6.47 GHz.

Comparisons of the transverse fields in the center of the cavity can be made with the mode chart of [11]. At 3.86 GHz the TE_{11} mode is evident for both polarizations. At 6.47 GHz, TE_{01} is the clear choice for y polarization, however, the x polarization shows no distinct mode. A closed cavity with the dimensions of the large central cavity region has resonance frequencies for the TE_{111} and TE_{011} modes of 3.576 GHz and 6.431 GHz respectively. Considering the fact that the large cylindrical cavity region of the sensor is far from being a closed right circular cylinder, these calculated frequencies are remarkably close to those found in the FDTD analysis.

Figures 12 - 15⁴ show electric field distributions in the xz plane (plane of the source), and in the yz plane. Comparing these figures shows that the field in the outer toroidal cavities are much more intense for the x polarized source than for the y polarized source for all frequencies except 6.47 GHz and in both xz and yz planes. This may be explained by observing that Figure 5 shows the mesh for the xz plane. An x polarized source at the detector location should produce greater z-directed fields because of reflection from the lower v-shaped filter area, whereas a y-polarized source would not. These z-directed fields easily propagate in the entrances to the outer toroidal sections.

Another notable feature of these field distributions is that for all but 6.47 GHz, the distributions show nulls at the lens, indicating the relatively high conductivity and dielectric constant, and thus high reflectivity, of this material. This information can be used for the third mode number, the number of half wavelengths along the length of the cavity, for resonance frequencies. The assumption of TE_{111} and TE_{011} modes at 3.58 GHz and 6.47 GHz (y polarization only) seems correct since there is only one half wavelength variation in the fields for these resonances.

TSAR Results

The first use of TSAR produced numerous runs on a full (no use of symmetry or a ground plane) model of the Celestron-8. The only difference between the TSAR model and the TEMAC3D model is that 7 pad cells were used for TSAR and its 2nd order Mur radiation boundaries as opposed to 5 pad cells for TEMAC3D with its 2nd order Liao radiation boundaries. A sample of the output x-directed fields at the eyepiece location and at the probe location are shown in Figures 16 and 17. These are the same positions as for the TEMAC3D fields. The exponentially increasing DC component at the probe locations continues to grow for longer run times and is physically not reasonable. Use of 10 pad cells, replacement of the glass below the primary mirror with air, use of perfect conductors as opposed to copper conductors, implementation of

⁴The scale for the magnitude of these fields has been set to emphasize the field variations at locations away from the source. As such, the fields in locations near the source have been clipped at the maximum scale reading.

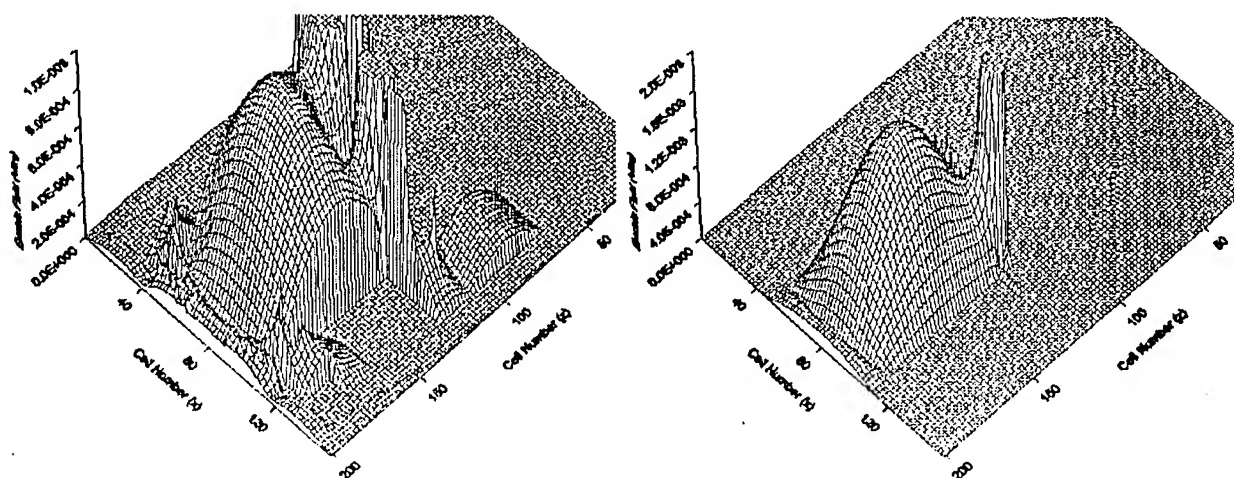


Figure 12: Electric field in the xz plane for x and y polarizations - 3.58 GHz.

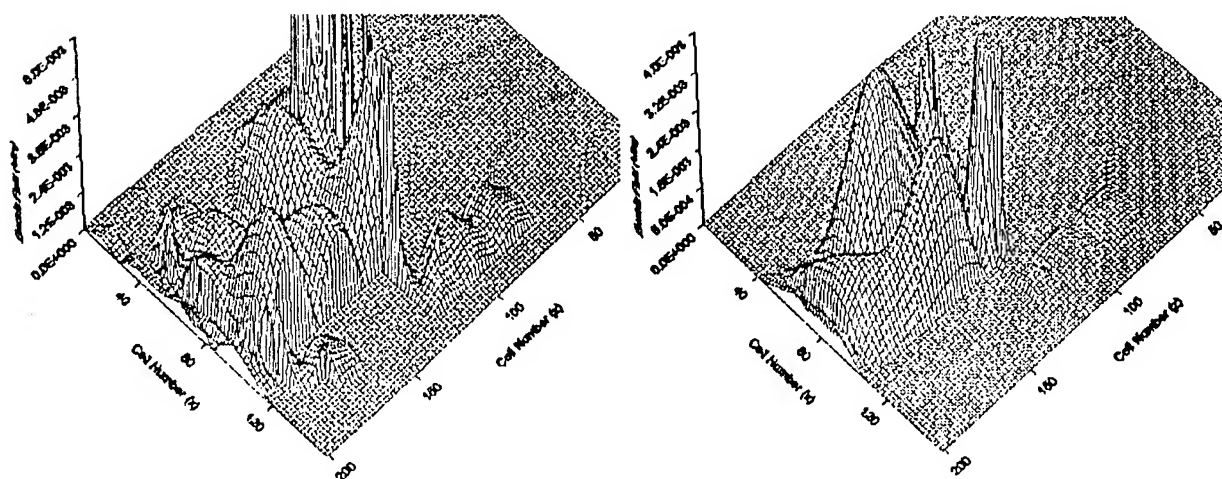


Figure 13: Electric field in the xz plane for x and y polarizations - 6.47 GHz.

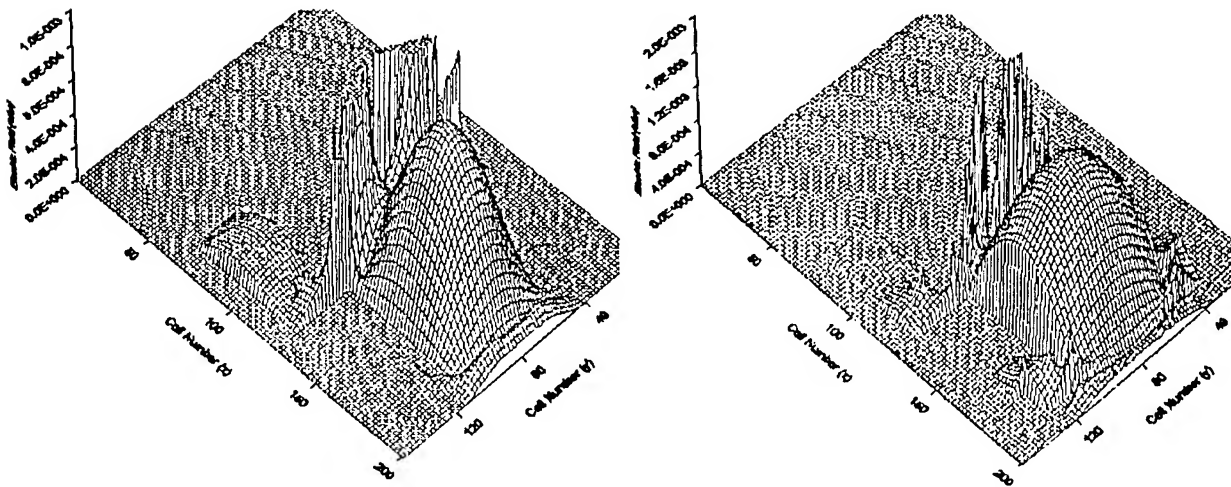


Figure 14: Electric field in the yz plane for x and y polarizations - 3.58 GHz.

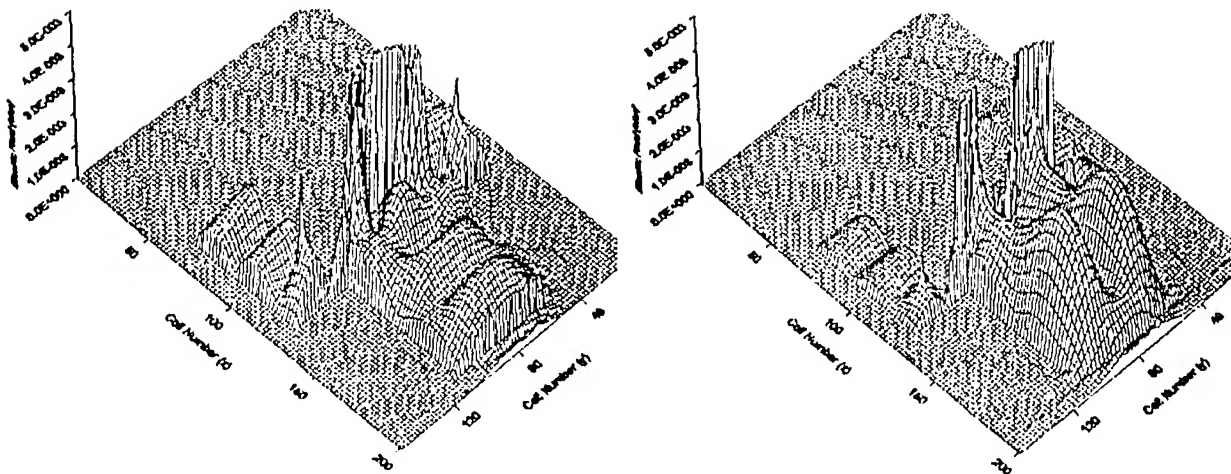


Figure 15: Electric field in the yz plane for x and y polarizations - 6.47 GHz.

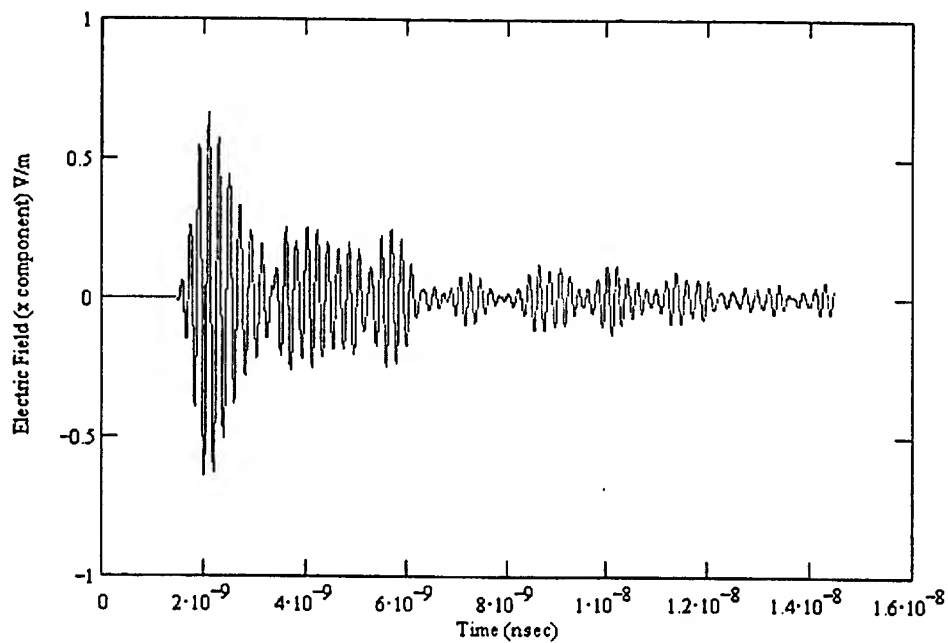


Figure 16: Field at the eyepiece location of the Celestron-8.

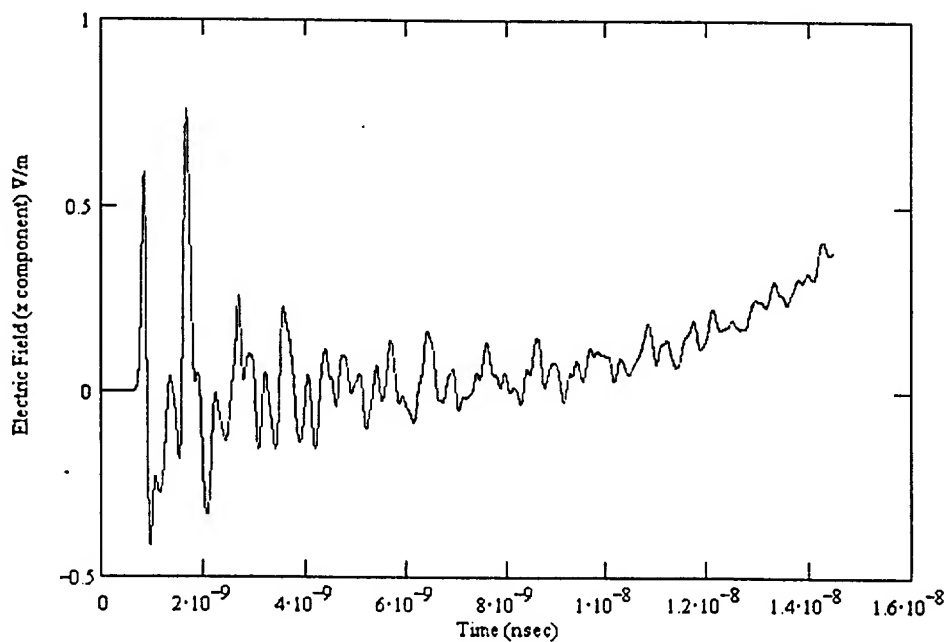


Figure 17: Field at the probe location of the Celestron-8.

longer pulse times for the Gaussian pulses, and specifying a smaller Courant number⁵ of 1/3 produced little if no change in this erroneous output.

These problems continued with a full model of the sensor. In addition to the variations cited above, use of a point radiator as opposed to a plane wave source yielded similar results - exponentially increasing DC components of certain field components. The decision was made to create models of the Celestron-8 and the sensor that took advantage of symmetry and, in the case of the sensor, add a ground plane at the base of the sensor to simulate the large body of the satellite. Anastasia was used to mesh 1/2, 1/4 or 1/8 of the full geometric model depending on the symmetry desired. Appropriate boundary conditions (perfect electric planes, perfect magnetic planes and absorbing boundaries) are then defined in the namelist file, "tsarin". For the scattering problem, plane waves are defined as for the fully meshed models. These simulations were successful and are reported below. It appears that for these particular scattering problems using the Celestron-8 and sensor models, TSAR does not do well with absorbing boundary conditions defined on all of the outer surfaces of the computational space.

The symmetric model of the Celestron-8 was excited with an x polarized plane wave incident on the window of the telescope. This is similar to the TEMAC3D model reported in [1] except for the symmetry planes. For the x polarized electric field excitation, the xz plane (the plane containing the electric field vector) is defined as a perfect magnetic conductor. The yz plane is then defined as a perfect electric conductor. The response for this model is shown, along with measured results from [3], in Figure 18. It is similar to the TEMAC3D results (Figure 3) but is not exactly the same. This is to be expected because, in addition to the use of symmetry and a ground plane for the TSAR simulation, TEMAC3D uses 2nd order Liao absorbing boundaries and TSAR uses 2nd order Mur absorbing boundaries. These results show that TSAR is working well with symmetric models. Since this is the main reason for using TSAR in the first place, TSAR can be used with confidence in future work where symmetry can be applied.

Unfortunately, there were no valid radiation simulation results. TSAR was modified so that it would produce files for specific values of ϕ for ϕ and θ polarized electric fields. The information in each file would be electric field as a function of θ . The code was run using a ground plane and one plane of symmetry, resulting in core dumps with no error codes generated. The pattern files were not written to disk and the far field files⁶ were filled with NaNQ which is an overflow or underflow. The analysis was run again using the original unmodified subroutines with the same results. A sine wave excitation was then used along with

⁵TSAR normally uses a Courant number of 1/2 whereas TEMAC3D uses $1/\sqrt{3}$. This is due to the differing radiation boundary conditions.

⁶These files contain time domain information on the electric fields at specified angles in the far field.

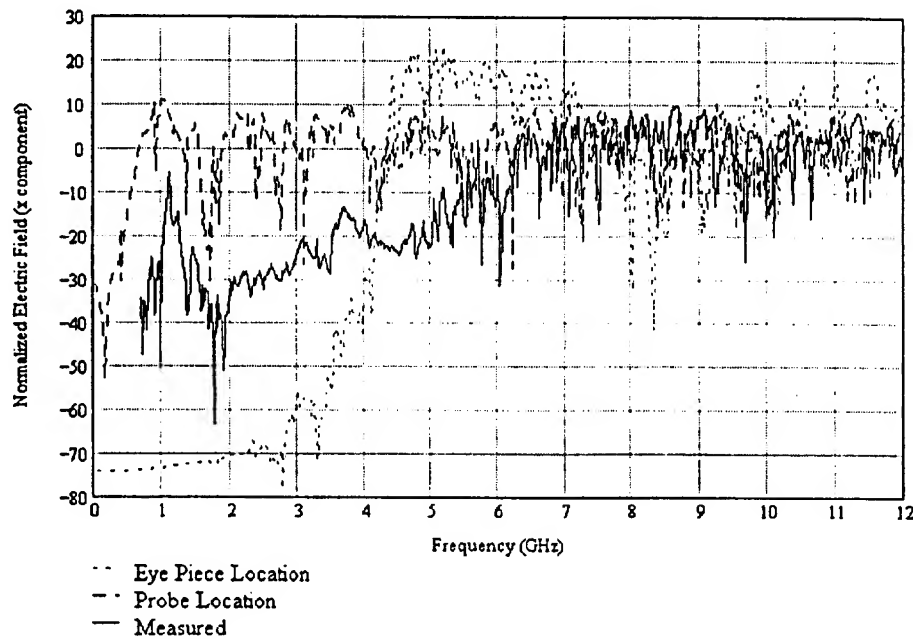


Figure 18: Plane wave response of the Celestron-8.

defining "slice sensors". In addition to the same results described above, these files contained field values of "0" throughout. To date, there is no solution for this problem.

The 1 mm mesh model of the sensor that was used for TEMAC3D was also used for TSAR with the exception that symmetry and 8 pad cells were used with TSAR. One symmetric model for TSAR defines two symmetry planes, one electric and the other magnetic, so that only 1/4 of the full model is meshed. Results for the thermopile detector location for this TSAR model are shown in Figure 19. The results are again similar to the TEMAC3D results shown in Figure 6. Of course, the presence or absence of the ground plane should not significantly affect the results for the scattering problem. The results are similar to the TEMAC3D results (Figure 7) as expected.

A similar symmetric model with a ground plane located at the bottom of the sensor was also created. Figure 20 shows the response at the center of the large cavity region of the sensor for the TSAR symmetric model. The TSAR symmetric model with the ground plane results are almost identical to these.

In all of the TSAR results given thus far, the models give zero field intensity for the x and z components at the locations noted. Since these locations are on a "perfect electric conductor" plane, this would naturally be the case. The presumption is then that the full model used for the TEMAC3D simulation does not have

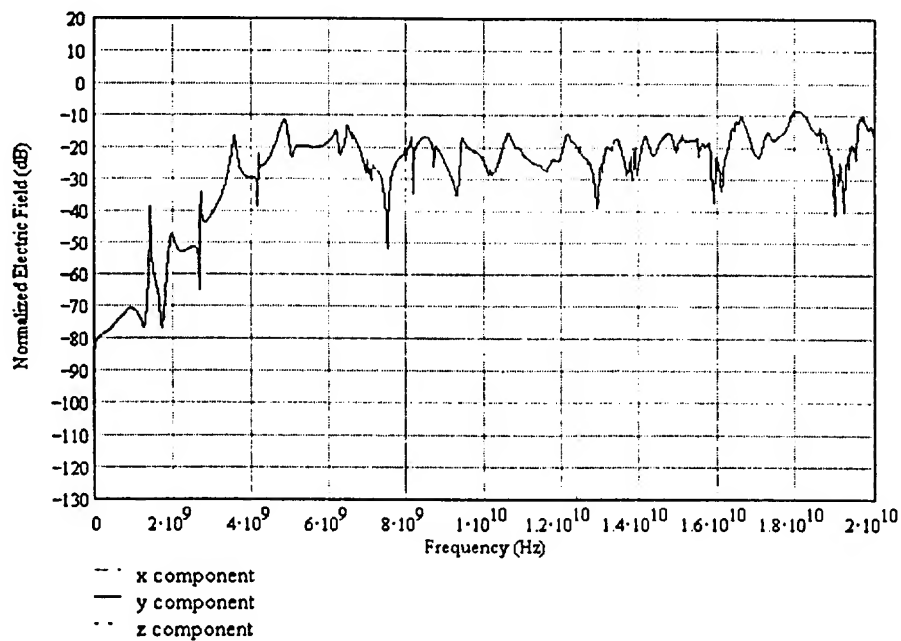


Figure 19: Plane wave response at the detector location of the Sensor.

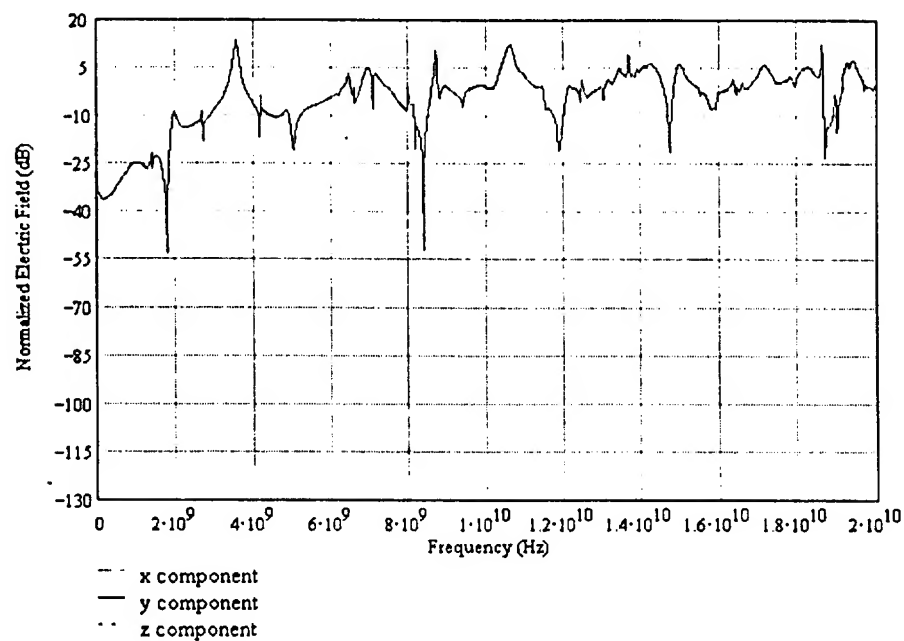


Figure 20: Response in the large cavity region of the Sensor without ground plane.

perfect symmetry and that small field intensities in the x and z directions are generated.

μ WaveLab Results

Methods of running μ WaveLab to best utilize the software in a timely manner were explored. The manual solution option in μ WaveLab allows the analysis to be run outside the graphical user interface. This increases the user's time efficiency in two ways. It allows the user to work on a completely different model while the analysis is running in the background and it also permits batch processing so that one analysis may fall on the heels of another when the user is unavailable to begin the next analysis. In order to run a solution manually, "manual analysis" must be selected on the analysis menu and a file name must be assigned when prompted. That file can then be run at any time. Batch processing may be achieved by writing UNIX script files containing each file to be analyzed.

μ WaveLab has the capability of determining port scattering parameters, radiation plot parameters in any direction and field quantities at predetermined locations at all of the selected analysis frequencies. The locations for field quantities are defined when the geometric model is created and are on surfaces of volumes. This differs from HFSS in that the port scattering parameters and radiation and field quantities are known everywhere for a single frequency run only. The scattering parameters only are generated for a multiple frequency sweep. After resonances are found from the port scattering parameters, a single frequency analysis at the resonance frequencies to determine field distributions and radiation plots is done.

μ WaveLab has the capability of solving for the eigenvalues (resonance frequencies) of a closed cavity. This capability has been used on two models, the actual geometry of the Celestron-8 telescope and on a simplified geometry of the sensor. The assumption that all outer walls, including the aperture, of the geometry are conductors is necessary for the eigenvalue problem. The first resonance frequency for the Celestron-8 was found to be 0.42218 GHz. This does not agree with results using TEMAC3D where the first resonance is at approximately 1 GHz. The simplified geometry of the sensor cross-section is taken to be only the large, central, cylindrical region. Many of the resonance frequencies for the sensor are close to those found using TEMAC3D but there are at least as many additional frequencies found using μ WaveLab. The purpose of this exercise was to see if the eigenvalue solver could be used to predict resonances of the large sensors presented here. In fact, calculation of a few of the lower frequency resonances assuming purely cylindrical cavities seems to be more effective. It was concluded that the eigenvalue solver is not a real asset for these types of problems.

Two models for Celestron-8 simulations were created, one with a probe excitation located in the

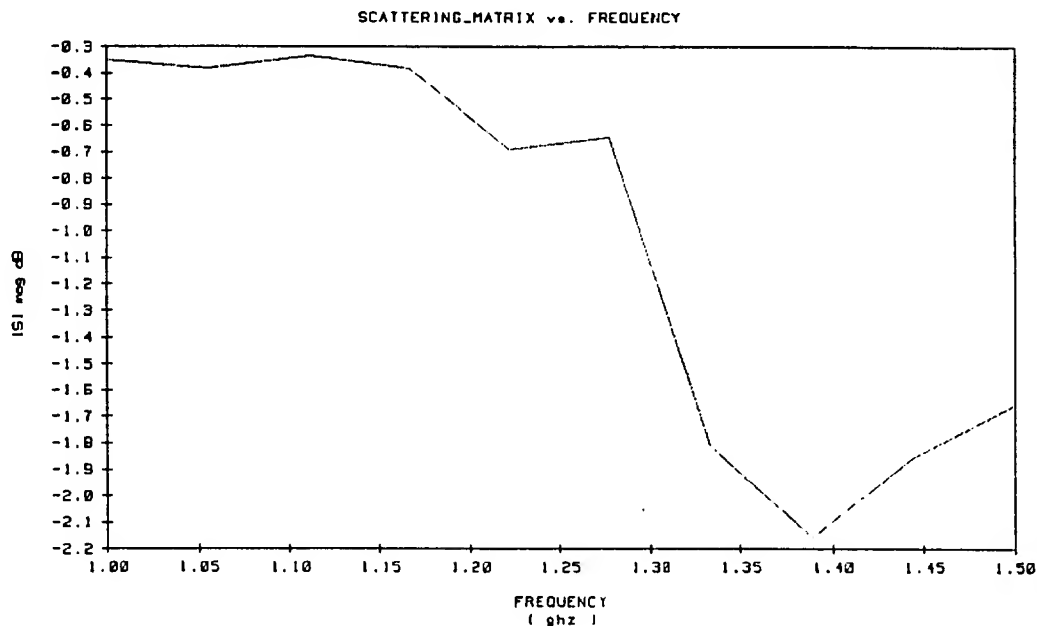


Figure 21: Reflection coefficient for the Celestron-8 model.

large cylindrical region of the cavity, and the other with waveguide excitation at the eyepiece location. The model for the Celestron-8 is the same as that used in HP HFSS and simulates tests at Phillips Lab [3]. The goal of the modeling is to take advantage of μ WaveLab's ability to use symmetry with radiation as well as its quadratic element meshing to reduce the size of the problem. After performing a frequency sweep from 1 to 1.5 GHz, a resonance in the correct range and the general shape of S_{11} versus frequency (Figure 21) is observed to agree with results from HP HFSS reported in [3].

The radiated power pattern for 1.35 GHz is shown in Figure 22. Even though this plot is for a frequency where the telescope is not resonant, the values are similar to the results reported for HP HFSS [1][8]. Figure 22 can also be compared with the results from TEMAC3D of Figure 4 at 1.45 GHz. Again, the frequencies are not exactly the same, but results are similar. Satisfaction with the capabilities of μ WaveLab and the validity of this model is high.

The Celestron-8 was also modeled with a circular waveguide excitation located at the eye piece. This effectively creates a model for frequencies above the cutoff frequency for this waveguide, 4.39 GHz. Attempts at running the analysis failed due to a meshing problem that remained after several attempts at fixing the problem. The models contained approximately 20,000 elements and were likely to fail during the analysis

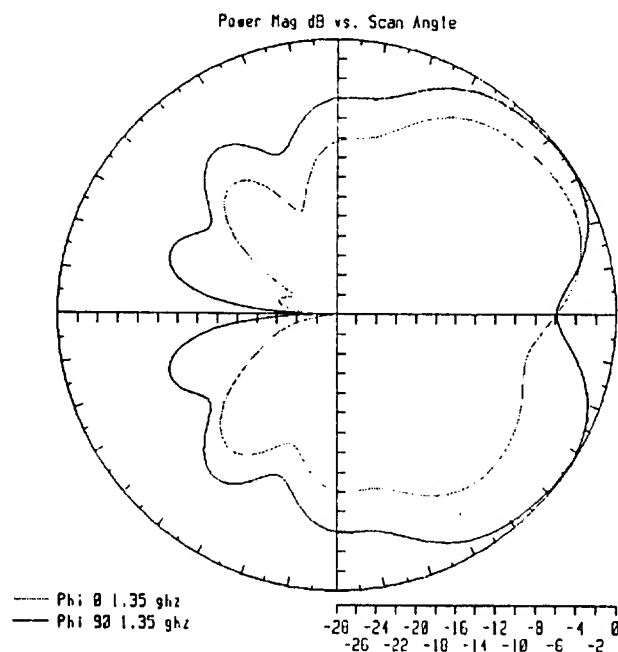


Figure 22: Power radiated for the Celestron-8 model.

due to lack of resources anyway. Attention was diverted to developing a full model of the satellite sensor.

Two models for the sensor simulations were created: one was a simplified model which did not contain the outer toroidal sections, the other was similar to the model created for TEMAC3D [10]. An added benefit to this approach is that the effects of the outer toroidal sections can be evaluated. The sensor was modeled so that the resonances at 3.58 GHz and 6.47 GHz that were found using TEMAC3D [1] could be investigated. Both H parallel and E parallel planes of symmetry⁷ (the plane of symmetry for this model is the yz plane) were used with the appropriate rectangular waveguide excitations at the location of one of the thermopile detectors in the sensor. A ground plane at the location of the satellite was also added. Figure 23 shows the geometry of the simplified sensor model. The layers to the right of the figure are, from left to right, Germanium filter, air and Mylar. Each layer is 3 mm thick. The model is a body of rotation as opposed to the detailed model used for TEMAC3D [1], and the ground plane is added at the right of the figure. Also notice that the outer toroidal cavities modeled in [1] are not present in this μ WaveLab model.

Electric field contours, port scattering parameters and radiation plots were generated for H parallel and E parallel symmetry models. For H parallel symmetry, the electric field polarization is x directed. The

⁷This is μ WaveLab terminology and is used for consistency with that software package. The standard terminology for an "H parallel" plane is a "perfect electric conductor" plane, and an "E parallel" plane is a "perfect magnetic conductor" plane.

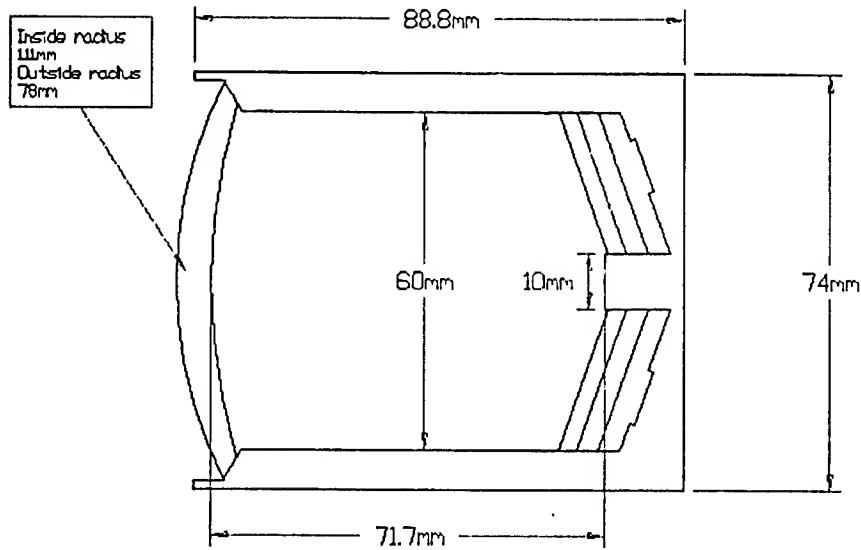


Figure 23: Model of the sensor used in μ WaveLab.

port scattering parameter, S_{11} , is shown in Figure 24. The resonance frequency of 3.42 GHz (TEMAC3D showed a resonance at 3.58 GHz [1]) was then investigated further by producing electric field contours at the predetermined surfaces shown in Figure 25. Comparisons with the field line charts shown in [11] can be made. The field intensity contours as presented by μ WaveLab are orthogonal to the field line representations shown in [11]. In the field line representation, the closely spaced lines represent areas of high field intensity corresponding to the lightly shaded areas in the μ WaveLab output. The view in the center of the large cavity in Figure 25, clearly shows that this resonance has a TE_{11} type mode structure in the xy planes. These field plots can also be compared to the results from TEMAC3D. The excitation source for those results is in the xz plane so that the y polarized results from TEMAC3D must be compared to these. The left view of Figure 25 is comparable to Figures 12 and 14 (y polarizations), and the right view of Figure 25 is comparable to Figure 10 (y polarization).

Figure 26 shows the radiation plot for 3.43 GHz on the left. This plot for x polarized excitation corresponds to the plot for y polarized excitation from TEMAC3D on the right. As such, the $\phi = 0^\circ$ plot for the μ WaveLab results corresponds to the $\phi = 90^\circ$ plot for the TEMAC3D results, and vice versa. The effect of the ground plane modeled in μ WaveLab is clearly shown. Slight reductions in gain at the angles approaching the ground plane are comparable to those shown for the TEMAC3D results. Also note that the μ WaveLab model is a simplified model as described above.

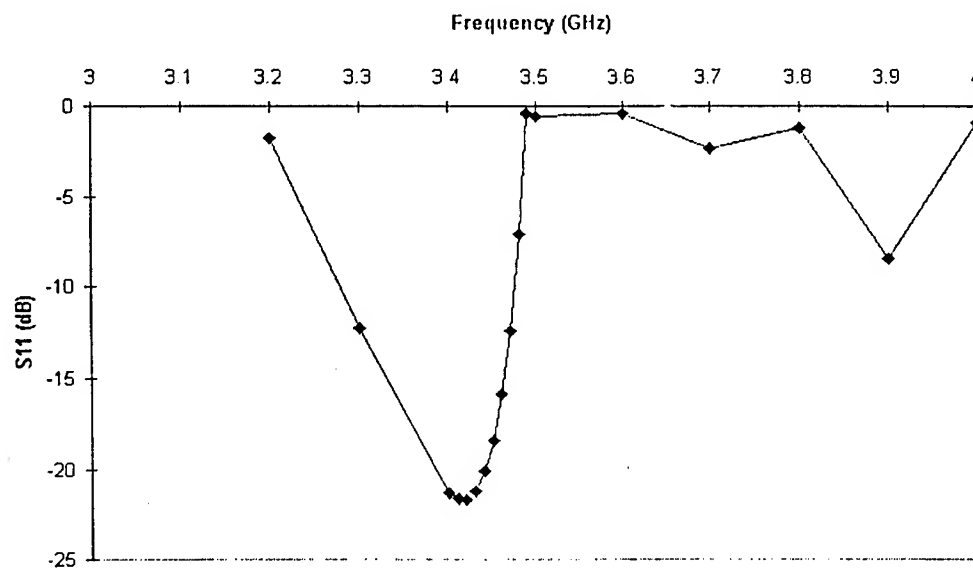


Figure 24: Scattering parameters for the H-parallel sensor model.

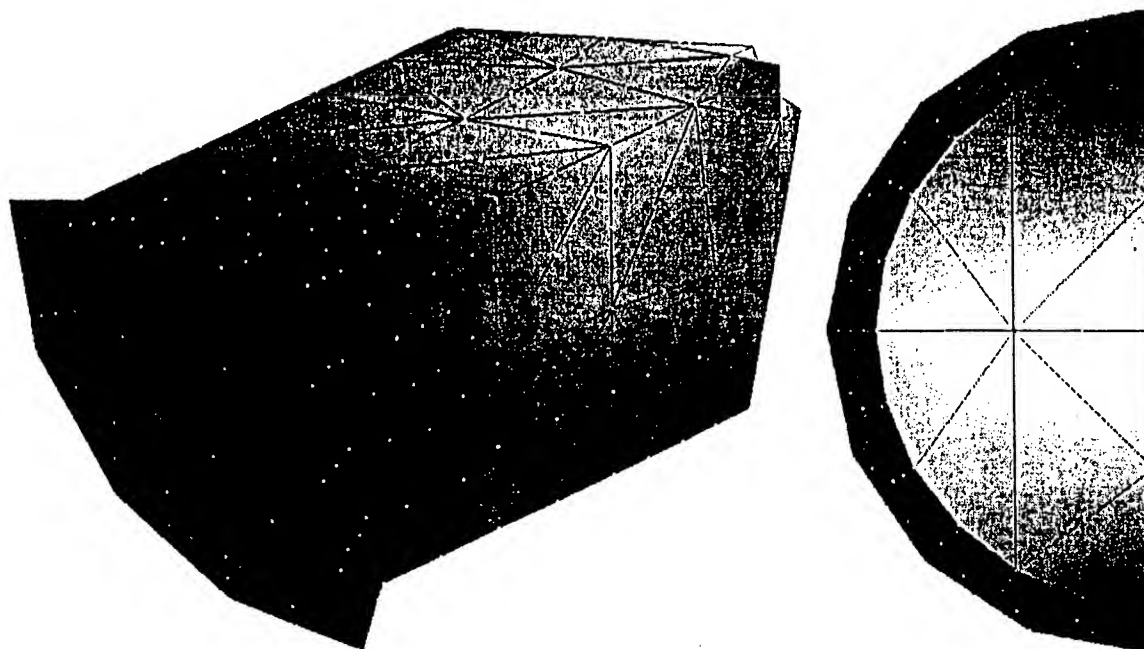


Figure 25: Electric field intensity - cutaway view and view at the center of the large cavity.

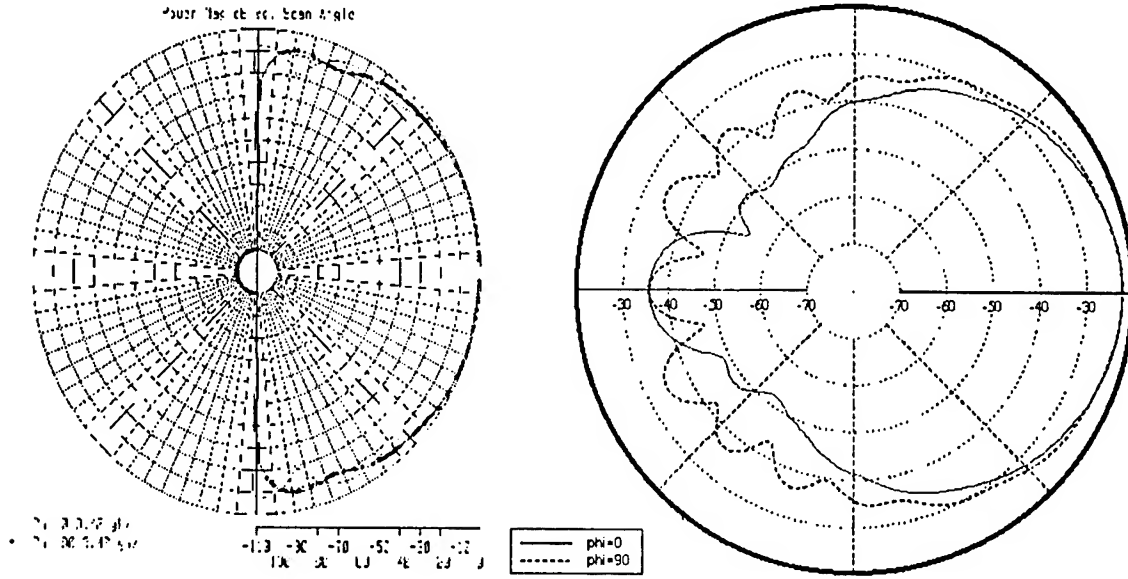


Figure 26: μ WaveLab (3.43 GHz) and TEMAC3D (3.58 GHz) radiation results.

The E parallel model is essentially the same as the H parallel model with the exception that the electric field excitation is in the y direction. This polarization is analogous to the x polarization of the TEMAC3D study [1]. The port scattering parameter, S_{11} , as a function of frequency is shown in Figure 27. This time, a resonance at 3.71 GHz is observed. The electric field contour plots for this type of symmetry are shown in Figures 28 and 29. Again, these need to be compared to the field line plots of [11] in the same manner as before. Comparisons can also be made with the results from TEMAC3D. Figures 28 and 29 compare to Figures 12 (y polarization) and 14, and 10 (x polarizations) respectively.

The radiation plot for this symmetry is shown in Figure 30 on the left compared to the x polarization plot of the TEMAC3D results on the right. The $\phi = 0^\circ$ plot of the μ WaveLab results corresponds to the $\phi = 90^\circ$ plot of the TEMAC3D results, and vice versa. Note that the μ WaveLab radiation plots are normalized so that the maxima are all 0 dB. Therefore, comparisons can only be made in the shape of the curves as opposed to absolute magnitudes.

Another model with smaller cells and closer radiation boundaries (the rule of thumb is that the radiation boundaries must be $\lambda/4$ from the radiators) was created for analysis in the 6 GHz range. All other aspects of the 6 GHz model are the same as for the 3 GHz model. Port scattering parameters are shown in Figure 31. Once again the resonance at 6.58 GHz compares well with the TEMAC3D resonance at 6.47 GHz. The field contours for this symmetry are presented in Figure 32 and can be compared to Figures 13 and 15, and

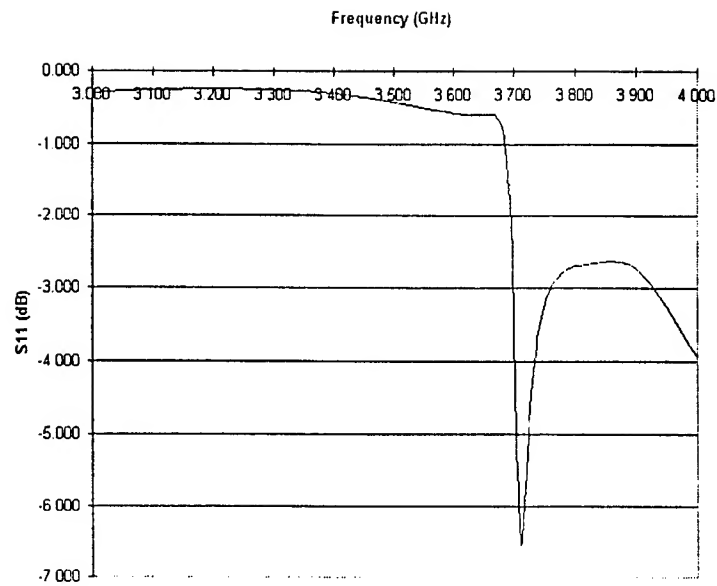


Figure 27: Scattering parameter for the 3 GHz E-parallel sensor model.

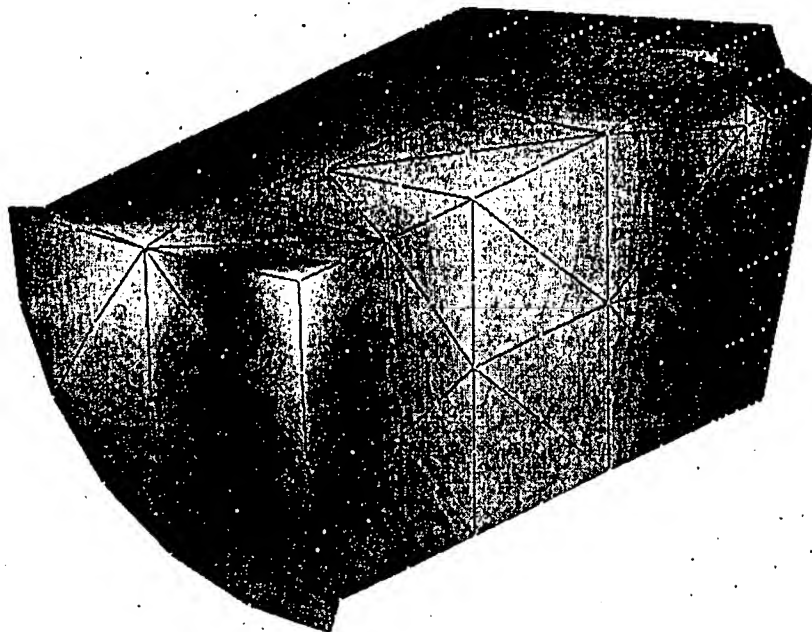


Figure 28: Electric field intensity - cut away view just below the lens.

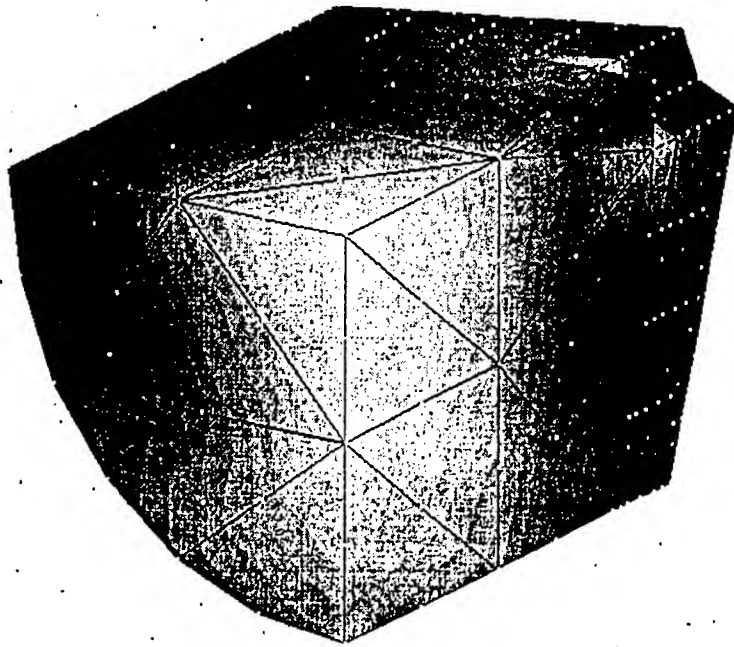


Figure 29: Electric field intensity - cut away view with top 1/3 of the cavity removed.

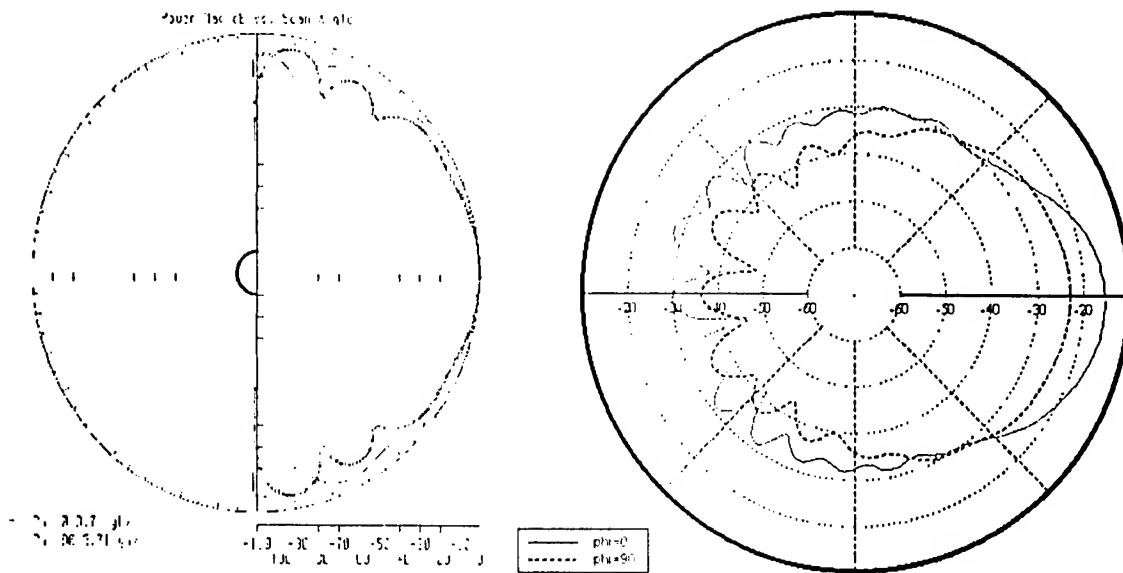


Figure 30: μ WaveLab (3.71 GHz) and TEMAC3D (3.58 GHz) radiation results.

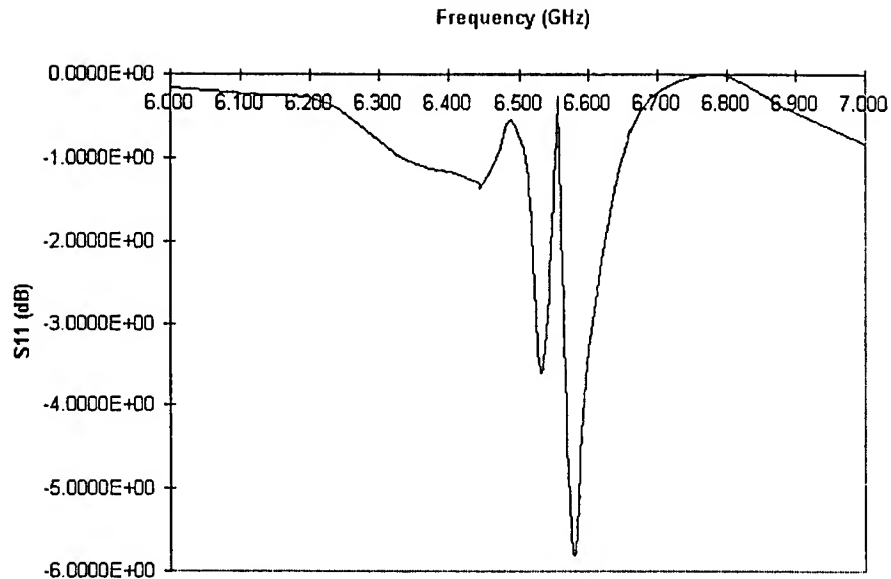


Figure 31: Scattering parameter for the 6 GHz H-parallel sensor model.

11 (all y polarizations) from the TEMAC3D results. Keep in mind that the μ WaveLab model is a simplified body of revolution model and, as such, is not the same as the TEMAC3D model.

Figure 33 compares the radiation plot for the sensor model with H parallel symmetry at 6.58 GHz on the left with the radiation plot from TEMAC3D on the right. The same rules as presented above for comparing the radiation plots in the 3 GHz range apply here. Notice that there is not as good agreement as was observed for the low frequency radiation plots. This can be explained by the fact that the μ WaveLab model is much simpler than the TEMAC3D model. The differences in the model results would naturally be more pronounced at the higher frequencies.

Port scattering parameters for the 6 GHz E parallel model are shown in Figure 34. The resonance at 6.59 GHz is very close to that of 6.47 GHz predicted by the TEMAC3D model. A field intensity plot for the 6.59 GHz resonance is shown in Figure 35. This can be compared to Figure 13 (x polarization) for the TEMAC3D results. The radiation plot is shown in Figure 36 on the left compared with the TEMAC3D results shown on the right. Once again, the same rules as presented above for comparing the radiation plots apply here. As for the H parallel symmetry, the radiation plot results do not compare well because of the differences in the models.

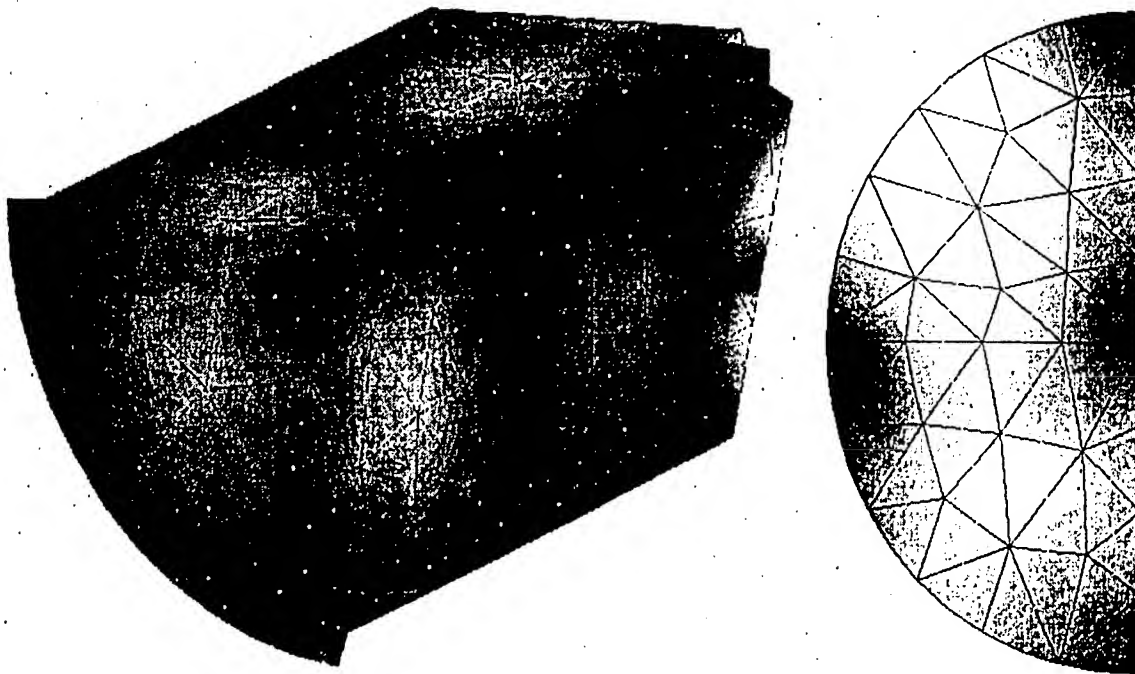


Figure 32. Electric field intensity - cutaway and top views.

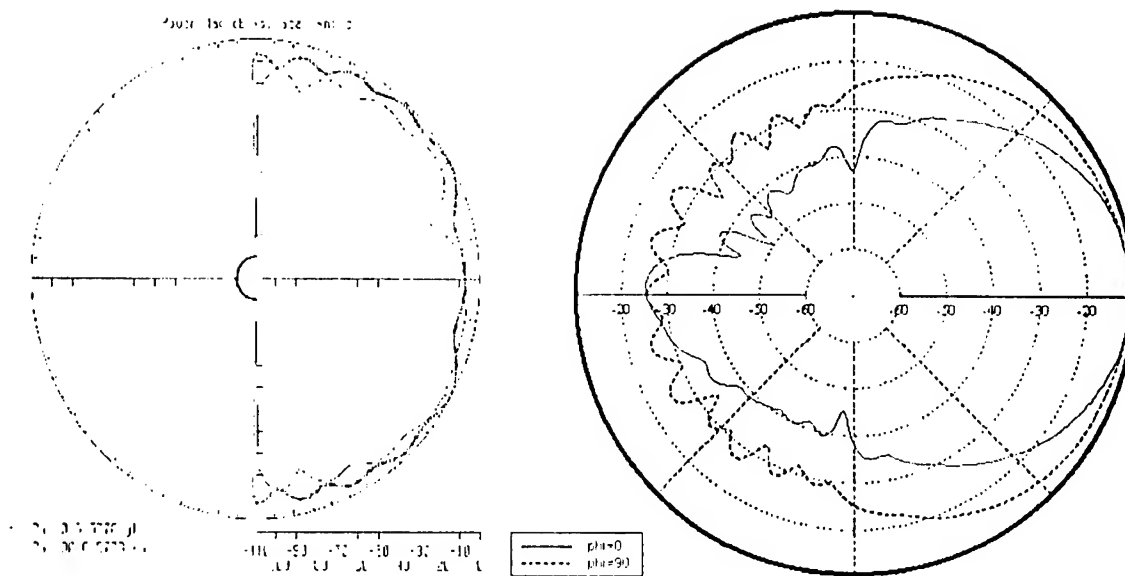


Figure 33. μ WaveLab (6.58 GHz) and TEMAC3D (6.47 GHz) radiation results.

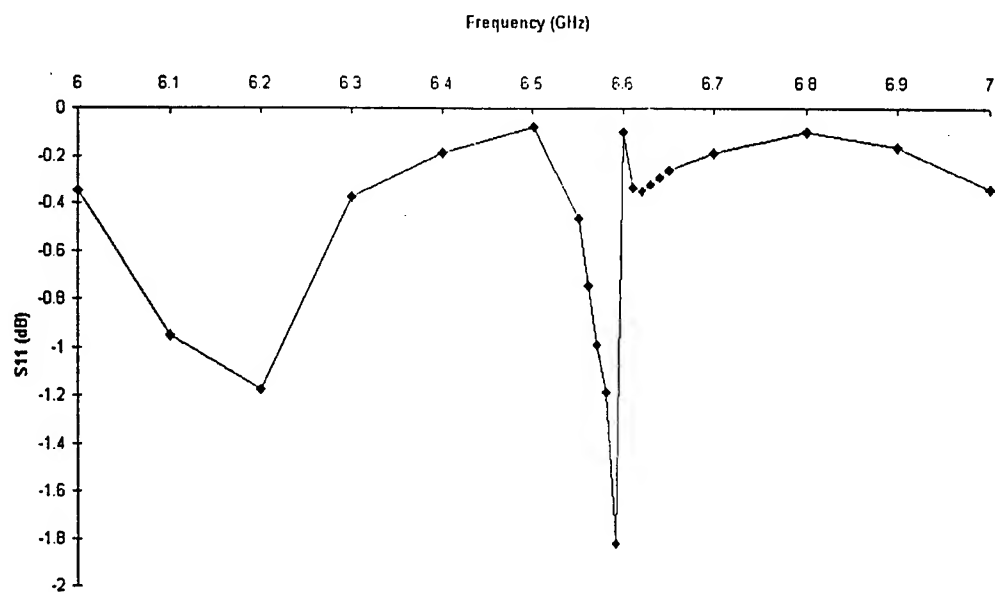


Figure 34: Scattering parameters for the 6 GHz E-parallel model.

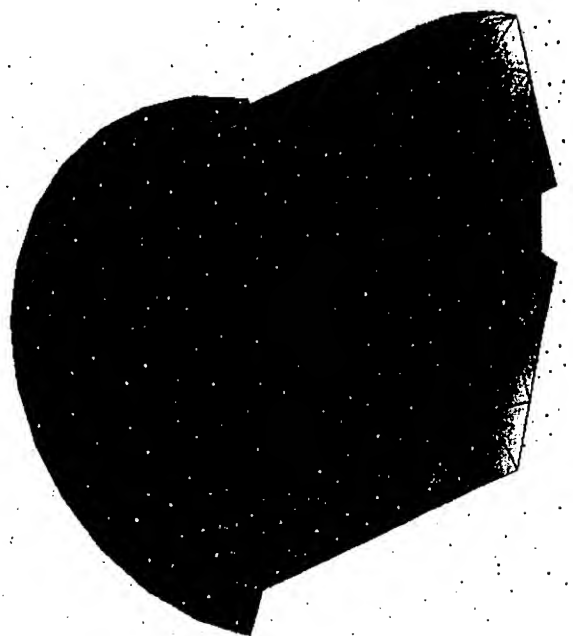


Figure 35: Electric field intensity at 6.59 GHz.

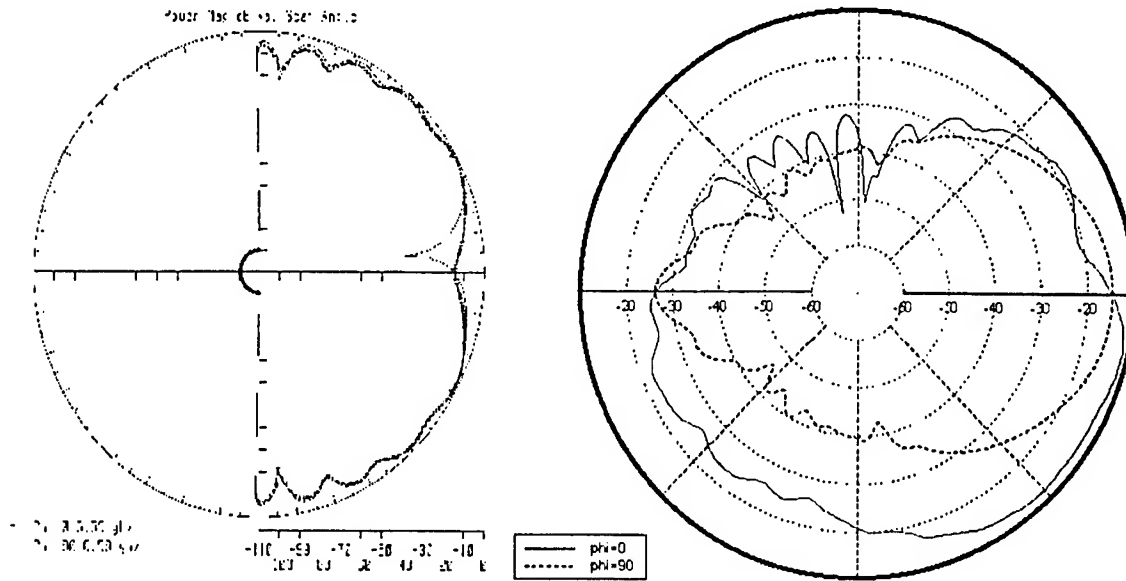


Figure 36: μ WaveLab (6.59 GHz) and TEMAC3D (6.47 GHz) radiation results.

The detailed models of the sensor similar to those reported in [1] were created so that the results of the analysis could be more reasonably compared to results obtained using other methods of analysis. However, this process was not entirely successful. At times the requirements for computer disk space were too great. Most of the problems that were not related to availability of disk space were with the 3 - 5 GHz E-parallel symmetry with a mesh containing 10,024 elements. The initial solution of the frequency sweep led to positive values (in dB) for S_{11} . This result, of course, was suspect not only due to the gain, but also because no resonances similar to the TEMAC3D results were found. Thinking that this result may be due to not modeling the loss in the germanium, its conductivity was incorporated into the model. The results of this model are presented below.

To better examine the resonance in the 6.5 GHz region, yet another model was generated for a frequency sweep between 4 and 6 GHz. This model surprisingly had less elements (7,903) than the previous one. This may be due to the different order in which the regions were meshed. If the radiating region was not meshed first, the computer would freeze up while attempting to mesh this region. The reason for this is not known. Therefore to generate a successful mesh required the meshing of the radiation region first. This model aborted in its solutions due to an error that Ansoft claimed to be a bug. Two viable work-arounds were recommended by Ansoft's technical support. The first was to try different element sizes. Several attempts at this produced the same error. The second method was to attempt meshing the cylindrical surface first

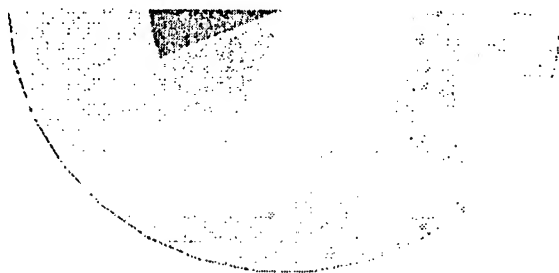


Figure 37: View of the port used for the full sensor model.

with a 2-D mesh as a seed for the 3-D mesh, and to delete the 2-D mesh after the 3-D mesh was complete. This also failed to produce results and the same error occurred.

At this point it became clear that one of the problems with the first model may have been that the elements in the Germanium may be too large due to its high dielectric constant of 14. A third mesh was generated in order to give smaller mesh elements in the Germanium regions. This mesh contained 32,400 elements and would have certainly failed due to lack of computing resources. The same error, however, that occurred in the second mesh occurred while attempting to analyze this mesh. And again all work-arounds recommended by Ansoft were unsuccessful.

The resulting successful geometric models that were created took advantage of half symmetry with either an E parallel or H parallel plane. In these models the germanium filter was modeled as in [1] which led to some difficulty in exciting the model. A port is the only means of exciting the cavity, so a waveguide must be used to do so. The waveguide was modeled as a circular wedge, that is, the cross-section of the waveguide was a portion of the face of the Mylar substrate. Figure 37 shows the port as the left triangle with the plane of symmetry to the top. This allowed for the solution of the lower frequency model. In summary, this sensor model differs from that of the previous section in that the outer toroidal regions and the filter regions are modeled as in [1], not as a body of revolution as in the simplified model. A ground plane was also added at the plane of the lens, not at the location of the satellite as in the simplified model.

Port scattering parameters were generated for H parallel symmetry and are shown in Figure 38. The resonance at 6.4 GHz was investigated further. Field plots are shown in Figure 39. Comparison of these plots to Figures 11 and 13 (y polarizations) show remarkable similarity. Again, the TE_{011} mode is clearly identifiable.

For the E parallel symmetry model, Figures 40 and 41 show S parameter results for the 3-5 GHz models

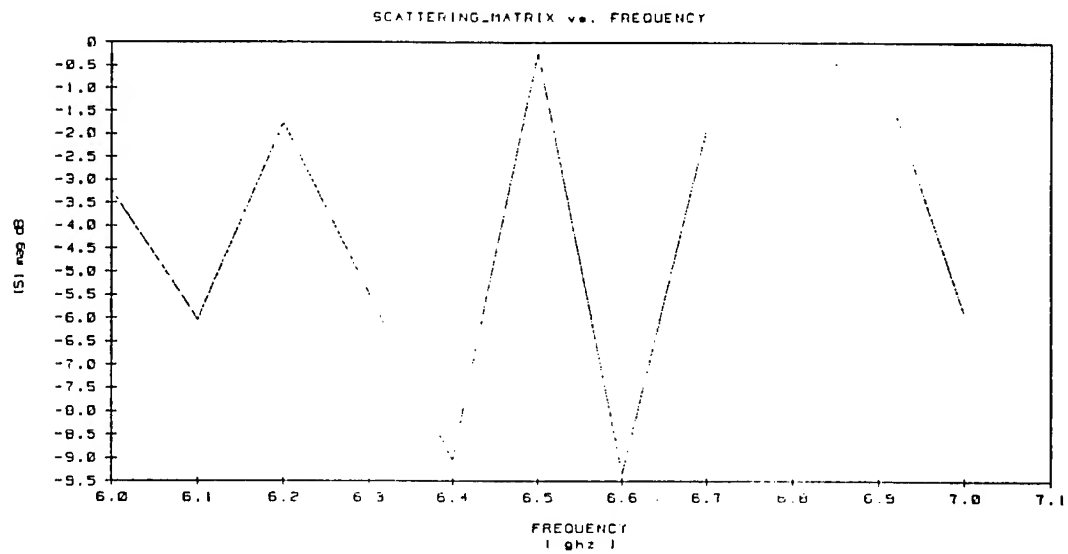


Figure 38: Scattering Parameters for the 6 - 7 GHz model.

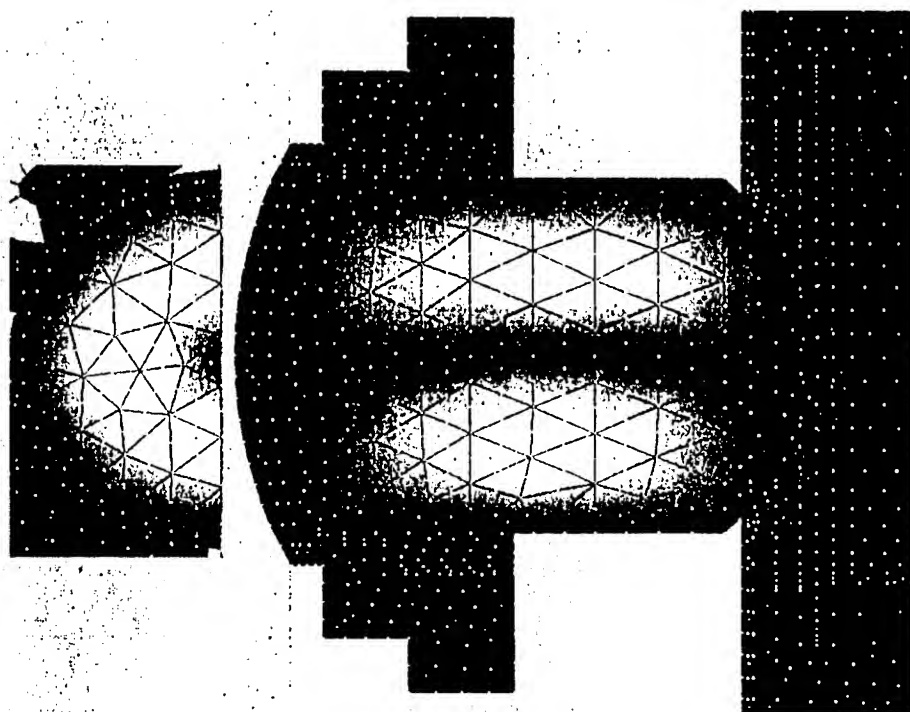


Figure 39: Electric field magnitude for the xy plane 1/3 below the lens, and the yz plane - 6.47 GHz.

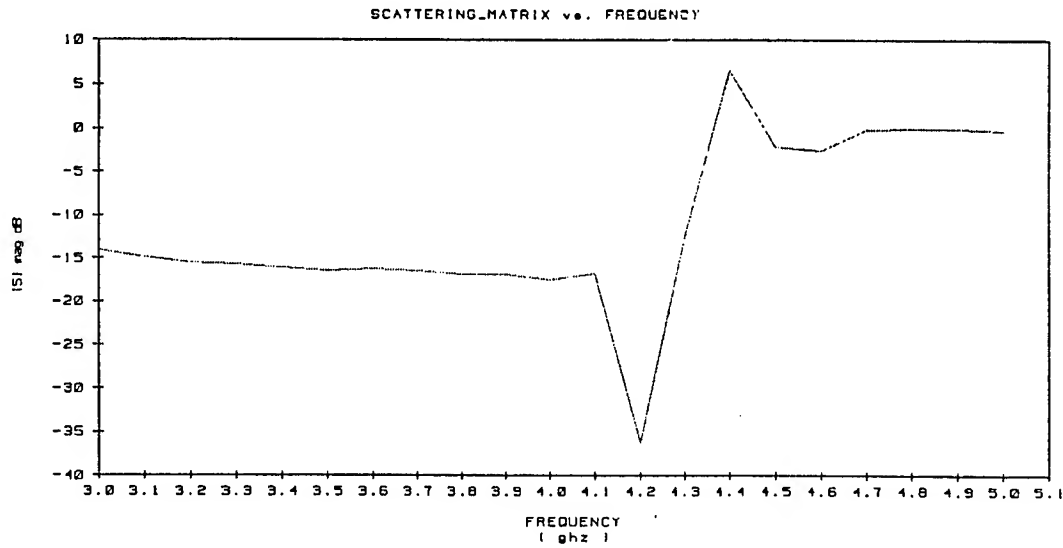


Figure 40: S_{11} for the sensor model with no loss.

without and with loss in the Germanium regions. Clearly, modeling of loss is important for this sensor in the FEM program. The scattering parameter plot for the 6-7 GHz model is shown in Figure 42. The resonance at 6.5 GHz was investigated further yielding the radiation plot shown in Figure 43. Compare this plot with Figure 36. Correlation is better than for the simplified model presented above.

Field contour plots are shown in Figure 44. Notice that the fields are capable of entering the lower toroidal cavity for this model. The field distribution in the central cavity can be compared to the TEMAC3D results of Figures 11 and 15 for the y polarization. The mode suggested is once again TE_{011} .

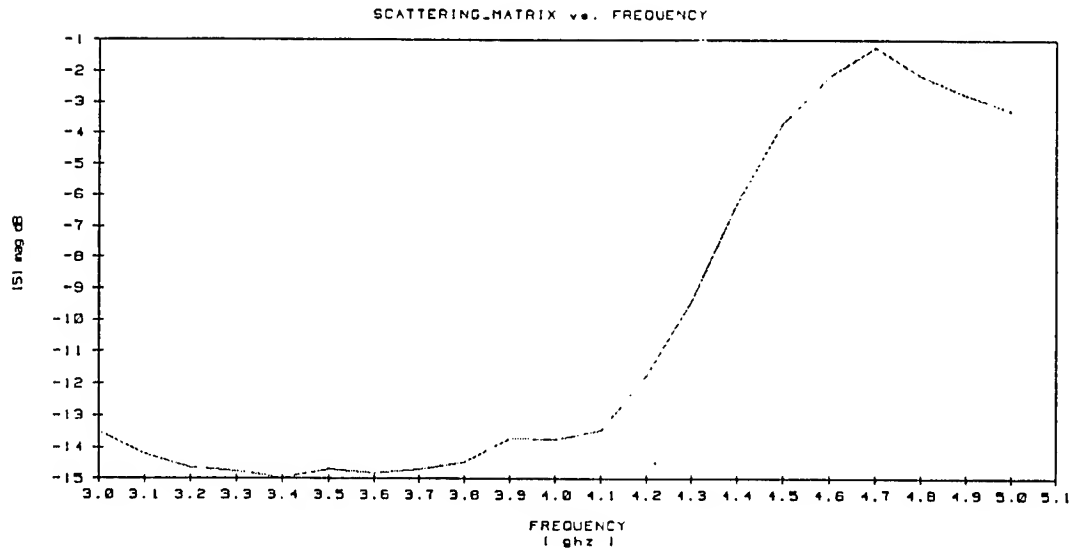


Figure 41: S_{11} for the sensor model with loss 3-5 GHz.

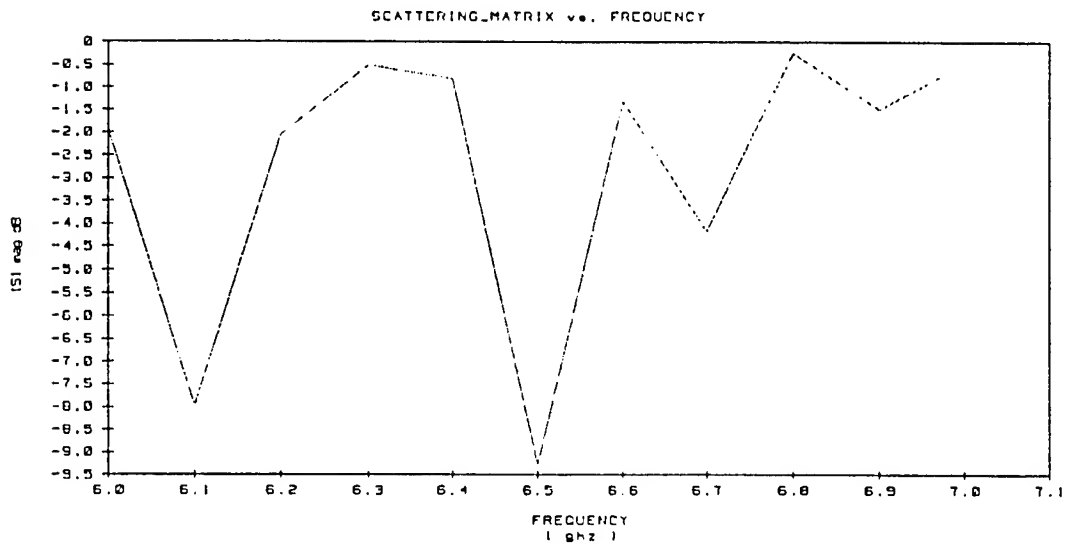


Figure 42: S_{11} for the sensor model with loss 6-7 GHz.

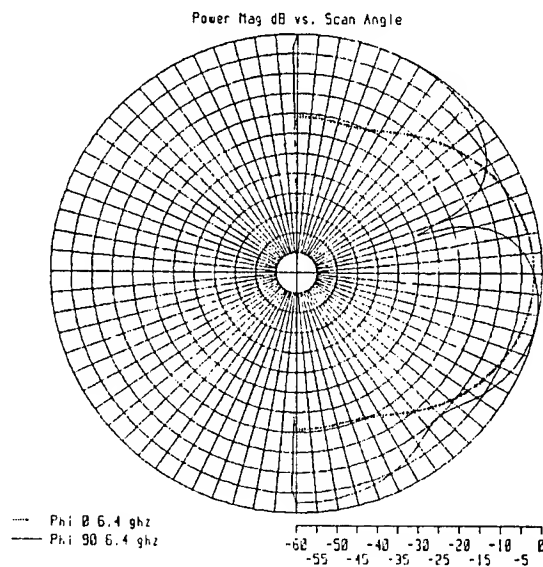


Figure 43: Radiation for the sensor, E parallel - 6.4 GHz.

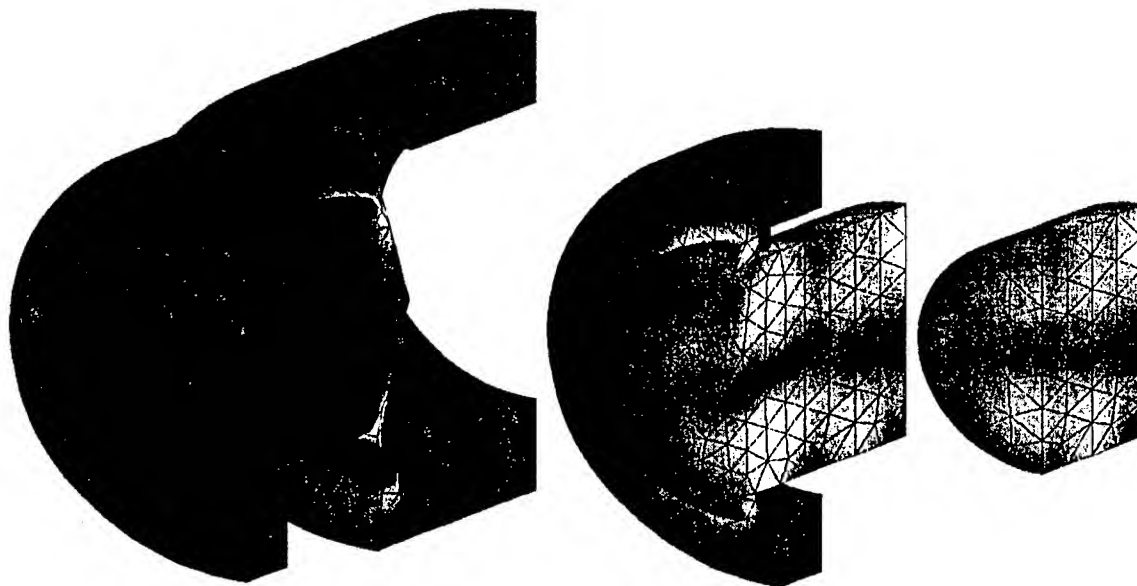


Figure 44: Field contours at 6.5 GHz with (a) lens removed, (b) lens and lower toroidal cavity removed, (c) lens, lower and upper toroidal cavities and 1/3 of central cavity removed.

Summary, Conclusions and Recommendations

The TSAR FDTD solver relies on the BRL-CAD, Anastasia and Image for pre-processing, and, in this study, Mathcad and Axum for post-processing. Unfortunately, problems with installation of the entire TSAR software suite were insurmountable, driving the use of a modified version of the TSAR FDTD solver from Sandia Laboratory. This version also had problems with a radiation model of both the Celestron-8 and the sensor. TSAR runs for the scattering problems with symmetry and a ground plane were, however, successful as validated by TEMAC3D.

Though the results of μ WaveLab for the most part have been accurate, the program has some drawbacks. First the bugs which prevented analysis on many of the models are a constant problem. The type of error which occurred most was a problem with the mesh near cylindrical walls. As cylindrical walls are pervasive in most of these problems, the error surfaces often. Next is the problem of excitation. The only way to excite the cavity is by means of a waveguide of some kind. This means first that the point of excitation must occur along a metal boundary of the model and second that the dimensions of the guide must permit passage of the frequencies being considered. This especially posed a problem at the lower frequencies as the maximum dimension available to place a waveguide in was barely large enough to fit a port valid at that frequency on. This may be one reason the results at the 3-5 GHz models performed so poorly. Finally, large computational resources are still necessary with FEM because of the need to solve a large matrix. For n unknowns (field quantities in the problem space), this results in a memory requirement of n^2 , where for the FDTD method, the memory requirement is n .

Significant findings from μ WaveLab were that it produced results consistent with TEMAC3D. The use of symmetry and second order finite elements allowed analysis at frequencies much higher than was achieved with IIP HFSS. Pre- and most post-processing can be accomplished with μ WaveLab. The HFSS capability of viewing fields on any plane in the problem space were not available with μ WaveLab. This capability is an asset because location and types of fields of interest are in general not known a priori. If this capability does not exist, the modeler must rely on experience to identify the likely locations and types of fields to be viewed. If that does not work, trial and error is the only alternative.

Based on prior studies cited and the results of this report, the conclusions are:

1. In general, the FDTD codes are the most computationally efficient for large open problems. Both TEMAC3D and TSAR run on UNIX platforms but could conceivably be ported to a PC running LINUX. The disadvantage for both codes is that they are tied to BRL-CAD for geometric modeling

and to Anastasia and Image for mesh generation and viewing. While BRL-CAD has been ported to AIX and resides on an IBM RS6000 at the University of Denver, Anastasia and Image have not been successfully ported to AIX (the attempt has been made) or to LINUX (yet to be tried). Anastasia and Image must still be used on a SUN platform at Phillips Laboratory. Both FDTD codes require external programs for FFTs and graphical presentation of data.

2. TSAR is required for large problems with symmetry or if a ground plane is necessary. Application of symmetry conditions reduces required computational resources and allows the high frequency limit of the simulation to be significantly extended. However, even though TSAR is capable of doing radiation problems, this feature does not work for the version of TSAR that has been installed at the University of Denver. A port to LINUX of the full TSAR Suite should be attempted.
3. TEMAC3D is better than TSAR for radiation problems which do not have to implement symmetry or a ground plane. Even though each simulation is done for only one frequency, the use of a separate program to generate any radiation pattern desired is a distinct advantage over TSAR which can have more than one frequency identified for the problem but with a limited number of radiation patterns. Desired radiation patterns are, in general, not known a priori. Both TSAR and TEMAC3D require definition of planes for field data prior to running the problem.
4. Ansoft μ WaveLab, limited to UNIX platforms and destined to be replaced by the Ansoft High Frequency Structure Simulator (HFSS) Version 5, is well suited to closed network parameter problems and single frequency radiation problems. As with TSAR and TEMAC3D, its field visualization capabilities are limited due to a priori definition of surfaces. Future use of Ansoft HFSS will overcome this deficiency. (HFSS will also be available for the PC.) Radiation and field plots can be generated in any plane desired. The high computational expense of doing frequency sweeps with large open problems put it at a distinct disadvantage. There is no capability of doing plane wave scattering problems.

The recommendations are: (1) In the absence of a comprehensive test and measurement program, various different numerical methods should be used for verification of results. (2) An FEM code such as Ansoft HFSS should be used for the closed optical train section of larger optical systems, and codes such as TEMAC3D and TSAR should be used for analysis of the open optical regions. (3) An attempt to port BRL-CAD and the TSAR Software Suite to LINUX should be accomplished. If successful, the extensive post-processing capabilities contained in the TSAR Software Suite could then be evaluated.

References

- [1] Ronald R. DeLyser, "FEM and FDTD Analysis of the Celestron-8 Telescope and a Satellite Sensor," Final Report, Contract F29650-96-W-0172, December, 1996.
- [2] R. R. DeLyser "Analysis of Complex Cavities Using The Finite Difference Time Domain Method", Final Report for the *Summer Faculty Research Program*, Sponsored by the Air Force Office of Scientific Research and Phillips Laboratory, September, 1996.
- [3] R. R. DeLyser and Peyman Ensaf, "Quality Factor Evaluation of Complex Cavities," Final Report, Summer Research Extension Program, Sponsored by Phillips Laboratory, December, 1995.
- [4] Ronald R. DeLyser, "Computational Evaluation of Optical Sensors," Final Report Contract F2965097W0130, November, 1997.
- [5] J.M. Putnam, L.N. Madgyesi-Mitschang and M.B Gedera, *CARLOS-3D Three Dimensional Method Of Moments Code*, McDonnell Douglas Aerospace-East, December 1992.
- [6] John H. Beggs, James D. Letterio and Sydney A. Blocher, Jr., *User Manual for XTEAR and TEMAC3D Computational Electromagnetic Time-Domain Codes*, available from Sydney A. Blocher, Jr., Phillips Laboratory/WSM, 3550 Aberdeen Ave. SE, Kirtland AFB, NM 87117.
- [7] R. R. DeLyser, P. Ensaf and P. McDaniel, "Method of Moments Analysis of the Celestron-8 Telescope," *The Twelfth Annual Review of Progress in Applied Computational Electromagnetics*, Naval Postgraduate School, Monterey, CA, 18-22 March, 1996.
- [8] R. R. DeLyser and H. Pohle, "Finite Element Method Analysis of the Celestron-8 Telescope," *The Twelfth Annual Review of Progress in Applied Computational Electromagnetics*, Naval Postgraduate School, Monterey, CA, 18-22 March, 1996.
- [9] K. S. Kuntz and R. J. Luebbers, "The Finite Difference Time Domain Method for Electromagnetics," CRC Press, Boca Raton, FL, 1993.
- [10] R. R. DeLyser, "Computational Evaluation of an Optical Sensor using the Finite Difference Time Domain Method," *The Thirteenth Annual Review of Progress in Applied Computational Electromagnetics*, Naval Postgraduate School, Monterey, CA, 17-21 March, 1997.
- [11] Constantine A. Balanis, "Advanced Engineering Electromagnetics," John Wiley & Sons, Inc., New York, 1989.

ANALYSIS AND INTERPRETATION OF
CONTRAIL FORMATION THEORY AND OBSERVATIONS

Andy Detwiler
Professor
Institute of Atmospheric Sciences

South Dakota School of Mines and Technology
501 East Saint Joseph Street
Rapid City, SD 57701-3995

Final Report for:
Summer Faculty Research Extension Program
Air Force Research Laboratory

Sponsored by:
Air Force Office of Scientific Research
Bolling Air Force Base, DC

and

Air Force Research Laboratory
Hanscom Air Force Base, MA

March, 1998

ANALYSIS AND INTERPRETATION OF CONTRAIL FORMATION THEORY AND OBSERVATIONS

Andy Detwiler
Professor
Institute of Atmospheric Sciences
South Dakota School of Mines and Technology
501 East Saint Joseph Street
Rapid City, SD 57701-3995

ABSTRACT

Gas turbine engine cycle calculations are used to estimate contrail factors in a range of flight environments at a range of power settings, for generic low-bypass and high-bypass turbofan engines. It is argued that the proper frame of reference for performing this calculation is that of an air parcel moving with the ambient winds. The most critical part of the contrail factor calculation is to estimate the change in total enthalpy such a parcel experiences as it is ingested by a gas turbine engine, compressed, heated, expanded, and exhausted. Using this frame of reference, it is seen that, contrary to assumptions made in current methods of contrail forecasting, the contrail factor is not constant for a given engine type. It varies even for the same engine at different power settings and flight conditions. The range of conditions investigated included flight at altitudes between 25000 and 50000 ft in a standard atmosphere, Mach numbers ranging from 0.4 to 0.9, and power settings from idle to military. The contrail factor ranges from 0.030 to 0.053 (g/kg)/°C for the low-bypass engine, and from 0.038 to 0.090 (g/kg)/°C for the high-bypass engine, depending on flight environment, Mach number, and power settings. Contrail factors are generally higher at lower power settings at a given Mach number, and higher at higher Mach numbers at a given power setting. Contrail factors tend to be higher at higher altitudes in general. In order to evaluate the contrail factor calculations based on cycle calculations, a set of contrail factors is diagnosed from a detailed set of opportunistic observations of contrails observed in near-threshold conditions for formation. The aircraft involved were mainly civil transport aircraft, and were powered with a variety of engine types. The range of contrail factors inferred from these observations is compared to the range of those computed from cycle calculations for different conditions. Reasonable agreement is found.

INTRODUCTION

Recent reviews (e.g. Schumann, 1996; Schrader, 1997) have noted that aircraft condensation trails, or contrails, have been observed since the early days of aviation. Combat requirements during the World War II era led to quantitative efforts to forecast the conditions in which contrails will form (Schumann, 1996). Detailed discussions of contrail formation forecasting by U.S. Air Force personnel and contractors appeared in the open refereed literature beginning in the 1950's (e.g. Appleman, 1953; Downie and Silverman, 1957; Pilie and Jiusto, 1958).

Contrails are an example of mixing cloud formation, a mode of cloud formation that has been studied and understood in a modern sense since early in this century. Despite the straightforward theory behind contrail formation, and despite the strong foundation laid by the early publications on this subject, to this day there still appear misguided treatments of contrail formation, as in Hanson and Hanson (1995). This report has three objectives, (1) discuss some of the misconceptions appearing in recent treatments of the theory of contrail formation, (2) develop a conceptual framework for analyzing contrail formation thermodynamically in a way that accounts for aspects of the problem not currently considered explicitly in Air Force operational forecasting, and finally (3) to compare predictions made using this framework to observations of contrail formation obtained during a recent Air Force Research Laboratory field program.

CONTRAIL FORMATION

Condensation trails form behind aircraft when they fly in sufficiently cold and humid air. These trails are an example of a cloud formed by isobaric mixing of warmer air that, while not saturated, contains a relatively high mixing ratio of water vapor, with colder air that also is not saturated and contains a relatively low mixing ratio of water vapor. Under suitable conditions it is possible for saturation to be reached in some mixtures of these two types of air. The process of cloud formation by mixing has been understood at least since the beginning of modern meteorology in this century and is described in detail in many of the classic modern texts (e.g. Geddes, 1921; Petterssen, 1956; Haltiner and Martin, 1957; Iribarne and Godson, 1981; Bohren and Albrecht, 1998).

It is important to note that when two parcels with different properties mix isobarically, it is vapor mixing ratio and enthalpy that are mixed in proportion to the mass of air of each of the two original types in the mixture. The state of the mixture is determined by this mixing of vapor and enthalpy. In most meteorological treatments of contrail formation (e.g. Appleman, 1953; Schrader, 1997), the mixing is described in terms of vapor mixing ratio and temperature. However, temperature is not a function of state, but enthalpy is a function of state. (See, e.g., Bohren and Albrecht, 1998.) Plume mixing described in terms of mixing of temperature is a reasonable approximation in a meteorological context because enthalpy is given by $C_p T$, where C_p is the specific heat of air at constant pressure. This specific heat is effectively constant and independent of temperature within the range of temperatures

encountered in the troposphere. If C_p is constant, then enthalpy is directly proportional to temperature and mixing can be described in terms of mixing of vapor mixing ratio and temperature.

In the context of contrail formation, however, mixing clouds form by mixing between parcels with temperatures differing by more than 1000 R in some instances. The specific heat of air, C_p , varies significantly over this range of temperatures, as shown in Figure 1. This variation has been incorrectly ignored in many treatments of contrail formation, including a recent treatment by this author! (Detwiler, 1996). It can be seen in Figure 1 that C_p varies by about 6% over the range of temperatures considered, which is typical of contrail formation circumstances. This means that the traditional contrail factor, the ratio of the vapor mixing ratio difference to the temperature difference between exhaust and environment, expressed as $(g/kg)/^{\circ}C$, is not constant over the entire range of possible exhaust temperatures.

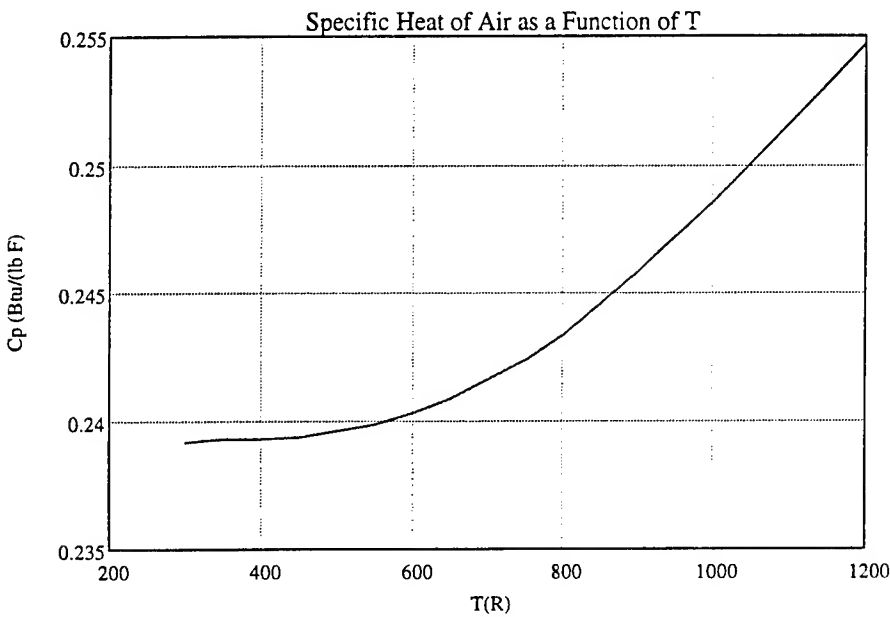


Figure 1. The variation of the specific heat of air at constant pressure, C_p , with temperature.

The process of contrail formation is illustrated below with a mixing diagram, derived from Figure 1 in Detwiler (1996), shown here as Figure 2. In Figure 2 mixing is shown in the framework of vapor mixing ratio and enthalpy. Isobaric mixing at 300 mb ambient total pressure is represented. Air characterized by mixing ratio and enthalpy represented on the diagram by Point A, mixing with air represented by Point B, will produce mixtures whose mixing ratio and enthalpy lie along a straight line connecting the two points. This line will be called the mixing line. (If

temperature were used on the horizontal axis, then the line would have slight curvature due to the variation of C_p with temperature. The mixing line on a mixing ratio versus temperature diagram will be essentially straight at the lower end, since C_p is essentially constant over the meteorological temperature range.) Its slope at any point along it is the traditional contrail factor if the horizontal axis is expressed in terms of temperature. Mixtures that are mostly A will lie near A on the diagram. Mixtures that are mostly B will lie near B. If the axes' scales on the diagram are linear, then the distance from the end points is inversely proportional to the proportion of that type of air in the mixture.

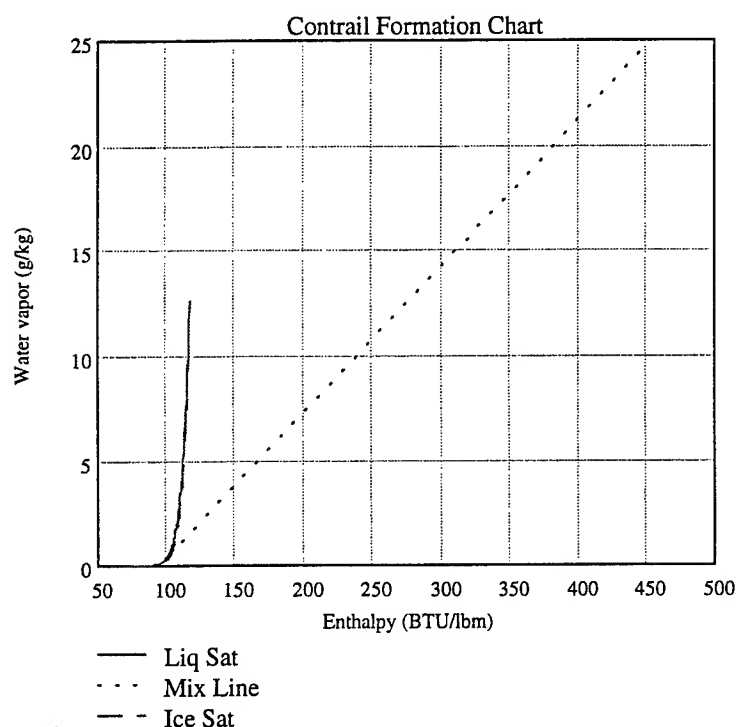


Figure 2. A diagram illustrating a hypothetical mixing line between air with vapor mixing ratio and enthalpy characteristic of high temperature gas turbine exhaust, and air with a mixing ratio and enthalpy characteristic of the upper troposphere. The exhaust has a temperature of 973 K (1751 R) while the tropospheric air has a temperature of 221 K (398 R) and a relative humidity of 40%. The contrail factor in this example has a value of 0.697 (g/kg)/(BTU/lbm), which is equivalent to 0.030 (g/kg)/°C near ambient conditions. At this scale, the saturation mixing ratio curves with respect to ice and liquid water are indistinguishable. The saturation mixing ratios as a function of temperature are computed using the Goff-Gratch formulae and are plotted against the enthalpy of air at that temperature.

Conditions near the lower end of the mixing line are shown in expanded scale in Figure 3. For this set of conditions, the mixing line crosses above the saturation mixing ratio line with respect to liquid water, and condensation is expected.

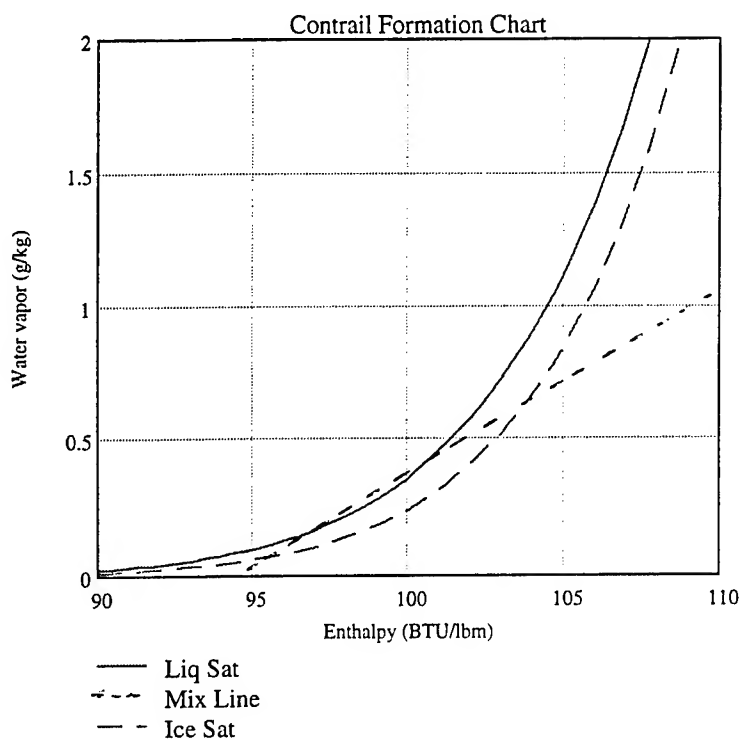


Figure 3. An expanded view of the lower end of the mixing line shown in Figure 2, indicating that liquid condensation will occur during mixing for the conditions specified above.

As discussed by many authors, most recently by Schrader (1997) and Jensen et al (1998), contrail formation will occur when the mixing line crosses the saturation mixing ratio line for liquid water. This indicates that some mixtures are supersaturated with respect to liquid water and condensation on suitable exhaust nuclei will occur. The slope of the mixing line for conditions near the ambient atmospheric temperatures, where condensation actually occurs, is equal to the traditional contrail factor. This slope can be expressed in terms of $(\text{g/kg})/^{\circ}\text{C}$, using Figure 2, if one divides enthalpy in the range of meteorological temperatures, by C_p in this temperature range, using appropriate units.

Detwiler (1996), among others, shows that the critical temperature for contrail formation, the highest temperature at which contrails will form at a given pressure level and relative humidity, is the temperature at which the slope of the curve of saturation mixing ratio versus temperature is just equal to the contrail factor. Since the standard meteorological value of C_p is valid at these temperatures, it is proper to divide the slope of the mixing line in mixing ratio-enthalpy space by C_p to find the slope in mixing ratio-temperature space.

ESTIMATING CONTRAIL FACTOR from ENGINE CYCLE DATA

Previous Work

Appleman (1953) estimated the slope of the mixing line by taking the ratio of water to heat produced during combustion without considering any of the details of engine operation. Appleman estimated that for every lbm of fuel burnt, 1.4 lbm of water, and 17974 BTU, were produced. The enthalpy of combustion is divided by C_p at typical ambient temperatures to estimate the temperature change due to combustion. The implicit assumptions in this approach are that all of the water and heat generated during combustion is contained in the gases leaving the exhaust nozzle, and that C_p is constant. While Appleman made his computation using data for a fuel used during World War II, Jiusto and Pilie (1958) in the same manner computed a contrail factor for JP-4, the most common military fuel in use then and now (very close in properties to Jet-A, the most common civilian fuel then and now), arriving at a value of 0.0295 (g/kg)/K. A detailed discussion of this procedure, along with some of the uncertainties associated with it, is presented in Detwiler (1996).

A different approach to estimating the contrail factor is to use measurements or calculations, based on the aircraft engine cycle, of the water generated by a particular rate of fuel combustion, and divide by the difference in enthalpy between the exhaust gases leaving the nozzle and the surrounding environment. Peters (1993) obtained engine manufacturer's data on several engines from which to calculate contrail factors in this manner. These engine types included the turbojet, and low- and high-bypass gas turbine engines. The data included tailpipe moisture and temperature, for a wide range of power settings, flight Mach numbers, and flight levels. He does not say so explicitly, but for the bypass engines it appears that he used numbers characteristic of the engine core exhaust. Other critical details not described in his report include the ratio of water created to fuel consumed, and whether the exhaust temperatures used were static or a total temperatures. He gives the following characteristic contrail factors for each type of engine:

non-bypass (turbojet)- 0.0360 (g/kg)/°C

low-bypass - 0.0400 (g/kg)/°C

high-bypass - 0.0490 (g/kg)/°C

Contrail factors can also be computed empirically from measured fuel flow m_f , engine air flow m_e , ambient static temperature T_a , and exhaust exit total (stagnation) temperature T_{E0} . One form of the estimate is presented in Saatzer (1995a)

$$CF = [1.3 m_f] / [(m_e)(T_{E0} - T_a)] \quad (1)$$

where “1.3” represents Saatzer’s assumption of the ratio of water mass generated per unit mass of fuel combusted (The fuel is assumed to be represented chemically as $(CH_2)_n$. One water molecule is produced for each CH_2 group oxidized. The ratio of molecular weights of water to CH_2 is 18/14 which is ~ 1.3 .) Other estimates of the ratio of water produced per unit of JP-4 or Jet-A fuel combusted, based on actual measurements of fuel composition, are as low as 1.22, as in Busen and Schumann, 1995. The fuel flow m_f multiplied by 1.3 is used to estimate the water added to the exhaust by combustion. Fuel flow can be neglected with respect to the air flow m_a , in the denominator of (1) for all practical calculations, as the air flow is usually not known to better than $\sim 2\%$, and typical maximum fuel/air ratios are 3-4%. The engine exit total temperature T_{E0} is a measure of the total energy, thermal plus directed kinetic energy of motion, created by combustion and added to the engine exhaust. The difference $(T_{E0} - T_a)$ is proportional to the energy added by combustion. (In fact, Saatzer assumes that C_p is independent of temperature and therefore that $(T_{E0} - T_a)$ is exactly proportional to the enthalpy of combustion.)

A several-month flight test program involving turbojet-powered T-33’s is described in Saatzer (1995a). Contrail factors were computed from engine measurements using equation (1) during climb, descent, and steady level flight. Contrail factors computed for the T-33 ranged from 0.025 to 0.039 $(g/kg)/^{\circ}C$. Factors as low as 0.025 were obtained during engine decelerations/descents, values near 0.032 in steady flight, and factors as high as 0.039 during accelerations/climbs. The low contrail factors during decelerations were transient and due to the fuel flow decreasing more quickly than the exhaust temperature. The reverse was true during accelerations. The median value of 0.032 $(g/kg)^{\circ}C^{-1}$ for steady flight is slightly higher than the value estimated from fuel properties, but lower than the value suggested by Peters (1993) for a turbojet. Good agreement was obtained between contrail factors inferred from the observed contrail onset environmental conditions, and those computed from aircraft operating parameters.

Building on the Previous Work

In this work, engine cycle data were computed for two engine configurations and a variety of flight conditions, following the line of investigation opened by Peters (1993). Contrail factors were first computed using a variation on (1), as described in Saatzer (1995a). It is presumed that Peters performed essentially the same calculation, although there is insufficient detail in Peters (1993) to verify this. One minor adjustment was that the constant factor in the numerator of (1) was reduced to 1.28, as justified in Detwiler (1996).

One difference between the present work and the previous work just described is that in the previous work the mixing process is incorrectly represented with a straight line connecting two different initial mixtures in vapor mixing ratio versus temperature space. As reported above, isobaric mixing is more correctly represented with such a

straight line in vapor mixing ratio versus enthalpy space. A computation of contrail factor in units of $(\text{g/kg})/^{\circ}\text{C}$, equivalent in definition to the contrail factor of Appleman (1953), can be made by dividing the slope of the mixing line in mixing ratio - enthalpy space, $(\text{g/kg})/(\text{BTU/lbm})$, by C_p ($\text{BTU}/(\text{lbm R})$) and then multiplying by 9/5.

When this contrail factor estimate is based on the ratio of water to heat produced during combustion, and the value of C_p employed is appropriate for upper tropospheric temperatures, then the contrail factor found is appropriate for estimating the threshold temperature for contrail formation by the matching-slope method, equivalent to the procedures of Appleman (1953), Jiusto and Pilie (1958), Jensen et al (1998), and others.

Comparing the results of the procedure followed by Peters (1993) and Saatzer (1995a) to the present work, the previously computed contrail factors are too low due to an underestimate of the enthalpy difference between environment and exhaust. The hotter the exhaust, the more the contrail factor will be underestimated if variation of C_p with temperature is ignored. For exhaust stagnation temperatures around 1750 R, the underestimate will be ~6%, resulting in an estimate of contrail onset temperature ~0.6 K too low (Detwiler, 1996).

Further refinements

Engines with separate exhaust streams

These first attempts at contrail factor estimation were subsequently modified. For bypass engines with separate unmixed exhaust streams, all of the water generated during combustion is in the core stream, but the enthalpy generated is distributed to both the core and bypass streams. In the results presented below, the contrail factor for turbofan cycles with separate exhausts is computed based on the core properties. Thus contrail factors for the core flow in turbofan cycles with separate exhausts represents a maximum possible contrail factor. Some mixing between core and fan stream may occur before contrail formation occurs aft of the engine. If mixing occurs, the appropriate contrail factor should be somewhere between the core contrail factor and a contrail factor representing completely mixed bypass and core streams. Saatzer (1995b) attributes the higher contrail factors for high-bypass turbofan engines compared to low-bypass engines, deduced during flight tests, to incomplete mixing of the separate streams prior to contrail formation.

Propulsion Efficiency

An important assumption in the computation of contrail factor from fuel properties is the assumption that all of the enthalpy added to the engine air stream during combustion is present in the exhaust leaving the engine. Detwiler (1996) reviewed the debate over this assumption. Schumann (1996), quoting earlier work by Schmidt in Germany during World War II, points out that some of the energy generated during combustion must be used to propel the

aircraft. This energy is not present in the near-field engine exhaust plume but dispersed in the wake of the aircraft outside of the engine exhaust plume. This separated energy eventually mixes back together, but not for many aircraft widths aft. Contrail formation typically occurs well before these separate regions mix back together.

Using a computation of propulsion efficiency to estimate the fraction of combustion energy in the aircraft wake outside of the exhaust plumes, and computing contrail factors using the Appleman approach but discounting this energy from the exhaust, Busen and Schumann (1995), Schumann et al (1996), Schumann (1996), and Jensen et al (1998) report reasonable agreement between estimated and observed contrail onset temperatures. These authors, in contrast to Saatzer, attribute the higher contrail factors for high-bypass compared to low-bypass engines, diagnosed from observations, to be due to higher propulsion efficiency for higher bypass engines.

An appropriate frame of reference for contrail factor calculations

After trying several approaches to estimating contrail factors based on engine cycle calculations, and observing some inconsistencies, it was decided to adopt a new reference frame for the calculations in order to simplify the interpretation of the results in terms of propulsion efficiency and separate exhaust streams. Busen and Schumann (1995), and Saatzer (1995 a), following Osterle (1956), and others, look at contrail formation in a reference frame moving with the engine. This is convenient in some respects, as total temperature and pressure measurements (in the case of real engines), and total temperature and pressure, and exit velocity, computations (in the case of cycle calculations) are all made in this reference frame. However, Figure 2 shows that contrail formation actually occurs in mixtures that are almost completely environmental air. If one assumes that turbulent mixing of heat and momentum proceed at the same rate, then this newly-formed contrail region should be moving almost with the environmental winds. Almost all of the directed kinetic energy in the exhaust plume, the thrust which the engine generates, will have been reduced to random thermal energy by the time contrail formation occurs. Thus the natural frame of reference for computing contrail factors is the one of the environment through which the aircraft is moving.

In this reference frame moving with the environmental winds, one can imagine a parcel of air lying in the path of an advancing jet engine. The parcel is overtaken by the engine, drawn into it, compressed, heated, has enthalpy injected by combustion, expands through the turbine and nozzle, is exhausted at a high speed, and is left behind mixing with the unaltered environment as the engine moves away.

The water vapor mixing ratio in this exhaust air is estimated as

$$1.28 \, m_f / (m_f + m_e) \quad (2)$$

The total enthalpy of this exhaust air is

$$H_{es} + \frac{1}{2} (v_e - v_p)^2 \quad (3)$$

where H_{es} is the static enthalpy of the exhaust at the exit plane, $C_{pe}T_{es}$. The C_{pe} is the specific heat at constant pressure at T_{es} , and the second term in (3) is the kinetic contribution to total enthalpy, in the reference frame of the air through which the engine is moving. It is assumed that this exhaust is brought to rest relative to the air around it by mixing with it, so that this total enthalpy, initially the sum of substantial static and kinetic parts, is converted to all static enthalpy at the point where contrail formation begins.

Saatzer (1995a), equation 6.5, gives a definition of exhaust total enthalpy equivalent to equation (3), above. However, in his subsequent calculations, e.g. equation 6.7 et seq, he appears to use total temperature in the aircraft frame of reference as the basis for estimating total enthalpy in the exhaust. This provides an overestimate of the total enthalpy in the exhaust in the frame of reference of the air through which the aircraft is moving, and yields an underestimate of the contrail factor, and more importantly, a contrail factor that is independent of airspeed.

In the reference frame of the air, there needs to be no additional correction for propulsion efficiency, as is employed by Busen and Schumann (1995), Jensen et al (1998), and others. In the frame of the engine, as used by these workers, exhaust speed relative to the engine plus static temperature, or equivalently the total temperature (abbreviated as EGT, exhaust gas temperature) determines the total enthalpy of the exhaust at the exit plane. A separate calculation of propulsion efficiency (see Schumann, 1996, or Detwiler, 1996, for a review) is required to correct for energy not in the exhaust plume of a moving engine. In the reference frame of the air through which the engine moves, no correction for propulsion efficiency is required. Note that in (3), as the aircraft speed more nearly approaches the exhaust speed (as it does for high-bypass ratio turbofan applications, and also for low-bypass engines at supersonic flight conditions), the enthalpy of the exhaust as seen in the reference frame of the environment through which the engine is moving, also decreases. In the unattainable limiting steady state where the exhaust is moving aft at the same speed the aircraft is moving forward, the thrust disappears, the propulsion efficiency becomes unity and the contrail factor becomes infinite.

As will be shown below, contrail factors estimated using this approach applied to calculated engine cycle are in reasonable agreement with contrail factors inferred from observations of contrail formation behind aircraft in steady flight. All of the results presented apply to steady-state conditions. Effects of transient conditions, such as the decelerations/accelerations discussed in Saatzer (1995a), are not accounted for in these calculations.

REVISED CONTRAIL FACTORS for LOW- and HIGH-BYPASS TURBOFAN ENGINES

Engine cycle calculations were performed with ONX/OFFX, a gas turbine engine cycle computation package that is a companion to Mattingly et al (1987). A variety of engine cycles were explored, with an emphasis on low-bypass and high-bypass turbofan engines based on examples given in Mattingly et al (1987). Both on-design and off-design operating points were computed. A particular set of initial parameters, including compressor pressure ratio and bypass ratio, was chosen, and then iterations were performed to find the engine parameters to optimize specific fuel consumption for a particular flight condition using ONX. Once the engine parameters were established for the design condition, OFFX was used to look at performance characteristics of this engine at other flight conditions.

Results of engine cycle computations also were obtained from Aeronautical Systems Center (ASC) for a typical low-bypass and a typical high-bypass engine. These results are more accurate than those obtained using ONX/OFFX because the ASC computations involve fewer simplifications.

Three estimates of a contrail factor, the ratio of water to enthalpy added to the air passing through the engine, are presented below for low-bypass and high-bypass engines for several flight conditions.

1. The first method follows the Appleman method. Here, it is assumed that 1.28 lbm of water and 18400 BTU are produced as a result of the combustion of 1 lbm of fuel, following Jiusto and Pilie (1958). In the standard units used by Appleman and followed by others since, the contrail factor if all of this water and enthalpy were in the exhaust would be 0.030 (g/kg)/C , independent of engine setting, flight condition, or any other variable associated with aircraft operation. For the comparisons to follow, the same assumption about water production is made for each method, so the relative comparisons would not change if a different ratio of water to fuel were assumed. The contrail factor computed using the traditional Appleman method is used as a reference. It is impossible for the exhaust to contain more energy than was generated by combustion, although due to parasitic flows, power extraction for accessories, etc., the energy in the exhaust could certainly be less than that generated by combustion. If the water-generated to fuel-combusted ratio is constant, and the energy in the exhaust must be less than or equal to the energy-to-fuel combusted ratio, then the contrail factor of an engine in operation should never be less than this "Appleman" factor, although it could be higher.
2. A second estimate is derived making the same assumption about water production, but estimating the enthalpy added to the air passing through the engine by taking the difference between the total enthalpy at station 9 (the exhaust plane) based on the cycle computation of the stagnation temperature there, and the static enthalpy in the environment. In this method, the exit-plane enthalpy is the enthalpy of the exhaust in the frame of reference moving with the engine.

3. The third method assumes the same relationship between fuel consumption and water production, but the enthalpy change in the air flowing through the engine is taken to be the total enthalpy in a reference frame relative to the air through which the engine moves, minus the static enthalpy in the environment.

Results for the low bypass engine are computed assuming complete mixing of the core and duct air flows prior to the exit plane. The situation is more complex for the high-bypass engine cycles. In some designs, the bypass and core streams are mixed prior to leaving the nozzle. In others, the fan stream exits upstream and concentric to the core stream. For this reason, contrail factors for the generic high-bypass engine are computed by both methods 2 and 3, for two extreme situations. The first (a) assumes that core air is mixing in an undiluted form with ambient air. The second (b) assumes that core and duct air are completely mixed prior to contrail initiation, and that this mixture has a mass-weighted average speed. In actuality, some, but not complete, mixing between core and duct air probably occurs in most cases prior to contrail initiation, and the observed contrail factor probably would lie between these two extremes in most installations.

Examples of results computed for a low-bypass engine over a range of flight conditions at 30 kft altitude in a standard atmosphere are shown in Figures 4 and 5. The contrail factor in Figure 4 is computed in the aircraft frame of reference (Method 2) while Figure 5 shows results computed in a frame of reference moving with the ambient air (Method 3).

In the aircraft frame of reference, Figure 4 shows that the contrail factor decreases with increasing flight Mach number, and generally increases with increasing power setting (PLA) at all flight Mach numbers except $M = 0.4$. At $M = 0.4$ and $M = 0.5$ there is very little dependence of contrail factor on power setting. The total range of variation is about $\pm 7\%$ from the mid-range of contrail factor values over the range of flight conditions examined. All computed factors are less than the Appleman factor estimated using Method 1. This relationship shows that these computations are incorrect. A contrail factor lower than that computed from fuel properties can only arise if there is higher enthalpy per unit of fuel consumed compared to the theoretical heating value. While it is possible for enthalpy to be lost from the engine air flow in parasitic flows (bleed air extraction, accessory power take-off, etc.) there is no way to add enthalpy to the flow beyond that released by fuel combustion.

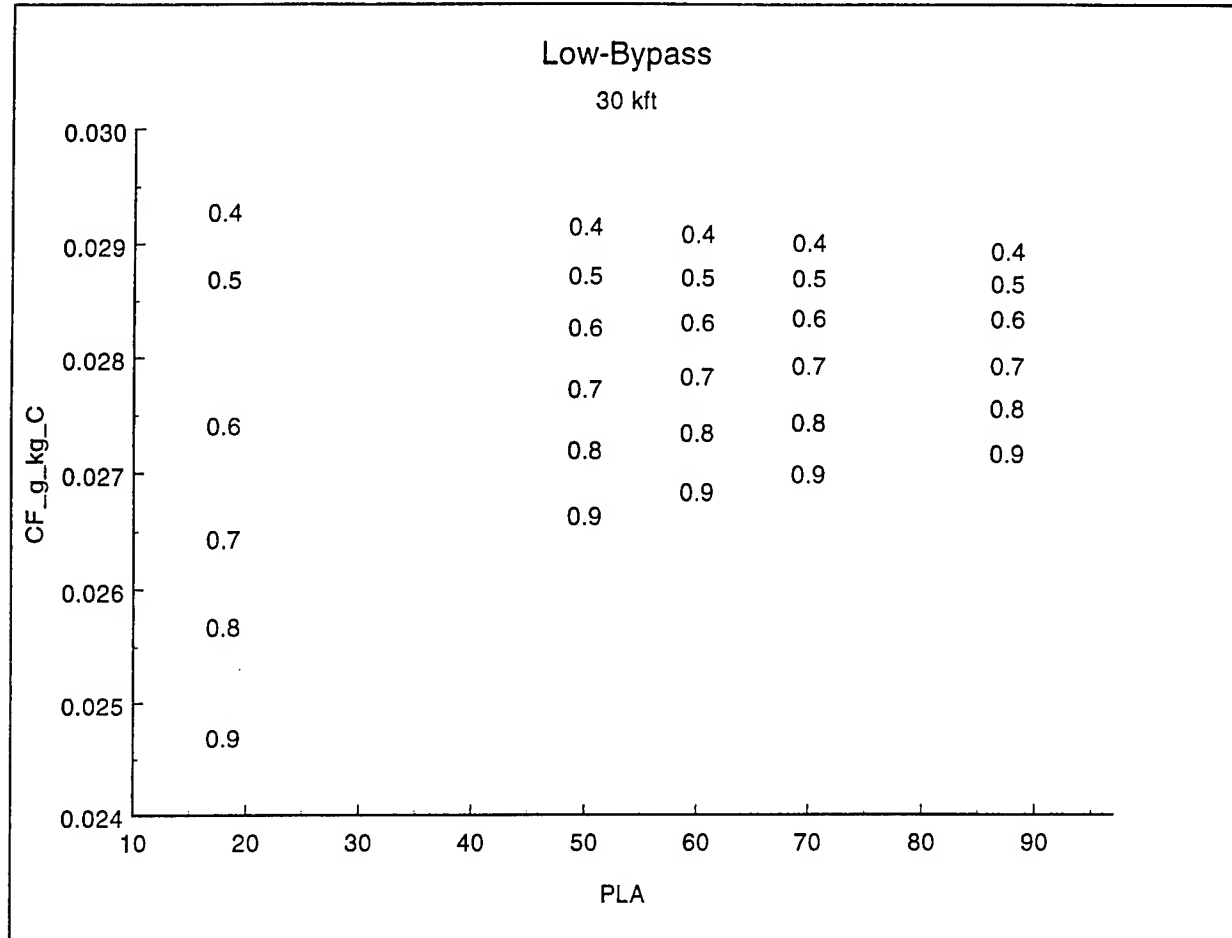


Figure 4. Contrail factors computed in the aircraft frame-of-reference for a low-bypass engine for 4 power settings (PLA). The engine is operating at 30000 ft MSL in a standard atmosphere. Results are shown for flight Mach numbers ranging from 0.4 to 0.9, at each power setting.

Figure 5 shows that contrail factors are generally higher when computed in the frame of reference of the air through which the aircraft is moving. None of the contrail factors are less than the “Appleman” contrail factor estimated using Method 1. The generally higher values arise because there is less total enthalpy in this reference frame, while the water content is the same as estimated using Method 2. There is small variation in contrail factor for $50 < \text{PLA} < 87.5$, but a big jump in contrail factor between $\text{PLA} = 50$ and $\text{PLA} = 18$. These “corrected” contrail factors generally increase with increasing flight Mach number at constant PLA because the exhaust is moving more slowly relative to the air as the aircraft speeds up. In other words, the exit plane exhaust speed becomes less in this reference frame as Mach number increases, lowering the total enthalpy in the exhaust. At a given Mach number, the “corrected” contrail factor increases with decreasing power setting for the same reason, that is, exhaust speed relative

to the air is decreasing as PLA decreases. The total range of variation of the "corrected" contrail factor is about +/- 25% over the range of conditions examined.

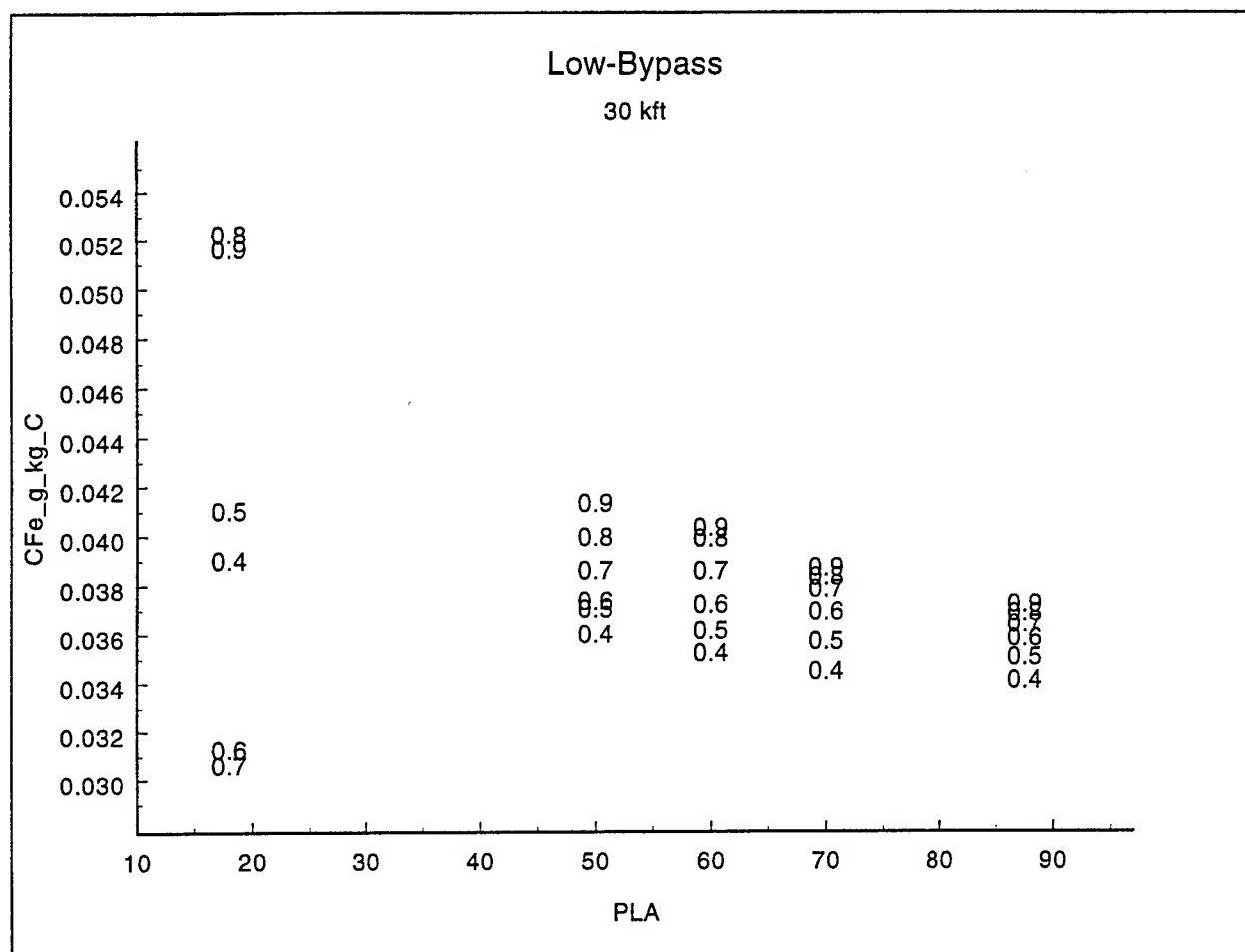


Figure 5. Results for contrail factor in a reference frame at rest relative to the air, in the same format as Figure 4.

Figures 6 and 7 show similar information to that given in Figures 4 and 5, for a range of altitudes between 25000 and 50000 feet in a standard atmosphere. The range of variation of contrail factor over the range of Mach numbers and power settings examined, diminishes somewhat with altitude. Overall mass flow through the engine diminishes with increasing altitude, and at the higher altitudes there is less variability in engine conditions over the same range of power settings. However, other major trends are as shown in Figure 4 and 5. Again, it is seen that Method 2 (Figure 6) yields unrealistic results because most of the contrail factors are less than the "Appleman" one, while Method 3 (Figure 7) yields more plausible estimates of contrail factors in that all factors are equal or greater than the Appleman one. The contrail factors at higher power settings are in the range estimated in Schrader (1997), based on flight test observations of low-bypass turbofan-equipped aircraft making contrails. They are lower than those estimated in Peters (1993)

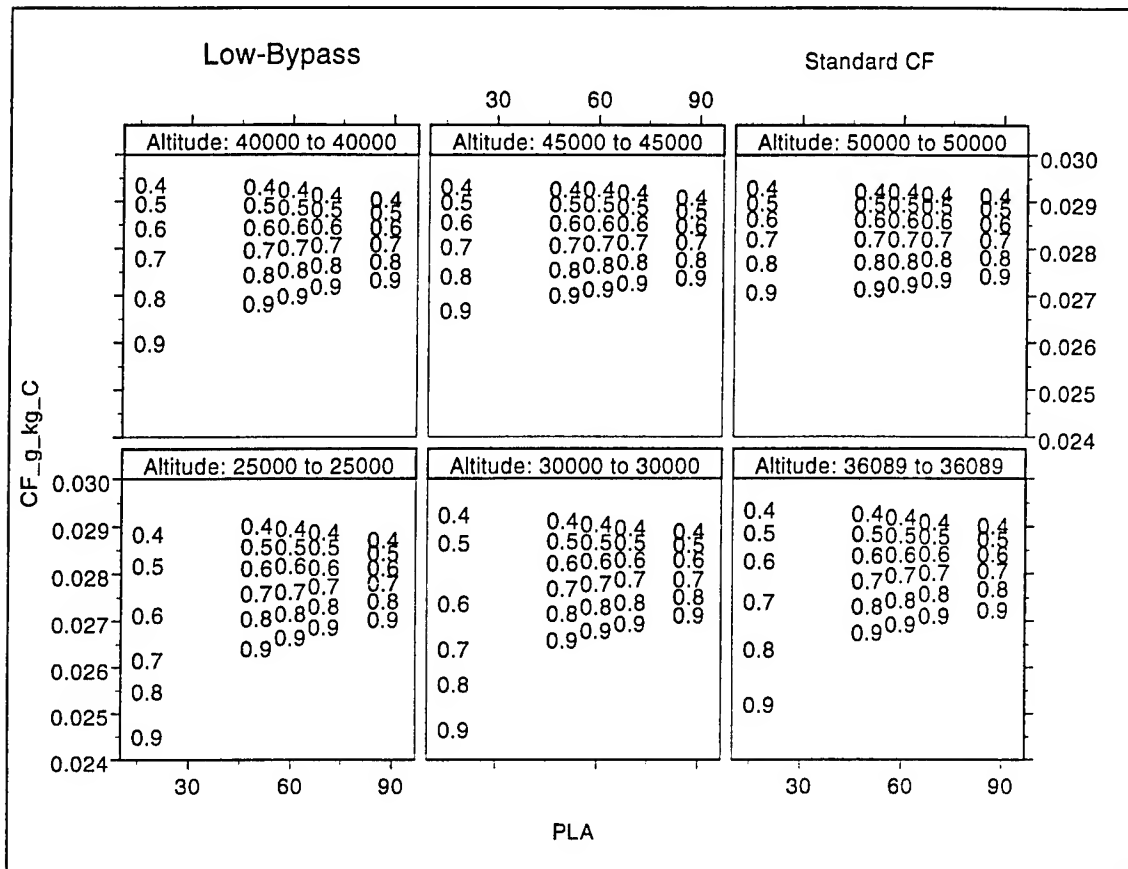


Figure 6. As in Figure 4, but showing estimates for a similar range of power setting and flight Mach number over a range of altitudes.

The situation is somewhat more complex for high-bypass engines, as 2 contrail factors can be computed for each reference frame. Figure 8 shows results for contrail factors estimated by Method 2a (aircraft reference frame, unmixed core air). Contrail factors are generally a factor of 2 higher than for the low-bypass engine. This is due to the fact that all of the water generated during combustion is in the core air, but a significant fraction of the energy is extracted to accelerate the duct air. Contrail factor decreases with increasing power setting because at higher power settings proportionally less energy is extracted to the duct air stream.

Figure 9 shows results for the “corrected” core contrail factor (method 3a). These corrected contrail factors are slightly higher than those shown in Figure 8, due to the lower total enthalpy in the exhaust in the frame of reference of the air. The range of variation at a given power setting is smaller than for the “standard” contrail factor. It is not possible to compare the estimates in Figure 8 and 9 to the fuel-property-based “Appleman” factor, because some fraction of the enthalpy released by combustion is present in the fan stream. However, by mixing the fan and core

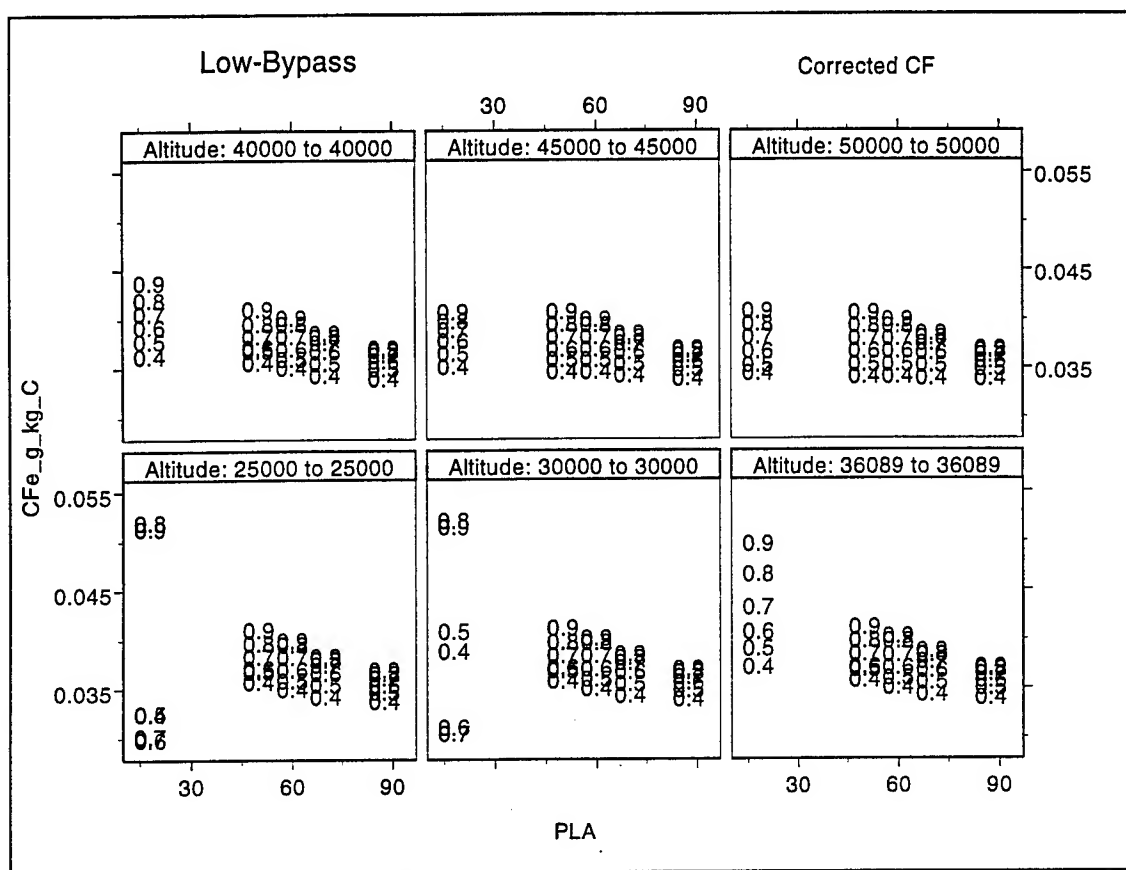


Figure 7. As in Figure 5, but for a range of altitudes.

streams for the high-bypass engine, and computing a contrail factor for the mixed exhaust, we have a situation where all enthalpy should be accounted for in the computation of the contrail factor. This mixing is used to construct Figure 10. Figure 10 shows standard contrail factors estimated assuming that core and duct air streams are completely mixed prior to contrail formation. They are much lower than the contrail factors shown in Figure 8, and for many conditions shown are less than the fuel-based "Appleman" factor. Ideally, the mixed stream contrail factors in Figure 10 should be very close to those in Figure 6 for the low-bypass engine, and both should be greater than or equal to the "Appleman" contrail factor, $0.030 \text{ (g/kg)}^\circ\text{C}$. The fact that for most conditions these contrail factors are less than the Appleman factor suggests that they are computed incorrectly.

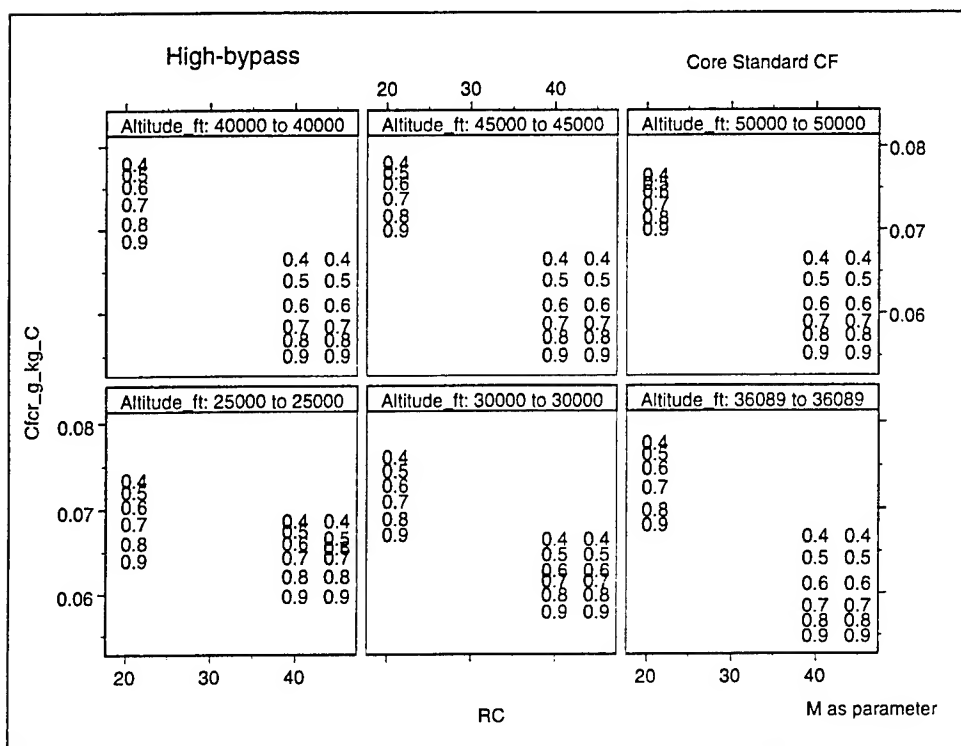


Figure 8. Contrail factors in the aircraft frame of reference estimated for the core stream of a high-bypass turbofan engine. Results are presented for 6 altitudes, three power settings (RC) and flight Mach numbers ranging from 0.4 to 0.9.

Figure 11 shows that the “corrected” contrail factors for the mixed streams are higher than the “standard” contrail factors for the mixed streams shown in Figure 10, but lower than the “corrected” contrail factors for the core streams shown in Figure 9. Compared to the results in Figure 10, the contrail factors are higher in Figure 11 because the total enthalpy in the exhaust is less in the frame of reference of the air. There is a stronger trend for decreasing contrail factor with increasing power setting in Figure 11 compared to Figure 10 because in Figure 11 the exhaust speed in the air frame of reference increases more dramatically with power setting.

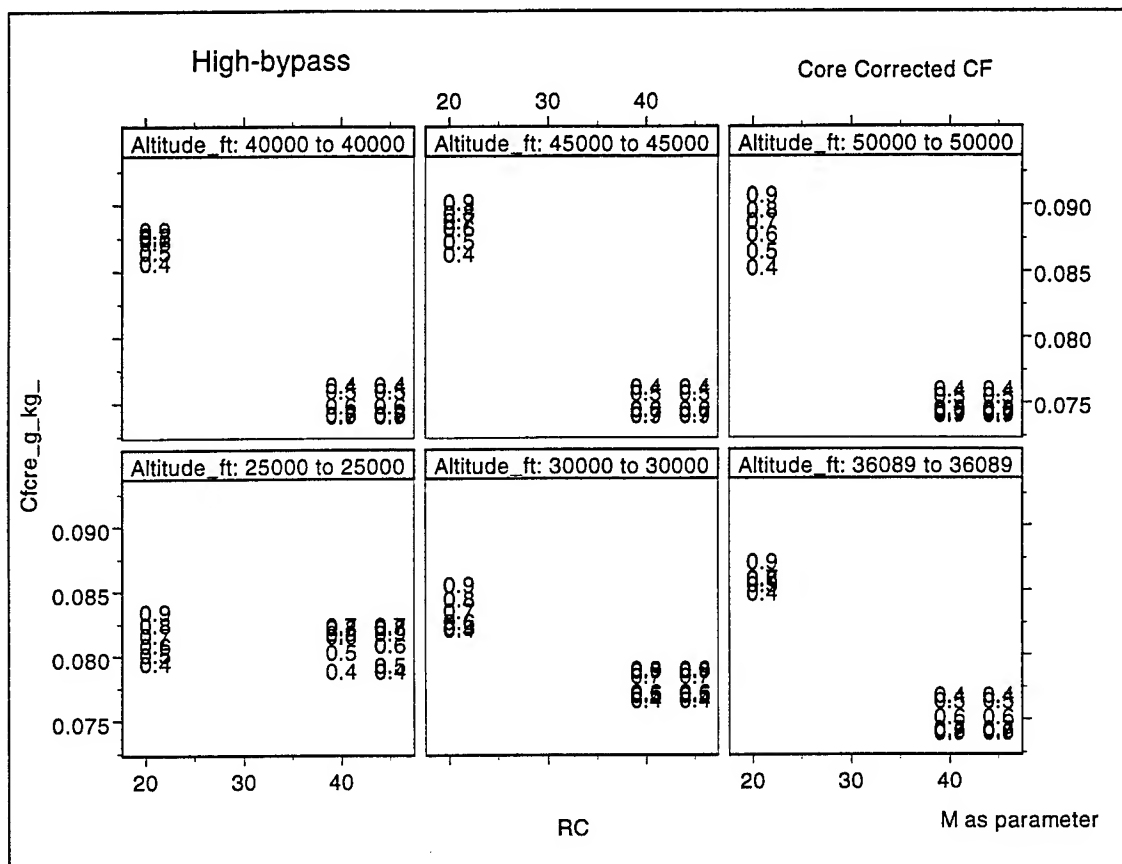


Figure 9. As in Figure 8, but for contrail factor computed in the reference frame of the air through which the aircraft is moving.

Most importantly, none of the mixed-stream contrail factors, in the reference frame of the air, are less than the fuel-based "Appleman" factor. The contrail factors shown in Figure 11 are generally lower than those estimated in Peters (1993) for high-bypass engines, but slightly higher than those given in Schrader (1997) as being deduced from flight tests. This suggests that the engines observed in these flight tests probably had well-mixed fan and core streams very close to the exit plane. It is possible that the assumption used above, that 1.28 kg of water are generated during the combustion of 1 kg of fuel, is a bit optimistic. A value of 1.22, as suggested in Busen and Schumann (1995) would lower the contrail factors in Figure 11 to a range closer to that suggested in Schrader (1997) for high-bypass engines.

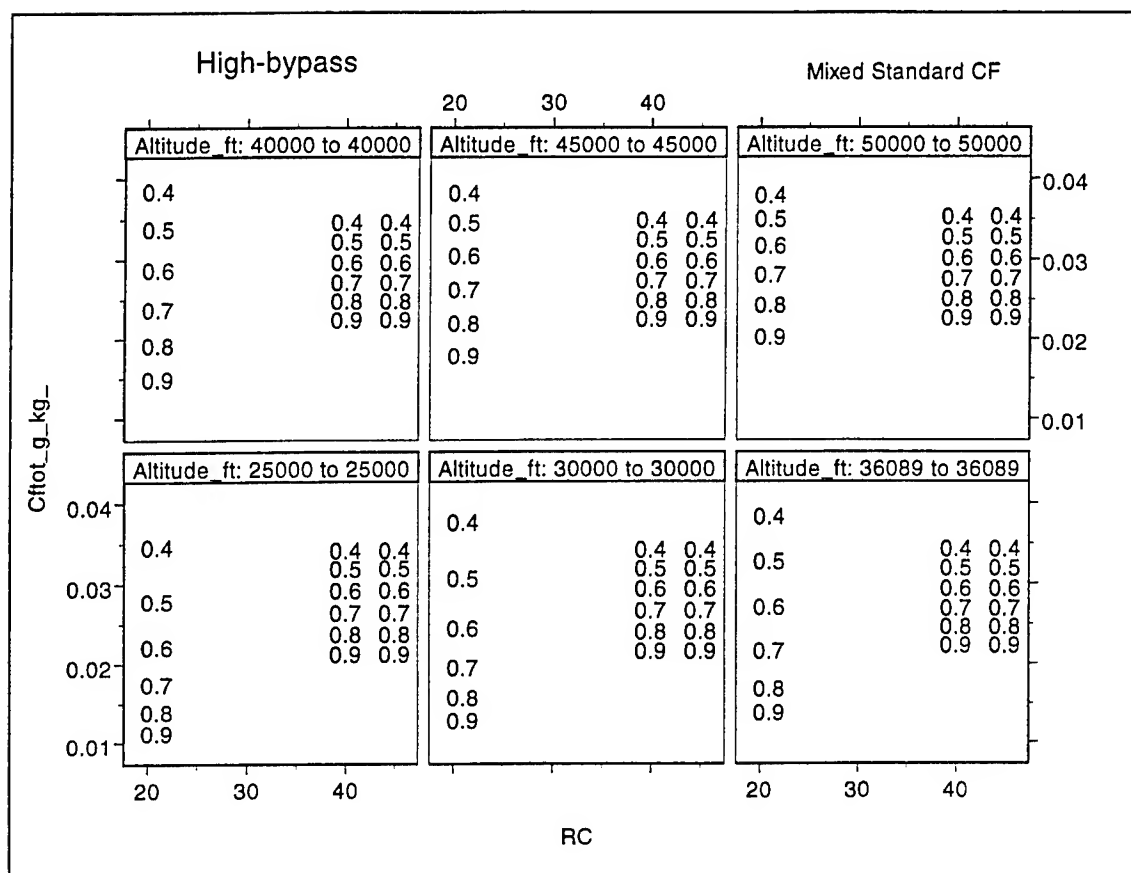


Figure 10. Contrail factors for the high-bypass engine computed in the reference frame of the engine, assuming fan and core streams are completely mixed prior to contrail formation.

DIAGNOSIS of CONTRAIL FACTORS from PHILLIPS LABORATORY CONTRAIL OBSERVATIONS

During the fall of 1995, the Air Force Phillips Laboratory (now Air Force Research Laboratory at Hanscom AFB) undertook an intensive observation campaign. (Jackson et al, 1997) Radiosondes were launched from 5 sites in the Boston area at intervals as small as 3 hours. Observers at these 5 sites observed aircraft and whether or not they were making contrails. Confirmation was obtained in real time from a nearby Federal Aviation Administration (FAA) en-route traffic control center of the altitude and aircraft type for each sighting by the observers.

There were 563 observations of aircraft in-flight made in a 2-week period. A summary of these data are shown in Figure 12. From this set, a subset of ~100 observations was extracted in which visual descriptions of the contrail observed were recorded. It was examined for short-lived contrails. Contrails that are short-lived (last less than a few seconds) are short-lived both because the air in which they form is dry and subsaturated with respect to liquid (and

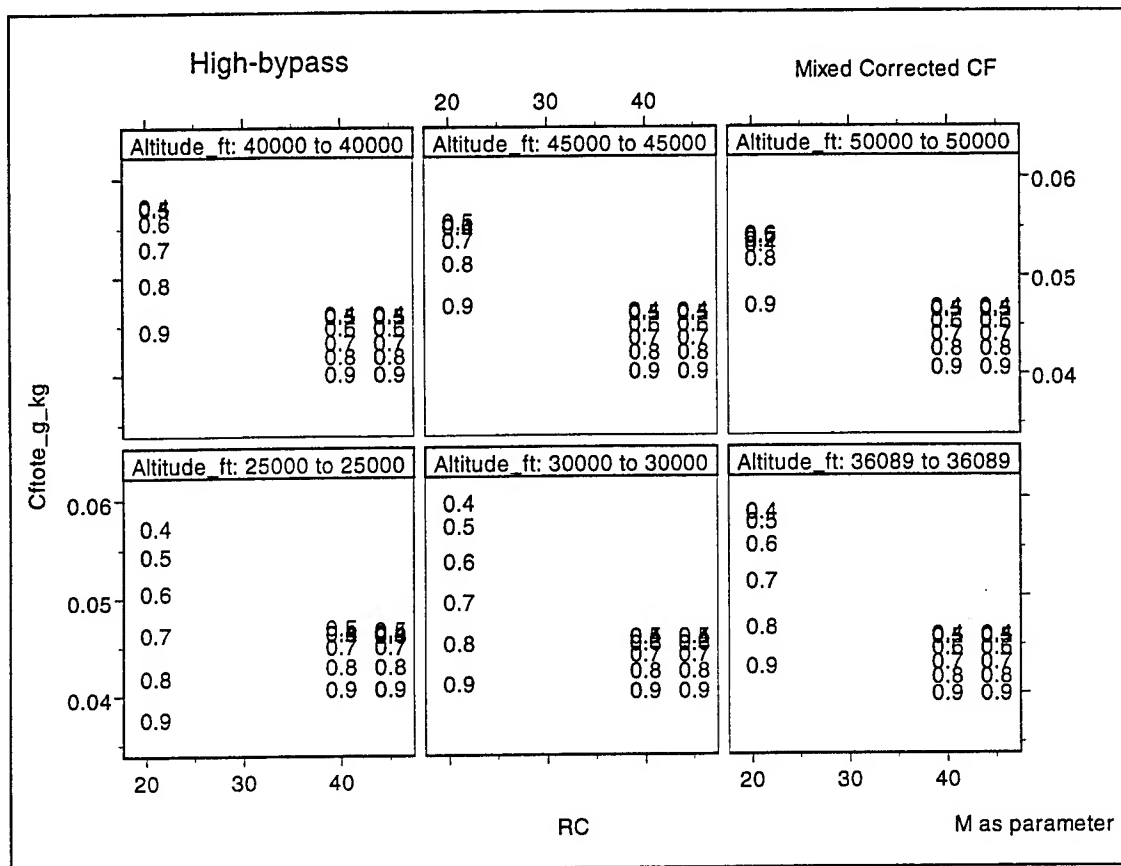


Figure 11. As in figure 10, but for the contrail factor computed in the reference frame of the air through which the aircraft is moving.

probably subsaturated with respect to ice), and because the conditions in which they are forming are at the very threshold for contrail formation. In the context of Figure 3, the mixing line is just tangent to the saturation mixing ratio curve and barely crosses above it. A group of 59 observations of short-lived contrails was selected for further analysis.

Environmental conditions in which short-lived contrails were observed were interpolated from the dense network of soundings to the location of the contrail observation. Looking at Figure 3, if the environmental condition is specified, and a line is drawn from it that is just tangent to the saturation mixing ratio curve in Figure 3, then the slope is determined for the mixing line describing the mixing that produced this non-persisting contrail. This slope is the contrail factor. This represents a lower limit to the contrail factor, as the contrail factor could actually be somewhat higher, and if the ambient air was dry enough, even if the mixing line passed markedly into the saturated region, the plume could mix out to a subsaturated state quickly and yield a short-lived contrail.

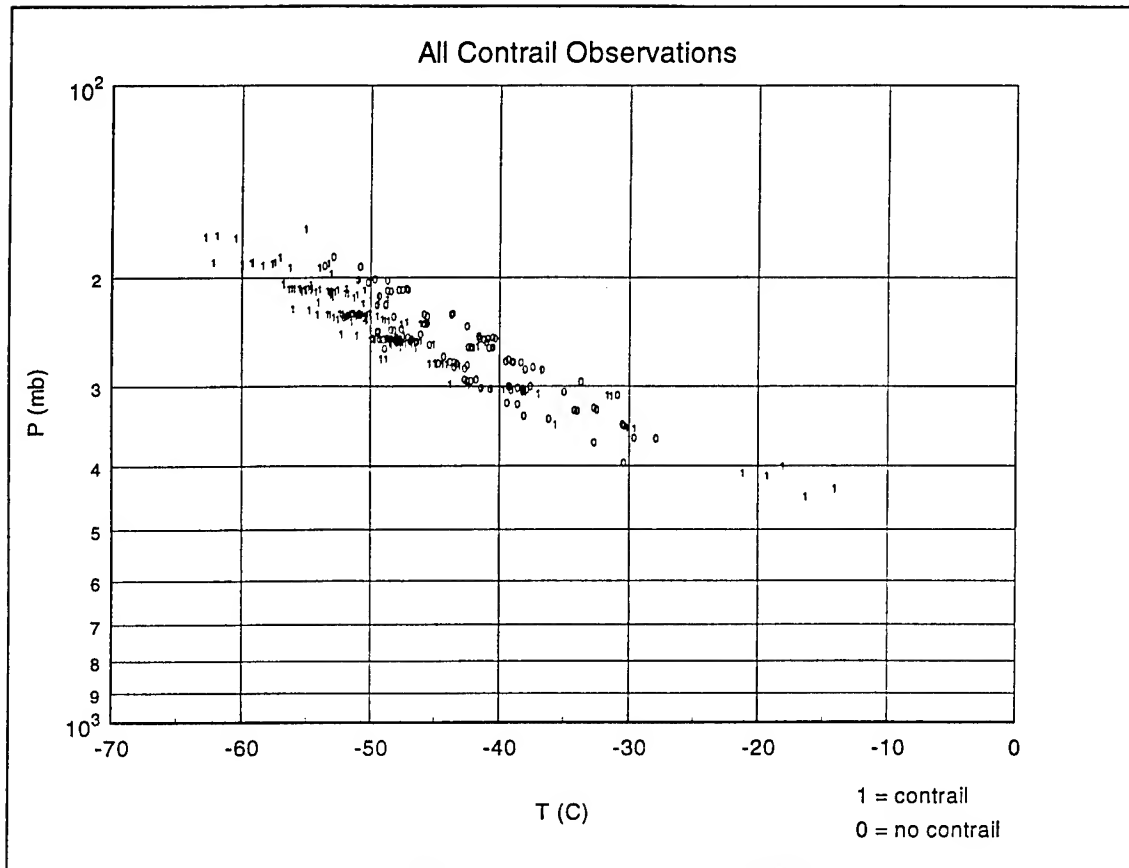


Figure 12. Aircraft observations as a function of ambient temperature and pressure.

From the aircraft type, as obtained from the FAA, an estimate was made of the bypass ratio of the engines on the observed aircraft. This estimate was made using Jane's All the World's Aircraft (Lambert, 1991). Many aircraft types may have different engines with a range of bypass ratios. In cases where more than one bypass ratio applied to the various engines in common use on aircraft of a given type, a mean bypass ratio was assigned to all aircraft of that type.

Contrail factors were inferred by a numerical iteration procedure analogous to fitting a line to the two known points on Figure 3, for each short-lived contrail observed during the study. The contrail factor estimates are summarized in Figure 13.

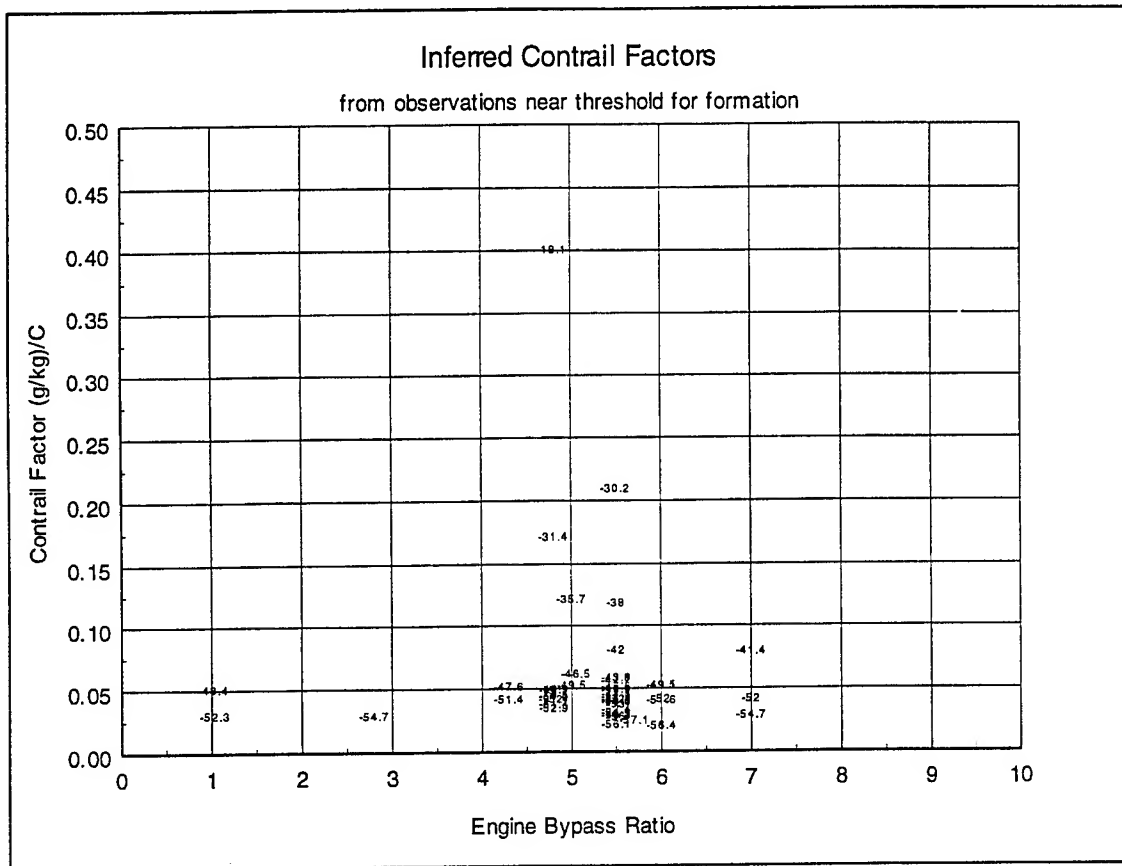


Figure 13. Inferred contrail factors based on 59 observations of short-lived contrails. The temperatures ($^{\circ}\text{C}$) at which the contrails were observed are plotted as a function of the deduced contrail factor and the estimated bypass ratio.

In general, the range of inferred contrail factors increases with increasing estimated bypass ratio. Most observations yield a contrail factor between 0.030 and 0.10 (g/kg)/C, consistent with estimates of contrail factors for low and high-bypass gas turbine engines in a reference frame moving with the air, given above. Some inferred contrail factors are less than 0.030 (g/kg)/C. However, the estimating procedure yields only a lower bound on the contrail factor, and so the actual factor in these cases could have been greater than the inferred one. Figure 14 shows only those observations yielding contrail factors less than 0.10 (g/kg)/C in order to make the lower contrail factor distribution more discernible. The range of variation of these observations agree very well with the theory for contrail factor calculation in the frame of reference moving with the air, as developed above.

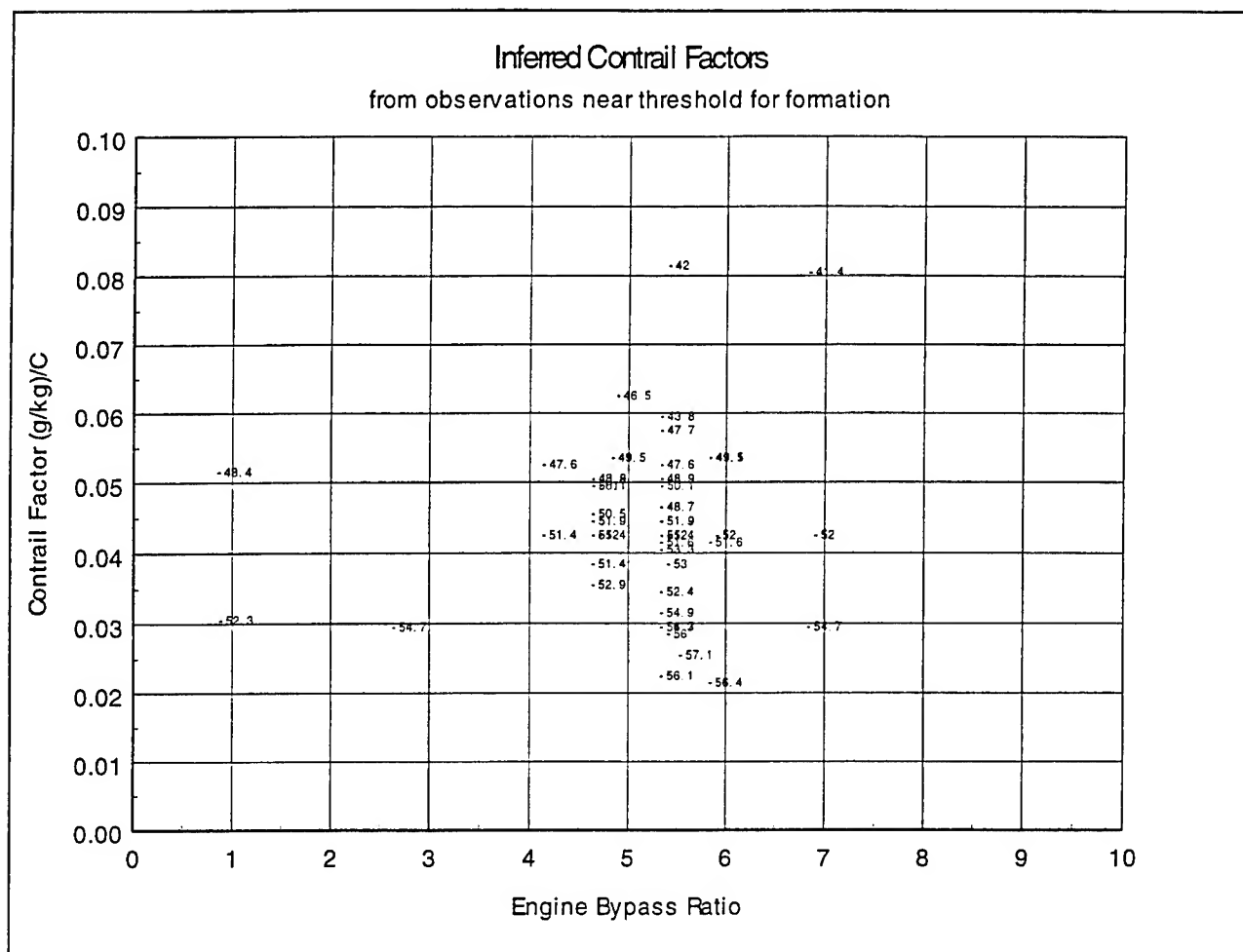


Figure 14. The region of Figure 13 corresponding to contrail factors less than 0.10 (g/kg)/C.

Five contrails in Figure 13 were observed at temperatures higher than -40 C. These observations yield inferred contrail factors much greater than 0.10 (g/kg)/C. They all were produced by high-bypass engined aircraft. These factors are not consistent with steady-state engine operation according to the generic high-bypass engine cycle data used in this study. It is possible they were produced by aircraft in non-steady-state flight or at a low power setting during a slow descent where the exhaust gas velocity was even closer to the forward airspeed than for the low power setting engine cycle data used in this study. A low throttle-setting and low exhaust speed could lead to a very low total enthalpy in the exhaust in the reference frame of the air, leading to very high contrail factors. It would be of interest to Air Force forecasters to study situations like this, as current contrail forecasting procedures would not recognize the possibility of contrail formation at such high temperatures, no matter what the humidity.

There are many uncertainties in inferring bypass ratios, and there are additional uncertainties in inferring contrail factor caused by uncertainties in the temperature, pressure, and most importantly humidity, in the contrail

environment. Humidities from radiosonde instrument packages at low temperatures are characteristically underestimated. An underestimate of humidity would yield an overestimate of contrail factor (see Figure 3).

Given these uncertainties, the bulk of the data presented in Figures 13 and 14 support the theory of computing the contrail factor using exhaust enthalpy in the reference frame of the air. Contrail factors computed in the aircraft frame of reference are generally lower than those estimated from the observational data set. Contrail factors computed in the reference frame of the air through which the aircraft is moving are generally higher, more variable, and closer to the range of those inferred from observations. The 5 observations that yield factors that exceed the contrail factors characteristic of high-bypass gas engines at the flight conditions investigated must have been characterized by a flight environment and/or flight settings outside the range of these conditions.

SUMMARY and CONCLUSIONS

A physically consistent procedure for computing contrail factors based in engine cycle calculations has been presented. It follows procedures used in past studies, with the exception that care is taken in the estimation of exhaust gas total enthalpy. The most important consideration is that the total enthalpy of the exhaust must be computed in the frame of reference of the air through which the engine is being carried by the aircraft. Contrail factors computed in this way are equal to or greater than the contrail factor of $0.030 \text{ (g/kg)/}^\circ\text{C}$ estimated assuming all water and enthalpy generated during combustion exits the tail pipe. They can be greater than this because some of the energy generated by combustion is used to propel the aircraft, and some is lost in parasitic flows. In contrast, contrail factors estimated assuming the EGT represents the total enthalpy in the exhaust yield contrail factors too low, particularly when the exhaust speed is relatively closer to the airspeed.

When exhaust gases have high exit speeds relative to the airspeed of the aircraft, fan and core streams are well-mixed, and there is little energy extracted in the form of parasitic flows, the contrail factor should approach $0.030 \text{ (g/kg)/}^\circ\text{C}$. For high-bypass engines, which move more air more slowly than low-bypass engines, contrail factors should be generally higher

It is seen that, contrary to assumptions made in current methods of contrail forecasting, the contrail factor is not constant for a given engine type for all flight conditions. It varies even for the same engine at different power settings and flight conditions. Cycle calculations were done for a range of conditions for a low-bypass and a high-bypass engine. This range included flight at altitudes between 25000 and 50000 ft in a standard atmosphere, Mach numbers ranging from 0.4 to 0.9, and power settings from idle to military. The contrail factors range from 0.030 to $0.053 \text{ (g/kg)/}^\circ\text{C}$ for low-bypass engines, and from 0.038 to $0.090 \text{ (g/kg)/}^\circ\text{C}$ for high-bypass engines, over this range of conditions. Contrail factors are generally higher at lower power settings at a given Mach number, and higher at

this range of conditions. Contrail factors are generally higher at lower power settings at a given Mach number, and higher at higher Mach numbers at a given power setting. Contrail factors tend to be higher at higher altitudes in general. Finally, contrail factors are generally higher for high-bypass ratio engines than for low-bypass engines.

Contrail factors are diagnosed from a detailed set of observations of contrails forming at threshold conditions for formation. These contrail factors are compared to those computed from cycle calculations. Generally good agreement is found between the range of contrail factors inferred from observations and those estimated from cycle calculations. A few observations of contrails forming at relatively high temperatures are represented by engine cycles or flight conditions inconsistent with those used in this study.

ACKNOWLEDGEMENTS

It was a pleasure to work with the former Atmospheric Sciences Division and others at what is now the Air Force Research Laboratory facility at Hanscom AFB while puzzling through this problem. Special thanks to Arthur Jackson, Brian Newton, Don Chisholm, Vincent Falcone, Edmond Dewan, Owen Cote, Arnold Barnes, and Alan Bussey, for a bit of help or encouragement every now and then. Will Delaney of the Aeronautical Systems Center at Wright-Patterson AFB provided the engine cycle calculations used. Thanks also to Paul Heberling of GE Aircraft Engine Business Group, Pat Saatzer of Northrup Grumman, and to Hillyer Norment, itinerant aerodynamicist, for additional data and insights into the problem.

REFERENCES

- Appleman, H. S., 1953: The formation of exhaust condensation trails by jet aircraft. *Bull. Amer. Meteorol. Soc.*, **37**, 47-54.
- Bohren, C. F., and B. A. Albrecht, 1998. *Atmospheric Thermodynamics*. Oxford University Press, NY. 322-324.
- Busen, R., and U. Schumann, 1995: Visible contrail formation from fuels with different sulfur contents. *Geophys. Res. Lett.*, **22**, 1357-1360.
- Detwiler, A., 1996. Evaluation of Engine-related Factors Influencing Contrail Prediction. Final Report for Summer Faculty Research Program Phillips Laboratory. Sponsored by Air Force Office of Scientific Research, Bolling Air Force Base, DC. 20 pp.

Downie, C. S., and B. A. Silverman, 1957. *Handbook of Geophysics for Air Force Designers*. Geophysics Research Directorate, Air Force Cambridge Research Laboratories, Air Research and Development Command, United States Air Force. 19-1 - 19-9.

Geddes, A. E. M., 1921. *Meteorology: An Introductory Treatise*. Blackie & Son, Ltd., London. 390 pp.

Hanson, H. M., and D. M. Hanson, 1995: A reexamination of the formation of exhaust contrails by jet aircraft. *J. Appl. Meteor.*, **34**, 2400-2405.

Jackson, A., B. Newton, D. Hahn, and A. Busey, 1997: Statistical contrail forecasting. *Preprints, 7th Conference on Aviation, Range, and Aerospace Meteorology*. 2-7 February, 1997, Long Beach, California. American Meteorological Society, Boston.

Jensen, E. J., O. B. Toon, S. Kinne, G. W. Sachse, B. E. Anderson, K. R. Chan, C. H. Twohy, B. Gandrud, A. Heymsfield, and R. C. Miake-Lye, 1998: Environmental conditions required for contrail formation and persistence. *J. Geophys. Res.*, **103**, 3929-3936.

Lambert, M., ed, 1991. *Jane's All the World's Aircraft, 81st edition*. Jane's Information Group, Inc., Alexandria, VA. 807 pp.

Mattingly, J. D., W. H. Heiser, and D. H. Daley, 1987. *Aircraft Engine Design*. American Institute of Aeronautics and Astronautics, Inc., New York, NY. 582 pp.

Osterle, F., 1956. *Condensation trail prediction*. AFCRC-TR-56-459. 25 pp.

Peters, J. L., 1993. *New Techniques for Contrail Forecasting*. AWS/TR--93/001. Available from Air Force Combat Climatology Center/DOL (Air Weather Service), Scott Air Force Base, Illinois 62225-5206. 31 pp.

Pilie, R. J., and J. E. Justo, 1958: A laboratory study of contrails. *J. Appl. Meteor.*, **15**, 149-154.

Saatzer, P. 1995a. *Final Report: Pilot Alert System Flight Test*. Northrup Grumman Corporation, B-2 Division, 8900 East Washington Boulevard, Pico Rivera, CA 90660-3783. (variously paged)

Saatzer, P., 1995b. Presentation to 2nd Meeting of Contrail Technology IPT. Offutt AFB, NE. (variously paged)

Schrader, M. L., 1997: Calculations of aircraft contrail formation critical temperatures. *J. Appl. Meteor.*, **36**, 1725-1729.

Schumann, U., 1996: On conditions for contrail formation from aircraft exhausts. *Meteorol. Z.*, **5**, 4-23.

Schumann, U., J. Strom, R. Busen, R. Baumann, K. Gierens, M. Krautstrunk, F. P. Schroder and J. Stingl, 1996: In situ observations of particles in jet aircraft exhausts and contrails for different sulfur-containing fuels. *J. Geophys. Res.*, **101**, 6853-6869.

MEASUREMENTS OF ION-MOLECULE REACTIONS AT VERY HIGH TEMPERATURES

Itzhak Dotan
Associate Professor
Department of Natural and Life Sciences

The Open University of Israel
16 Klousner St.
Ramat-Aviv, Tel Aviv, Israel

Final Report for:
Summer Faculty Research Program
Phillips Laboratory

Sponsored by:
Air Force Office of Scientific Research
Bolling Air Force Base, D.C.
and
The Open University of Israel
Ramat-Aviv, Tel-Aviv, Israel

March 1998

MEASUREMENTS OF ION-MOLECULE REACTIONS AT VERY HIGH TEMPERATURES

Itzhak Dotan
Associate Professor
Department of Natural and Life Sciences
The Open University of Israel

Abstract

We have developed a flowing-afterglow apparatus for the study of ion-molecule reactions at high temperatures (HTFA). Using this apparatus we have studied the rate constants for eight reactions over the temperature range 300-1800K. Comparing to previous drift tube measurements allows the rate constants for vibrationally excited neutrals to be derived.

MEASUREMENTS OF ION-MOLECULE REACTIONS AT VERY HIGH TEMPERATURES

Itzhak Dotan

Introduction

The need for understanding the chemical behavior of plasmas has spawned the development of techniques for studying ion-molecule reactions at elevated temperatures. High temperature ion chemistry occurs in the ionosphere, in combustion situations, in plasma chemical reactors, and in plasmas associated with atmospheric reentry and hypersonic flight. In the case of atmospheric reentry, e.g., a plasma may envelope the vehicle and interfere with radio communication. Computer models are used to describe the complicated chemistry in these plasma situations, such as reentry, but the models require accurate and meaningful kinetics data in order to describe and predict the plasma properties. While there is a wealth of ion chemical kinetics data available in the literature, very little covers temperatures above 300 K, and such data above 900 K are essentially nonexistent. High temperature kinetics data are often required for modeling plasmas at elevated temperatures because extrapolation of low temperature data is unreliable.

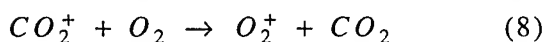
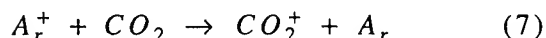
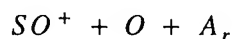
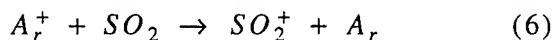
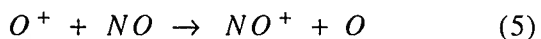
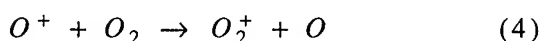
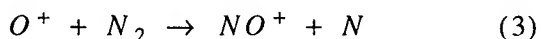
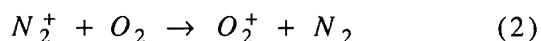
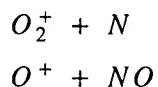
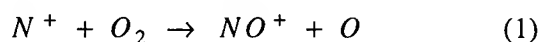
One way to circumvent the temperature limitation has been to study reactions at elevated ion energy in drift tubes and ion beam apparatuses. These techniques have been highly successful and produced an abundance of data on many systems. However, results from these techniques offer only a guide for predictions on the behavior of reaction rate constants and product branching fractions at elevated temperatures because it is the translational energy (and perhaps the internal energy of the ion) that is raised in ion beam and drift tube experiments. It has been shown that temperature and kinetic energy often have differing effects on reactivity. We have studied many systems as functions of both temperature and kinetic energy and have observed a variety of behaviors, e.g., sometimes increasing temperature increases reactivity while kinetic energy decreases reactivity. In other cases, increasing temperature decreases reactivity more effectively than does kinetic energy. Thus in some cases kinetic energy dependence may be misleading indicators of temperature dependence, and clearly there is a need for measurements at true temperatures.

While the kinetics of most ion-molecule reactions have been measured only at room temperature, there has been a considerable amount of work in studying temperature dependence of ion-molecule reactions over the range between 80-600 K. These temperature dependence studies have shown interesting features including the important observation that rate constants for ion-molecule reactions frequently decrease with increasing temperature, presumably because the lifetime of the reaction complex decreases with collision energy.

There have been only two studies where rate constants of ion-molecule reactions were measured above 600 K. The first set of measurements was made at the NOAA Aeronomy Laboratory in 1974 using a flowing afterglow apparatus designed to operate over the temperature range 80-900 K. A total of 9 reactions were studied up to 900 K, all involving simple systems. The second experiment was carried out at the University of Pittsburgh in a static drift tube designed to operate up to 1500 K. Measurements were made up to 930 K on two reactions that had been previously studied by the NOAA group. Measurements were not made above 930 K due to thermionic emission of alkali ions from the drift tube walls.

Recently, in the Philips Laboratory we have constructed a flowing afterglow to study ion-molecule reactions at temperatures from 300 to 1800 K. In this report I describe the experimental setup and the results of 8 reactions studied as a function of temperature up to 1800 K.

The following reactions were studied:



Experimental

The measurements were made in a high temperature flowing afterglow. This apparatus has been described in detail recently [4] and just a brief description is given here. Ions are created by electron impact in the upstream, cooled section of a ceramic flow tube. A helium buffer carries the ions downstream where the flow tube is heated by a commercial furnace. After the gases have reached the equilibrium temperature, the reactant gas is added. The bulk of the gas is pumped by a Roots blower, a small fraction is sampled; the ions are analyzed by a quadrupole mass filter and detected by an electron multiplier. The decay of the primary ion signal as a function of the reactant neutral gas concentration yields the rate constant. The only significant change in the instrument since the detailed description was published has been to slightly lengthen the flow tube upstream of the furnace. This allowed for measurements up to 1800 K by increasing the distance between the hot zone and the sealing gaskets and o-rings. Two minor changes included the use of a turbopump on the ion lens region and a separate pump for the vacuum box. The system is described in Fig. 1.

All the ions were made from their parent neutral gas. Sufficient gas was added to ensure That the production of ions was complete before the reactant inlet. Insufficient gas resulted in curvature to the data, indicating a problem. The helium was passed through a liquid nitrogen trap to reduce the water vapor concentration. The reactant neutrals, except for NO, were used without further purification. No was passed through a silica gel trap at 170K to reduce contamination. No attempt to measure the product ions made except to confirm the appearance of products known from other results. We estimate the error in the measurements as $\pm 25\%$ and $\pm 15\%$ in the total and relative error, respectively.

Results and Discussion

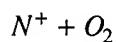


Figure 2 shows the rate constants for the reaction of N^+ with O_2 as a function of temperature. The rate constants increase with temperature from 300K to 1000 K, above which they level out at the collision rate within our error limits, the measured rate constants being about 10% higher than the collisional value. It was not possible to determine the products of the reaction but other studies [5,6] have indicated that branching is 43%, 51%, and 6% into the 3 channels, respectively.

The rate constant for this reaction has been measured in a number of studies. [2, 5-10] Of particular interest to the present study is the NOAA study of the temperature dependence up to 900 K [2] and several drift tube studies [5, 9, 10] of the rate constant as a function of average kinetic energy. In Fig. 2, we plot the NOAA data as a function of temperature [2] and kinetic energy. [10] The drift tube collision are converted to an effective temperature by the relation $(3/2)kT_{\text{translation}} = KE_{\text{centerofmass}}$. $T_{\text{translation}}$ is used to plot the data.

The NOAA temperature data agree with the present results within our 15% relative error. Numerous room temperature measurements are also in agreement with all the above mentioned data. [2, 5-10] The NOAA drift tube data plotted in Fig. 2 are in good agreement with the temperature dependence data at low field. However, the drift tube data show little or no dependence on kinetic energy at the energies of interest in this study. Between 1000 K and 1600 K, the temperature data are about a factor of 2 higher than the drift tube data. The drift tube data from Johnsen et al. [9] are very similar to the NOAA data and are a repeat of the NOAA experiment. [5]

Differences in rate constants as a function of temperature and drift electric field at a given translational energy is the same in both experiments. We have studied the internal energy dependences of numerous reactions using this technique and found that differences as large as observed here are usually attributed to vibrational excitation. However, if we assume that all vibrationally excited O_2 reacts at the Langevin rate, [11] there is not enough vibrational excitation in O_2 to account for the difference in data. The curve labeled maximum in Fig. 2 assumes that the $v=0$ rate constant is $5.5 \times 10^{-10} \text{ cm}^3 \text{ s}^{-1}$ (the average drift tube data) and that the $v>1$ rate constant is $1.1 \times 10^{-9} \text{ cm}^3 \text{ s}^{-1}$ (the average of the present data at temperature over 1000 K, just slightly greater than the Langevin rate).

Since vibrations cannot fully account for the increase in reactivity, one or more of several possibilities must also help explain the reactivity difference:

- 1) One of the data sets may be in error. However, two temperature dependent studies and three drift tube studies are in good agreement. In addition, comparison of results from our laboratory and the NOAA laboratory almost uniformly shows excellent agreement. [4] This seems to indicate the effect is real.
- 2) Increasing rotational excitation leads to larger rate constants. The large rotational effects we have observed previously have fallen into two categories: endothermic reactions where rotational and translational energy are equivalent forms of energy or reactions involving species with large rotational constants. Neither case seems to fit the present situation. There are some product states of reaction 1 that are nearly thermoneutral and production of the diatomic product in $v=1$ would be endothermic, namely $NO^+(^3\Sigma^+) + O(^3P)$ and $O_2^+(^2\Pi_g) + N(^2D)$. [12] O'Keefe et al. [13] have found no evidence of the former and that the latter channel accounts for 15% of the total reactivity at 300 K. Howorka et al. [5] found that the total channel producing O_2^+ increases with kinetic energy indicating that the $O_2^+ + (^2\Pi_g) + N(^2D)$ channel may become more important with increasing energy. Rotational energy may then be efficient at driving this channel. However, rotational and translational would not be equivalent forms of energy, in contrast to what we have observed in previous studies involving endothermic reactions.
- 3) The populations of the spin orbit states of N^+ will vary more with temperature than with kinetic energy with respect to the buffer rather than with respect to the reactant. [14] For the experiments shown in Fig. 2 the buffer is He and the kinetic energy with respect to the buffer is considerably less than the kinetic energy with respect to the center of mass of the reactants. The equilibrium population of the 3P_0 , 3P_1 , and 3P_2 states of N^+ at 300 K are 17, 39 and 43% respectively. At 1000 K the populations are 13, 35, and 52%, respectively. These differences also cannot explain all of the difference between the temperature and kinetic energy data.

Therefore, we are led to conclude that the observed effect is due to a complicated function of all three sources of internal energy which is difficult to unravel. Another possibility is that the charge transfer channel occurs at a very long range for either

vibrationally excited O_2 or the higher level N^+ spin states so that these rate constants would be appreciably larger than the Langevin value.

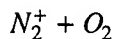


Figure 3 shows the rate constants for the reaction of N_2^+ with O_2 as a function of temperature. The rate constants decrease with temperature up to about 1000 K and increase above that. The reaction produces exclusively O_2^+ . Numerous other studies of the rate constant for this reaction have been made. In Fig. 3 we show data from the NOAA laboratory as a function of temperature [2] from 300 to 900 K and as a function of translational temperature measured in a drift tube. [10] Other measurements are similar. [12, 14, 15, 17, 20, 22, 40]. The NOAA temperature dependent data are similar to the present data, being essentially identical at lower temperatures and about 15% larger than the present data at 900 K, well within our error limits.

At low temperatures (<1000 K), the drift tube rate constants are larger than either set of thermal rate constants at the same translational temperature but show the same trend (i.e. decreasing rate constant with increasing temperature) as the thermal data. Above a translational temperature of 1000 K, the drift tube data continue to decrease until a minimum is reached at 3000-4000 K, in contrast to the increase seen for the temperature data above 1000 K.

We attribute the disparity at low temperatures between the drift tube and the thermal rate constants at a given translational temperature to the difference in reactant internal energy in the two types of experiments. Below 1000 K the internal energy is predominantly the rotational energy, vibrations being mainly in the ground states. To elucidate the role of reactant rotational energy upon reactivity, we replotted the rate constants from Fig. 3 as a function of the sum of average translational and rotational energy in Fig. 4. For this, the thermal data are plotted vs. $(7/2)kT$ and the drift tube data are plotted versus the original kinetic energy plus $2kT$ (with $T=300$ K). As can be seen in Fig 4 this results in extremely good agreement at energies below 0.3 eV. This agreement indicates that rotational and translational energy are equally detrimental to reaction at low energies. We have seen these two types of energy being equally important previously, although usually in the role of increasing the rates of endothermic reactions. We have seen other examples where both rotational and translational energy may have caused the rate constant to decrease but the effect was

never as large as observed here, usually just at the maximum of our relative uncertainty. Therefore, any conclusion we made was tentative.

A qualitative explanation for this negative dependence of the rate constants upon reactant energy can possibly be found in the mechanism suggested by Scherbarth and Gerlich [18] to account for the similar energy dependence observed in the reaction of Ar^+ with O_2 . Briefly stated, this mechanism assumes that the reactants approach on an attractive potential energy surface to form an intermediate complex which may either separate back to reactants or jump at a crossing seam to the potential energy surface for the products. If the latter surface is repulsive, the probability of the complex exiting via the product channel would increase with the lifetime of the complex (i.e. the number of times the trajectory crosses the seam). Since increasing either translational or rotational energy of the reactants shortens the lifetime of the complex, one would expect a decreasing fraction of collision to lead to product formation as the reactant energy (either translational or rotational) is increased.

From the data shown in figure 4, it is also possible to derive information on how vibrational energy effects the reactivity. Several previous studies have shown that N_2^+ vibrations do not affect the rate constant for charge transfer [15, 19] presumably because the overlap between states of N_2^+ and N_2 in the same vibrational level are good and the $N_2^+(v)$ reactant results in a $N_2(v)$ product. Therefore, the difference between the temperature and kinetic energy data above 0.3 eV is mainly due to vibrational excitation of O_2 in the HTFA experiment above 1000 K.

From the two data sets and calculated O_2 vibrational populations as a function of temperature, it is possible to derive the rate constants for vibrationally excited O_2 . The rate constant at a given temperature can be written as

$$k(T) = \sum k_i \cdot \text{pop}(i)$$

where, $k(T)$ is the measured rate constant as a function of temperature, k_i is the rate constant for a particular vibrational state, and $\text{pop}(i)$ is the population of that state. For the N_2^+ reactions with O_2 we can derive vibrational energy effects in two ways. The first is to assume that all vibrational excitation behaves similarly. For this case, we take k_0 as the drift tube data, calculate the fraction of O_2 that is vibrationally excited from the known temperature, and solve for a $k_{v \geq 1}$. The results are shown in Fig. 4 as the $\text{O}_2(v \geq 1)$ rate. At the lowest energies the rate constants are found to rise relatively

rapidly with increasing energy, probably an artifact of using small differences between the drift tube data and the present results to derive the rate constants. At higher energies, the rate constants for O_2 ($v \geq 1$) are about a factor of 6 larger than those for $v=0$ and increase slightly with increasing energy.

Production of $O_2^+(a^4\Pi_u)$, which is endothermic by 0.577 eV for ground state reactants, is essentially thermoneutral for O_2 ($v=2$). Production of this state has been invoked to explain the kinetic energy dependence of this reaction at energies above 1 eV [20]. Production of $O_2^+(a^4\Pi_u)$ has been observed in the similar reaction of Ar^+ with O_2 [18]. Therefore it is totally feasible that the increase in the rate constant we observe with increasing temperature is dominated by an increase in the O_2 ($v \geq 2$) population and not O_2 ($v = 1$). By assuming that the $v = 1$ and $v = 0$ rate constants are the same, we derive rate constants for O_2 ($v \geq 2$). The results of this calculation are also shown in Fig. 4. The roughness in the two curves for vibrationally excited O_2 is due to the small bump in the present data and gives an indication of the accuracy of the derived rate constants. The derived rate for ($v \geq 2$) is roughly independent of energy with a rate constant of approximately $1.5 \times 10^{-10} \text{ cm}^3 \text{ s}^{-1}$. This represents a very large increase in the rate constant compared to $v = 0$, but the value is reasonable considering that production of a new electronic state would be involved. The Franck Condon factors for production of the $a^4\Pi_u(v = 2)$ state are large supporting this interpretation. Also lending support to the ($v \geq 2$) interpretation is the fact that an appreciable population of $v = 2$ (1%) exists just about at the minimum in the temperature dependent data, while at the same temperature the $v = 1$ population of $v = 1$ is 14%. While the ($v \geq 2$) explanation is attractive for the reasons given above, it is not possible to rule out either case, and in fact something in between the two cases is likely.

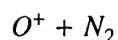


Figure 5 shows the rate constants for the reaction of O^+ with N_2 as a function of temperature. The rate constants are very small, reaction occurring on the order of 1 in 10^3 collisions. At low temperature the rate constants decrease with temperature and show a minimum in the 1100-1300 K range before rising steeply at higher

temperature. The results are in excellent agreement with the previous measurements made at temperatures up to 900 K. Shown are the data from the NOAA [2] laboratory. The results of Chen *et. al.*[3] Are similar. Several drift tube studies were made of this reaction [10, 21, 22]. Plotted in Fig 5 are the data of Albritton *et al.*, [21] the most recent and thorough drift tube measurement. The other studies are similar, except that the rate constants near the minimum in the Albritton *et al.* Study are slightly smaller. The drift tube data were taken as a function of ion kinetic energy and converted to effective translational temperature by $KE=1.5 kT$. The drift tube data agree with the present data within experimental uncertainty up to 1300 K. Above 1300K the present thermal results increase much faster than the drift tube results, in which only the ion translational energy is increased.

Comparing drift tube results to pure temperature results allows information on internal energy dependence of the reactivity to be derived. Any difference in rate constant at the same translational temperature is due to internal energy. For the reaction of N_2 with O^+ this means the N_2 internal energy. The good agreement between the pure temperature and kinetic energy data at low temperatures (<1000 K) shows that N_2 rotational energy has at most a small role in controlling the reactivity, since only a small fraction of N_2 is vibrationally excited.

The difference at the same translational temperature between the drift tube studies and the present at high temperature is due to N_2 vibrations becoming excited in the thermal experiments. N_2 ($v=1$) is already populated to a small extent by 1000 K, yet no clear enhancement in the rate constant is observed until 1300 K. Since there is only a relatively small difference in the $v=1$ population between 1200 and 1300 K, the data suggest that the increase may in fact come from a large rate enhancement for the $v=2$ state which changes in population by almost a factor of 2 over this temperature range. The speculation that the increase is due to $v=2$ is confirmed by the experiments of Schmeltekopt *et. al.*[3, 4] In their experiment, the reactants' translational and rotational temperatures were fixed at 300 K while the N_2 vibrational temperature was varied from 300 to 6000 K by means of a microwave discharge. The measured rate constants increased slightly from 1000-1200 K and dramatically above that. From their data they derived vibrational state specific rate constant for v from 0-11. They found the $v=1$ rate constant to be about the same as the $v=0$ rate constant. The rate constant for $v=2$ increased by about a factor of 40 from the $v=0$ and 1 values. The rate constant continued to increase for higher v 's until a value close to the collisional value

was reached for $v=6$. This shows that the increase in our pure temperature data is due almost exclusively to $v=2$, present in only small abundance.

The two nonthermal experiments can be combined to compare with the present data. The NOAA vibrational temperature data were report relative to the 300 K rate constant. Scaling these data points to the drift tube translational temperature ($T_{vib} = T_{trans}$) rather than scaling to the 300 K rate constant allows a thermal rate constant to be predicted with both vibrational and translational effects included. This ignores the effects of rotational excitation (shown above to be at most a small effect). This also assumes that the translational energy dependence of the vibrationally excited species are the same as that for $v=0$. The results of this prediction are shown in Fig. 5. Very good agreement is found. Unsatisfactory agreement is obtained (not shown) if the vibrational temperature data are plotted relative to the 300 K rate constant. This shows that both vibrational and translational energy are important in controlling the rate constant in this temperature range and that the assumption of similar translation dependence for different states is reasonable. The reason for the strong increase at $v=2$ is at present unexplained.

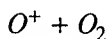


Figure 6 shows the rate constants for the reaction of O^+ with O_2 as a function of temperature. The rate constants are small, although they are about a factor of 10 larger than those for the O^+ with N_2 reaction. At low temperature, the rate constants decrease with temperature and show a minimum in the 800-1100 K range before rising at higher temperature. Error bars of ± 25 are shown. Several previous studies of the temperature dependence of this reaction have been made. At NOAA, the reaction was studied from 100 to 900 K [2, 25, 26] Chen *et. al* [3] studied the reaction from 300 to 700 K. The most recent NOAA results are shown in Fig 6, the other results being in good agreement with them. The present data agree with the previous study within 15% at all temperatures except 900 K. At 900 K the present results are 27% higher than the NOAA results, still within the combined uncertainty.

In addition to the temperature studies, several drift tube studies have been made [10, 21, 22]. The results from the two NOAA studies are essentially the same, and the McFarland *et al.* [10] data taken in a helium buffer are plotted in Fig. 6 as well as the Johnsen and Biondi [2] data. At low translational temperatures, the rate constants taken in the drift tube studies are slightly larger than those found for the pure

temperature dependence at most effective temperatures. This is especially true for the data of Johnsen and Biondi. However, the main difference between the data is that the minimum in kinetic energy (outside the range of the data plotted in Fig 6) is much broader and occurs at higher translational temperatures (~1600 K) than the minimum for the pure temperature data. The pure temperature rate constants also increase much faster with increasing temperature than do the drift tube data. These differences are due to the O_2 vibrations becoming excited at high temperatures. The slight offset between the pure temperature and kinetic energy data makes a direct derivation of the internal energy dependence of the reaction slightly complicated. In order to facilitate this comparison we scaled the drift tube data so that the present results and the drift tube data coincide at the lowest translational temperature studied, namely, 400 K. Figure 7 shows this comparison including only the present results and the data from McFarland *et al.* for simplicity. The scaling factor for the drift tube data is 0.8, or a 20% offset, which is within the uncertainty of either data set.

In order to facilitate the derivation of vibrational energy effects, the two data sets are fit to the following expression:

$$k = A_1(300 / T)^n + A_2 \exp(-E_a / kT)$$

where A_1 , A_2 , n , and E_a are adjustable constants. The results of this fitting are shown in Fig 7 as solid lines and, as can be seen, are very accurate representations of the data. Below the minimum in the pure temperature data, there is excellent agreement between the present results and the scaled drift tube results. This shows that O_2 rotations do not play a major role in controlling the reactivity. At temperatures above the minimum, the pure temperature data clearly lie above the drift tube data. The separation occurs at a temperature where the O_2 vibration starts to become excited indicating that excited O_2 vibrations increase the reactivity.

From the two fits and the O_2 vibrational population as a function of temperature, it is possible to derive the rate constants for vibrationally excited O_2 . The rate constant at a given temperature can be written as $k(T) = \sum k_i \cdot \text{pop}(i)$, where $k(T)$ is the measured rate constant as a function of temperature, k_i is the rate constant for a particular vibrational state, and $\text{pop}(i)$ is the population of that state. We take k_0 as the drift tube data, assume that all vibrationally excited O_2 reacts at the same rate, and derive the fraction of O_2 that is vibrationally excited from the known temperature. The results are shown in Fig 7 and represent the translational temperature dependence of the $v>0$ rate constant. The data show an initial rise that probably has to do with the fact that below

1200 K the drift tube data and the present results are similar and therefore the derivation depends on a small difference between two large numbers. At 1200 K and above, the present data continue to rise but at a much slower rate, roughly paralleling the translational temperature dependence for $v=0$, i.e., the drift tube data, but a factor of 4-5 larger.

On the basis of thermochemistry we know that the O^+ reaction with $O_2(v''=0)$ can produce O_2^+ in states from $v'=0-7$ and the O^+ reaction with $O_2(v''=1)$ can produce O_2^+ in states from $v'=0-8$. Frequently, charge transfer is fastest when the process is energy resonant. Therefore, in order to compare Franck-Condon factors it is useful to compare the product states for $O_2^+(v')$ for the $O_2(v''=1)$ reaction to the $O_2^+(v'-1)$ for the $O_2(v''=0)$ reaction. In this way the energy resonances are approximately equal. As v' increases the energy gap becomes smaller, and finally for $v'=7$ and 8 for $O_2(v''=0)$ and $O_2(v''=1)$, respectively, the energy gap reduces to a few tens of wave numbers. For these near resonant products states and the two next closest resonant states, the Franck-Condon factor ratio is in the 4-5.6 region, values very close to the experimental rate constant ratio. While this agreement may be fortuitous, it does provide a simple explanation for the rate constant increase. If the above explanations is true, the product states will be highly vibrationally excited, a result that can be checked experimentally in a beam apparatus. The exact nature of the rate increase awaits a detailed molecular dynamics calculation beyond the scope of this study.



The charge transfer reaction



has been studied intensively using flowing afterglow [27], flow-drift tube [21, 28] and static drift tube techniques [29]. The reaction has been found to be very slow at room temperature ($k = 8 \times 10^{-13} \text{ cm}^3 \text{ S}^{-1}$). Flow drift tube data [21, 28] start at 0.3ev center of mass kinetic energy ($k = 3 \times 10^{-12} \text{ cm}^3 \text{ S}^{-1}$) and increase very fast to a value of $2 \times 10^{-10} \text{ cm}^3 \text{ S}^{-1}$ at 3.5ev center of mass kinetic energy. The gap between room temperature and 0.3ev center of mass kinetic energy has been covered by the static drift experiment of Graham et al. [29]. Their results show that the rate constants do

not vary between room temperature and 1000K and increase steeply above 1000K. These results are a little unusual since generally we do not find such a wide minimum. Recently Le Garrec et al. [30] measured the reaction, using a CRESU machine, as a function of temperature between 23 and 160K. The rate constants decrease in this range from a value of $3 \times 10^{-11} \text{cm}^3 \text{S}^{-1}$ at 23K to $3 \times 10^{-12} \text{cm}^3 \text{S}^{-1}$ at 160K.

We have used the HTFA machine [4] to measure the reaction between room temperature and 1400K, thus covering the gap between the flowing afterglow and flow-drift-tube data.

Figure 8 shows the rate constants for the reaction of O^+ ions with NO as a function of temperature. The rate constants increase from a value of $8 \times 10^{-13} \text{cm}^3 \text{S}^{-1}$ at 300K to $2.6 \times 10^{-12} \text{cm}^3 \text{S}^{-1}$ at 1400K. In the same figure we also plotted NOAA's data measured in a flow-drift tube apparatus [21, 28], Pittsburgh data using static drift tube (29) and Rennes data using CRESU machine [30]. Combining all these sets of data we can establish the minimum in the rate constants to be between 300-400K. There is a very good agreement between our room temperature data, Pittsburgh data and the room temperature flowing afterglow point [27]. Above 500K Pittsburgh's data seems to be a little slower than the present and NOAA's data, but the three sets are within the combined experimental error.

Comparing temperature to kinetic energy dependence of rate constants could lead to the role of vibrationally excited species in driving the reaction. For the $\text{O}^+ + \text{NO}$ reaction we cannot come to any quantitative conclusions since the data is too scattered. The pure temperature dependence data seems to be a little higher than the kinetic energy data, thus hinting to the effect of vibrationally excited NO in driving the reaction.

The reaction proceeds via two separate mechanisms. At the low temperature a long lived complex is formed so that sufficient curve crossing occur to allow the complex to exit in an exothermic channel $\text{NO}^+(\text{}^1\text{S}) + \text{O}(\text{}^3\text{S}, \text{}^1\text{D}, \text{}^1\text{P})$. At higher temperatures ($T > 300\text{K}$) the complex is not being formed and the process is a direct one appearing to have an endothermic threshold. This has been rationalized by Ferguson [31] to be a consequence of the correlation of $\text{O}^+(\text{}^4\text{S})$ and $\text{NO}(\text{}^2\pi)$ with the excited states $\text{}^3\text{A}_1$, $\text{}^3\text{B}_1$ of NO_2^+ which lie slightly above the reactants in energy [32]. The reaction does not occur via non-adiabatic electron jump due to the low Frank-Condon factor.

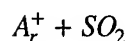
We fit the CRESU and the HTFA data sets to the following expression:

$$k = A_1(300/T)^n + A_2\exp(-E_a/kT)$$

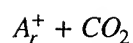
where A_1 , A_2 , n and E_a are adjustable constants. The fitting is shown in Fig 9, it is not a very good one due to some errors in the high temperature points of the CRESU machine. (NO was not purified in their experiment [33]).

These results support the mechanism suggested above since the activation energy is, within the experimental error, similar to the endothermicity of the process leading from $O^+(^4S) + NO(^2P)$ to $NO_2^+(^3A_1, ^3B_1)$. (About 0.1ev).

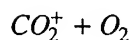
On top of the above described reactions we have measured three more reactions, for which we still have not analyzed the data.



The results for this reaction are shown in Fig. 10. Up to about 900K the rate constants decrease with increasing temperature. At this temperature range there is no difference between the flow-drift tube [34] and the HTFA data. About 900K and up to 1400K the HTFA rate constants increase by about a factor of 2 whereas the flow-drift tube rate constants continue to decrease and start increasing only above 4000K.



The results for this reaction are shown in Fig. 11. Here again there is a very good agreement between the HTFA and flow-drift tube [35] data up to 600K. Above that temperature the HTFA rate constants decrease much faster than the flow-drift-tube data.



The results for this reaction are shown in Fig. 12. Here we compare the HTFA data with flow-drift-tube data taken at three temperature [36]. Here we find a similar behavior to the reaction $A_r^+ + SO_2$ i.e at low temperatures (up to about 600K) there is

no significant difference between the four sets of data; above 600K the HTFA rate constants increase by about a factor of 6 up to 1600K where as the drift tube rate constants start increasing at a higher temperature.

The results of the last three reactions will be analyzed in the near future and we shall try and find the role of the internal excitation in driving the reactions.

CONCLUSIONS

The rate constants for a few ion-molecule reactions have been measured for the first time at temperatures up to 1800K. The results clearly show that drift-tube studies do not model kinetics at high temperatures adequately. The problem arises mainly from the fact that vibrations are not excited in drift-tube measurements. However, combining the present high temperature data with previous drift tube results allows rate constants for vibrationally excited molecules to be derived.

References

1. J.M. Farrar and W.H. Sanders, Jr., "Techniques for the study of Ion-Molecule Reactions". (Wiley, New-York, 1988).
2. W. Lindinger, F.C. Fehsenfeld, A.L. Schmeltekopf and E.E. Ferguson, J.G.R. 79 4753 (1974).
3. A. Chen, R. Johnsen and M.A Biondi, J. Chem. Phys. 69, 2668 (1978).
4. P.M. Hierl, J.F. Friedman, T.M. Miller, I. Dotan, M. Menendez-Barreto, J.V. Seely, J.S. Williamson, F. Dale, P.L. Mundis, R.A. Morris, J.F. Paulson and A.A. Viggiano, Rev. Sci. Instrum. 67 2142 (1996).
5. F. Howorka, I. Dotan, F.C. Fehsenfeld and D.L. Albritton, J. Chem. Phys. 73 758 (1980).
6. D. Smith, N. G. Adams and T.M. Miller, J. Chem. Phys. 69 308 (1978).
7. A.L. Farragher, Trans. Faraday Soc. 66, 1411 (1970).
8. M. Tichy, A.B. Rakshit, D.G. Lister, N.D. Twiddy, N.G. Adams and D. Smith, Int. J. Mass. Spectrom. Ion Phys., 29 231 (1979).
9. R. Johnsen, H.L. Brown and M. A. Biondi, J. Chem. Phys. 52 5080 (1970).
10. M. McFarland, D.L. Albritton, F.C. Fehsenfeld, E.E. Ferguson and A.L. Schmeltekopf, J. Chem. Phys. 59 6620 (1973).
11. G. Gioumousis and D.P. Stevenson, J. Chem. Phys. 29 294 (1958).
12. P.H. Krupenie, J. Phys. Chem. Ref. Data 1 423 (1972).

13. A. O'keefe, G. Mauclaire, D. Parent and M.T. Bowers, J. Chem. Phys. 84 215 (1986).
14. E.A. Mason and E.W. McDaniel, "Transport properties of ions in gases" (John Wiley and Sons, Inc. New-York, 1988).
15. E. Alge and W. Lindinger, J.G.R. 86 871 (1981).
16. P. Gauchered, J.B. Marquette, C. Rebrion, G. Poisant, G. Dupeyrat and B.R. Rowe, Chem. Phys. Lett. 132 63 (1986).
17. J.W. Dreyer and D. Perner, Chem. Phys. Lett. 12 299 (1971).
18. R. Scherbarth and D. Gerlich, J. Chem. Phys. 90 1610 (1989).
19. E.E. Ferguson, R. Richter and W. Lindinger, J. Chem. Phys. 89 1445 (1988).
20. R.H. Schultz and P.B. Armentrout, J. Phys. Chem. 95 121 (1991).
21. D.L. Albritton, I. Dotan, W. Lindinger, M. McFarland, J. Tellinghuisen and F.C. Fehsenfeld, J. Chem. Phys. 66 410 (1977).
22. R. Johnsen and M.A. Biondi, J. Chem. Phys. 59 3504 (1973).
23. A.L. Schmeltekopf, Planet. Space Sci. 15 401 (1967).
24. A.L. Schmeltekopf, E.E. Ferguson and F.C. Fehsenfeld, J. Chem. Phys. 48 2966 (1968).
25. D.B. Dunkin, F.C. Fehsenfeld, A.L. Schmeltekopf and E.E. Ferguson, J. Chem. Phys. 49 1365 (1968).
26. E.E. Ferguson, Rev. Geophys. Space Phys. 12 703 (1974).

27. D.B. Dunkin, M. McFarland, F.C. Fehsenfeld and E.E. Ferguson, J.G.R. 76 3820 (1971).
28. M. McFarland, D.L. Albritton, F.C. Fehsenfeld, A.L. Schmeltekopf and E.E. Ferguson, J.G.R. 79 2005 (1974).
29. E. Graham, R. Johnsen and M.A. Biondi, J.G.R. 80 2338 (1975).
30. J.L. LeGarrec, V. Lepage, B.R. Rowe and E.E. Ferguson, Chem. Phys. Lett. 270 66 (1997).
31. E.E. Ferguson, "Interactions between Ion and Molecules", Piere Ausloos (Ed.), Plenum Press p. 320 (1974).
32. C.R. Brondle, D. Neumann, W.C. Price, D. Evans, A.W. Potts and D.G. Streets, J. Chem. Phys. 53 705 (1970).
33. B.R. Rowe, Private Communication.
34. I. Dotan, D.L. Albritton and F.C. Fehsenfeld, J. Chem. Phys. 64 4334 (1976).
35. I. Dotan and W. Lindinger, J. Chem. Phys. 76 4972 (1982).
36. E.E. Ferguson, J.M. Van Doren, A.A. Viggiano, R.A. Morris, J.F. Paulson, J.D. Stewart, L.S. Sunderlin and P.B. Armentrout, Int. J. Mass. Spectrom. Ion Proc. 117 261 (1992).

FIGURE CAPTIONS

Fig. 1 - High Temperature Flowing Afterglow Apparatus

Fig. 2 - Rate constants for the reaction of N^+ with O_2 .

The NOAA kinetic energy data are from McFarland et.al. (10) and the temperature data are from Lindinger et al. (2). k_L is the Langevin collisional rate constant. "Maximum for $v>0$ " assumes that the $v=0$ rate constants are given by "NOAA (KE)" and that all vibrationally excited O_2 reacts at the Langevin rate.

Fig.3 - Rate constants for the reaction of N_2^+ with O_2 . The NOAA (KE) kinetic energy data are from McFarland et al.(10) and the NOAA (T) temperature data are from Lindinger et al. (2).

Fig 4 - Rate constants for the reaction of N_2^+ with O_2 as a function of rotational and vibrational energy. The curves marked $v \geq 0$ and $v \geq 1$ are derived rate constants for vibrationally excited O_2 as described in the text.

Fig 5 - Rate constants for the reaction of O^+ with N_2 .

The NOAA temperature data are from Lindinger et. al. (2) and the drift tube data from Albritton et al. (21). The predicted values are described in the text.

Fig 6 - Rate constants for the reaction of O^+ with O_2 . The NOAA temperature data are taken from Lindinger et al. (2) and Ferguson (26). The NOAA kinetic energy data are from McFarland et al. (10) and J&B refers to drift tube work of Johnsen and Biondi. (22).

Fig 7 - Rate constants for the reaction of O^+ with O_2 . The NOAA kinetic energy data are from McFarland et al. (10) The solid lines through the data represent fits to the expression $k = A_1(300/T)^n + A_2 \exp(-E_a/kT)$. The derivation of the rate constants for O_2 ($v>0$) is described in the text.

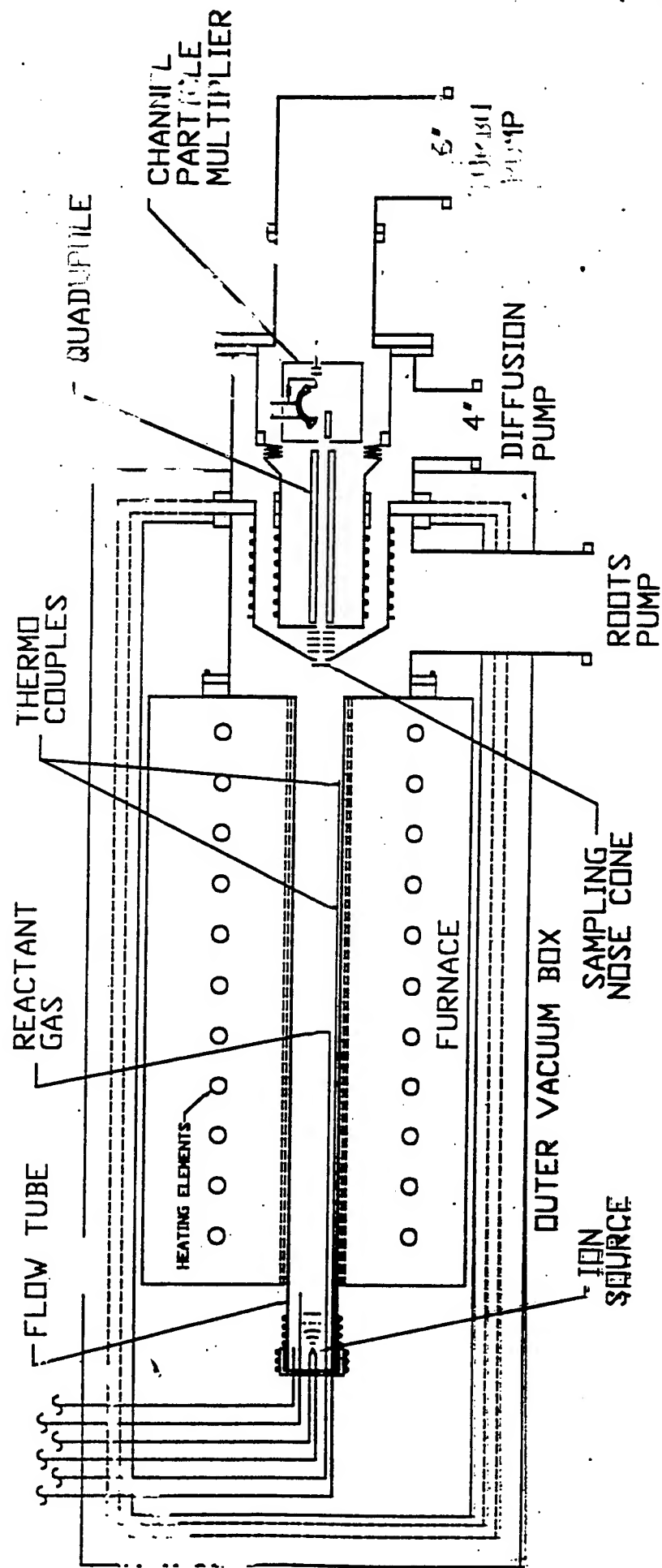
Fig 8 - Rate constants for the reaction of O^+ ions with NO. Rennes data are from Le Garrec et al. (30), NOAA data from Albritton et al. (21) and Pittsburgh data from Graham et al. (29).

Fig 9 - Rate constants for the reaction of O^+ ions with NO. Rennes data are from Le Garrec et al. (30). The solid line through the data represents a fit to the expression $k = A_1(300 / T)^n + A_2 \exp(-E_a / kT)$.

Fig 10 - Rate constants for the reaction of A_r^+ ions with SO_2 . NOAA data are from Dotan et al. (34).

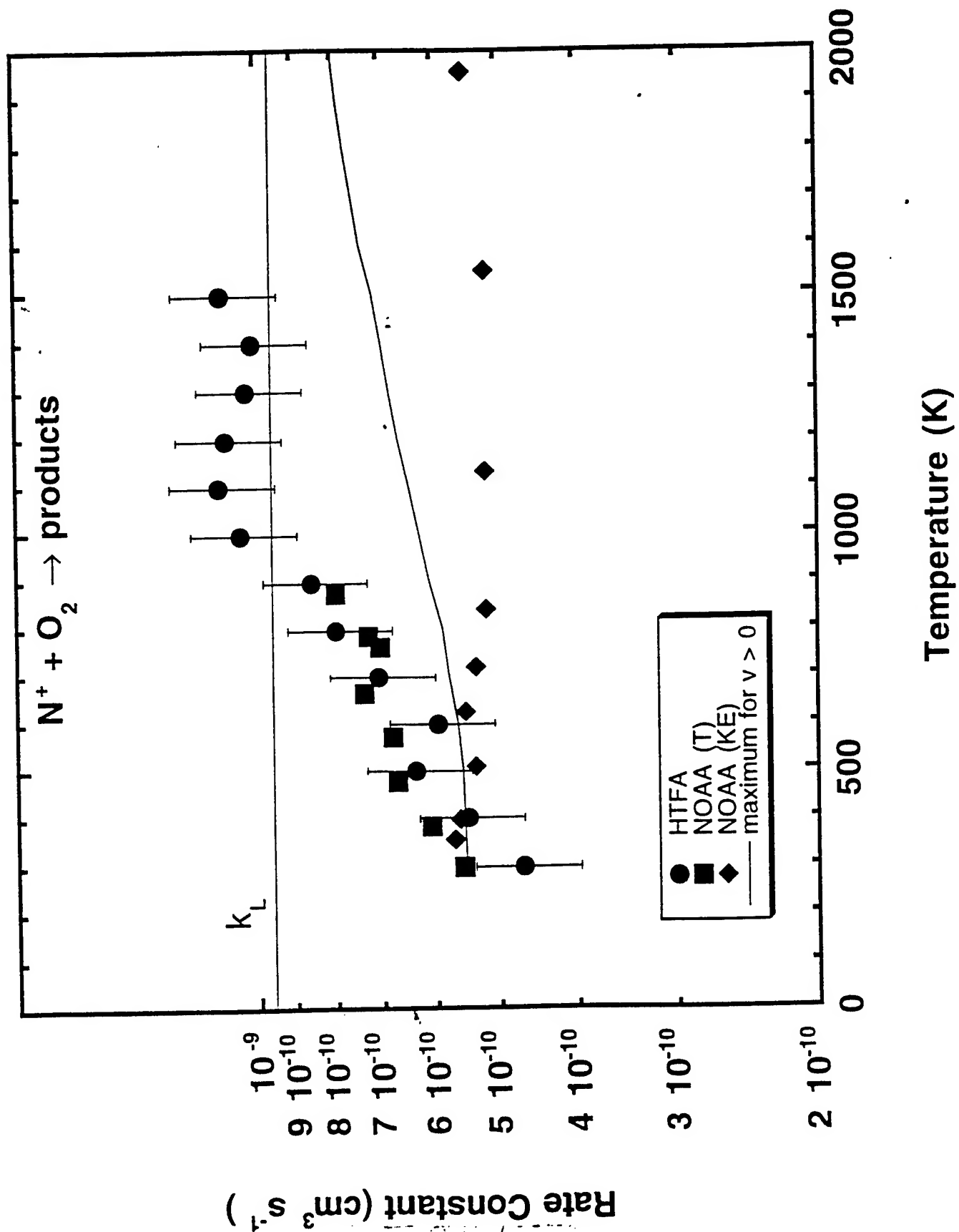
Fig 11 - Rate constants for the reaction of A_r^+ ions with CO_2 . NOAA data are from Dotan and Lindinger (35).

Fig 12 - Rate constants for the reaction of CO_2^+ ions with O_2 . Drift data are from Ferguson et al (36).



HIGH TEMPERATURE FLOWING AFTERGLOW

Fig. 1



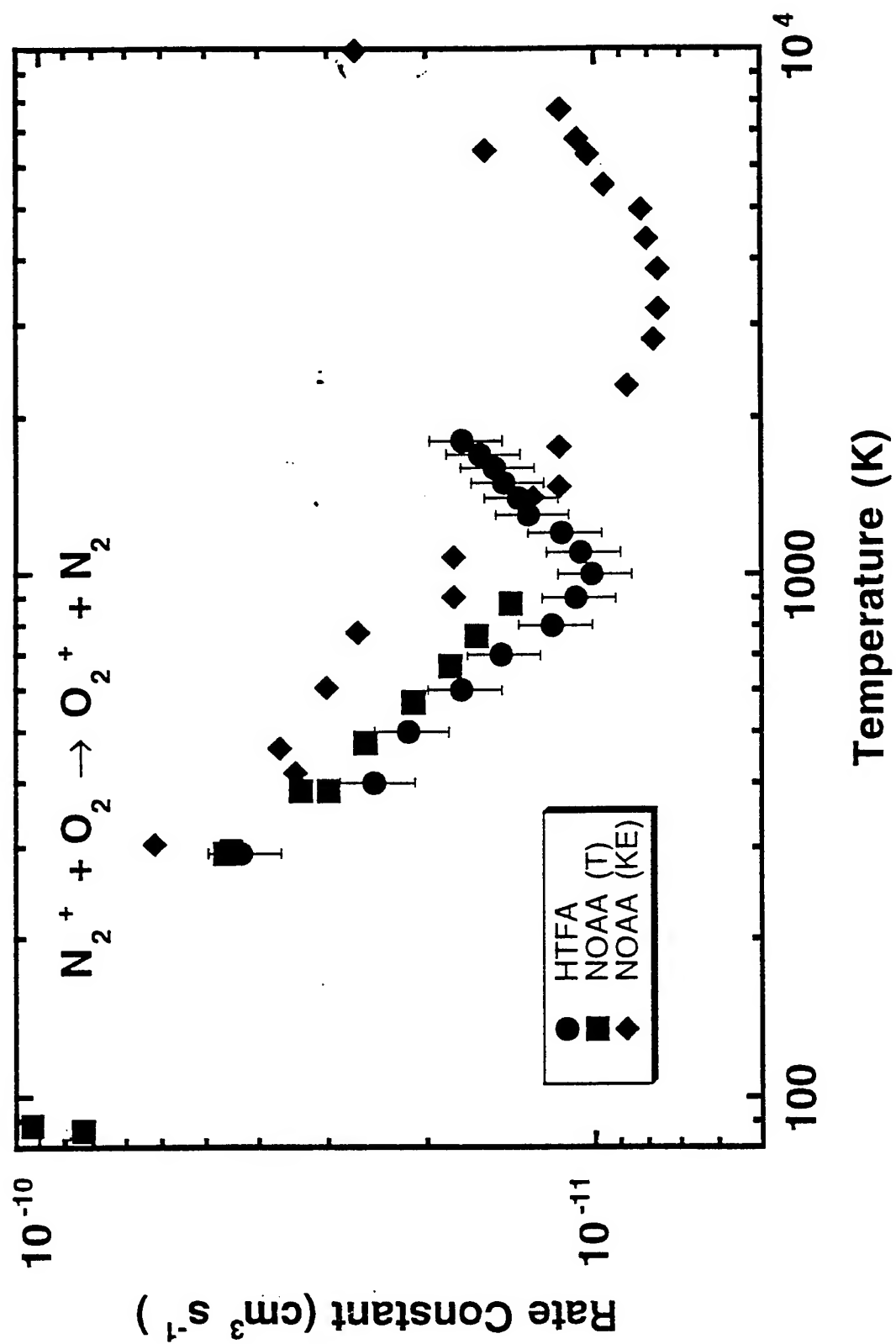


Fig. 3

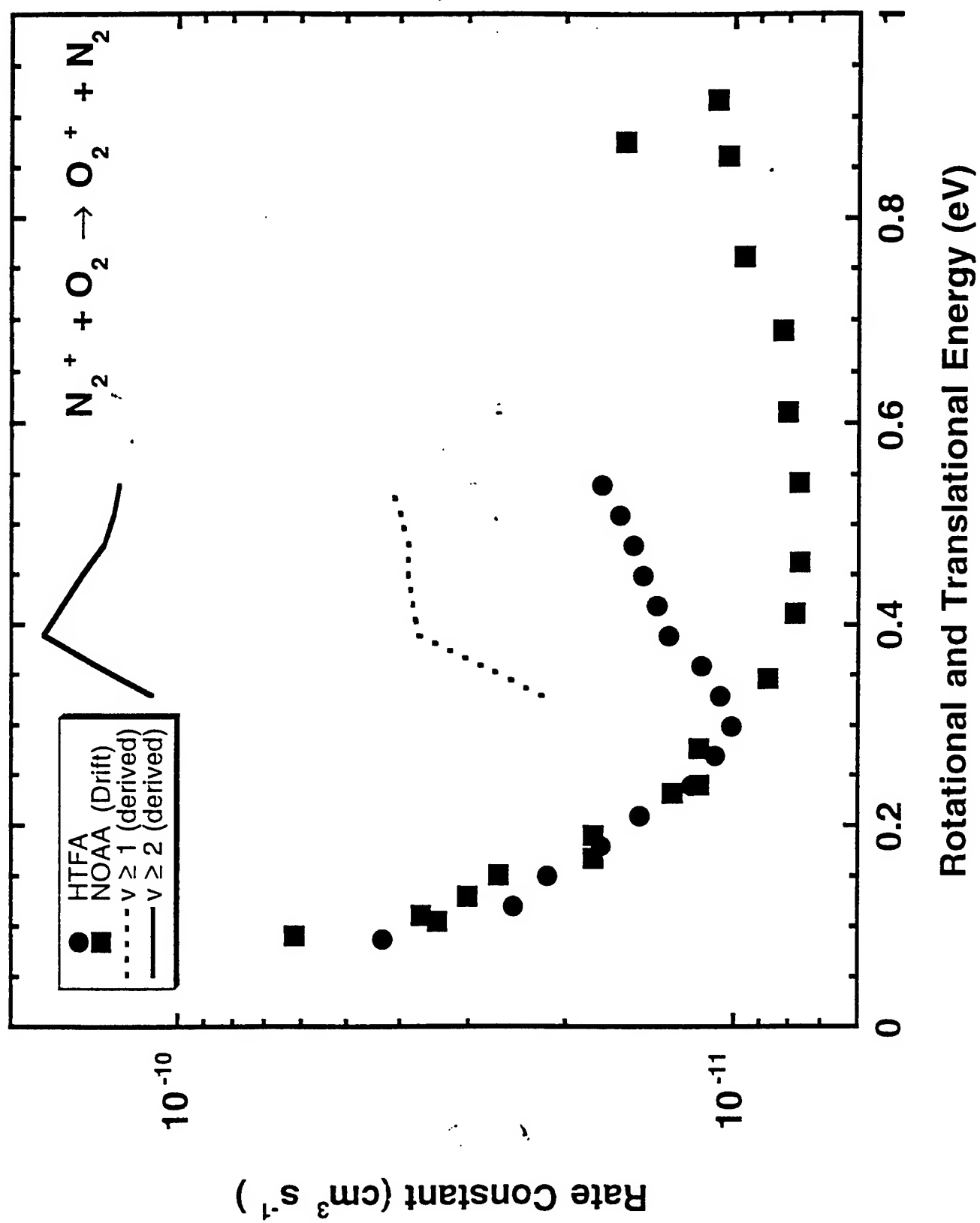


Fig. 4

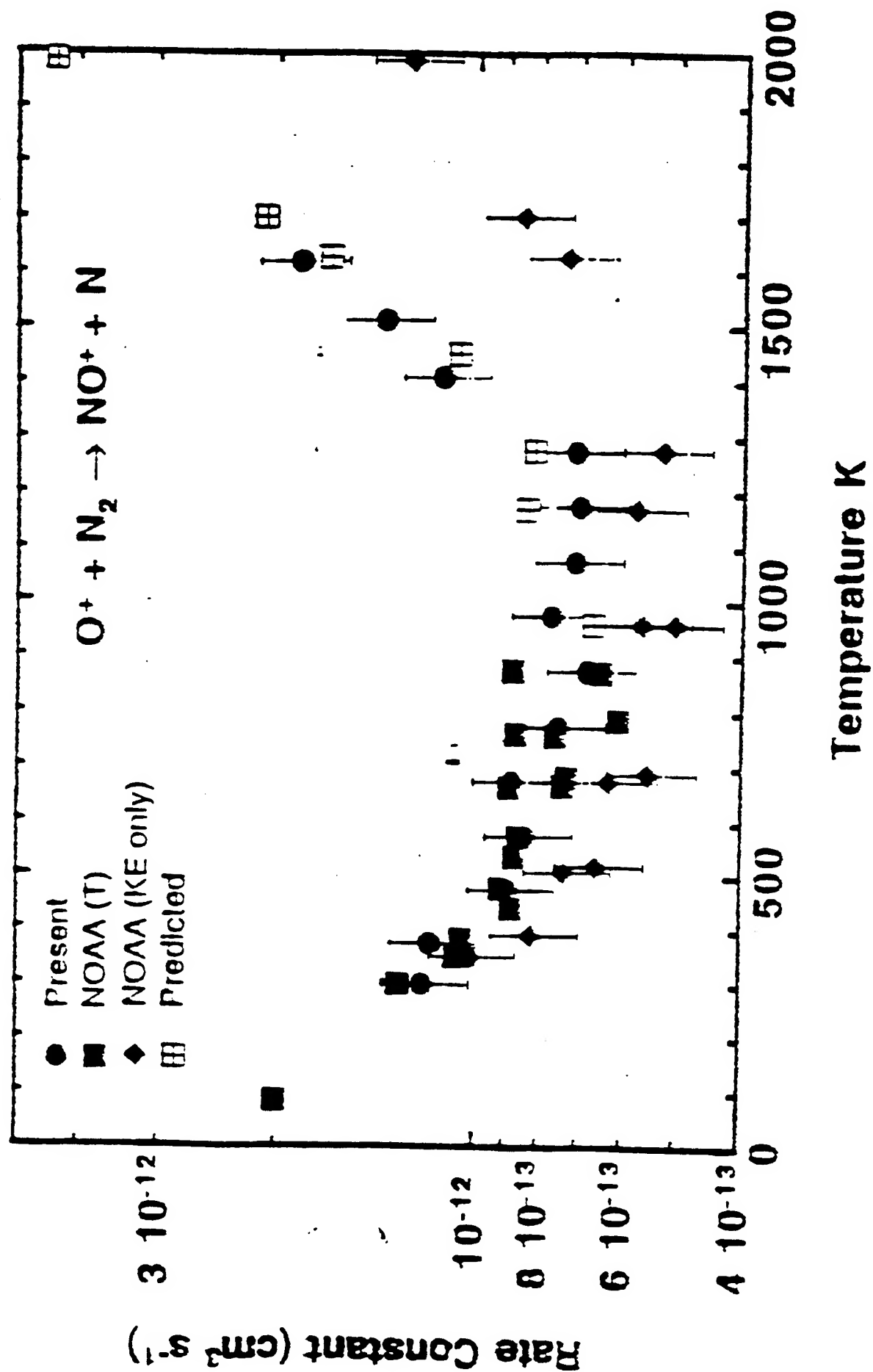


Fig. 5

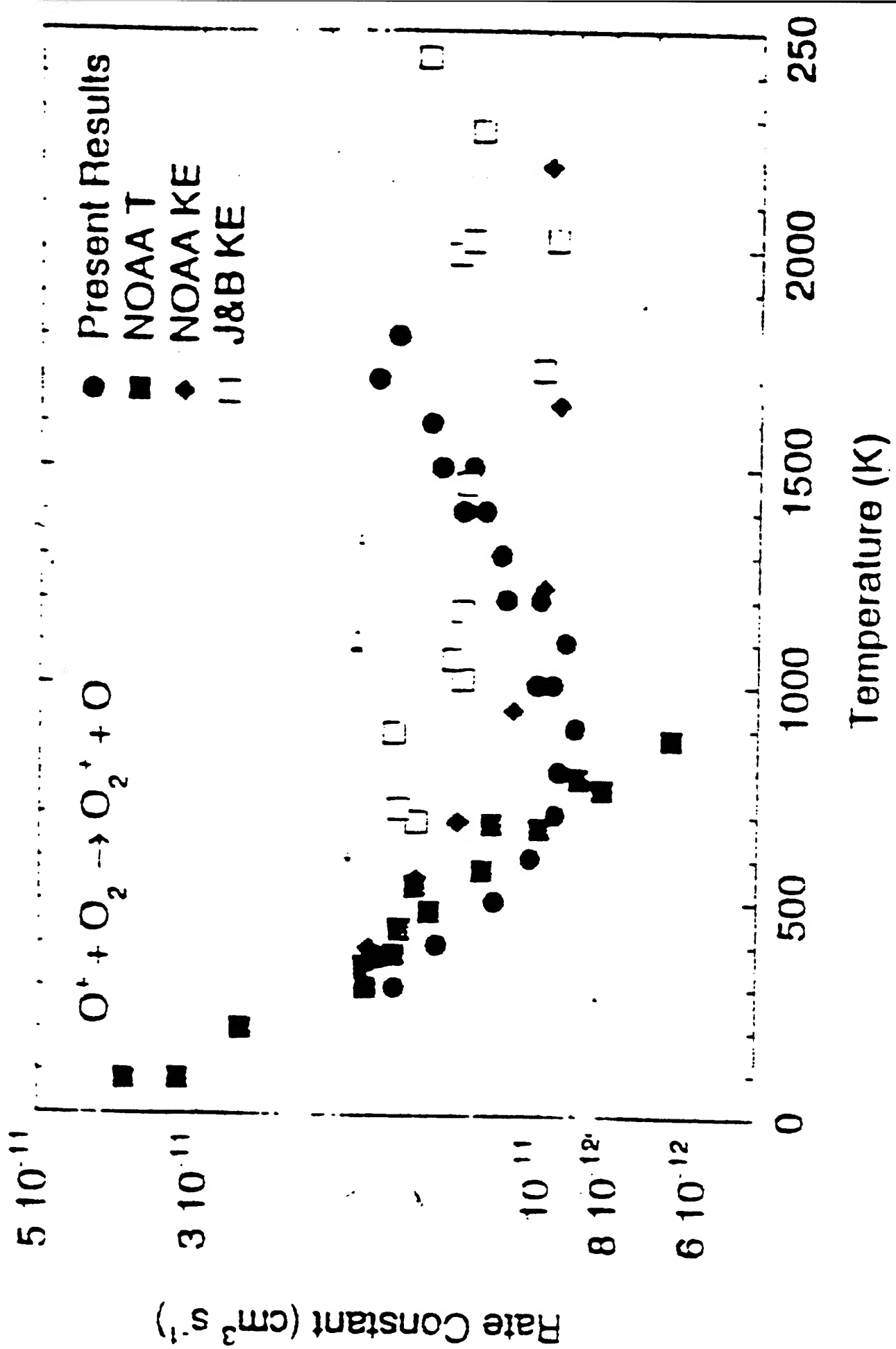


Fig. 6

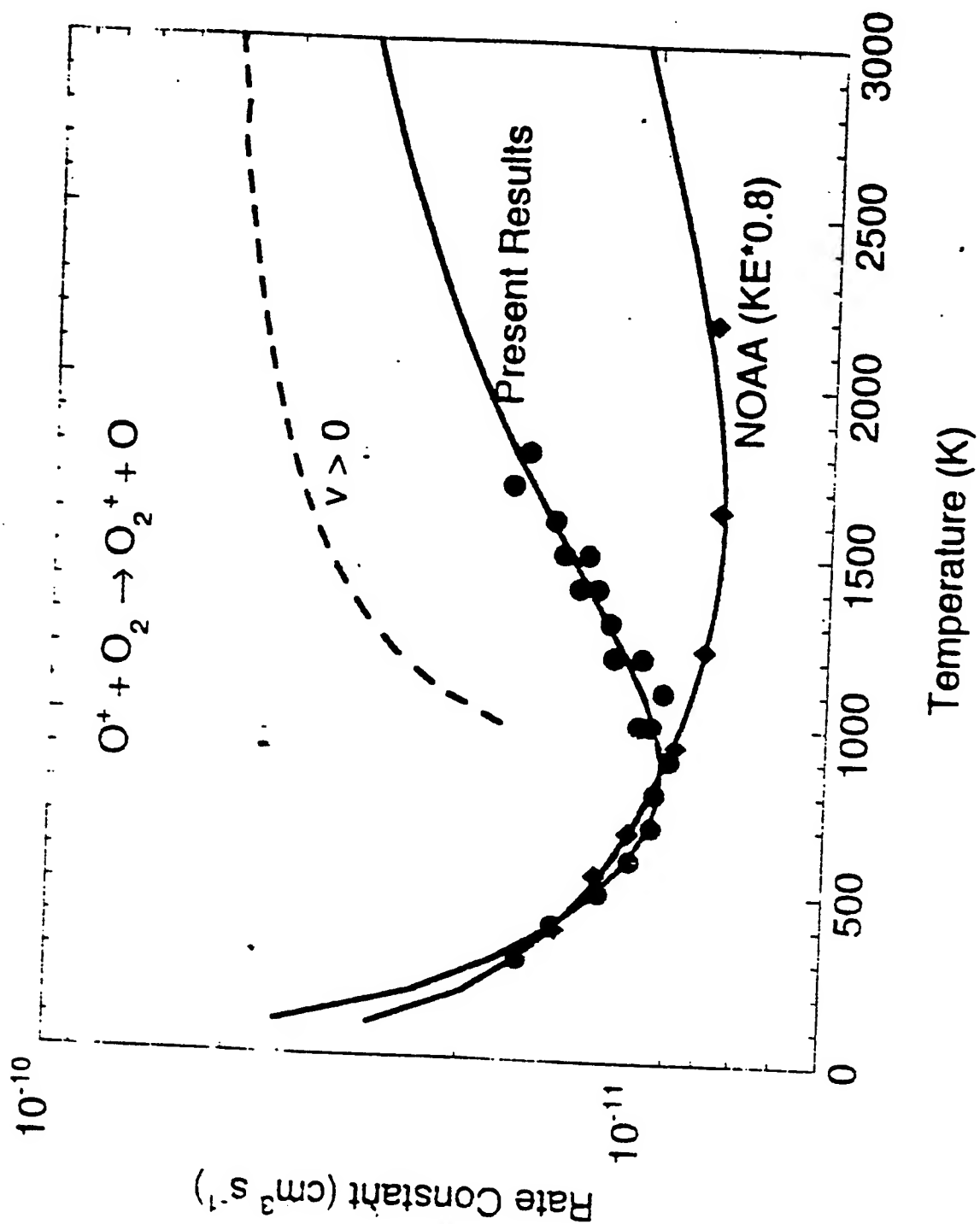


Fig. 7

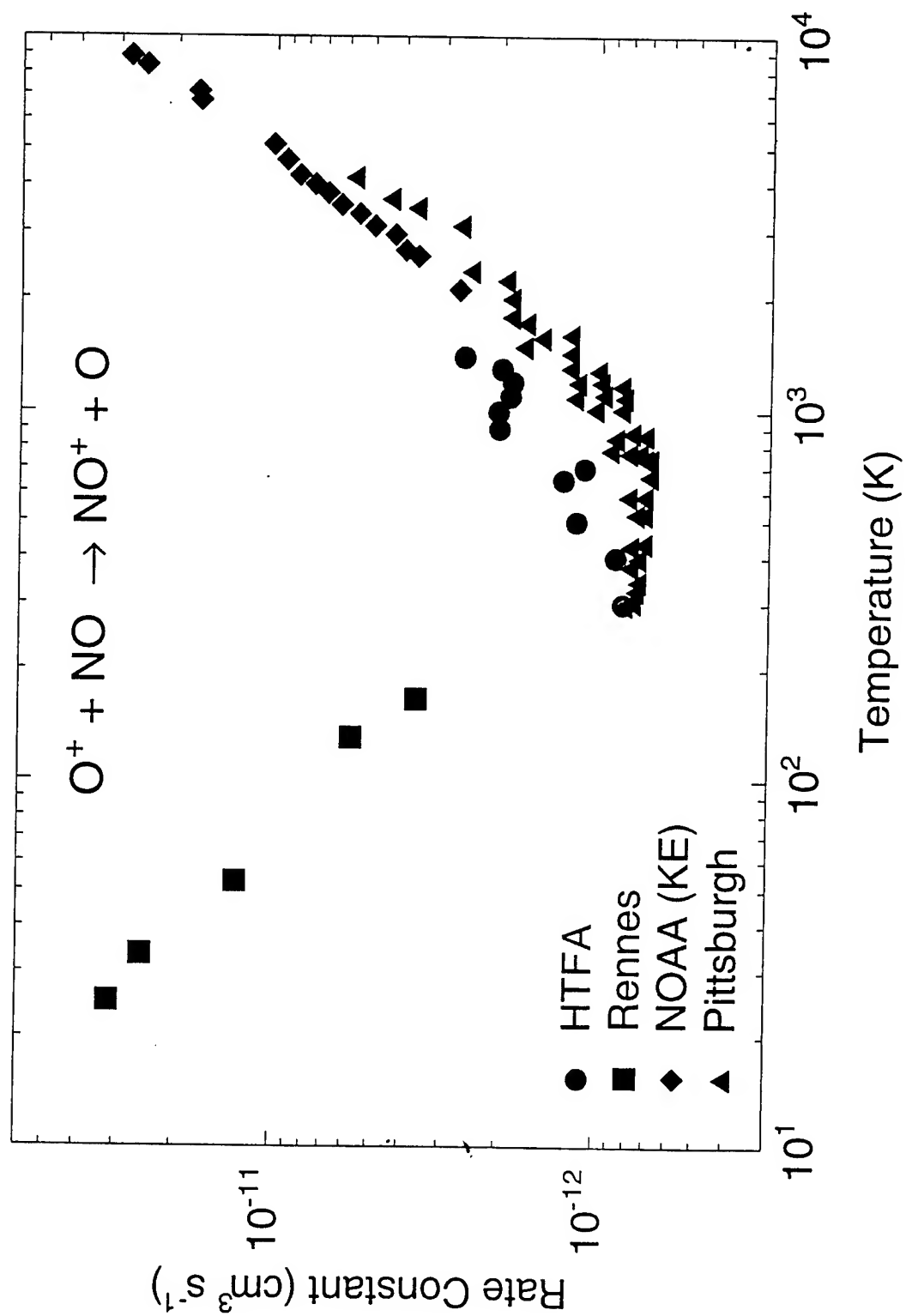


Fig. 8

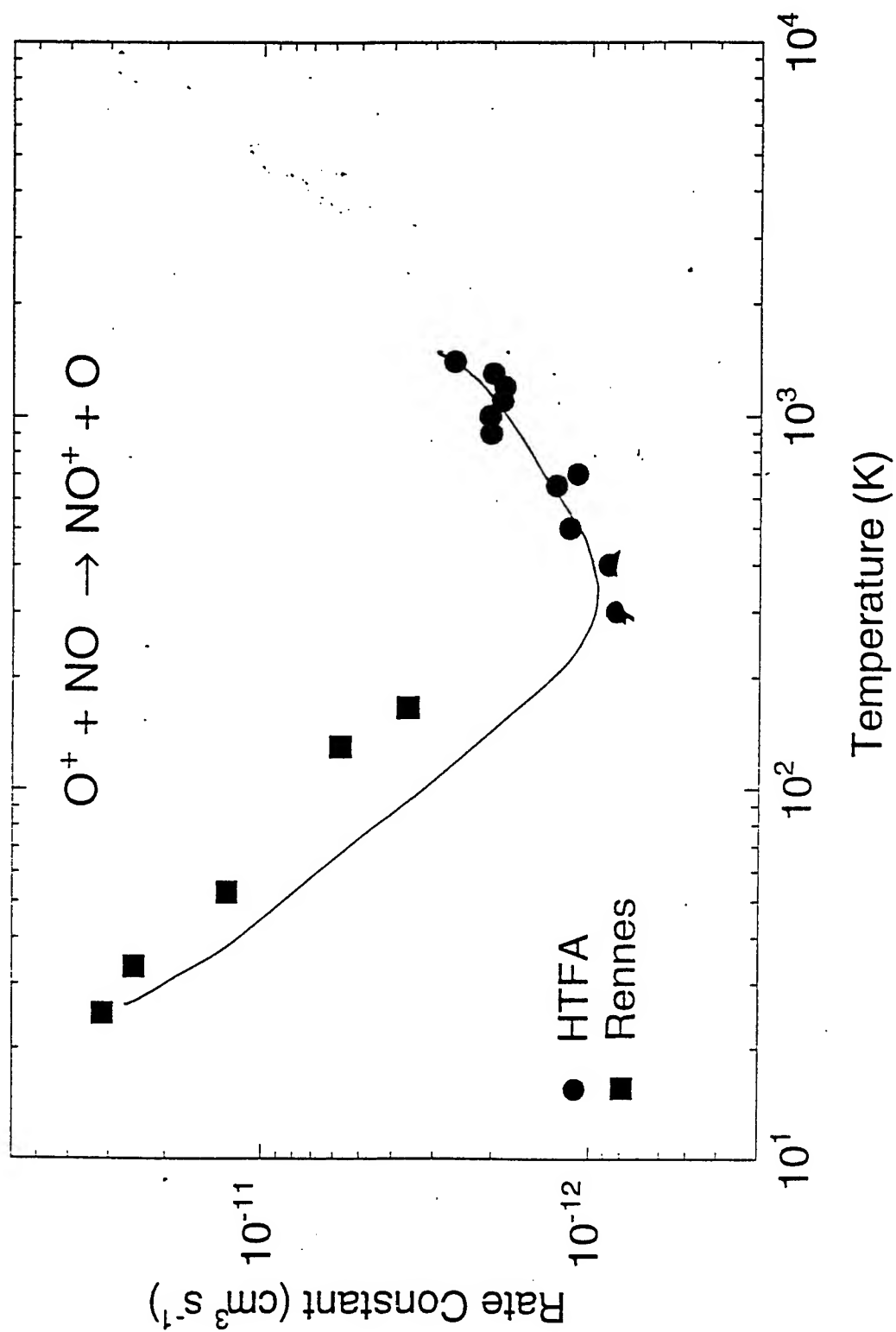


Fig. 9

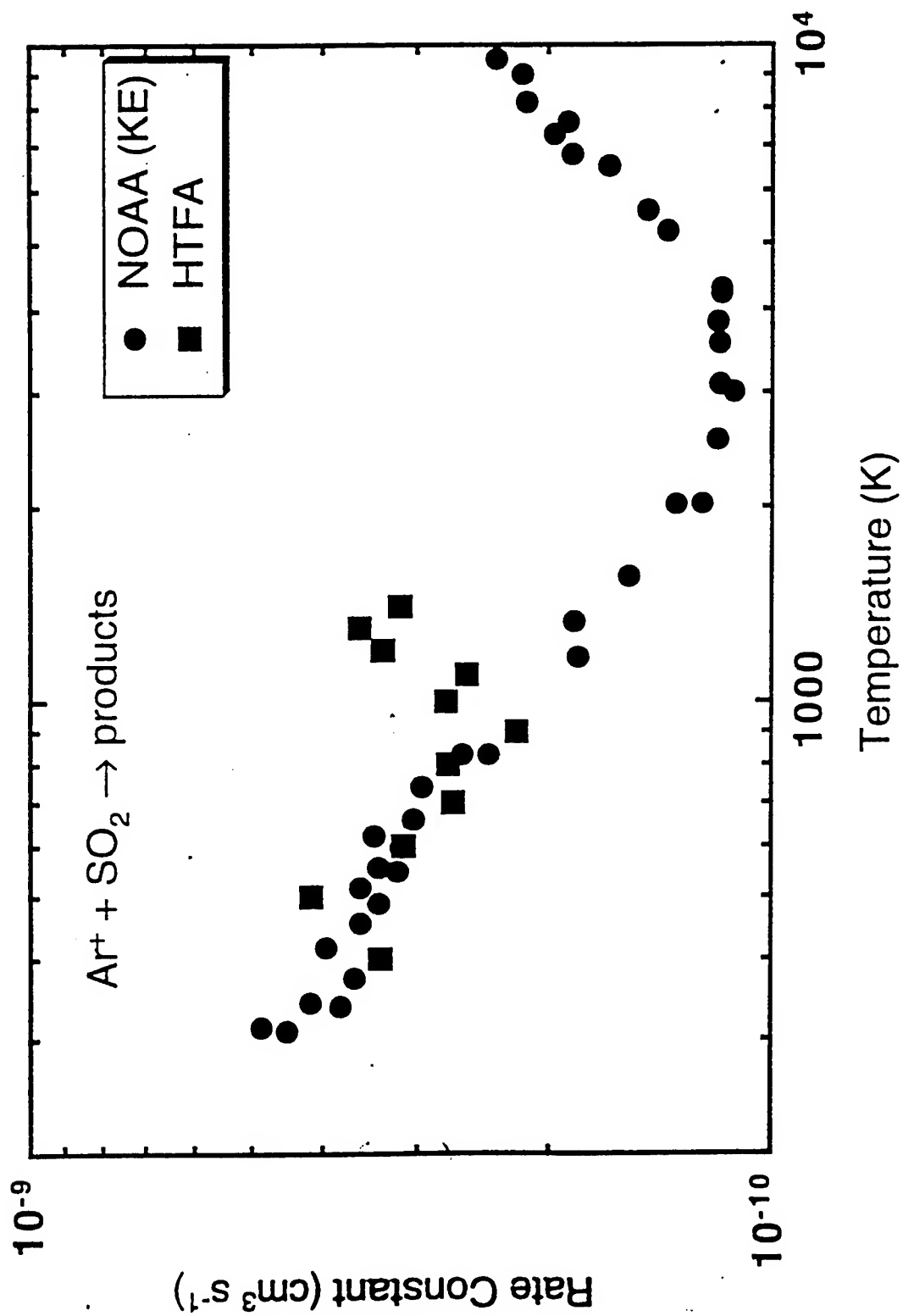


Fig. 10

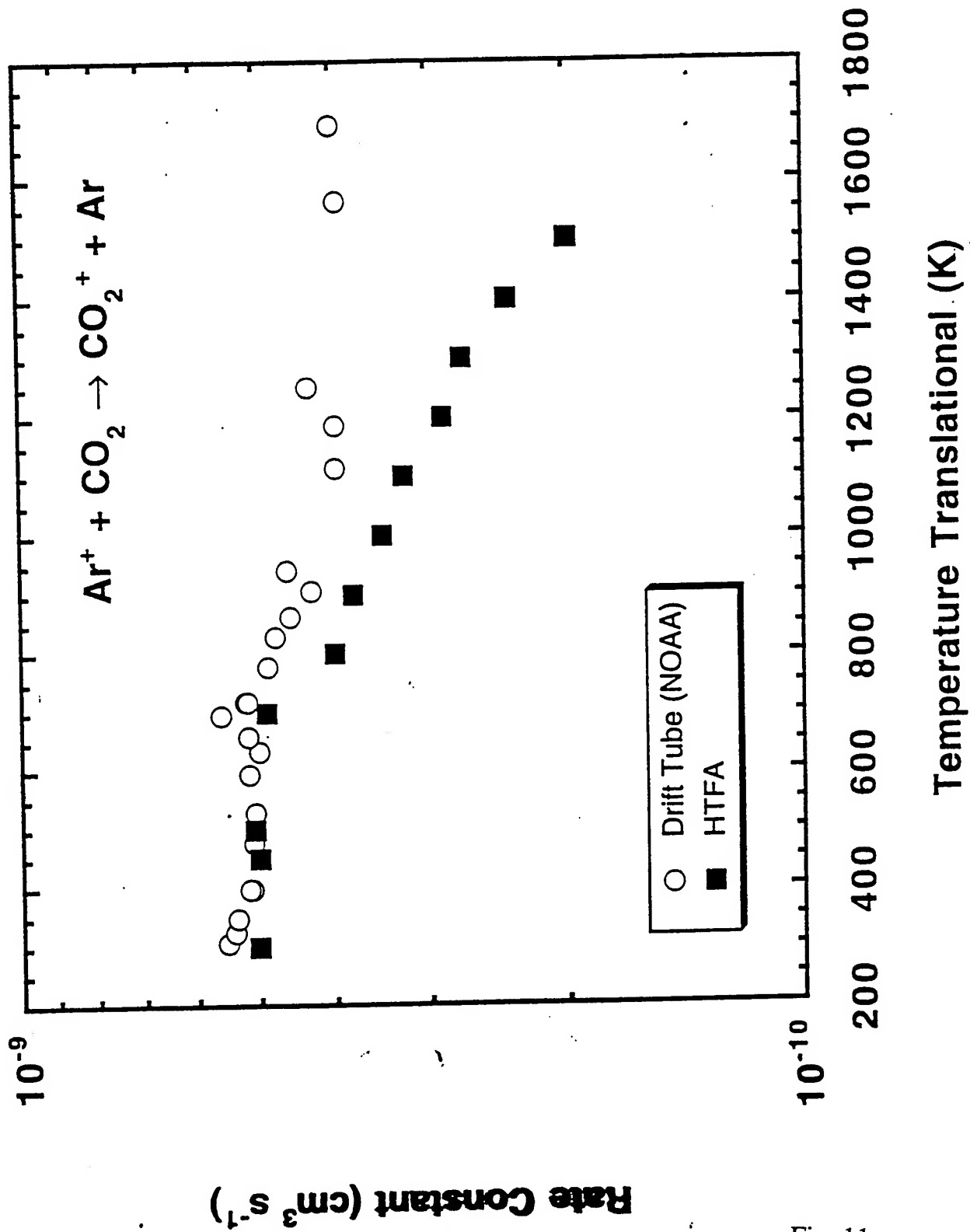


Fig. 11

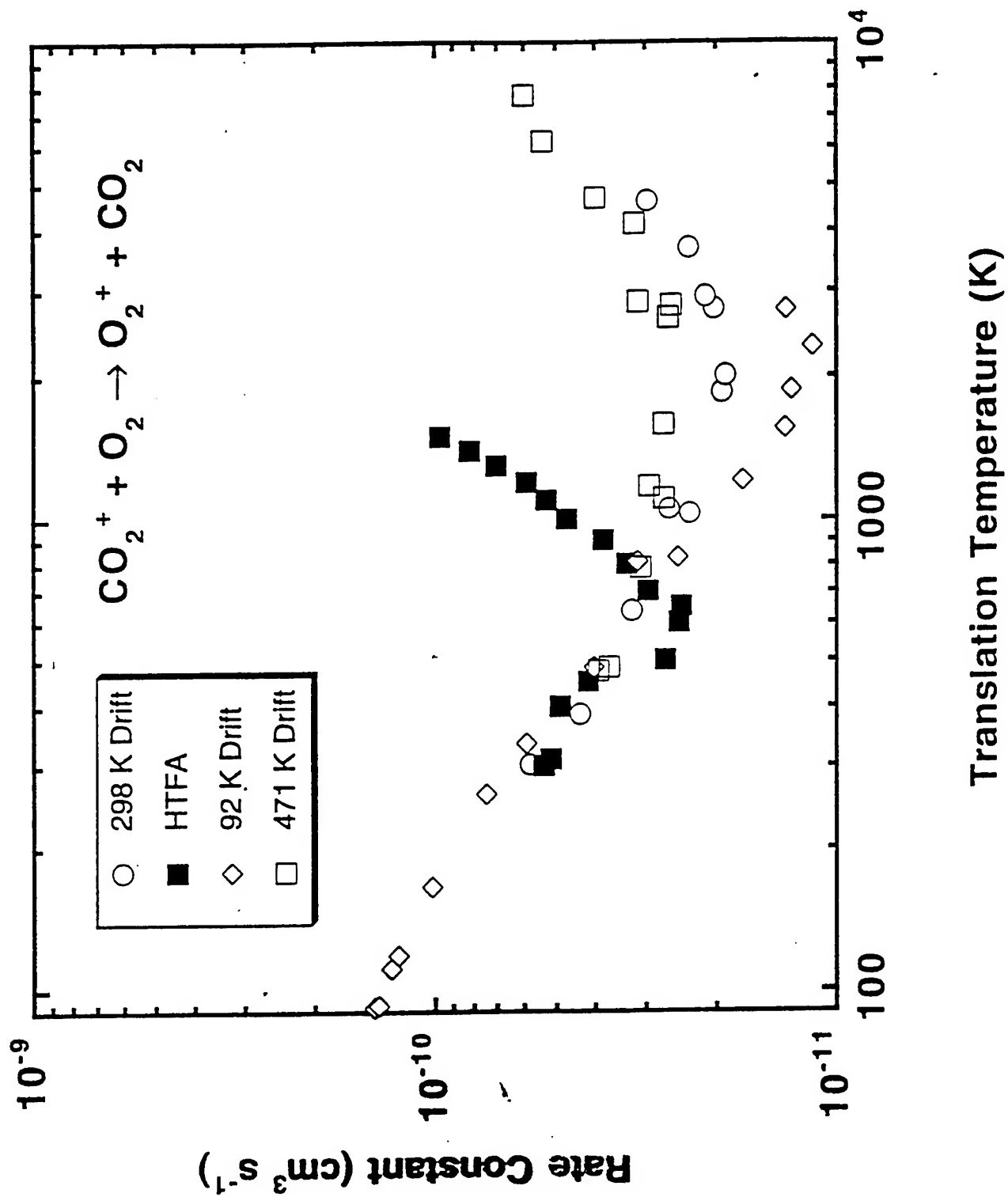


Fig. 12

ELECTROMAGNETIC MODELING OF COMPLEX DIELECTRIC/METALLIC MINES IN A LAYERED EARTH

**George W. Hanson
Associate Professor
Department of Electrical Engineering and Computer Science**

**University of Wisconsin-Milwaukee
3200 North Cramer Street
Milwaukee, Wisconsin 53211**

**Final Report for:
Summer Faculty Research Extension Program
Phillips Laboratory
Kirtland Air Force Base**

**Sponsored by:
Air Force Office of Scientific Research
Bolling Air Force Base, DC**

and

**Phillips Laboratory
Kirtland Air Force Base**

December 1997

ELECTROMAGNETIC MODELING OF COMPLEX DIELECTRIC/METALLIC MINES IN A LAYERED EARTH

George W. Hanson
Associate Professor
Department of Electrical Engineering and Computer Science
University of Wisconsin-Milwaukee

Abstract

An accurate electromagnetic model of a buried dielectric/metallic mine has been developed as an aid to the development of target detection and identification technologies for military and humanitarian weapons cleanup efforts. An integral equation model for the buried mine configuration has been formulated and numerically solved exploiting an efficient numerical technique to compute important electromagnetic features. The implemented method is applicable to the determination of a mine's natural resonant frequencies and eigencurrents/fields, which can be used for detection and identification schemes. The influence of the layered earth background environment, into which the target (mine) is embedded, on natural modal characteristics has been ascertained. Further development of this technique (ongoing by current graduate students) will yield results of significant value in guiding the design of future detection and identification technologies for the buried mine problem.

ELECTROMAGNETIC MODELING OF COMPLEX DIELECTRIC/METALLIC MINES IN A LAYERED EARTH

George W. Hanson

Contents

I.	Problem Significance.....	4
II.	Project Description.....	5
III.	Brief Overview of Previous Work	6
IV.	Theoretical Formulation of Electromagnetic Model	
	A. Formulation of Integral Equation Model	7
	B. Special Computational Considerations	12
V.	Results.....	13
VI.	References	14

I. Problem Significance

The detection of potentially dangerous hidden objects is of great importance. Even specifically considering the mine problem, there are many different scenarios to consider. For instance, the detection of unexploded ordnance (UXO) is a very difficult problem for military range cleanup. According to the Department of Defense, there are approximately nine million acres of past and present test ranges that contain unexploded ordnance [1], including Air Force property. This problem is of increasing concern to civilians due to the Base Realignment and Closure (BRAC) Program, under which some military bases have been closed and the land returned to the public or private sector. It is estimated that 1,200-1,700 Formerly Used Defense Sites (FUDS) are contaminated [1]. The possibility of UXOs on land returned to private or public use is certainly disturbing. This is not to imply that the military purposely releases land with UXO contamination, but the extent of the regions affected, together with the difficulty of absolutely assuring removal of all UXO material (due to imperfect detection technology) renders the release of contaminated land likely.

Aside from the possibility of UXO on FUDS within the United States, the detection of land mines in foreign countries is a significant problem for humanitarian cleanup efforts. There are now over 50 million abandoned, yet active, land mines in over 60 countries around the world [2]. These mines kill some 10,000 civilians each year, and injure many more. Unfortunately, in many countries mines continue to be set at an astounding rate. Current technology for mine detection is unsatisfactory, being imprecise, dangerous, and expensive.

Separate from the buried mine issue, the identification of hidden objects is of great concern for safety in airports, courtrooms, prisons, etc.. Current detectors are only useful for determination of the presence of sufficient quantities of metallic material. Since non-metallic materials are being incorporated into weapons to avoid detection, technologies to detect and identify such materials need to be improved.

The above described problems represent an important subset of the wide range of scenarios which require detection and identification technology improvement. Due to the considerable variation of object shapes and material properties which must be detected and identified, and the range of background environments into which the objects may be embedded, no single

technology will prove to be completely satisfactory. In a general situation, it may be necessary to employ a suite of technologies, based on electromagnetic, acoustic, chemical, and nuclear mechanisms, to achieve accurate detection and identification. Even within the electromagnetic domain, for example, a range of approaches may be required. A combination of low frequency (object small compared to wavelength), resonance (object comparable to wavelength), and high frequency (object large compared to wavelength) frequency-domain methods may be useful, in addition to wideband and transient methods. Within the above, detection and identification can be based upon singularity characteristics (magnetic or electromagnetic) or actual electromagnetic imaging (optical, microwave, etc.), although the latter is generally a more difficult problem.

II. Project Description

The work performed here concerns the electromagnetic modeling of primarily dielectric bodies embedded in an inhomogeneous background environment. The specific problem of buried dielectric mines is addressed here, although with slight modification other objects/environments can be considered. The type of mine considered is primarily dielectric, with small amounts of metallic material incorporated to model springs or wires which are found on some mines. The proposed method of analysis is fullwave, and can be applied to a range of frequencies for the determination of singularities and scattering response, which can be used for detection and identification schemes [3],[4]. The principal idea is to determine the electromagnetic characteristics of interest, such as natural frequencies, and the influence of the background environment on those quantities. Given a specific shape of interest, the influence of the background material layering and constitutive parameters on the resonance characteristics can be determined. The determination of natural frequencies allows one to determine the correct frequency range which will provide a strong response from the object, and the natural modes (natural currents or fields) provide information as to what type of waveform polarization is necessary to strongly excite the body [5]. The influence of the background environment on the object's natural characteristics is important to consider, since the object will rarely be in free-space, physically. It may happen, though, that the object will behave electrically as if it were in free space (or a homogeneous space) in some situations. In other situations, the background

environment will need to be accounted for explicitly.

III. Brief Overview of Previous Work

There has been a considerable amount of interest in the development of appropriate techniques for detecting and identifying buried objects or bodies. Geophysical sensing technologies have been developed for the detection and identification of various types of geological bodies or features, such as underground oil reserves, mineral deposits, and other structures of interest. The detection and identification problem for the buried mine, either conducting or nonconducting, has received less attention. Current metallic mine detectors use standard "metal detector" technology, which is inaccurate in the detection phase and provides no identification capability. Dielectric mines provide a more difficult problem, and no system has been developed which operates in a satisfactory manner. A brief compilation of research papers is provided [6]-[11], which detail some recent work in this direction. It should be noted that [10],[11] are particularly relevant to the problem and solution method proposed here. This work represents a significant extension of previous efforts in several ways. The model developed is an exact, three-dimensional description of the problem, including an arbitrary multi-layered earth with a general dielectric body. Most, but not all, previous efforts considered a two-dimension problem. All previous work utilized a simpler half-space model of the earth/air interface, and neglected other soil layers which often exist. The mine includes metallic material to model wires, whereas previous work has considered either metallic objects or dielectric objects, but no mixed conducting/dielectric bodies. The project particularly concentrates on natural modal properties, which are valuable in the identification problem, but have not been characterized for the buried mine.

IV. Theoretical Formulation of Electromagnetic Model

A. Formulation of Integral Equation Model

In this section a brief description of the theoretical formulation for the considered problem is provided. In the following development, all electromagnetic quantities will be assumed to obey Maxwell's equations in the two-sided Laplace transform domain, governed by the transform pair

$$\begin{aligned} F(s) &= \int_{-\infty}^{\infty} F(t) e^{-st} dt \\ F(t) &= \frac{1}{2\pi j} \int_{\Omega_0 - j\infty}^{\Omega_0 + j\infty} F(s) e^{st} ds \end{aligned} \quad (1)$$

where $s = \Omega + j\omega$, and Ω, ω are real quantities.

Consider the geometry shown in Fig.1, which depicts a closed surface S bounding volume V containing a generally inhomogeneous and anisotropic medium characterized by $\tilde{\epsilon}(\vec{r}), \mu_0$. The medium external to S is assumed for simplicity to be isotropic but generally inhomogeneous. The layered exterior medium case corresponds to the buried dielectric body problem assuming the ground can be approximated as consisting of planar layers. In each layer, as well as internal to S , material loss can be accommodated by defining the permittivity to be complex as $\epsilon \rightarrow \epsilon + \sigma/s$ for real conductivity σ .

A wave impedance and propagation constant can be defined for the j -th exterior region,

$$\begin{aligned} \gamma_j &= s[\mu_0 \epsilon_j]^{1/2} \\ Z_j &= [\mu_0 \epsilon_j^{-1}]^{1/2} \end{aligned} \quad (2)$$

and formally extended to the interior region

$$\begin{aligned} \tilde{\gamma}(\vec{r}) &= s[\mu_0 \tilde{\epsilon}(\vec{r})]^{1/2} \\ \tilde{Z}(\vec{r}) &= [\mu_0 \tilde{\epsilon}^{-1}(\vec{r})]^{1/2} \end{aligned} \quad (3)$$

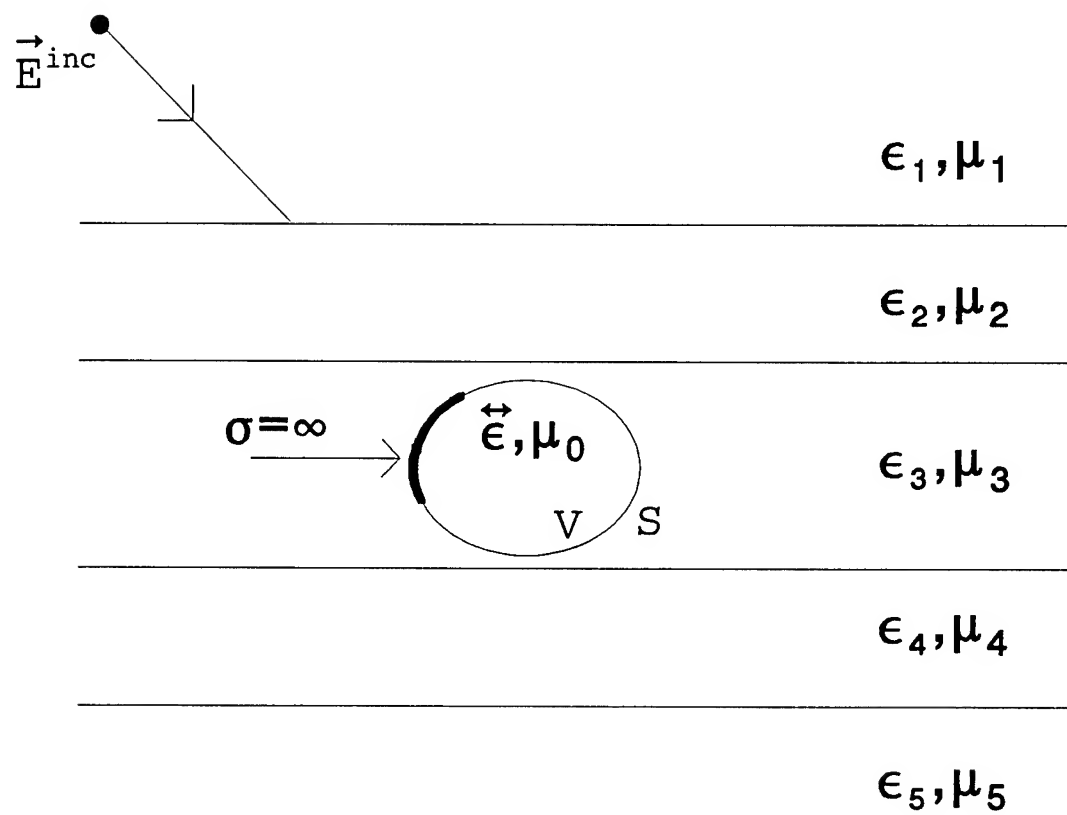


Fig. 1. General dielectric/conducting body in multilayered media.

noting the following combinations

$$\begin{aligned}\gamma_j Z_j &= s\mu_0, \quad \tilde{\gamma} \cdot \tilde{Z} = \tilde{I} s\mu_0, \\ \gamma_i Z_j^{-1} &= s\epsilon_j, \quad \tilde{\gamma} \cdot \tilde{Z}^{-1} = s\tilde{\epsilon}\end{aligned}\quad (4)$$

The relationship between the electric field and an electric current source can be written as

$$\vec{E}(\vec{r}, \gamma_o) = -\langle \tilde{Z}^e(\vec{r}|\vec{r}', \gamma_o) ; \vec{J}(\vec{r}') \rangle \quad (5)$$

where \langle , \rangle denotes integration of the two terms separated by the comma over common spatial coordinates, and the symbol above the comma indicates the real scalar product. The propagation constant γ_o is merely symbolic, and represents dependance on all of the exterior region layers, i.e., $\gamma_o \equiv \{\gamma_1, \gamma_2, \gamma_3, \dots\}$. The electric dyadic Green's function, $-\tilde{Z}_{\alpha\beta}^e(\vec{r}|\vec{r}', \gamma_o)$, provides the α -th component of field at \vec{r} due to the β -th component of a Hertzian current element at \vec{r}' . In general, the Green's dyadic can be written as

$$\tilde{Z}^e(\vec{r}|\vec{r}', \gamma_o) = s\mu_0 \{ \tilde{g}(\vec{r}|\vec{r}', \gamma_o) + \tilde{L}_\delta \gamma^{-2} \delta(\vec{r} - \vec{r}') \} \quad (6)$$

where the first term is evaluated in a principle value sense for a specified exclusion volume. The second term is the depolarizing dyad contribution, which depends on the shape of the exclusion volume as well as the material properties of the region which includes the source current (with the appropriate value of propagation constant assigned to γ). Details concerning (6), as well as general forms of the principal value term for homogeneous and layered media surround regions are provided in Appendix B of [12].

Next, a set of coupled integral equations which model the dielectric/metallic body completely contained within one layer of the surround environment can be formulated [13],[14],[15]. As a specific example, consider the geometry depicted in Fig. 2. A dielectric disk resembling a dielectric mine is shown, along with some thin metallic pieces that represent wires or springs. The IEs for this geometry are formed by enforcing boundary conditions along the surface of the wires and field conditions in the dielectric region. The boundary and field conditions are given

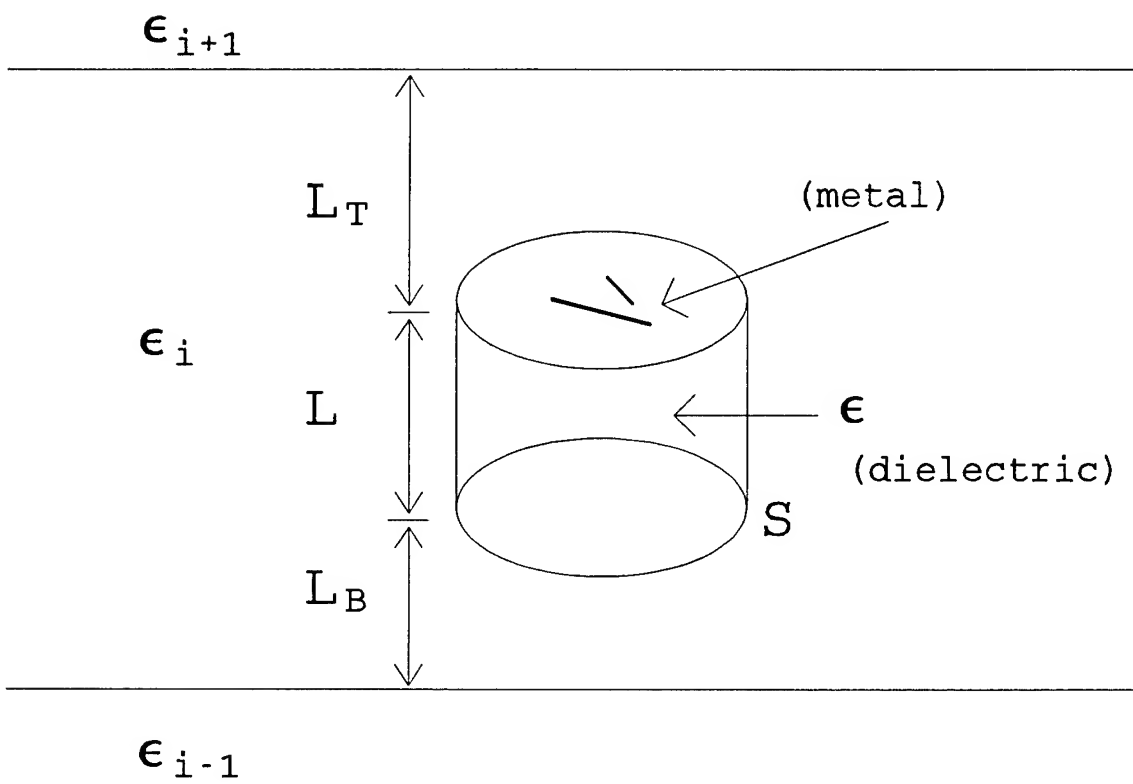


Fig. 2. Example of a buried dielectric mine with arbitrary conducting wires.

by

$$\begin{aligned} \hat{\alpha} \cdot \left\{ \sum_{n=1}^N \vec{e}_{in}^s(\vec{r}) + \vec{e}_d^s(\vec{r}) \right\} &= -\hat{\alpha} \cdot \vec{e}^{inc}(\vec{r}) \quad \dots \forall \vec{r} \in l_m, m=1..N \\ \vec{e}(\vec{r}) - \sum_{n=1}^N \vec{e}_{in}^s(\vec{r}) - \vec{e}_d^s(\vec{r}) &= \vec{e}^{inc}(\vec{r}) \quad \dots \forall \vec{r} \in V \end{aligned} \quad (7)$$

where l_m extends over the m 'th wire, V denotes the space occupied by the dielectric, $\hat{\alpha}$ is a unit vector tangential to the wire, \vec{e}_{in}^s is the scattered electric field maintained by conduction current on the n 'th wire, \vec{e}_d^s is the scattered electric field due to equivalent polarization current in the inhomogeneous dielectric region, \vec{e} is the total electric field in the dielectric region, and \vec{e}^{inc} is the incident electric field maintained by remote sources with the wires and dielectric region absent, but in the presence of the multilayered background environment. In the above, the first equation represents $2N$ scalar equations which force the total tangential electric field to be zero along the m 'th perfectly conducting wire. The next equation represents three scalar equations which force the total electric field at every point within the dielectric region to equal the incident field plus the field maintained by the various currents. The radiation condition is enforced, along with boundary conditions at the other planar interfaces, by the Green's function for the background environment.

The volume equivalence principle is used to account for the inhomogeneous dielectric region embedded in the background layering [16],[14]. The dielectric region is replaced by a homogeneous region containing equivalent polarization currents which reside in the space previously occupied by the dielectric and vanish outside of that region, as depicted in [15]. The equivalent currents are

$$\vec{J}_e^{eq}(x,z) = j\omega[\vec{\epsilon}(x,z) - \epsilon_c \vec{I}] \cdot \vec{e}(x,z) \quad (8)$$

A coupled set of IE's is formed by substituting the relations (5) and (8) into the set of boundary and field conditions (7), resulting in

$$\hat{\alpha} \cdot \left\{ \sum_{n=1}^N \int \tilde{\mathbf{Z}}^e(\bar{\mathbf{r}}|\bar{\mathbf{r}}') \cdot \bar{\mathbf{J}}_{in}(\bar{\mathbf{r}}') d\mathbf{l}' \right\} + s \int_{V_d} \tilde{\mathbf{Z}}^e(\bar{\mathbf{r}}|\bar{\mathbf{r}}') \cdot \bar{\mathbf{e}}(\bar{\mathbf{r}}') dV' = -\hat{\alpha} \cdot \bar{\mathbf{e}}^{inc}(\bar{\mathbf{r}}) \quad \begin{matrix} \bar{\mathbf{r}} \in l_m \\ m=1..N \end{matrix} \quad (9)$$

$$\begin{aligned} \bar{\mathbf{e}}(\bar{\mathbf{r}}) - \sum_{n=1}^N \int \tilde{\mathbf{Z}}^e(\bar{\mathbf{r}}|\bar{\mathbf{r}}') \cdot \bar{\mathbf{J}}_{in}(\bar{\mathbf{r}}') d\mathbf{l}' - s \int_{V_d} \tilde{\mathbf{Z}}^{eq}(\bar{\mathbf{r}}|\bar{\mathbf{r}}') \cdot \bar{\mathbf{e}}(\bar{\mathbf{r}}') dV' \\ = \bar{\mathbf{e}}^{inc}(\bar{\mathbf{r}}') \quad \forall \bar{\mathbf{r}} \in V_d \end{aligned} \quad (10)$$

where

$$\tilde{\mathbf{Z}}^{eq} = \tilde{\mathbf{Z}}^e \cdot [\bar{\epsilon} - \epsilon_c \bar{\mathbf{I}}] \quad (11)$$

The coupled set of IE's (9) and (10) can be solved using the method of moments (MoM). The conduction currents ($\bar{\mathbf{J}}_m$) on each wire can be expanded in overlapping piecewise sinusoidal (PWS) functions. The electric field in the dielectric region can be expanded as entire domain basis functions. A galerkin solution is implemented by testing each scalar IE with the appropriate function, leading to a matrix system. To determine natural frequencies, the impressed field term is set to zero and a numerical root search is performed to find the complex value of ω which forces the determinate of the impedance matrix to vanish.

B. Special Computational Considerations

Entire-domain basis functions are used to render the computational solution of (9) and (10) tractable. If the basis functions are carefully chosen, based upon mathematical and physical considerations, the numerical solution of the integral equation system can be made much more efficient than if the standard subdomain basis functions are used [17]. Entire-domain basis functions have been used in the solution of conducting wire and patch models, but generally have not been applied to the dielectric body problem. We have found in this work that the cavity-type entire-domain basis functions utilized here results in a small matrix size which is computationally efficient. The entire-domain scheme is also free of fictitious excess-charge within the problem domain, which can result from the utilization of sub-domain basis functions. Considering that

many mine shapes are well modeled by simple geometrical shapes that are amenable to the entire-domain approach, it is not surprising that this technique works very well for the buried mine problem considered here.

V. Results

The integral equation (7) for a dielectric region embedded in multilayered media was numerically solved using a set of entire-domain cavity modes. The cavity modes should be valid for expanding the electric fields for the cases $\epsilon/\epsilon_i > 1$ (PMC wall approximation) and $\epsilon/\epsilon_i < 1$ (PEC wall approximation). Results for rectangular regions and cylindrical regions have been obtained for each case, and results are being prepared for journal publication. Several examples will be included here to illustrate the accuracy and efficiency of the method. Fig. 3 shows a convergence plot for the complex resonant frequency of a rectangular dielectric region (39.5 x 23.0 x 13.5 cm). The dielectric inside the region has $\epsilon = 2.5\epsilon_0$, whereas the surrounding region has $\epsilon = 12.0\epsilon_0$. PEC modes were used for field expansion in a Galerkin solution. It can be seen that the resonant frequency converges very quickly with increasing the number of basis functions, resulting in efficient computation. Fig. 4 shows similar results for a PMC case, (7.45 x 7.45 x 2.98 cm) with the inner region characterized by $\epsilon = 79.46\epsilon_0$, whereas the surrounding region has $\epsilon = \epsilon_0$. Fig. 5 shows results for a cylindrical PMC resonator (radius 5.25 mm, height=4.6 mm, $\epsilon = 38\epsilon_0$) residing in air. Fig. 6 provides an indication of the accuracy of the method. A cylindrical resonator (radius=4.55 mm, height=4.04 mm, $\epsilon = 37.1\epsilon_0$) is positioned on a grounded dielectric layer of thickness h having $\epsilon = 2.22\epsilon_0$. Results are compared with another author's theoretical results (cross) and experimental results (triangle) [18]. Our method is seen to be in good agreement with measurements.

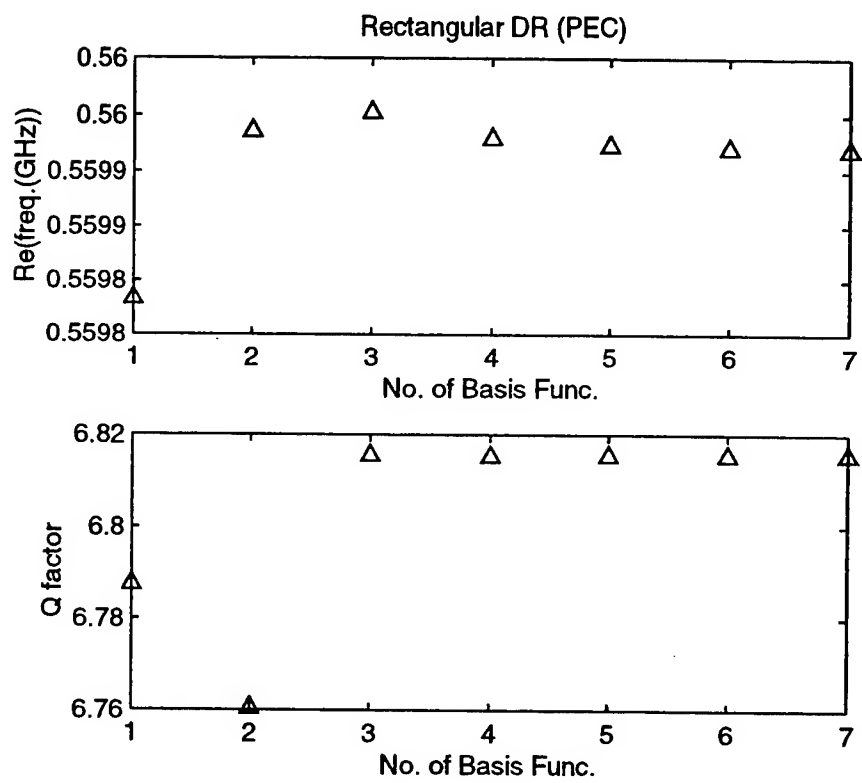


Fig. 3

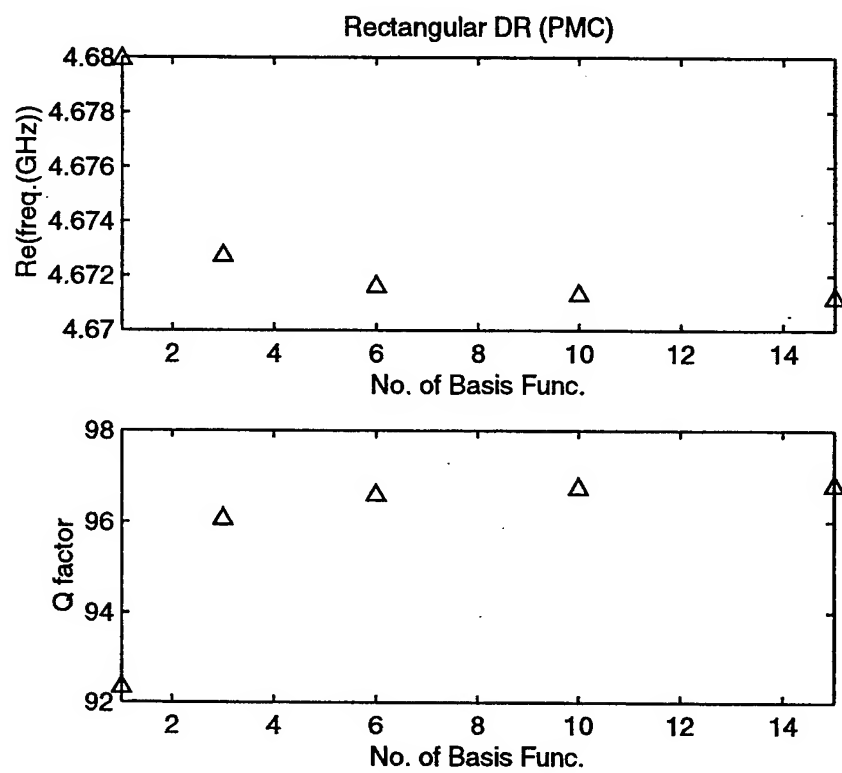


Fig. 4

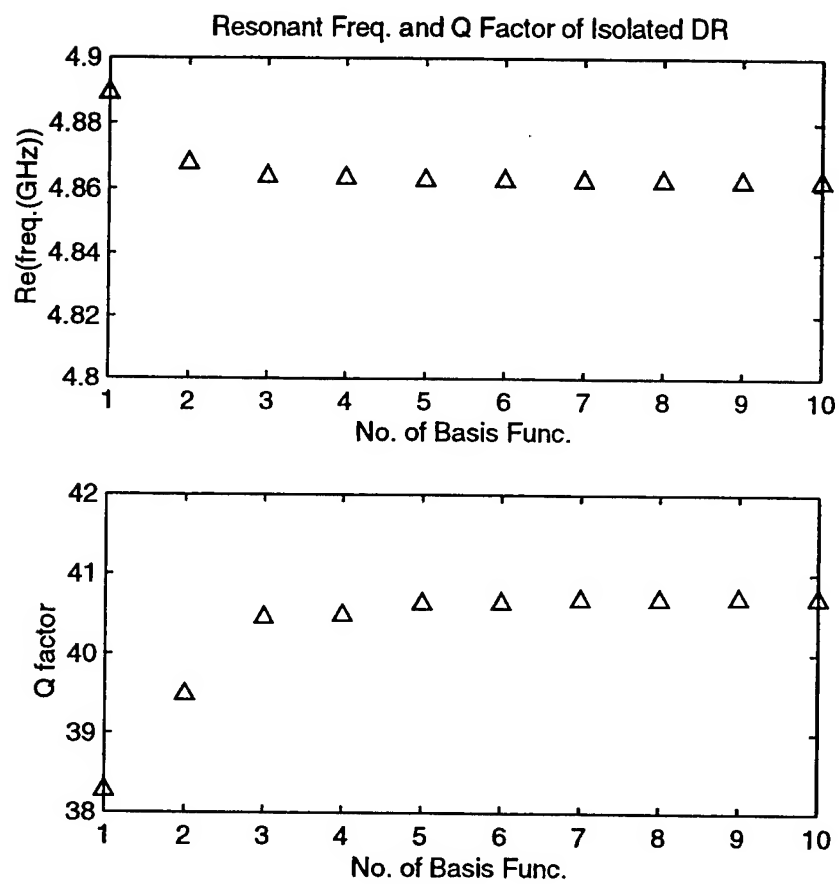


Fig. 5

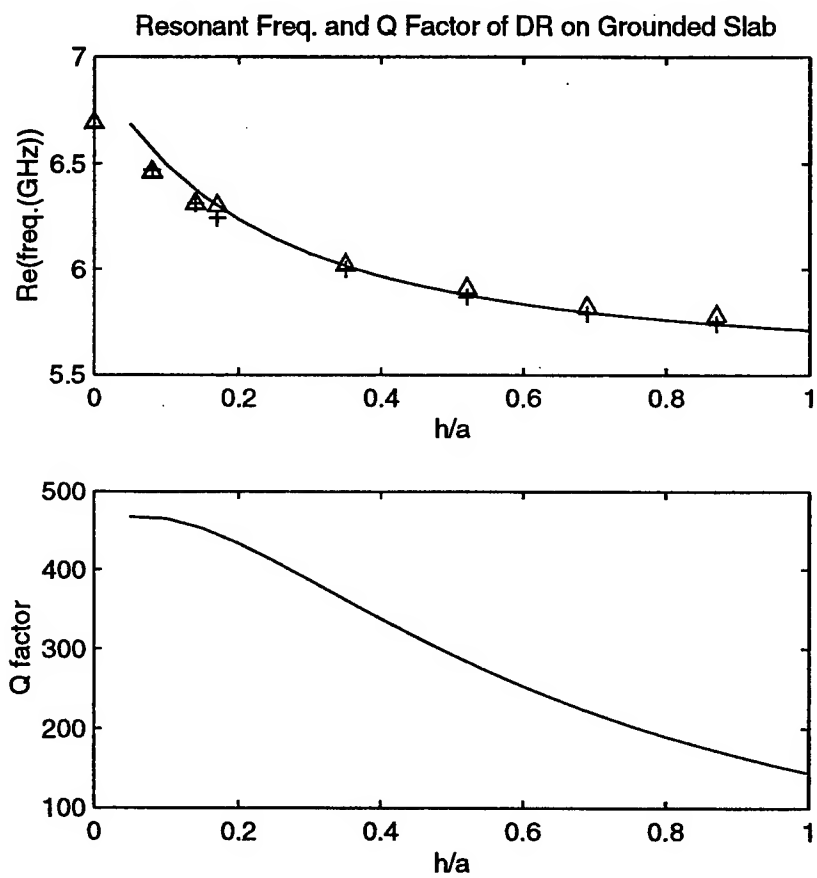


Fig. 6

VI. References

1. Military Munitions Working Group Final Report, *Western Governors Association*, June 1996.
2. Proceedings of *The Detection of Abandoned Land Mines*, Edinburgh, UK, Oct. 1996.
3. C. E. Baum, "Discrimination of Buried Targets Via the Singularity Expansion," Interaction Note 521, *Phillips Laboratory Note Series*, Kirtland AFB, Aug., 1996.
4. C. E. Baum, "Signature-Based Target Identification," Interaction Note 500, *Phillips Laboratory Note Series*, Kirtland AFB, Jan., 1994.
5. C. E. Baum, "Comparative System Response to Resonant and Unipolar Waveforms," Interaction Note 509, *Phillips Laboratory Note Series*, Kirtland AFB, Nov., 1994.
6. D. A. Hill, "Near-Field Detection of Buried Dielectric Objects," *IEEE Trans. Geosci. Remote Sensing.*, vol. 27, pp. 362-368, July 1989.
7. D. A. Hill, "Electromagnetic Scattering by Buried Objects of Low Contrast," *IEEE Trans. Geosci. Remote Sensing.*, vol. 26, pp. 195-203, March 1988.
8. J. Schneider, J. Brew, and I. Peden, "Electromagnetic Detection of Buried Dielectric Targets," *IEEE Trans. Geosci. Remote Sensing.*, vol. 29, pp. 555-562, July 1991.
9. G. A. Ellis and I. Peden, "An Analysis Technique for Buried Inhomogeneous Dielectric Objects in the Presence of an Air-Earth Interface," *IEEE Trans. Geosci. Remote Sensing.*, vol. 33, pp. 535-540, May 1995.
10. S. Vitebskiy and L. Carin, "Moment-Method Modeling of Short-Pulse Scattering from and the Resonances of a Wire Buried Inside a Lossy, Dispersive half-Space," *IEEE Trans. Antennas Propagat.*, vol. 43, pp. 1303-1312, Nov. 1995.
11. S. Vitebskiy, K. Sturgess, and L. Carin, "Short-Pulse Plane-Wave Scattering from Buried Perfectly Conducting Bodies of Revolution," *IEEE Trans. Antennas Propagat.*, vol. 44, pp. 143-151, Feb. 1996.
12. G.W. Hanson and C.E. Baum, "A Volumetric Eigenmode Expansion Method for Dielectric Bodies," Interaction Note 517, *Phillips Laboratory Note Series*, Kirtland AFB, Aug. 1996.
13. J. H. Richmond, "Scattering by a Dielectric Cylinder of Arbitrary Cross Section Shape," *IEEE Trans. Antennas Propagat.*, v. AP-13, pp. 334-341, March 1965.

14. G.W. Hanson, "Complex Media Microstrip Ridge Structures: Formulation and Basic Characteristics of Ferrite Structures," *IEEE Trans. Microwave Theory Tech.*, vol. 44, pp. 1563-1568, Sept. 1996.
15. G.W. Hanson, "Propagation Characteristics of a Microstrip Transmission Line on an Anisotropic Material Ridge," *IEEE Trans. Microwave Theory Tech.*, vol. 43, pp. 2608-2613, Nov. 1995.
16. R. F. Harrington, Time-Harmonic Electromagnetic Fields, McGraw-Hill, 1961.
17. D. I. Kaklamani and N. K. Uzunoglu, "Scattering from a Conductive Rectangular Plate Covered by a Thick Dielectric Layer and Excited from a Dipole Source or a Plane Wave," *IEEE Trans. Antennas Propagat.*, vol. 42, pp. 1065-1075, Aug. 1994.
18. R.K. Mongia, "Resonant Frequency of Cylindrical Dielectric Resonator Placed in an MIC Environment," *IEEE Trans. Microwave Theory Tech.*, vol. 38, pp. 802-804, June 1990.

STRATOSPHERIC STRUCTURE-FUNCTION
PARAMETERS FROM AIRCRAFT DATA

Mayer Humi
Professor
Department of Mathematical Sciences

Worcester Polytechnic Institute
100 Institute Road
Worcester, MA 01609

Final Report for:
Summer Extension Faculty Research Program
Phillips Laboratory

Sponsored by:
Air Force Office of Scientific Research
Bolling Air Force Base, DC

and

Phillips Laboratory

December, 1997

Stratospheric Structure-Function Parameters from Aircraft Data

Mayer Humi

Department of Mathematical Sciences

Worcester Polytechnic Institute

Worcester, MA 01609

December 19, 1997

Abstract

In this paper we present a model for the computation of the structure function parameters [1] and the local Richardson number [2] for stratospheric flow. Due to the nature of aircraft data available the model applies Boussinesq-Kolmogorov turbulence modeling hypothesis to recover the (vertical) gradients of the flow. We test the predictions of the model using the data collected by NASA during the 1989 AASE mission [3].

1 Introduction

For many practical applications it is useful to know the refractive index structure function [1, 4]

$$\overline{[n(\mathbf{x}, t) - n(\mathbf{x} + \mathbf{r}, t)]^2}$$

where $n(\mathbf{x})$ is the fluctuating refractive index. In the inertial range this structure function depends only on r and has the form $C_N^2 r^{2/3}$ (C_N^2 is referred to as the 'refractive structure function parameter'). In the absence of humidity (e.g. in the high stratosphere) the fluctuations in $n(\mathbf{x})$ are due to the fluctuations in the potential temperature Θ and $C_N^2 \sim C_T^2$ where C_T^2 is the structure function parameter for the potential temperature [1]. In the inertial range C_T^2 is related to the temperature spectra $\Phi_T(k)$ by

$$\Phi_T(k) = 0.25 C_T^2 k^{-5/3} = \beta \epsilon^{-1/3} \chi_\theta k^{-5/3} \quad (1.1)$$

where k is the wave number and ϵ, χ_θ are the molecular destruction rates of the turbulent kinetic energy and potential temperature, respectively..

Using the results obtained in [1] for the planetary boundary layer $\beta \sim 0.4$ and hence

$$C_T^2 = 1.6 \epsilon^{-1/3} \chi_\theta. \quad (1.2)$$

Following the model presented in [1] χ_θ and ϵ are related to the flow gradients and cospectra by the following relations

$$\chi_\theta = -2 \overline{\theta w} \frac{\partial \Theta}{\partial z} \quad (1.3)$$

$$\epsilon = -\overline{uw} \frac{\partial U}{\partial z} - \overline{vw} \frac{\partial V}{\partial z} + \frac{g}{T_0} \overline{\theta w} \quad (1.4)$$

(Upper case variables U, V, W represent components of the large scale flow and Θ the mean potential temperature. Lower case variables represent the fluctuating turbulent residuals of these quantities).

We observe that the average value of C_T^2 can be obtained from spectral analysis (using eq. (1.1)). However the 'local' values of C_T^2 (which depend on local averages as expounded in [1]) require the computation of χ_θ, ϵ and therefore the evaluation of the **vertical** gradients.

Similarly the Richardson number Ri which measures the stability of the geophysical flow against temperature stratification [2] is defined as

$$Ri = \frac{g}{\Theta} \frac{\partial \Theta}{\partial z} / \left[\left(\frac{\partial U}{\partial z} \right)^2 + \left(\frac{\partial V}{\partial z} \right)^2 \right] \quad (1.5)$$

and its computation also requires the **vertical** flow gradients.

In the past aircraft data collection missions to the stratosphere [3, 5, 6] used one meteorological probe. Accordingly they provide only the flow gradients along the horizontal flight path. Our objective in this paper is to present a model which surmount this difficulty and thus allows us to calculate the local values

of C_T^2 and Ri in the stratosphere. To this end the model utilizes the Boussinesq-Kolmogorov hypothesis [7] coupled with the Smagorinski model for the turbulent eddy viscosity [8].

To test this model against actual data we use the AASE 5 Hertz data which was collected by the 1989 NASA ER2 arctic mission [3, 9]. We note that this data set have several shortcomings (which we discuss at length in Section 3). Nevertheless we shall show that by using appropriate filtering techniques this data can be used at least as a "testing ground" for the model presented in this paper.

The plan of the paper is as follows: In Section 2 we present the model for the computation of the flow gradients and the local values of C_T^2 and Ri . In Section 3 we discuss the AASE data, its shortcomings and its decomposition (using the Karhunen-Loève (K-L) algorithm [8, 19]) into mean, wave and turbulent components. In particular we apply several tests to confirm that the "turbulent component" actually represents turbulence. Using these turbulent residuals we then compute C_T^2 and Ri along the flight path of the ER2.

2 Computation of the flow gradients

The statistical approach to turbulence modeling splits the flow variables $\tilde{\mathbf{U}}, \tilde{T}$ (where \tilde{T} is the temperature) into a sum

$$\tilde{\mathbf{U}} = \mathbf{U} + \mathbf{U}' + \mathbf{u}, \quad \tilde{T} = T + T' + t \quad (2.1)$$

where \mathbf{U}, T represent the mean (large scale) flow, \mathbf{U}', T' represent waves and \mathbf{u}, t "turbulent residuals" [16]. The turbulent residuals are then used to form the averaged Reynold's stress tensor

$$\bar{\tau}_{ij} = \overline{u_i u_j}. \quad (2.2)$$

(In the following we use (x, y, z) and (x_1, x_2, x_3) interchangeably to represent the spatial coordinates). Boussinesq-Kolmogorov (B-K) postulate [7] relates $\bar{\tau}_{ij}$ and $\overline{u_i t}$ to the gradients of the mean flow as follows:

$$\bar{\tau}_{ij} = \frac{1}{3} K \delta_{ij} - \nu_T \left(\frac{\partial U_i}{\partial x_j} + \frac{\partial U_j}{\partial x_i} \right) \quad (2.3)$$

$$\overline{u_i t} = -\kappa \frac{\partial T}{\partial x_i} \quad (2.4)$$

where

$$K = \bar{\tau}_{ii} = \tau_{11} + \tau_{22} + \tau_{33}. \quad (2.5)$$

In these equations κ is a constant and ν_T is the turbulent eddy viscosity.

From the data collected by an airplane flying along a "straight horizontal" line in the stratosphere (which we take as the x-axis) we can compute (after an appropriate decomposition of the data) $\frac{\partial U}{\partial x}, \frac{\partial V}{\partial x}, \frac{\partial W}{\partial x}, \frac{\partial T}{\partial x}$, the

six independent components of $\bar{\tau}_{ij}$ and $\overline{u_i t}$. Eqs (2.3), (2.4) and the continuity equation for incompressible flow

$$\frac{\partial U}{\partial x} + \frac{\partial V}{\partial y} + \frac{\partial W}{\partial z} = 0 \quad (2.6)$$

can be used then (at least in principle) to evaluate ν_T and the ("missing") gradients that are needed to compute C_T^2 and Ri

To see how this is done we first write eqs (2.3) explicitly;

$$\frac{1}{3}K - \bar{\tau}_{11} = 2\nu_T \left(\frac{\partial U}{\partial x} \right) \quad (2.7a)$$

$$\frac{1}{3}K - \bar{\tau}_{22} = 2\nu_T \left(\frac{\partial V}{\partial y} \right) \quad (2.7b)$$

$$\frac{1}{3}K - \bar{\tau}_{33} = 2\nu_T \left(\frac{\partial W}{\partial z} \right) \quad (2.7c)$$

$$\bar{\tau}_{12} = -\nu_T \left(\frac{\partial U}{\partial y} + \frac{\partial V}{\partial x} \right) \quad (2.7d)$$

$$\bar{\tau}_{13} = -\nu_T \left(\frac{\partial U}{\partial z} + \frac{\partial W}{\partial x} \right) \quad (2.7e)$$

$$\bar{\tau}_{23} = -\nu_T \left(\frac{\partial V}{\partial z} + \frac{\partial W}{\partial y} \right) \quad (2.7f)$$

observe that the averages referred to in these equations should be interpreted as **local** averages (in a "short window") around the point \mathbf{x} under consideration.

Since $\frac{\partial U}{\partial x}$ is known we can use (2.7a) to compute ν_T . Then from (2.7b), (2.7d), (2.7e) we compute $\frac{\partial V}{\partial y}$, $\frac{\partial U}{\partial y}$ and $\frac{\partial U}{\partial z}$. The continuity eq. (2.6) and eq. (2.7c) provide then two methods to compute $\frac{\partial W}{\partial z}$ and thus act as a check for the validity of B-K hypothesis for the flow under consideration.

Finally, eq. (2.7f) remains as one equation in two unknowns. To resolve this difficulty we shall assume that

$$\frac{\partial W}{\partial x} = \frac{\partial W}{\partial y} \quad (2.8)$$

(i.e. assume that the gradient of W in the x - y plane is isotropic) and this will allow us to compute an estimate for $\frac{\partial V}{\partial z}$. We note that this last quantity is utilized only in the last step of the computation of Ri .

As to the temperature gradients we use (2.4) to obtain

$$\frac{\partial T}{\partial z} = \frac{\overline{wt}}{\overline{ut}} \cdot \frac{\partial T}{\partial x} \quad (2.9)$$

The attempt to implement the algorithm described above numerically for actual geophysical flows yields however strong variations in the value of ν_T (and hence for the gradients). To overcome this difficulty we introduced a "more stable" numerical scheme to compute ν_T . This is accomplished by using Smagorinski eddy viscosity model [8] where

$$\nu_T = \ell^2 (2D_{ij}D_{ij})^{1/2}, \quad D_{ij} = \frac{1}{2} \left(\frac{\partial U_i}{\partial x_j} + \frac{\partial U_j}{\partial x_i} \right). \quad (2.10)$$

To motivate this choice we observe that aircraft measurements of a flow at fixed intervals can be considered as “large eddy measurements” as no information is available about the flow in between the grid points.

Eq. (2.10) has the advantage of utilizing all the components of $\bar{\tau}_{ij}$ in the computation of ν_T . In fact from eq. (2.3) we have

$$4\nu_T^2 D_{ij} D_{ij} = \sum_{i,j} \left(\frac{1}{3} K \delta_{ij} - \bar{\tau}_{ij} \right)^2. \quad (2.11)$$

Using (2.10) to eliminate $(D_{ij} D_{ij})$ in (2.11) leads then to

$$\nu_T^2 = \ell^2 \left[\sum_{i,j} \left(\frac{1}{3} K \delta_{ij} - \bar{\tau}_{ij} \right)^2 / 2 \right]^{1/2}. \quad (2.12)$$

In this equation ℓ is of the order of the “grid size” (i.e. interval between measurements) which introduces a parameter in the computation of ν_T . Using eq. (2.12) to compute ν_T we now have two ways to evaluate $\frac{\partial U}{\partial x}$, one directly from the data and the other from eq. (2.7a). Once again this can be used to verify the validity of the B-K hypothesis for the given data set.

Two strategies can be used now to compute C_T^2 . The first one is to follow Wyngaard-Kosovic model [1]. In this model

$$C_T^2 = \alpha \frac{\overline{w\theta^2}}{\tau \Lambda^{2/3}} \quad (2.13)$$

where τ is the local kinematic shear, Λ is the local Monin-Obukov length and α is a numerical parameter. (Based on PBL data α was set to 19 in [1]).

$$\tau = \overline{uw^2} + \overline{vw^2} \quad (2.14)$$

$$\Lambda = \frac{-\tau^{3/2}}{\beta(g/T)\bar{\theta}w} \quad (2.15)$$

(β is the Von-Karman constant). The only modifications we applied to this scheme for stratospheric flow is to redefine τ to contain all the strain components, i.e.

$$\tau^2 = \overline{uw^2} + \overline{vw^2} + \overline{uv^2}. \quad (2.16)$$

We also determined α so that the mean value of C_T^2 is equal to the value obtained from spectral estimates. ($\alpha \sim 0.1$).

It should be observed that in this scheme we do not utilize the flow gradients directly to compute C_T^2 . However the second algorithm to compute C_T^2 which is based on eqs. (1.2), (1.3), (1.4) requires these gradients.

As to the computation of Ri we use eqs. (1.5), (2.9) but note that

$$\frac{\partial \Theta}{\partial z} = \frac{\Theta}{T} \left(\frac{\partial T}{\partial z} + \frac{g}{C_P} \right). \quad (2.17)$$

In summary we presented here a model for the computation of C_T^2 and Ri from aircraft data. This model contains two parameters α and ℓ^2 .

3 A case study

Previous studies of the stratosphere and its structure parameters were conducted by many researchers e.g. Lilly et al [5], Woodman and Rastogi [13], Fakao et al [14] and Dewan [12].

In this section however we restrict ourselves to one case study where we apply the model described above to compute the local values of C_T^2 and Ri in the stratosphere. To this end we use the data collected by the ER2 flight on Feb. 9, 1989 during the AASE mission to the arctic. We note that the AASE data as well as that obtained from latter missions was analyzed recently by Bacmeister et al [9]. (This paper gives a detailed description of this data and also contains a lengthy list of references which we shall not duplicate here).

Two objections might be raised against the use of the AASE data in our context. First there are concerns about its accuracy especially for frequencies above 1 Hertz [15]. Second some previous studies [5] concluded that the outer scale of turbulence in the stratosphere must be of the order of 10-50m [5] while the resolvable scale in the AASE data is 80m.

Our answer to the first objection is that our results in this case study should be viewed as preliminary (and we can only hope that better data will improve our results). To overcome the second objection (at least partially) we shall apply the K-L decomposition [18, 19] to the data and demonstrate that this technique can be used to separate it into mean, wave and turbulent residuals. Several tests [10, 11] are then used to verify that the turbulent residuals so obtained actually represent turbulence in the stratosphere.

3.1 K-L decomposition

The K-L decomposition algorithm (or PCA) was used by many researchers (for a review see [19]). Here we shall give only a brief overview within our context.

Let be given a time series X (of length N) of some geophysical variable. We first determine a time delay τ for which the points in the series are decorrelated. Using τ we create n copies of the original series

$$X(k), X(k + \tau), \dots, X(k + (n - 1)\tau).$$

(To create these one uses either periodicity or choose to consider shorter time-series). Then one computes the auto-covariance matrix $R = (R_{ij})$

$$R_{ij} = \sum_{k=1}^N X(k + i\tau)X(k + j\tau). \quad (3.1)$$

Let $\lambda_0 > \lambda_1, \dots > \lambda_{n-1}$ be the eigenvalues of R with their corresponding eigenvectors

$$\phi^i = (\phi_0^i, \dots, \phi_{n-1}^i), \quad i = 0, \dots, n - 1.$$

The original time series T can be reconstructed then as

$$X(j) = \sum_{k=0}^{n-1} a_k(j) \phi_0^k \quad (3.2)$$

where

$$a_k(j) = \frac{1}{n} \sum_{i=0}^{n-1} X(j+i\tau) \phi_i^k. \quad (3.3)$$

The essence of the K-L decomposition is based on the recognition that if a large spectral gap exists after the first m_1 eigenvalues of R then one can reconstruct the mean flow (or the large component) of the data by using only the first m_1 eigenfunctions in (3.2). A recent refinement of this procedure due to Ghil et al [18] is that the data corresponding to eigenvalues between $m_1 + 1$ and up to the point m_2 where they start to form a “continuum” represent waves.

Thus the original data can be decomposed into mean flow, waves and residuals (i.e. data corresponding to eigenvalues $m_2 + 1, \dots, n - 1$ which we wish to interpret at least partly as turbulent residuals).

For the data under consideration we carried out this decomposition using a delay τ of 1024 points (approximately 40km separation) for all the geophysical variables. The resulting eigenvalues and data decomposition for the temperature is presented in Figs. 1-4. Figs. 5,6 present the Fourier transform of the wave and turbulent components. In this decomposition $n = 96$, $m_1 = 6$ and $m_2 = 14$. Similar decompositions were carried out for the components of the velocity field (and they confirm the validity of B-K hypothesis for stratospheric flow).

3.2 The interpretation of the residuals

The residuals of the time series which are reconstructed as

$$X^r(j) = \sum_{k=m_2+1}^{n-1} a_k(j) \phi_0^k$$

contain (obviously) the measurement errors in the data. However we shall show that primarily they should be interpreted as representing turbulence. To this end we utilize the tests devised by Axford [10] and Dewan [11]. According to these tests turbulence data is characterized by low coherence between u, v, w and a phase close to zero or π between w and θ . (A phase close to $\pi/2$ is characteristic of waves). Figs. 7,8,9 demonstrate that the coherence between the residuals of u, v, w is less than 0.1. Fig. 10 gives a scatter plot of the phase between w and θ . This figure is less definitive as there are still quite a few points in the wave sector ($\pi/4, \frac{3\pi}{4}$). However out of the 150 points in this plot 105 are in the “turbulence sector”.

These tests show that to a large extent the residuals that were obtained from the K-L decomposition represent actual 3-D turbulence.

3.3 Computation of C_T^2, Ri

Using the residuals obtained above and by applying the algorithm described in Section 2 we can now compute C_T^2 and Ri along the flight path of the ER2. The results are shown in Figs. 11,12. It is evident from these figures that there exist large local variations in the values of C_T^2 and Ri in the stratosphere. These variations

are totally masked when an averaged value for these parameters is computed from the whole time-series. (These averaged values are $C_T^2 = 0.3 \cdot 10^{-4}$, $Ri = 0.14$). These results confirm previous studies [12, 17] which suggested that the flow in the stratosphere is strongly stably stratified with intermittent thin patches of 3-D turbulence.

Acknowledgement

The author is deeply indebted to O. Coté for many conversations and guidance. Part of this research was carried out while the author was in residence at Phillips Labs (Hanscom AFB).

References

- [1] Wyngaard, J. and Kosovic, B. - 1994, Similarity of structure function parameters in the stably stratified boundary layer, *Boundary Layer, Mer.* **71** p. 277-296.
- [2] Dutton, J. and Panofsky, H. - 1970, Clear air turbulence, *Science* **167** p. 937-943.
- [3] Chan, K.R., Bowen, S.W., Bui, T.P., Scott, S.G. and Day, J. Dean -1990, Temperature and wind measurements and model atmospheres of 1989, Airborne Arctic Stratospheric Experiment, *Geophys. Res. Lett.* **17**, p. 341-344.
- [4] Tatarskii, V. - 1967, Wave propagation in turbulent medium (Dover, NY).
- [5] Lilly, D.K., Waco, D.E. and Adelfang, S-I - 1974, Stratospheric mixing estimated from high altitude turbulence measurements, *J. Appl. Meteor.*, **13**, p. 488-493.
- [6] Hocking, W.K. - 1985, Measurement of turbulent energy dissipation rates in the middle atmosphere by radar techniques: A review *Radio Sci.* **20**, p. 1403-1422.
- [7] Warsi, Z.U.A., - 1992, Fluid Dynamics (CRC Press, Florida).
- [8] Smagorinski, J. - 1983, General circulation experiments with primitive equations, *Mon. Weather Rev.* **91**, p. 91-164.
- [9] Bachmeister, J.T. et al - 1996, Stratospheric horizontal wave number spectra of winds, potential temperature and atmospheric tracers observed by high altitude aircraft, *J. Geophys. Res.* **101**, p. 9441-9470.
- [10] Axford, D.N. - 1971, Spectral analysis of aircraft observation of gravity waves, *Q.J. Royal Met. Soc.* **97**, p. 313-321.

- [11] Dewan, E.M. - 1985, On the nature of atmospheric waves and turbulence, *Radio Sci.* **20**, p. 1301-1307.
- [12] Dewan, E.M. - 1981, Turbulent vertical transport due to thin intermittent mixing layers in the stratosphere and other stable fluids, *Science* **211**, p. 1041-1042.
- [13] Woodman, R.F. and Rastogi, P.R. - 1984, Evaluation of effective eddy diffusion coefficients using radar observations of turbulence in the stratosphere, *Geophys. Res. Lett.*, **11**, p. 243-246.
- [14] Faukao, S. et. al. - 1994, Seasonal variability of vertical eddy diffusivity in the middle atmosphere, *J. Geophys. Res.* **99**, p. 18973-18987.
- [15] Murphy, D.M. - 1989, Time offsets and power spectra of the ER-2 data set from the 1987 Airborne Antarctic ozone experiment, *J. Geophys. Res.* **94**, p. 16737-16748.
- [16] Einaudi, F. and Finnigan, J.J. - 1993, Wave turbulence dynamics in stably stratified boundary layer, *J. Atmos. Sci.* **50**, p. 1841-1864.
- [17] Sidi, C. - 1993, Wave-turbulence coupling, *Proc. Nato Adv., Res Workshop*, Leon, Norway, May 25-30, 1992, ed. E.V. Thrane, T.A. Blix and D.C. Fritts, Dordrecht, Kluwer Academic Publishers., p. 291-304.
- [18] Ghil, M. and Taricco, C. - 1997, Advanced spectral analysis methods, In G. Cini Castagnoli and A. Provenzale (eds.), *Past and Present Variability of the Solar-Terrestrial System: Measurement, Data Analysis and Theoretical Models*, Societ Italiana di Fisica, Bologna, & IOS Press.
- [19] Penland, C., Ghil, M. and Weickmann, K.M. - 1991, Adaptive filtering and maximum entropy spectra, with application to changes in atmospheric angular momentum, *J. Geophys. Res.*, **96**, p. 22659-22671.

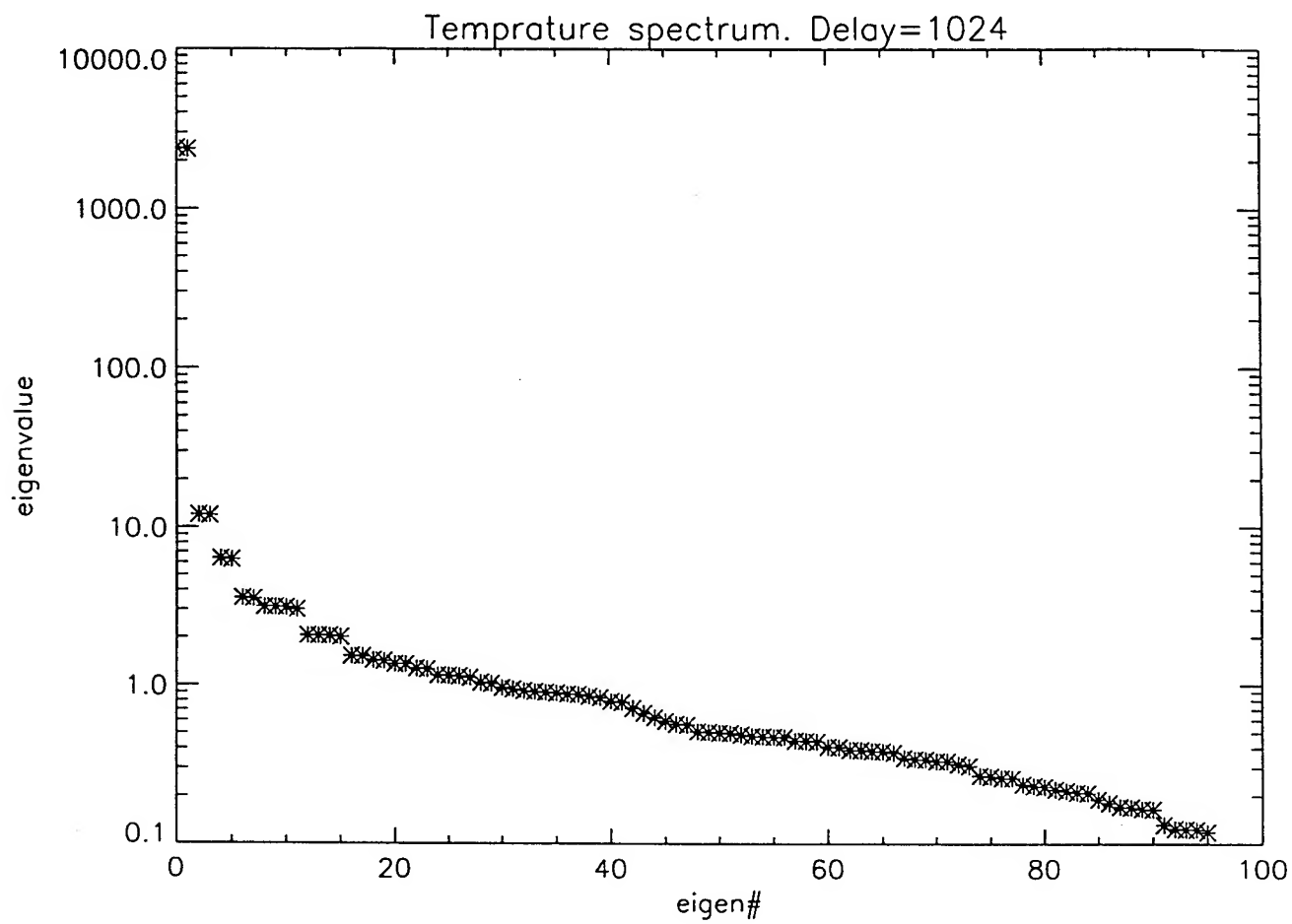


Fig. 1

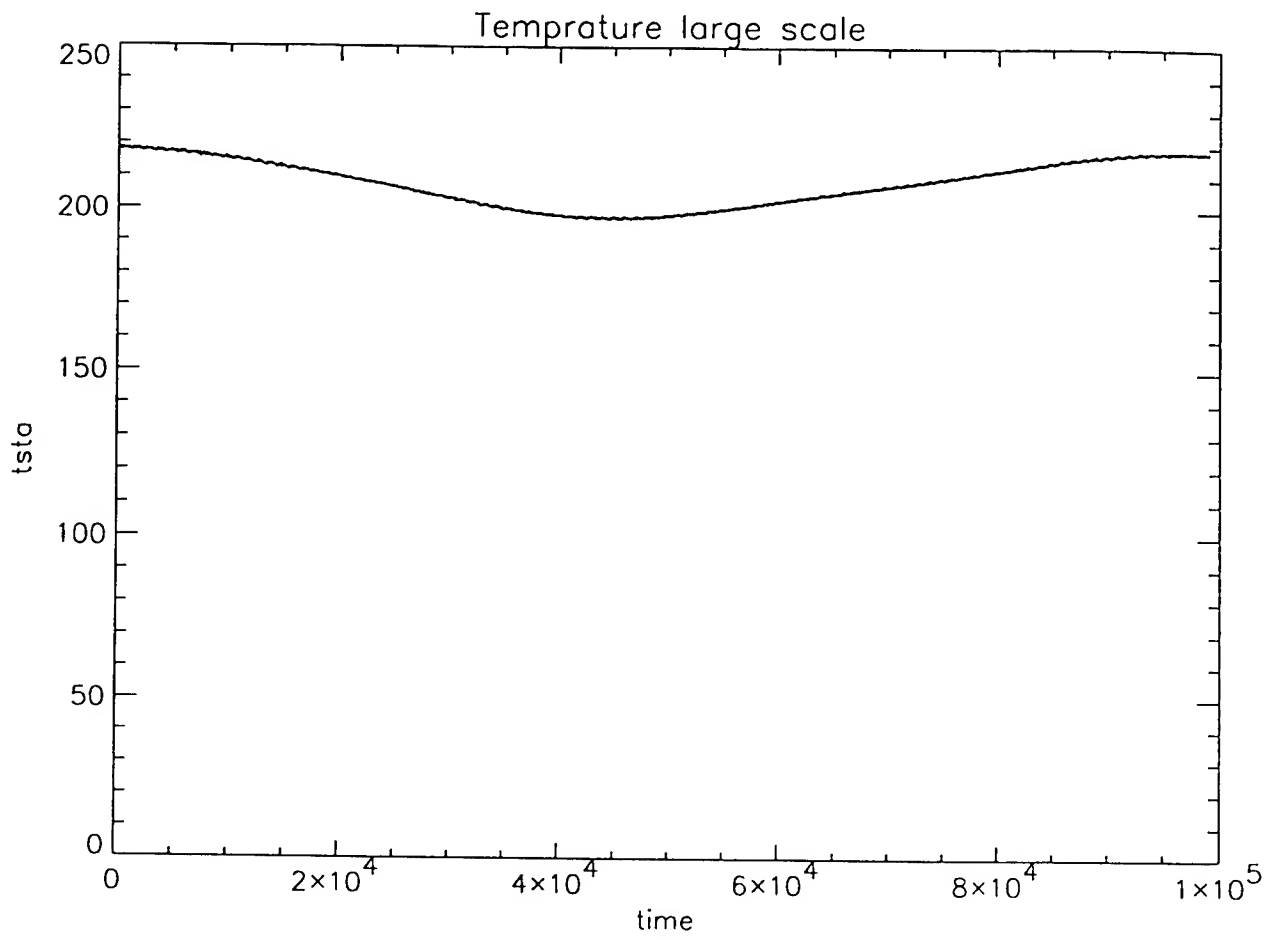


Fig. 2

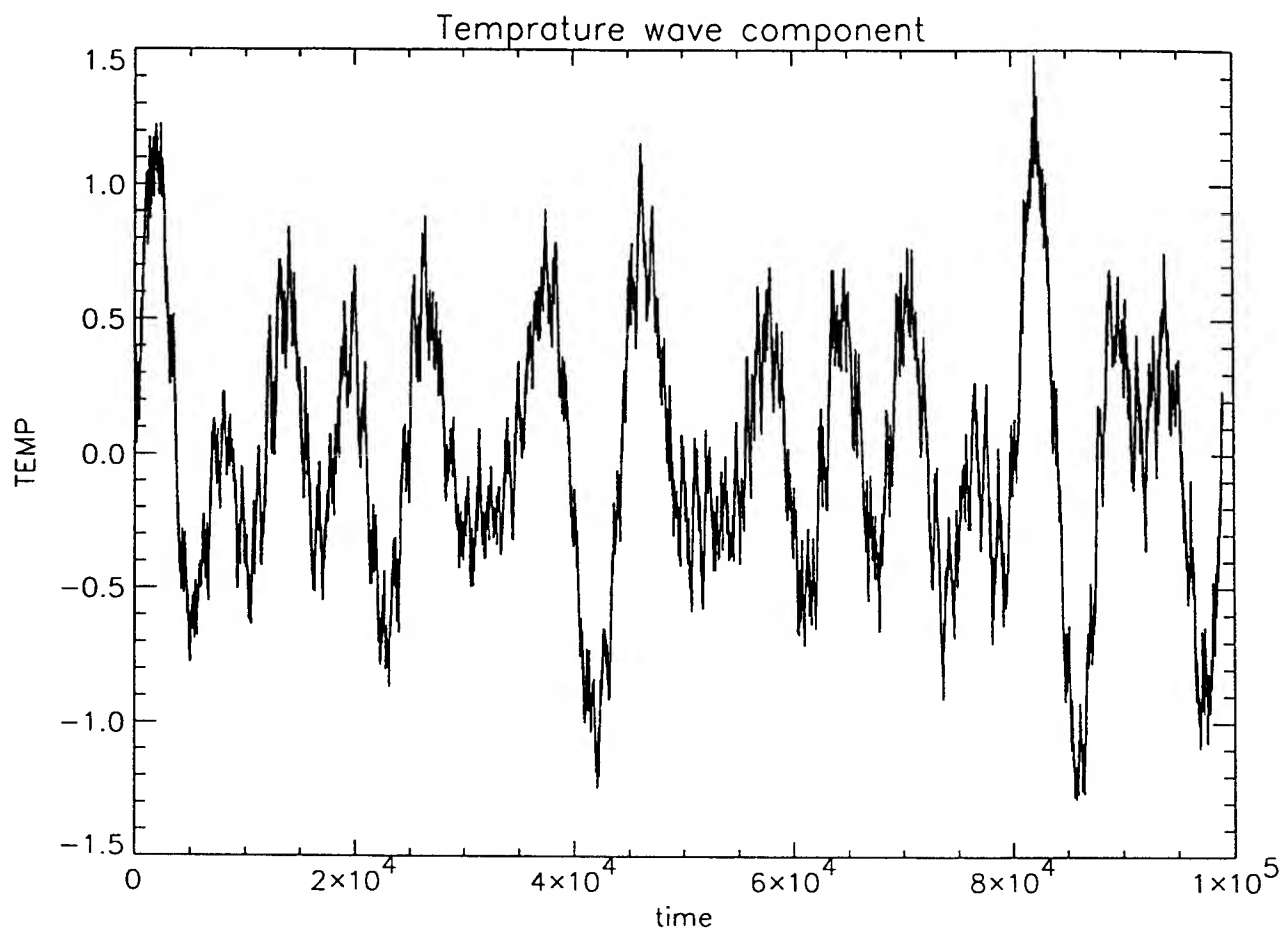


Fig. 3

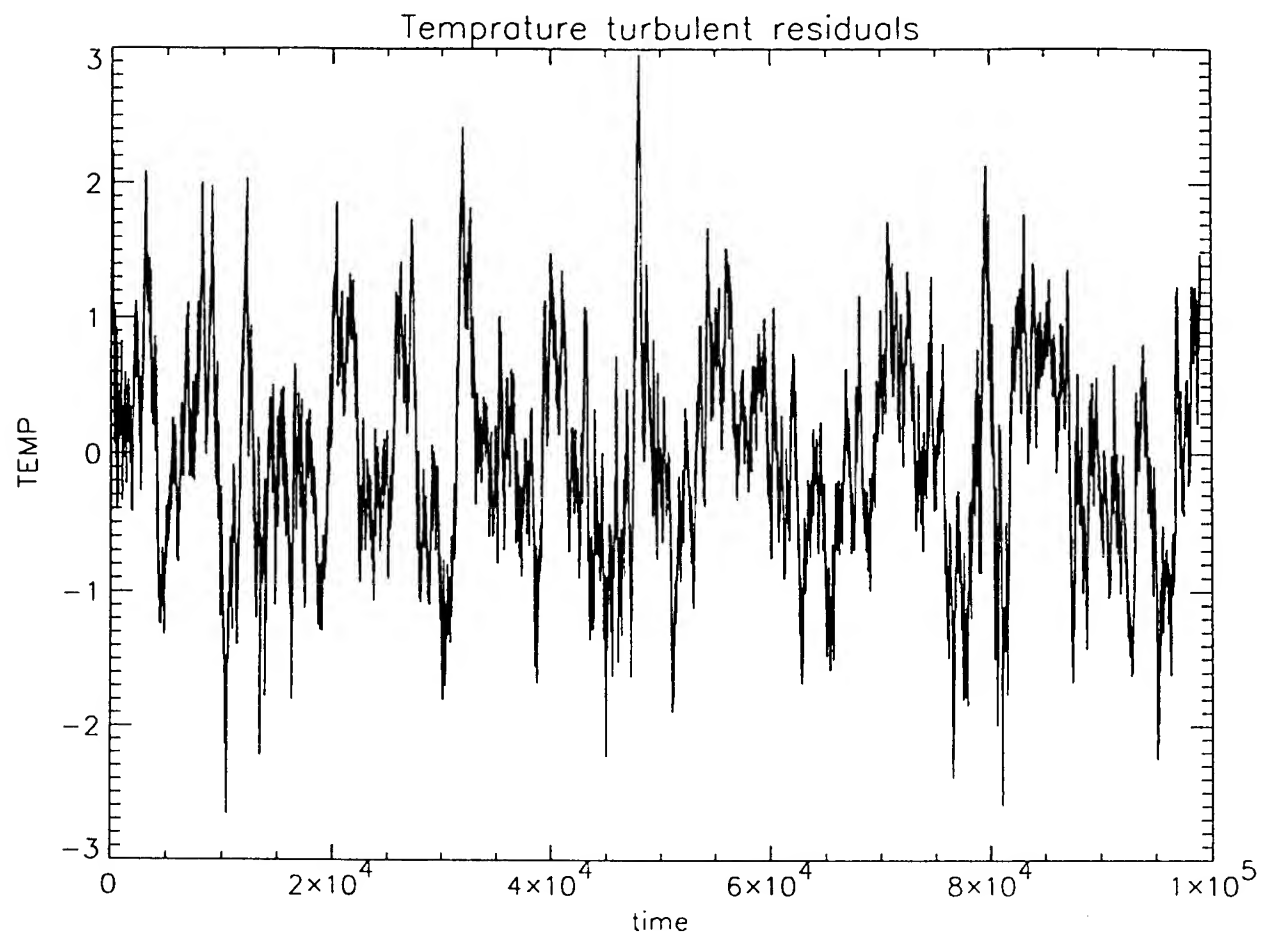


Fig. 4

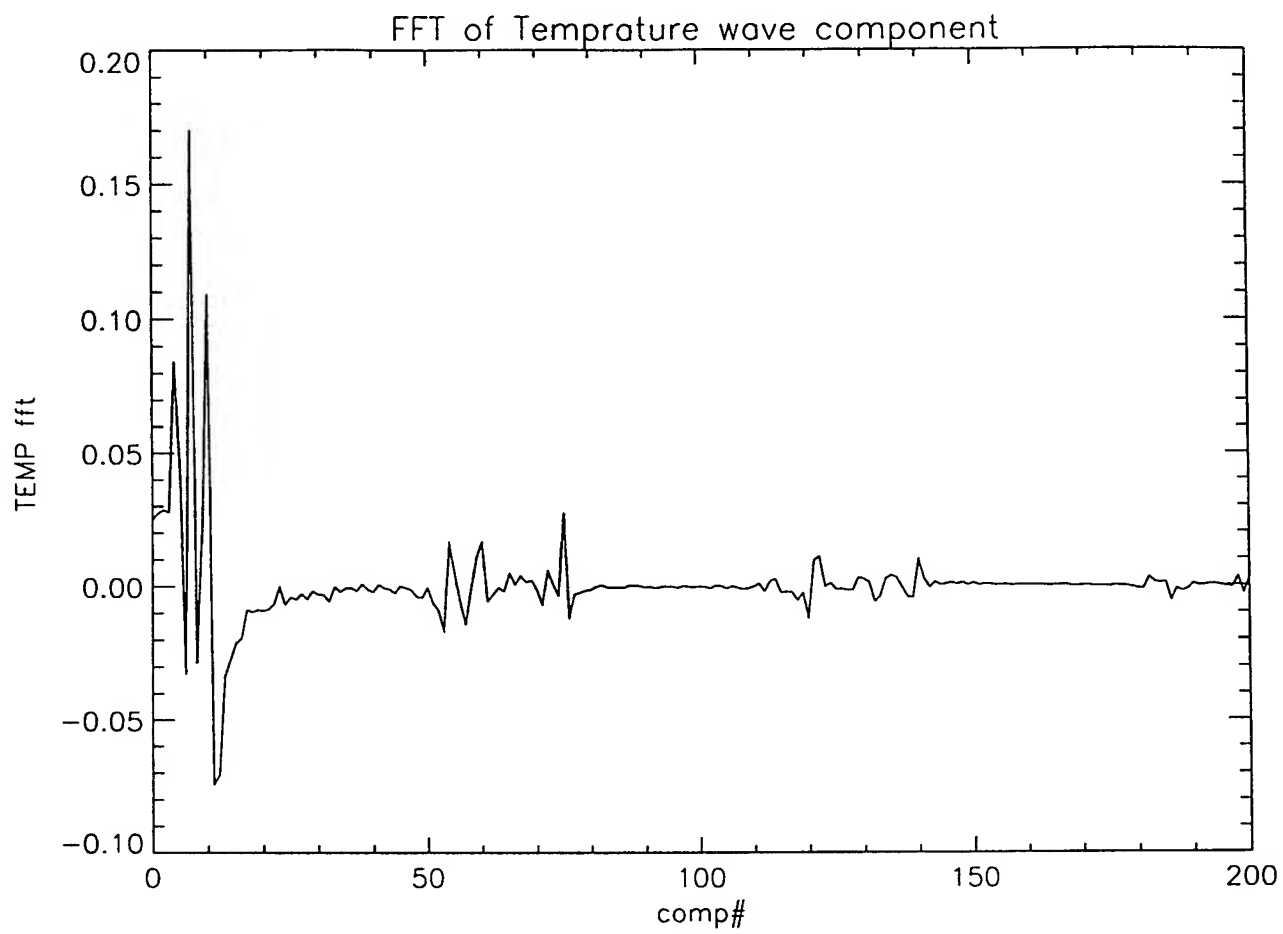


Fig. 5

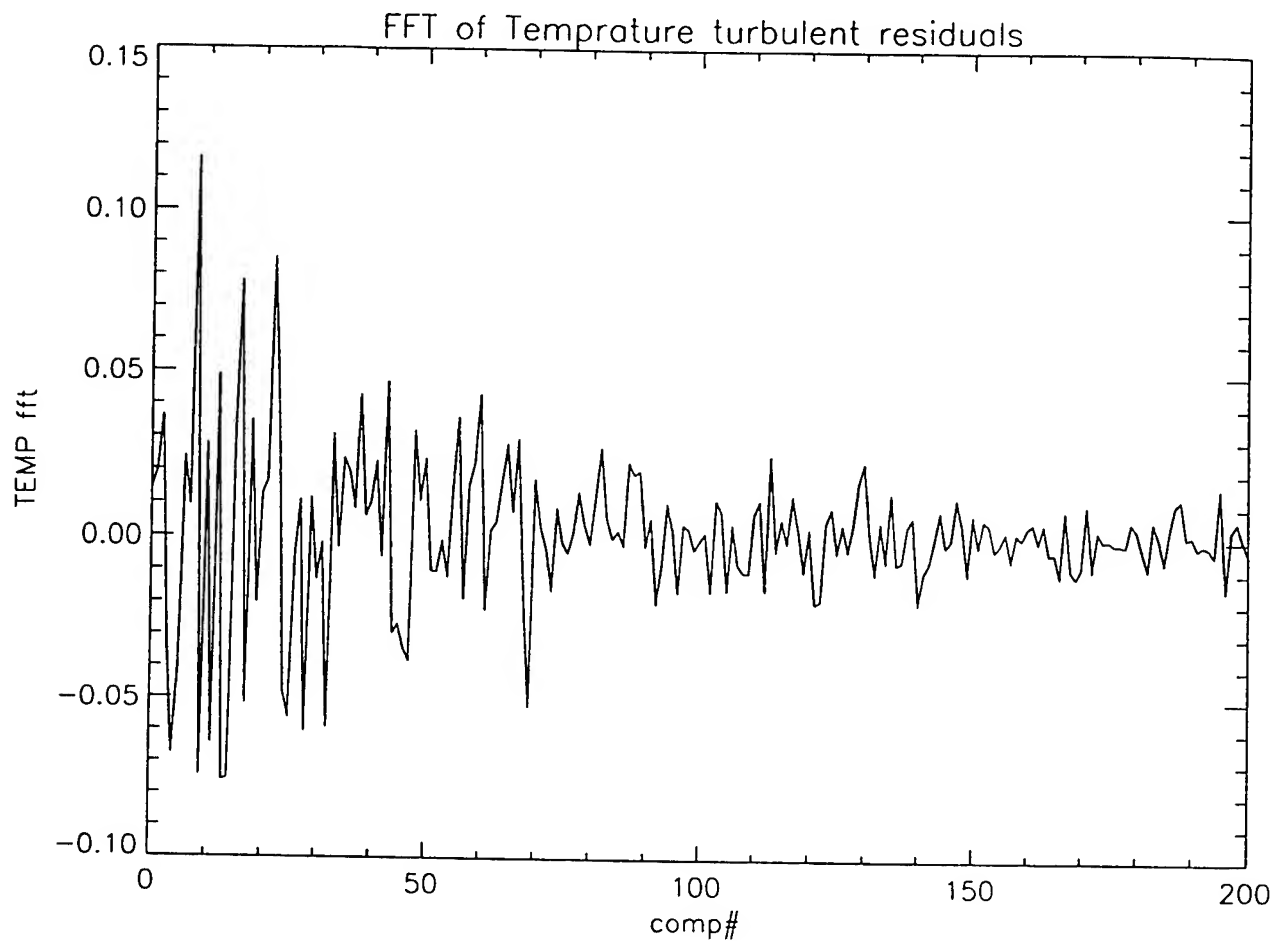


Fig. 6

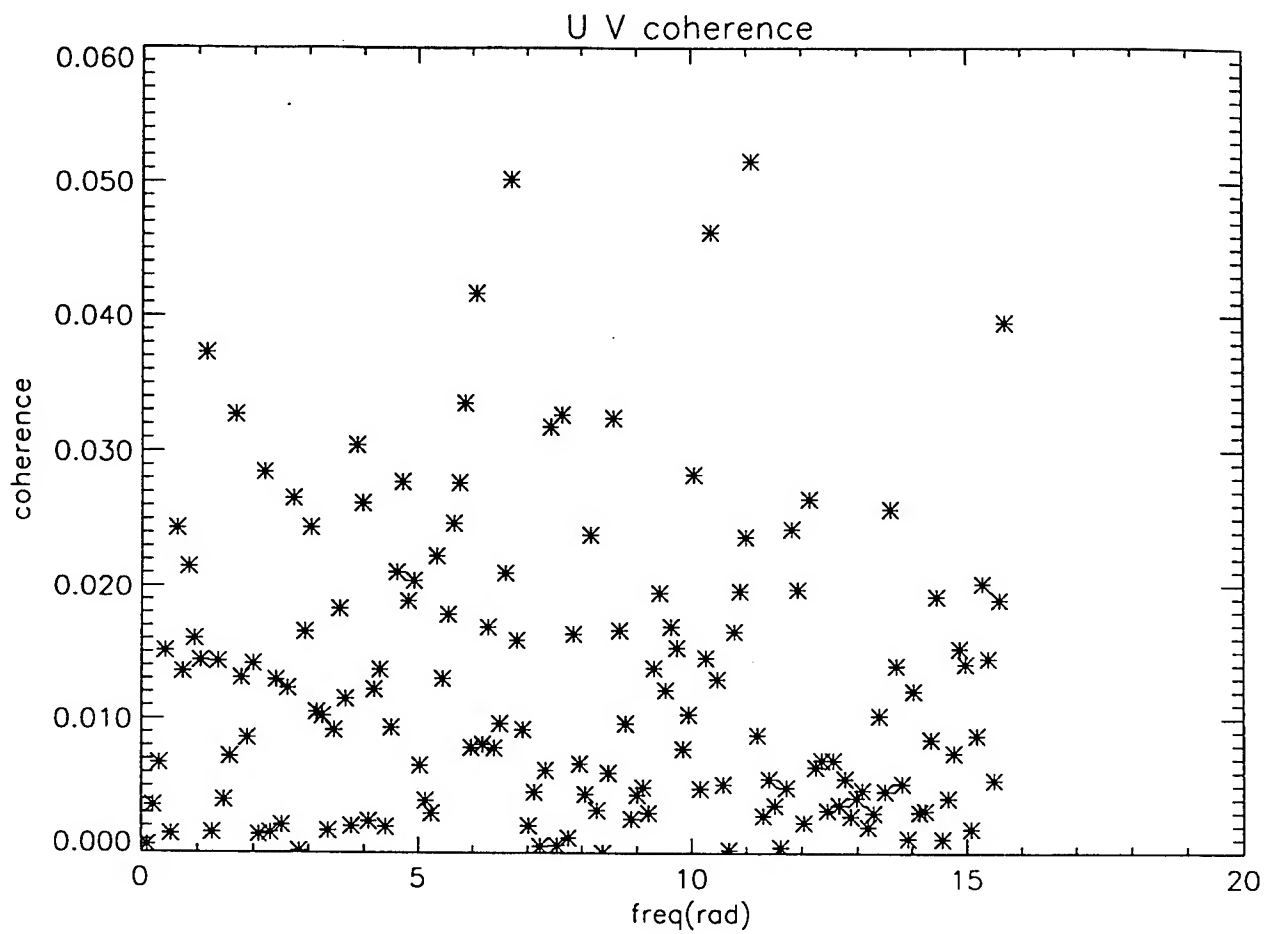


Fig. 7

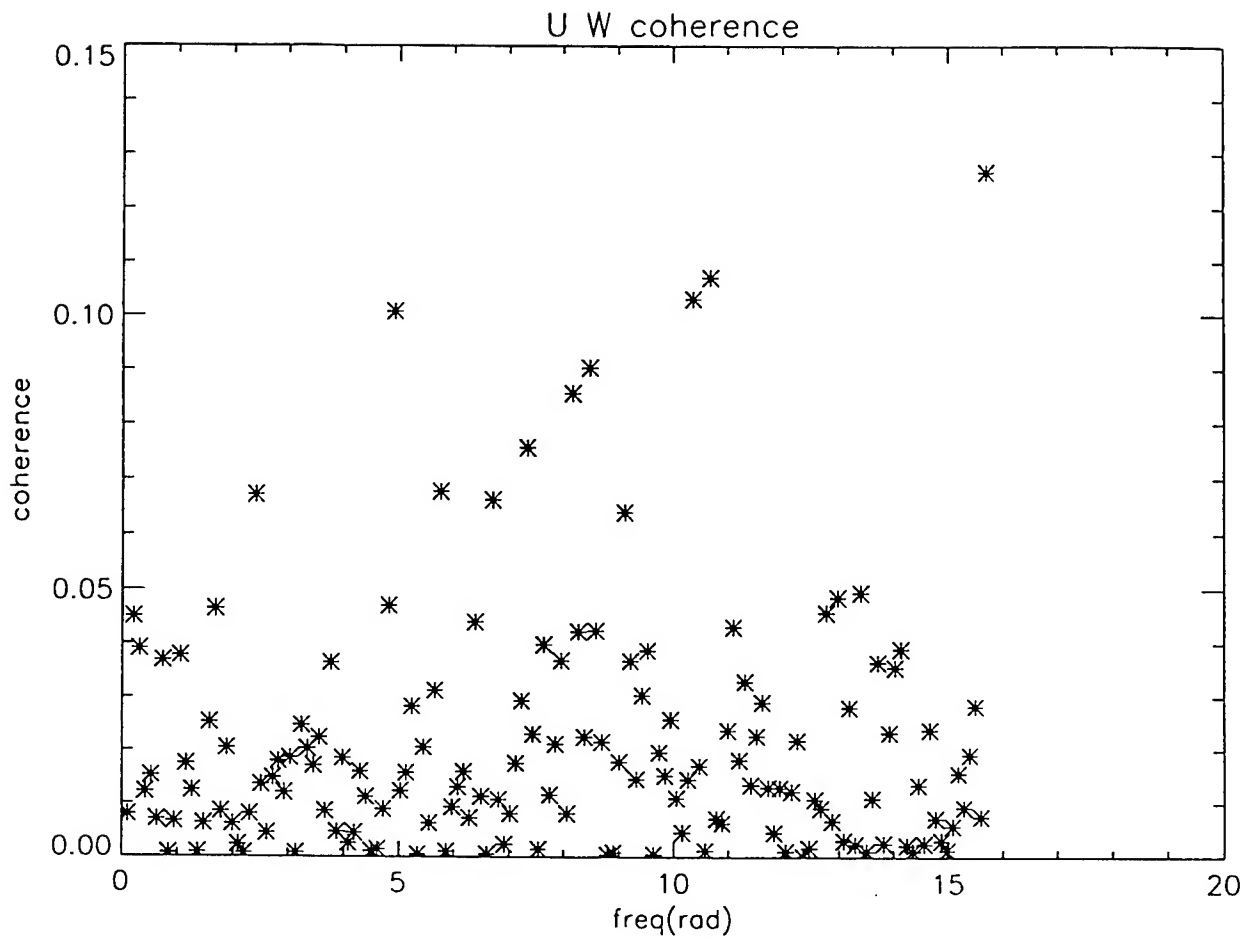


Fig. 8

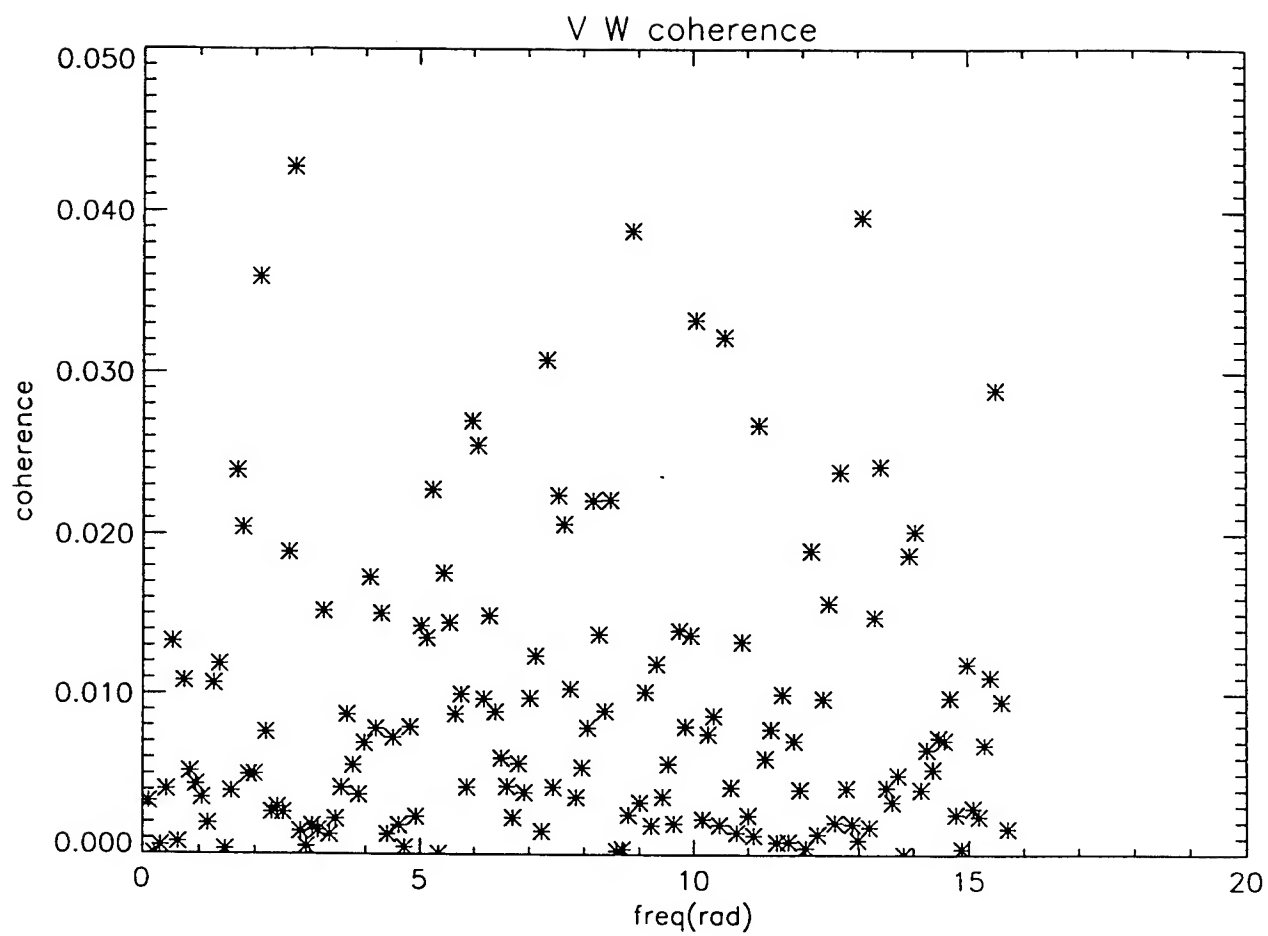


Fig. 9

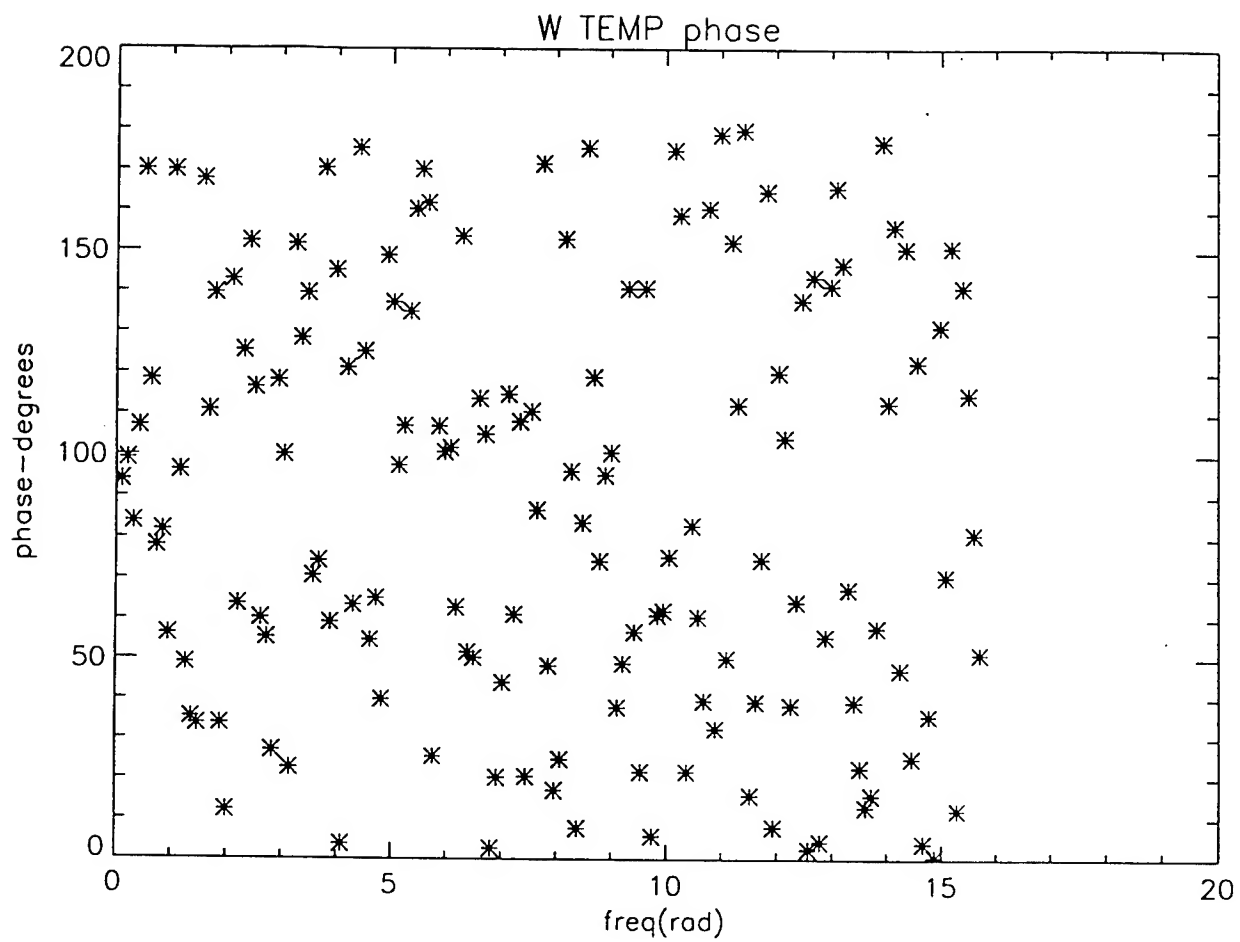


Fig. 10

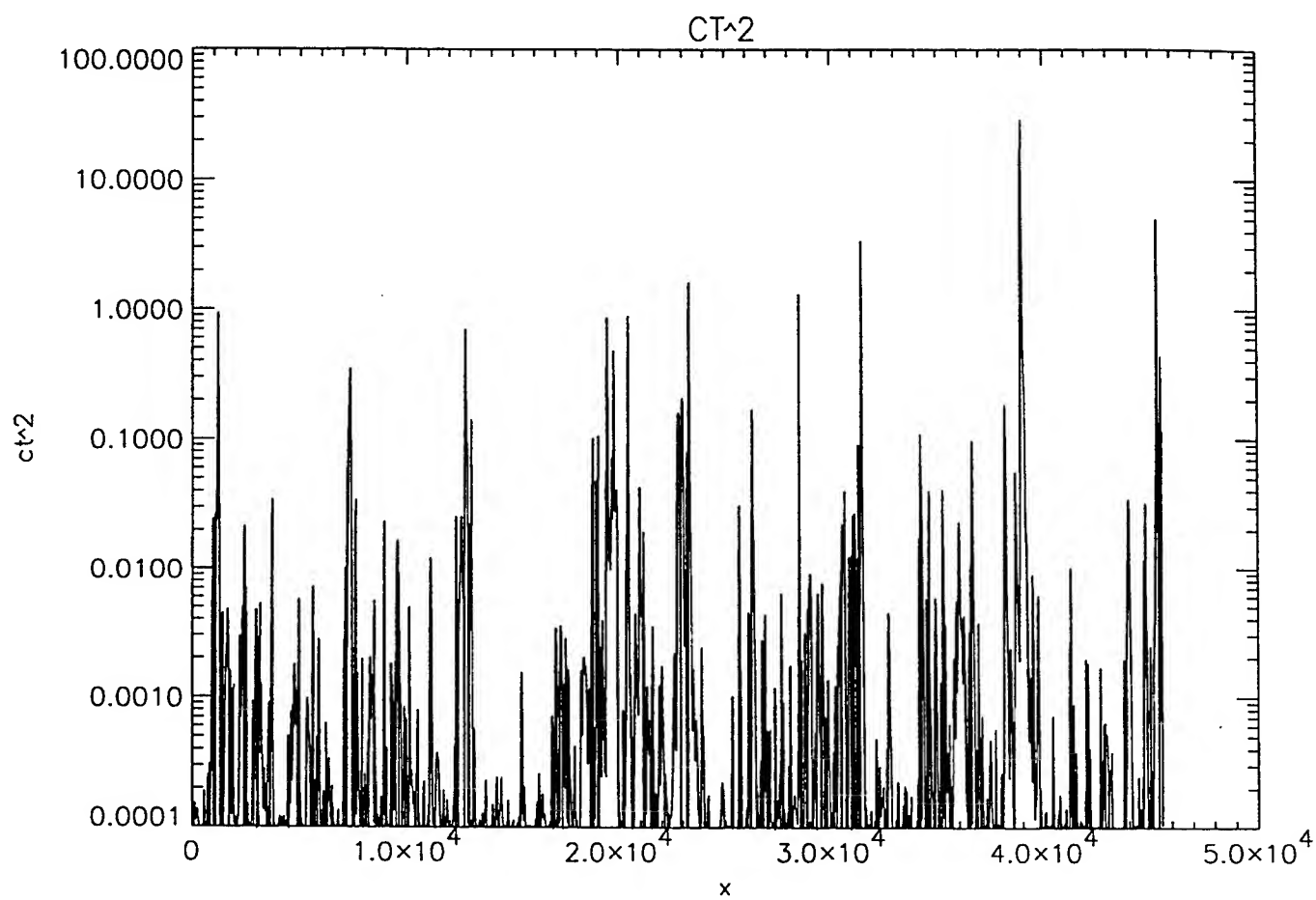


Fig. 11

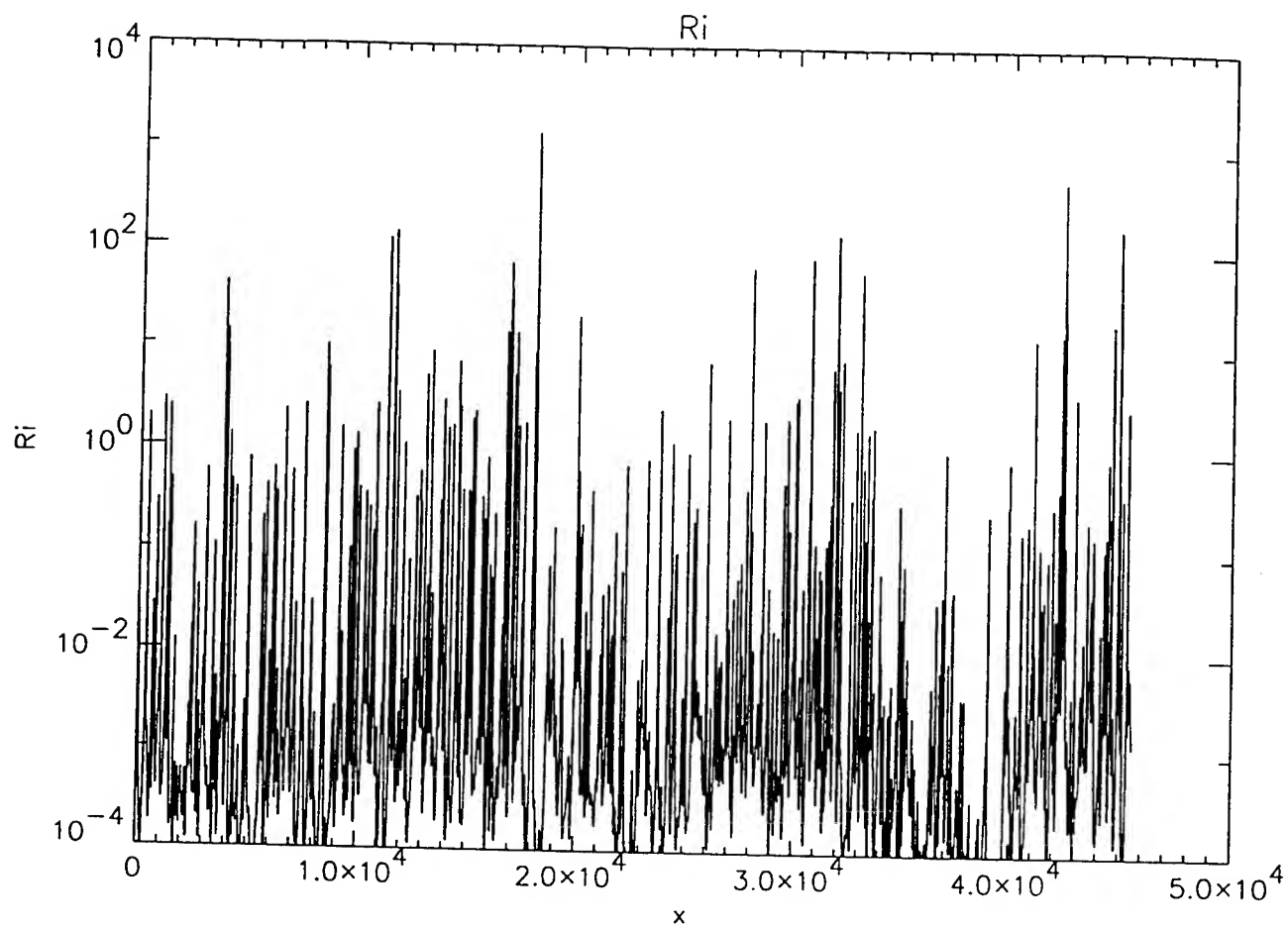


Fig. 12

SHAPE CONTROL OF AN
INFLATED THIN CIRCULAR DISK:
Experimental Investigation

C. H. M. Jenkins, Ph.D., P.E.
Associate Professor
Mechanical Engineering Department

South Dakota School of Mines and Technology
Rapid City, SD 57701

Final Report for:
Summer Faculty Research Program
Phillips Laboratory

Sponsored by:
Air Force Office of Scientific Research
Bolling Air Force Base, DC

and

Phillips Laboratory

December 1997

SHAPE CONTROL OF AN INFLATED THIN CIRCULAR DISK:
Experimental Investigation

C. H. M. Jenkins, Ph.D., P.E.
Associate Professor
Mechanical Engineering Department
South Dakota School of Mines and Technology

Abstract

Space-based inflatable technology is of current interest to NASA and DOD, and in particular to the Air Force and Phillips Laboratory. Potentially large gains in lower launch costs, through reductions in structure mass and volume, are driving this activity. Diverse groups are researching and developing this technology for radio and radar antennae, optical telescopes, and solar power and propulsion applications. Regardless of the use, one common requirement for successful application is the accuracy of the inflated surface shape. The work reported here concerns a preliminary nonlinear finite element and experimental analysis of shape control of an inflated thin circular disk. Shape modification was achieved through enforced boundary displacements, which resulted in moving the inflated shape towards a desired parabolic profile. Conclusions and recommendations are provided.

SHAPE CONTROL OF AN INFLATED THIN CIRCULAR DISK: Experimental Investigation

Christopher H. M. Jenkins

1. INTRODUCTION

There currently exists renewed interest in applications of inflatable structures in space. With increased pressure to reduce costs associated with design, fabrication, and launch of space structures, DOD and NASA are taking a new look at space-based inflatable structures. Applications for inflatable structures in space include lunar and planetary habitat, RF reflectors and waveguides, optical and IR imaging, solar concentrators for solar power and propulsion, sun shades, and solar sails [see, e.g., Grossman and Williams, 1990; Cassapakis and Thomas, 1995].

For many of these applications, particularly those involved with communications, imaging, power, and propulsion, accurate maintenance of the inflatable surface shape is critical. Surface accuracy ranges from a few percent of wavelength for low frequency applications, to a fraction of a percent of wavelength for visual wavelengths [see Hedgepeth, 1982]. The likelihood of achieving such tolerances by purely passive means is small.

For example, the AF Phillips Laboratory has recently undertaken the task of creating a large optical quality membrane telescope. The membranes on these telescopes will range in thickness from 10 - 150 micrometers. The maximum acceptable peak-to-peak figure error over the entire surface will range from 10 - 20 micrometers. (This value assumes that a certain amount of secondary adaptive optics will be used to correct image errors.) Passive and active means for reducing the figure error are under investigation.

In what follows, background information on highly compliant structures and their analysis is first given. Then we review the problem of the inflation of an initially plane, circular membrane, with deformations limited to those that admit only small strains but moderately large rotations. (We purposefully exclude here any consideration of the associated problems of the inflation of annular membranes or circular plates, or of large strain deformation; see Jenkins and Leonard [1991], and Jenkins [1996a] for additional details on these topics.) Next we discuss the use of finite element analysis to demonstrate the effects of boundary (rim) control on the deformed

shape of an inflated circular membrane. Experimental work is then described which correlates with the FEM analysis. Results are presented, and finally conclusions are provided.

Background

Structures formed from thin-walled material can be found in a diverse array of applications, from biological organisms to architectural structures to aerospace craft. Depending on the degree of bending resistance inherent in such structures, as well as the degree of participation of in-plane and bending reactions to loads, for certain analytical purposes they may be modeled successfully as membranes, whose unique feature is the absence of any resistance to bending.

For structures whose bending resistance is very small indeed (and we take here as fundamental that all real structures have some finite bending resistance, no matter how small), compressive stresses result in a localized buckling or wrinkling. Hence, a further modeling restriction can be made that limits the membrane to allowable stresses greater than zero only, i.e., a no-compression membrane. The structure is then modeled as carrying loads only in tension or in tension fields [see Jenkins and Leonard, 1991; Jenkins, 1996a].

Finite element methods have made significant contributions to the analysis of large deformation, nonlinear structural problems. Yet the analysis of membrane structures that undergo large displacements during loading remains a difficult problem for which current finite element methods are unsuitable. The primary difficulties lie in the fact that the structural system is underconstrained, and stable equilibrium conditions only exist for loading fields that are orthogonal to the set of unconstrained degrees of freedom (see Kuznetsov, 1991). Furthermore, configurations exist that are not in the vicinity of such an equilibrium state. Consequently, large rigid body motions with concomitant, large configuration changes, must take place before elastic response is obtained.

A class of pneumatic envelopes provides dramatic examples of underconstrained systems: the stowed versus deployed configurations in air bags, balloons, parachutes, or reflectors. There are several difficult aspects of the analysis of pneumatic envelopes. First of all, while structural stiffness is provided by structural components such as the skin, and any reinforcing elements such as cables or tapes, this stiffness can only be engaged in specific loaded configurations, and the

stability of the structural system only exists under such loading. The structural system is thus said to be underconstrained.

Furthermore, the unloaded configuration may be far from any static equilibrium condition in solution space. Constraints are usually unilateral so that a structurally impossible state is obtained under a reversal of the load from an equilibrium state.

Even in a loaded configuration, the structural function of the skin may degenerate from a state of bi-axial tension, for which the membrane model is appropriate, to a state of uni-axial tension (since compression cannot be accommodated by thin films or cables). Under this latter condition the skin will wrinkle. This condition may be appropriately modeled by a tension field model which ignores the detail of the wrinkling but properly models the structural performance of the skin [Jenkins and Leonard, 1993]. Experimental verification is a challenge under such conditions, since any contact with the structure readily disturbs that which was to be measured [Jenkins, 1995; Jenkins, et al., 1995; Jenkins, 1996b].

2. MECHANICS OF INFLATED MEMBRANES

The problem of the inflation of an initially plane membrane with circular boundary begins with Hencky [1915]. Earlier, Föppl [1907] had arrived at equilibrium equations for a membrane plate. These equations were essentially modified von Kármán plate equations [1910] with the bending rigidity set to zero. Figure 2-1 represents a plane elastic sheet with circular boundary of radius a . The geometry is rotationally symmetric (axisymmetric); we also assume the loading to be a symmetric pressure p . The sheet has modulus E , thickness h , and Poisson's ratio ν .

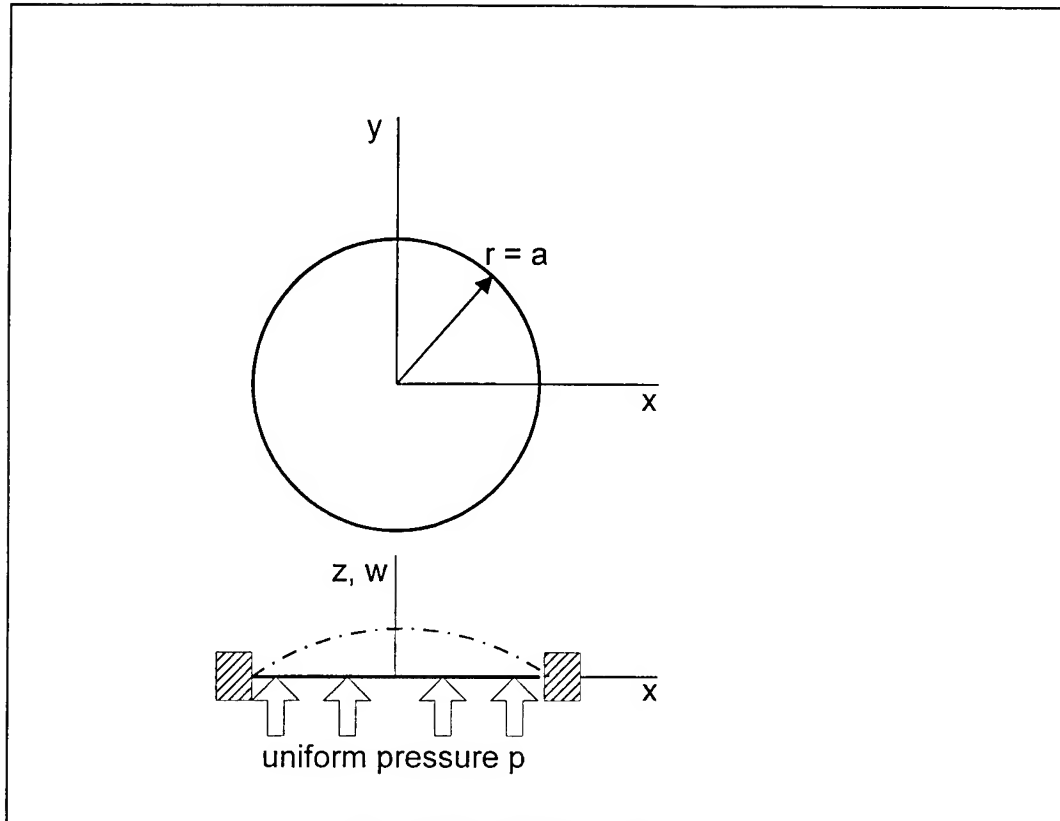


Figure 2-1. Definition Sketch.

The von Kármán plate equations are based upon strains which have nonlinearity introduced through rotations (squares of slope):

$$\epsilon_r = \frac{du}{dr} + \frac{1}{2} \left(\frac{dw}{dr} \right)^2 \quad (1)$$

$$\epsilon_\theta = \frac{u}{r} \quad (2)$$

where u and w are displacements in the r and z directions, respectively.

The von Kármán plate equations in axisymmetric form can be written as:

$$D \left(\frac{d^2}{dr^2} + \frac{1}{r} \right)^2 w - \frac{h}{r} \frac{d}{dr} \left(\frac{d\Phi}{dr} \frac{dw}{dr} \right) = p \quad (3)$$

$$r \frac{d}{dr} \left(\frac{d^2 \Phi}{dr^2} + \frac{1}{r} \frac{d\Phi}{dr} \right) + \frac{E}{2} \left(\frac{dw}{dr} \right)^2 = 0 \quad (4)$$

where $D = Eh^3/12(1-\nu^2)$ is the bending rigidity, and Φ is a stress function to which the stress resultants in the radial and circumferential direction are related respectively by:

$$N_r = \frac{1}{r} \frac{d\Phi}{dr}, N_\theta = \frac{d^2 \Phi}{dr^2} = \frac{d}{dr} (r N_r) \quad (5)$$

Linear elastic constitutive relations are assumed. It is important to note that the above equations are not *geometrically exact*, in that several assumptions have been made with regard to the geometry of the deformed configuration.

Hencky provided a solution of the above for the case of zero boundary displacements ($u = 0 = w$ at $r = a$) and $D = 0$ by assuming power series for stresses and transverse displacement. Little interest in the Hencky problem seems to have taken place until the 1940's, when, in conjunction with a study on air-supported roofs, Stevens [1944] performed an experimental investigation on a 10 inch radius by 0.014 inch thick cellulose acetate butyrate inflated circular membrane. Stevens compared his results for the deflected membrane shape (which were apparently empirical in nature) with Hencky's. Apparently Chien [1948] provided slight corrections to Hencky's solutions for maximum values of stress and transverse deflection [see also Kao and Perrone, 1971].

Cambell [1956] allowed an arbitrary initial tension in the membrane. Dickey [1967] re-examined the Hencky problem, this time using a nonlinear integral equation formulation. Dickey provided a plot of $u(r)$ for various values of the Poisson's ratio. Weil and Newmark [1955] provide some experimental evidence that validate Dickey's predictions. We discuss later the important relationship of $u(r)$ with the surface precision.

Kao and Perrone [1971] used a relaxation method, developed earlier by Shaw and Perrone [1954], to solve the Hencky problem [see also Kao and Perrone, 1972]. Schmidt and DaDeppo [1974] and Schmidt [1974] used a perturbation analysis based on odd powers of r (actually r/a), in conjunction with the Marguerre shallow shell equations (which collapse to the von Kármán plate equations when there exists no initial curvature), to determine the maximum values of the stress and transverse displacement in the Hencky problem. In a series of articles, Storakers [1983] uses a

power series in even powers of r (or r/a) for stresses and transverse displacement (odd powers of r for $u(r)$).

Validity of the Föppl-von Kármán formulation for certain regimes of deformation is discussed by Weinitschke [1980]. For the case of the axisymmetric deformation of an annular membrane, Weinitschke considered a parameter k , (essentially the so-called nondimensional load parameter), where

$$k = \left(\frac{2r_a p}{Eh} \right)^{\frac{1}{3}} \quad (6)$$

and r_a is the radius of the outer edge of the membrane. Comparisons were made between the Föppl and the large rotation Reissner shell (with zero bending stiffness) theories. For values of $k > \frac{1}{2}$, the difference between theories exceeds 10%. The appropriateness of a Reissner-like theory for $k > \frac{1}{2}$ is reiterated in Weinitschke [1987]. [See also Storakers (1983); for further details on the Reissner theory see Weinitschke (1989); see also Ciarlet (1980) for further justification of the von Kármán equations.] Pujara and Lardner [1978] showed that linear (Hookean) and nonlinear (Mooney-Rivlin) elastic constitutive relations provide essentially similar Hencky results up to w_0/a equal to about 0.3.

3. NUMERICAL ANALYSIS

It has been observed in inflatable reflectors, that their service shape deviates from the desired parabolic shape as a function of position on the reflector. This leads to the so-called “W-curve” discussed in more detail below. Hence, one fundamental motivation for shape control of a circular disk is to minimize the surface deviation from the desired target parabola [Jenkins et al. (1998a, 1998b); Jenkins and Marker (1997); Marker and Jenkins (1997)].

It was seen above that the initially plane disk does not have an inflated shape that is parabolic. Questions naturally arise then about how could one move the shape to be more parabolic. More generally, the following question might be posed: Given “N” actuators equally spaced around the rim of an inflated disk (or disk pair), what combination of actuations would result in optimizing a desired effect at some location on the disk? Below we provide some results from an initial investigation of that question.

One quarter of the balloon upper surface was modeled because of symmetry of the structure. Model construction, analysis, and post processing were conducted using the nonlinear FEM code ABAQUS. The model was situated in the first quadrant of the xy plane, and therefore x and y symmetry boundary conditions were applied, as shown in Figure 3-1, noting that coordinates x, y and z are represented by 1, 2 and 3, respectively, in ABAQUS.

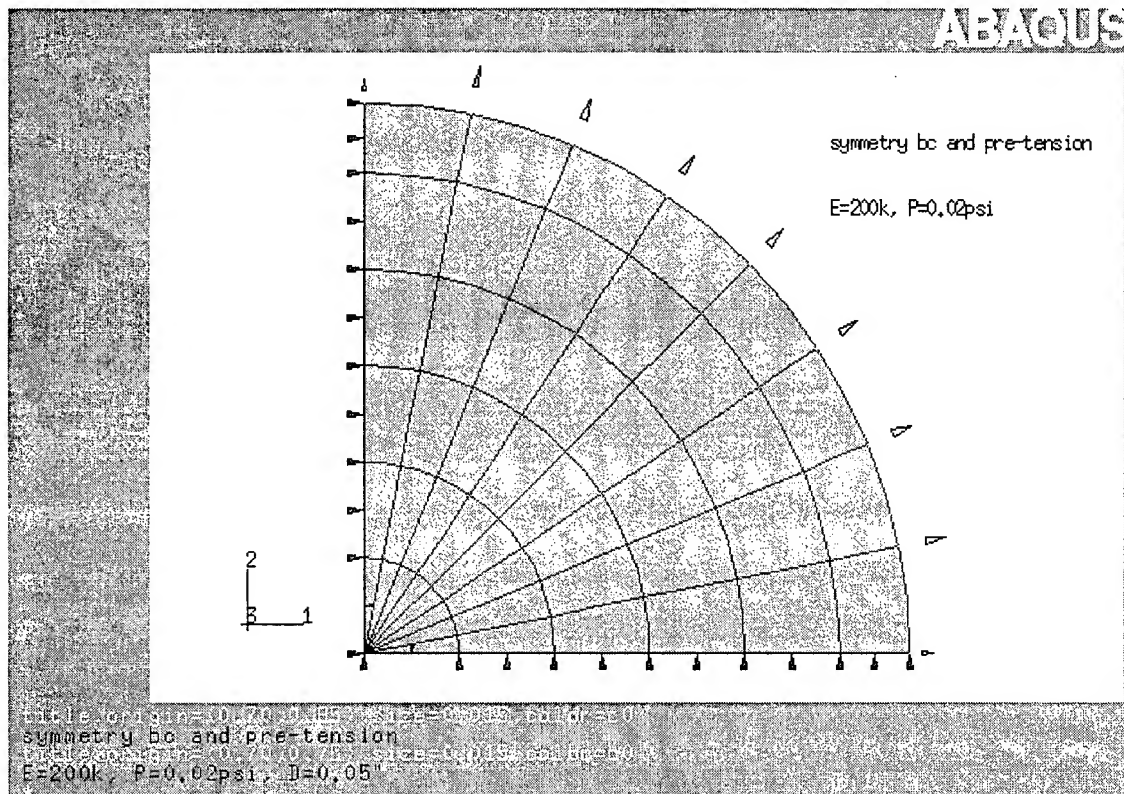


Figure 3-1 FEM model of one quarter of a balloon upper surface, showing mesh, boundary conditions and prestresses at its rim, noting that the node number at the center (lower-left corner) is 100.

As pressure was applied, large deflection occurred in the 3-direction. The model consisted of 48 second-order membrane elements and 157 nodes. For convenience, the model edge along the 1-direction was also called the horizontal line (abbreviated as horiln), Lines

oriented at 22.5 and 45 degrees with respect to the 1-direction were named as line 225 (ln225) and middle line (midln), respectively.

Linear elastic properties were assumed in the present modeling: Young's modulus $E = 200$ ksi, Poisson's ratio $\nu = 0.4$. The geometric dimensions of the model were: membrane thickness $t = 0.00125$ inch, and radius $a = 8.60$ inch. The pressure used was 0.02 psi.

Analysis procedures

The analysis was completed with 4 steps, that replicated what would take place experimentally. From step 1 to step 3, inflation of the balloon was completed. A deflected meridian curve was obtained, which provided a basis to compare with those later obtained under so-called rim control, i.e., imposed boundary displacements.

1) Step 1

Prestress was first applied to the surface with a load of 0.031 lb at each respective point of the rim, as shown Figure 3-1, which resulted in a Mises stress in the membrane of 14 to 18 psi (Figure 3-2) and a rim outward displacement of 0.0005 inch (Figure 3-3).

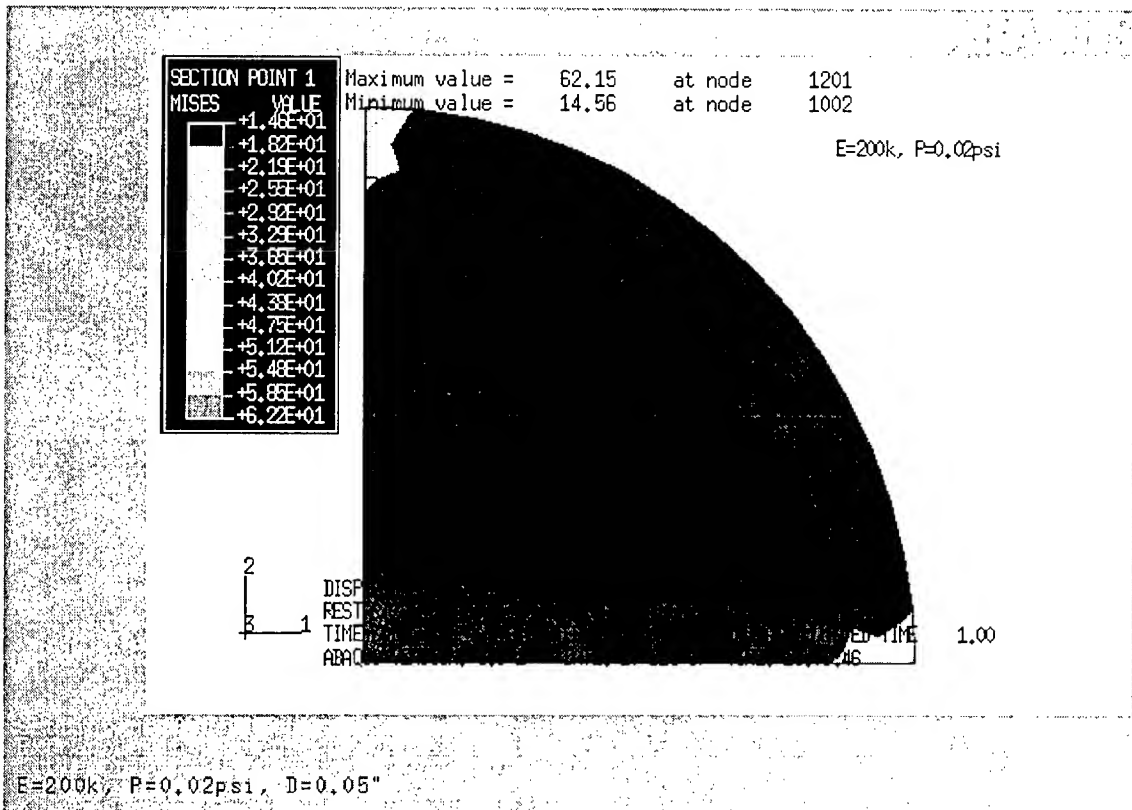


Figure 3-2 The stress in the membrane was around 14 to 18 psi after prestressing.

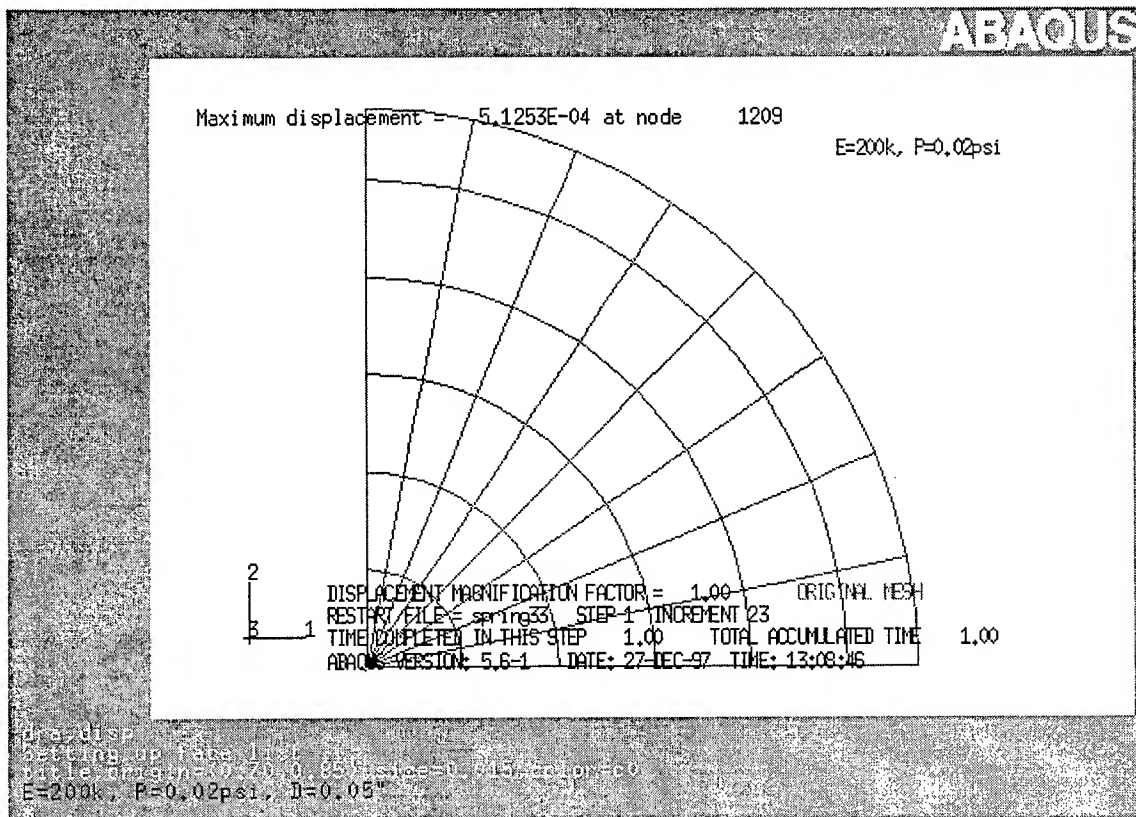


Figure 3-3 A rim displacement of 0.00051 inch was achieved after prestressing.

2) Step 2

The rim displacement resulted from prestressing was fixed. Spring elements were used to initiate deflection of membrane elements under a pressure of a small fraction of 0.02 psi.

3) Step 3

Spring elements were removed from the model and a full pressure of 0.02 psi was applied. A maximum deflection of 0.4733 inch resulted at the center (Figure 3-4), and Mises stress in the membrane of 482 to 701 psi with the maximum located at the center of the surface (Figure 3-5).

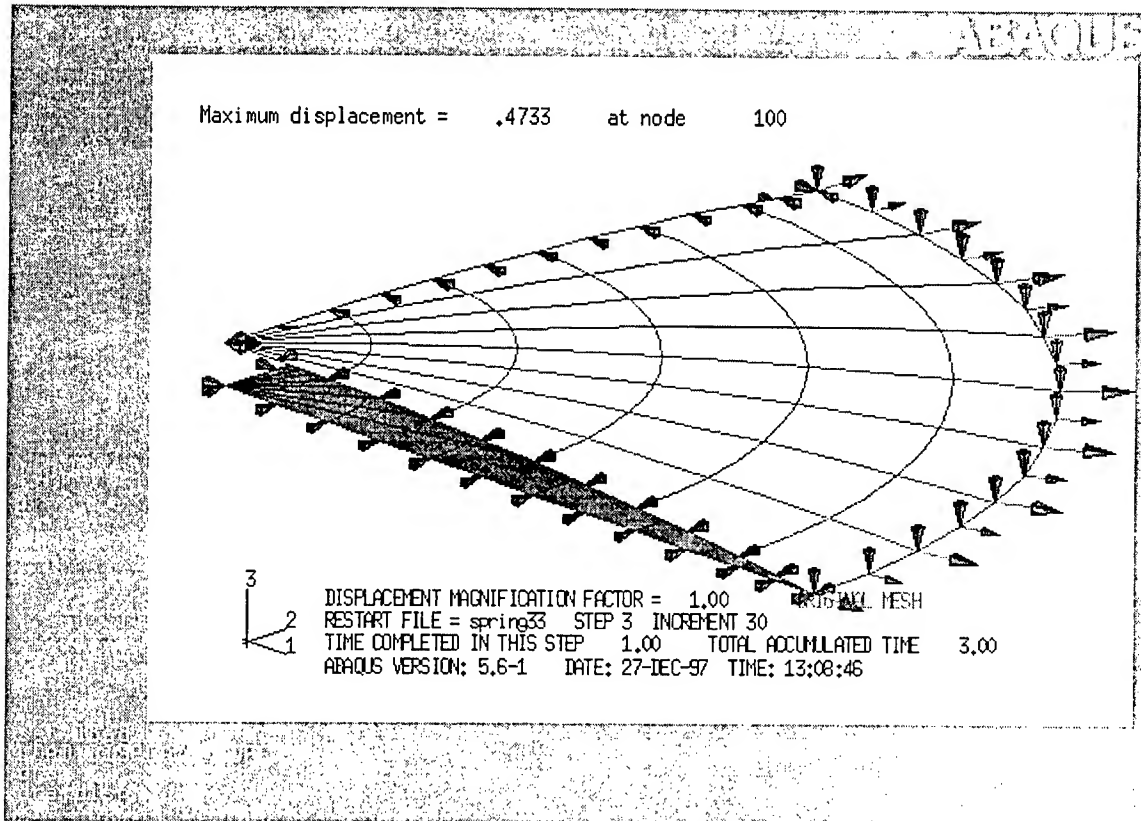


Figure 3-4 A maximum deflection of 0.4733 inch at the center was achieved under a pressure of 0.02 psi, noting that boundary conditions and prestress are still shown.

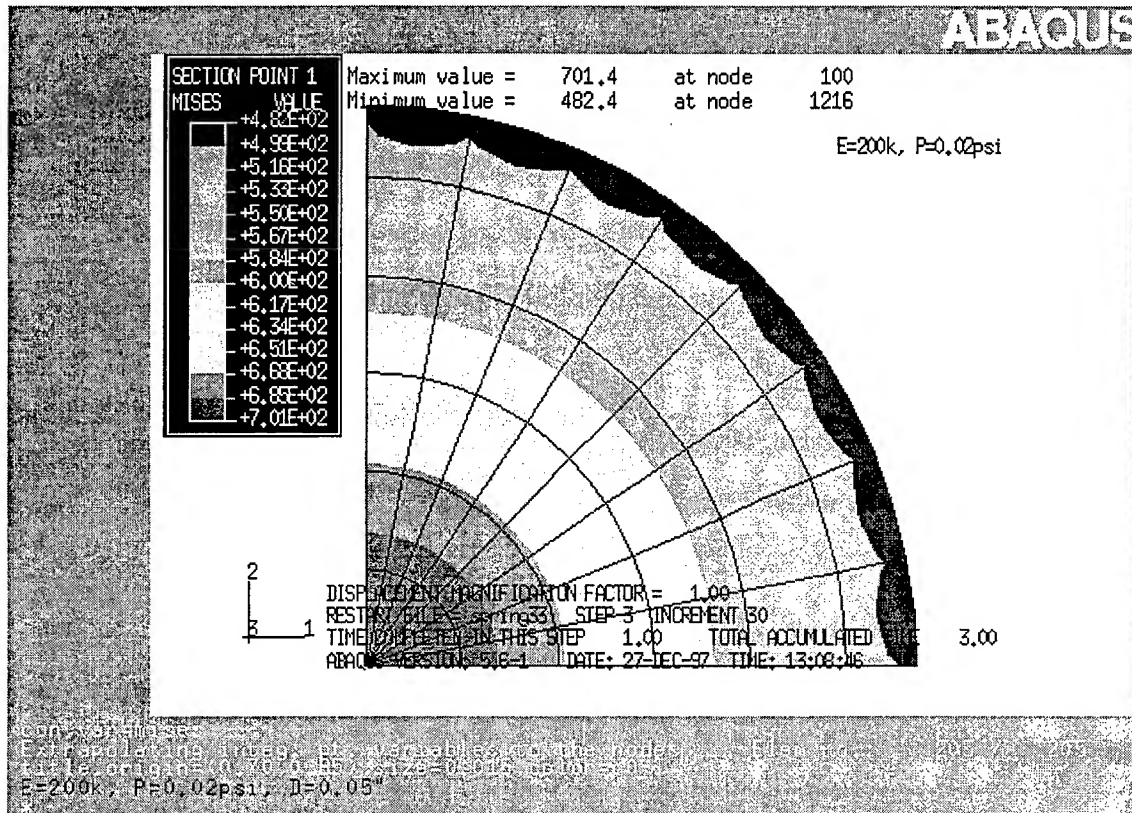


Figure 3-5 Mises stress was around 480 to 700 psi under a pressure of 0.02 psi.

4) Step 4

Imposed outward radius displacements of 0.05 inch at certain positions of model rim (radius = 8.6 inches) were applied. Detailed results will be described below.

4. EXPERIMENTAL ANALYSIS

An experiment was conducted to verify the FEM model described above. Funding limited the sophistication of the experiment performed; however, results gathered confirm the model and provide a foundation for future experimental work. The experimental setup consisted of a mylar balloon and the following subsystems (see Figure 4-1):

Support frame and rings

This system provides support to the balloon while allowing mount locations for tension wires. The frame supports two concentric rings, attached together and which pivot with in the frame, thus allowing both the rings to be in either horizontal or vertical positions. The clamping

devices are mounted on the outer ring, while the inner ring supports the tensioning cable and the balloon.

Tensioning system

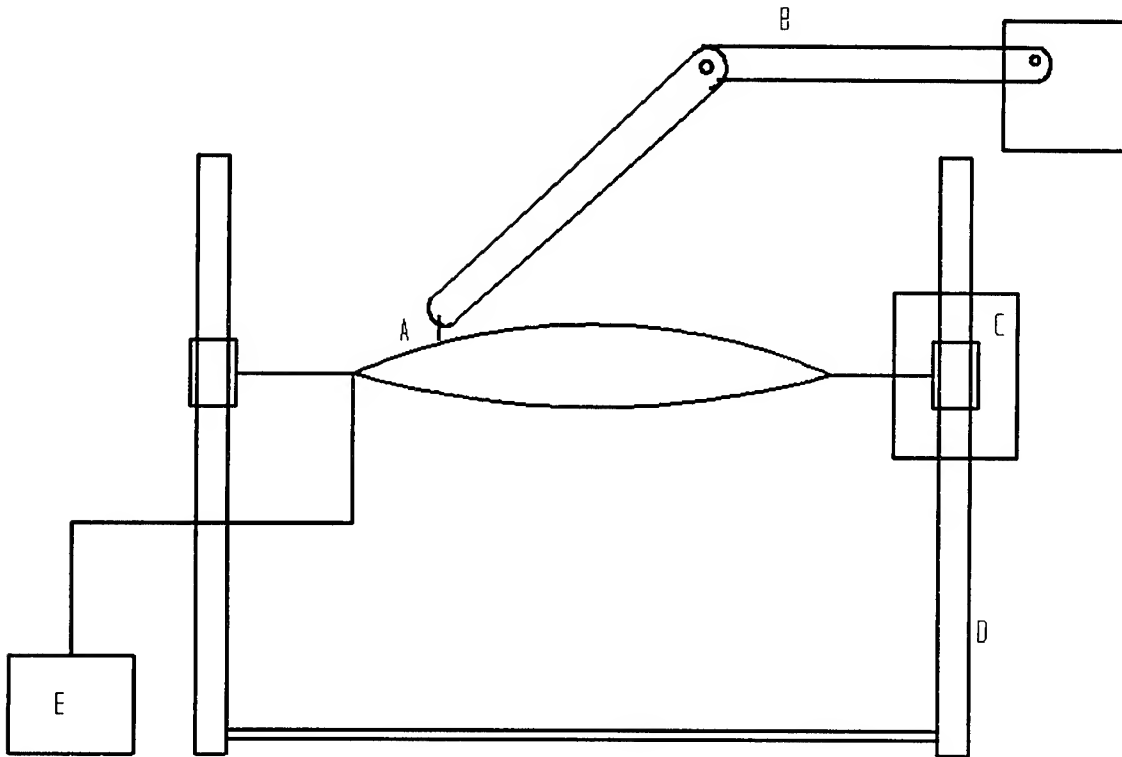


Figure 4-1. Schematic of experimental setup. A = Capacitance sensor ; B = robot; C = Tensioning system; D = Support system; E = Pressure system.

The tensioning system is necessary to apply some prestress in the balloon before inflation, and also for creating the required boundary displacements. A "weight and pulley" tensioning system has been chosen for its ease of use and versatility. It consists of a smooth inner ring surrounding the balloon, which acts as a "pulley" to the weighted tension lines

attached directly to the boundary of the balloon. Braided Kevlar line is used for the tensioning lines, which are radially attached to the balloon at a spacing of 11.25° see Fig. 4-2). With the rings in a horizontal position, a weight of 22.97gm (0.0615lb) are attached to the other end of the line, after it passes through the clamping device.

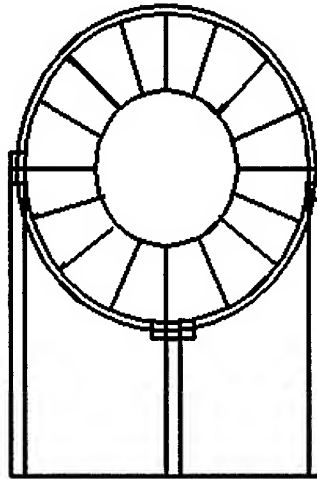


Figure 4-2. Tensioning system schematic(vertical position)

These lines can then be clamped off in order to secure the lines in a constant tension as the balloon prepares to be rotated to its mapping (vertical) position. The clamping devices are used are much like a cable clamp to secure the tension lines during the vertical orientation of the balloon. A schematic of this setup can be seen in the figure below.

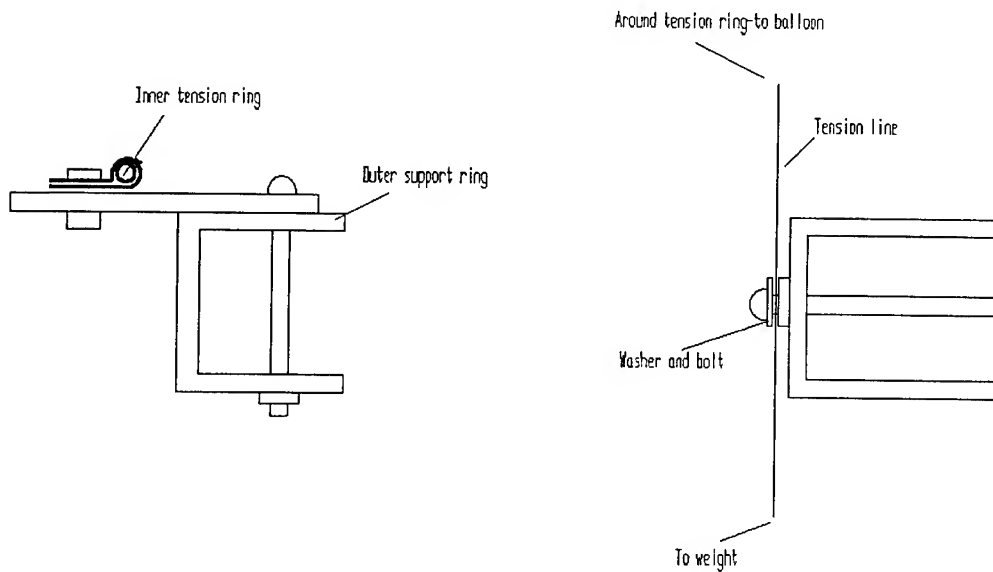


Figure 4-3. Clamping mechanism

The line travels over the tension ring, then down between the two washers and through the bolt. To create the boundary displacement, there is a provision for pulling along the 0, 45 and 90-degree lines around the balloon, through use of turnbuckle system.

Pressure control

Maintaining a constant pressure during the surface mapping is an essential requirement for this experiment. The pressure control system consists of a hand regulator/bleed valve ("dynamic system"), which produces the required accuracy. The system also includes a valve closer to the balloon to allow for measuring the pressure inside the balloon at static conditions. Both the dynamic and static systems were verified using a U-tube manometer with the resolution of 1/10 th of an inch H₂O (0.0036 psi) to check the specified input pressure. To achieve a certain pressure, the pressure regulator is adjusted until the desired pressure is reached, as shown by the U-tube, while the bleed valve is opened to allow for air flow. The combination of the pressure and bleed valve have been verified to provide a constant pressure over a time period of 1 hour. The second valve is also used to check the pressure inside the balloon, simply by closing this valve for a pressure static condition.

Robot measurement system

The profile mapping system consisted of an industrial robot, controlled by a personal computer, and a Capacitec sensor. This robotic mechanism is used under close loop control, with two degrees of freedom that are accurate to 0.00039 in (0.01mm).

The heart of the measurement system is the capacitance displacement sensor (Capacitec model HPT-75). This cylindrically-shaped non-contact sensor, of 1.9 mm (0.075 in) core diameter, acts as one-half of a capacitor, while the membrane surface (conductive mylar) acts as the other half. An AC voltage is applied between the sensor core and the membrane surface, and a self-contained single channel amplifier card within a PC measures the capacitance of this sensor/membrane circuit. A scaled DC voltage is returned to an output terminal on the card, to be read for data acquisition. The sensor has linearity and repeatability of $\pm 0.2\%$ and $\pm 0.01\%$ of full scale, respectively, and a maximum range of about 3 mm (0.12 in).

Data acquisition system

The principle of the Capacitec sensor is to measure the voltage corresponding to the sensor's distance from the surface. In this experiment, the goal was to achieve a fixed voltage for different measuring positions around the balloon surface, thus mapping the balloon profile along a meridian.

To collect the data, the LabVIEW (data acquisition program) and AML (robot control program) software package were used. The AML software was used to control the robot movement directly from the computer. The robot can move in X and Z directions by entering the desired coordinates in the program. This program has a precision to control the robot movement to 0.01 mm.

The sensor is connected to the robot arm through the hole in a plate at the end of the arm. Two nuts, one on each side of the plate, securely mount the sensor to the robot. The ground line is clamped to the balloon. Dan.vi, a program under LabVIEW software, gives the voltage reading of the sensor in both graphical and numerical forms.

After the balloon was completely inflated, the robot was moved toward one edge of the balloon, and the voltage reading from the sensor was observed. In this experiment 6 volts was taken as the reference voltage, and at that position the X and Z coordinates were recorded. In a

similar way, the X and Z coordinates of the diametrically opposite edge were also recorded. The Z coordinate should be the same for both edge positions, to make sure that the balloon surface is parallel to the sensor axis. From these two positions it is easy to calculate the center X coordinate of the balloon. To map the semi profile of the balloon, 15 points were taken from center to edge, and the Z coordinate for every point was measured at the reference voltage. These data are analyzed to get the surface profile of the balloon.

Experimental Procedure

The first step of the experiment is to mount the balloon. To attach the tensioning lines to the balloon, a template was made so that the lines will be in radial directions. Index tabs were used to attach the strings to the balloon, and Kevlar line was used. After the balloon was prepared, it was mounted on the support frame in horizontal position, with a uniform tension load at the other end of each string. Then the tension lines were clamped in the frame. The clamps were tightened a little more than finger tight in order to get some prestress in the balloon.

The second step is the inflation process. The balloon was inflated to a desired pressure by adjusting the regulator. The bleed valve was open to maintain contain pressure inside the balloon. At this point, the entire system was left for 1/2 hour to allow the balloon to achieve the desired pressure, and to observe any pressure difference.

Third, the measuring device, i.e., the personal computer, Capacitec sensor, and the industrial robot were prepared. When ready, the frame was flipped to the mapping (vertical) position, and again the pressure inside the balloon was checked.

Finally the robotic arm with the sensor was brought toward the balloon as discussed previously, and the mapping is begun. These data are used to analyze the balloon profile and deviation from the parabola with inflation only. After these measurements were done, the balloon was flipped horizontally to apply the boundary displacements at the 0, 45, and 90 lines. Then the balloon is flipped vertically again to measure the surface now resulting from the boundary displacements. The entire process was done with the balloon inflated at the same pressure. The data are then analyzed to see the effect of boundary displacements on the surface profile.

5. RESULTS AND DISCUSSION

FEM deflection data before and after imposing the boundary displacements are listed in Table 5-1.

Radius	w^*	w_0^{**}	$w_{3(horiln)}^{***}$	$w_{3(ln225)}^{***}$
0	0.4733	0.1521	0.4095	0.4095
0.75	0.47	0.151	0.4066	0.4066
1.50	0.4603	0.1475	0.3978	0.3978
2.25	0.4439	0.1417	0.383	0.383
3.00	0.4208	0.1337	0.3621	0.3622
3.75	0.3908	0.1233	0.3351	0.3355
4.50	0.3535	0.1106	0.3009	0.3034
5.25	0.3087	9.56E-02	0.26	0.2642
6.00	0.2558	7.82E-02	0.2087	0.2215
6.75	0.1944	5.85E-02	0.1401	0.181
7.50	0.1236	3.65E-02	6.51E-02	0.1353
8.05	6.49E-02	1.89E-02	2.25E-02	4.12E-02
8.60	0.00E+00	0.00E+00	0.00E+00	0.00E+00

* Before imposing displacements

** Imposing displacements on entire rim

*** Imposing displacements at 3 positions of 0, 45 and 90 degrees on the rim

Table 5-1 FEM deflection of respective meridian curves before and after imposing displacements (in inch).

Deviation of FEM results from parabolic curve

The deflection of the meridian curve of the model without imposed displacements was obtain after completing the analysis of Step 3 discussed in Section 3. As an FEM meridian curve (hereafter referred to as FEM curve), w , was found under a certain pressure, p , the intersection points between the curve and coordinate axes, i.e., the maximum deflection, w_0 , at the center of

the balloon surface and the radius, a , of the surface can be used to define the corresponding parabolic curve (hereafter referred to as parabola), w_p according to the equation

$$w_p = w_0 \left(1 - \frac{r^2}{a^2}\right) \quad (7)$$

A comparison of an FEM curve under a pressure of 0.02 psi with its corresponding parabola shows that the FEM curve has larger deflection than the parabola, as showing in Figure 5-1. The difference between these curves, $w-w_p$, is a “W” shaped curve, as also shown in the same figure, noting that only a half of the “W” curve is shown due to symmetry, and the curve has been magnified by 10 times for convenience.

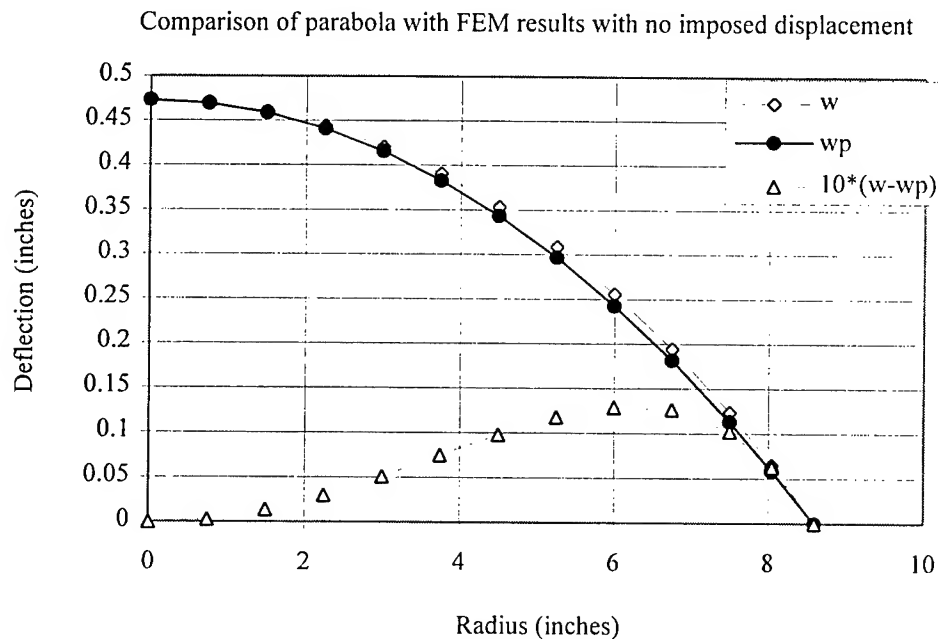


Figure 5-1 A comparison between FEM meridian curve and its corresponding parabola, noting that the deviation of the FEM curve from the parabola is a “W” curve which is magnified by 10 times in the figure.

In the following text, as far as the word deviation is used, it is always referred to a difference between an FEM curve and its corresponding parabola. Normalization of the

deviation and model radius will be employed for general understanding of the deflection tendency with and without rim control.

Reduction of the deviation through rim control

The deviation of a meridian curve from its corresponding parabola can be reduced through rim control. Specifically, 0.05 inch outward radial displacements were imposed on certain positions along the rim of the model. Two cases of imposed positions on the rim were investigated:

- 1) at 0, 45 and 90 degrees; and
- 2) a uniform displacement imposed on the entire rim.

The following symbols will be used in some figures (noting that “n” denotes “normalized”, “p” denotes “parabola”, “0” denotes “uniform rim displacement” and “3” denotes “under the case of 3 positions on the rim”):

w_n , normalized deflection before imposing a displacement

w_{np} , normalized parabola corresponding to w_n ;

w_{0n} , normalized deflection after a displacement was imposed on entire rim;

w_{0np} , normalized parabola corresponding to w_{0n} ;

w_{3n} , normalized deflection of a meridian curve along which one of the 3 displacements were imposed on the rim;

w_{3np} , normalized parabola corresponding to w_{3n} ;

$w_{3(\ln225)n}$, normalized deflection of $\ln225$ after 3 displacements were imposed on the rim;

$w_{3(\ln225)np}$, normalized parabola corresponding to $w_{3(\ln225)n}$.

Imposed displacements at 0, 45, and 90 degrees

After 0.05-inch displacements were imposed at the positions of 0, 45, and 90 degrees, the maximum deflection of the model was reduced to 0.4095 inch, as shown in Figure 5-2, 13% less than that before imposed boundary displacements. In the same figure, boundary conditions including the imposed displacement directions are also indicated. Deflections of lines of $\ln r$, $\ln225$ and mid \ln were plotted in Figure 5-3. For comparison, the FEM meridian curve before imposed boundary displacement, denoted as mid $\ln0$, is also included in the figure.

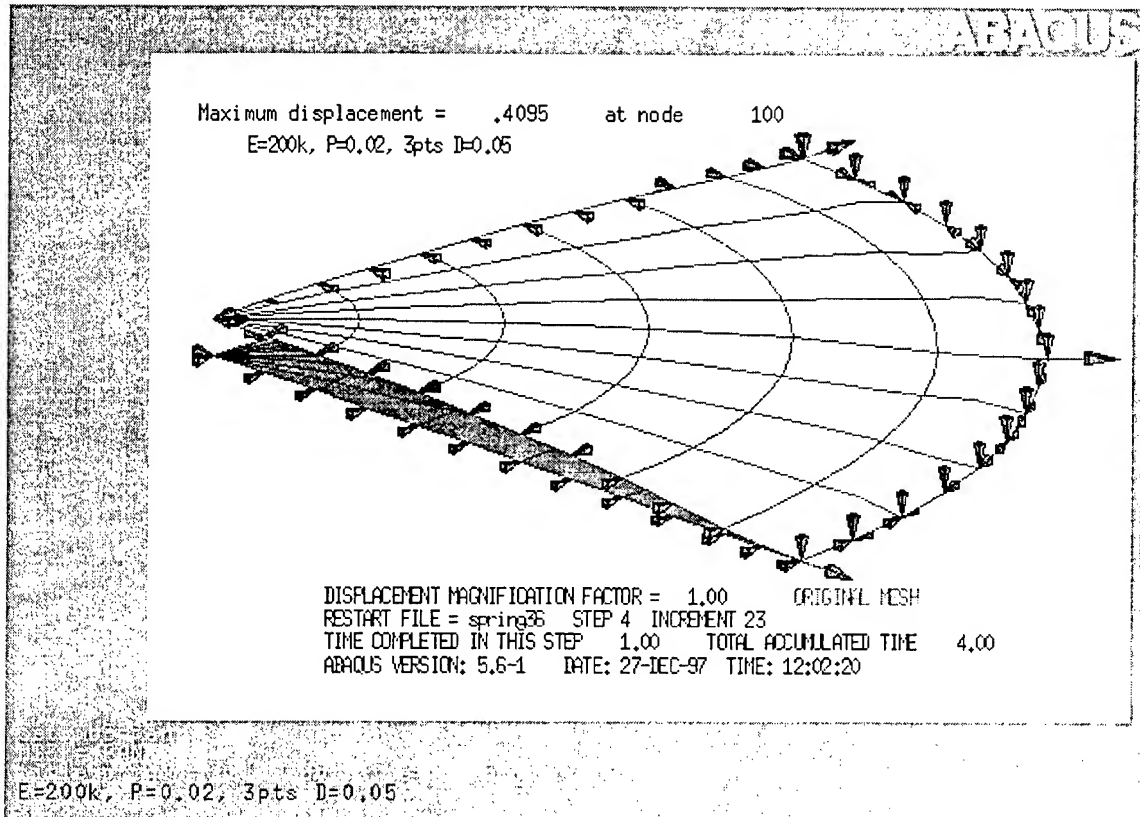


Figure 5-2 The maximum deflection was reduced by 13% after an imposed displacement of 0.05 inch applied at 3 positions on the rim.

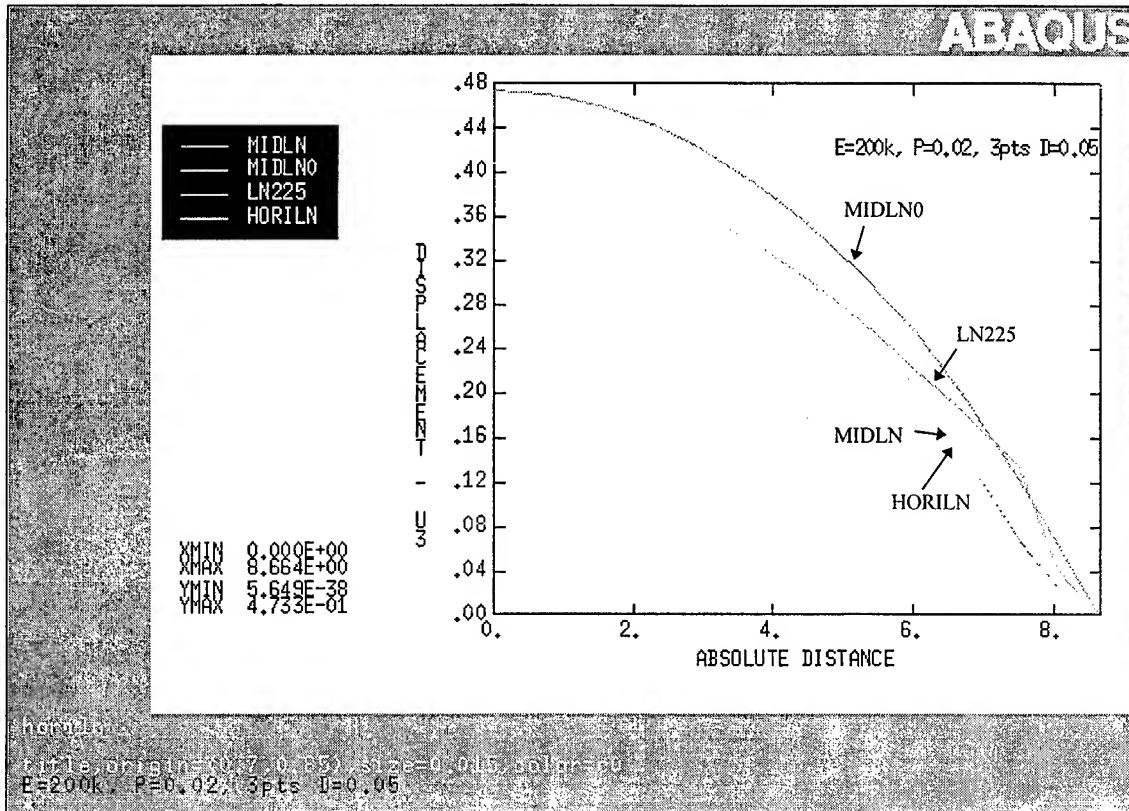


Figure 5-3 FEM meridian curves at 0, 22.5, and 45 degrees.

It is found that there was a bulge in midln and a concavity in horiln, which were close to the rim. In order to have a full conception of the shape of the model in this state, profiles of circumferential curves with radii of 1.50, 3.00, 4.50, 6.00, 7.50 and 8.60 inches, respectively, are given in Figure 5-4, showing that when the radius was greater than 6 inches, these curves were no longer of constant z-deflection.

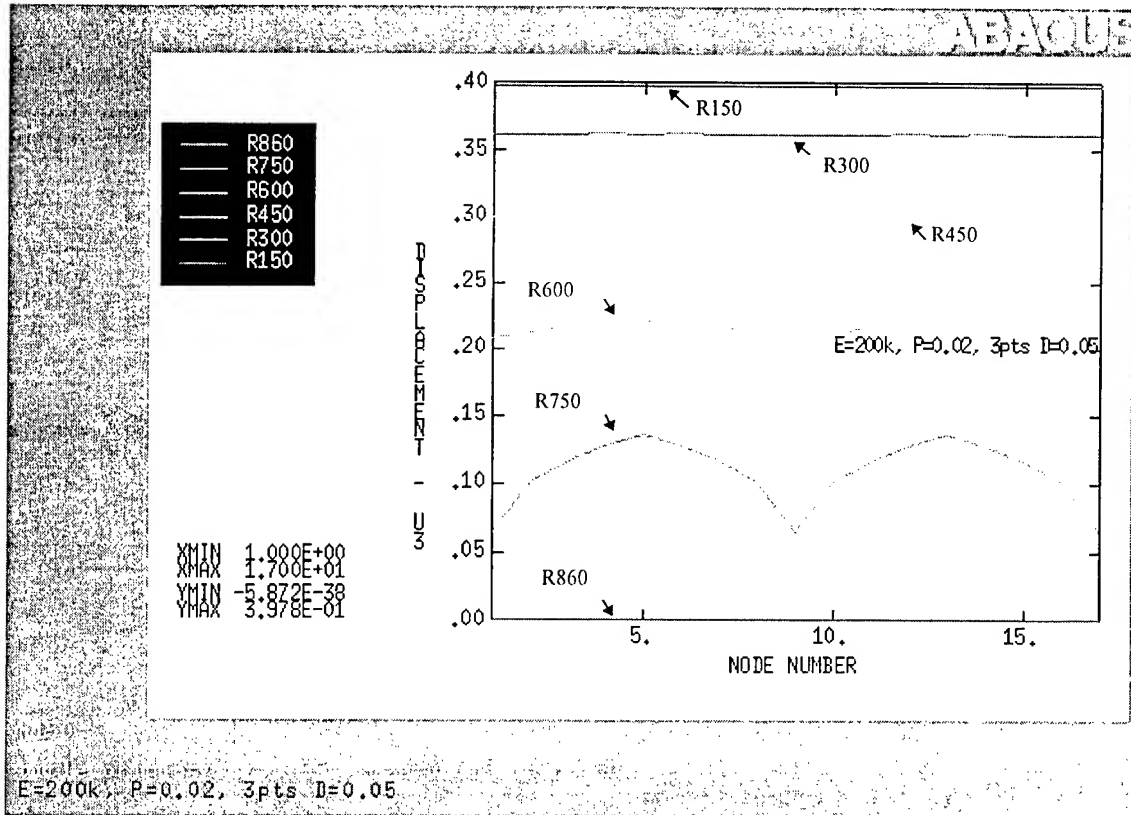


Figure 5-4 Deflections along circular lines with various radii. R150 = 1,50 inch radial position, etc.

The deviations of hor1ln and ln225 were reduced in an area with a radius 60% of the balloon radius as shown in Figure 5-5.

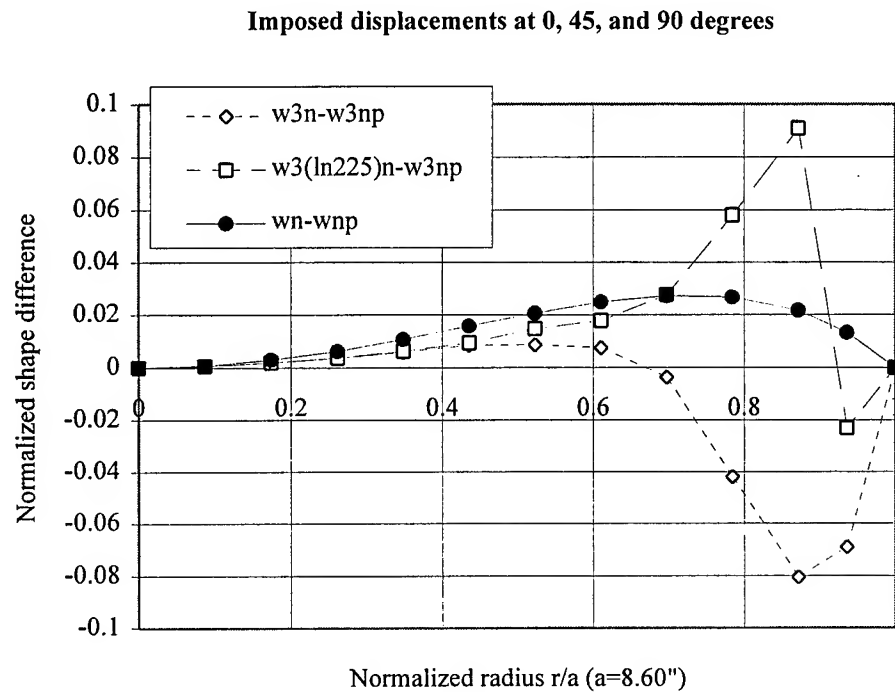


Figure 5-5 Deviations of horiln and ln225 were reduced in the area with a radius 60% of the model radius.

Displacement imposed on entire rim.

After 0.05 inch outward displacement was imposed on the entire rim, as shown in Figure 5-6, the maximum deflection was 0.1521 inch, a reduction of 68% compared with the deflection of 0.4722 inch before the displacement. The deviation was also dramatically reduced, as seen from Figure 5-7. Before boundary displacements, the deviation was 2.7%; the deviation became 0.1% after uniform displacements. Stress distribution was almost uniform, as shown in Figure 5-8, and increased by 3 times compared with that before boundary displacements.

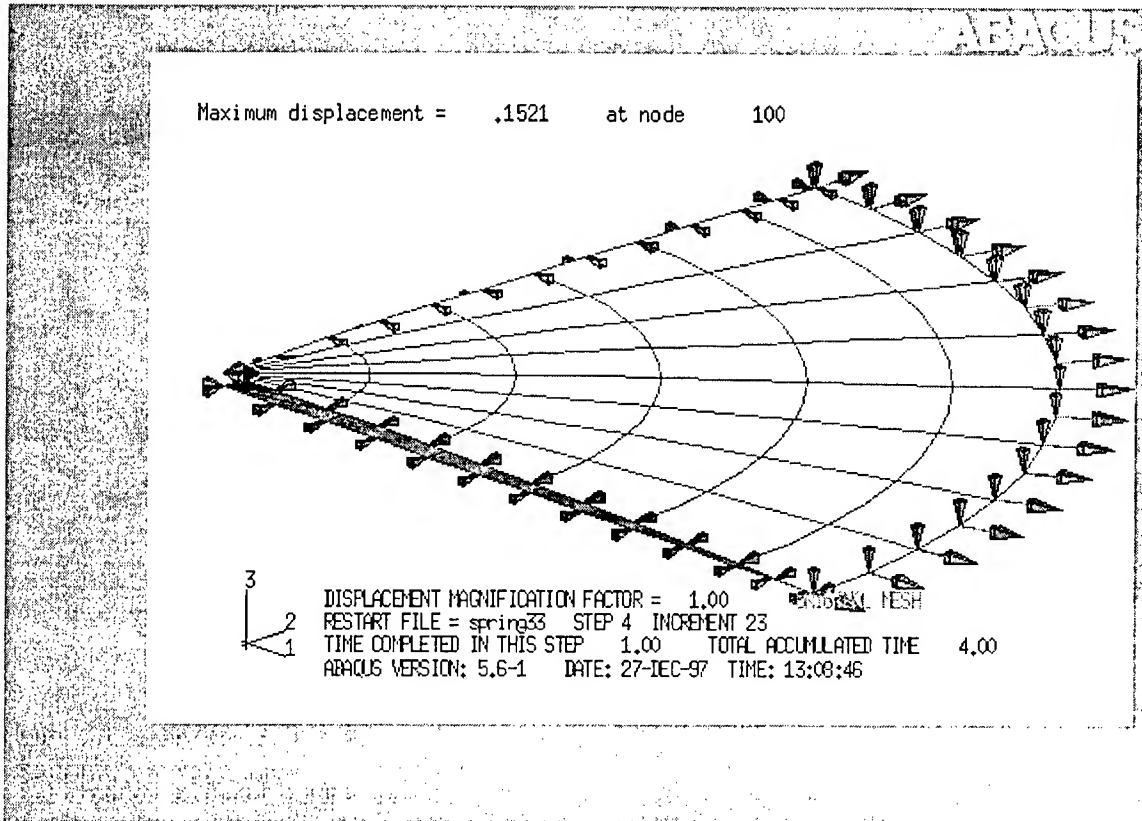


Figure 5-6 The maximum deflection was greatly reduced after a displacement of 0.05 inch was uniformly imposed on the rim of the model.

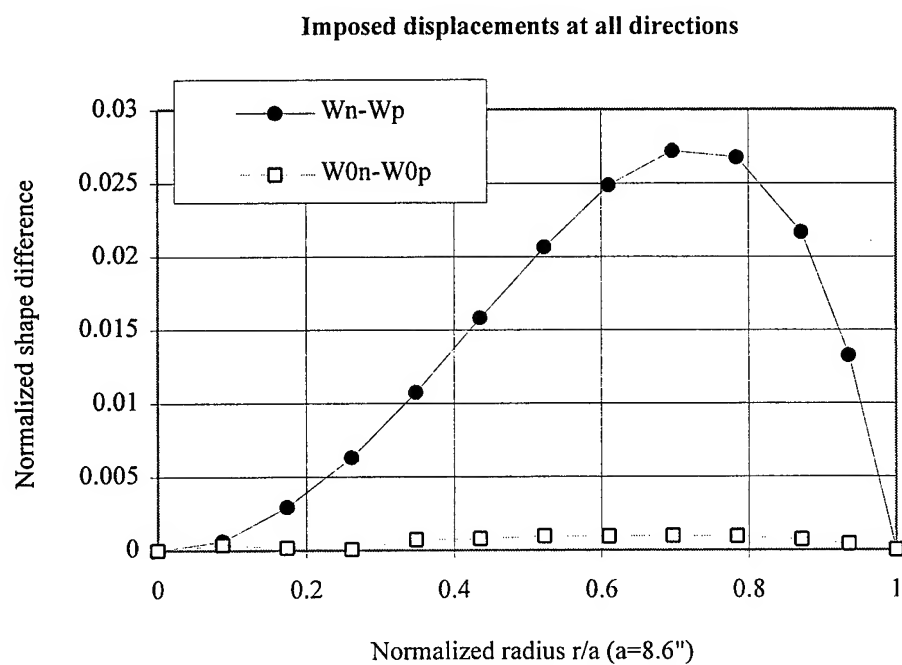


Figure 5-7 The maximum deviation from parabola was reduced to 0.1% after a displacement of 0.05 inch was uniformly imposed on entire rim, compared with 2.7% before boundary displacements.

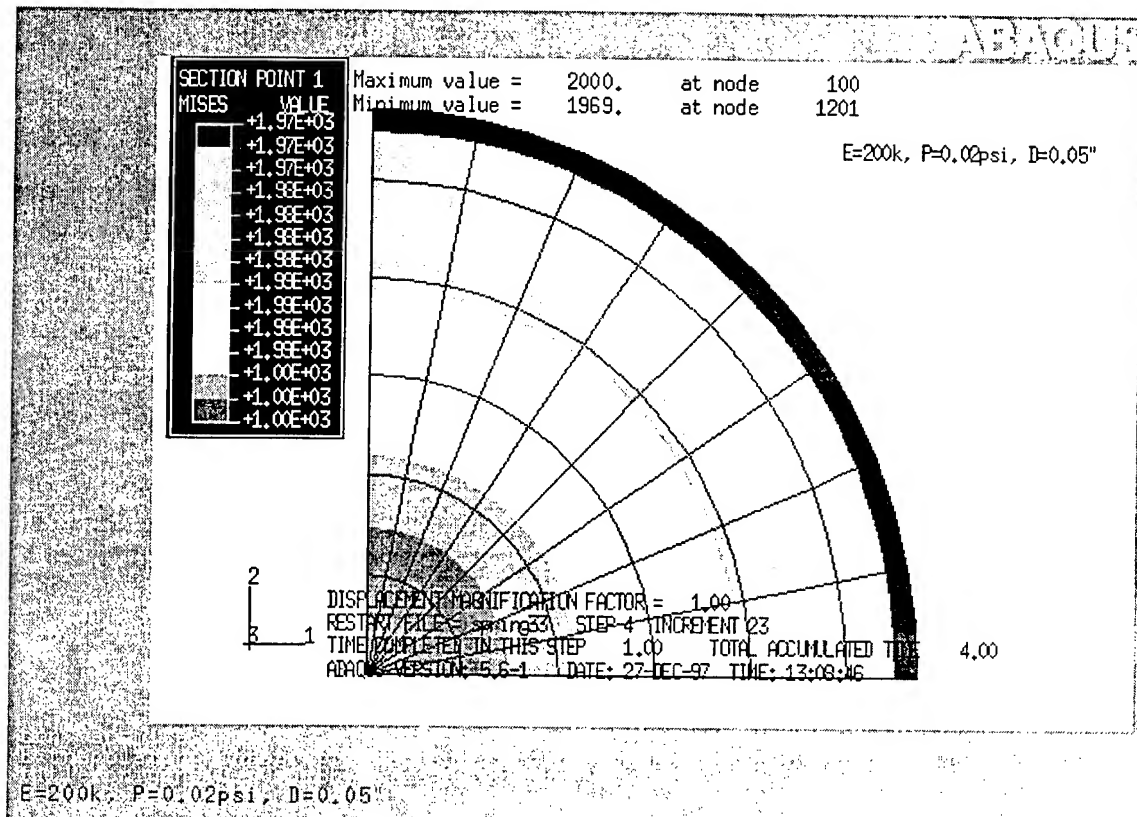


Figure 5-8 Stress in the model was almost uniform after an outward radial displacement of 0.05 inch was uniformly imposed on the entire rim.

The experimental results are presented below in graphical manner, and show how the pressure and boundary displacements effect the balloon profile.

Effect of pressure

In Figure 5-9, the experimentally measured profile (w_e) of the balloon along a meridian at two constant pressures are shown, along with the desired parabolic shape (w_p), and the deviation from the parabola ($w_e - w_p$). The parabola plotted here is drawn to fit through the apex and boundary of the balloon profile. Both the vertical displacements and the radial positions are normalized with respect to their maximum values, to make the effects clearer. Then both Fig. 5-9a and 5-9b are compared in 5-9c to show the effect of pressure on the profile of the balloon. From this third figure it can be seen that at the higher pressure the profile is closer to the desired shape; however, this may be an artifact of too low a pressure in the first case (Fig.5-9a).

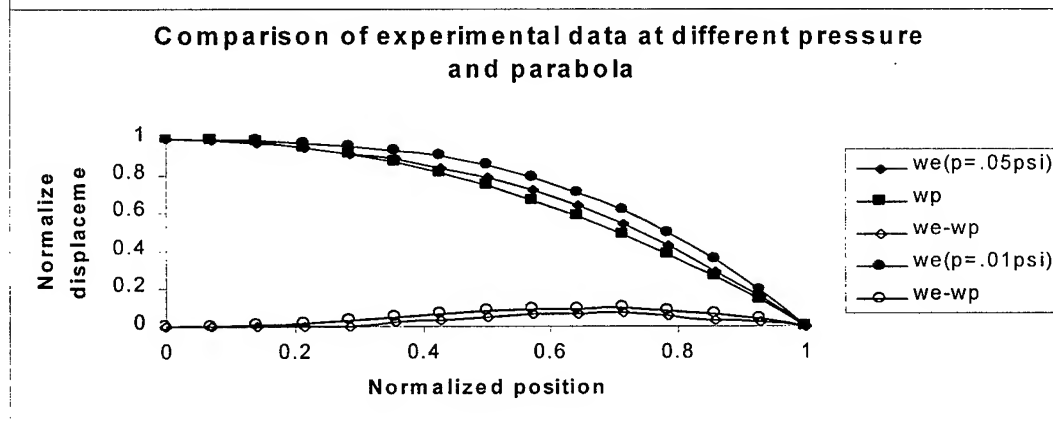
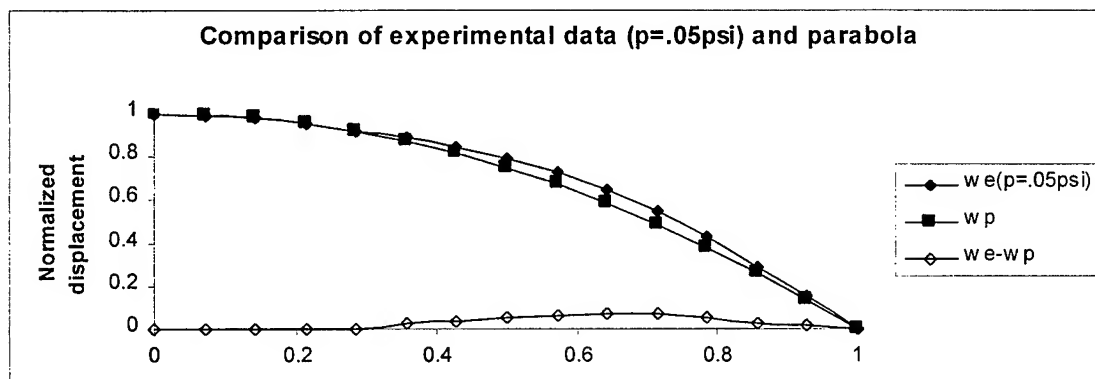
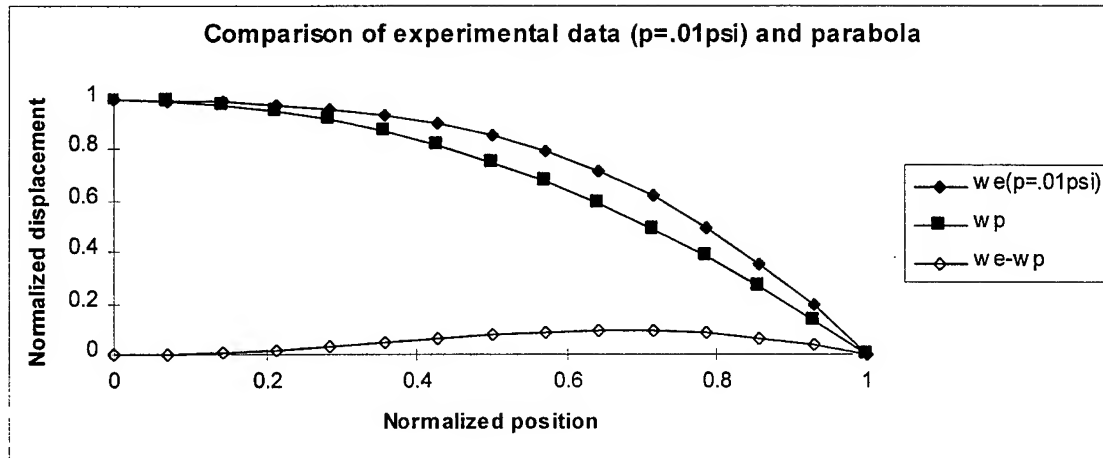


Figure 5-9 Experimentally measured profiles. a) $p = 0.01\text{psi}$; b) $p = 0.05\text{psi}$; c) comparing a) and b).

Effect of boundary displacements

Two experiments at different pressures were conducted to see the effect of boundary displacement on surface profile, and the results are plotted in Fig. 5-10. The results show that the profile of the balloon with the boundary displacement is closer to the parabola than the inflation only case. This is the same trend seen in the FEM model.

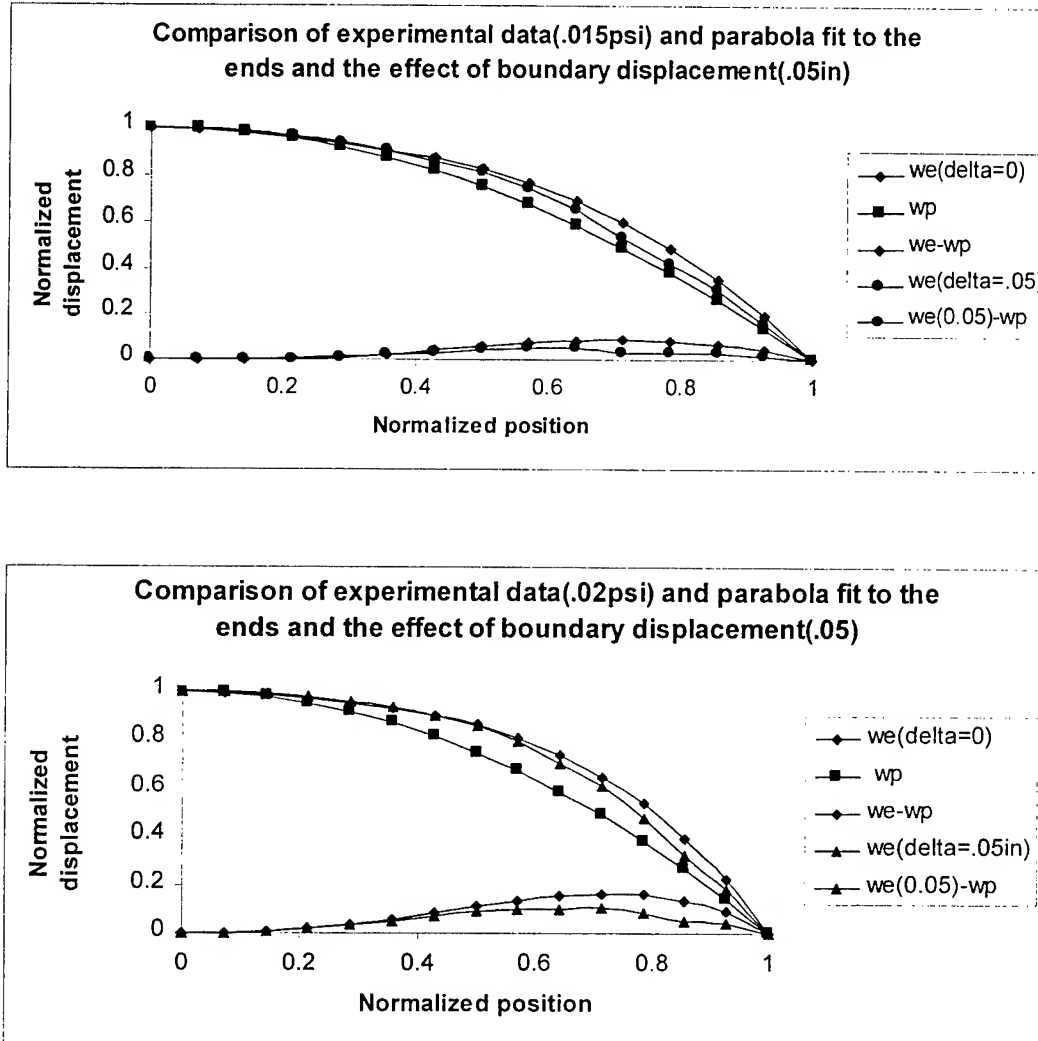


Figure 5-10. Experimentally measured profiles with the boundary displacement of 0.05 in a) $p = 0.015\text{psi}$; b) $p = 0.02\text{ psi}$.

6. CONCLUSIONS

Inflatable structures have been used for many years in terrestrial applications, from sports stadium roofs to automotive airbags. Inflatable will achieve their greatest potential, however, in space-based applications. Along with their high strength to weight ratio, the capability of reduced launch mass and volume make inflatables highly desirable candidates for space-based structures.

This investigation has focused on initial inquiries into the shape control of inflatable structures, specifically a thin inflated disk. It has been shown that the shape of an initially plane circular disk is not inherently parabolic. Radial displacements at the boundary can, however, move the surface toward a parabolic shape. Moreover, this effect is pronounced at locations distant from the locations where the discrete boundary displacements are applied. The so-called "W-curve" has been shown to be reduced by imposed outward radial displacements at the boundary.

7. ACKNOWLEDGMENTS

The author gratefully acknowledges the AFOSR Summer Faculty Research Program for their support of this investigation. The author is especially grateful to Dr. Linfa Yan and Mr. S. M. Faisal for their work on this project; to Lt. Jonathan Bishop, PL/VTs, for his help and support during this investigation; and to Mr. Dan Marker, PL/LI, for the many helpful discussions regarding space-based inflatable applications.

8. REFERENCES

- Cambell, J.D. (1956), "On the theory of initially tensioned circular membranes subjected to uniform pressure," *Q J Mech Appl Math* **9**, 84-93.
- Cassapakis, C., and Thomas, M. (1995). "Inflatable structures technology development overview," *AIAA* 95-3738.
- Chien, W.Z. (1948), "Asymptotic behavior of a thin clamped plate under uniform normal pressure at very large deflection," *Sci. Rep. Natn. Tsing Hua Univ.* A5, 71-94.
- Ciarlet, P.G. (1980), "A justification of the von Kármán equations," *Arch Rat Mech Anal* **73**, 349-389.

- Dickey, R.W. (1967), "The plane circular elastic surface under normal pressure," *Arch Rational Mech Anal* **26**, 219-236.
- Föppl, A. (1907), "Vorlesungen über technische Mechanik," *B.G. Teubner*, Bd. 5., p. 132, Leipzig, Germany.
- Grossman, G., and Williams, G. (1990). "Inflatable concentrators for solar propulsion and dynamic space power," *J Solar Energy Engineering* **112**, 229-236.
- Hencky, H. (1915), "Über den Spannungszustand in kreisrunden Platten," *Z. Math. Phys.* 63, 311-317.
- Hedgepeth, J.M. (1982). "Accuracy potentials for large space antenna reflectors with passive structures," *J Spacecraft* **19**(3), 211-217.
- Jenkins, C.H., Marker, D.K., and Wilkes, J.M. (1998a), "Improved surface accuracy of precision membrane reflectors through adaptive rim control," *AIAA Adaptive Structures Forum*, Long Beach, CA (to appear).
- Jenkins, C.H., Wilkes, J.M., and Marker, D.K. (1998b), "Surface accuracy of precision membrane reflectors," *Space 98*, Albuquerque, NM (to appear).
- Jenkins, C. H., and Marker, D. K. (1997), "Surface precision of inflatable membrane reflectors," *J Solar Energy Engr* (in review).
- Jenkins, C.H. (1996a), "Nonlinear Dynamic Response of Membranes: State of the Art -- Update," *Appl Mech Rev* 49 (10), S41-S48.
- Jenkins, C.H. (1996b). "Experimental Measurement of Wrinkling in Plane Elastic Sheets," *1996 Spring Conference*, Society of Experimental Mechanics, Nashville, TN.
- Jenkins, C.H. (1995). "Membrane Wrinkling: Theoretical Predictions and Experimental Verifications," (invited), *Symposium on Advances in Mechanics of Elastic and Bioelastic Membranes* at the Int Mech Engr Conf Expo, ASME, San Francisco, CA.
- Jenkins, C.H., Spicher, W., and Vedoy, A. (1995). Evaluation of membrane wrinkling by noncontact measurement," *Proc 24th Midwestern Mechanics Conf*, Ames, IA.
- Jenkins, C.H., and Leonard, J.W. (1993). Dynamic wrinkling of viscoelastic membranes, *J Appl Mech* **60**, 575-582.

- Jenkins, C.H. and Leonard, J.W. (1991), "Nonlinear Dynamic Response of Membranes: State of the Art," *Appl Mech Rev* 44, 319-328.
- Kao, R., and Perrone, N. (1972), "Large deflections of flat arbitrary membranes," *Comput Struct* 2, 535-546.
- Kao, R., and Perrone, N. (1971), "Large deflections of axisymmetric circular membranes," *Int J Solids Struct* 7, 1601-1612.
- Kuznetsov, E.M. (1991). *Underconstrained structural systems*, Springer-Verlag, New York.
- Marker, D. K., and Jenkins, C. H. (1997), "On the systematic "W" profile error in uncompensated isotropic membrane reflectors," *25th Midwestern Mechanics Conf*, Rapid City, SD.
- Pujara, and Lardner, T.J. (1978), "Deformations of elastic membranes--effect of different constitutive relations," *Z Angew Math Phys* 29, 315-327.
- Schmidt, R. (1974), "On Berger's method in the non-linear theory of plates," *J Appl Mech* 41, 521-523.
- Schmidt, R., and DaDeppo, D.A. (1974), "A new approach to the analysis of shells, plates, and membranes with finite deflections," *Int J Non-Linear Mech* 9, 409-419.
- Shaw, F.S., and Perrone, N. (1954), "A numerical solution for the non-linear deflection of membranes," *J Appl Mech* 21, 117-128.
- Stevens, H.H. (1944), "Behavior of circular membranes stretched above the elastic limit by air pressure," *Experimental Stress Analysis* 2, 139-146.
- Storakers, B. (1983), "Small deflections of linear elastic circular membranes under lateral pressure," *J Appl Mech* 50, 735-739.
- Timoshenko, S., and Woinowsky-Krieger, S. (1959). *Theory of plates and shells*. McGraw-Hill.
- von Kármán, T. (1910), "Festigkeitsproblem im Naschinenbau," *Encyk D Math Wiss* IV, 311-385.
- Weil, N.A., and Newmark, N.M. (1955), "Large plastic deformations of circular membranes," *J Appl Mech* 22, 533-538.
- Weinitschke, H.J. (1989), "Stable and unstable axisymmetric solutions for membranes of revolution," *Appl Mech Rev* 42, S289-S294.

Weinitschke, H.J. (1987), "On finite displacements of circular elastic membranes," *Math Method Appl Sci* **9**, 76-98.

Weinitschke, H.J. (1980), "On axisymmetric deformations of nonlinear elastic membranes," in *Mechanics Today* **5**, 523-542, Pergamon Press, Oxford.

**NUMERICAL SIMULATION OF ELECTROMAGNETIC WAVE
TRANSFORMATION IN A DYNAMIC MAGNETIZED PLASMA**

**Dikshitulu K. Kalluri
Professor
Department of Electrical Engineering**

**Joo Hwa Lee
Department of Physics and Applied Physics**

**University of Massachusetts Lowell
1 University Avenue
Lowell, MA 01854**

**Final Report for:
Summer Research Extension Program
Phillips Laboratory / Geophysics Directorate**

**Sponsored by:
Air Force Office of Scientific Research
Bolling Air Force Base, Washington DC**

and

Phillips Laboratory / Geophysics Directorate

December 1997

Numerical Simulation of Electromagnetic Wave Transformation in a Dynamic Magnetized Plasma

Dikshitulu K. Kalluri
Professor
Department of Electrical Engineering
Joo Hwa Lee
Department of Physics and Applied Physics
University of Massachusetts Lowell

Abstract

Finite-Difference Time Domain (FD-TD) algorithms are developed to study the transformation of an electromagnetic wave by a dynamic (time-varying) inhomogeneous magnetized plasma medium. One dimensional code is used to verify the results obtained earlier using approximate-analytical results based on (a) WKB method for slow rise time of the profile (b) Green's function technique for rapid switching of the plasma medium. Spectrum analysis using an enhanced Fast Fourier Transform (FFT) technique is used to obtain the amplitude and the frequencies of the new modes generated by the switching of the medium.

A three dimensional FD-TD code, valid for arbitrary variation in space and time of (a) plasma density, (b) direction and strength of static magnetic field, and (c) collision frequency, is developed. The accuracy and the stability of the three dimensional code is being examined by studying the mode coupling in a rectangular plasma cavity containing the dynamic inhomogeneous magnetized plasma. The code will be used to study the remarkable transformation of an electromagnetic wave and explore its applications.

Numerical Simulation of Electromagnetic Wave Transformation in a Dynamic Magnetized Plasma

Dikshitulu K. Kalluri
Joo Hwa Lee

1 Introduction

The FD-TD method [1]-[3] has become a very powerful method to analyze electromagnetic problems due to its simplicity and accuracy. It is a natural representation of Maxwell's equations in a discretized form.

In this report, we study the effects of time-varying and space-varying magnetized plasma medium on an electromagnetic wave. Most time-varying plasma problems do not have exact solutions and are likely to be described by high-order differential equations. Hence, only very simple problems are solved exactly and many problems are left unsolved. Due to their high-order complexity, approximate solutions have been given in several forms. WKB methods [4]-[5] are used for slowly varying plasmas and Green's function methods [6] are used for fast-profile plasma problem. These solutions are not verified in some cases because numerical solutions usually give the total fields. The WKB solution for some of the modes has very weak field amplitudes and they are hard to detect in the total fields. So, we need to find a tool to analyze the weak components (modes) from the output signals in the computer simulations. Green's function methods for fast profile can give very good approximate solutions for small perturbations. When the perturbations are large, the solution tends to degrade quickly.

In this report we will verify the validity of the solutions given by WKB methods and Green's function methods to ensure the validity of the numerical and analytical

approaches. This will be done by the FD-TD method to find time series for the total fields. The frequencies and the amplitudes of the various modes will be obtained by using a modified FFT method.

2 One Dimensional FD-TD Algorithm

2.1 One Dimensional Equations

Consider a magnetoplasma medium with time-varying and space-varying plasma frequency in one dimension. The Maxwell's equations and the constitutive relation for the plasma medium [7] are given by

$$\nabla \times \mathbf{E} = -\mu_0 \frac{\partial \mathbf{H}}{\partial t}, \quad (1)$$

$$\nabla \times \mathbf{H} = \epsilon_0 \frac{\partial \mathbf{E}}{\partial t} + \mathbf{J}, \quad (2)$$

$$\frac{\partial \mathbf{J}}{\partial t} = \epsilon_0 \omega_p^2(z, t) \mathbf{E} + \omega_b \times \mathbf{J}. \quad (3)$$

The electromagnetic wave is assumed to be propagating in z -direction and the static magnetic field is also assumed to be in z -direction. The natural modes of this case are circularly polarized waves. For the specific example of a right circularly polarized wave (R-wave), the fields may be written as:

$$\mathbf{E} = (\hat{x} - j\hat{y})E(z, t), \quad (4)$$

$$\mathbf{H} = (j\hat{x} + \hat{y})H(z, t), \quad (5)$$

$$\mathbf{J} = (\hat{x} - j\hat{y})J(z, t), \quad (6)$$

where $j = \sqrt{-1}$.

From (1)-(3) and (4)-(6), we will get the following one dimensional equations:

$$\frac{\partial H}{\partial t} = -\frac{1}{\mu_0} \frac{\partial E}{\partial z}, \quad (7)$$

$$\frac{\partial E}{\partial t} = -\frac{1}{\epsilon_0} \frac{\partial H}{\partial z} - \frac{1}{\epsilon_0} J, \quad (8)$$

$$\frac{dJ}{dt} = \epsilon_0 \omega_p^2(z, t) E + j\omega_b J. \quad (9)$$

These equations (7), (8), and (9) are valid for both isotropic ($\omega_b = 0$) and magnetized plasmas ($\omega_b \neq 0$).

2.2 Grid Generation

We can use several grid configurations to discretize (7)-(9). Let $z = k\Delta z$ and $t = n\Delta t$. We can use the standard Yee's grids for E and H [1]. As (9) implies, E and J lie on the same space coordinate but will be offset by $\frac{1}{2}$ time step.

2.3 FD-TD Formulation

Using central difference formulas we generate the following approximations for (7)-(9).

$$\frac{H|_{k+\frac{1}{2}}^{n+\frac{1}{2}} - H|_{k+\frac{1}{2}}^{n-\frac{1}{2}}}{\Delta t} = -\frac{1}{\mu_0} \frac{E|_{k+1}^n - E|_k^n}{\Delta z}, \quad (10)$$

$$\frac{E|_k^{n+1} - E|_k^n}{\Delta t} = -\frac{1}{\epsilon_0} \frac{H|_{k+\frac{1}{2}}^{n+\frac{1}{2}} - H|_{k-\frac{1}{2}}^{n+\frac{1}{2}}}{\Delta z} - \frac{1}{\epsilon_0} J|_k^{n+\frac{1}{2}}, \quad (11)$$

$$\frac{J|_k^{n+\frac{1}{2}} - J|_k^{n-\frac{1}{2}}}{\Delta t} = \epsilon_0 \omega_p^2|_k^n E|_k^n + \frac{j\omega_b}{2} (J|_k^{n+\frac{1}{2}} + J|_k^{n-\frac{1}{2}}). \quad (12)$$

These equations reduce to

$$E|_k^{n+1} = E|_k^n - \frac{\Delta t}{\epsilon_o \Delta z} \left(H|_{k+\frac{1}{2}}^{n+\frac{1}{2}} - H|_{k-\frac{1}{2}}^{n+\frac{1}{2}} \right) - \frac{\Delta t}{\epsilon_o} J|_k^{n+\frac{1}{2}}, \quad (13)$$

$$H|_{k+\frac{1}{2}}^{n+\frac{1}{2}} = H|_{k+\frac{1}{2}}^{n-\frac{1}{2}} - \frac{\Delta t}{\mu_o \Delta z} \left(E|_{k+1}^n - E|_k^n \right), \quad (14)$$

$$J|_k^{n+\frac{1}{2}} = \frac{1 + j\omega_b \Delta t / 2}{1 - j\omega_b \Delta t / 2} J|_k^{n-\frac{1}{2}} + \frac{\Delta t \epsilon_o}{1 - j\omega_b \Delta t / 2} \omega_p^2|_k^n E|_k^n. \quad (15)$$

Initial conditions are given at $n = 1/2$ for J and H and $n = 0$ for E .

2.4 Spectrum Analysis using an Enhanced FFT

A spectrum analysis is a useful tool to extract information on signals. Usually a Fast Fourier Transform (FFT) is used to compute the scattering coefficients in the scattered fields when an electromagnetic wave is propagating in different media [8]. A pulsed incident wave is assumed and its power spectrum or amplitude spectrum is computed. After scattering takes place, the power spectrum of the scattered fields is obtained and the ratio of the two spectra gives the scattering coefficients as a function of frequency. This method allows us to find the frequency response over a wide range. However, the frequency accuracy is limited to the sampling frequency that is half the inverse of the sampling rate. We may assume that the frequency of a given mode is likely to lie between two adjacent frequencies determined by the FFT analysis. Therefore, the maximum error in the frequency estimation is half the frequency spacing. This frequency error may not be serious for the modes whose amplitudes are large enough. However, small amplitude modes can be buried or undetectable due to the errors of poor frequency estimations. This will result in misinterpretation of the results. In

order to remedy this problem, we need to estimate accurately the frequencies in the signals.

Let s be a signal with N samples.

$$s_n = s(t_n), \quad n = 1, 2, \dots, N. \quad (16)$$

s_n is assumed to be written as

$$s_n = \sum_{m=1}^M A_m e^{2\pi i f_m t_n}. \quad (17)$$

where M is the number of modes, A_m is the amplitude, and f_m is the frequency of a mode. Let FFT be a fast Fourier transform operator given by:

$$s_k = FFT(s) = \frac{1}{N} \sum_{n=1}^N s_n e^{-2\pi i (n-1)(k-1)/N}. \quad (18)$$

Our object is to find A_m and f_m as accurately as possible. We may think of a least square method:

$$SSE = \sum_{n=1}^N \left| s_n - \sum_{m=1}^M A_m e^{2\pi i f_m t_n} \right|^2. \quad (19)$$

However, this equation is nonlinear in A_m and f_m and therefore is not easy to handle.

The authors have used the following procedures to find these parameters accurately:

Step 1 Let $A_m = 0$ for $m = 1, 2, \dots, M$.

Step 2 Repeat Step 3 to 5 for $m = 1, 2, \dots, M$

Step 3
$$\hat{s}_n = s_n - \sum_{l=1, l \neq m}^M A_l e^{2\pi i f_l t_n} \quad \text{for } n = 1, 2, \dots, N.$$

Step 4 Choose the frequency that gives the maximum amplitude by the $FFT(\hat{s}_n)$ and call it f_m .

Step 5 Accurately find the frequency by maximizing $|A_m|$ given by (20) in the neighborhood of the frequency f_m using an optimization technique available in MATLAB as *fmin*.

$$A_m = \frac{1}{N} \sum_{n=1}^N \hat{s}_n e^{-2\pi j f_m t_n}, \quad (20)$$

Step 6 Repeat Step 2 to Step 5 if the following condition is not satisfied:

$$\sum_{n=1}^N \left| s_n - \sum_{l=1}^M A_l e^{2\pi j f_l t_n} \right|^2 < tolerance. \quad (21)$$

This procedure eliminates the mutual interference between two adjacent components and accurately finds frequencies and amplitudes. Figures 2 and 3 are examples of the signal analysis by the above procedure. Figure 2 shows the real and imaginary parts of a signal $s(t)$. Figure 3 shows the power spectral density of $s(t)$. The broken line is obtained by an ordinary FFT method [8]. This reveals two distinct peaks and two small peaks. The solid line is obtained by the new method and shows four distinct peaks. For the strong modes there exist small differences in frequencies and amplitudes between the two methods. For the weakest mode, the difference between the two methods is huge, about 40dB, which means the conventional method may not produce accurate result for the weak signal. In this figure, the residual signal by the new method is below -100dB, which assures the accuracy of the new method. This method has a slow convergence when two frequencies are very close.

Note that we need to use a complex signal to distinguish reflected waves from transmitted waves. However the problems under discussion generate complex time series.

3 Unbounded Isotropic Plasma

3.1 Simulation of an Unbounded Isotropic Plasma

Simulation of an unbounded problem by FD-TD requires a special treatment since an infinite space is taken into consideration. For a space-invariant time-varying medium, the simulation can be simplified by noting that the wavenumber is conserved during a temporal change of the plasma medium [9]. This implies that the wavelength λ of the waves in the plasma medium remains the same in the entire procedure. Hence the waves have the following property:

$$E(t, z) = E(t, z + \lambda), \quad (22)$$

$$H(t, z) = H(t, z + \lambda), \quad (23)$$

$$J(t, z) = J(t, z + \lambda). \quad (24)$$

Therefore, we choose λ as the size of the spatial domain. As a result,

$$E|_K^n = E|_0^n, \quad (25)$$

$$H|_{\frac{1}{2}}^{n+\frac{1}{2}} = H|_{K+\frac{1}{2}}^{n+\frac{1}{2}}. \quad (26)$$

The computation molecules (13) and (14) at both boundaries will be given as

$$E|_1^{n+1} = E|_1^n - \frac{\Delta t}{\epsilon_o \Delta z} \left(H|_{1+\frac{1}{2}}^{n+\frac{1}{2}} - H|_{K-\frac{1}{2}}^{n+\frac{1}{2}} \right) - \frac{\Delta t}{\epsilon_o} J|_1^{n+\frac{1}{2}}, \quad (27)$$

$$H|_{K+\frac{1}{2}}^{n+\frac{1}{2}} = H|_{K+\frac{1}{2}}^{n-\frac{1}{2}} - \frac{\Delta t}{\mu_o \Delta z} (E|_1^n - E|_K^n). \quad (28)$$

3.2 Sudden Creation

It is assumed that the incident wave (source wave) is propagating in free space in the positive z direction with the frequency ω_0 :

$$E = e^{j(\omega_0 t - k_0 z)}, \quad (29)$$

$$H = e^{j(\omega_0 t - k_0 z)}, \quad (30)$$

$$J = 0, \quad (31)$$

where $k_0 = \omega_0 / c$. To simplify the computation we may assume $c = \epsilon_0 = \mu_0 = 1$. For $t < 0$, the entire space is considered to be free space and at $t = 0$, the entire space is assumed to be converted into a plasma medium with the plasma frequency ω_p . By the sudden creation of the plasma medium, new waves are generated [7] and their properties are summarized in Table 1.

Table 1 Summary of Frequencies and amplitudes for the sudden switching case

MODE	Initial Values	Mode 1	Mode 2	Mode 3
Frequency	ω_0	$\omega_1 = +\sqrt{\omega_0^2 + \omega_p^2}$	$\omega_2 = -\sqrt{\omega_0^2 + \omega_p^2}$	$\omega_3 = 0$
E	1	$E_1 = \frac{\omega_1 + \omega_0}{2\omega_1}$	$E_2 = \frac{\omega_1 - \omega_0}{2\omega_1}$	$E_3 = 0$
H	1	$H_1 = \frac{\omega_0}{\omega_1} \frac{\omega_1 + \omega_0}{2\omega_1}$	$H_2 = -\frac{\omega_0}{\omega_1} \frac{\omega_1 - \omega_0}{2\omega_1}$	$H_3 = \frac{\omega_p^2}{\omega_0^2 + \omega_p^2}$
J	0	$J_1 = -j \frac{\omega_p^2}{\omega_1} \frac{\omega_1 + \omega_0}{2\omega_1}$	$J_2 = j \frac{\omega_p^2}{\omega_1} \frac{\omega_1 - \omega_0}{2\omega_1}$	$J_3 = j \frac{\omega_0 \omega_p^2}{\omega_0^2 + \omega_p^2}$

In the FD-TD simulation, we also assume that $\omega_0 = 1$ for convenience. The FD-TD results are shown in Figures 4-7. Both frequencies and amplitudes are well matched.

3.3 Slow Creation

The plasma frequency is slowly varied from 0 to a certain value. Generally an exact solution to this slowly-varying plasma creation problem does not exist. However, the WKB method can be used to obtain the amplitudes of the new waves. We assumed an exponential plasma profile for the simulation:

$$\omega_p^2(t) = \omega_{p0}^2 (1 - e^{-t/T_r}). \quad (32)$$

where T_r is the rise time. In this profile, a WKB solution for the electric fields is given by [10]

$$E_1 = \left(1 - j \frac{\omega_{p0}^2}{8T_r \omega_0^3} \left(\frac{\omega_0^2}{\omega_0^2 + \omega_p^2(t)} \right) \right)^{1/4}, \quad (33)$$

$$E_2 = j \frac{\omega_{p0}^2}{8T_r \omega_0^3} \left(\frac{\omega_0^2}{\omega_0^2 + \omega_p^2(t)} \right)^{1/4}. \quad (34)$$

The results are shown in Figs. 8 and 9. As expected, WKB solutions match with the FD-TD solution for large T_r . However we see in Fig. 9 a deviation in the curves for T_r larger than 70. This is because the FD-TD simulation has been obtained to a certain accuracy. When this accuracy is improved, they match well.

3.4 Rapid Creation – Linear Profile

When the switching action is fast, the WKB method may not be suitable. Also exact solutions for the fast switching profiles do not exist in general. A different approach has been used to handle this kind of problem [6]. A Green's function method

gives an approximate solution by using a perturbation technique. The difference function between the actual profile and a reference profile is used to generate a perturbation series. The reference profile must have an exact solution. By its nature, this method has two fundamental limitations. One is the second order approximation can become very complicated. The other is that it is hard to determine its range of validity. By using the FD-TD method, we can easily verify their accuracy and validity ranges.

A linear profile as shown in Fig. 10 is an example of a problem having an exact solution that can be used to test the validity of the three methods, i.e., WKB, Green's function method, and FD-TD. Figures 11 and 12 show such comparisons. The FD-TD and theoretical results agree in the wide range of rise time of the plasma profile. Green's function solutions are given in [6] and (33) and (34) are used for the WKB method. It is seen that for the fast profile (T_r is small) the Green's function method is valid while for the slow profile (T_r is large) the WKB method is valid.

3.5 Rapid Creation – Hump Profile

A hump profile has been used to show applicability of the Green's function method [6] because it could handle complicated profiles. The FD-TD solutions are compared with the Green's function method in Figs. 13 and 14. Figure 13a shows the sketch of the hump file.

3.6 Periodic Plasma Slab

Interaction of an electromagnetic wave with a rapidly created spatially periodic plasma was studied by S. P. Kuo and James Faith [11]. It can be extended to the magnetized plasma slab.

In a periodic isotropic plasma slab, the wave can be represented as:

$$E(z) = \begin{cases} A \exp[-jkz] + B \exp[+jkz], & -l < z < l \\ C \exp[-jk\eta(z-l)] + D \exp[+jk\eta(z-l)] & l < z < l+d \end{cases} \quad (35)$$

where η is the index of refraction, L is the separation between two adjacent slabs, d is the width of the slab, and $l = (L-d)/2$. Due to the periodicity, the wave has to satisfy the Bloch wave condition [11]-[12]:

$$E(z) = e^{j\beta L} E(z+L) \quad (36)$$

where β is the propagation constant.

Applying boundary conditions at $z = l$ and $z = -l$ and (36), the dispersion relation can be obtained as [11]:

$$\cos \beta L = \cos k\eta d \cos 2kl - \frac{1}{2} \left(\eta + \frac{1}{\eta} \right) \sin k\eta d \sin 2kl, \quad (37)$$

where

$$\begin{aligned} \beta L &= k_0 L + 2m\pi \\ \frac{\beta}{k_0} &= 1 + \frac{2m\pi}{k_0 L} \end{aligned} \quad (38)$$

Based on this relation, we can construct the electric fields for $t > 0$ as

$$E(z, t) = \sum_{m=-\infty}^{m=+\infty} \left[A_m e^{j(\omega_m t + \beta_m z)} + B_m e^{j(\omega_m t - \beta_m z)} \right]. \quad (39)$$

It is noted from (36) that for any β we have the following condition:

$$e^{-j\beta_m L} = e^{-j(k_0 + \frac{2\pi m}{L})L} = e^{-j(k_0 L + 2\pi m)} = e^{-jk_0 L} = \text{const.} \quad (40)$$

Hence we can simulate the problem easily without having infinite cells, but one cell with a free space and a plasma slab. In the Yee's cell, we may write FD-TD equations as

$$E|_{K+1}^n = E|_1^n e^{-jk_0 L}, \quad (41)$$

$$H|_0^{n+\frac{1}{2}} = H|_K^{n+\frac{1}{2}} e^{jk_0 L}. \quad (42)$$

These relations as well as (37) hold for magnetized plasma media where η is given by

$$\eta = \sqrt{1 - \frac{\omega_{p0}^2}{\omega(\omega - \omega_b)}}. \quad (43)$$

In free space, $k_m = |\omega_m|/c$. Therefore, (39) can be written as

$$E(z, t) = \sum_{m=-\infty}^{m=+\infty} e^{j\omega_m t} [A_m e^{-jk_m z/c} + B_m e^{jk_m z/c}] \quad (44)$$

In plasma, $|\omega_m| = \eta k_m c$ and (39) becomes

$$E(z, t) = \sum_{m=-\infty}^{m=+\infty} e^{j\omega_m t} [C_m e^{-jk_m \eta_m z} + D_m e^{jk_m \eta_m z}] \quad (45)$$

Work is in progress to extend the results obtained by Kuo [11] to the case of a switched spatially periodic magnetized plasma medium with particular emphasis on the effect of the collision frequency and the mode amplitudes.

4 Plasma Slab Problem

4.1 PML

The effect of spatial boundaries may be studied by considering the slab problem. It is an one dimensional problem, however we need to define the appropriate outer boundary for the truncating the lattice [3] and thus limit the size of the field computation domain. At the boundaries of the lattice a suitable boundary condition must be used to simulate its extension to infinite. The waves propagating outward must be terminated at the boundaries without any reflections. Such a boundary condition is called absorbing

boundary condition (ABC). The most recent advance in material-based ABC's was put forward by Berenger [2]. His ABC, termed the perfectly matched layer (PML) absorbing boundary condition, appears to yield a major improvement in the reduction of boundary reflections compared to any ABC proposed previously.

4.2 FD-TD Simulation of Switched Plasma Slab

Using FD-TD algorithm and PML condition we simulated the frequency shifting property of a plasma slab and the result is in agreement with our analytical results obtained earlier for the case of sudden switching. Work is in progress for the case of an arbitrary profile of the plasma density in the slab.

5 Three Dimensional Resonator

5.1 Three Dimensional FD-TD for a Magnetoplasma with Collisions

The governing equations are given [7] by (1), (2), and (46),

$$\frac{d\mathbf{J}(\mathbf{r},t)}{dt} + \nu(\mathbf{r},t)\mathbf{J}(\mathbf{r},t) = \epsilon_0\omega_p^2(\mathbf{r},t)\mathbf{E}(\mathbf{r},t) + \boldsymbol{\omega}_b(\mathbf{r},t) \times \mathbf{J}(\mathbf{r},t). \quad (46)$$

where $\boldsymbol{\omega}_b$ the gyrofrequency and written in cartesian components as

$$\boldsymbol{\omega}_b = \omega_x \hat{x} + \omega_y \hat{y} + \omega_z \hat{z}. \quad (47)$$

In (46) ν is the collision frequency. The FD-TD equations by the Yee's formula are given by

$$\begin{aligned} \frac{\partial E_x}{\partial t} \Big|_{i+\frac{1}{2},j,k}^{n+\frac{1}{2}} &= \frac{1}{\Delta t} \left(E_x \Big|_{i+\frac{1}{2},j,k}^{n+1} - E_x \Big|_{i+\frac{1}{2},j,k}^n \right) = -\frac{1}{2\varepsilon_0} \left(J_x \Big|_{i+1,j,k}^{n+\frac{1}{2}} + J_x \Big|_{i,j,k}^{n+\frac{1}{2}} \right) + \\ &\frac{1}{\varepsilon_0} \left[\frac{1}{\Delta y} \left(H_z \Big|_{i+\frac{1}{2},j+\frac{1}{2},k}^{n+\frac{1}{2}} - H_z \Big|_{i+\frac{1}{2},j-\frac{1}{2},k}^{n+\frac{1}{2}} \right) - \frac{1}{\Delta z} \left(H_y \Big|_{i+\frac{1}{2},j,k+\frac{1}{2}}^{n+\frac{1}{2}} - H_y \Big|_{i+\frac{1}{2},j,k-\frac{1}{2}}^{n+\frac{1}{2}} \right) \right] \end{aligned} \quad (48)$$

$$\begin{aligned} \frac{\partial E_y}{\partial t} \Big|_{i,j+\frac{1}{2},k}^{n+\frac{1}{2}} &= \frac{1}{\Delta t} \left(E_y \Big|_{i,j+\frac{1}{2},k}^{n+1} - E_y \Big|_{i,j+\frac{1}{2},k}^n \right) = -\frac{1}{2\varepsilon_0} \left(J_y \Big|_{i,j+1,k}^{n+\frac{1}{2}} + J_y \Big|_{i,j,k}^{n+\frac{1}{2}} \right) + \\ &\frac{1}{\varepsilon_0} \left[\frac{1}{\Delta z} \left(H_x \Big|_{i,j+\frac{1}{2},k+\frac{1}{2}}^{n+\frac{1}{2}} - H_x \Big|_{i,j+\frac{1}{2},k-\frac{1}{2}}^{n+\frac{1}{2}} \right) - \frac{1}{\Delta x} \left(H_z \Big|_{i+\frac{1}{2},j+\frac{1}{2},k}^{n+\frac{1}{2}} - H_z \Big|_{i-\frac{1}{2},j+\frac{1}{2},k}^{n+\frac{1}{2}} \right) \right] \end{aligned} \quad (49)$$

$$\begin{aligned} \frac{\partial E_z}{\partial t} \Big|_{i,j,k+\frac{1}{2}}^{n+\frac{1}{2}} &= \frac{1}{\Delta t} \left(E_z \Big|_{i,j,k+\frac{1}{2}}^{n+1} - E_z \Big|_{i,j,k+\frac{1}{2}}^n \right) = -\frac{1}{2\varepsilon_0} \left(J_z \Big|_{i,j,k+1}^{n+\frac{1}{2}} + J_z \Big|_{i,j,k}^{n+\frac{1}{2}} \right) + \\ &\frac{1}{\varepsilon_0} \left[\frac{1}{\Delta x} \left(H_y \Big|_{i+\frac{1}{2},j,k+\frac{1}{2}}^{n+\frac{1}{2}} - H_y \Big|_{i-\frac{1}{2},j,k+\frac{1}{2}}^{n+\frac{1}{2}} \right) - \frac{1}{\Delta y} \left(H_x \Big|_{i,j+\frac{1}{2},k+\frac{1}{2}}^{n+\frac{1}{2}} - H_x \Big|_{i,j-\frac{1}{2},k+\frac{1}{2}}^{n+\frac{1}{2}} \right) \right] \end{aligned} \quad (50)$$

$$\begin{aligned} \frac{\partial H_x}{\partial t} \Big|_{i,j+\frac{1}{2},k+\frac{1}{2}}^n &= \frac{1}{\Delta t} \left(H_x \Big|_{i,j+\frac{1}{2},k+\frac{1}{2}}^{n+\frac{1}{2}} - H_x \Big|_{i,j+\frac{1}{2},k+\frac{1}{2}}^{n-\frac{1}{2}} \right) = \\ &-\frac{1}{\mu_0} \left[\frac{1}{\Delta y} \left(E_z \Big|_{i,j+1,k+\frac{1}{2}}^n - E_z \Big|_{i,j,k+\frac{1}{2}}^n \right) - \frac{1}{\Delta z} \left(E_y \Big|_{i,j+\frac{1}{2},k+1}^n - E_y \Big|_{i,j+\frac{1}{2},k}^n \right) \right] \end{aligned} \quad (51)$$

$$\begin{aligned} \frac{\partial H_y}{\partial t} \Big|_{i+\frac{1}{2},j,k+\frac{1}{2}}^n &= \frac{1}{\Delta t} \left(H_y \Big|_{i+\frac{1}{2},j,k+\frac{1}{2}}^{n+\frac{1}{2}} - H_y \Big|_{i+\frac{1}{2},j,k+\frac{1}{2}}^{n-\frac{1}{2}} \right) = \\ &-\frac{1}{\mu_0} \left[\frac{1}{\Delta z} \left(E_x \Big|_{i+\frac{1}{2},j,k+1}^n - E_x \Big|_{i+\frac{1}{2},j,k}^n \right) - \frac{1}{\Delta x} \left(E_z \Big|_{i+1,j,k+\frac{1}{2}}^n - E_z \Big|_{i,j,k+\frac{1}{2}}^n \right) \right] \end{aligned} \quad (52)$$

$$\begin{aligned} \frac{\partial H_z}{\partial t} \Big|_{i+\frac{1}{2},j+\frac{1}{2},k}^n &= \frac{1}{\Delta t} \left(H_z \Big|_{i+\frac{1}{2},j+\frac{1}{2},k}^{n+\frac{1}{2}} - H_z \Big|_{i+\frac{1}{2},j+\frac{1}{2},k}^{n-\frac{1}{2}} \right) = \\ &-\frac{1}{\mu_0} \left[\frac{1}{\Delta x} \left(E_y \Big|_{i+1,j+\frac{1}{2},k}^n - E_y \Big|_{i,j+\frac{1}{2},k}^n \right) - \frac{1}{\Delta y} \left(E_x \Big|_{i+\frac{1}{2},j+1,k}^n - E_x \Big|_{i+\frac{1}{2},j,k}^n \right) \right] \end{aligned} \quad (53)$$

$$\begin{aligned} \frac{dJ_x}{dt} \Big|_{i,j,k}^n + \nu J_x \Big|_{i,j,k}^n &= \frac{1}{\Delta t} \left(J_x \Big|_{i,j,k}^{n+\frac{1}{2}} - J_x \Big|_{i,j,k}^{n-\frac{1}{2}} \right) + \frac{\nu}{2} \left(J_x \Big|_{i,j,k}^{n+\frac{1}{2}} + J_x \Big|_{i,j,k}^{n-\frac{1}{2}} \right) \\ &= \frac{\varepsilon_0 \omega_p^2}{2} \left(E_x \Big|_{i+\frac{1}{2},j,k}^n + E_x \Big|_{i-\frac{1}{2},j,k}^n \right) + \frac{\omega_y}{2} \left(J_z \Big|_{i,j,k}^{n+\frac{1}{2}} + J_z \Big|_{i,j,k}^{n-\frac{1}{2}} \right) - \frac{\omega_z}{2} \left(J_y \Big|_{i,j,k}^{n+\frac{1}{2}} + J_y \Big|_{i,j,k}^{n-\frac{1}{2}} \right) \end{aligned} \quad (54)$$

$$\begin{aligned} \frac{dJ_y}{dt} \Big|_{i,j,k}^n + \nu J_y \Big|_{i,j,k}^n &= \frac{1}{\Delta t} \left(J_y \Big|_{i,j,k}^{n+\frac{1}{2}} - J_y \Big|_{i,j,k}^{n-\frac{1}{2}} \right) + \frac{\nu}{2} \left(J_y \Big|_{i,j,k}^{n+\frac{1}{2}} + J_y \Big|_{i,j,k}^{n-\frac{1}{2}} \right) \\ &= \frac{\epsilon_0 \omega_p^2}{2} \left(E_y \Big|_{i,j+\frac{1}{2},k}^n + E_y \Big|_{i,j-\frac{1}{2},k}^n \right) + \frac{\omega_z}{2} \left(J_x \Big|_{i,j,k}^{n+\frac{1}{2}} + J_x \Big|_{i,j,k}^{n-\frac{1}{2}} \right) - \frac{\omega_x}{2} \left(J_z \Big|_{i,j,k}^{n+\frac{1}{2}} + J_z \Big|_{i,j,k}^{n-\frac{1}{2}} \right) \end{aligned} \quad (55)$$

$$\begin{aligned} \frac{dJ_z}{dt} \Big|_{i,j,k}^n + \nu J_z \Big|_{i,j,k}^n &= \frac{1}{\Delta t} \left(J_z \Big|_{i,j,k}^{n+\frac{1}{2}} - J_z \Big|_{i,j,k}^{n-\frac{1}{2}} \right) + \frac{\nu}{2} \left(J_z \Big|_{i,j,k}^{n+\frac{1}{2}} + J_z \Big|_{i,j,k}^{n-\frac{1}{2}} \right) \\ &= \frac{\epsilon_0 \omega_p^2}{2} \left(E_z \Big|_{i,j,k+\frac{1}{2}}^n + E_z \Big|_{i,j,k-\frac{1}{2}}^n \right) + \frac{\omega_x}{2} \left(J_y \Big|_{i,j,k}^{n+\frac{1}{2}} + J_y \Big|_{i,j,k}^{n-\frac{1}{2}} \right) - \frac{\omega_y}{2} \left(J_x \Big|_{i,j,k}^{n+\frac{1}{2}} + J_x \Big|_{i,j,k}^{n-\frac{1}{2}} \right). \end{aligned} \quad (56)$$

In Equations (54)-(56), $J_x \Big|_{i,j,k}^{n+\frac{1}{2}}, J_y \Big|_{i,j,k}^{n+\frac{1}{2}}, J_z \Big|_{i,j,k}^{n+\frac{1}{2}}$ can not be expressed in terms of the values of previous time steps but become simultaneous equations that we must avoid. We can avoid this by introducing a matrix equation. After simplifying and combining (54)-(56) we can construct a matrix equation as

$$\begin{aligned} \begin{bmatrix} \frac{1}{\Delta t} + \frac{\nu}{2} & \frac{\omega_z}{2} & -\frac{\omega_y}{2} \\ -\frac{\omega_z}{2} & \frac{1}{\Delta t} + \frac{\nu}{2} & \frac{\omega_x}{2} \\ \frac{\omega_y}{2} & -\frac{\omega_x}{2} & \frac{1}{\Delta t} + \frac{\nu}{2} \end{bmatrix} \begin{bmatrix} J_x \Big|_{i,j,k}^{n+\frac{1}{2}} \\ J_y \Big|_{i,j,k}^{n+\frac{1}{2}} \\ J_z \Big|_{i,j,k}^{n+\frac{1}{2}} \end{bmatrix} &= \\ \begin{bmatrix} \frac{1}{\Delta t} - \frac{\nu}{2} & -\frac{\omega_z}{2} & \frac{\omega_y}{2} \\ \frac{\omega_z}{2} & \frac{1}{\Delta t} - \frac{\nu}{2} & -\frac{\omega_x}{2} \\ -\frac{\omega_y}{2} & \frac{\omega_x}{2} & \frac{1}{\Delta t} - \frac{\nu}{2} \end{bmatrix} \begin{bmatrix} J_x \Big|_{i,j,k}^{n-\frac{1}{2}} \\ J_y \Big|_{i,j,k}^{n-\frac{1}{2}} \\ J_z \Big|_{i,j,k}^{n-\frac{1}{2}} \end{bmatrix} &+ \frac{\epsilon_0 \omega_p^2}{2} \begin{bmatrix} E_x \Big|_{i+\frac{1}{2},j,k}^n + E_x \Big|_{i-\frac{1}{2},j,k}^n \\ E_y \Big|_{i,j+\frac{1}{2},k}^n + E_y \Big|_{i,j-\frac{1}{2},k}^n \\ E_z \Big|_{i,j,k+\frac{1}{2}}^n + E_z \Big|_{i,j,k-\frac{1}{2}}^n \end{bmatrix}. \end{aligned} \quad (57)$$

In (57), $\nu, \omega_x, \omega_y, \omega_z$, and ω_p^2 are the values at the grid point $P \Big|_{i,j,k}^n$. The final FD-TD

equations for E and H follow:

$$H_x \Big|_{i,j+\frac{1}{2},k+\frac{1}{2}}^{n+\frac{1}{2}} = H_x \Big|_{i,j+\frac{1}{2},k+\frac{1}{2}}^{n-\frac{1}{2}} - \frac{\Delta t}{\mu_0 \Delta y} \left(E_z \Big|_{i,j+1,k+\frac{1}{2}}^n - E_z \Big|_{i,j,k+\frac{1}{2}}^n \right) + \frac{\Delta t}{\mu_0 \Delta z} \left(E_y \Big|_{i,j+\frac{1}{2},k+1}^n - E_y \Big|_{i,j+\frac{1}{2},k}^n \right) \quad (58)$$

$$H_y|_{i+\frac{1}{2},j,k+\frac{1}{2}}^{n+\frac{1}{2}} = H_y|_{i+\frac{1}{2},j,k+\frac{1}{2}}^{n-\frac{1}{2}} - \frac{\Delta t}{\mu_0 \Delta z} (E_x|_{i+\frac{1}{2},j,k+1}^n - E_x|_{i+\frac{1}{2},j,k}^n) + \frac{\Delta t}{\mu_0 \Delta x} (E_z|_{i+1,j,k+\frac{1}{2}}^n - E_z|_{i,j,k+\frac{1}{2}}^n) \quad (59)$$

$$H_z|_{i+\frac{1}{2},j+\frac{1}{2},k}^{n+\frac{1}{2}} = H_z|_{i+\frac{1}{2},j+\frac{1}{2},k}^{n-\frac{1}{2}} - \frac{\Delta t}{\mu_0 \Delta x} (E_y|_{i+1,j+\frac{1}{2},k}^n - E_y|_{i,j+\frac{1}{2},k}^n) + \frac{\Delta t}{\mu_0 \Delta y} (E_x|_{i+\frac{1}{2},j+1,k}^n - E_x|_{i+\frac{1}{2},j,k}^n) \quad (60)$$

$$\begin{aligned} E_x|_{i+\frac{1}{2},j,k}^{n+1} &= E_x|_{i+\frac{1}{2},j,k}^n - \frac{\Delta t}{2\epsilon_0} (J_x|_{i+1,j,k}^{n+\frac{1}{2}} + J_x|_{i,j,k}^{n+\frac{1}{2}}) + \\ &\frac{\Delta t}{\epsilon_0 \Delta y} (H_z|_{i+\frac{1}{2},j+\frac{1}{2},k}^{n+\frac{1}{2}} - H_z|_{i+\frac{1}{2},j-\frac{1}{2},k}^{n+\frac{1}{2}}) - \frac{\Delta t}{\epsilon_0 \Delta z} (H_y|_{i+\frac{1}{2},j,k+\frac{1}{2}}^{n+\frac{1}{2}} - H_y|_{i+\frac{1}{2},j,k-\frac{1}{2}}^{n+\frac{1}{2}}) \end{aligned} \quad (61)$$

$$\begin{aligned} E_y|_{i,j+\frac{1}{2},k}^{n+1} &= E_y|_{i,j+\frac{1}{2},k}^n - \frac{\Delta t}{2\epsilon_0} (J_y|_{i,j+1,k}^{n+\frac{1}{2}} + J_y|_{i,j,k}^{n+\frac{1}{2}}) + \\ &\frac{\Delta t}{\epsilon_0 \Delta z} (H_x|_{i,j+\frac{1}{2},k+\frac{1}{2}}^{n+\frac{1}{2}} - H_x|_{i,j+\frac{1}{2},k-\frac{1}{2}}^{n+\frac{1}{2}}) - \frac{\Delta t}{\epsilon_0 \Delta x} (H_z|_{i+\frac{1}{2},j+\frac{1}{2},k}^{n+\frac{1}{2}} - H_z|_{i-\frac{1}{2},j+\frac{1}{2},k}^{n+\frac{1}{2}}) \end{aligned} \quad (62)$$

$$\begin{aligned} E_z|_{i,j,k+\frac{1}{2}}^{n+1} &= E_z|_{i,j,k+\frac{1}{2}}^n - \frac{\Delta t}{2\epsilon_0} (J_z|_{i,j,k+1}^{n+\frac{1}{2}} + J_z|_{i,j,k}^{n+\frac{1}{2}}) + \\ &\frac{\Delta t}{\epsilon_0 \Delta x} (H_y|_{i+\frac{1}{2},j,k+\frac{1}{2}}^{n+\frac{1}{2}} - H_y|_{i-\frac{1}{2},j,k+\frac{1}{2}}^{n+\frac{1}{2}}) - \frac{\Delta t}{\epsilon_0 \Delta y} (H_x|_{i,j+\frac{1}{2},k+\frac{1}{2}}^{n+\frac{1}{2}} - H_x|_{i,j-\frac{1}{2},k+\frac{1}{2}}^{n+\frac{1}{2}}). \end{aligned} \quad (63)$$

5.2 Three dimension FD-TD Grid

To implement the FD-TD algorithm given by (57)-(63) in a rectangular resonator, we need to extend Fig. 1 to the three dimensional space. J can be placed in the center of the cubic unit cell of the Yee space lattice as shown in Fig. 15. Figure 16 shows two planes for visualizing the implementation of the boundary conditions. Assigning zero values to the field components at the boundaries automatically satisfy the boundary conditions on the walls of the rectangular resonator bounded by perfect conductors.

5.3 Numerical Stability

One important aspect of FD-TD algorithm is the optimum choice of the time step. Too large a time step will result in numerical instability. Figure 17 shows the maximum time step as a function of the final plasma frequency.

5.4 Magnetized Plasma in the Cavity

We are presently simulating the mode coupling when the plasma, in addition, is magnetized. A complete report will be published soon.

6 Conclusion

We have seen that the FD-TD method can easily simulate various problems and give very accurate solutions. Analyzing the solution by FD-TD has been done usually by FFT method that has its limitation of resolutions. A new analyzing tool is presented that can solve conventional limitations. It resolves several modes even if some of them have low amplitudes.

7 Reference

- [1] K. S. Yee, "Numerical solution of initial boundary value problems involving Maxwell's equations in isotropic media," *IEEE Trans. on Antennas Propagation*, vol. AP-14, pp. 302-307, May 1966.
- [2] Jean-Pierre Berenger, "A Perfectly Matched Layer for the Absorption of Electromagnetic Waves, *Journal of Computational Physics*, **114**, pp. 185-200, 1994.

- [3] Allen Taflove, *Computational Electrodynamics-The Finite-Difference Time-Domain Method*, Artech House, Boston, 1995.
- [4] Dikshitulu K. Kalluri, Venkata R. Coteti, and Andrew M. Sessler, "WKB Solution for Wave Propagation in a Time-Varying Magnetoplasma Medium: Longitudinal Propagation," *IEEE Trans. On Plasma Science*, vol. 21, no. 1, 1993.
- [5] Joo Hwa Lee and D. K. Kalluri, "Modification of an Electromagnetic Wave by a Time-varying Switched Magnetoplasma Medium: Transverse Propagation," *IEEE Transaction on Plasma Science*, Feb. 1998.
- [6] Tom T. Huang, Joo Hwa Lee, Dikshitulu K. Kalluri, and Keith M. Groves, "Wave Propagation in a Transient Plasma - Development of a Green's Function," *IEEE Trans. On Plasma Science*, Feb. 1998.
- [7] D. K. Kalluri, *Electromagnetics of Complex Media*, Boca Raton, CRC Press, to be published in Aug., 1998.
- [8] Karl S. Kunz and Raymond J. Luebbers, *The Finite Difference Time Domain Method for Electromagnetics*, CRC, Boca Raton, 1993.
- [9] C. L. Jiang, *IEEE Transaction on Antennas Propagation*, vol. AP-23, pp. 83-, 1975.
- [10] Joo Hwa Lee, "Wave Propagation in a Time-Varying Switched magnetoplasma Medium: Transverse Propagation," *MS-Thesis, University of Massachusetts Lowell*, 1994.
- [11] S. P. Kuo and James Faith, "Interaction of an electromagnetic wave with a rapidly created spatially periodic plasma," *Physical Review E*, vol. 56, no 2, pp. 1-8, 1997.
- [12] Pochi Yeh, *Optical Waves in Layered Media*, John Wiley & Sons, New York, 1988.

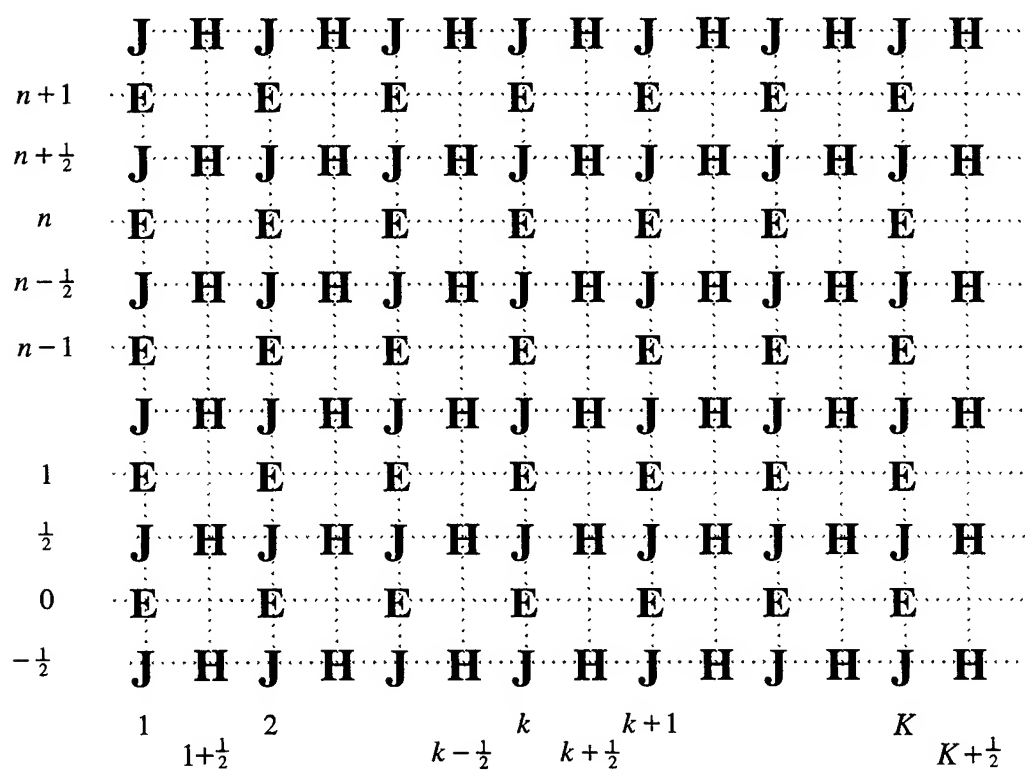


Figure 1. Position of E , H , and J for one dimensional problem.

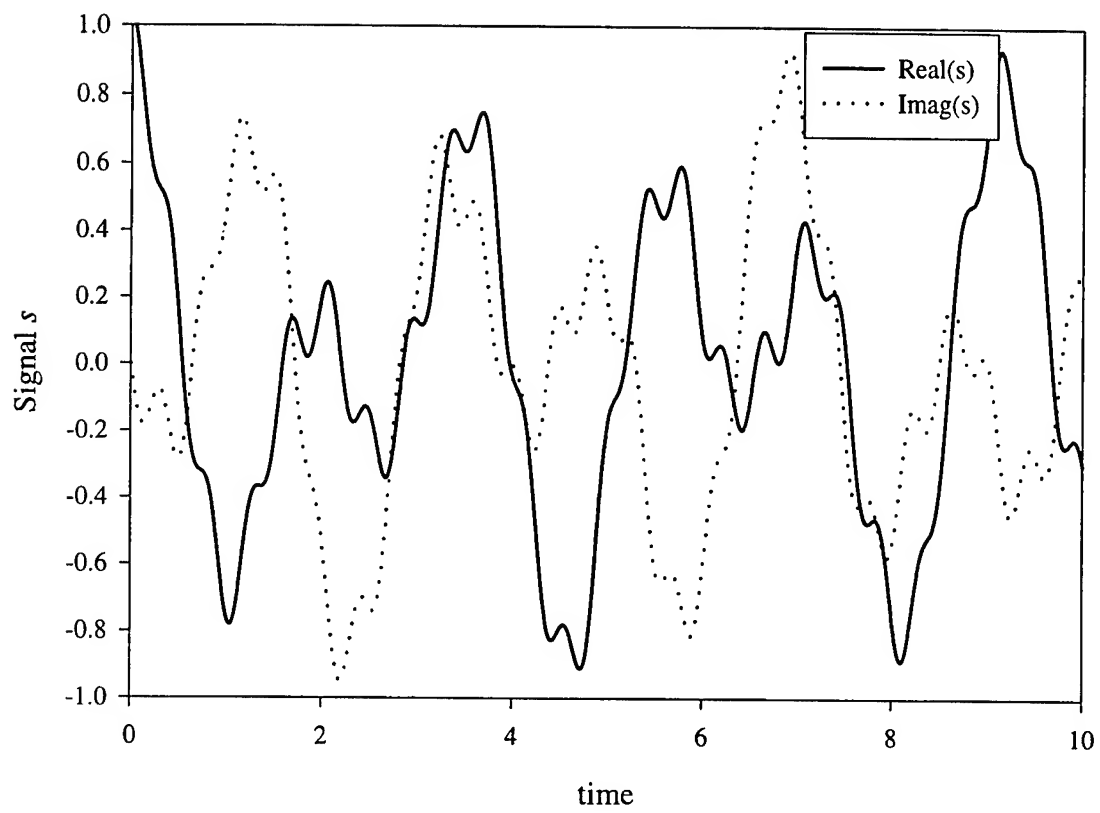


Figure 2. Complex signal in time.

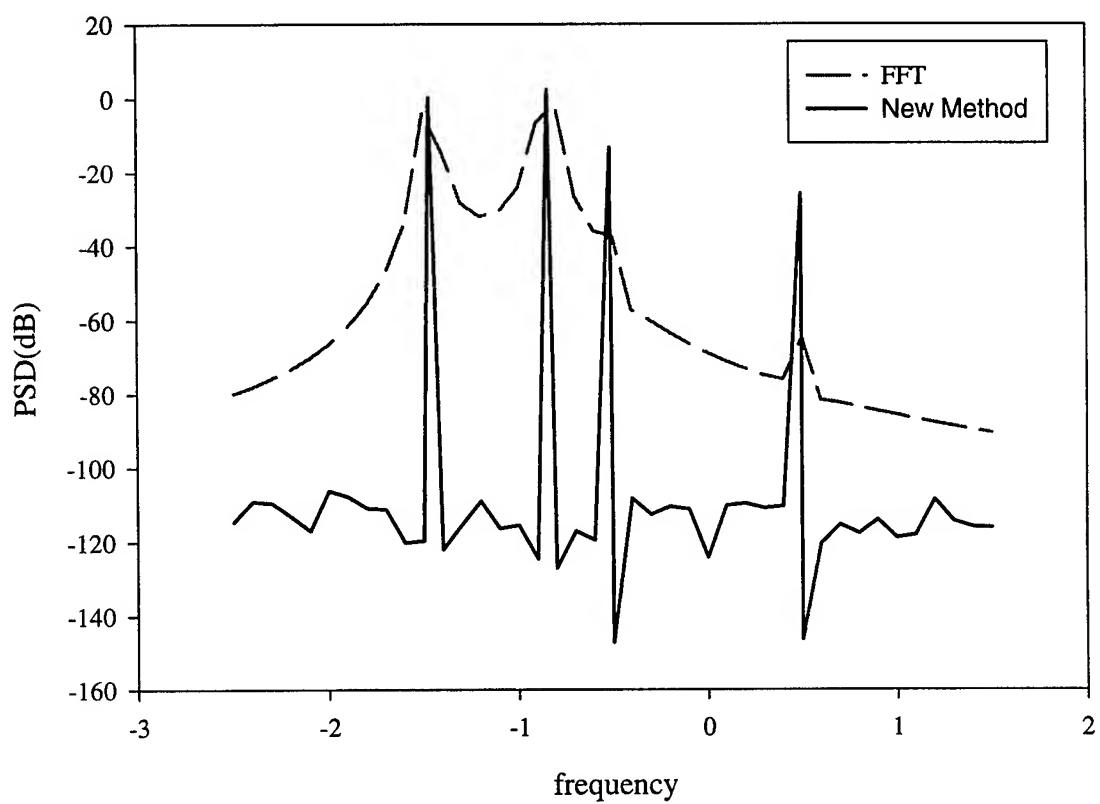


Figure 3. Power Spectral Density.

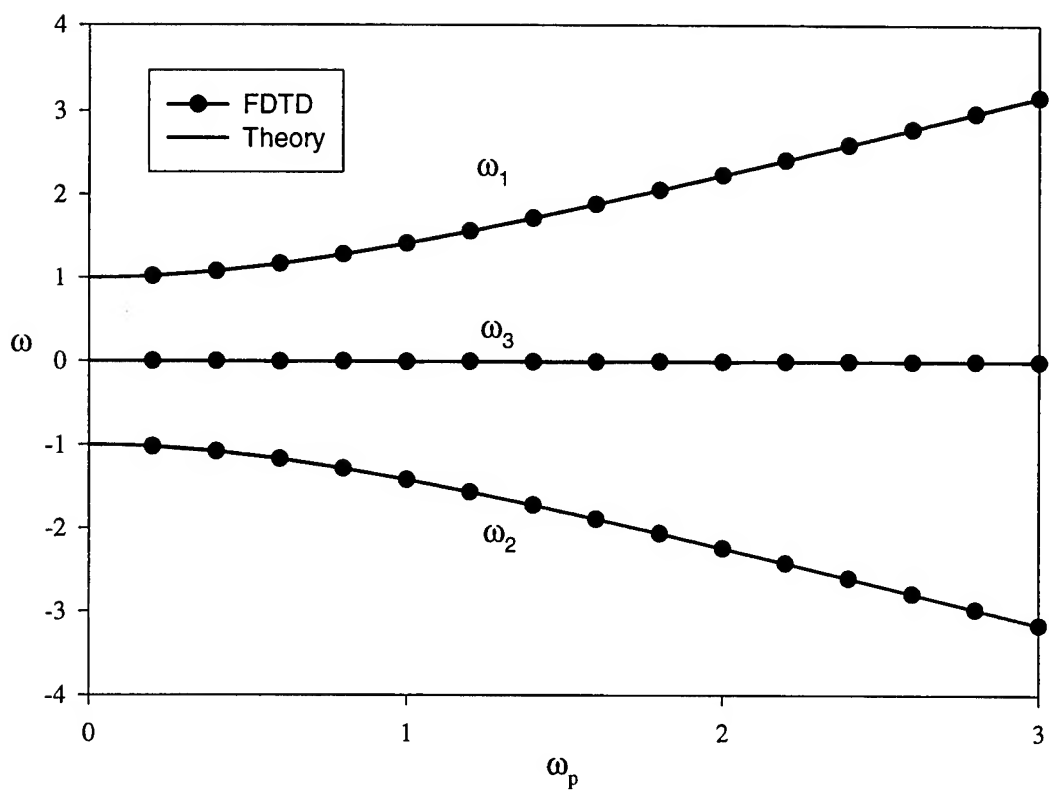


Figure 4. New frequencies after creation of the plasma.

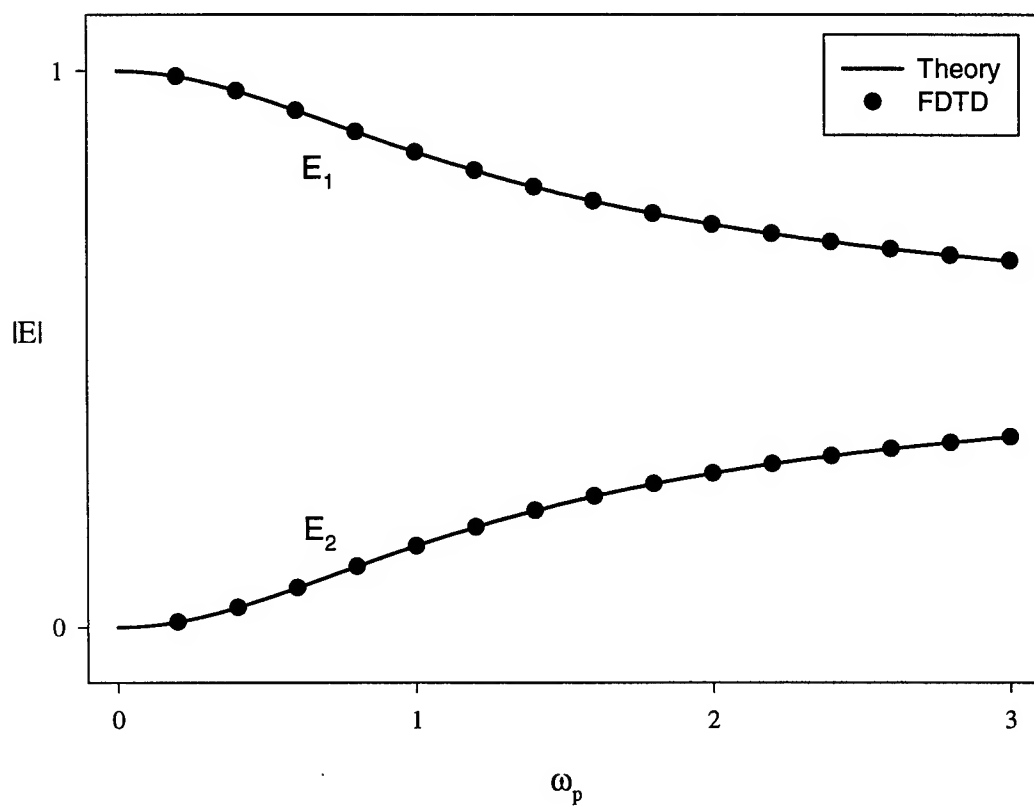


Figure 5. Electric fields vs. plasma frequency for the sudden switching case.

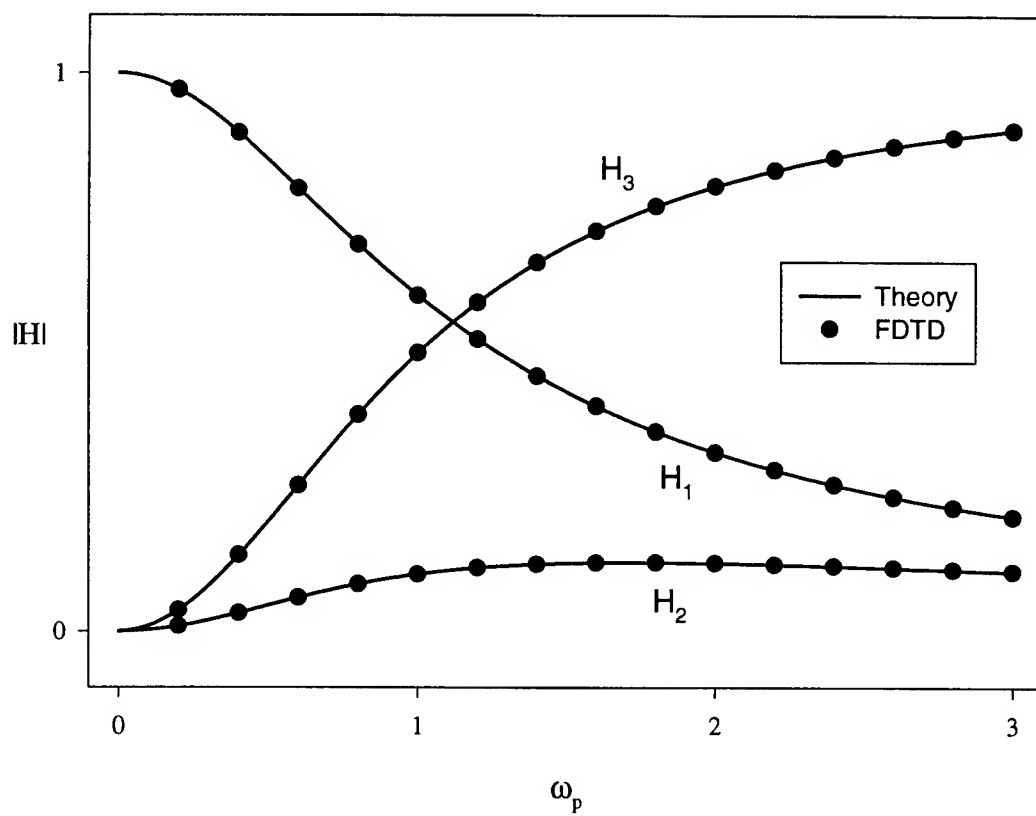


Figure 6. Magnetic fields vs. plasma frequency for the sudden switching case.

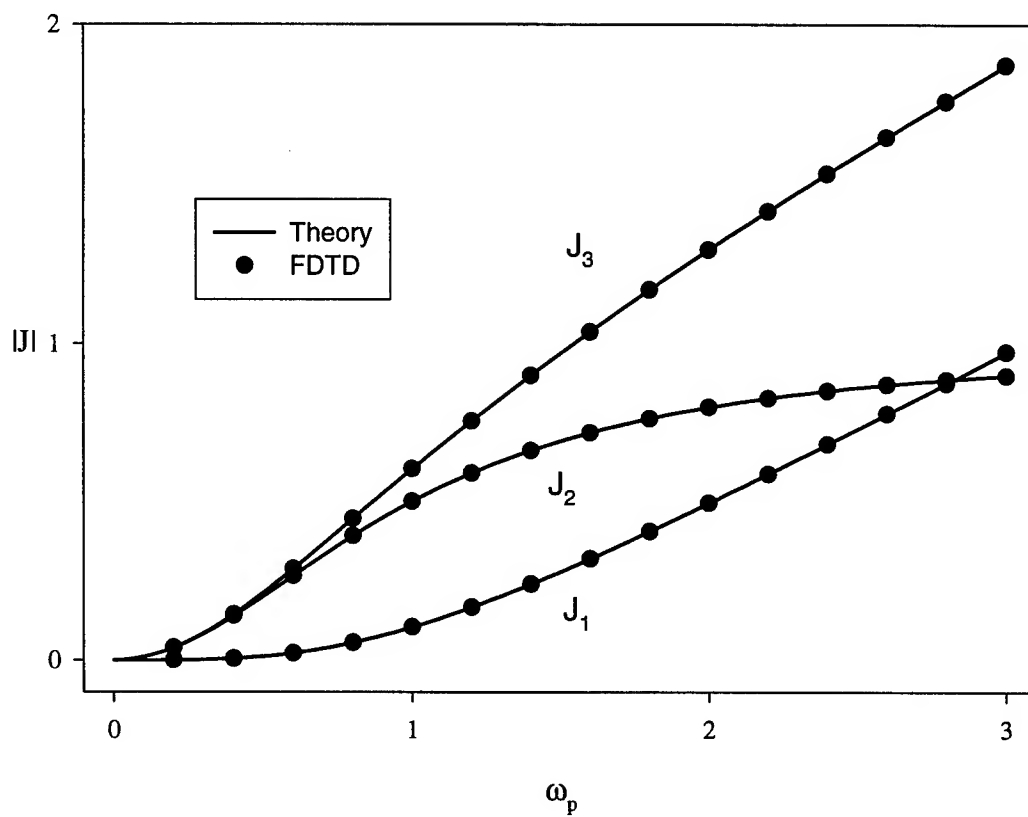


Figure 7. Current densities vs. plasma frequency for the sudden switching case.

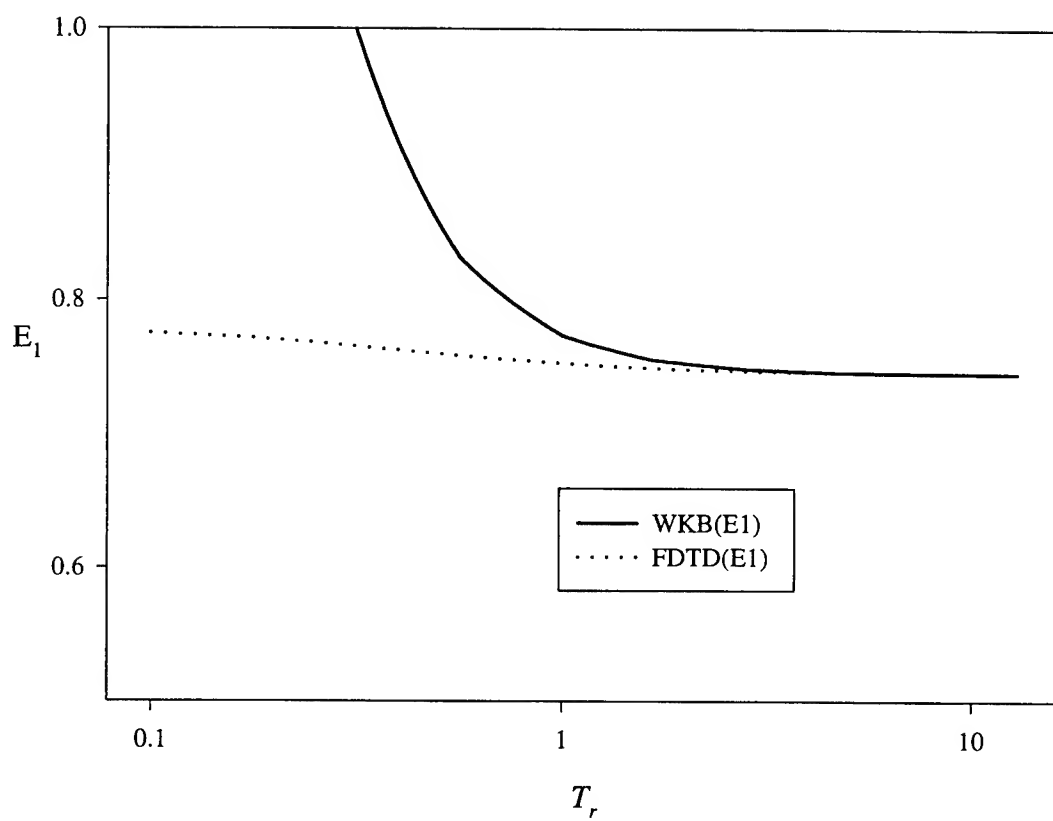


Figure 8. Comparison of transmitted electric fields for arbitrary rise time.

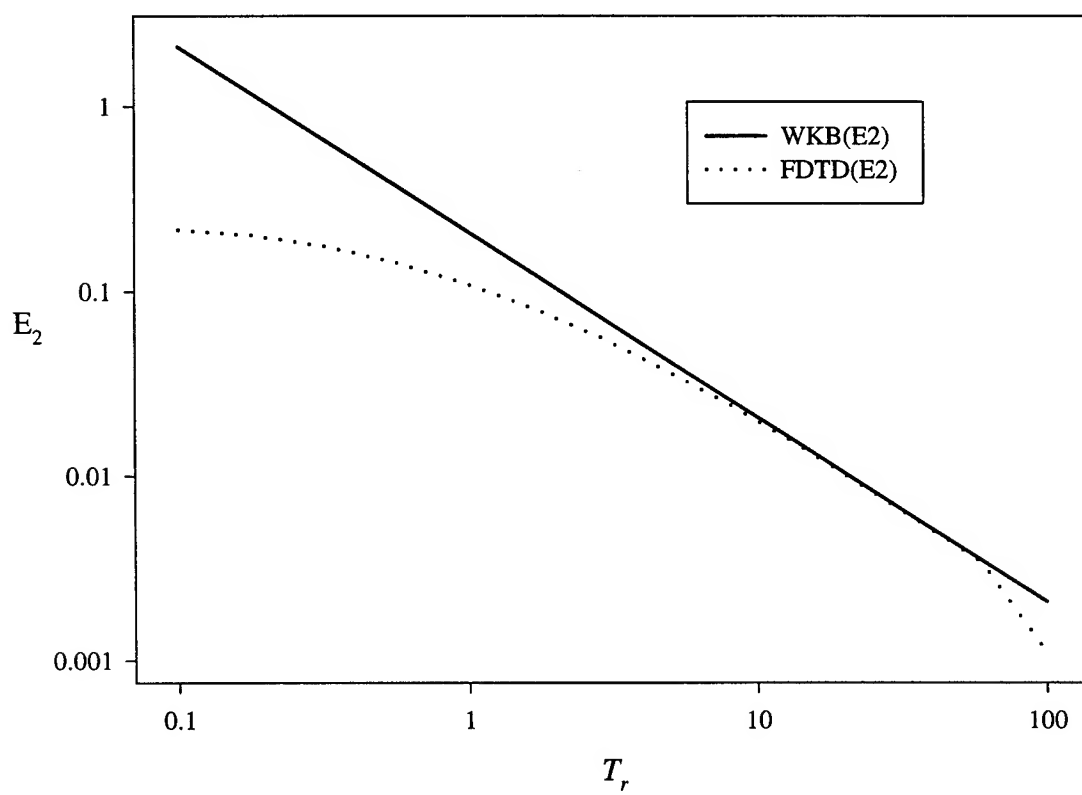


Figure 9. Comparison of reflected electric fields for arbitrary rise time.

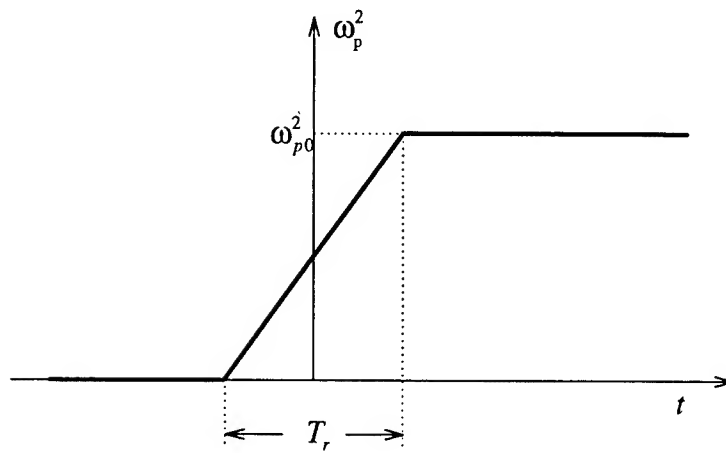


Figure 10. Plasma frequency for a linear profile.

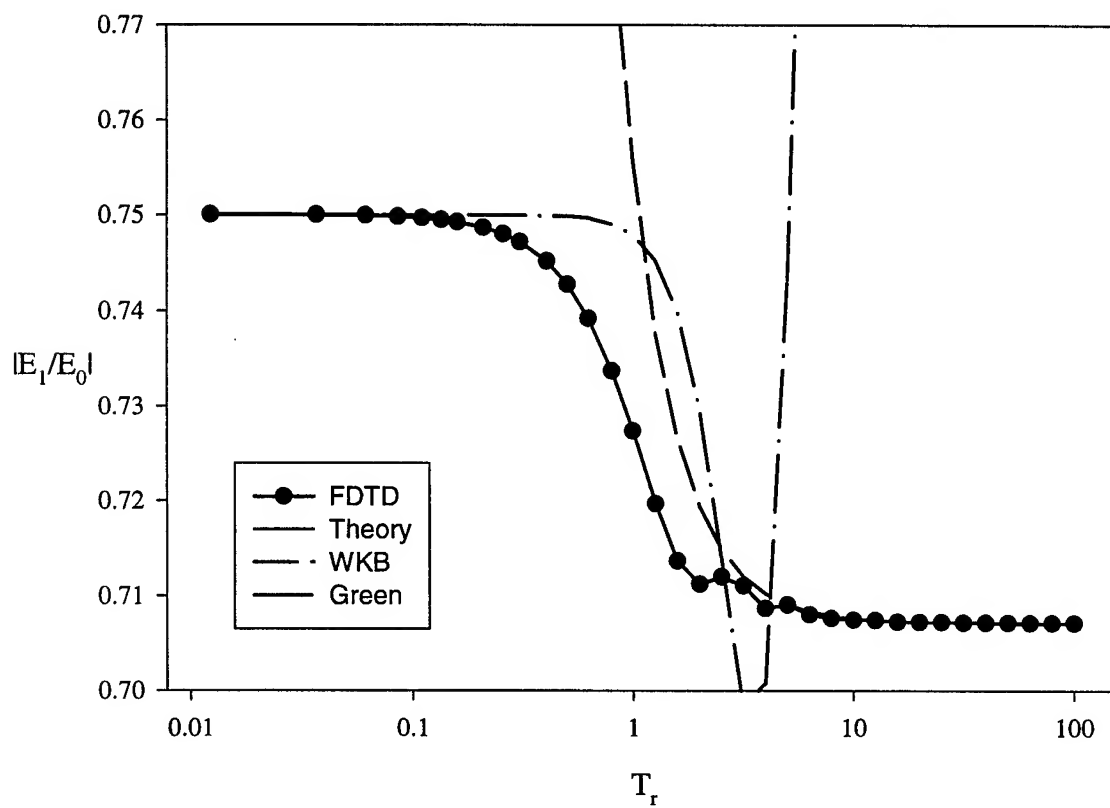


Figure 11. $|E_1/E_0|$ for a linear profile.

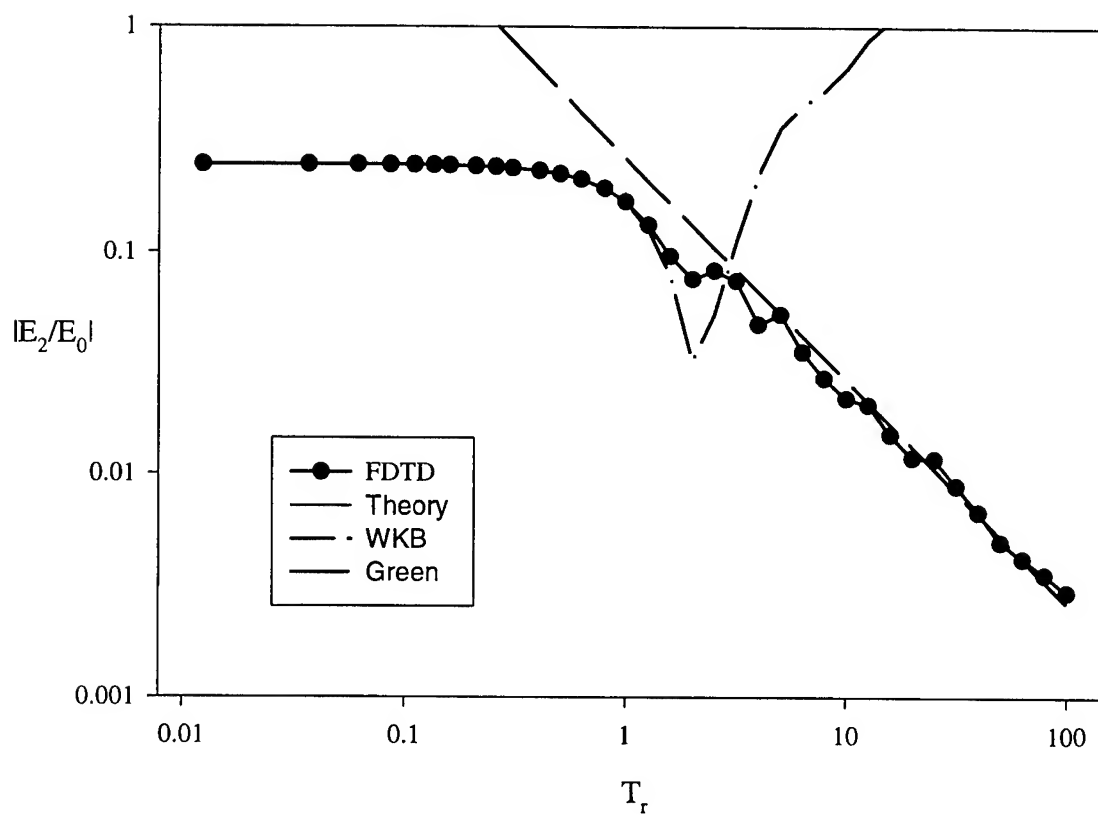


Figure 12. $|E_2/E_0|$ for a linear profile.

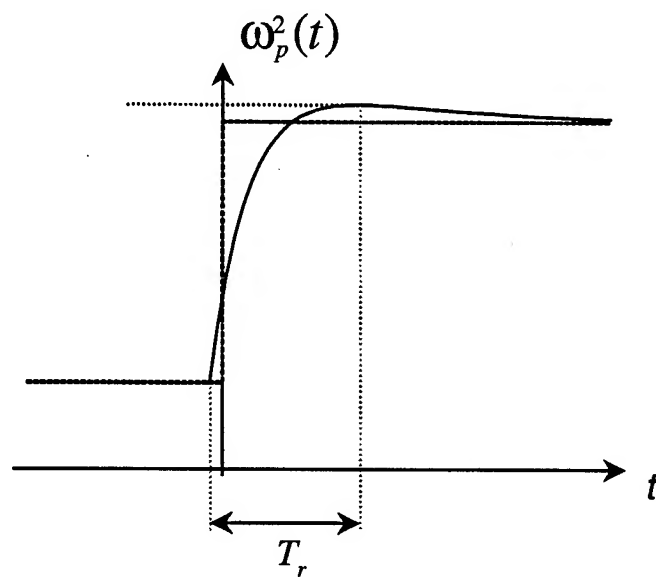


Figure 13a. Sketch of a hump profile.

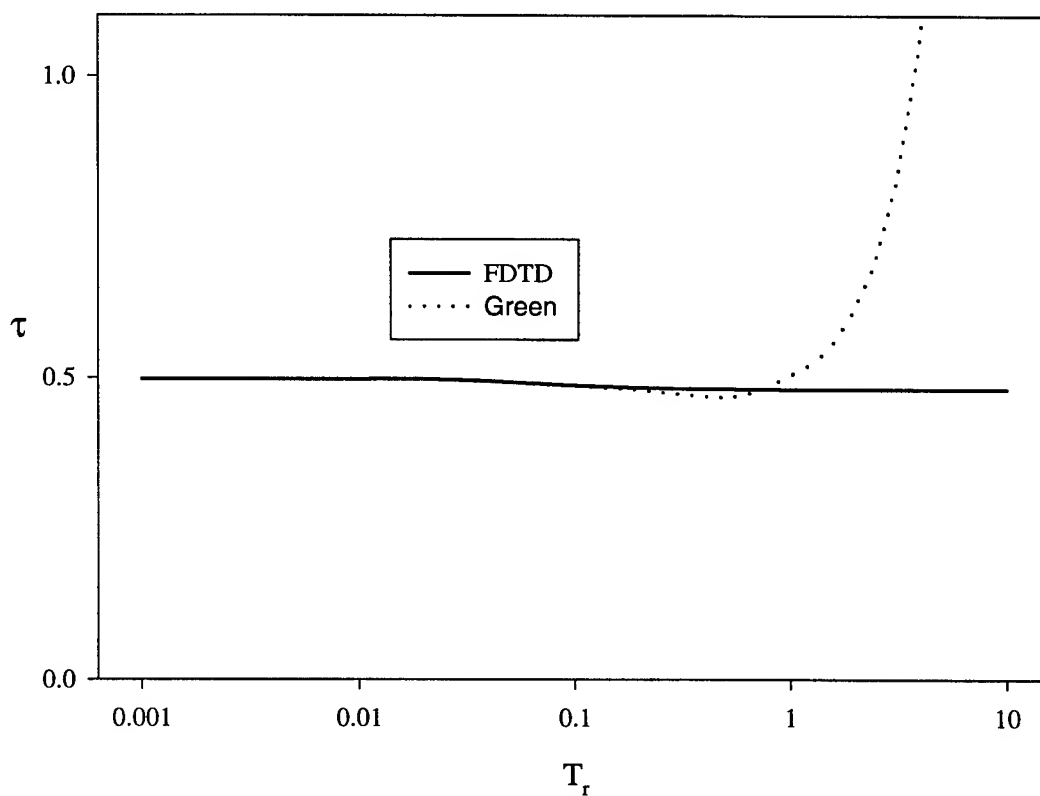


Figure 13b. Power transmission coefficient τ for a hump profile.

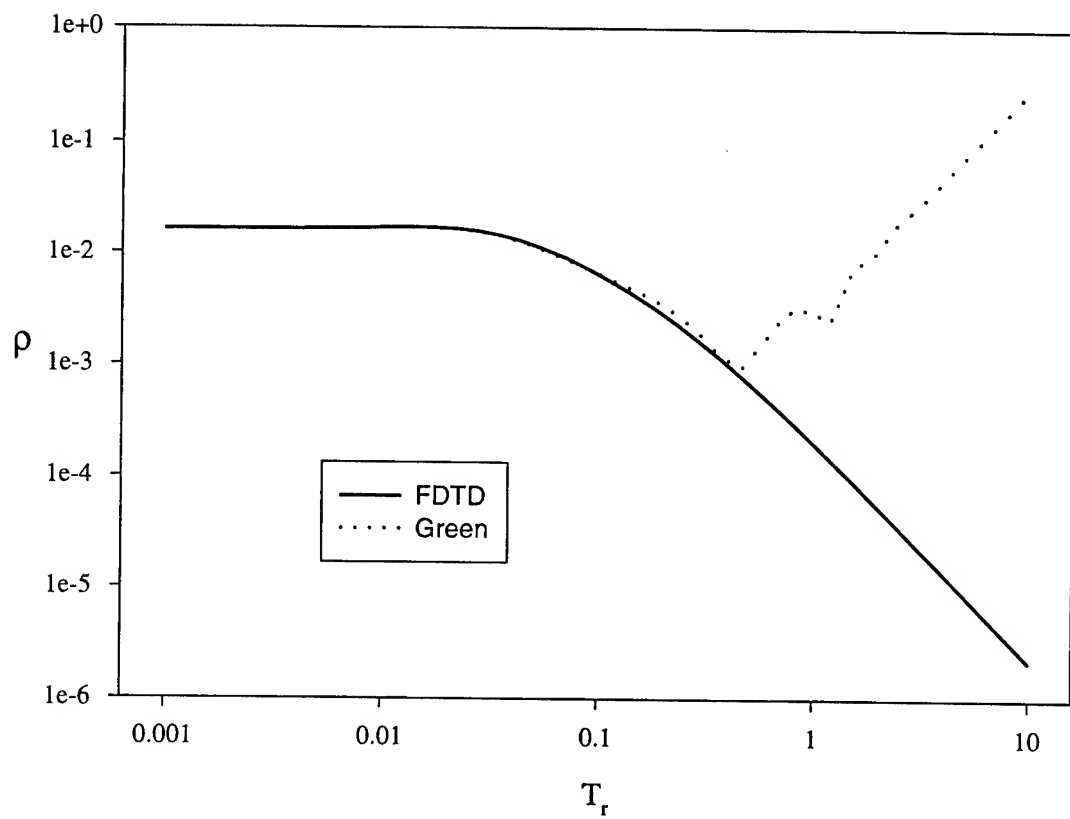


Figure 14. Power reflection coefficient ρ for a hump profile.

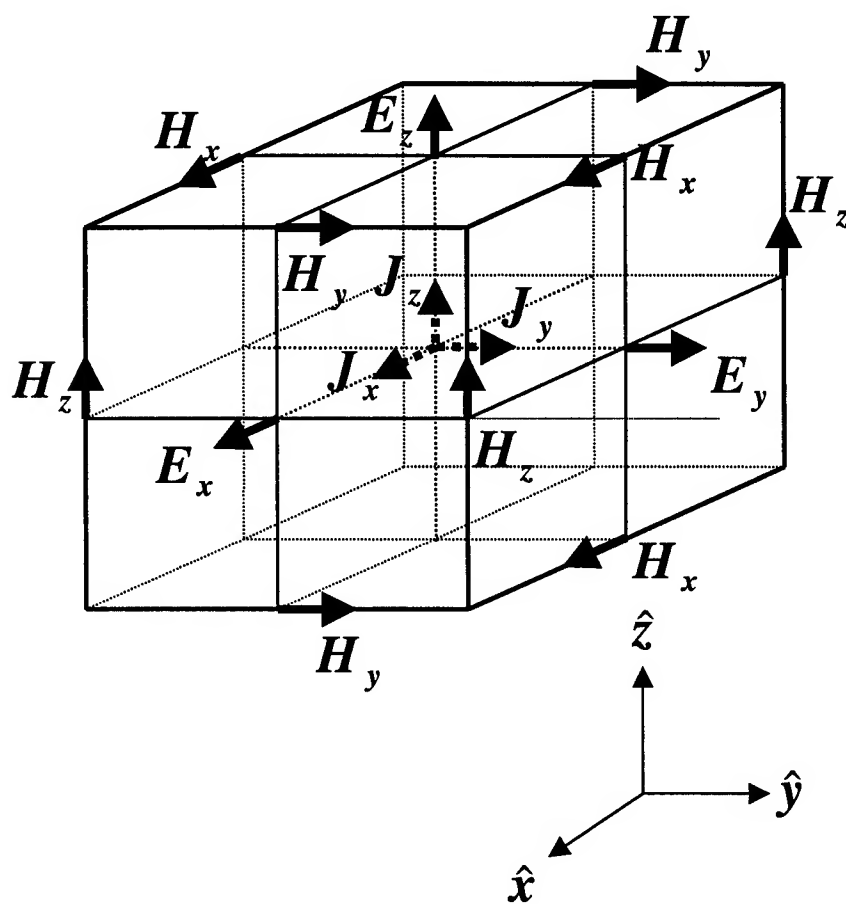


Figure 15. Position of the electric and magnetic field vector components and current density field about a cubic unit cell.

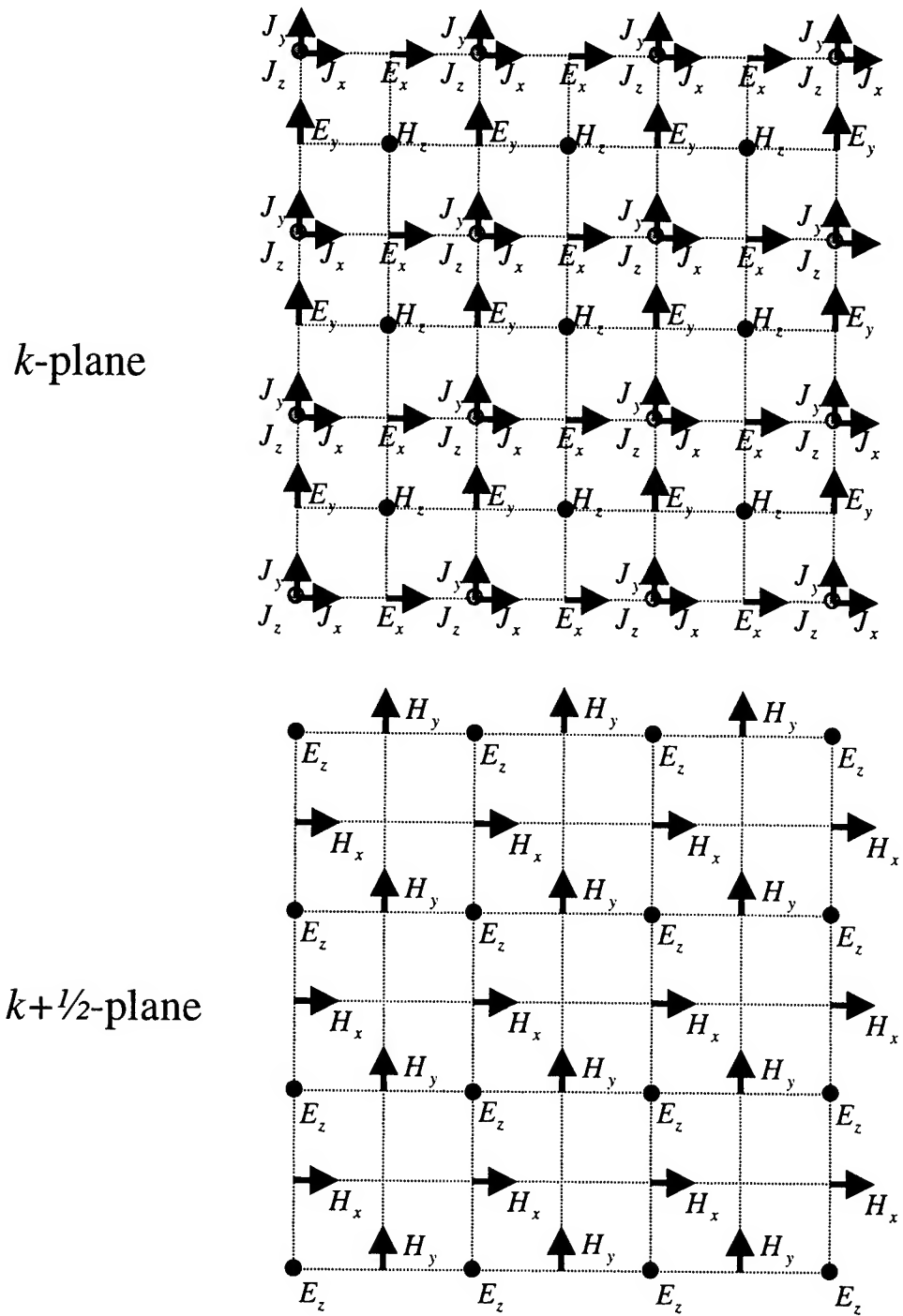


Figure 16. Construction of planes for the automatic implementation of the boundary conditions.

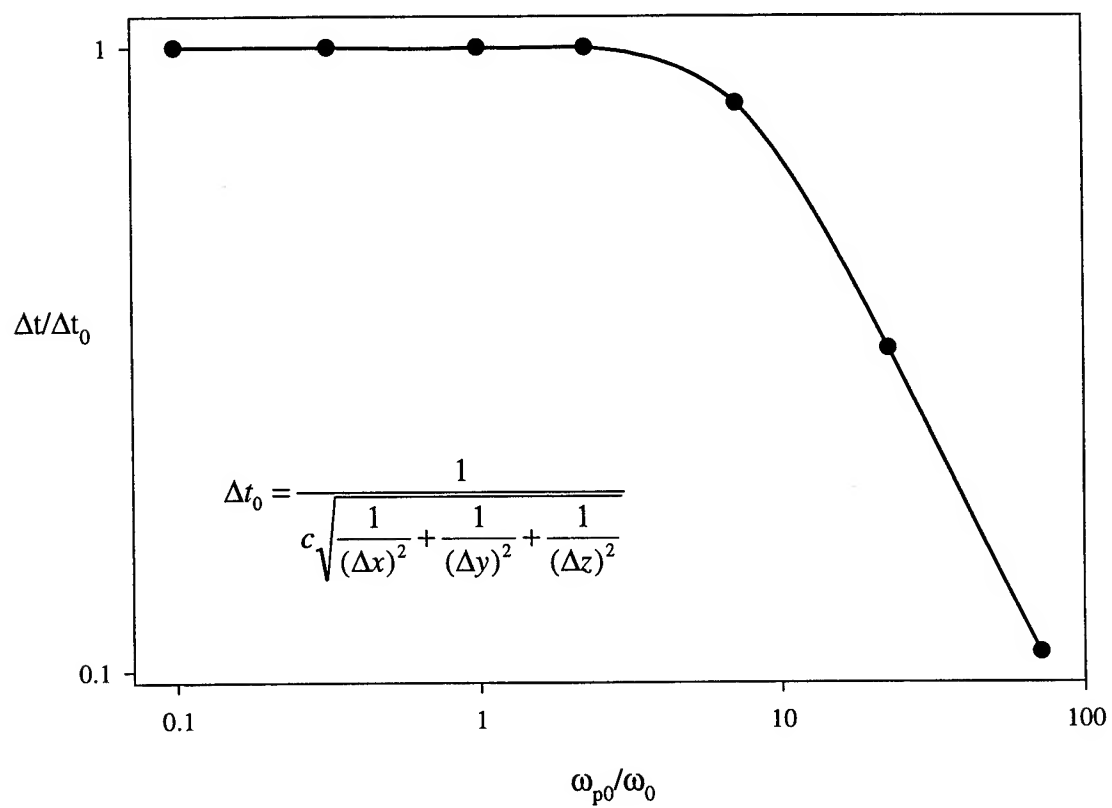


Figure 17 Maximum time step vs. the plasma frequency.
The optimum value Δt is normalized with respect to Δt_0
which is the 'magic' time step in free space. See [3].

IMPROVED CHEMICAL OXYGEN-IODINE LASER (COIL) CUTTING MODELS TO
OPTIMIZE LASER PARAMETERS

K. Farooq and A. Kar
Center for Research and Education in Optics and Lasers (CREOL)

University of Central Florida
4000 Central Florida Boulevard
Orlando, Fl 32816

Final Report for:
Summer Faculty Research Program
Phillips Laboratory

Sponsored by:
Air Force Office of Scientific Research
Bolling Air Force Base, DC

and

Phillips Laboratory

December 1997

IMPROVED CHEMICAL OXYGEN-IODINE LASER (COIL) CUTTING MODELS TO OPTIMIZE LASER PARAMETERS

K. Farooq, Graduate Student

and

Aravinda Kar, Assistant Professor

Center for Research & Education in Optics and Lasers (CREOL)

University of Central Florida.

Abstract

Molten material is removed in many laser applications such as laser grooving and laser cutting. An assist gas is usually used to remove the molten material from the laser material interaction zone. The effect of assist gas pressure on the material removal rate is investigated in this paper for laser cutting and grooving applications. The model for melt depth is based on the overall energy balance, and the cut depth is obtained by considering the effect of the assist gas. The model for kerf width is based on the modified Rosenthal solution taking into account the melting effect. The cut depths reach a constant value beyond a critical pressure if the kerf width is of the order of nozzle width and through cuts are assumed. Most of the molten material is removed by the assist gas at pressures below this critical pressure. The model predicts on the basis of the Prandtl or Meyer relation that the cutting speed decreases when the assist gas pressure exceeds a critical value if the kerf dimensions are smaller than the nozzle dimensions.

IMPROVED CHEMICAL OXYGEN-IODINE LASER (COIL) CUTTING MODELS TO OPTIMIZE LASER PARAMETERS

Khizar Farooq and Aravinda Kar

Introduction

Melt removal during laser materials processing is modeled in this study, and the model results are compared to experimental data for a Chemical Oxygen-Iodine Laser (COIL) of wavelength $1.315\mu m$. The basic principle of COIL has been discussed briefly by Kar et al¹. Two important applications of melt removal are laser cutting and laser grooving. The effects of assist gas pressure on laser cutting have been studied by Chrysosolouris and Choi², Biermann et al.³ and Molian and Baldwin⁴. Schuocker and Abel⁵ presented a mathematical model for the material removal process during laser cutting. The physical mechanism of the process has been discussed by Schuocker⁶. Mathematical models for the evaporative cutting have been developed by Modest and Abakian⁷, Bang and Modest⁸, and Roy and Modest⁹. Belic and Stanic¹⁰, and Belic¹¹ analyzed the laser cutting process with a simple model involving empirical parameters. The purpose of this paper is to model the effects of assist gas pressure on the cut depth and kerf width. This work is based on the model in Ref. [12] where several physical effects such as the convection and shock wave phenomena have been neglected. These effects are analyzed in this study to show that the cutting speed decreases when the assist gas pressure is increased above a critical value leading to the shock formation above the substrate surface.

Mathematical model for melt and cut depths

A. Energy and mass balance equations

The proposed model is based on the lumped parameter technique¹² in which the overall energy and mass balances are considered instead of the pointwise distribution. The overall energy and mass balance equations are, respectively, written as

$$AP\tau = \rho w_k(d_m - d_c)(v + V_m)\tau \left[c_p(T_m - T_0) + L_m + c_p(T_a - T_m) \right] + \rho w_k d_m v \tau \beta L_b + f_d \rho v w_k d_m \tau \left[c_p(T_m - T_0) + L_m + c_p(T_a - T_m) \right] + E_{cond} + E_{conv} \quad (1)$$

$$\rho w_k v d_m \tau = \rho w_k (v + V_m) (d_m - d_c) \tau + f_d \rho w_k v d_m \tau \quad (2)$$

The mass of the metal vapor is not included in the mass balance Eq. (2) because it is very small as compared to the mass of the melt. The first, second and third terms on the right side of Eq. (1) represent the total amount of material processed (melted and boiled). The first term accounts for the energy associated with the material that leaves the depressed region at the base of the kerf as shown in the Fig. 1, as a result of the impinging jet ; whereas the second term accounts for the energy required to boil a fraction of the molten material. The third term accounts for the energy loss as a result of the splashing or entrainment of molten droplets by the assist gas, and the sticking of molten layers to the side walls of the kerf. f_d denotes a fraction of the total amount of material melted by the laser beam. E_{cond} is the energy loss from the melt to the surrounding solid region in the workpiece due to heat conduction. E_{conv} is the convective heat loss from the melt to the assist gas at the free surface of the liquid metal. P is the power of incident laser beam and A is the absorptivity of the substrate. T_m , T_a and T_0 are respectively the melting temperature, characteristic temperature of the melt pool and ambient temperature. d_m and d_c represent the melt and cut depths respectively. L_m , L_b , c_p and V_m are respectively the latent heat of melting, latent heat of boiling, specific heat capacity of the substrate at constant pressure and the average velocity of liquid metal in the kerf. The laser-substrate interaction time is defined as $\tau = l/v$ where l is the length of the rectangular laser spot and v is the scanning velocity. l is measured in the scanning direction.

The energy loss due to the heat conduction is determined by using the Fourier law of heat conduction and is given by the following expression¹

$$E_{cond} = d_m \left[\frac{w_k k + 2lk}{2(\alpha\tau)^{1/2}} \right] (T_m - T_0)\tau \quad (3)$$

where k is the thermal conductivity and α is the thermal diffusivity of the workpiece.

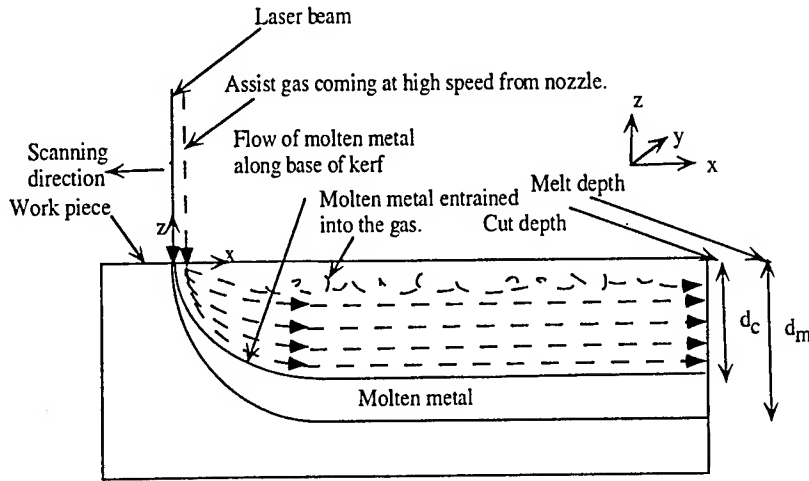


FIG. 1. High speed assist gas is carving out a kerf in molten metal.

Heat loss due to convection as a result of the assist gas flowing over the melt surface is given by

$$E_{conv} = \bar{h} w_k d_m (T_s - T_u) \tau \quad (4)$$

where T_s is the surface temperature of the melt and T_u is the temperature of the assist gas at the nozzle exit, which will be determined later. T_s is an unknown, however, it is taken to be the characteristic temperature of the melt, T_a , in the subsequent calculations. This overestimates the heat loss due to convection but the convection heat loss is still found to be insignificant as shown later. The average heat transfer coefficient, \bar{h} is estimated by using the following expression that is applicable to a single slot nozzle¹³

$$\bar{h} = \frac{3.06 Pr^{0.42} Re^m k_g}{D_h \left[\frac{y}{W} + \frac{H}{W} + 2.78 \right]} \quad \text{for} \quad \begin{bmatrix} 3000 \leq Re \leq 90,000 \\ 2 \leq H/W \leq 10 \\ 4 \leq y/W \leq 20 \end{bmatrix} \quad (5a)$$

where

$$m = 0.695 - \left[\left(\frac{y}{2W} \right) + \left(\frac{H}{2W} \right)^{1.33} + 3.06 \right]^{-1} \quad (5b)$$

Pr , k_g are respectively the Prandtl number and thermal conductivity of the gas. y is the perpendicular distance from the line running lengthwise through the center of the nozzle. W is the width of the nozzle and H is the height of the nozzle from the workpiece. The Reynolds number, Re is given by $Re = V'_g D_h / \nu_g$, where V'_g and ν_g are respectively the velocity and kinematic viscosity of the gas at the nozzle exit. The hydraulic diameter, D_h is given by $D_h = 4A_c/P_c$, where A_c and P_c are the cross-sectional area and perimeter of the nozzle respectively. k_g , ν_g and Pr are evaluated at one atmospheric pressure and temperature T_u .

B. Gas dynamic analysis for the assist gas

The assist gas expands after leaving the nozzle depending on the ambient pressure, and its velocity, V'_g is given by ^{14,15}

$$V'_g = M^* \sqrt{\frac{2\gamma}{\gamma+1} RT_0} \quad \text{for } j = u \text{ or } d \text{ as discussed below.} \quad (6)$$

where γ is the specific heat ratio which is also known as the isentropic index. It is given by $\gamma = c'_p / c'_v$ where c'_p and c'_v are the specific heat capacities of assist of the assist gas at constant pressure and volume respectively. For diatomic gases such as Nitrogen, $\gamma = 1.4$.

R is the universal gas constant and T_0 is the room temperature which is taken as 300 K in this study. M_j^* is a dimensionless velocity of the assist gas depending on its flow conditions. The critical pressure, P^* , is defined as $P^* = P_0 \left(\frac{\gamma + 1}{2} \right)^{\frac{\gamma}{\gamma - 1}}$ where P_0 is the ambient pressure. Depending on the assist gas pressure at the nozzle mouth, P_n , three kinds of flow situations of interest are listed below.

(i) Supersonic flow ($P_n > P^*$) in which the shock wave is formed between the nozzle and substrate surface: This may occur in grooving, or through cuts of small kerf width relative to the nozzle dimensions. The dimensionless velocity at the upstream of the shock wave is given by¹⁴

$$M_u^{*2} = \frac{(\gamma + 1)}{(\gamma - 1)} \left[1 - \left(\frac{P_0}{P_n} \right)^{\frac{\gamma - 1}{\gamma}} \right] \quad (7)$$

The dimensionless velocity at the downstream of the shock wave, M_d^* is given by the Prandtl or Meyer relation¹⁶, $M_d^* = 1 / M_u^*$. It should be noted that the dimensionless velocity at the upstream of the shock front is taken equal to the dimensionless velocity at the nozzle exit. The velocity with which the assist gas enters the kerf is obtained from Eq. (6) by setting $M_j^* = M_d^*$. The dimensionless velocity M_j^* is related to the Mach number M_j through the following relation¹⁵.

$$M_j^2 = \frac{\frac{2}{\gamma + 1} M_j^{*2}}{1 - \frac{\gamma - 1}{\gamma + 1} M_j^{*2}} \quad (8)$$

where $j = u$ or d signifies the upstream and downstream conditions respectively. The temperatures T_u and T_d of the assist gas at the upstream and downstream of shockfront, respectively, are given by the following expressions¹⁵

$$\frac{T_0}{T_j} = 1 + \frac{\gamma-1}{2} M_j^2 \quad j = u \text{ or } d \quad (9)$$

(ii) Supersonic flow ($P_n > P^*$) in which the shock wave is formed at the kerf inlet: The velocity V'_g at the nozzle exit is obtained from Eq. (6) by setting $M_j^* = M_u^*$. The flow will be sonic inside the kerf even though the flow is supersonic outside the kerf. This situation is encountered for through cuts of uniform width comparable to the nozzle width. This is the maximum gas velocity that can be attained in the kerf for material removal to achieve the highest cutting rate.

(iii) Subsonic flow ($P_n < P^*$): The velocity V'_g at the nozzle exit is obtained from Eq. (6) by setting $M_j^* = M_u^*$. In through cuts, the velocity of the gas inside the kerf can be calculated by treating the kerf as a convergent or divergent nozzle if the kerf tapers in or out respectively.

C. Melt flow

The assist gas removes the energy from the laser-material interaction zone through two mechanisms: (i) Surface effect which involves the convective cooling at the free surface of the melt, and (ii) Bulk effect which refers to the removal of energy contained in the melt that is flushed away by the assist gas. The average velocity of the molten metal is calculated by considering the Poiseuille flow of the melt¹⁷.

$$V_m = -\frac{1}{12\mu} \left(\frac{dp}{dx} \right) w_k^2 \quad (10)$$

The viscosity of the molten metal, μ depends on temperature as $\mu = \mu_0 \exp\left[E/(RT_a)\right]$

where μ_0 and E are constants and their values can be found in Ref. [18]. The pressure gradient dp/dx in the metal is estimated by taking it to be the pressure gradient of the assist gas as it flows over the melt surface. Corner flow theory is used to analyze the assist gas

velocity. A stagnation point exists below the gas jet, and the gas accelerates as it moves away from this point. The velocity of an ideal fluid flowing along a 90° corner of stationary solid surface is given by^{17, 19} $V_c = V_g' l / H$ at a distance l from the stagnation point. In the present case of melt removal, the assist gas transfers momentum to the liquid metal to induce flow in the melt giving rise to a moving boundary for the gas flow instead of the stationary surface used in the corner flow theory. This will significantly reduce the assist gas velocity compared to the value of V_c given by the above expression. To account for this effect, V_c is taken to be $V_c = F V_g' l / H$ where F is a fraction ($0 < F \leq 1$). The pressure gradient is approximated as follows by using the Bernoulli equation,

$$\frac{dp}{dx} \approx \frac{\Delta p}{l} = \frac{\rho_0 V_c^2}{2l} = \frac{\rho_0 l}{2} \left(\frac{F V_g'}{H} \right)^2 \quad (11)$$

where ρ_0 is taken as the density of the assist gas at one atmospheric pressure and temperature 300 K.

The characteristic temperature of the melt, T_a in Eqs. (1) and (4) is obtained by considering the stefan condition at the solid-liquid interface which yields¹

$$T_a - T_m = \varepsilon \frac{\rho L_m}{2kl} v w_k + \varepsilon \frac{T_m - T_0}{2(\alpha w_k)^{1/2}} (v w_k)^{1/2} \quad (12)$$

ε is the average thickness of the recast layer in the kerf and is taken to be 0.1 mm in this study. Combining Eqs. (1) and (2) and utilizing Eqs. (3), (4) and (12), the melt depth is found to be

$$\frac{d_m}{p} = \frac{A_0}{v w_k + A_1 (v w_k)^2 + A_2 (v w_k)^{3/2} + A_3 (v w_k)^{1/2} + A_4 (\bar{h} v w_k^2) + A_5 (\bar{h} v^{1/2} w_k^{3/2}) + A_6 \bar{h} w_k} \quad (13)$$

where the coefficients are defined as

$$A_0 = \frac{A}{a_0} \quad (14a)$$

$$A_1 = \frac{\rho^2 c_p L_m \varepsilon}{2a_0 kl} \quad (14b)$$

$$A_2 = \frac{\rho \varepsilon c_p (T_m - T_0)}{2a_0 (\alpha l w_k)^{1/2}} \quad (14c)$$

$$A_3 = \left[\frac{w_k k + 2kl}{2a_0 (\alpha l w_k)^{1/2}} \right] (T_m - T_0) \quad (14d)$$

$$A_4 = \frac{\rho L_m \varepsilon}{2a_0 kl} \quad (14e)$$

$$A_5 = \frac{\varepsilon (T_m - T_0)}{2a_0 (\alpha l w_k)^{1/2}} \quad (14f)$$

$$A_6 = \frac{(T_m - T_u)}{a_0} \quad (14g)$$

and

$$a_0 = \rho [c_p (T_m - T_0) + L_m + \beta L_b] \quad (14h)$$

For a rectangular laser spot of length $l = 1.7 \text{ mm}$ and width $w = 1.2 \text{ mm}$, the thermophysical data listed in Tables I and II and the assumptions that $T_0 = 300 \text{ K}$, $\varepsilon = 0.1$ mm, $\beta = 0.1$ and $w_k = w$, the coefficients in expressions (14b-h) are found to be $a_0 = 1.24 \times 10^{10} \text{ [J/m}^3]$, $A_1 = 233.35 \text{ [s/m}^2]$, $A_2 = 3.29 \text{ [s}^{1/2}/\text{m}]$, $A_3 = 0.0033 \text{ [m/s}^{1/2}]$, $A_4 = 6.50 \times 10^{-5} \text{ [m.s.K/J]}$, $A_5 = 9.18 \times 10^{-7} \text{ [m}^2\text{.K.s}^{1/2}/\text{J}]$ and $A_6 = 1.26 \times 10^{-7} \text{ [m}^3\text{.K/J]}$. To carrying out the order of magnitude analysis, these coefficients are multiplied by the respective terms to obtain $A_1(\nu w_k)^2 = 1.34 \times 10^{-7} \text{ [m}^2/\text{s}]$, $A_2(\nu w_k)^{3/2} = 3.87 \times 10^{-7} \text{ [m}^2/\text{s}]$, $A_3(\nu w_k)^{1/2} = 1.62 \times 10^{-5} \text{ [m}^2/\text{s}]$, $A_4 \bar{h} \nu w_k = 2.07 \times 10^{-9} \text{ [m}^2/\text{s}]$, $A_5 \bar{h} \nu^{1/2} w^{3/2} = 1.46 \times 10^{-9}$

$[\text{m}^2/\text{s}]$ and $A_6 \bar{h} w_k = 1.67 \times 10^{-7} [\text{m}^2/\text{s}]$ where $v = 1.2 \text{ m/s}$. The value of \bar{h} is calculated for the largest nozzle of length 22 mm and width $W = 1 \text{ mm}$ for the conditions at which the assist gas attains sonic velocity at the kerf inlet. For this situation the temperature of the gas is found to be $T_u = 250 \text{ K}$ by taking the Mach number $M_u = 1$ in Eq. (9). The distance between the nozzle and workpiece (H) and the parameter y are taken as 6 mm and 20 mm respectively in Eq. (5a). The average value of the heat transfer coefficient, $\bar{h} = 1708 [\text{W}/\text{m}^2\text{K}]$ under these conditions. These magnitudes indicate that the terms involving A_3 is dominant in affecting the melt depth compared to the rest of the terms. Therefore, Eq. (13) can be simplified as

$$\frac{d_m}{P} = \frac{A_0}{vw_k + A_3(vw_k)^{1/2}} \quad (15)$$

The assist gas removes the melt to produce a slot of depth d_c in the case of laser grooving. d_c is equal to the thickness of the workpiece for laser cutting applications. The mass balance Eq. (2) relates d_c to d_m as given below.

$$d_c = \left(\frac{V_m + f_d v}{V_m + v} \right) d_m \quad (16)$$

The splashing function f_d is not a constant. It is zero when the assist gas pressure is zero and progressively increases as the pressure increases. Since the gas pressure affects the melt velocity V_m , the splashing function is defined in terms of V_m as follows,

$$f_d = \frac{(1 - X_d)V_m}{X_d v + V_m} \quad (17)$$

where X_d is a suitable constant. Utilizing Eqs. (10), (15), (17) and setting $w_k = w$ in Eq. (10), Eq. (16) can be written as

$$d_c = \left(\frac{-\left(\frac{dp}{dx}\right)w^2}{-\left(\frac{dp}{dx}\right)w^2 + 12X_d\mu v} \right) d_m \quad (18)$$

TABLE I. Typical values of thermophysical properties of iron. Due to the lack of availability of high temperature data, these values were used in this study to obtain various results for 400 series stainless steel workpiece¹⁸.

Thermophysical properties	Values of thermophysical properties
Density, ρ	7870 kg m ⁻³
Melting point, T_m	1809 K
Boiling point, T_b	3133 K
Specific heat, c_p	456 J Kg ⁻¹ K
Thermal conductivity, k	78.2 W m ⁻¹ K ⁻¹
Thermal diffusivity, $\alpha = k/(\rho c_p)$	2.18×10 ⁻⁵ m ² s ⁻¹
Latent heat of melting, L_m	2.72×10 ⁵ J Kg ⁻¹
Latent heat of boiling, L_b	6.10×10 ⁶ J Kg ⁻¹
Dynamic viscosity, μ_0	0.3699 m N s m ⁻²
Activation Energy, E	41.4 kJ mol ⁻¹

TABLE II. Thermophysical properties of nitrogen¹³.

Thermophysical properties	Values of thermophysical properties
Pressure, P_0	1.013×10^5
Density, ρ_0 (300 K, 1 atm)	1.1233 kg m^{-3}
Kinematic viscosity, ν_g (250 K, 1 atm)	$11.48 \times 10^{-6} \text{ m}^2/\text{s}$
Prandtl number, Pr (250 K, 1 atm)	0.727
Thermal Conductivity, k_g (250 K, 1 atm)	$22.2 \times 10^{-3} \text{ W m}^{-1} \text{ K}^{-1}$

Model for kerf width

The width of the slot, which is referred to as kerf width in laser cutting applications, produced due to melt removal by an assist gas is obtained by modifying the Rosenthal equation for temperature distribution²⁰. The Rosenthal model is based on a point heat source, a semi-infinite workpiece, no heat losses due to convection and radiation, and no melting of the workpiece. To account for the reduction in temperature due to the melting of the workpiece and the removal of the superheated melt from the laser-material interaction zone, the Rosenthal equation is modified by incorporating a factor f_m , $0 < f_m \leq 1$, as given below.

$$T - T_0 = \frac{PA}{2\pi k} e^{-\frac{vx}{2\alpha}} \cdot \frac{e^{-\frac{vr}{2\alpha}}}{r} \quad (19)$$

where $r = \sqrt{x^2 + y^2 + z^2}$. The melt width is approximated by determining the width of the region at the substrate surface ($x = z = 0$) within which the temperature is above the melting temperature. To obtain a simple expression for the melt width w_m , r is set equal to $w_m/2$ in the denominator and is taken as $w/2$ in the exponent in Eq. (19), which reduces Eq. (19)

to the following form.

$$w_m = f_m \frac{A}{\pi k (T_m - T_0)} e^{\left(\frac{vw}{4\alpha} \right)} \quad (20)$$

Some of the molten material flows along the walls of the slot or kerf and most of it is splashed out by the assist gas (see Fig. 2). This produces a slot or kerf of width w_k which is related to the melt width w_m by the following mass balance equation.

$$\rho v w_m d_m \tau = \rho (V_m + v) (w_m - w_k) d_m \tau + f_w \rho v w_m d_m \tau \quad (21)$$

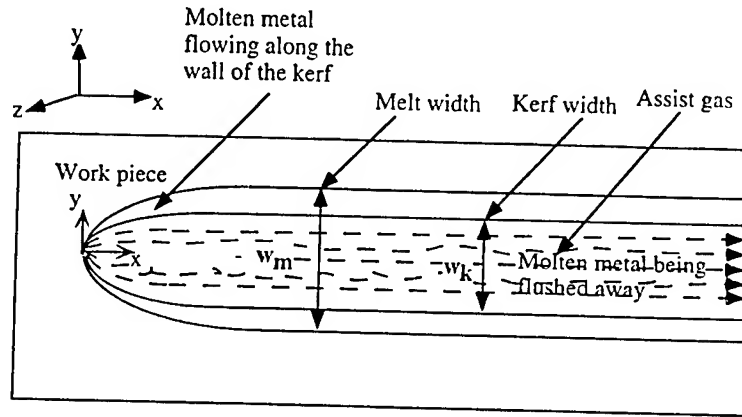


FIG. 2. Top view of the work piece showing how assist gas has squeezed metal along the walls of the kerf.

The first term on the right hand side of this equation corresponds to the amount of material sticking along the kerf walls while the second term represents the amount splashed out. Here f_w is a splashing function of similar nature as in the case of the cut depth. It is zero when the assist gas pressure is zero and increases progressively as the pressure increases. As in section II, f_w is defined in terms of V_m in the following way,

$$f_w = \frac{(1 - X_w) V_m}{X_w v + V_m} \quad (22)$$

where X_w is a suitable constant. Utilizing Eqs. (10), (22) and setting $w_k = w$ in Eq. (14), the expression for the kerf width can be written as follows from Eq. (21).

$$w_k = \left(\frac{-\left(\frac{dp}{dx}\right)w^2}{-\left(\frac{dp}{dx}\right)w^2 + 12X_w\mu v} \right) w_m \quad (23)$$

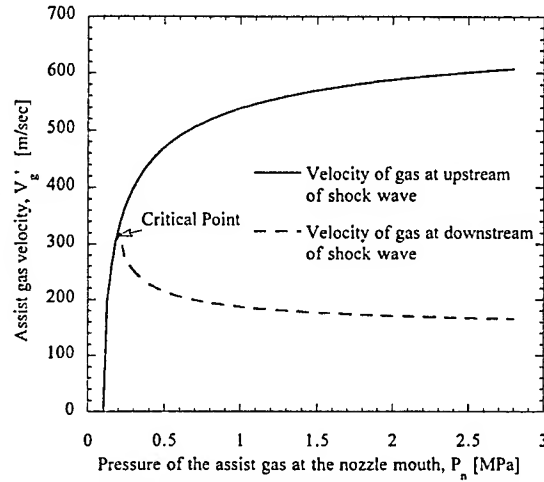


FIG. 3. Plot of Prandtl or Meyer relationship as a function of assist gas pressure at the nozzle mouth. The upper and lower curves indicate the velocity of gas at upstream and downstream side of the shock respectively.

Results and discussion

The melt and cut depths and the kerf width are calculated by using the above models and the data listed in Tables I and II. The results are compared with experimental data to verify the models. Details of the experimental set up and procedure have been presented in Ref. [1]. The values of the parameters, F , X_d , f_m and X_w are chosen to be $F=0.05$, $X_d=X_w=0.02$ and $f_m=0.27$ to obtain similar trends as experimental data. The physical meaning of choosing $X_d=X_w=0.02$ is that this choice leads to maximum cut depth over a wide range of cutting speed for sonic gas velocity at the inlet of the kerf of uniform width.

Figure 3 is a plot of the Prandtl or Meyer relation for the case in which the assist gas attains a critical speed at about 0.2 MPa gas pressure at the nozzle mouth and a shock wave is formed at an intermediate location between the nozzle and workpiece. The curve bifurcates at this critical speed. The upper curve represents the assist gas velocity at the upstream of the shock wave and the lower curve denotes the velocity downstream. The velocity of the downstream gas is always less than the critical speed of the gas. Figure 3

indicates that the velocity with which the assist gas enters the kerf decreases if a shock front is formed between the nozzle and workpiece. This reduces the effectiveness of the assist gas in removing the molten material.

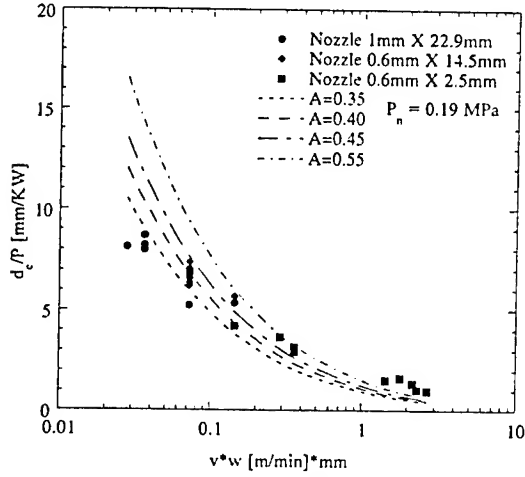


FIG. 4. Verification of the scaling law for cut depth with the experimental data.

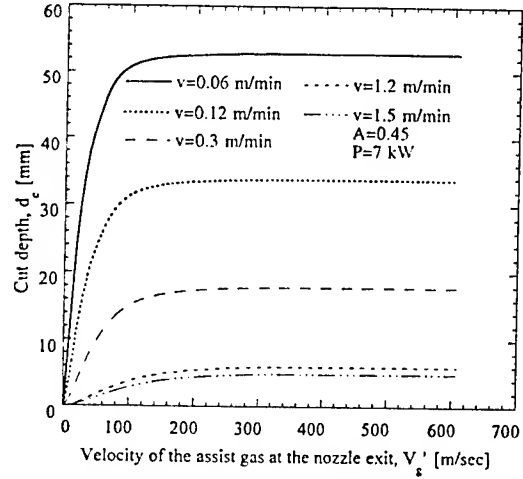


FIG. 5. Variation of cut depth with the assist gas velocity at the nozzle exit for different scanning velocities.

Figure 4. shows the cut depth per unit power (d_c/P) as a function of the product of laser beam width and scanning velocity v . Four different absorptivity values in the range of 0.35 to 0.55 are used. The theoretical curves closely follow the experimental data and validates the theory. Figure 5 represents the variation in the cut depth with assist gas velocity at the nozzle exit. The curves show zero cut depth for zero gas velocity, rise sharply and then attain constant values. This can be explained on the basis of the kerf geometry which is assumed to be nontapered through cut. Due to this the velocity of the assist gas remains equal to the critical value in the kerf even though the velocity of the gas may be supersonic outside the kerf. The curves indicate that the maximum cut depth is achieved at gas velocities much lower than the critical speed. At higher scanning speeds the maximum cut depth is achieved at higher gas velocities though still less than the critical speed because the gas jet interacts with the workpiece for shorter duration. Figure 6 denotes the corresponding results in terms of the gas pressure at the nozzle mouth and essentially explains the same fact as in Fig. 5. Figure 7 shows the variation in the cut depth

with the scanning velocity. The cut depth drops sharply for higher scanning speeds because the laser-material interaction time decreases and therefore, laser beam deposits less energy on the workpiece when the beam is scanned at the higher speeds.

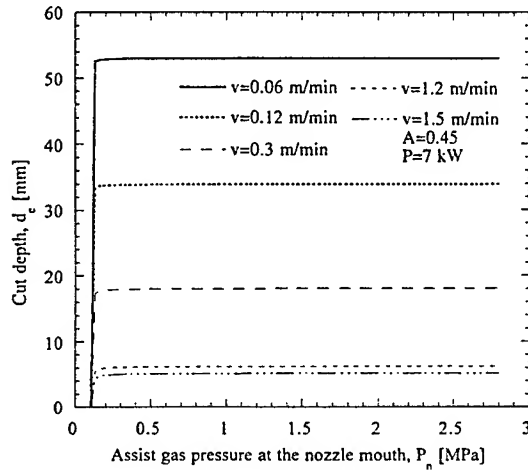


FIG. 6. Variation of cut depth with pressure of assist gas at the nozzle mouth at different scanning velocities

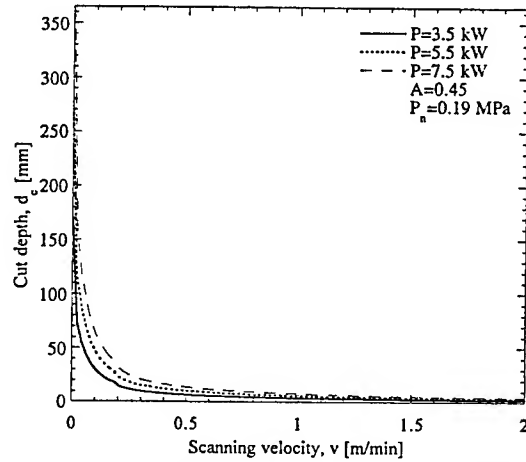


FIG. 7. Trends showing cut depth varying with the scanning velocity at different laser power.

The kerf width per unit power (w_k/P) is plotted against the product of the laser beam width w and the scanning velocity v in Fig. 8. Experimental data and model results show similar trends. Figures 9 and 10 examine the kerf width as a function of the assist gas velocity at the nozzle exit and pressure at the nozzle mouth respectively. The kerf width rises sharply as the gas velocity or pressure increases, and then attains a constant value as the sonic velocity is approached due to the geometry of the kerf already mentioned above in the case of the cut depth (Fig. 5). Figure 11 shows that the kerf width decreases as the scanning velocity increases because of less energy deposition on the workpiece at higher scanning speeds.

Figure 12 examines the cutting speed as a function of the assist gas pressure at the nozzle mouth, and the model results are compared with experimental data taken from the Ref. [21]. The results are shown for two cases involving 2 mm and 3 mm cut depths. The experimental data indicate that the cutting speed increases as the gas pressure is increased

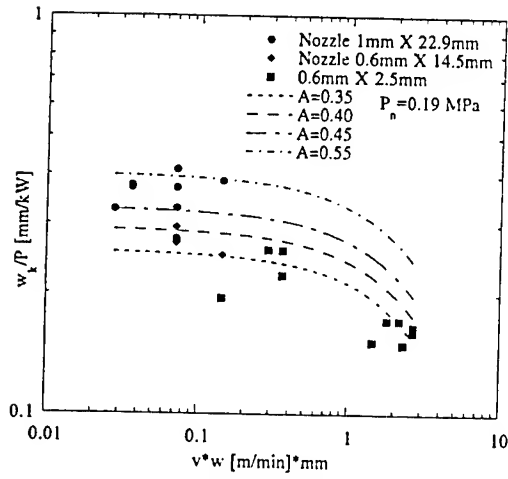


FIG. 8. Verification of scaling law for cut depth with experimental data.

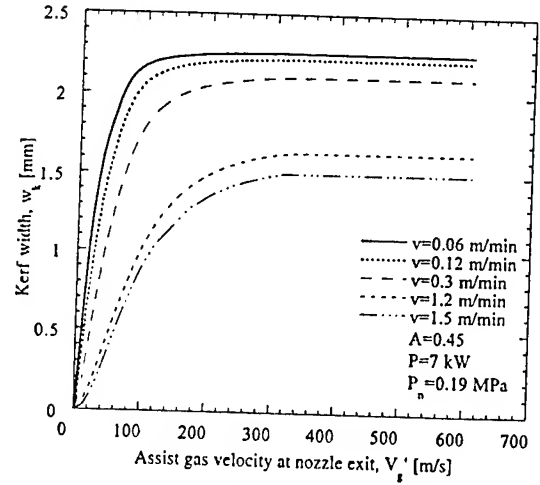


FIG. 9. Variation of kerf width with the assist gas velocity at nozzle exit for different scanning velocities.

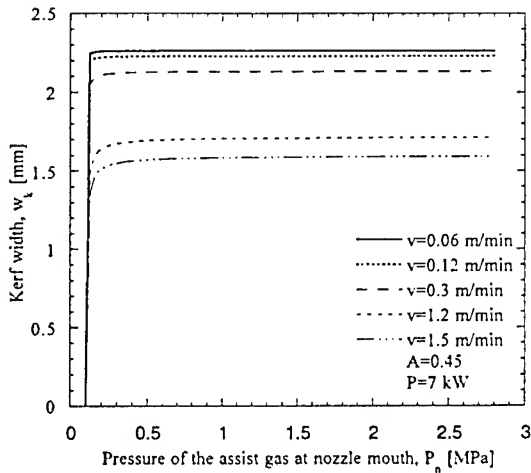


FIG. 10. Variation of kerf width with the assist gas pressure at the nozzle mouth for different scanning velocities

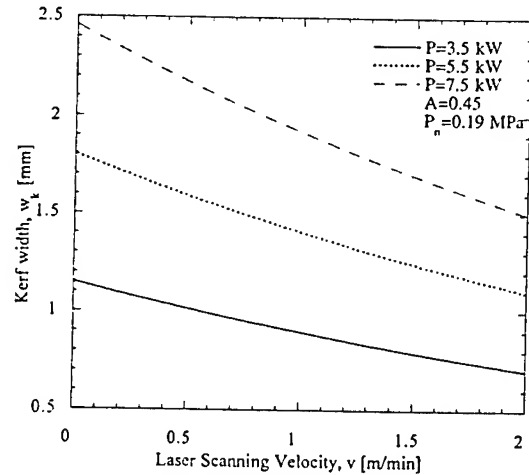


FIG. 11. Trends showing kerf width varying with the scanning velocity at different laser powers.

upto the critical pressure (0.2 MPa) and then drops on further increase of pressure. This trend is predicted by the present model on the basis of the assumption that a shock wave is formed at an intermediate location between the nozzle and workpiece for supersonic gas flow. The flow is then governed by the Prandtl or Meyer relation and the velocity of the gas at kerf inlet is always less than the critical velocity. In the pressure range $0.1 < P_n < P^* = 0.2$ MPa the velocity of the metal V_m is calculated on the basis of M_u^* , and V_m is determined by using M_d^* for $P_n \geq P^*$. It may be noted that the effective nozzle-to-plate distance becomes $H/2$ for supersonic gas flow because the shock wave is assumed to form halfway between the nozzle and workpiece. It is also assumed that the kerf is of nontapered geometry and that the size of the laser spot is $0.25\text{mm} \times 0.25\text{mm}$. For this spot size X_d is chosen to be 0.0088.

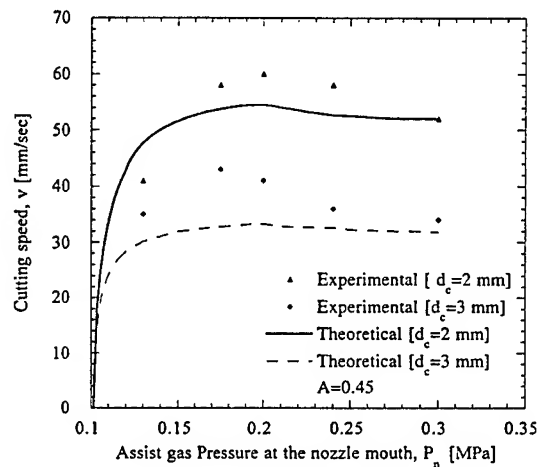


FIG. 12. Experimental data taken from Ref. [21] is compared with the theoretical results for 2mm and 3mm depths of cut, for a laser spot size of dimensions 0.25mm X 0.25mm

Conclusions

Models for melt and cut depths and kerf width are presented for laser grooving and cutting applications. Experimental data for both cut depth and kerf width validate the model predictions. The cutting speed reaches a maximum value at a certain pressure of the assist gas. It decreases when the gas pressure is increased beyond the critical pressure for certain geometry of the kerf, and nozzle dimensions.

REFERENCES:

- ¹A. Kar, J. E. Scott and W. P. Latham, *J. Laser Appl.* **8**, 125 (1996).
- ²G. Chryssolourius and W. C. Choi, in *CO₂ Lasers and Applications* edited by J. D. Evans and E. V. Locke (Society of Photo-Optical Instrumentation Engineers-The international Society for Optical Engineering, Bellingham, Washington, 1989) Vol. 1042, pp.86-96.
- ³B. Biermann, S. Biermann and H. W. Bergmann, *J. Laser Appl.* **3**, 13 (1996).
- ⁴P. A. Molian, M. Baldwin, *J. Laser Appl.* **4**, 9 (1992).
- ⁵D. Schuocker and W. Abel, in *SPIE Proc. Industrial Applications of High Power Lasers*, (SPIE, Bellingham, Washington, 1984) Vol. 455, pp. 88-95.
- ⁶D. Schuocker, *The Industrial Laser Annual Handbook* (PennWell Books, Tulsa, Oklahoma, 1987), Edited by D. Belforte and M. Levitt, pp. 65-79.
- ⁷M. F. Modest and H. Abakians, *J. Heat Transfer.* **108**, 602 (1986).
- ⁸S. Y. Bang and M. F. Modest, *J. Heat Transfer.* **113**, 663 (1991).
- ⁹S. Roy, M. F. Modest, *Int. J. Heat Mass Transfer* **36**, 3515 (1993).
- ¹⁰I. Belic, J. Stanic, *Optics and Laser Technology.* **19**, 309 (1987).
- ¹¹I. Belic, *Optics and Laser Technology.* **21**, 277 (1989).
- ¹²A. Kar, J. A. Rothenflue, W.P. Latham, *J. Laser Appl.* **9**, (1997).
- ¹³F. P. Incropera, D. P. DeWitt, *Introduction to heat transfer* (John Wiley & Sons, 2nd edition, New York, 1990), pp. 402-403, A 20.
- ¹⁴A. G. Grigoryants, *Basics of Laser Material Processing* (CRC Press, Boca Raton, 1994), pp.281-298.
- ¹⁵A. H. Shapiro, *The Dynamics and Thermodynamics of Compressible Fluid Flow I* (John Wiley and Sons, New York, 1953), pp. 73-158.
- ¹⁶I. G. Currie, *Fundamental mechanics of Fluids* (McGraw-Hill Inc, 2nd edition, New York 1993), pp. 354-355.
- ¹⁷W. F. Hughes and J.A. Brighton, *Theory and Problems of Fluid Dynamics* (Schaum's

Outline Series, New York, 1967), pp. 88-89, 116-117.

¹⁸E. A. Brandes, *Smithells Metal Reference Book* (Butterworth & Company, Boston, 1983), pp. 14.7-14.8, 8.2, 14.1.

¹⁹L. M. Milne-Thomson, *Theoretical Hydrodynamics* (The MacMillan Company, 4th Edition, New York, 1966), pp.149-150.

²⁰D. Rosenthal, *Welding. J.* **20**, 220s (1941).

²¹W. M. Steen, *Laser Material Processing* (Springer-Verlag, London, 1991), pp. 89-90.

**CHARACTERIZATION OF THERMOPLASTIC
INORGANIC-ORGANIC HYBRID POLYMERS**

Andre Lee
Associate Professor
Dept. of Materials Science and Mechanics

Michigan State University
3514 Engineering Building
E. Lansing, MI. 48824

Final Report for:
1996 SUMMER RESEARCH EXTENSION PROGRAM (96-0129)
PHILLIPS LABORATORY
SUBCONTRACT 97-0843

Sponsored by:
AIR FORCE OFFICE OF SCIENTIFIC RESEARCH
Bolling Air Force Base, D.C.

and

Phillips Laboratory

December, 1997

CHARACTERIZATION OF THERMOPLASTIC INORGANIC-ORGANIC HYBRID POLYMERS

Andre Lee
Associate Professor
Department of Materials Science and Mechanics
Michigan State University

Abstract

The properties of nano-structured plastics are determined by complex relationships between the type and size of the nano-reinforcement, the interface and chemical interaction between the nano-reinforcement and the polymeric chain, along with macroscopic processing and microstructural effects. Recently, families of functionallized polyhedral oligomeric silsesquioxane (POSS) macromers bearing various polymerizable organic groups that can be chemically attached to common polymer such as polystyrene to form random copolymer. These hybrids show many interesting physical and thermal properties differ than the host organic polymers. However, due to rigid nature of inorganic component, it is often difficult to characterize desired properties using conventional thermal-physical techniques. In this study, we use techniques such as positron annihilation lifetime spectroscopy (PALS) as a quantitative method to examine thermal transitions and nanoscopic structure of these hybrid copolymers. In addition to hybrid thermoplastic polymers, we also examined thermal and viscoelastic responses of thermoset epoxy reinforced with epoxy-functionallized POSS. It was found that POSS cages provide topological constraints that hinder the motion of crosslink junctions. Thus, we were able to improve thermal performance of epoxy with no additional difficulty in processing. Furthermore, high temperature mechanical performance was also improved.

CHARACTERIZATION OF THERMOPLASTIC INORGANIC-ORGANIC HYBRID POLYMERS

Andre Lee
Associate Professor
Department of Materials Science and Mechanics
Michigan State University

INTRODUCTION

The design of new materials with enhanced properties continues to be a driver for the investigation of hybrid materials. As hybrid materials are copolymers based on inorganic and organic comonomers, they display enhanced properties by bridging the property space between two dissimilar types of materials. A typical hybrid material will contain a crosslinked inorganic phase covalently bound with an organic phase. Depending on the relative amounts of two components, the properties of the resulting hybrid are intermediate between that of an inorganic and an organic polymer. Such methodology can be used to create either plastic inorganics or toughened plastics, and is superior to traditional blending methods. However, as most hybrid materials are obtained through a so-call "sol-gel" type process. This approach can only be use to create crosslinked polymers. Therefore a more general approach to material chemistry is desired.

Polyhedral Oligomeric Silsesquioxanes (POSS) reagents, monomers and polymers represent such emerging technology as a new chemical feedstock for the preparation of nano-reinforced hybrid plastics. The establishment of broad chemical trees of monomeric POSS reagents and resins based on well-defined POSS cages affords new chemical feedstocks for the modification of properties in nearly all traditional organic polymeric materials.

POSS reagents combine a hybrid inorganic-organic composition with nano-sized cage structures having dimensions comparable to those of most polymeric segments or coils. Hence incorporation of POSS reagents into linear thermoplastic or thermoset networks can be used to

modify the composition, local structure, and chain mobility in polymeric systems. These modifications can ultimately affect the thermal, oxidative, and dimensional stability of many polymeric resins thus upgrading their properties for numerous high performance engineering applications. The current difficulty for further advancement of these materials is the concern about the processing into engineering structures. In this study, we are to examine two different approaches: (1) melt processing of thermoplastic type hybrid materials, and (2) thermal casting process for thermoset high crosslink density, high performance hybrids.

BACKGROUND

Positron Annihilation Lifetime Spectroscopy

The successful application of positron annihilation lifetime spectroscopy (PALS) as a quantitative method for studying the structural characteristics of polymeric materials depends on an understanding of the behavior of the positron injected into the substance. It has found that in all known polymers the positron exist as a free positron or form a bound state with the electrons from the medium, which is then known as positronium (Ps). The typical lifetime of the positron is in the range 0.3 to 0.5 nano-seconds, while the lifetime of Ps depends on the spin state. The singlet state or parapositronium (p-Ps) annihilates in 0.1 to 0.2 nano-seconds, and investigations show that its lifetime, τ_1 , as well as the π^+ lifetime, τ_2 , are not sensitive to temperature and structural changes. The triplet state or orthopositronium (o-Ps) has an intrinsic vacuum lifetime of about 140 nano-seconds, which in amorphous polymers is reduced to τ_3 about 1.5 to 3 nano-seconds, by "pick-off" annihilation with an electron from the surrounding molecules. The fraction of the positron forming o-Ps (I_3), and τ_3 both depend on the temperature and structural changes in the host glass. It is widely accepted that o-Ps exhibits a strong tendency to localize in microvoids or small holes, where the electron density is

lower than that in the bulk, and it has been found that τ_3 increases with an increase in the hole volume.

The positronium formation process in polymeric solids is not well understood. The most popular models, i.e., those due to Ore and Spur, use completely different approaches to explain the process of o-Ps formation and there is no clear evidence in favour of one or the other at the present time. The experimental results show that in porous resins and other porous materials I_3 is proportional to the total surface area of the pores. It is assumed that in glassy polymers I_3 is correlated to the density of holes in the material, but the exact nature of this correlation, however, is not known.

Viscoelastic Responses and Physical Aging

Amorphous polymers and the amorphous regions of crystalline polymers undergo a process known as physical aging. For all glassy materials, when cooled from temperature T_0 above the glass transition temperature, T_g to a temperature T_a below T_g , the material exhibits a slow but significant evolution in its mechanical properties. Since no chemical degradation of material can be invoked, such evolution of properties has come to be called "physical aging". The occurrence of physical aging has been attributed to the non-equilibrium state of glass caused when the amorphous polymer is quenched from above to below its T_g . The non-equilibrium nature of glass makes it thermodynamically unstable. As a result, the thermodynamic properties such as specific volume, or enthalpy decreases with the aging, or annealing time in the glassy state as the polymer molecules strive to attain their equilibrium packing and conformation. The changes in mechanical performance are attributed to the changes in the thermodynamic properties. The phenomena reported most extensively in the literature are concerned with the gradual increases of the isochronal viscoelastic modulus due to shifts in the relaxation response as aging proceeds, the reduction in the creep rate,

the increase of strength under tension or multi-axial deformation, and to a lesser extent, the decrease of the impact fracture energy of the aged materials.

In the "free-volume" theory of the glass transition, the material relaxation time, τ , is primarily determined by free volume, v_f and not by temperature directly. As the material is quenched from above to below T_g , to a first approximation, the value of v_f at T_g is frozen-in and v_f no longer decreases as temperature further cooled to aging temperature T_a . Hence the modulus of polymer at the glassy state remain constant as function of temperature. However at T_a , due to effect of physical aging, the modulus slowly increases with time as the specific volume slowly decreases. The interpretation by the free-volume theory is physical aging is related to slow relaxation of free volume towards its equilibrium. The time required for free volume to reach equilibrium and the rate of aging are related to excess amount of free volume and its distribution, respectively.

As mentioned above, the physical aging affects the viscoelastic response of the polymer by shifting the mechanical, dielectric, etc. relaxation (or retardation) curves to longer time. The amount of shift is a_c , the aging rate is generally define by the double logarithmic shift rate μ :

$$\mu = d \log a_c / d \log t$$

As glassy polymer approach structural equilibrium, the viscoelastic responses cease to shift to longer time. Therefore, it is refer to as "structural equilibrium state". The time to reach this equilibrium may be control by the molecular nature of glassy structure. With the addition of POSS cages, we are to examine the impact of nano-clusters on the overall relaxation of polymeric glasses.

EXPERIMENTAL

Styryl POSS Macromers and Copolymers

The synthesis four POSS macromers containing a single styrene group of $P_1R_7Si_8O_{12}$ with P is

the styrene group and R is either (cyclohexyl, $c\text{-C}_6\text{H}_{11}$) or (cyclopentyl, $c\text{-C}_5\text{H}_9$). These macromers were synthesized in the same manner from the known trisilanols $\text{R}_3\text{Si-O}_3(\text{OH})_3$, and the appropriate trichlorosilane PSiCl_3 . The purity of POSS-styryl macromers was verified using proton NMR. Various amounts of POSS-macromers were used to produce random copolymers of different mole fraction of POSS segment. The random copolymers were synthesized using the additional polymerization technique with AIBN as initiator. The reaction time of 64 hours at 60°C . The molecular weight was characterized using gel permeation chromatography and a combination of refractive index and multi-angle laser light scattering measurements with a Wyatt Technologies DAWN spectrometer.

Epoxy POSS Macromers and Epoxy Networks

Meta-chloroperbenzoic acid (MCPBA) was added to a solution of $(c\text{-C}_6\text{H}_{11})_3\text{Si-O}_3\text{CH}_2\text{CH}=\text{CH}_2$ in methylene chloride and stirred at 23°C for 3 days. The methylene chloride was removed from the reaction mixture by rotary evaporation and the resulting solid was placed into methanol and stirred for 24 hours. The POSS-epoxide product, which is insoluble in methanol, was collected by vacuum filtration, washed with methanol and dried under vacuum to give of mono-functional POSS-epoxide. The product was verify by ^1H NMR.

The nano-reinforced epoxy network glasses used in this study have up to 9 weight percent of POSS-macromer described above. The conventional epoxy resins used in this study were two different di-functional epoxies (diglycidyl ether of bisphenol A, DGEBA; Dow Chemical D.E.R. 332, and 1,4-butanediol diglycidyl ether, BDGE; Shell Chemical Heloxy 67). The curing agent used was the diamine-terminated polypropylene oxide; Huntsman Chemical Jeffamine D230. It is important to note here that the molar ratio of epoxide (the contribution from DER332 and Heloxy 67 combined) and hydrogen (from Jeffamine D230) were equal to one for all epoxy network investigated

in this study. The DGEBA epoxide monomer was first heated at 60°C for two hours to melt any crystals present. First, POSS-epoxide/Heloxyl 67/D230 was mixed together and stirred by hand. The mixture was heated at 60°C for 3 hours to promote the reaction between the amines and epoxide functionalities. The preheated DER332 was then added to the mixture and stirred by hand till clear. The mixture was then degassed in a vacuum for 10 minutes at room temperature. This resin mixture was then poured into a glass tube with a diameter of 12.7 mm and cured in an air oven at 100°C for 4 hours, then slowly cooled in oven overnight to room temperature.

Positron Annihilation Lifetime Spectroscopy

The PALS measurements of the series of specimens were performed by using a conventional fast-timing coincidence method in a temperature-controlled chamber at a constant temperature of $25 \pm 1^\circ\text{C}$. The thermal response was investigated by heating the material up to 480°K. The cooling was provided by the addition of LN_2 . All spectrum were collected at a constant temperature with acquisition time of 3 hours. Due to the long measurement time needed for a thermal scan (about 84 hours), sample was first saturated with positron radiation for 6 hours to properly measurement of I_3 . The positron source [$\sim 1 \times 10^4$ Bq ($\sim 30 \mu\text{Ci}$) of ^{22}Na] was deposited on the surface of an annealed single-crystal copper disc. As a result, I_3 measured herein is approximately half of that determined with the source sandwiched between two samples. The spectra were acquired and stored in a MicroVAX-based multichannel analyzer. The lifetime spectra were resolved into three components by using PFPOSFIT program.

Differential Scanning Calorimetry

Heat flow and glass transition measurements were performed with a TA Instrument 2920 differential scanning calorimeter. This calorimeter is based on the modern modulation technique. By apply a sine wave on top of heating ramp (an analytical Fourier transformation method), one can

separate reversible and non-reversible heat flow. Any thermal transition such as glass transition appears as a slope discontinuity on the non-reversible heat flow trace. This calorimeter was used in this study to resolve glass transition for polymer containing high mole fraction of POSS segments, which can not be examine using conventional DSC. The sample was first heated to 250°C from 50°C at a rate of 5°C/minute, with modulation of 1 Hz and amplitude of $\pm 1^\circ\text{C}$. The glass transition temperature was determined as the inflection point of the glass transition region on the DSC thermograms.

Small-Strain Stress Relaxation

Mechanical tests were performed using a computer-controlled servo-hydraulic testing machine (Instron model 1321) equipped with an oven for temperature control. The temperature measurements taken at the top and bottom surfaces of the samples showed a gradient of less than 0.3°C. Oven stability was observed to be better than $\pm 0.2^\circ\text{C}$ for over 3 day period. The tensile test specimens were first annealed for 30 minutes at 105°C (at less 20°C above the DSC determined T_g) to erase any aging that occurred during storage and were then placed in the testing machine at the testing temperature, and the samples were then monitored as they aged.

All mechanical tests were carried out in uniaxial extension under stress relaxation conditions.

A small strain was applied periodically at aging time, t_a , that double with each test; i.e., $t_a = 30$ minutes, 60 minutes, 120 minutes, etc. The duration, t_d , of the deformation was varied so that the ratio of t_d/t_a was constant throughout the aging experiment. The value of t_d/t_a in this study was 0.05. A short duration time was used so that the changes that occurred in polymer structures during the mechanical experiment would be minimal and hence would not influence the measurements. The small-strain stress relaxation technique was used to examine the effect of PSS cages on the viscoelastic response of polymeric glasses during physical aging. The applied strain used here was 0.001 and was measured

with an extensometer. The load was measured with an 1000 lbs. capacity load cell.

RESULTS AND DISCUSSION

Linear Thermoplastic Styryl-POSS copolymers

Differential Scanning Calorimetry

Calorimetric measurements were performed for all styryl-POSS copolymer with both cyclohexyl and cyclopentyl-substituted POSS cages. Previously, it was reported that no DSC observable glass transition for copolymer with high mole fraction of POSS segments. However, using the modulation DSC technique it was clear that one can determine the glass transition temperature even for POSS-homopolymer (see Figure 2). Therefore, without any difficulty we can obtain T_g for copolymer with 16 mole percent of POSS segments. All DSC traces were depicted in Figures 2 - 7. The glass transition temperature for all specimen studied was depicted in Figure 8. The following observations were made:

1. In general as amount of POSS segments in copolymer increases the glass transition increases. Moreover, the transition remains sharp, which indicate the copolymer was not phase separated in the length scale of DSC experiment.
2. From Figure 8, we suggest that cyclohexyl substituted POSS cages provided a more effective impact on the glass transition temperature. However, the molecular detail for why cyclohexyl is more effective than cyclopentyl is still not clear at this time.

PALS results

In Figure 9, we depict the value of τ_3 at room temperature (25°C) for POSS copolymers with varying mole fraction of POSS segments. As mentioned above that the value of τ_3 directly reflect the size of free volume. As we increase the mole fraction of POSS segment in the copolymer, the value

of τ_3 increase. Hence the results in Figure 9 suggest that the presence of POSS cages hinder the packing of polymeric coils.

Figure 10, we depict the value of τ_3 as a function of temperature. Similar to the DSC experiments, we observed a change in slope at temperature near the glass transition temperature as reported by DSC. It is interesting to point out here that the physics of between these two experimental methods are complete different. DSC is based on the difference in heat flow above and below glass transition, while the value of τ_3 is related to the size of hole. For sample with higher mole fraction of POSS segments, it became more difficult to determine the exact value of glass transition temperature. However, this difficulty is not presence for PALS measurement. In Figures 11 and 12, we showed τ_3 versus temperature for samples with 16 mole percent of POSS segments. The change in slope can easily be determined.

Another piece of information that can be obtain using PALS is the number of holes. Which is represent by the value of I_3 . In Figure 13, we plotted I_3 versus temperature for 8 mole percent POSS- MPS copolymers. Here, we observed another change of slope at temperature near 200°K. It is not clear as to the molecular origin of this change. It is possible relate to the so call β transition in polystyrene.

Crosslinked Thermoset POSS-Epoxy

DSC study

Calorimetric measurements were performed for network glass containing 5 and 9 weight percent of a mono-functional POSS-epoxy nano-reinforcements. Measurement of glass transition is routinely used as part o resinous material characterization and provides direct insight into the mobility of polymer chains and junctions. Although here we use only mono-functional POSS epoxy, but due to the size of POSS cages, the mobility of network junctions were hindered. Thus, as weight fraction

of POSS cage increases the glass transition temperature (mid-point of the specific heat transition) also increase. Unlike in the linear thermoplastic copolymers, the onset temperature of glass transition was not observed to change. This suggests that the presence of POSS cages within the network slows down the transition from glassy-like behavior to rubbery-like behavior. Hence the material maintains its modulus longer at elevated temperatures. However, since the onset temperature is principally governed by the difunctional epoxy-amine junctions and is therefore not affected by the presence of mono-functional POSS cages that chemically attached to the network.

Isothermal Aging - Stress Relaxation Experiments

The relaxation modulus curve displayed in Figure 17 are representative of the results obtained with the epoxy network glass aged at a temperature below the glass transition temperature. They correspond to aging times of 0.5 hour, 1 hour, 2 hours, and up to 64 hours, as indicated. In general, for a given sample, it is always possible to shift the relaxation curve obtained at different aging times horizontally along the time axis to form a time-aging time master curve, as shown in Figure 17. To compare the relaxation modulus curves obtained at different temperatures and between the various epoxy compositions, the relaxation modulus curve was fitted with a stretched exponential Kohlrausch-William-Watt type function:

$$E(t) = E_0 \{ \exp[-(t/\tau)^\beta] \}$$

where E_0 is the zero-time tensile modulus, τ is the characteristic relaxation time, and β is the shape parameter related to the breadth of the stress relaxation modulus curve. The numerical analysis for the curve fits at each experimental condition was performed using Kalidagraph™ non-linear least-square data analysis software on a personal computer. We found that the value of β and E_0 remained constant despite the differing amounts of mono-functional POSS-epoxy that had been added into the glassy network. In contrast, the breadth of the glass transitions was observed to increase with higher

loading of POSS-epoxy in the network. Furthermore, it is interesting to note that when tested at different aging temperatures, the value of β was not affected by the amount of POSS-epoxy presence. In Figure 18, we depict the relaxation modulus curves for different loading of POSS-epoxy monomers after 64 hours of isothermal aging at a temperature of 63.9°C. It is clear that these relaxation curves can be superimposed with only horizontal shift along the time axis. Furthermore, it is interesting to point out that the value of E_r is not affected by the presence of the inorganic nano-reinforcements. This may be in part a reflection of the mono-functional nature of POSS-epoxy used in this study. Despite the ability of the POSS cages to hinder the relaxation motion of network junctions from a chain terminus location within the network, they do not contribute to the overall deformation process of such glassy networks from this position. Interestingly such mono-functional POSS-epoxide may be useful for enhancing glass transition without increasing crosslinking density and potentially detracting from the desirable mechanical properties of such epoxy networks.

The characteristic relaxation time, τ , of the networks was also obtained using the above KWW function from the data of the stress relaxation experiments. From Figure 17, we shown that as the isothermal aging time increase the value of τ also increases. This is a common phenomenon of glass-forming materials in the nonequilibrium glassy state. As the material gradually relaxes into its equilibrium state, the molecular mobility is impacted. Hence, the characteristic relaxation time is expected to increase with increased isothermal aging time until the material reaches its structural equilibrium state. Therefore, the rate of change in τ is use as a measure for how a glassy system approaches its structural equilibrium state. In Figure 19, we constructed a double-logarithmic plot of τ versus aging time at a given test temperature for the epoxy glasses containing different loading of the POSS nano-reinforcements. Similar plots but at different testing temperature is shown in Figures 20 and 21. For aging temperature well below T_g , the double logarithmic rate of change in the

characteristic relaxation times does not appear to be affected by the presence of POSS cages. However, at any given aging time, the networks containing higher loading of the POSS nano-reinforcements have higher characteristic relaxation time values. Increased relaxation time is also to be expected given the fact that the POSS-reinforced network also shows higher values of T_g .

To examine the effect of POSS cages on the molecular mobility, it is necessary for the system to be in the same thermodynamic state, i.e., the difference between testing temperature and the T_g is the same. In Figure 22, we show a double logarithmic plot of characteristic relaxation time versus aging time for stress relaxation experiments performed at a temperature 9°C below the respective T_g . For neat resin sample, we observed a change in the slope of characteristic relaxation time versus aging time after 32 hours. This is an indication that the sample is close to its final structural equilibrium. However, for sample with 9 weight percent of POSS-epoxy, the relaxation modulus curve continued to shift to longer times, i.e. no change in the slope of characteristic relaxation time versus aging time. After 64 hours of isothermal aging, the sample had not yet reached its structural equilibrium point. From this observation, we proposed that the presence of POSS cages provide topological constraints to the network junctions which prevent or severely retard the process which the network can reach the structural equilibrium. Given that the physical size of POSS-cages approach those of most polymer dimension the inability of such a network to relax can be anticipated. Therefore, the time needed to reach structural equilibrium is longer for sample with POSS cages attached to the network chains.

CONCLUSIONS

The synthesis of soluble, thermoplastic hybrid materials from well-defined inorganic cluster containing only a single polymerization site has been developed. Styryl-based POSS derivatives were

successfully copolymerized with methylstyrene. Detail thermal analysis was carry out using modern DSC technique. We were able to determine the glass transition temperature for those copolymers with high loading f POSS segments. It was determine that these copolymers form single phase system and copolymers with more POSS segments has higher value of T_g .

Using PALS technique, the glass transition temperature of styryl-based POSS copolymer was easily determined. This is due to the different physics involving with measurements. Result shows that average size of hole increases with POSS contain as determine by PALS. This suggests that the presence f POSS cages prevent the formation of random polymer coils. The detail of POSS-based copolymer is to be investigator further using small angle neutron scattering (SANS) technique.

Commonly used DEGBA epoxy resins were formulated with mono-functional POSS-epoxy nano-reinforcements and subsequently cured into structural thermoset network with amine-terminated agents. DSC result shows that the value of T_g increases with increased loading of the mono-functional POSS epoxy into the network. This increase in T_g without increasing the degree of crosslinking within the network may be of technological important, which are to be investigated in the future.

The networks were subjected thermal quenching and aging experiments at temperature below T_g . At a constant temperature below the T_g of the system, it is possible to age these glassy networks to the point where they reach a structural equilibrium. However the topological constraints provided by the presence of POSS-reinforcements, slows down the motion of the network junctions and hence the time needed t reach structural equilibrium is dramatically increased relative to that for non-reinforced networks.

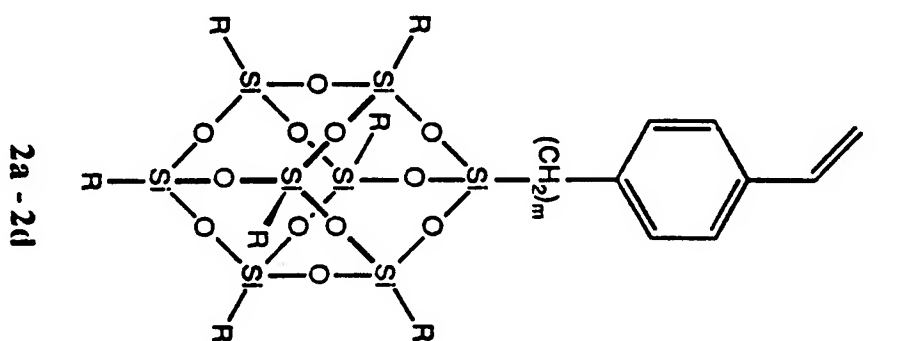
ACKNOWLEDGMENTS

The Air Force Office of Scientific Research through the Summer Faculty Research Extension Program supported this research. The author also likes to express his thanks to Dr. JD Lichtenhan of Phillips Laboratory for many useful discussions during this period of research.

Figure Captions

- Figure 1. Schematic of Styryl-POSS/Methylstyrene Copolymers
- Figure 2. Reversible heat flow trace and heat capacity trace obtained using modulated DSC for homopolymer of Styryl-POSS with cyclohexyl group. A T_g of 379.2°C is depicted.
- Figure 3. Heat capacity trace obtained using modulated DSC for homopolymer of Styryl-POSS with cyclopentyl group. A T_g of 372.0°C is depicted.
- Figure 4. Reversible heat flow trace and heat capacity trace obtained using modulated DSC for copolymer of Styryl-POSS/MPS with 4 mole percent of POSS segment. A T_g of 109.0°C is depicted.
- Figure 5. Reversible heat flow trace and heat capacity trace obtained using modulated DSC for copolymer of Styryl-POSS/MPS with 8 mole percent of POSS segment. A T_g of 118.9°C is depicted.
- Figure 6. Reversible heat flow trace and heat capacity trace obtained using modulated DSC for copolymer of Styryl-POSS/MPS with 16 mole percent of POSS segment. A T_g of 134.5°C is depicted.
- Figure 7. Reversible heat flow trace and heat capacity trace obtained using modulated DSC for copolymer of Styryl-POSS(cyclopentyl)/MPS with 16 mole percent of POSS segment. A T_g of 112.4°C is depicted.
- Figure 8. T_g of Styryl-POSS/MPS copolymers versus POSS segment content as obtained using DSC. Filled symbols represent cyclopentyl system and open symbols represent cyclohexyl system.
- Figure 9. τ_h (Average size of holes) as measured using PALS at room temperature for styryl-POSS/MPS copolymers versus POSS segment content. A blend is cyclohexyl system and B blend is cyclopentyl system.
- Figure 10. τ_h (Average size of holes) as a function of temperature of styryl-POSS/MPS copolymers with 8 mole percent of POSS segments. Square symbols represent cyclopentyl system and circle symbol represent cyclohexyl system.
- Figure 11. τ_h (Average size of holes) as a function of temperature of styryl-POSS(cyclohexyl)/MPS copolymers with 16 mole percent of POSS segments.
- Figure 12. τ_h (Average size of holes) as a function of temperature of styryl-POSS(cyclopentyl)/MPS copolymers with 16 mole percent of POSS segments.

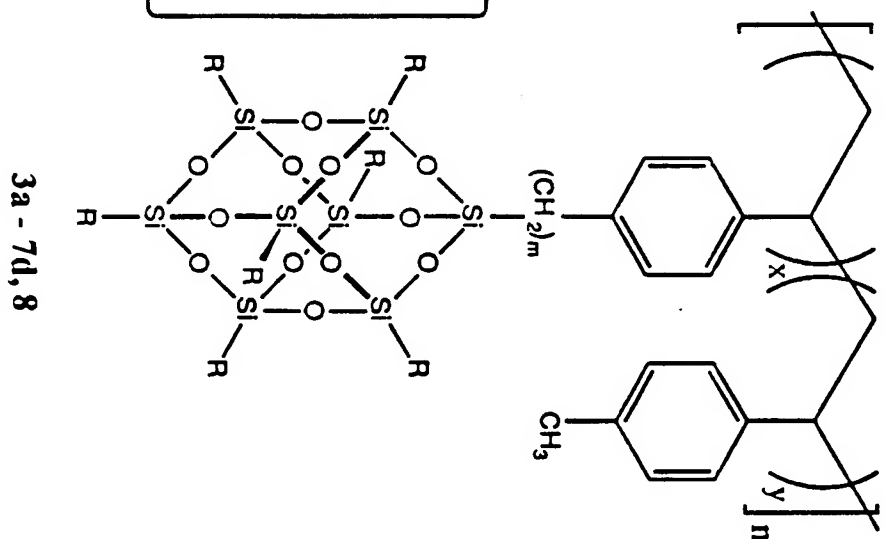
- Figure 13. I_3 (number of holes) as a function of temperature of styryl-POSS/MPS copolymers with 8 mole percent of POSS segments. Square symbols represent cyclopentyl system and circle symbol represent cyclohexyl system.
- Figure 14. PHVF ($\tau_3 * I_3$ or total hole volume) as a function of temperature for styryl-POSS (cyclohexyl)/MPS copolymers.
- Figure 15. PHVF ($\tau_3 * I_3$ or total hole volume) as a function of temperature for styryl-POSS (cyclopentyl)/MPS copolymers.
- Figure 16. Schematic of curing cycle of POSS-epoxy system.
- Figure 17. Small-strain stress relaxation modulus curves for DGEBA/D230/Heloxy67/9wt% POSS-Epoxy glass at aging temperature of 63.9°C. Master curves offset by an arbitrary shift for clarity.
- Figure 18. Small-strain stress relaxation modulus curves for DGEBA/D230/Heloxy67/x wt% POSS-Epoxy glass after 64 hours of isothermal aging at a temperature of 63.9°C.
- Figure 19. Characteristic relaxation time versus Aging time for DGEBA/D230/Heloxy67/x wt% POSS-Epoxy glasses at a testing temperature of 54.1°C.
- Figure 20. Characteristic relaxation time versus Aging time for DGEBA/D230/Heloxy67/x wt% POSS-Epoxy glasses at a testing temperature of 58.9°C.
- Figure 21. Characteristic relaxation time versus Aging time for DGEBA/D230/Heloxy67/x wt% POSS-Epoxy glasses at a testing temperature of 63.9°C.
- Figure 22. Characteristic relaxation time versus Aging time for DGEBA/D230/Heloxy67/x wt% POSS-Epoxy glass at testing temperature of 9°C below its respective T_g .



AIBN / 4-Methylstyrene / 60 °C

Approximate Mole % Used in Polymer Synthesis			
Mol % 2	Mol % 4-Methylstyrene	Copolymer	
100 %	0 %	3a-d	
80 %	20 %	4a-d	
50 %	50 %	5a-d	
20 %	80 %	6a-d	
10 %	90 %	7a-d	
0 %	100 %	8	

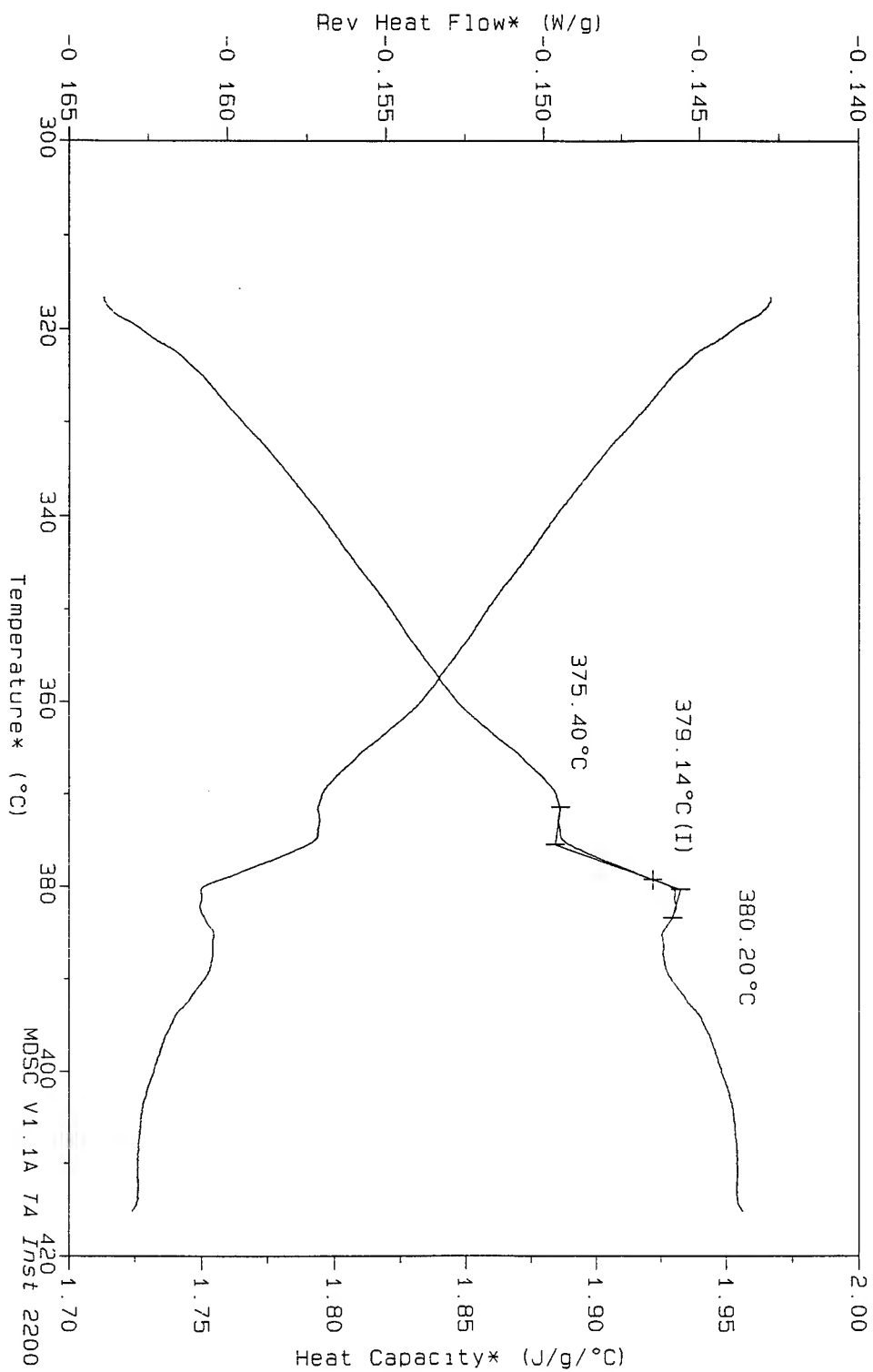
#a R = *c*-C₆H₁₁, m = 2
 #b R = *c*-C₅H₉, m = 2
 #c R = *c*-C₆H₁₁, m = 0
 #d R = *c*-C₅H₉, m = 0



Sample: CY7T8POSSPS-100
Size: 14.1000 mg
Method: HEATING TO 450 LEE
Comment: N2 PURGE 50ML/MIN

DSC

File: C:\VLP05S1.011
Operator: A. LEE
Run Date: 22-Sep-96 06:40

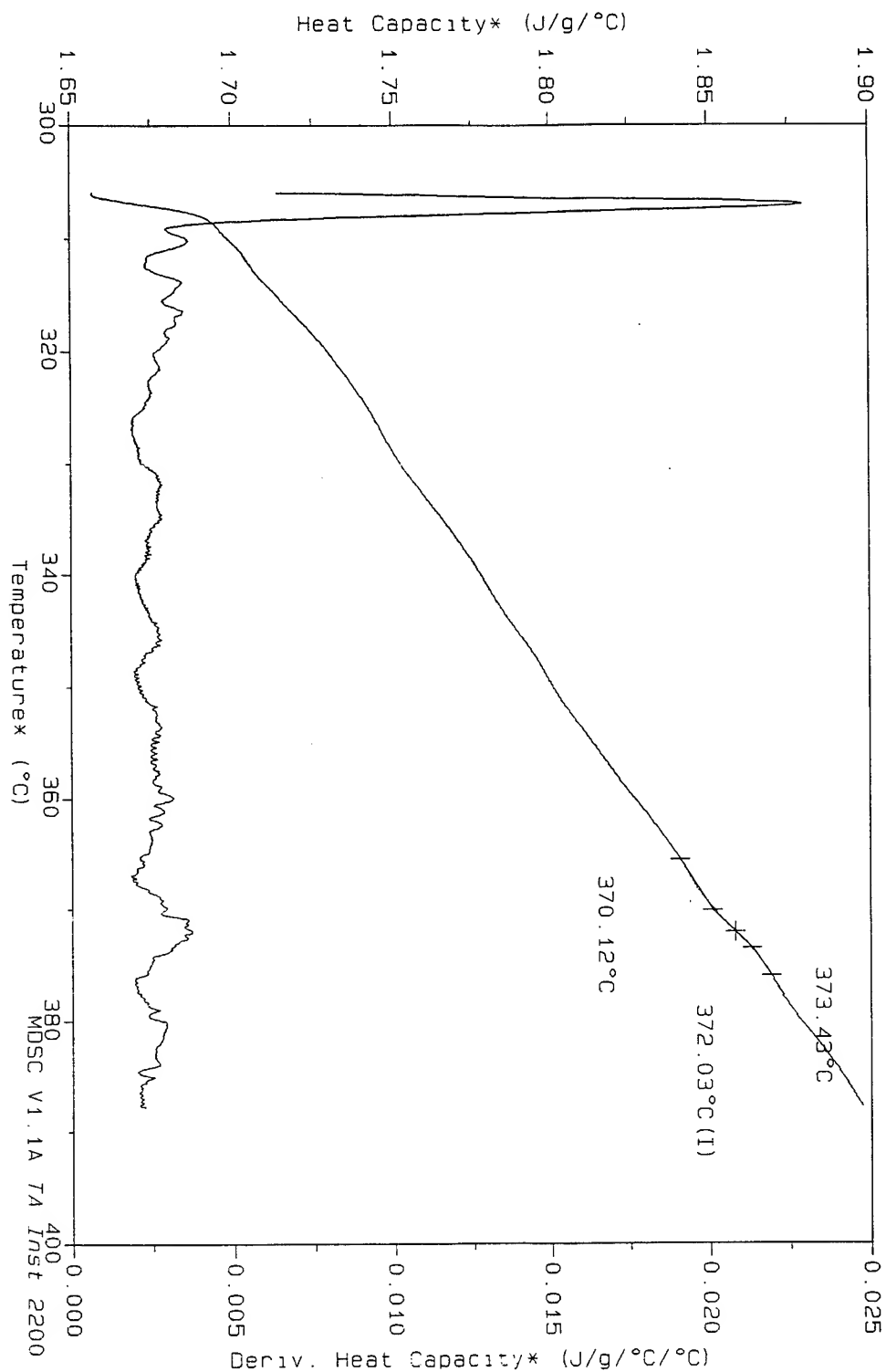


Sample: CP718POSSPS-100
Size: 6.1000 mg
Method: MOD 5°C/MIN TO 250°C LEE
Comment: N2 PURGE 50ML/MIN

DSC

File: C:\AYLP05S1.009
Operator: A LEE
Run Date: 22-Sep-96 04:06

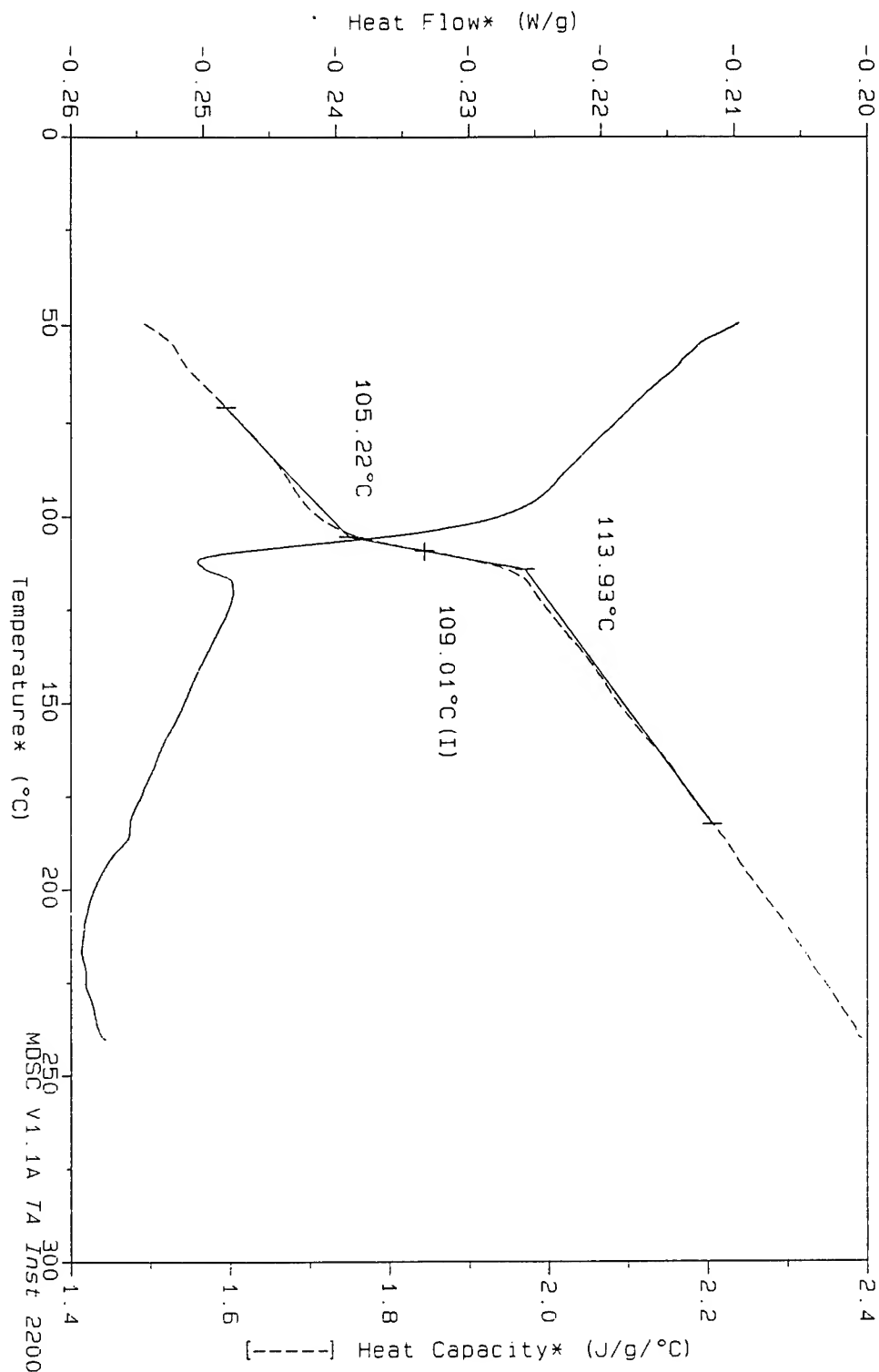
Handwritten: 1.000



Sample: CY7T8PS/4
Size: 4.6000 mg
Method: MOD 5°C/MIN TO 250°C LEE
Comment: N2 PURGE 50ML/MIN

DSC

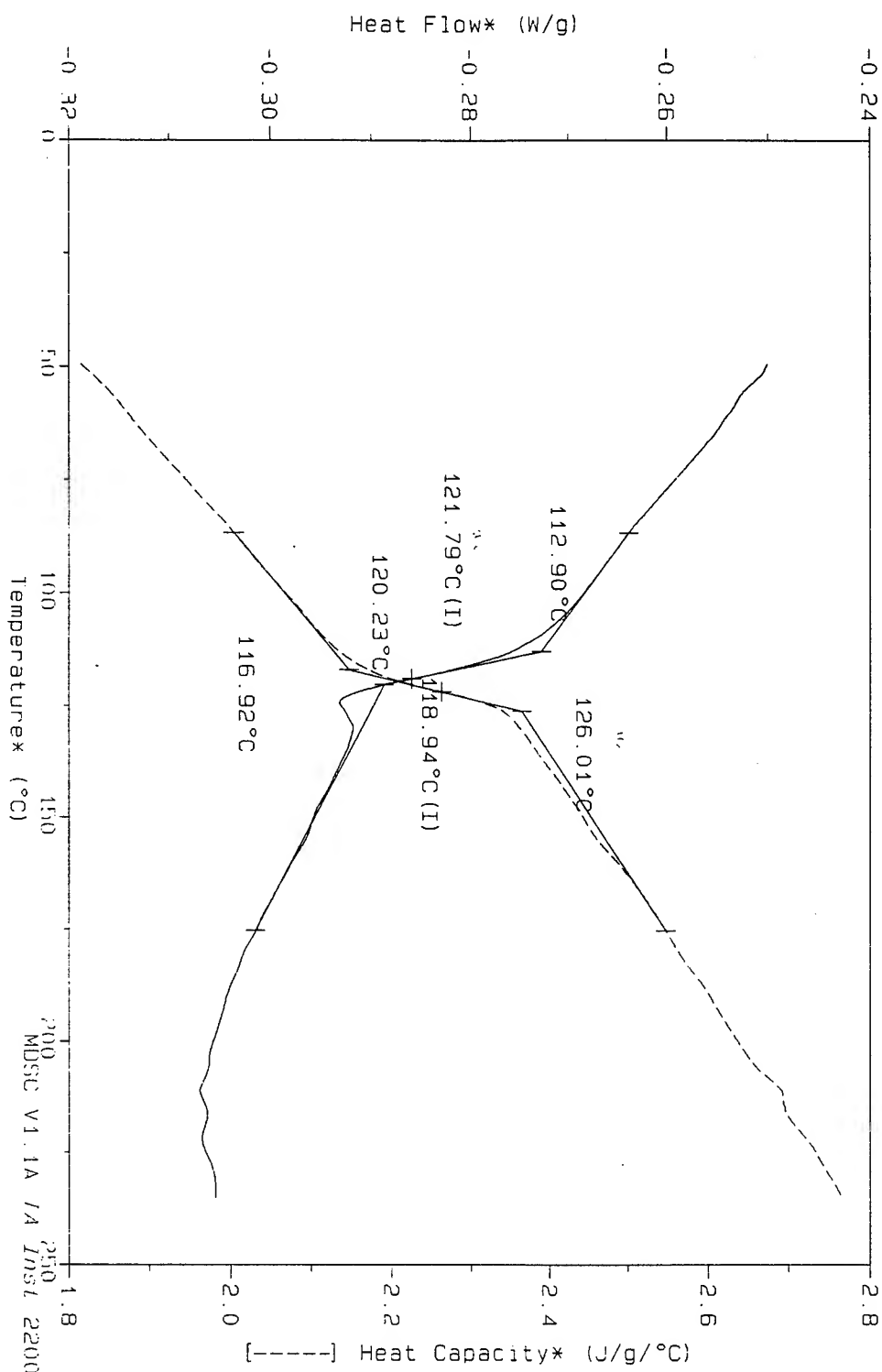
File: C:\YLPOSS1.005
Operator: A LEE
Run Date: 16-Sep-96 07:22



Sample: CY718PS/B
Size: 3.8000 mg
Method: MOD 5°C/MIN TO 250°C LEE
Comment: N2 PURGE 50ML/MIN

DSC

File: C:\VLP05S1.003
Operator: A LEE
Run Date: 15-Sep-96 05:26

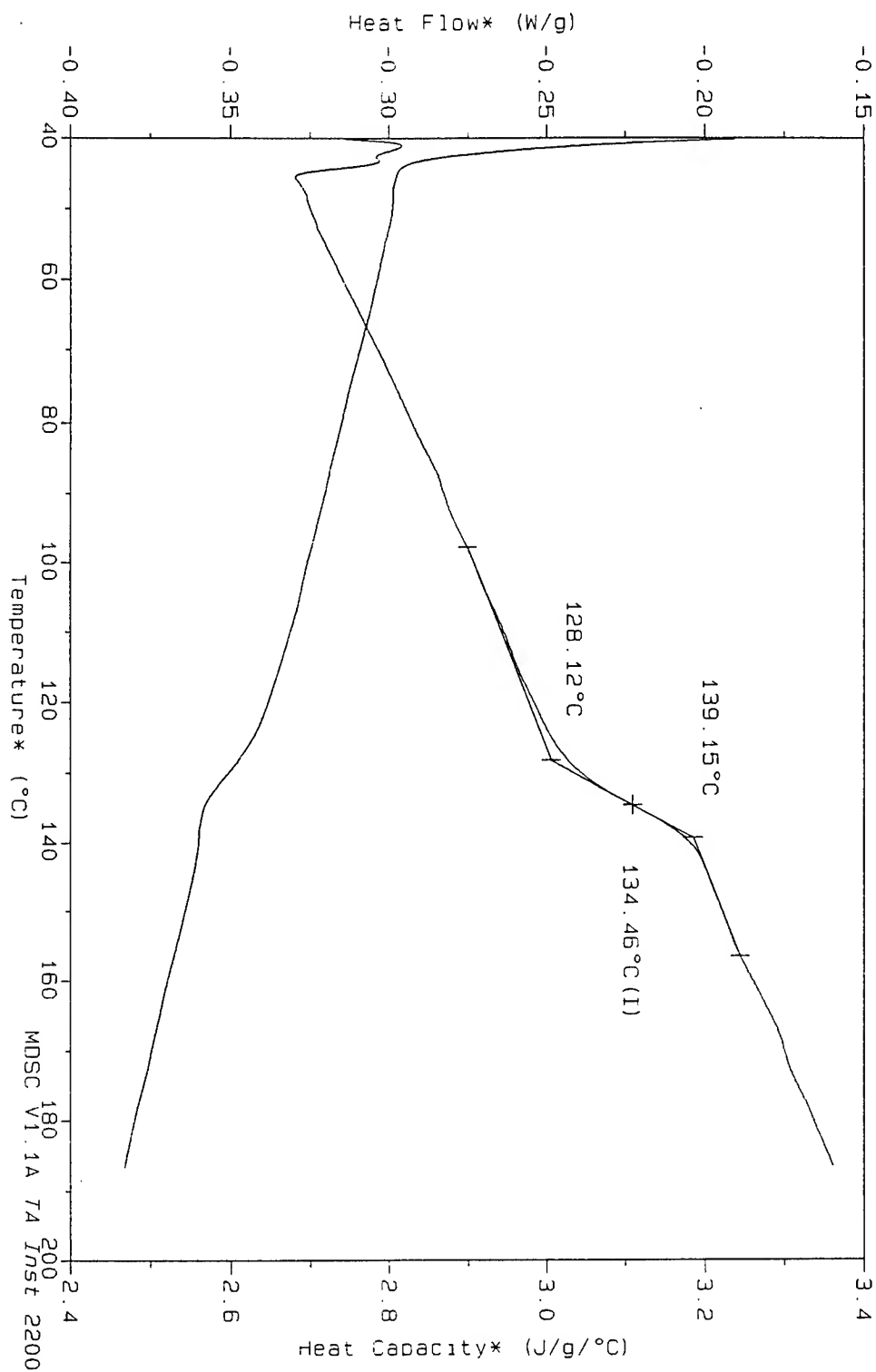


Sample: CY7T8POSSPS/16%
Size: 3.1000 mg
Method: MOD 5°C/MIN TO 250°C LEE
Comment: N2 PURGE 50ML/MIN

DSC

File: C:\YLPOSS1.010
Operator: A. LEE
Run Date: 22-Sep-96 05:09

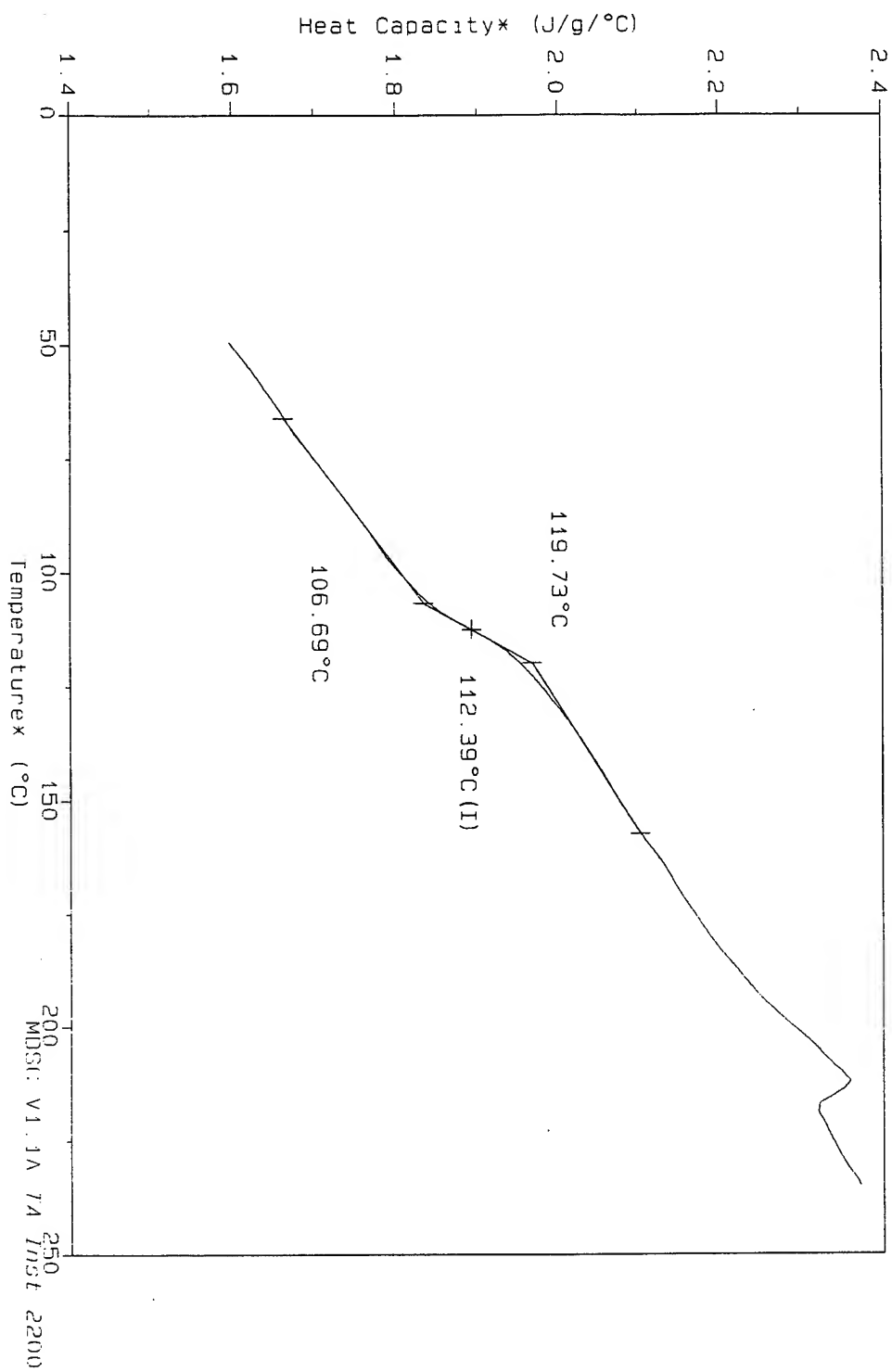
Handwritten: Heat



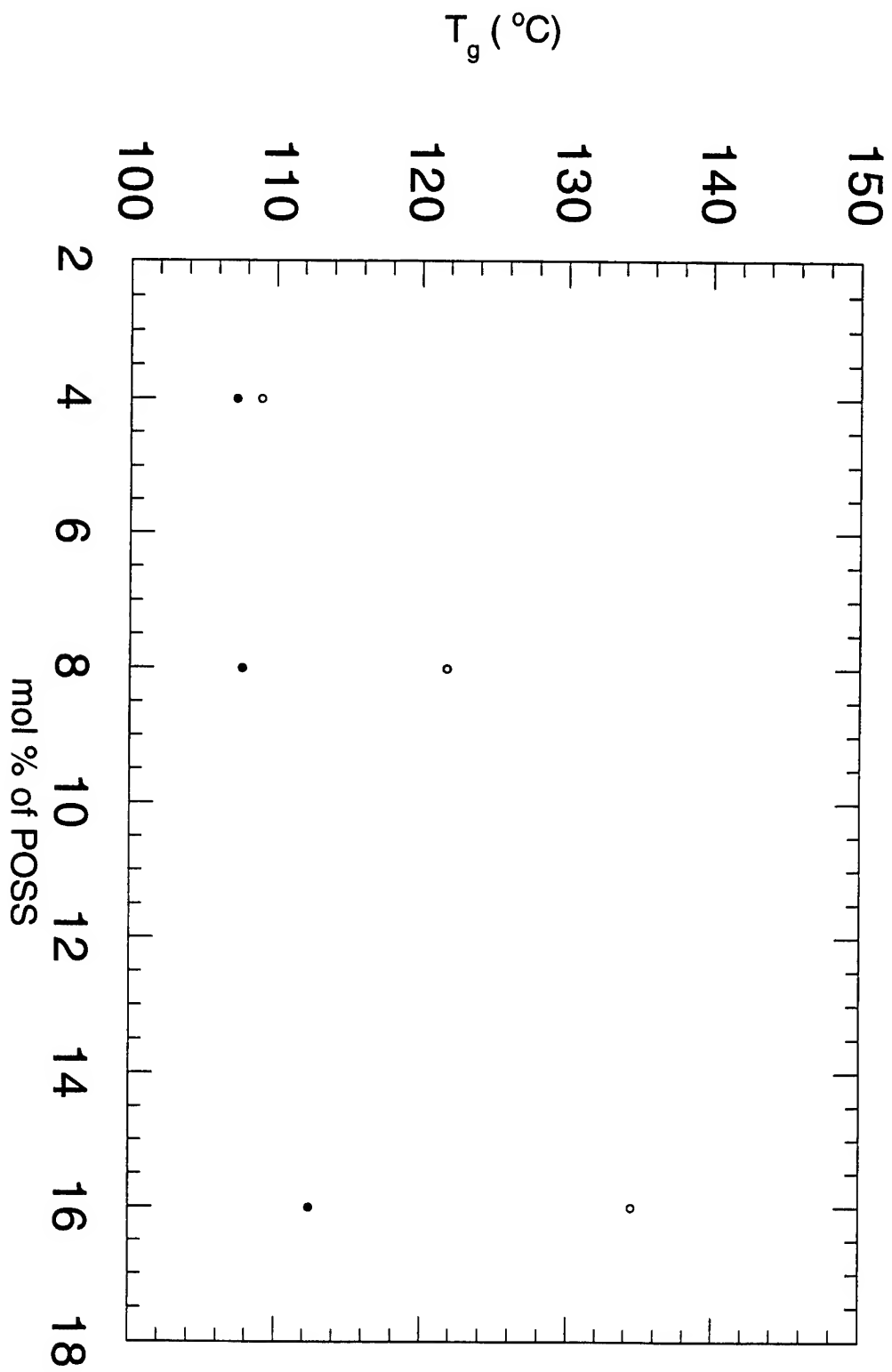
Sample: CP8T8PS/16
Size: 5.8000 mg
Method: MOD 5°C/MIN TO 250°C LEE
Comment: N2 PURGE 50ML/MIN

DSC

File: C:\VLP05S1.002
Operator: A LEE
Run Date: 15-Sep-96 03:31



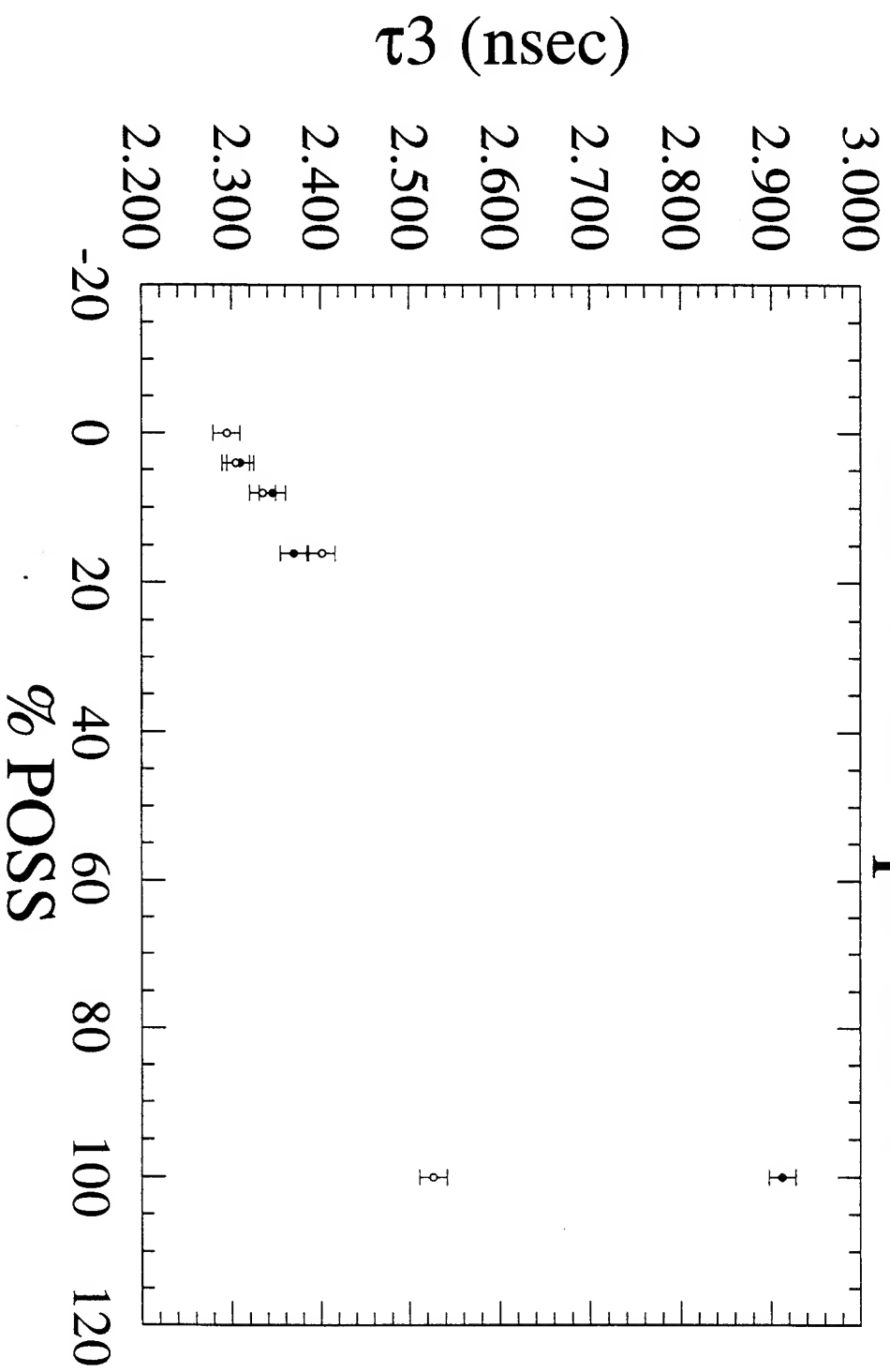
DSC Results



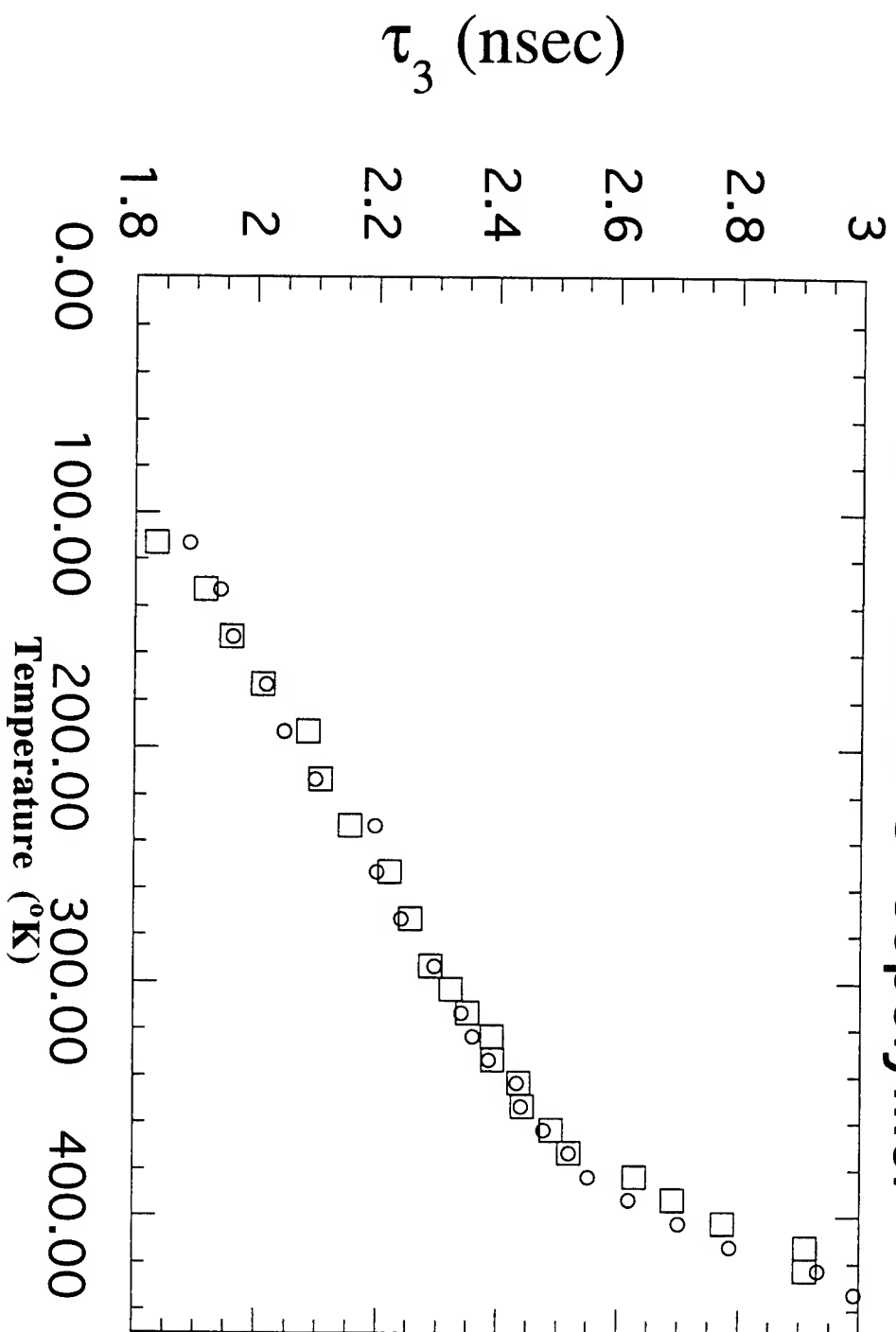
PALS

• "A" blend
◦ "B" blend

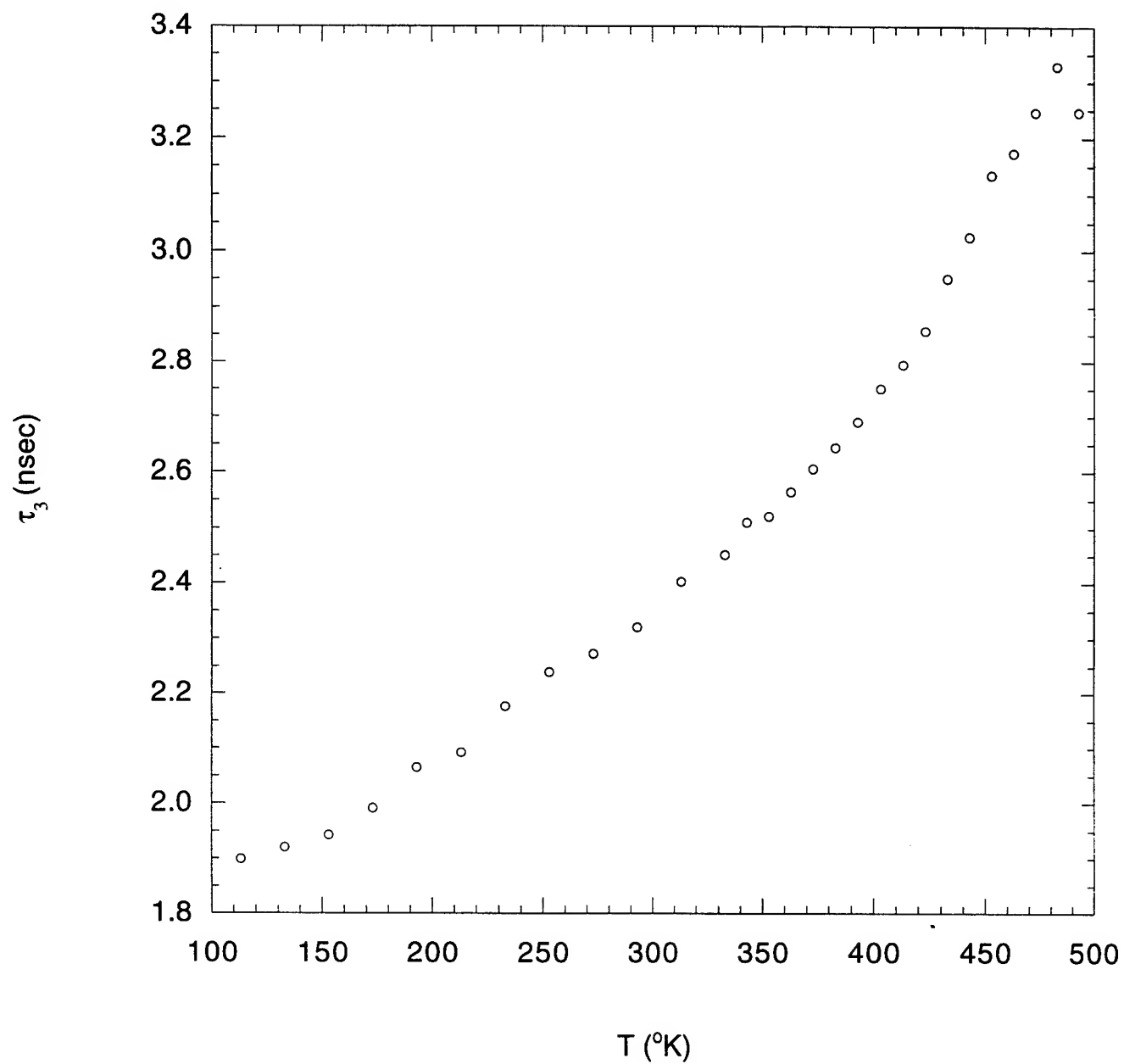
Room Temperature



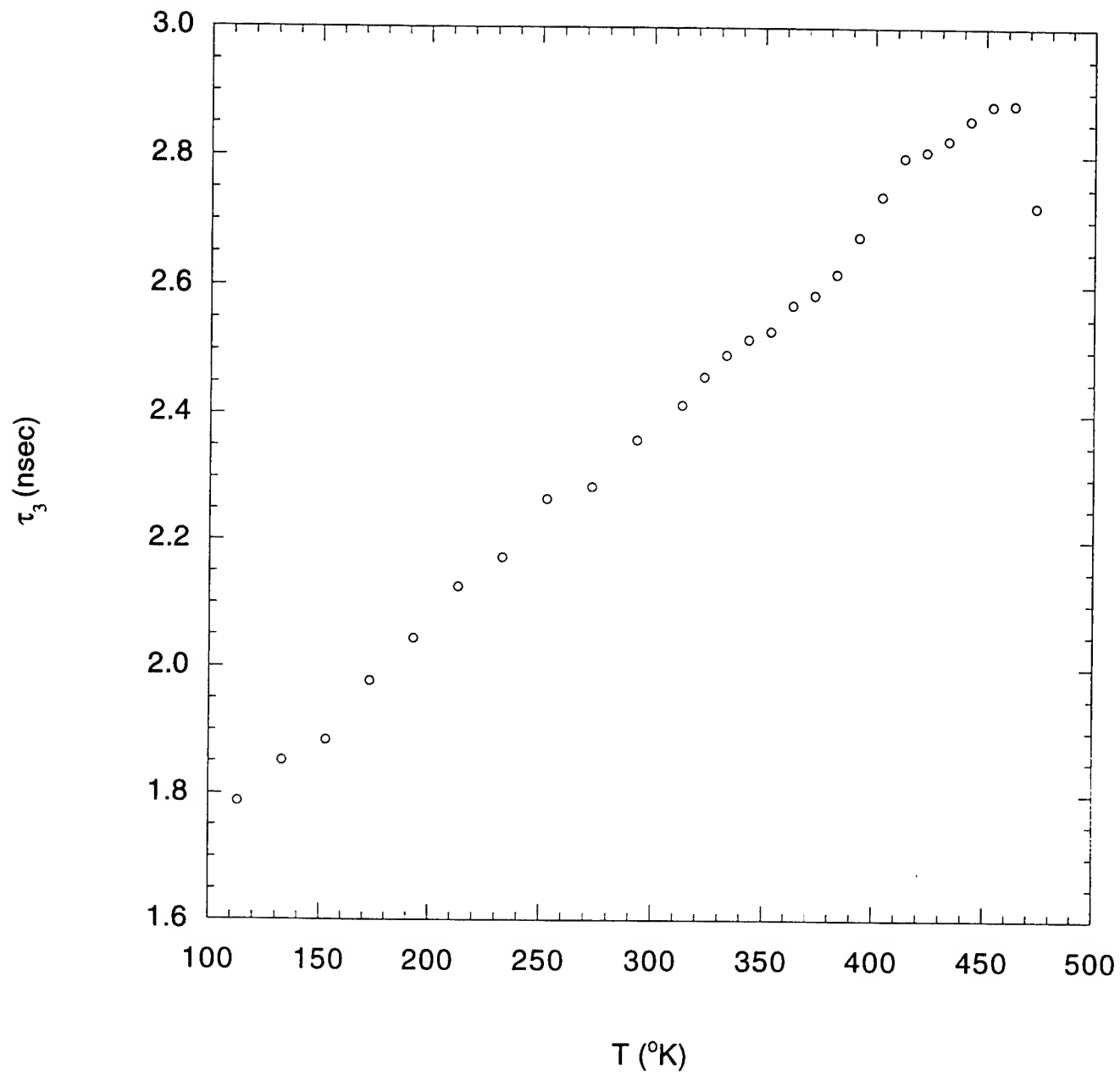
8% Poss/MPs copolymer



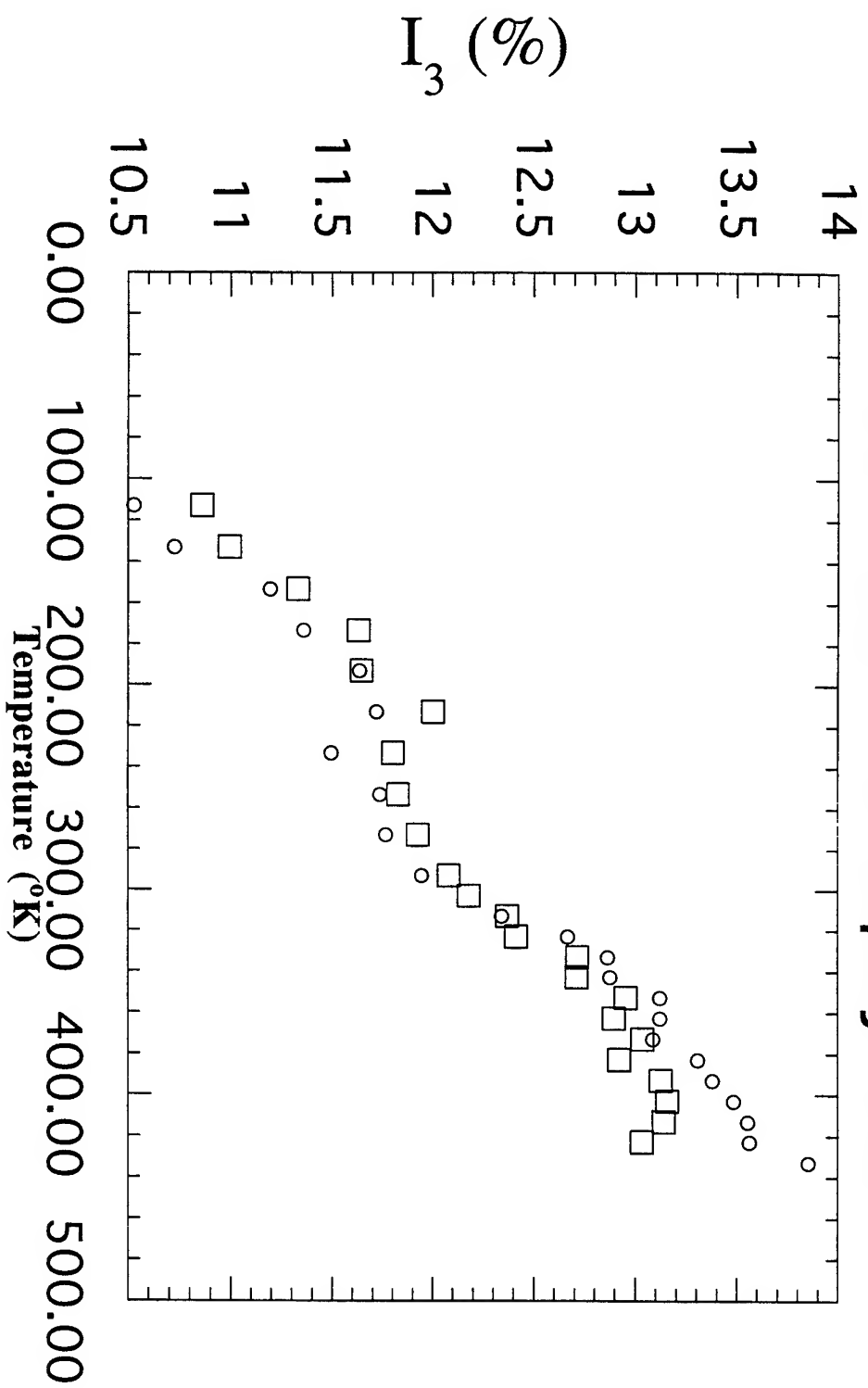
A POSS/MPS 16%



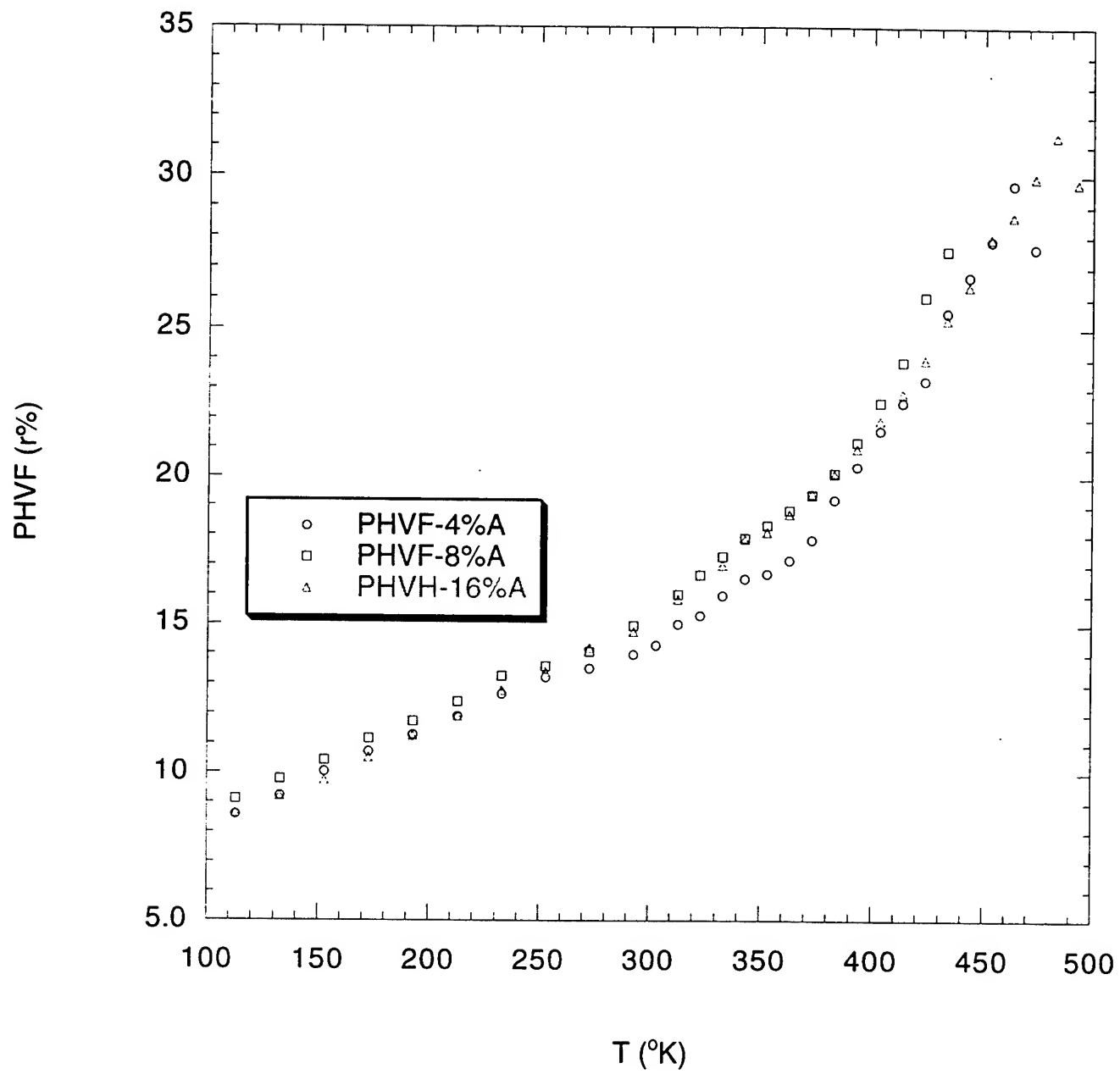
B POSS/MPS 16%



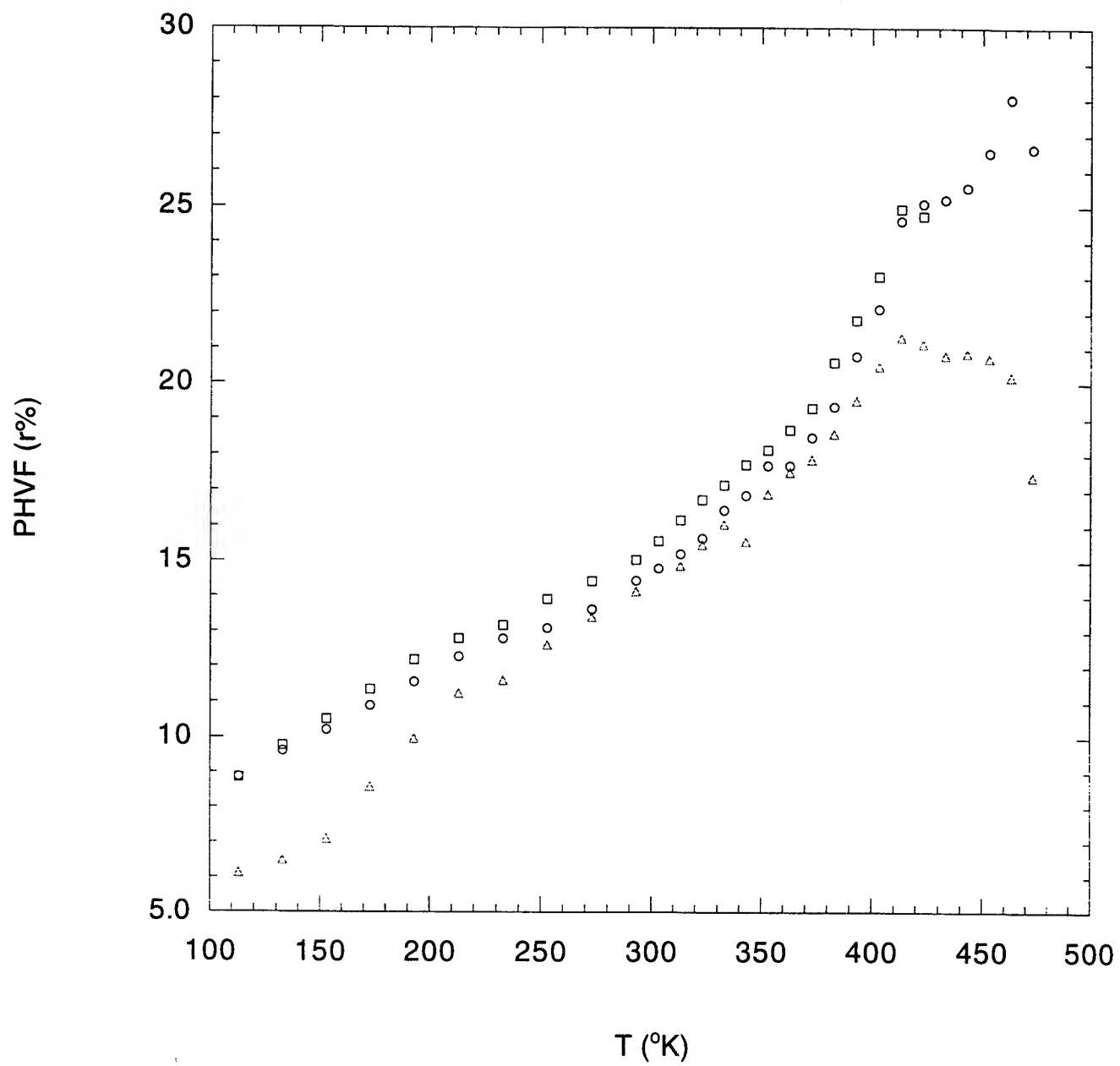
8% Poss/MPs copolymers

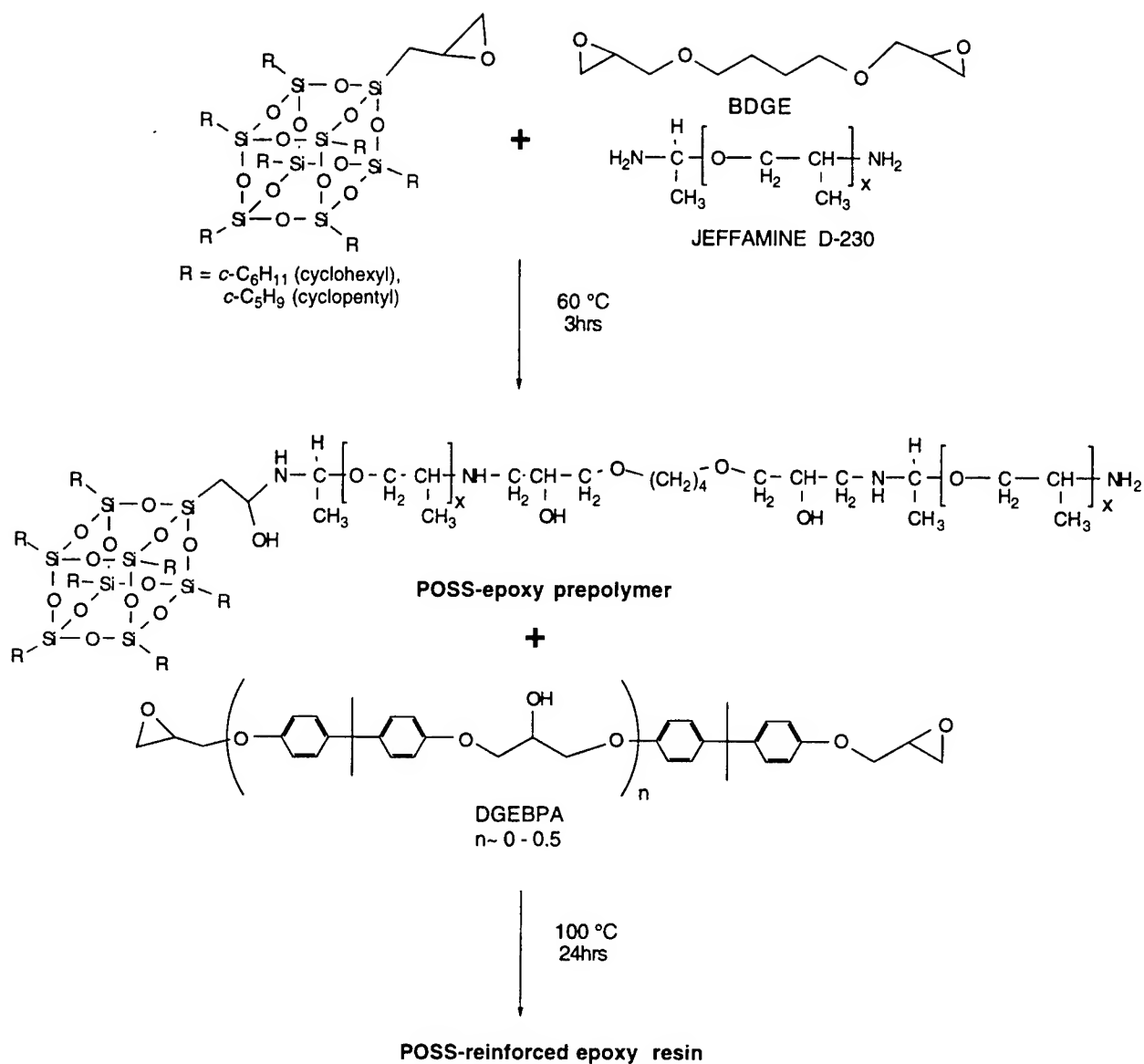


APOSS/MPS

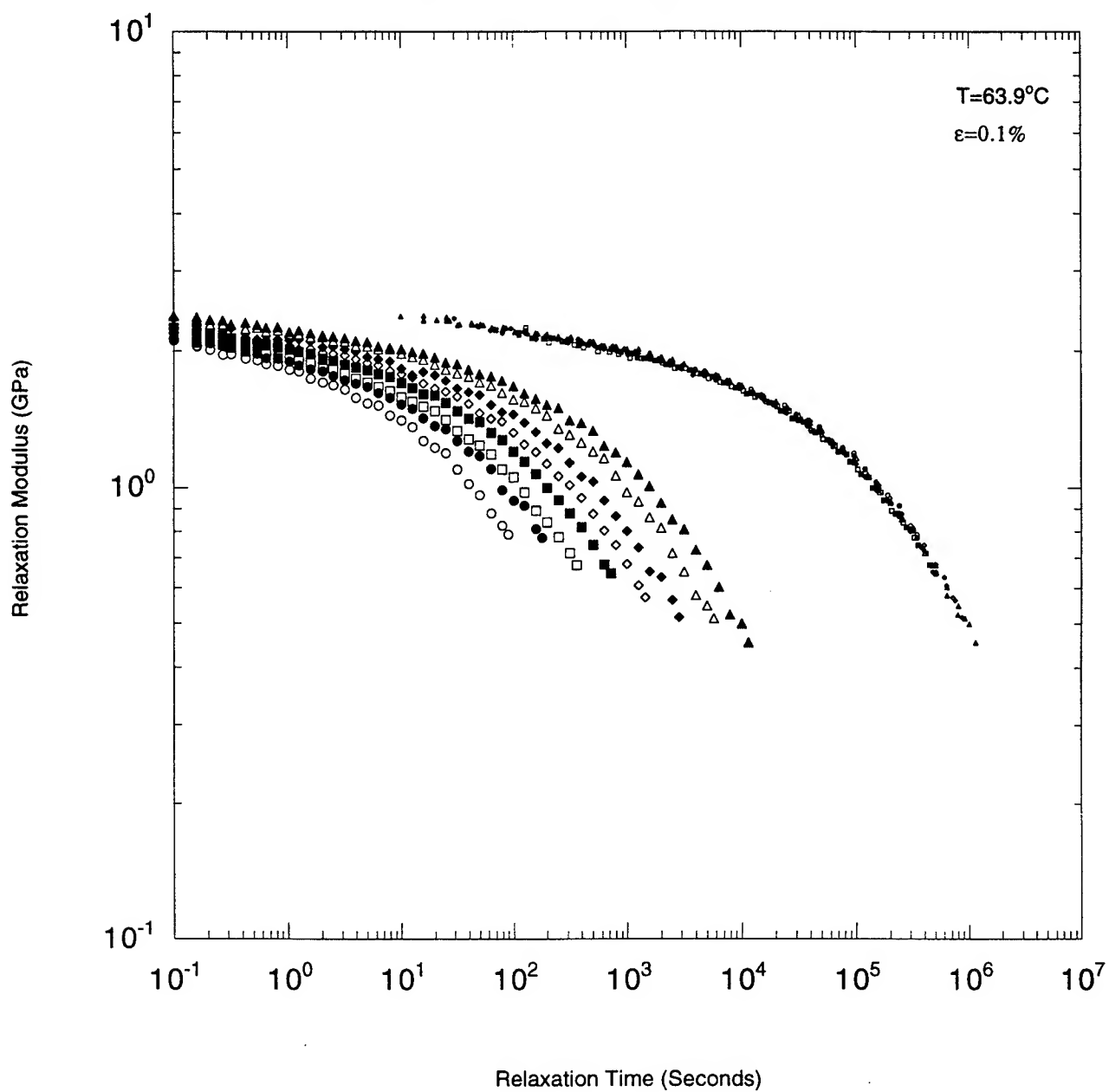


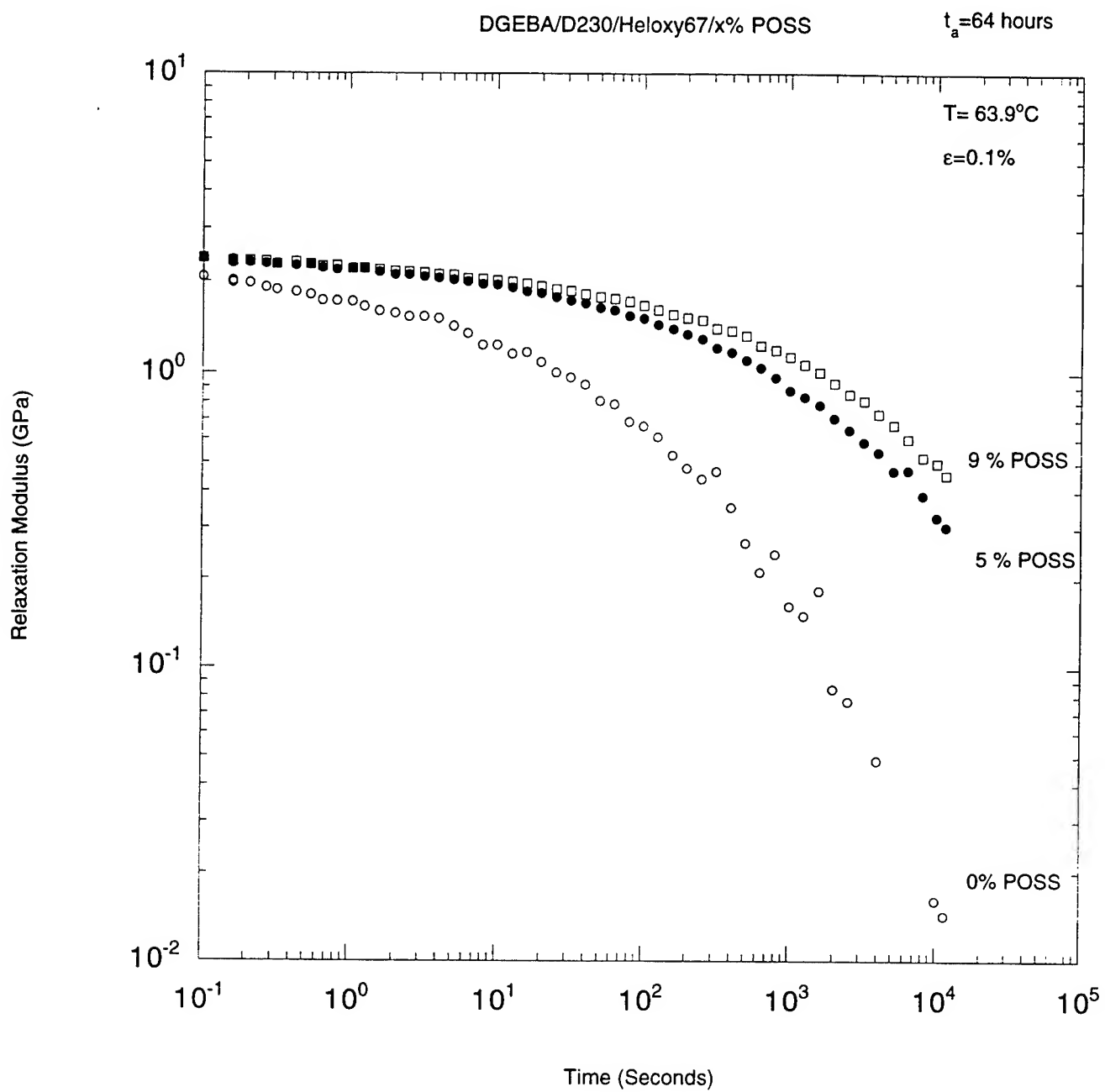
B POSS/MPS

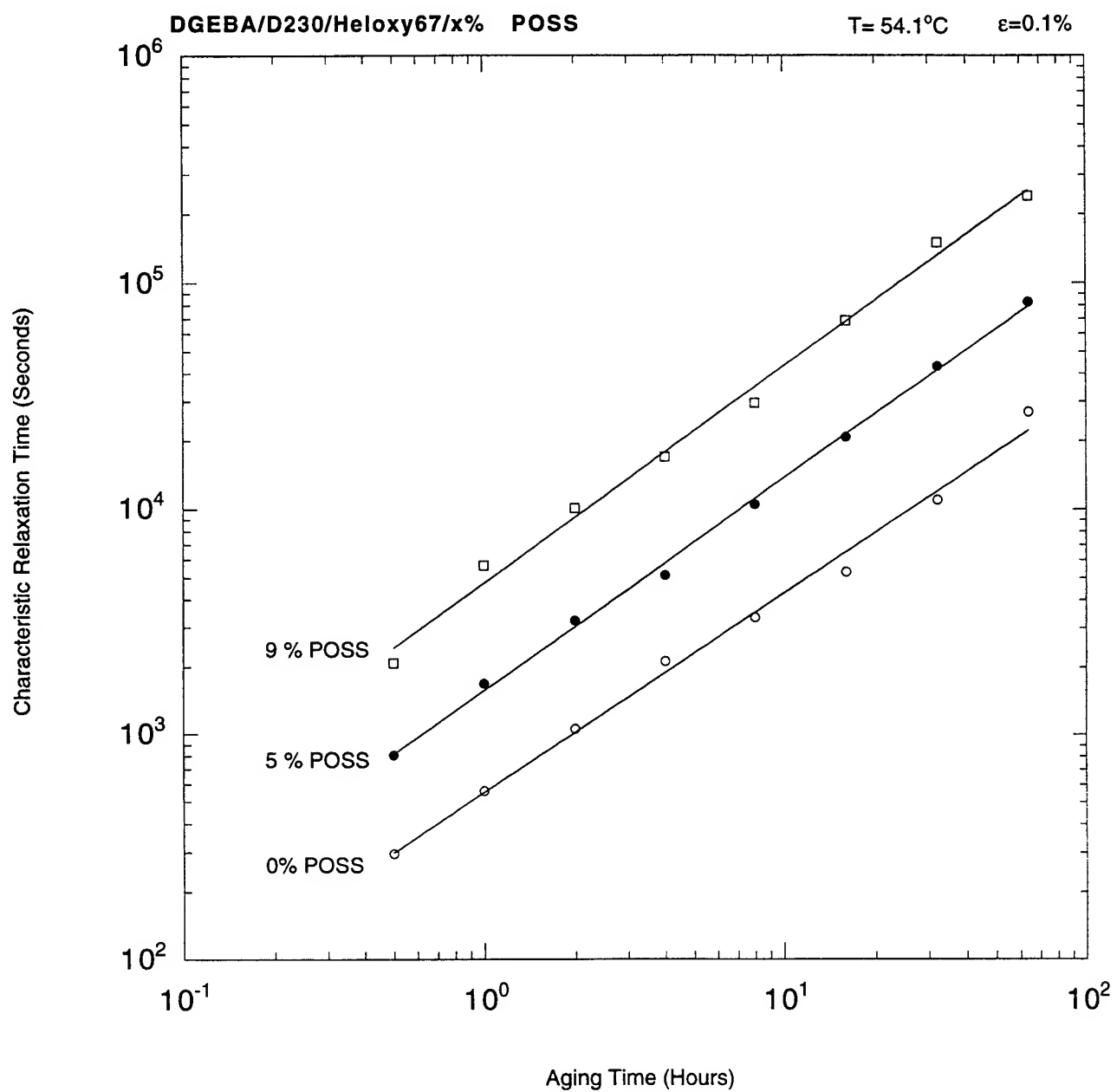


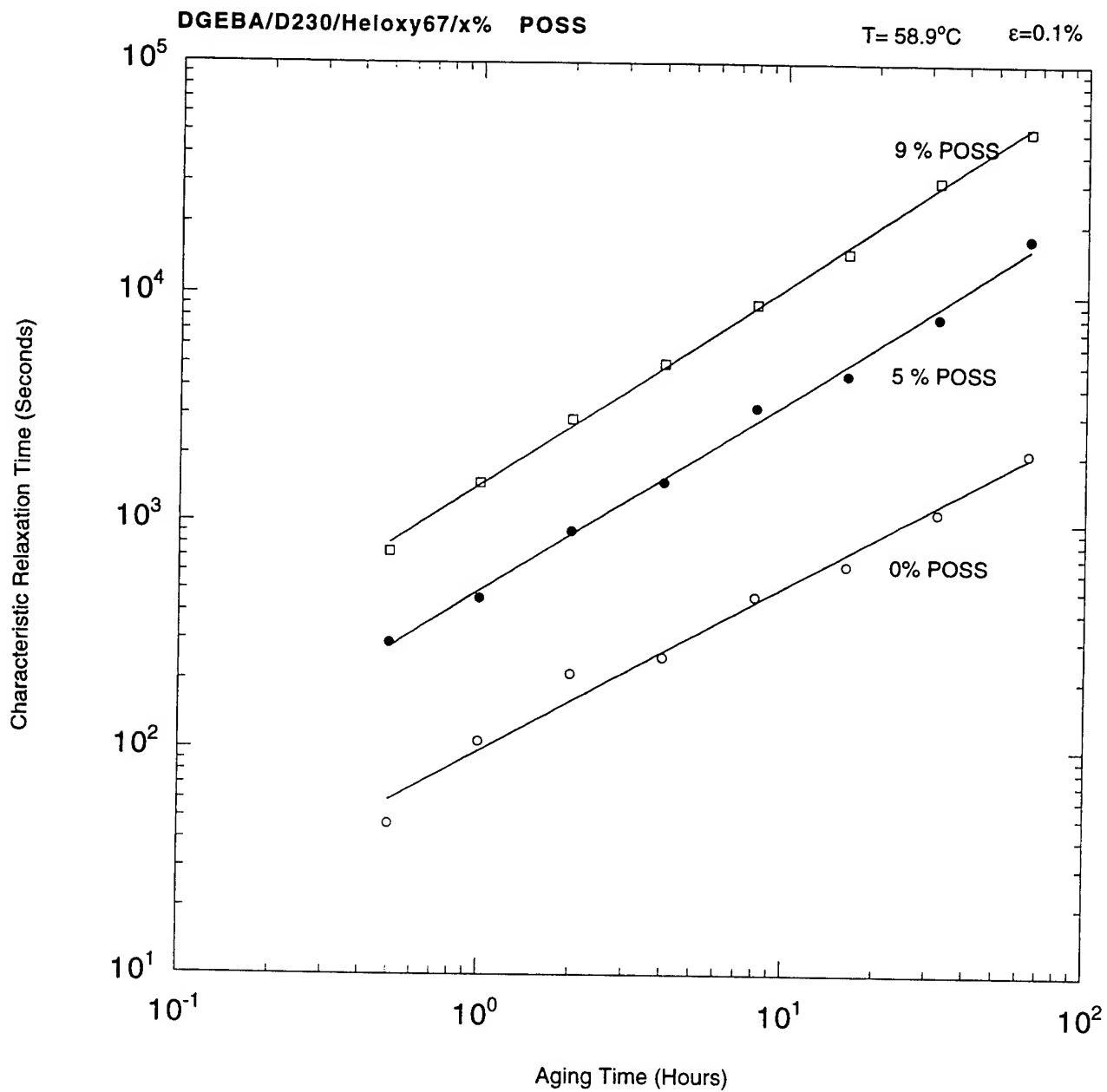


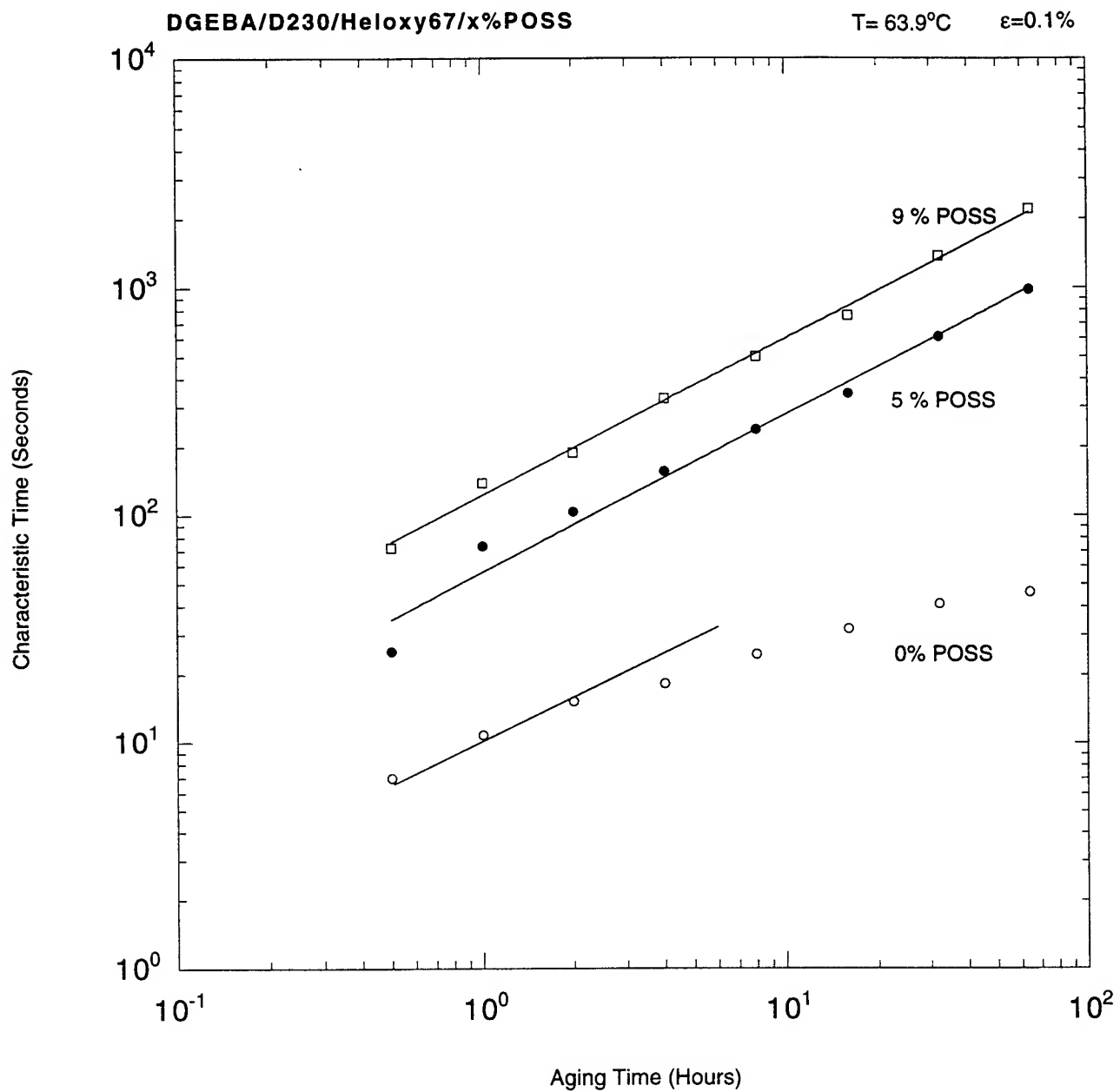
DGEBA/D230/Heloxys67/10%POSS

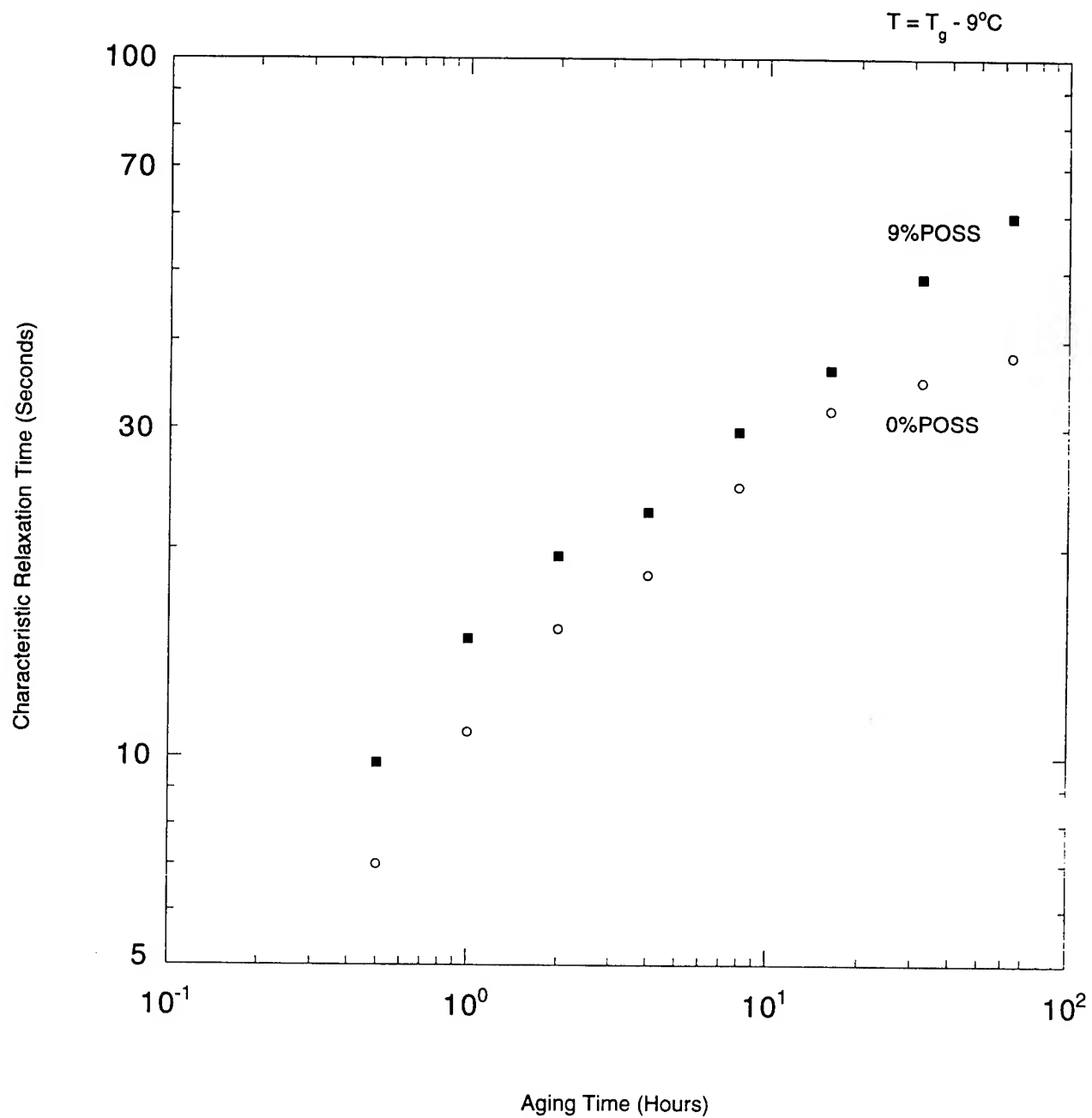












IMPROVEMENT IN FRACTURE PROPAGATION MODELING
FOR STRUCTURAL BALLISTIC RISK ASSESSMENT

Feng-Bao Lin
Associate Professor
Department of Civil and Environmental Engineering

Polytechnic University
6 Metrotech Center
Brooklyn, NY 11201

Final Report for:
Summer Research Extension Program
Phillips Laboratory

Sponsored by:
Air Force Office of Scientific Research
Bolling Air Force Base, DC

and

Phillips Laboratory

December 1997

IMPROVEMENT IN FRACTURE PROPAGATION MODELING FOR STRUCTURAL BALLISTIC RISK ASSESSMENT

Feng-Bao Lin

Associate Professor

Department of Civil and Environmental Engineering

Polytechnic University

Abstract

A numerical simulation of the firing of a solid propellant rocket motor has been performed. The emphasis is on the fracture modeling of the motor. A two-dimensional model was analyzed using a finite element program equipped with the nonlocal smeared cracking model to simulate the fracture behavior. Solid propellants are inhomogeneous materials, and the influence of the fracture process zone needs to be considered. The geometrical data for the finite element model were obtained from previous studies conducted by Thiokol Corporation. The numerical results of this study agree with Thiokol's test measurements. Debonding is not considered in this study. This nonlocal smeared cracking model may be included in the FEINT program to improve Thiokol's three-dimensional predictions of motor firing.

IMPROVEMENT IN FRACTURE PROPAGATION MODELING FOR STRUCTURAL BALLISTIC RISK ASSESSMENT

Feng-Bao Lin

Introduction

The firing of a solid rocket propellant motor is a complex process and its risk assessment requires an integration of advanced technologies in diverse disciplines. A numerical simulation of its firing involves burnback, internal ballistics, and structural analysis, in which one has to consider thermostrain, nonlinear constitutive relationship, large deformation, rate effect, interface modeling, debond and crack propagation, void growth, as well as the interactions between them. One essential aspect in the ballistic risk assessment is that cracks and voids in a propellant grain and debonds between propellant and insulator can exist in a motor that could constitute a risk to its successful firing. These inherent anomalies could affect the performance of the motor, increase the bore pressure, and thus act as stress raisers and influence its structural response. In order to predict, from a structural point of view, whether it is safe to fire a motor that contains those defects, fracture mechanics modeling would be a required component in the motor risk assessment system.

Thiokol Corporation under contract with Phillips Laboratory conducted a very thorough study on the ballistic risk assessment of solid rocket propellant motors between June 1988 and May 1995 [Graham, et al, 1995]. The result of that study is an integrated computer software named Structural/Ballistic Analysis System (SBAS). This program includes structural analysis codes: TEXLESP-2D and TEXLESP-3D [Collingwood, et al, 1988]; burnback analysis codes: RECESS and SURF; internal ballistics analysis codes: RECESS, ITTIB, and VOLFIL; crack/debond combustion codes: CCM and CDCA; and heat transfer codes: HEAT, ASCHAR, and SINDA. Furthermore, interfaces are provided for the following general commercial structural analysis codes: ABAQUS, ANSYS, NASTRAN, and TEXPAC. Any of these commercial codes can be selected to perform a structural analysis instead of using TEXLESP. The executive module for SBAS is the FEINT program. FEINT provides preprocessing (geometry definition, mesh generation, boundary conditions, material properties), analysis execution, and postprocessing (deformed geometry plots, contour plots, vector plots, XY plots). FEINT also provides interfaces between the various codes mentioned above.

One of the primary goals of Thiokol's study was to have a better qualitative and quantitative understanding of the influence of defects on the structural response of solid rocket propellant motor. This would provide a means of assessing the effect of motor defects on a static test firing and provide the test engineers with a rational evaluation of the risks of firing the motor so that actions can be taken to minimize damage to expensive test facilities.

Thirteen static firing tests of specially designed subscale motors were carried out in the Thiokol's program. To check the accuracy of the numerical simulations, Thiokol used the FEINT program to predict each motor performance before the firing test. The test measurements included pressure, strain, and deformation. The pressure measurements

and the real-time radiography (RTR) observations together provided the best indication of the growth defects. In their study, the numerical predictions of the crack criticality were accurate, but debond and crack initiation and propagation speeds were generally overpredicted. It can be concluded that defects are critical to the performance of solid rocket propellant motors, but considerable discrepancies between numerical predictions and test results exist, specially in the three-dimensional simulations.

Thus, it appears necessary to include in FEINT additional fracture mechanics models to improve the accuracy of the predictions. These fracture models should reflect the highly strain rate, temperature, and time dependent mechanical behavior of solid propellants. The inhomogeneity of the propellant, which may induce inelastic fracture process zones, may have an essential influence on motor's firing performance. The adopted fracture models should have the capability to simulate this nonlinear behavior.

In this study, a nonlocal smeared cracking model [Bazant and Lin, 1988] was used to simulate the effect of the fracture process zone. Using a finite element program equipped with the nonlocal smeared cracking model, two-dimensional models studied by Thiokol [Graham, et al, 1995] under the Structural/Ballistic Risk Assessment Methodology program were analyzed to see if the nonlocal model can better predict Thiokol's test results.

Current Fracture Mechanics Models in FEINT

The fracture module in FEINT consists of three different fracture analysis methods:

1. Crack closure integral method - This method calculates the energy release rate G based on the work required to reverse crack propagation by an amount ΔA :

$$G = \frac{dW}{dA} - \frac{dU}{dA} = \frac{\Delta W_c}{\Delta A} \quad (1)$$

The work required to reverse the crack, W_c , is the area under the force displacement curve. If the material behavior is such that the force-displacement path from the open crack state to the closed crack state is unique, as in a linear elastic material, then the crack closure integral may be applicable.

2. Crack opening displacement method - This method computes the stress intensity factors from the crack tip opening displacements [Anderson and Abrahamson, 1984], and is similar to that used by ANSYS. the method is applicable to cracks in isotropic linear elastic materials only. Base on the LEFM, the crack opening displacements Δv , Δu , and Δw near the crack tip, where Δ indicates displacement differences between two crack surfaces, are related to the stress intensity factors K_I , K_{II} , and K_{III} by:

$$\Delta v = \frac{(1+\kappa) K_I}{\mu\sqrt{2\pi}} \sqrt{r}, \quad \Delta u = \frac{(1+\kappa) K_{II}}{\mu\sqrt{2\pi}} \sqrt{r}, \quad \Delta w = \frac{4K_{III}}{\mu\sqrt{2\pi}} \sqrt{r} \quad (2)$$

where μ is the shear modulus, κ equals $(3 - \nu)/(1 + \nu)$ for plane stress problems and equals $(3 - 4\nu)$ for plane strain problems, and ν is the Poisson's ratio. Taking the natural log of both sides of the equations and solving for K as $r \rightarrow 0$ yields:

$$K_I = \frac{\mu\sqrt{2\pi}}{(1 + \kappa)} e^{(\ln(\Delta v) - \frac{1}{2}\ln(r))}, \quad K_{II} = \frac{\mu\sqrt{2\pi}}{(1 + \kappa)} e^{(\ln(\Delta u) - \frac{1}{2}\ln(r))}, \quad K_{III} = \frac{\mu\sqrt{2\pi}}{4} e^{(\ln(\Delta w) - \frac{1}{2}\ln(r))} \quad (3)$$

3. J-integral method - This method is based on the virtual crack extension method proposed by Parks [1974, 1977], and supports linear and nonlinear material behavior, including thermal strains and large deformation. The J-integral method implemented in FEINT also accounts for distributed loads on the crack surfaces. The procedure assumes that steady state conditions exist around the crack tip. This method can also calculate the energy release rate, stress intensity factors, and the speed of crack propagation if the necessary properties have been defined. Internodal constraints are ignored and should not be used inside the outermost contour of elements.

The J-integral is defined as the decrease in total energy, P , per unit area of crack extension, A , i.e.,

$$J = - \partial P / \partial A \quad (4)$$

Total potential energy is a function of material reference positions X , displacements u , and external loads f . For linear elastic materials, it can be shown that the J-integral is equal to the energy release rate G . For a virtual crack extension, δA , the above equation can be written in terms of virtual quantities as

$$J \delta A = - \delta P|_{u=const.} = (\delta W_E - \delta W_I)|_{u=const.} \quad (5)$$

where W_E and W_I are the work due to external and internal forces, respectively. Here, $u = \text{constant}$ means to keep the same displacements u during the virtual crack extension. This is due to the fact that the terms associated with δu vanish because the finite element solution yields the minimum potential energy, i.e., $\delta P / \delta u = 0$.

Internal work $W_I = \int_V U dV$, where U is the strain energy density and V is the entire volume of the solid under consideration. The variation of the internal work equation gives

$$\delta W_I = \int_V U \delta(dV) + \int_V \delta U dV \quad (6)$$

For linear elastic materials, $U = \frac{1}{2} \sigma \epsilon$ and $\delta U = \sigma \delta \epsilon$. For nonlinear materials, U depends on the material constitutive

relationship and loading history, and is generally available as a step-by-step accumulation result from the analysis program. δU can be evaluated from a Taylor series expansion as $\delta U = \sigma \delta \epsilon + \frac{1}{2} \delta \sigma \delta \epsilon$. Since $\delta \sigma$ is unknown, the first order approximation $\delta U = \sigma \delta \epsilon$ is used, where Cauchy stress and the variation of the small strain induced by virtual crack extension are utilized in FEINT. It would be more accurate if the actual material model is used to determine δU .

Only load in the vicinity of the crack will contribute to δW_E because a virtual crack extension produces displacement changes only in a small region near the crack tip. Restrict loads in the vicinity of the crack to normal pressure on the crack surface, and assume no change in load magnitude during the virtual crack extension. Then, we have

$$\delta W_E = \int_S pn \cdot u \, dS - \int_{S_0} pn \cdot u \, dS_0 \quad (7)$$

where p is the normal pressure applied to the current deformed crack surface, S_0 is the deformed crack surface, S is the deformed and extended crack surface, and n is the unit surface normal vector. Fig. 1 shows a virtual crack extension by perturbing the crack tip node. Note that the energy method does not allow the separation of K_I , K_{II} , K_{III} in mixed mode situations, unless two of these fields are zero, i.e., a single mode fracture problem.

In FEINT, three crack tip mesh types can be generated around a crack tip: focused mesh, rectangular mesh, and zipper mesh (Fig. 2). The rectangular mesh was used in the Thiokol study for two-dimensional models.

Fracture Predictions in the Subscale Motor Test Program

In Thiokol's study, the subscale motor program was particularly focused on the study of the effect of defects. This motor was designed to encourage defect propagation during firing. The motor case, made of filament wound nylon in a low-modules epoxy matrix, is highly flexible, and thus provides large strains in the propellant grain under ignition pressurization to allow crack or debond propagation. The case can reach 10 percent hoop strain prior to failure at about 900 psi of hydroburst test pressure. Meanwhile, catastrophic failure is not desired, so the motor is provided with thick internal insulation to protect the case from early flame exposure.

Numerical predictions using the FEINT program were made before each of thirteen static firing tests of subscale motors. The pressure measurements and the real-time radiography (RTR) observations provided the best indication of the growth of defects. A baseline motor without defects was first tested and the test data were recorded. For numerical simulation, a coarse finite element model was used initially, allowing numerous analyses with different material properties and assumptions in order to match the test measurements as closely as possible. Then a fine finite element model was created and the best properties and analysis assumptions were used to predict the motor fracture behavior and to find the fracture parameters. The flow charts of this analysis approach are shown in Fig. 3.

The results of large deformation structural analyses using ABAQUS based on the material properties determined

in the coarse mesh were used to calculate the debond fracture energy at each step. A plot of debond fracture energy versus time was obtained. This debond fracture energy history was then used to calibrate a debond growth speed model using a modified power law, in which the crack speed is proportional to the difference between the current fracture energy and the critical energy, raised to a power:

$$\frac{da}{dt} = A (J - J_c)^q \quad (8)$$

In this model, both the critical fracture energy, J_c , and the crack speed coefficient, A , are rate dependent. This rate dependence is handled by making them another power law functions of the effective propellant modulus. The coefficients obtained by fitting the finite element results having a initial 0.1", with the baseline motor test data were:

$$J_c = 0.00015 E_{eff}^{1.2}, \quad A = 1 \times 10^{-8} E_{eff}^{2.4}, \quad q = 0.83 \quad (9)$$

Unexpectedly, the fracture parameters fit to the static motor firing test data is considerably different from those obtained from laboratory specimen tests for a similar propellant material (Fig. 4). The critical fracture energy obtained from the static firing is lower than the laboratory data by an order of magnitude. Thiokol commented that it was not known whether the differences were from the material itself or because of the different configuration and loading between the motor and a laboratory specimen. However, if the critical fracture energy is a material property, it shall not be specimen geometry or loading configuration dependent. Additional work is needed in identifying realistic fracture properties of propellant. The properties obtained from the first motor static firing test were used in the subsequent numerical simulations.

Based on the test results and the failure analysis of the first motor, the motor was redesigned to include the addition of flaps at both ends of the grain and an increase in the nozzle throat diameter. Fig. 5 shows the flow chart for the subsequent analyses. Fracture energy calculated from the structural analysis was used to determine whether the debond or crack would propagate and how fast based on the debond speed model. The coupled burnback/ballistics analysis calculated the pressure history, which was applied as a load in the structural analysis. The latter in turn provided strains as a function of the pressure, creating strain histories for computing time-dependent effective moduli for the propellant, the insulator, and the case.

Table 1 shows different defects and FEM models used in the subscale motor tests. Fig. 6 shows the subscale motor configuration. For the motors without defects, the predictions agreed well with the test data. But for those with cracks or debonds, they did not match well. Three predicted noncritical cracks and two predicted critical cracks were tested. The criticality of bore cracks was predicted correctly, but crack propagation speeds were much overpredicted. Debond propagation was predicted for all four axisymmetric debond motors, but was observed in none of them. A known natural debond in one motor was predicted to propagate; it did not. However, a similar debond in another motor

propagated extensively. The differences between predictions and test measurement in tests 10, 11, and 12 are shown in Fig. 7.

Fracture Mechanics Models for Solid Rocket Propellant Motors

A solid rocket propellant may be classified as a viscoelastic material. Its mechanical behavior is highly time, strain-rate, and temperature dependent. A good fracture mechanics model should be able to capture these characteristics. The conventional J-integral [Rice, 1968] will uniquely characterize the crack-tip conditions in a viscoelastic material only for a given failure time. This means a critical J value, J_{cr} , taken from a laboratory test is relevant to a structure only if they have similar failure times. Thus, it is difficult to apply such data to structural components. To account for the time dependence of viscoelastic materials, Schapery [1984] proposed a characterizing parameter, J_v , and showed that J_v uniquely defines the crack-tip conditions, making it a suitable fracture criterion for a wide range of rate-sensitive materials. By limiting the dependence of the time-shift factor on the stress or by choosing specific power-law forms for the constitutive response, Schapery [1990] further showed that J_v is path independent for nonlinearly viscoelastic materials with constitutive equations based on a reduced time, and is a candidate parameter for the characterization of the crack-tip fields. Bencher and his co-workers [1995] measured the fracture toughness of H-24 propellant at three different strain rates and three selected temperatures using Schapery's time-dependent viscoelastic approach. They concluded that J_v appears to provide an appropriate measure of the toughness of that propellant.

A J-integral value can be computed from its elastic and plastic components from measurements of the applied load and load-point displacement using [Anderson, 1991]

$$J = \frac{(K_I)^2}{E'} + \frac{\eta}{h b} \int_0^{\delta} P \cdot d\Delta \quad (10)$$

where E' equals E or $E/(1 - \nu)$ in plane stress or plane strain problems, respectively, h is the uncracked ligament length, b is the specimen thicknesses, P is the applied load, Δ is the load-point displacement, and η is a geometry-dependent factor.

The viscoelastic integral J_v can be calculated from the same formula by integrating a load vs. pseudoelastic displacement ($p - \Delta^*$) curve rather than a load vs load-point displacement ($p - \Delta$) curve. The $P - \Delta^*$ curve is converted from a $p - \Delta$ curve by removing the creep displacements arising from the material's viscous behavior that occur during the fracture test. This was achieved by conducting a stress relaxation test at each of the relevant temperatures, and dividing the measured stress by the constant strain to calculate the effective Young's modulus as a function of time, $E(t)$. Then, the pseudoelastic displacement for a constant-displacement-rate fracture test is given by

$$\Delta^e = \frac{\bar{E}(t)}{E_R} \Delta \quad (11)$$

where reference modulus E_R is defined as the short-time relaxation modulus taken at time=0, and $E(t)$ is independent of the strain applied in the stress relaxation test and the $P-\Delta^e$ curve after removing the relaxation strains will be linear.

Another critical aspect is the influence of inelastic fracture zone. The linear elastic stress analysis indicates that tensile stress at a sharp crack tip approaches infinity. Since material cannot withstand infinitely large stress, an inelastic zone must exist in front of the crack tip. In the inelastic zone, some fracture process, such as microcracking or microvoid formation, occurs. Thus, the zone is also named as the fracture process zone. For homogeneous materials, because the size of the fracture zone is negligible compared to the overall dimensions of the member examined, the effect of the zone is usually ignored, and thus linear elastic fracture mechanics (LEFM) can be approximately applied. However, this nonlinearity localized at the crack tip is usually more prominent in inhomogeneous materials since the fracture process zone spreads to a relatively large size due to the heterogeneity nature of the materials. Solid rocket propellants possess a microstructure dictated by agglomerates of filler particles embedded in polymer matrix, and are considered as inhomogeneous materials. In order to better simulate the fracture behavior of solid rocket propellant motors, consideration of the fracture process zone. While LEFM requires only one fracture parameter to characterize the crack tip behavior, it requires more than one parameter to account for the influence of fracture process zone. Several models have been proposed:

1. Fictitious crack model - An early attempt to model the behavior in the fracture process zone was presented by Dugdale and is considered to be an extension of the linear elastic behavior to ductile materials. Because of its assumption of elastic perfectly plastic behavior, this model cannot accurately represent damage in inhomogeneous composites since it fails to account for factors such as microcracking and particle pullout. Hilleborg [1776] proposed a fictitious crack model, which is considered more suitable for inhomogeneous materials. The model is based on applying a cohesive stress, which decreases with the increment of the crack opening displacements rather than a constant value, on the crack surface near the crack tip. The fracture parameters of this model include the tensile strength, f_t , the crack opening displacement beyond which cohesive stress vanishes, w_c , and the energy release rate, G_F . G_F is defined as the area under the cohesive stress versus crack opening displacement, $\sigma - w$, curve, i.e.,

$$G_F = \int_0^{w_c} \sigma(w) dw \quad (12)$$

Different $\sigma - w$ relations were introduced since, such as linear, bilinear, and exponential decay. The relation varies with materials and has to be determined experimentally.

2. Size-effect model - For members that follow the strength criterion or yield criterion, the log-log plot of peak loads versus member sizes represents a horizontal line, i.e., there is no size effect. The linear elastic fracture mechanics yields the strongest possible size effect which corresponds to a straight inclined line of slope $-1/2$. For materials that exhibit distributed cracking (fracture process zone), the size effect plot represents a smooth transition from the horizontal line for the strength criterion to the inclined straight line for the linear elastic fracture mechanics [Bazant and Pfeiffer, 1987]. Since test results vary with member sizes due to the size effect, it is difficult to find material fracture parameters. Thus, the size-effect model extrapolates the experimental data to those for the infinite specimen and based on that defines two fracture parameters G_f and c_f , the critical energy release rate and the critical effective crack extension for the infinite specimen, respectively. [Bazant and Kazemi, 1990]. To determine these two fracture parameters, at least three different sizes of geometrically similar specimens have to be tested. Bazant and Lin [1988] analyzed fracture tests on specimens of various sizes by finite elements using a nonlocal smeared cracking model. Their numerical results agreed well with the size-effect law.

3. Two-parameter fracture model - As the load applied to a specimen increase from zero to its maximum value, the crack length changes from a_0 to a_c , where a_0 is the initial crack length and a_c is the critical effective crack length at the peak load. LEFM can then be used to present a criterion for failure:

$$\sigma_{Nc} = \frac{K_{Ic}}{F\sqrt{\pi a_c}} \quad (13)$$

where σ_{Nc} is the nominal failure stress (the peak value of the nominal stress), K_{Ic} is the critical stress intensity factor for the specimen, and F is a geometry-dependent function. It has been shown that the value of K_{Ic} remains constant for specimens of the same material. However, the value of a_c depends on specimen size and geometry, and cannot be used as a structure-independent material parameter. Jenq and Shah [1985] found that when structures of the same material fail, values of the elastic part of the crack tip opening displacement are approximately constant, regardless of the size of the structure. Based on their observation, they proposed the two-parameter fracture model, and claimed that the criterion for failure of a structure can be expressed as simultaneous satisfaction of

$$K_I(\sigma_{Nc}, a_c) = K_{Ic}^s, \quad CTOD(\sigma_{Nc}, a_c) = CTOD_c \quad (14)$$

where CTOD represents the elastic crack tip opening displacement at the location of initial crack tip. Functions for K_I and CTOD on the left side of the above two equations in terms of applied load and crack length are based on LEFM and can be found in LEFM manuals for various structure geometries. Both K_{Ic} and $CTOD_c$ are regarded as material fracture parameters that are independent of structural size and geometry. The value of critical length a_c is determined by equating the unloading compliance of applied load versus crack mouth opening displacement at the peak load to the initial compliance, so its value is somewhere between the actual crack length and the length of the actual crack as well

as the fracture process zone.

Nonlocal Smeared Cracking Model

In this study, the author used a nonlocal smeared cracking model [Bazant and Lin, 1988] to simulate the effect of the fracture process zone. The cracking is modeled by adjustments of material stiffness. This approach is called smeared cracking. To avoid spurious mesh sensitivity and convergence to an incorrect failure mode with zero energy dissipation, which is typical of the classical smeared cracking model, several alternatives have been proposed. One of them is the coupling of the crack band model [Bazant and Oh, 1983] with a nonlocal continuum approach. The idea is that the nonlocal treatment should be applied only to those variables which cause strain softening, while the other variables, especially the elastic strain, should be local. In this form of nonlocal approach, the differential equations of equilibrium with the boundary conditions retain their standard form, no extra boundary conditions need to be introduced, the continuity requirements for finite elements remain the same as for the local formulation, and spurious zero-energy periodic instability modes, which cause problems for the original nonlocal formulation, do not exist. Also the method produces numerical results in agreement to the size effect.

In two-dimensional cases, the crack band model may be characterized by the stress-strain relation:

$$\begin{bmatrix} \epsilon_{11} \\ \epsilon_{22} \\ \gamma_{12} \end{bmatrix} = \begin{bmatrix} C_{1111} & C_{1122} & 0 \\ C_{2211} & C_{2222} & 0 \\ 0 & 0 & C_{1212}/\beta \end{bmatrix} \begin{bmatrix} \sigma_{11} \\ \sigma_{22} \\ \sigma_{12} \end{bmatrix} + \begin{bmatrix} \epsilon^f \\ 0 \\ 0 \end{bmatrix} \quad (15)$$

in which ϵ^f is the fracturing strain; ϵ_{11} , ϵ_{22} , and γ_{12} are the normal strains and the shear angle; σ_{11} , σ_{22} , and σ_{12} are the normal and shear stresses; C_{ij} are the initial elastic compliances; and the numerical subscripts refer to the cartesian coordinates x_1 and x_2 . Assuming isotropy, we have $C_{1111} = C_{2222} = 1/E'$, $C_{1122} = C_{2211} = \nu'/E'$, $C_{1212} = 2(1+\nu)/E$, in which for plane stress $E' = E$, $\nu' = \nu$, and for plane strain $E' = E/(1 - \nu^2)$, $\nu' = \nu/(1 - \nu)$.

The cracks are assumed to be parallel and normal to the axis x_1 . We introduce the classical hypothesis that, at the time the cracks start to form, the direction of the cracks is fixed as normal to the maximum principal stress σ_1 at that instant and remains constant afterwards. If σ_1 does not rotate, σ_{12} remains zero; however in general σ_1 may rotate, and in that case one must take into account the shear stiffness due to aggregate interlock on rough crack surfaces. This is done by multiplying the shear compliance C_{1212} with an empirical coefficient β , called the shear retention factor.

It has been shown [Bazant and Oh, 1983] that Eq. 15 is equivalent to:

$$\begin{bmatrix} \epsilon_{11} \\ \epsilon_{22} \\ \gamma_{12} \end{bmatrix} = \begin{bmatrix} C_{1111}/(1-\omega) & C_{1122} & 0 \\ C_{2211} & C_{2222} & 0 \\ 0 & 0 & C_{1212}/\beta \end{bmatrix} \begin{bmatrix} \sigma_{11} \\ \sigma_{22} \\ \sigma_{12} \end{bmatrix} \quad (16)$$

in which the normal stiffness C_{1111} in the direction normal to the cracks is reduced by the coefficient $(1 - \omega)$, where ω represents what is known in continuum damage mechanics as damage and may be regarded as the cracked area fraction; $\omega = 0$ corresponds to the initial state of no cracking (zero damage); and $\omega = 1$ corresponds to the final state of complete cracking (complete damage). Comparing Eqs. 15 and 16, we note that $\epsilon^f = [\omega C_{1111} / (1 - \omega)] \eta$. Diverse assumptions may be adopted for unloading : secant unloading, linear and exponential strain softening.

The nonlocal continuum is a continuum for which at least some variables are defined by spatial averaging. Only those variables that cause strain softening should be considered as nonlocal. This means that the damage should be made nonlocal. This is accomplished by specifying it as a function of the average (nonlocal) strain, which is defined by spatial averaging as follows:

$$\overline{\epsilon}_{11}(x) = \frac{1}{V_r(x)} \int_V \alpha(s-x) \langle \epsilon_{11}(s) \rangle dV = \int_V \alpha'(x,s) \langle \epsilon_{11}(s) \rangle dV \quad (17)$$

in which

$$V_r(x) = \int_V \alpha(s-x) dV, \quad \alpha'(x,s) = \frac{\alpha(s-x)}{V_r(x)} \quad (18)$$

The overbar is a label for the nonlocal variables, V = volume of the entire body, $\alpha(x)$ given weighting function which is treated as a material property, and s = general coordinate vector. V_r has approximately but not exactly the same meaning as the representative volume in the statistical theory of heterogeneous materials. The pointed brackets $\langle \rangle$ denote the positive part of the variable.

Calculations converge better if the weighting function is smooth. A suitable choice is the normal (Gaussian) distribution :

$$\alpha(x) = e^{-(k|x|/l)^2} \quad (19)$$

in which k is a constant whose value is $k = 2$ for the case of two dimensions; $|x|^2 = x^2 + y^2$; and l is the characteristic length of the material, which may be interpreted as the radius of a circle on which the uniform distribution $\alpha = 1$ has the same volume as the normal distribution function extending to infinity in the plane.

If the body is finite, the normal distribution function obviously extends beyond the boundary. This is handled by deleting the region outside the body from the integration domain V , both for the calculation of the average (Eq. 17) and for the calculation of the representative volume (Eq. 18). This fact causes V_r to depend on location x .

In finite element calculations, the integrals in Eqs. 17 and 18 are approximately evaluated as finite sums over all the integration points of all the elements in the structure. However, the integration points whose distances from the point x exceed approximately $2l$ may be omitted since for them the value of α is negligible.

The nonlocal damage is considered a function of the nonlocal normal strain:

$$(1 - \bar{\omega})^{-1} = \Phi(\bar{\epsilon}_{11}) \quad (20)$$

Thus, the nonlocal constitutive equation with local strain takes the form:

$$\begin{bmatrix} \epsilon_{11} \\ \epsilon_{22} \\ \gamma_{12} \end{bmatrix} = \begin{bmatrix} C_{1111}/(1-\bar{\omega}) & C_{1122} & 0 \\ C_{2211} & C_{2222} & 0 \\ 0 & 0 & C_{1211}/\beta \end{bmatrix} \begin{bmatrix} \sigma_{11} \\ \sigma_{22} \\ \sigma_{12} \end{bmatrix} \quad (21)$$

Two-dimensional Finite Element Modeling

A two-dimensional model studied by Thiokol was analyzed using a nonlocal smeared cracking model. The model was analyzed assuming plain strain conditions. The finite element mesh is shown in Fig. 8, and the detail of the mesh around the crack tip is shown in Fig. 9. The model includes a 0.3" deep bore crack and has 1386 4-node quadrilateral elements with 1501 nodes. Transitional quadrilateral elements were used in the modeling (Fig. 9). The material properties used in the analysis are as follows. For propellant, effective Young's modulus is 800 psi and Poisson's ratio is 0.499. For insulator, Young's modulus is 1000 psi and Poisson's ratio is 0.499. For motor case, effective Young's modulus is 375,000 psi and Poisson's ratio is 0.4. The characteristic length, l , of the propellant obtained from best fit of the test results is 0.5". Isotropic conditions were assumed in this study.

To simulate the burning of the propellant, the interior bore diameter is increased piece wise every two seconds similar to those used in Thiokol's study (Fig. 10). Fig. 11 and Fig. 12 shows the size of the fracture process zone obtained from the nonlocal finite element analysis at the internal bore pressure of 160 psi and 300 psi, respectively.

Fig. 13 shows the comparison of internal pressure between test results and nonlocal simulations. Fig. 14 shows the comparison between Thiokol's predictions and nonlocal simulations. The comparison of hoop strain is shown in Fig. 15.

Discussion and Conclusions

In order to achieve a successful numerical simulation of the firing performance of a solid propellant rocket motor, it is essential to have adequate constitutive relations for the materials that form the motor (propellant, insulator, adhesive liner, and case). A linear elastic model is the simplest one, but cannot achieve a good prediction. More elaborated models may include plastic effects, viscoelasticity, and viscoplasticity. Temperature-dependent material properties and rate effect should also be included to have a better prediction. Cracks, voids, and debonds (adhesive cracks) compound the difficulty of the modeling. Their existence alters the ballistics performance by exposing a larger burning surface area. Proper fracture criteria to determine when a crack will propagate and, if so, which direction and how far the crack will go have to be sought. The modeling of debond or adhesive crack propagation is even more complex because it involves two different materials at the crack tip.

Schapery's J_v integral was particularly developed for viscoelastic materials. It is suggested to incorporate this integral into FEINT as a fracture toughness to predict if a crack will propagate. To include the effect of the fracture process zone, we may consider the nonlocal smeared cracking approach, Hillerborg's fictitious crack model, or Jenq and Shah's two-parameter model. In Thiokol's subscale motor test program, the crack propagation speeds were generally overpredicted. Liu and Ravi-Chandar [1996] showed that a power law relationship exists between mode I stress intensity factor and the crack growth speed. It was also observed in Thiokol's test program that some motor failures were caused by splitting of the insulator at the flap tip, rather than the crack propagation in the propellant, allowing the flame to burn through the aft dome. It is suggested that a future numerical analysis should take into account the effect of the sharp tip caused by making a flap in the insulator.

The nonlocal smeared cracking model has been used successfully for cementitious materials. This model could be applied to the simulation of the firing of a solid propellant rocket motor. The numerical simulations of this study show fair agreement with the experimental results. To improve the fracture behavior predictions, we may incorporate the nonlocal model in the FEINT program. In this way, we can take advantage of all the modules of FEINT to take into account various aspects of the complex motor firing process. Also, it is essential to obtain realistic fracture parameters experimentally in order to further improve the numerical simulation.

References

1. P. Anderson and L.P. Abrahamson, "Methods for Energy Release Rate Calculation, CPIA Report 41 A, V.1, pp. 193-199, 1984.
2. T.L. Anderson, *Fracture Mechanics: Fundamentals and Applications*, 1st Ed., CRC Press, Boca Raton, FL, pp. 373-513, 1991.
3. Z.P. Bazant and M.T. Kazemi, "Determination of Fracture Energy, Process Zone Length, and Brittleness Number from Size Effect with Application to Rock and Concrete," *International Journal of Fracture*, V. 44, No. 2, pp. 111-131, 1990.
4. Z.P. Bazant and Feng-Bao Lin, "Nonlocal Smeared Cracking Model for Concrete Fracture," *ASCE, Journal of Structural Engineering*, V. 114, No. 11, pp. 2493-2510, 1988.
5. Z.P. Bazant and B.H. Oh, "Crack band theory for fracture of concrete," *Materials and Structures, RILEM, Paris*, 16, pp. 155-177, 1983.
6. Z.P. Bazant and P.A. Pfeiffer, "Determination of Fracture Energy from Size Effect and Brittleness Number," *ACI Materials J.*, V. 84, pp. 463-480, 1987.
7. C.D. Bencher, R.H. Dauskardt, and R.O. Ritchie, "Microstructural Damage and Fracture Processes in a Composite Solid Rocket Propellant," *Journal of Spacecraft and Rockets*, V. 32, No. 2, pp. 328-334, 1995.
8. G.A. Collingwood, T. Sato, S.A. Geddie, A.M. Ratte, and E.B. Becker, "TEXLESP-2D User's Manual," Morton Thiokol, Inc, and University of Texas at Austin, MSFC-RPT-1564, 1988.
9. T.C. Derbidge, "One-dimensional Compressible Flow in a Variable Area Duct With Mass Addition," Master's Degree Thesis, Department of Mechanical Engineering, University of Utah, Salt Lake City, Utah, 1971.
10. R.P. Graham, M.P. Iverson, D.P. Clark, D.A. Isaac, and J.B. Endicott, "Structural Ballistic Risk Assessment Methodology - Final Report for Period June 1988 to May 1995," Thiokol, Publication No. 951026, prepared for Phillips Laboratory, Edwards Air Force Base, 1995.
11. A. Hillerborg, M. Modeer, and P.E. Peterson, "Analysis of Crack Formation and Crack Growth in Concrete by Means of Fracture Mechanics and Finite Elements," *Cement and Concrete Research*, V. 6, No. 6, pp. 773-782, 1976.
12. Y.S. Jenq and S. P. Shah, "Two Parameter Fracture Model for Concrete," *Journal of Engineering Mechanics*, V. 111, No. 10, pp. 1227-1241, 1985.
13. C.T. Liu and K. Ravi-Chandar, "Local Fracture and Crack Growth Behavior in a Particulate Composite Material," *Journal of Reinforced Plastics and Composites*, V. 15, pp. 196-207, 1996.
14. Y.C. Lu, V. Yang, and K.K. Kuo, "User's Manual of Crack/Debond Combustion Anomaly (CDCA) Code," Pennsylvania State University, 1992.
15. D.M. Parks, "A Stiffness-Derivative Finite Element Technique for Determination of Crack Tip Stress Intensity Factors," *International Journal of Fracture*, V. 10, pp. 487-501, 1974.
16. D.M. Parks, "The Virtual Crack Extension Method for Non-Linear Material Behavior," *Computer Methods in Applied Mechanics and Engineering*, V. 12, pp. 353-364, 1977.

17. J.R. Rice, "A Path Independent Integral and the Approximate Analysis of Strain Concentration by Notches and Cracks," *Journal of Applied Mechanics*, V. 35, pp. 379-386, 1968.
18. R.A. Schapery, "Correspondence Principles and a Generalized J-Integral for Large Deformation and Fracture Analysis of Viscoelastic Media," *International Journal of Fracture*, V. 25, pp. 195-223, 1984.
19. R.A. Schapery, "On Some Path-Independent Integrals and their Use in Fracture of Nonlinear Viscoelastic Media," *International Journal of Fracture*, V. 42, pp. 189-207, 1990.

Table 1: Subscale Motor Tests

Test No.	Test Date	Description	Nozzle Throat, ϕ	FEM Model
1	5/17/93	Original baseline, no flaps, no flaws	2.0 in.	Axisymmetric
2	7/13/94	Redesign baseline, with flaps, no flaws	2.3 in.	Axisymmetric
3	7/14/94	Full-length bore crack, 0.3 in. deep	2.3 in.	Gen. Plane Strain
4	7/19/94	Full-length bore crack, 0.35 in. deep	2.0 in.	Gen. Plane Strain
5	3/13/95	Buried debond, axisym., 0.75 in. wide	2.3 in.	Axisymmetric
6	3/14/95	Buried debond, axisym., 0.75 in. wide	2.3 in.	Axisymmetric
7	3/15/95	Voids, 0.72 x 0.47 x 0.30 in. and smaller	2.3 in.	3-D
8	3/16/95	Edge debond, axisymmetric, 1.0 in. deep	2.3 in.	Axisymmetric
9	3/17/95	Edge debond, axisymmetric, 1.0 in. deep	2.3 in.	Axisymmetric
10	3/17/95	Half-circle plane bore crack, $r = 0.4$ in.	2.1 in.	3-D
11	3/20/95	Half-circle plane bore crack, $r = 0.6$ in.	2.1 in.	3-D
12	3/22/95	Half-circle plane bore crack, $r = 1.7$ in.	2.1 in.	3-D
13	3/27/95	0.3-in. axisym. edge and natural debonds	2.3 in.	3-D

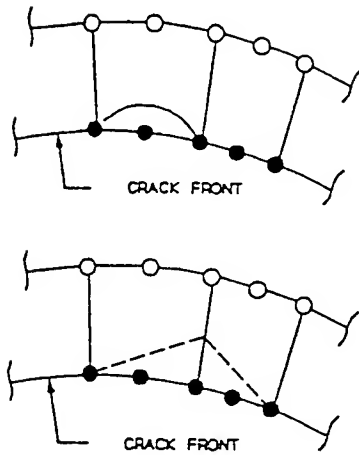


Fig. 1 Crack Tip Perturbation for Computing J-integral.

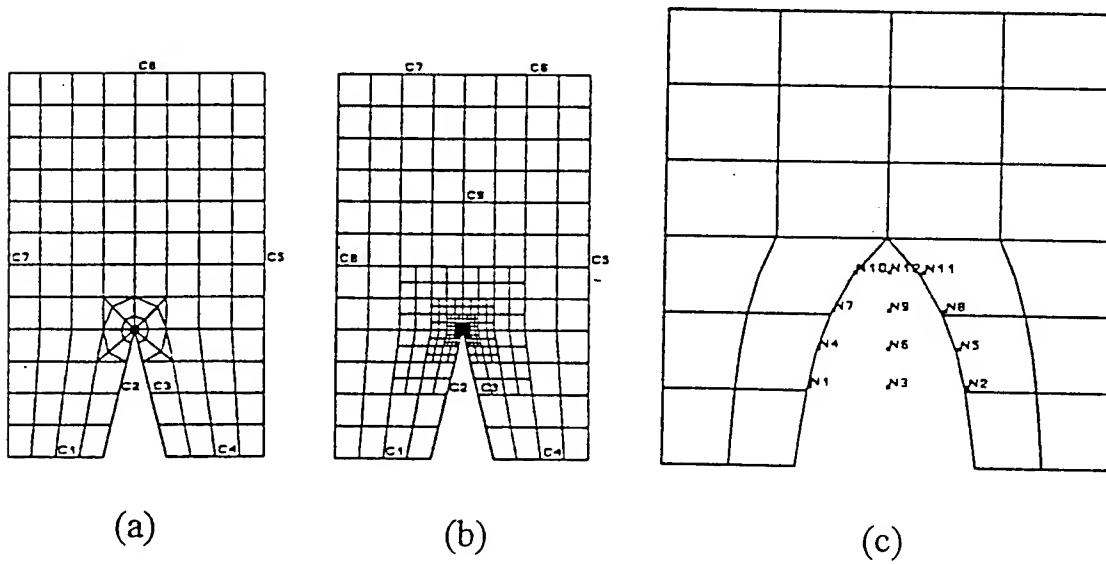


Fig. 2 Three Crack Tip Mesh Types Available in FEINT: (a) Focused Mesh, (b) Rectangular Mesh, and (c) Zipper Mesh.

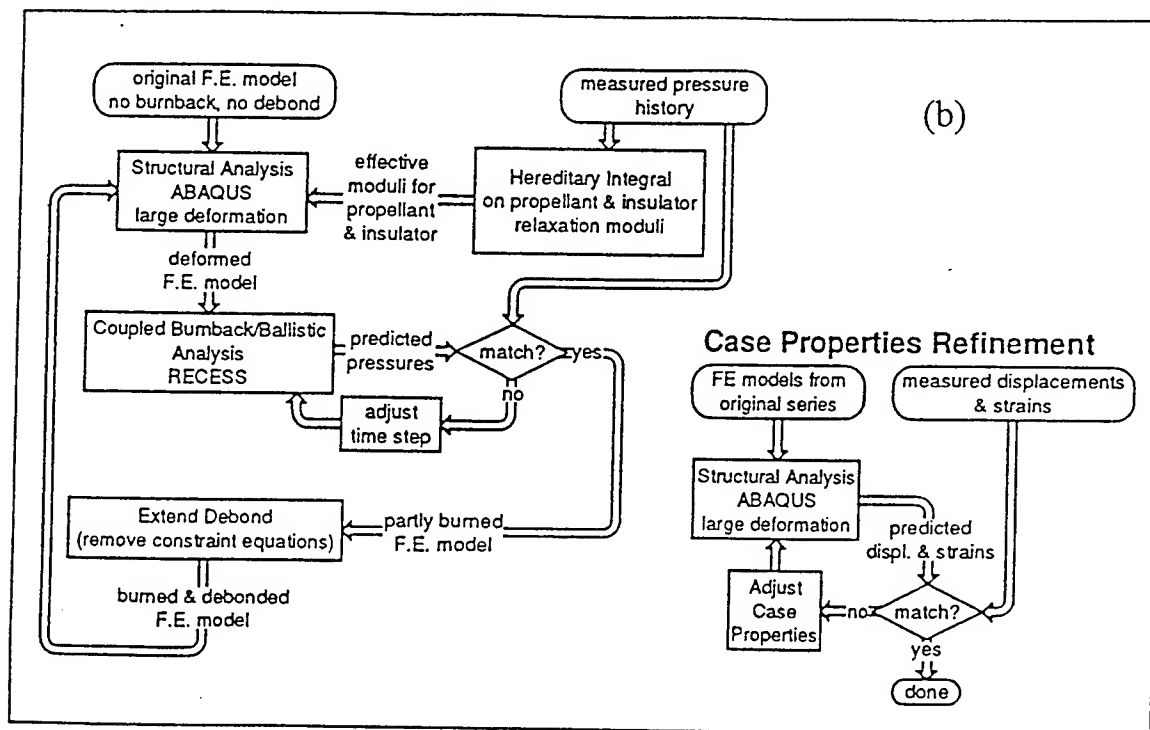
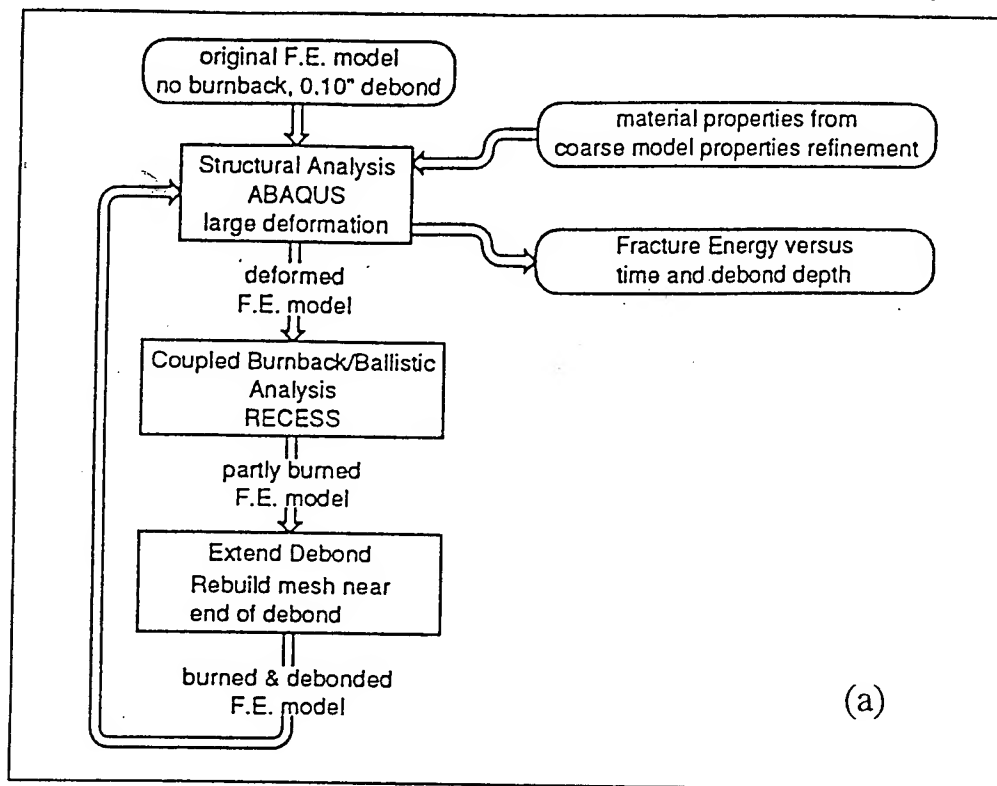


Fig. 3 Numerical Analysis Flow for Baseline Motor Analysis: (a) Coarse Model Analysis Flow, (b) Fine Model Analysis Flow.

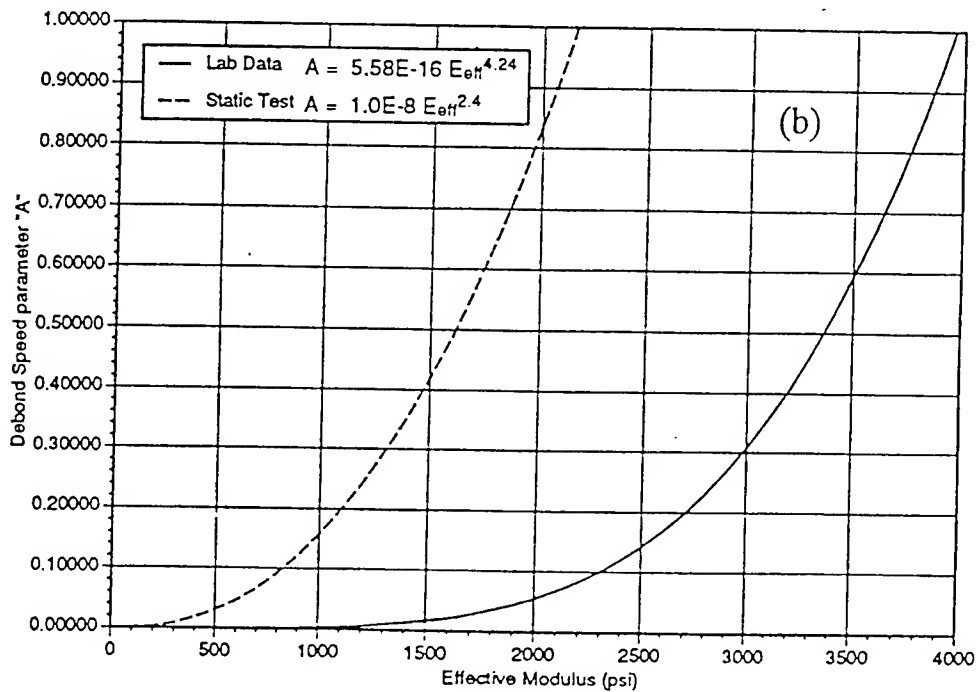
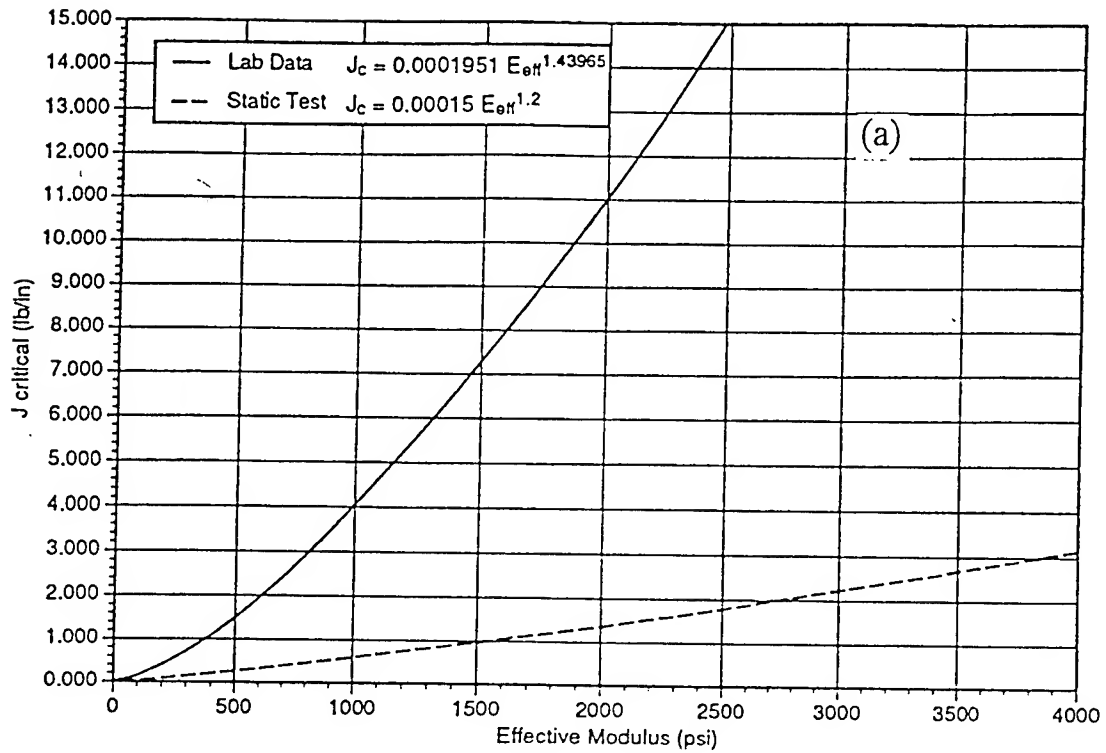


Fig. 4 Fracture Parameters Obtained from Motor Firing Tests and Laboratory Specimen Tests: (a) Critical J-integral Value versus Effective Modulus, (b) Debond Speed Parameter A versus Effective Modulus.

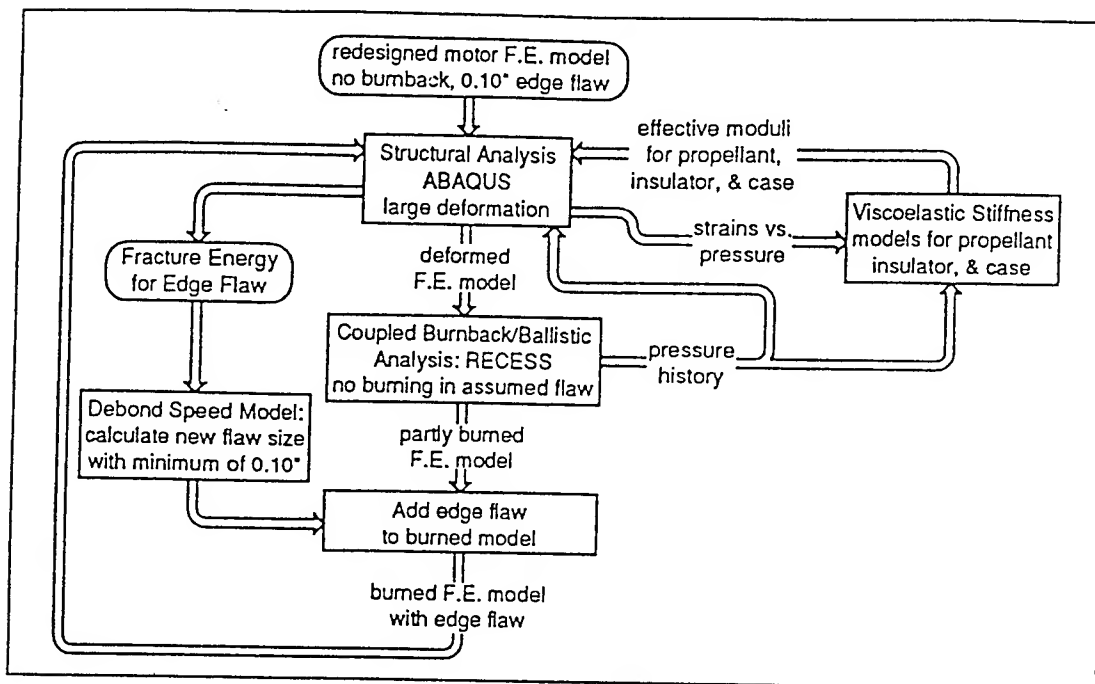


Fig. 5 Numerical Analysis Flow for Redesigned Motor Analysis.

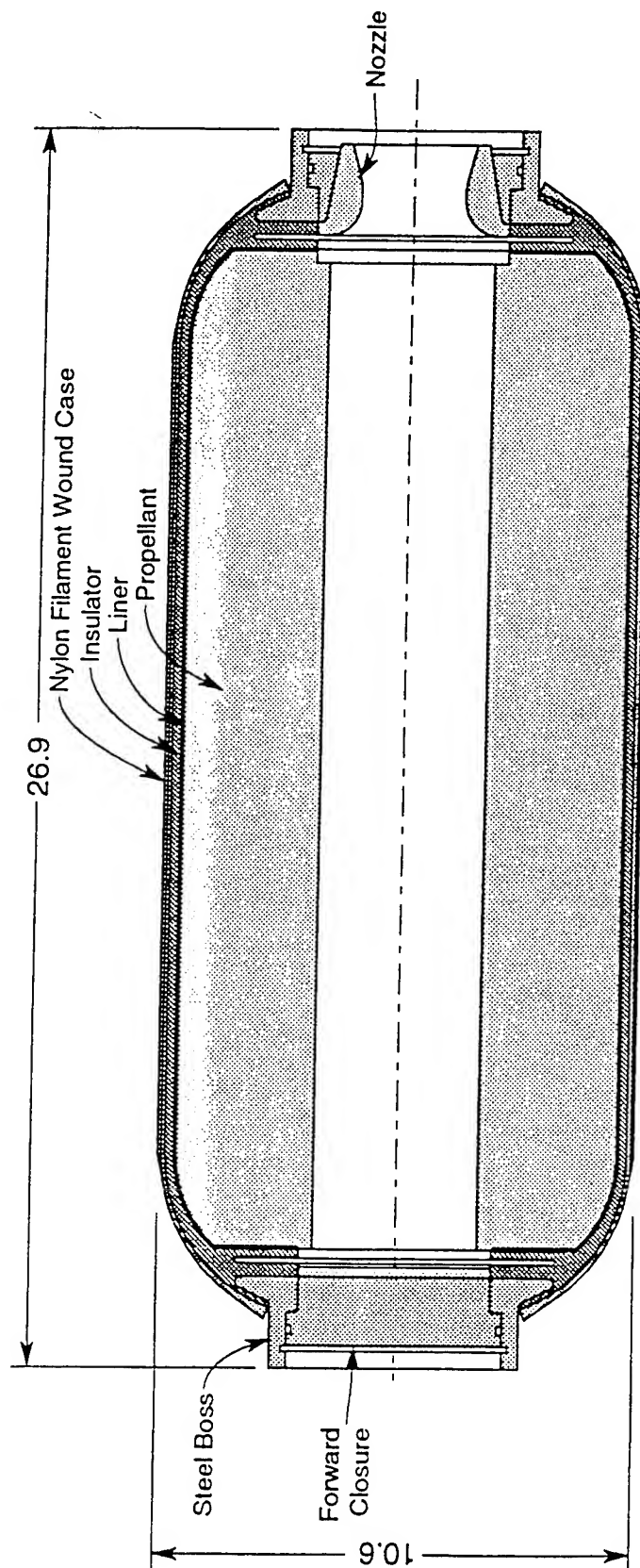


Fig. 6 Subscale Motor Configuration.

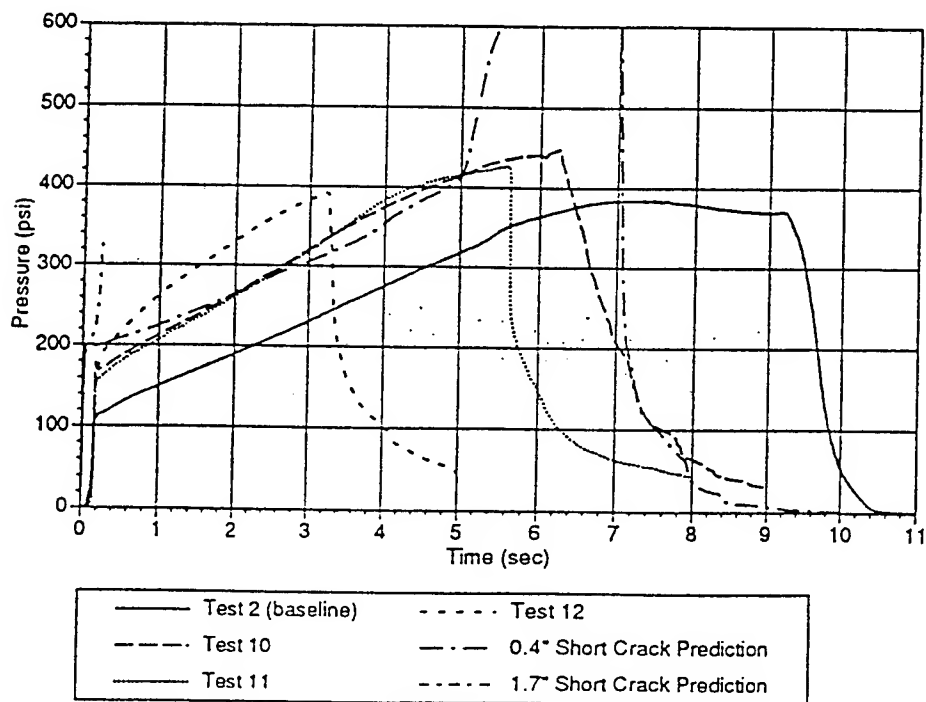


Fig. 7 Numerical Prediction and Test Measurement for Subscale Motor Test 10, 11, and 12.

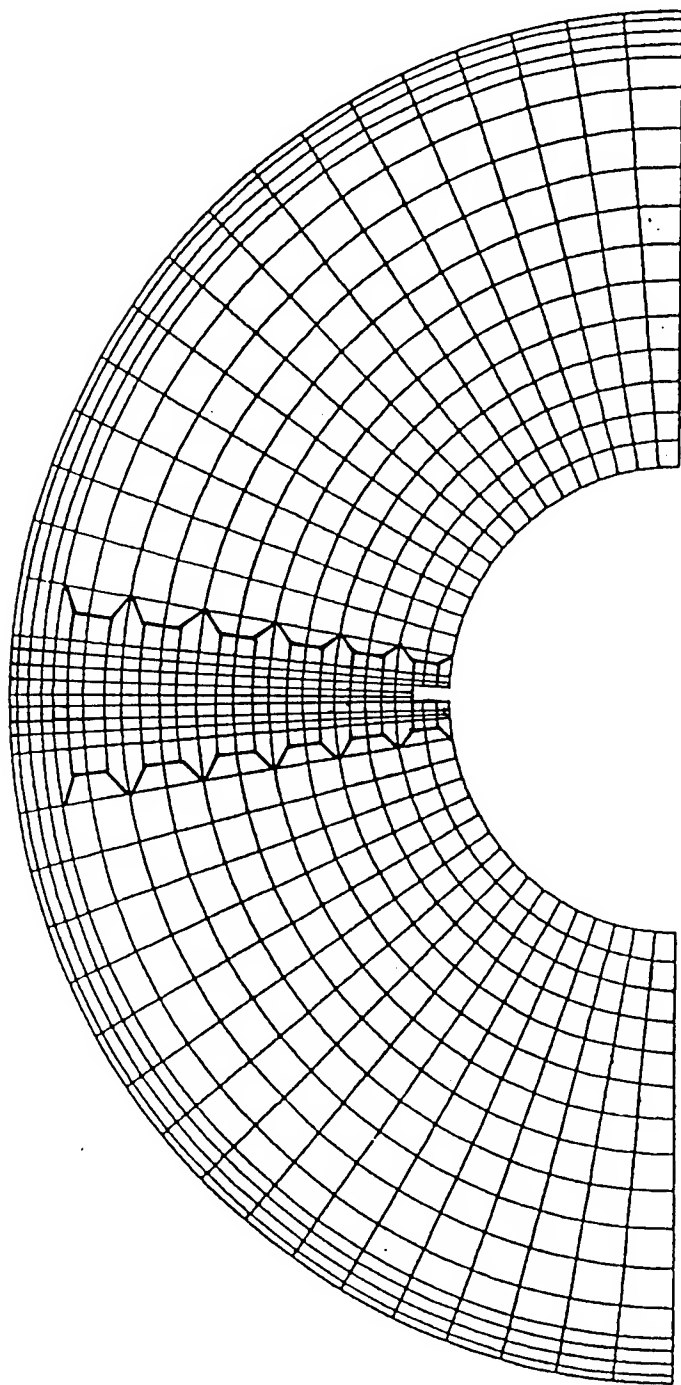


Fig. 8 Finite Element Model (Half Circle with 0.3-inch crack is shown)

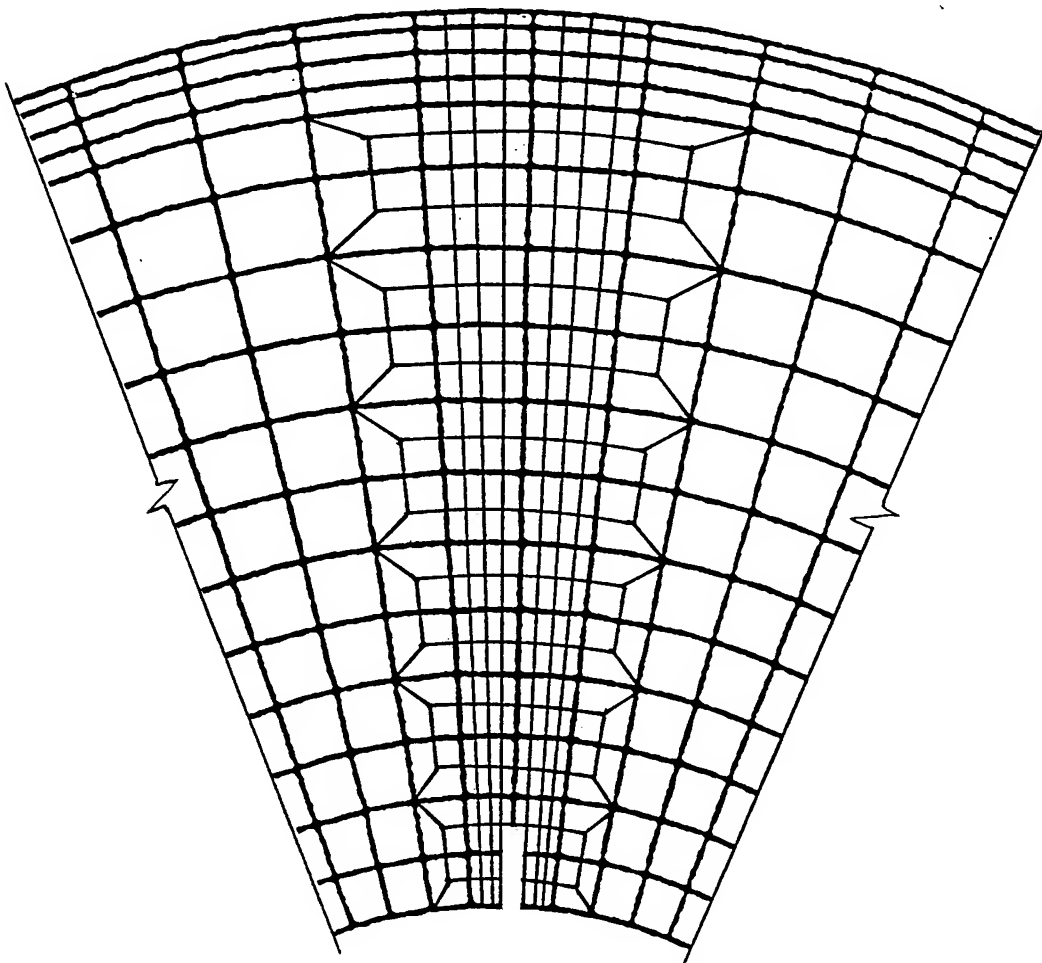


Fig. 9 Crack Tip Model Used in this Study.

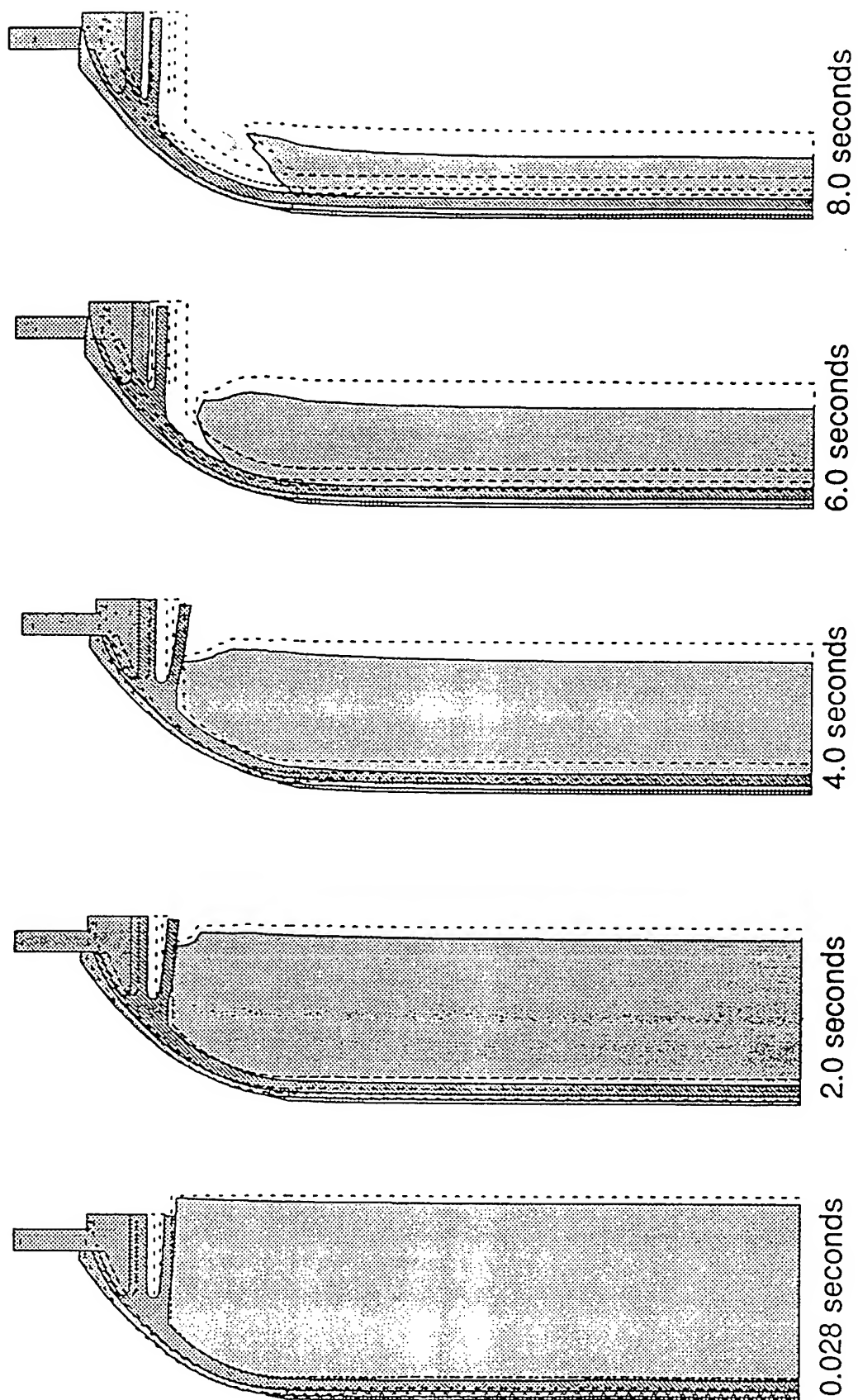


Fig. 10 Sequence of Models for Motor Analysis.

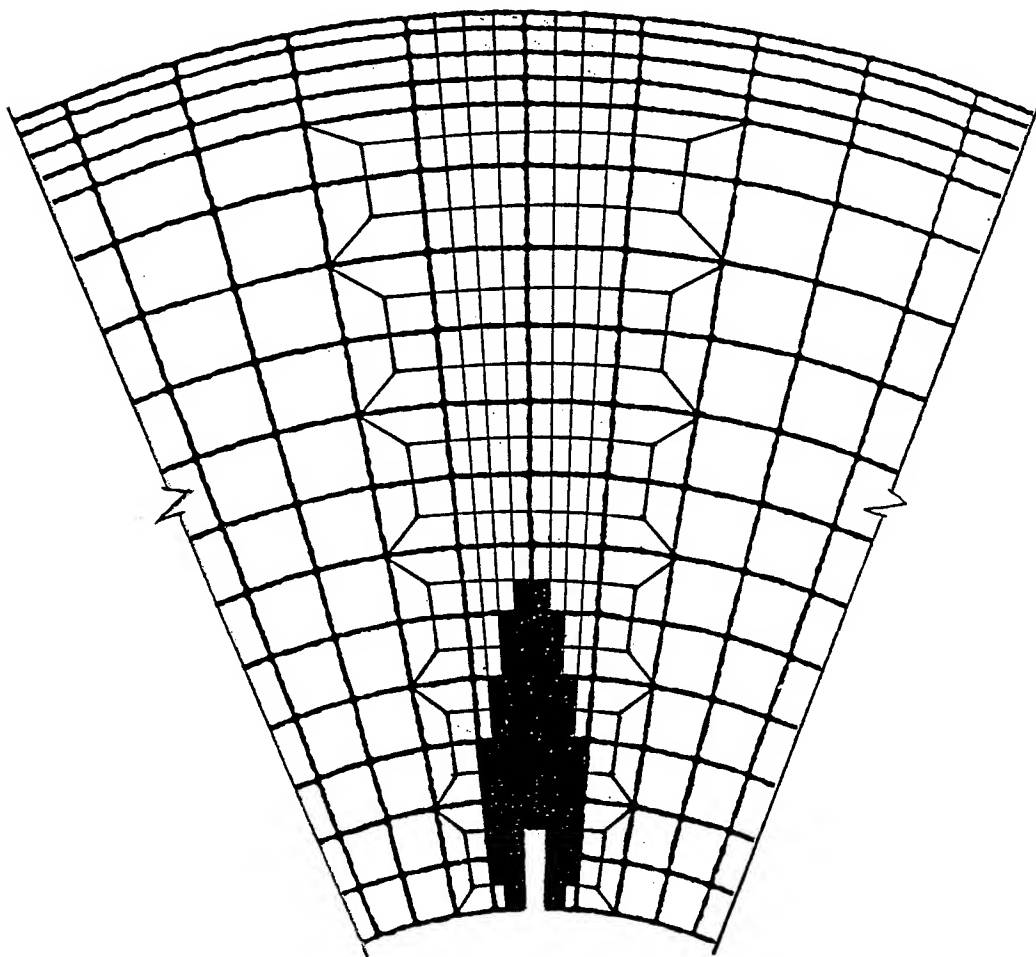


Fig. 11 Fracture Process Zone at a Internal Pressure of 160 psi (2 seconds)

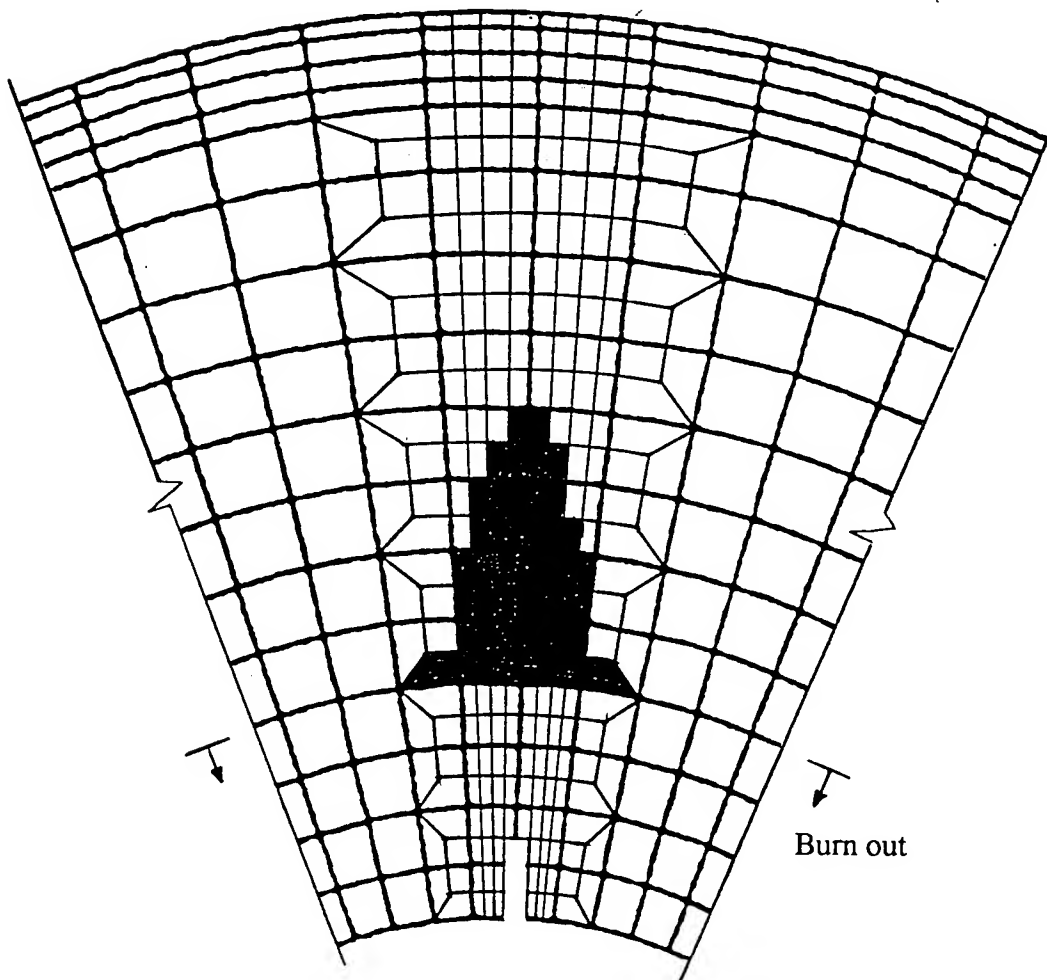


Fig. 12 Fracture Process Zone at a Internal Pressure of 300 psi (4 seconds)

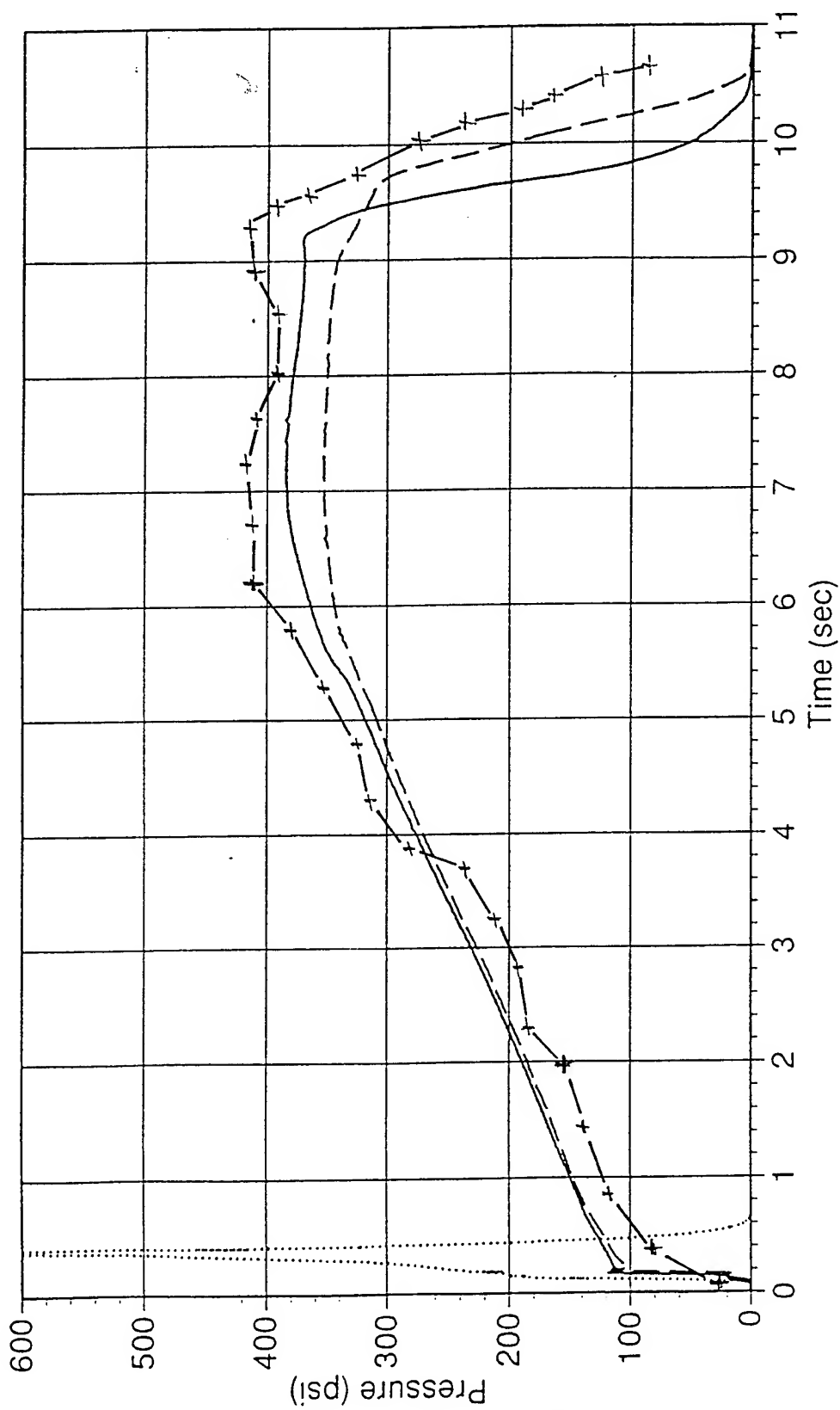


Fig. 13 Comparison Between Test Results and Nonlocal Numerical Simulation.

— Test 2 (Baseline)
 - - - Test 3
 Test 4
 + + + Nonlocal Numerical Simulation

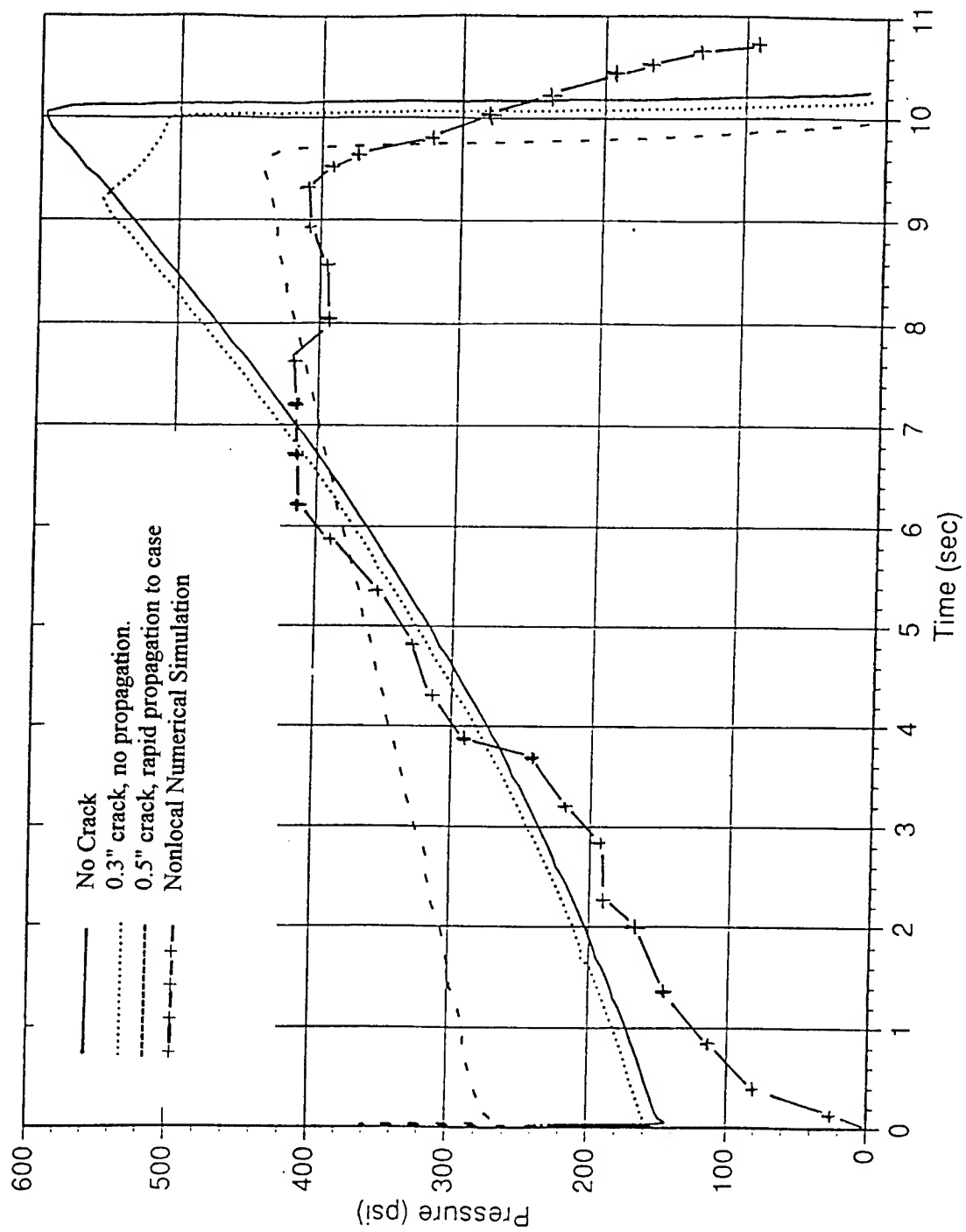


Fig. 14 Comparison Between 2-D Thiokol's Predictions and Nonlocal Numerical Simulation.

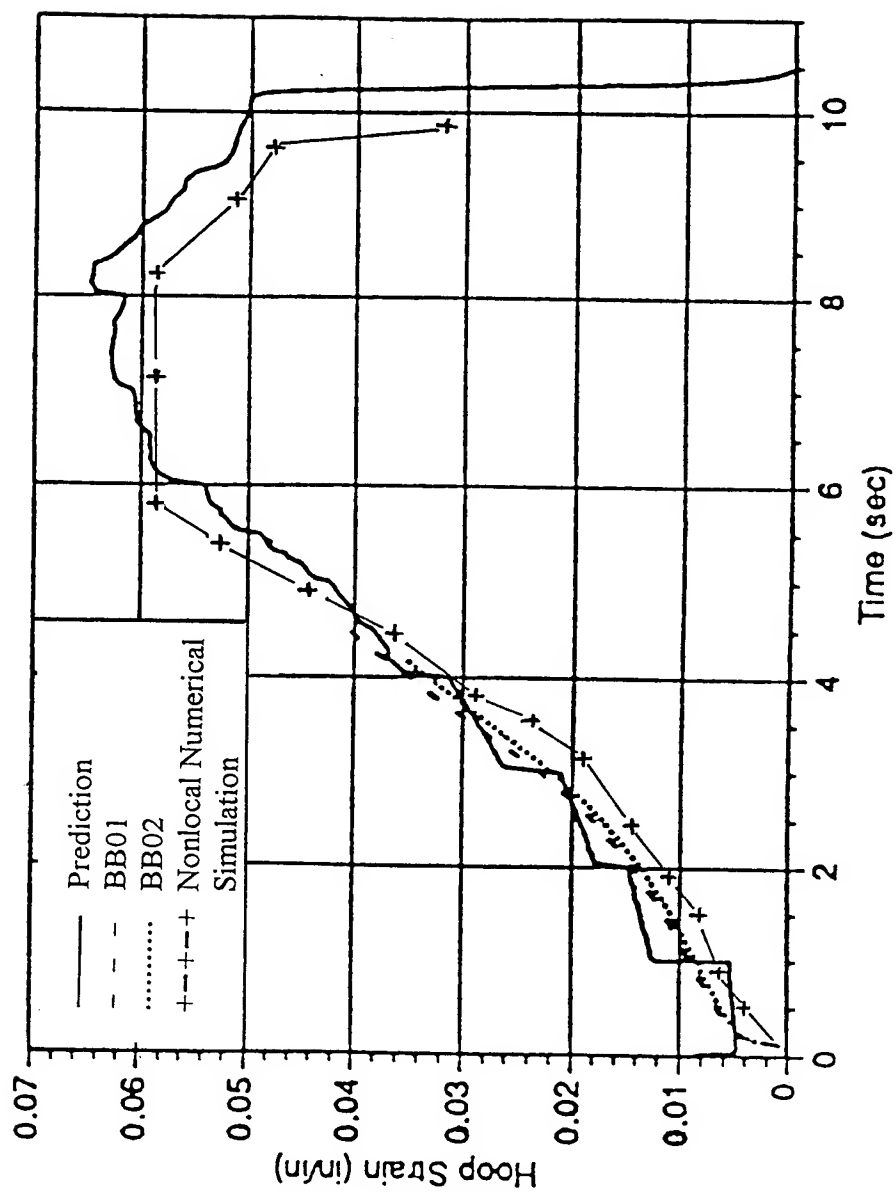


Fig. 15 Comparison of Hoop Strain Among Test Results, Thiokol's Predictions, and Nonlocal Numerical Simulation

CROSS SECTIONAL AREA ESTIMATION OF ORBITAL DEBRIS

Ronald A. Madler
Assistant Professor
Department of Aerospace Engineering

Embry-Riddle Aeronautical University
3200 Willow Creek Road
Prescott, Arizona 86301-3720

Final Report for:
1997 Summer Research Extension Program
Air Force Research Laboratory

Sponsored by:
Air Force Office of Scientific Research
Bolling Air Force Base, DC

and

Air Force Research Laboratory

March 1998

CROSS SECTIONAL AREA ESTIMATION OF ORBITAL DEBRIS

Ronald A. Madler
Assistant Professor
Department of Aerospace Engineering
Embry-Riddle Aeronautical University

Abstract

The physical characteristics of breakup debris are essential to properly estimate the orbital debris environment and its hazard to spacecraft. This paper examines methods of determining certain physical characteristics utilizing ground based fragmentation debris. A well-defined and easily repeatable method of determining the cross sectional area of ground based fragmentation debris has been defined. This method expands on previous methods of obtaining and modeling physical characteristics of debris. The results of these measurement methods are compared. This report presents methods and results of direct measurements of the cross sectional area of fragmentation debris.

CROSS SECTIONAL AREA ESTIMATION OF ORBITAL DEBRIS

Ronald A. Madler

Introduction

There exists a need to quantify and characterize the hazard posed to orbiting assets by space debris. Currently there are approximately 9,500 objects being tracked by the United State Space Command's (USSPACECOM) Space Surveillance Network (SSN). The majority of these tracked objects are operational and fragmentation debris. The tracked objects in orbit as of June 1996 are categorized as follows: satellite fragmentation debris (39%); inactive payloads (24%); rocket bodies (18%); operational debris (11%); active payloads (6%); anomalous event debris (2%).¹ A much larger population of objects below the detection threshold is known to exist from the approximately 150 on-orbit satellite breakups that have occurred to date. Although not trackable, they still pose a threat to space operations. Hence, it is important to be able to model the fragments from these on-orbit fragmentation events.

The relationships between mass, area, and size are important because these values affect the decay of resident space objects (RSOs), the expected collision rate, the hazard to other RSOs, and the observability of the debris. The relationships between mass, number, and size have been examined extensively.²⁻⁶ Cross sectional area for fragments is important to model fragment behavior, but is difficult to determine. Several researchers have examined observations of on-orbit fragmentation debris, but great uncertainties exist in determining area of these objects due to the long distance to the objects and the many unknowns.⁷⁻¹⁰

This report examines a method to determine the cross sectional area of debris fragments at a large number of orientations, from which an average value can be determined. The method has been used on various shapes of known area. The cross sectional areas of some of the fragments also have been measured with other methods to verify the results.

Methodology

A set of simulated debris was obtained for this project from a hypervelocity impact test. Shot CU-6470, a hypervelocity impact conducted at the Arnold Engineering Development Center (AEDC), was examined in cooperation with the University of Colorado and the owners of the fragments, NASA/JSC. The physical parameters of size, mass, and area were determined for these fragments. Also, some simple shapes were obtained and used, including a sphere, cube, slender rod, cylinder, and flat plate.

Previous characterization of debris object size has focused on a pieces characteristic dimensions. When obtaining three characteristic dimensions, the first dimension is the longest dimension of an object, the second dimension is the longest dimension orthogonal to the first, and the third dimension is the longest dimension orthogonal to the first two. The first two dimensions are demonstrated in Figure 1. The average of these three dimensions is THE characteristic dimension and is usually referred to as the debris diameter.

Previous methods of determining the area for this research using a shadowgraph technique and using a planimeter.^{11,12} The shadowgraph method relates light intensities, with and without a fragment, to determine the cross sectional area seen at various orientations. Although this method resulted in useful data, it is time consuming and difficult to repeat as it requires the use of a special dark room and light sensing equipment. The planimeter is a mechanical device that determines area by tracing the outline of an object. A variety of random images containing a reference of known area and debris are taken and printed out. The planimeter is then used to trace the debris and reference. Comparing these values gives a cross sectional area. This device produces useful results when several pictures of a fragment are analyzed; however, it is extremely time consuming.

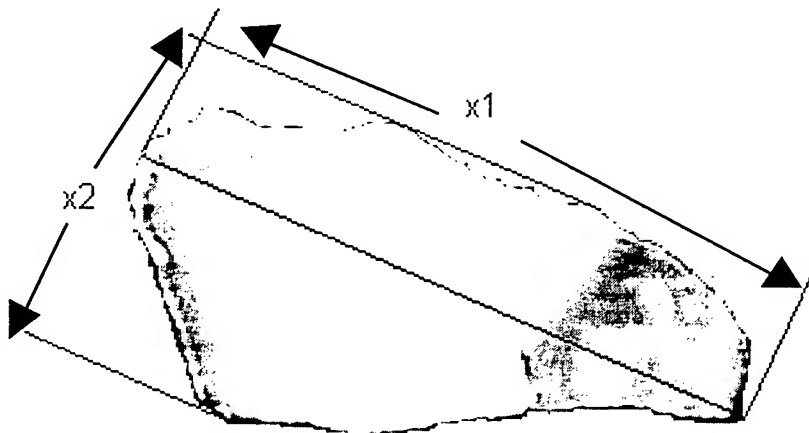


Figure 1: Characteristic dimension measurement

By determining the cross sectional area of a fragment at many orientations, an average area and normalized relative area frequency (NRAF) distribution can be directly computed. NRAF distributions will be discussed in more detail in the results section of this report. This process can be carried out using a digital image method (DIM) wherein digital images of a debris piece are obtained at many orientations. These images can then be run through a digital image analysis software package to compute the average area and area distribution quickly and accurately.

Image Acquisition

The setup for image acquisition is crucial to the speed and accuracy of the DIM. A uniform background and lighting must be set in place before images are taken. The background color of choice is a flat black. The reasoning behind this choice of background is that black, by its nature, will absorb all or nearly all light frequencies (color). In this way, the light reflected from the debris piece and reference will best stand out for image analysis. An attempt at creating a uniform background (few lines or creases) will also increase the speed and accuracy of the DIM by making the edge detection easier. A good uniform lighting source is also important as shadows can also make the debris outline difficult to follow. Two overhead fluorescent lights are used along with two high wattage halogen lights. A smaller mobile halogen is placed on the floor for bottom lighting.

A reference of known cross sectional area must be placed near the debris piece. The prime choice is a white sphere, as it will reflect the most light and has the same cross sectional area at every orientation. The reference is used as a known area in the digital image analysis process to compare and determine the area of the debris piece. This is necessary because the focal length and distance from the camera to object may change from image to image. The change in focal length is due to the fact that, in order to utilize all resolution possible, the camera is zoomed so that the reference and debris piece fill the image. This being the case, as the area seen changes the amount of zoom changes as well. The debris piece and reference object are placed on the top of two thin, black stands. The stands are located at the center of the area in which images will be taken. The stand holding the debris piece remains fixed in one location while the stand holding the reference is moved about the debris piece to ensure that the reference is always located to the left of the debris piece, which is necessary for the automated version of the image analysis process.

A fairly large number of images must be taken of the debris to ensure a good statistical sample. The location of the digital camera for the images must simulate all possible orientations (looking at the debris piece from every possible viewpoint) for the average area to be correct. A geodesic framework is used to generate the viewing coordinates so that all look angles are given an equal and correct weighting. The geodesic model of choice is the icosahedron, as utilized by the Aerospace Corporation in their model for a uniform satellite fragmentation.¹³ An icosahedron has 12 vertices, 20 faces, and is symmetrical about a central plane. Because of the symmetry of vertices, only the top half of the icosahedron geometry is needed with the debris piece and reference at the center. The reason for this can be seen by imagining looking at your hand from the front and back: both sides show the same area, although their exact surfaces may be different. By dividing the faces into several equilateral triangles, and including the centroids of the triangles, a total of 66 image locations can be attained. However, as the debris piece lies at the center of the virtual icosahedron, the points around the center are duplicated. For the same reason that only 5 of the 10 points at the center are used. Thus a total of 61 images can be taken. To create a more complete and accurate representation of each debris piece, 61 images are taken at the above locations, the debris piece's orientation is changed, and 61 more images are taken. Also, 6 additional images are taken corresponding to three orthogonal viewing directions, front

and back, with the thought that some day the 3 view may help in creating a 3-D model of the piece. Thus, a total of 128 images are acquired for each debris piece.

The camera used to acquire the images is a Kodak DC120. It has a picture resolution of 1.2 million pixels, a CCD resolution of 836,400 pixels, and a 3X zoom lens equivalent to a 35mm camera. A 10 MB picture card is used to hold all pictures in one shooting. Once the pictures have been taken they are downloaded for analysis.

Image Analysis

Once the images are downloaded to the workstation, Matlab and the image analysis toolbox are used to process the images. An extensive program was written in Matlab to analyze the digital images with as much automation as possible. Complete automation is possible, but is limited by the quality of the digital images themselves. The images which cannot be processed automatically are flagged for manual analysis.

There are several steps necessary to determine the area of an object by comparing it to a reference of known area. The main steps involve image separation, edge detection, and pixel counting. Several methods for each of the steps were tested to determine the most accurate one. Figure 2 on the following page shows a comparison of the results of using different threshold and area methods for one test object. The resultant areas are compared to results using a planimeter. As seen the maximum difference is less than five percent, which is considered to be a close value. The final process uses up to three methods of determining cross sectional area to further reduce any errors within one method. Total processing time can take from 1 to 3 minutes per image, depending on computer speed and image size.

The program can run in multiple variations of automated modes or manual check modes. It can run all images at once, or a few images at a time until all images are completed. The program completes a series of steps to calculate the area of a debris piece. Once the process to be used has been defined by the user, the images are read in and analyzed one at a time. This process can be summarized as:

- an image is read into Matlab
- the green matrix is extracted
- a threshold level is chosen to create a binary image
- the reference and debris are separated into two images
- an edge of each image is found
- the pixels within each image are counted
- a best fit circle is created from the reference image and an area calculated in pixels
- pixel values are compared and an area is computed

The final results from running all images consist of the average area, a list of all areas seen, and a list of normalized areas which make up the NRAF. A sample of an image analyzed by this program is shown in Figure 3.

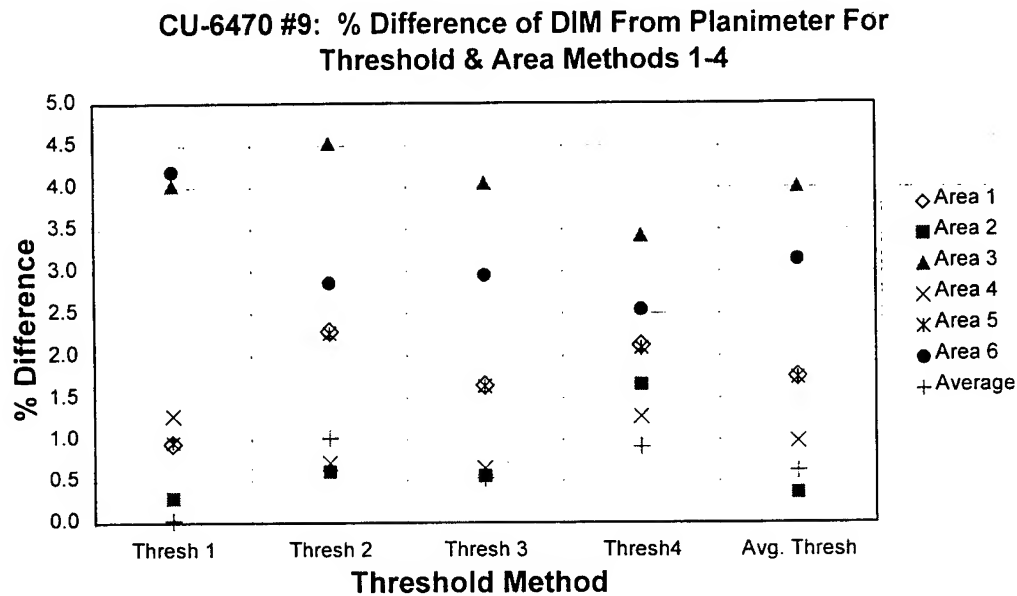


Figure 2: Threshold and area method determination for debris piece CU-6470 #9.

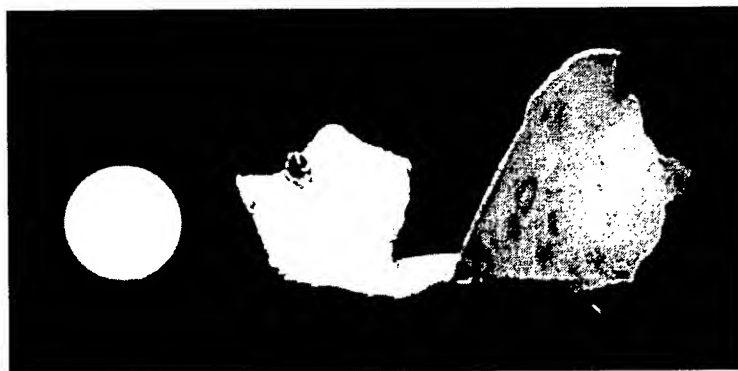


Figure 3: Sample image of reference sphere and CU-6470 Piece #2.

Calibration

To calibrate the DIM and compare results for useful relationships, the DIM observations of standard shapes (sphere, cube, rod, and flat plate) were compared with their "ideal" characteristics. The "ideal" characteristics were simulated with a program which utilizes a random number generator to create a large number of orientations for an object. The area can be determined using an equation describing the object's area at a given orientation. For ease of calculations 3000 random orientations are chosen from which the area can be calculated. An average area and

NRAF distribution can then be determined. Table 1 shows resultant average area values and error using the DIM and ideal results using this program for some standard shapes. The maximum error is less than ten percent.

Shape	DIM	Ideal	Actual	% Error DIM	% Error Ideal
Sphere	1.7398	1.7294	1.7294	0.5993	0.0009
Cube	3.3159	3.3613	3.3750	1.7517	0.4051
Rod	1.0670	0.9831	1.0201	4.5968	3.6253
Flat Plate	7.2305	8.0593	8.0000	9.6183	0.7416

Table 1: Average area comparison for DIM, ideal program, and actual value.

The area of several shapes were determined and compared against actual areas or areas determined by a planimeter to determine common errors for individual images. The results are shown in Table 2. As can be seen the greatest error or difference is less than ten percent.

Shape	DIM	Actual	% Error
Sphere	1.683	1.729	2.674
Rod	1.171	1.250	6.332
Cylinder	4.422	4.500	1.732
Flat Plate	16.048	16.000	0.301

Shape	DIM	Planimeter	% Difference
P4	3.843	3.529	8.911
CU-6470 #9	4.686	4.883	4.031
G2	1.358	1.387	2.084

Table 2: Individual image analysis of several objects.

The NRAF for the image analysis program can be compared to the ideal mathematical model as another means of calibration. A comparison for a flat plate is shown below in Figure 4. The results are seen to agree quite well.

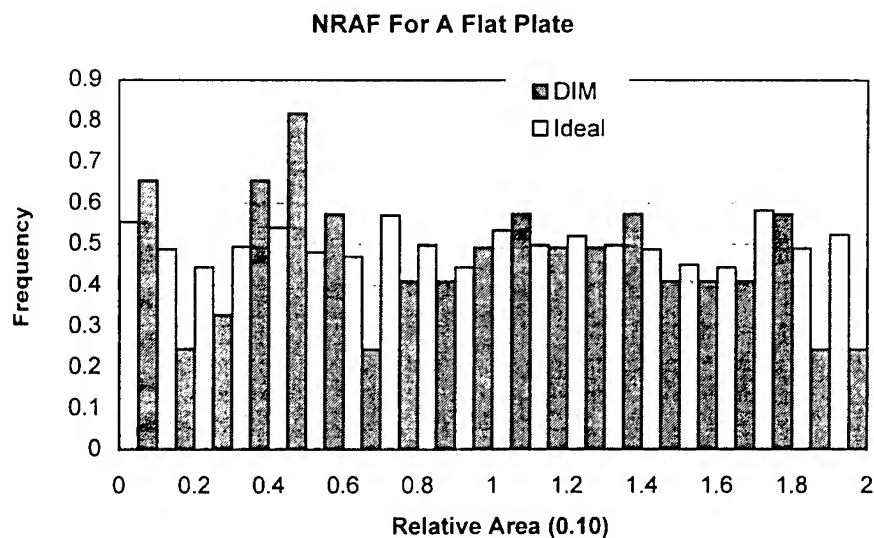


Figure 4: Normalized relative area frequency (NRAF) distribution

Results

A number of objects were analyzed using the DIM. The average area and area distributions are examined here. These results are compared to results from an earlier method, those measured with a planimeter, as well as some characteristic shapes and simple models.^{11,12}

Average Area Distribution

The average area for several debris pieces was found using the DIM, shadowgraph, and planimeter methods. These methods compute the area of a debris piece at several orientations. The mean is then computed for the respective debris. Figure 5 shows the measured average area versus diameter for the fragments examined. The diameter is the characteristic dimension as discussed earlier.

As can be seen in Figure 5, there appears to be a fairly regular relationship between the "characteristic" dimension and the average area for the CU-6470 debris fragments. Several types of relationships have been fit to this data. It is thought that a power law should provide the most meaningful fit to the data. The power law equation becomes: $\text{Area} = 0.859 * (\text{diameter})^{1.69}$. Where the area is in cm^2 and the diameter is in cm. Looking at the log-linear data space shown in Figure 6, however, makes us wonder if there should be different relationships depending on the size regime of the object. Further analysis of more fragments is necessary to fully understand the relationships and its variation.

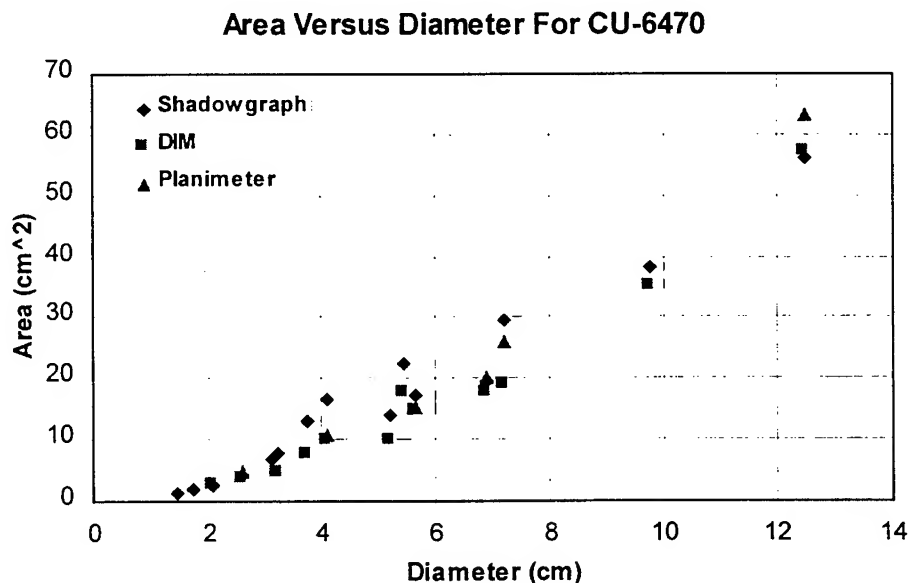


Figure 5: Measured average cross sectional areas versus diameter for CU-6470 objects.

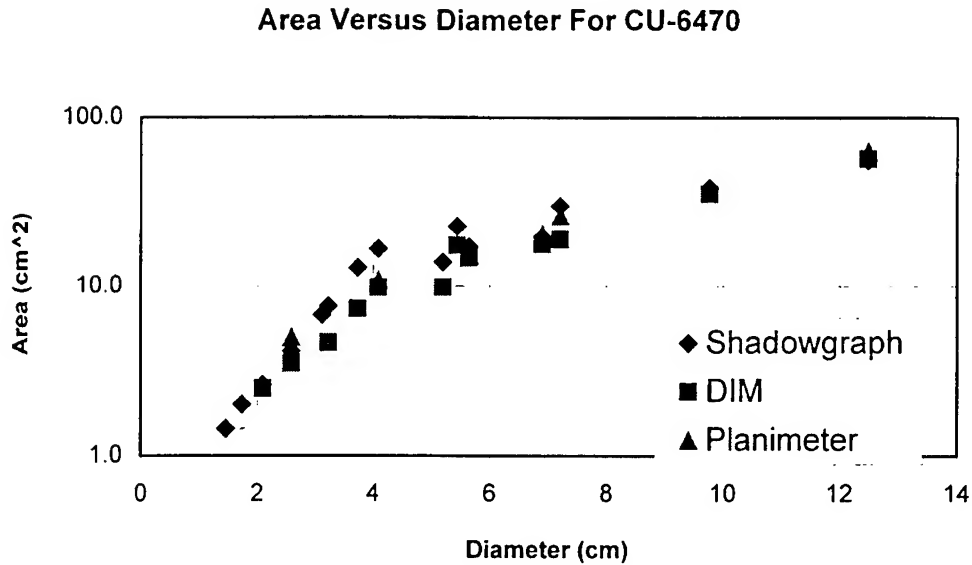


Figure 6: Log of Measured average cross sectional areas versus diameter for CU-6470 objects.

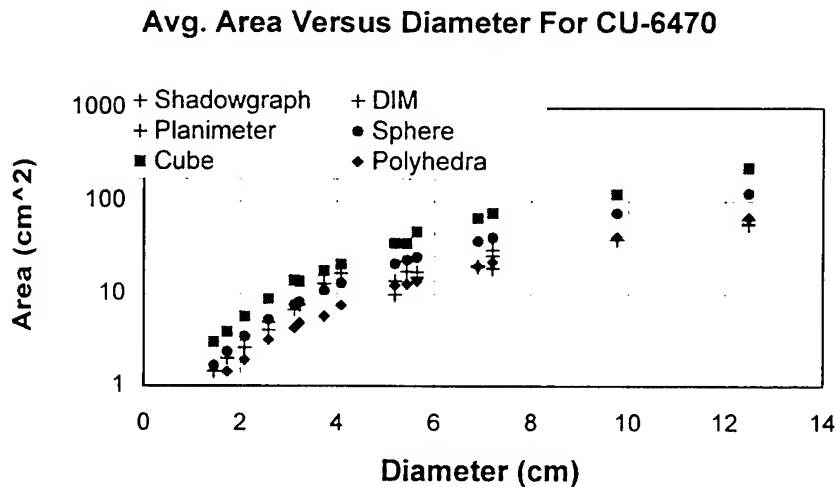


Figure 7: Log of estimated and measured average cross sectional area versus diameter for CU-6470 objects.

From a modeling point of view it is desirable to have a simple relationship between fragment dimension and average cross section as found earlier. Often the cross sectional area has been estimated by assuming that the debris object is a sphere with diameter equal to the characteristic dimension. Figure 7 shows estimated average areas based on the characteristic dimensions along with the measured average areas. It can be seen that the classic assumption yields reasonable estimates for the cross sectional area for all but the largest objects. The only shape that appears to work better is the polyhedral shape. The estimated average areas come from: assuming the object to

be a sphere with the characteristic dimension as the diameter, assuming a cube with sides equal to the measured dimensions, and a polyhedral with the measured dimensions representing the main axes. The polyhedral shape can be thought of as two rhombus based pyramids attached at the base. It can be seen that the measurements generally lie between the sphere and polyhedral shape values. A spheroid shape is slightly better than the spherical model, but not enough to justify its increased complexity.

Normalized Relative Area Frequency Distribution

The normalized relative area frequency (NRAF) distributions for several objects from the CU-6470 shot have been determined. A non-dimensional relative area is found by dividing each measured area by the average area for that piece. The relative area distribution curve is normalized so that the area under the curve is equal to one. The NRAF can then be compared for all pieces regardless of the actual area.

The NRAF distributions are interesting in that they appear to depend on the "shape" of the object. Figures 8 to 10 show the idealized (theoretical) NRAF distributions and the DIM measured NRAF distributions for several idealized shapes: sphere, cube, and flat plate. The "ideal" distributions come from a Monte-Carlo simulation using 3000 random orientations. The DIM distributions are slightly spread out with respect to the ideal distributions due to the small errors in estimating the area.

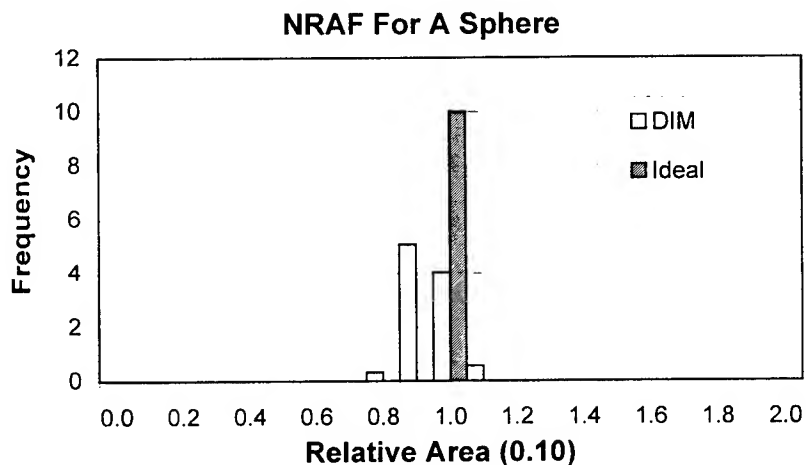


Figure 8: Idealized and measured NRAF distributions for a sphere

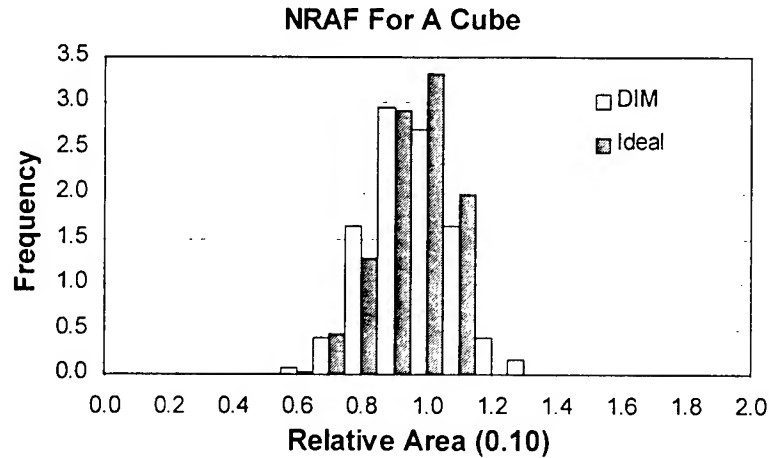


Figure 9: Idealized and measured NRAF distributions for a cube.

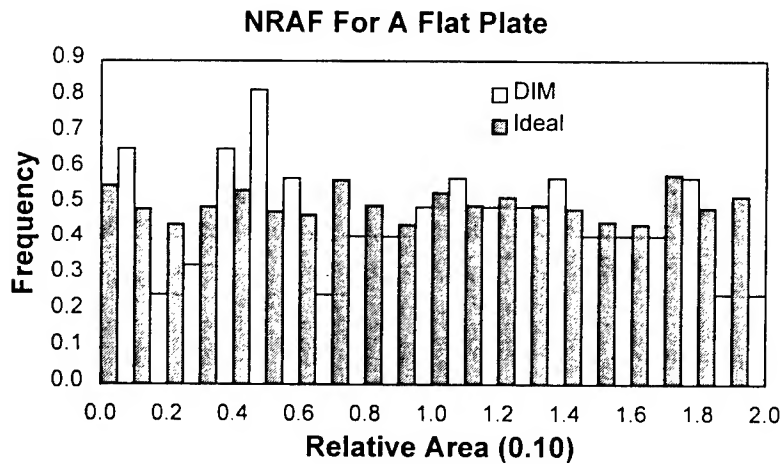


Figure 10: Idealized and measured NRAF distributions for a flat plate.

Shape Factor

The shape of debris affects the lethality, decay, and ability to observe debris objects.¹⁴ A preliminary shape factor derived from the NRAF and aspect ratio distributions has been developed. The aspect ratio is the ratio of the characteristic dimensions of an image. These factors may help in modeling the lethality, decay and observability of fragments and will be explained in this section.

Figure 11 compares the NRAF distribution of CU-6470 Piece #9 to that of a flat plate. It can be seen that the distributions are similar. The differences at the ends are easily explained by the slight curvature of Piece #9, which is shown in Figure 1. This slight curvature means that the "edge on" images will always have a greater area than the edge of an idealized flat plate. Therefore there will be no small area measurements and the average area will be slightly higher than for a flat plate. This slightly higher average and the slight curvature also mean that there will be few observations of large areas.

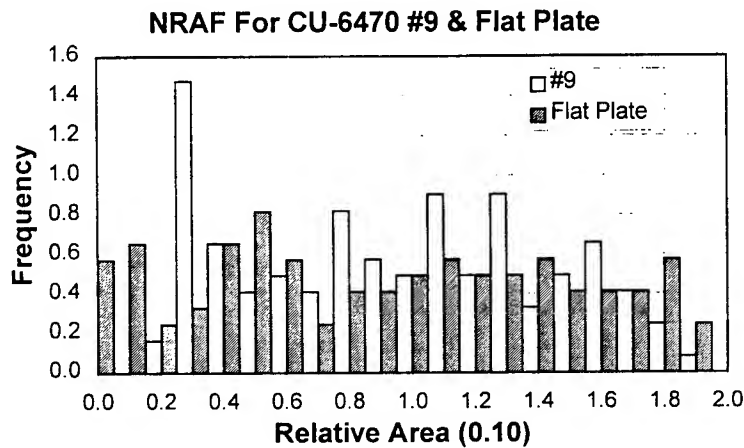


Figure 11: NRAF distribution for CU-6470 Piece #9 and DIM results for a flat plate.

This can be contrasted to the NRAF distribution shown in Figure 12 for Piece #6, which is crumpled. This more "shapely" object has a distribution more like a cube or a rod. Figure 13 compares the NRAF for objects that had highly twisted shapes ("shapely" pieces such as 2, 4, 6, and a sphere) with those pieces that were more plate-like ("flatter" pieces 9, 12, and flat plate). The data for this figure was taken from DIM data for the specified objects. The NRAF distributions differ depending on the shape of the object. This makes sense when compared with the NRAF for the ideal shapes.

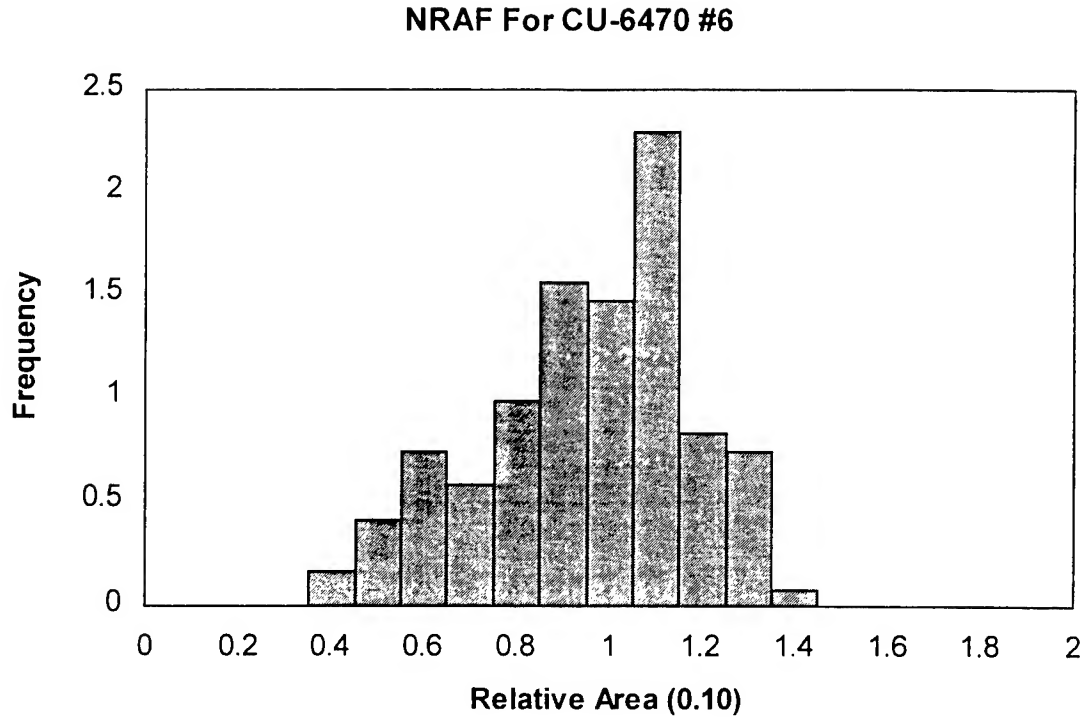


Figure 12: NRAF for a crumpled piece, #6

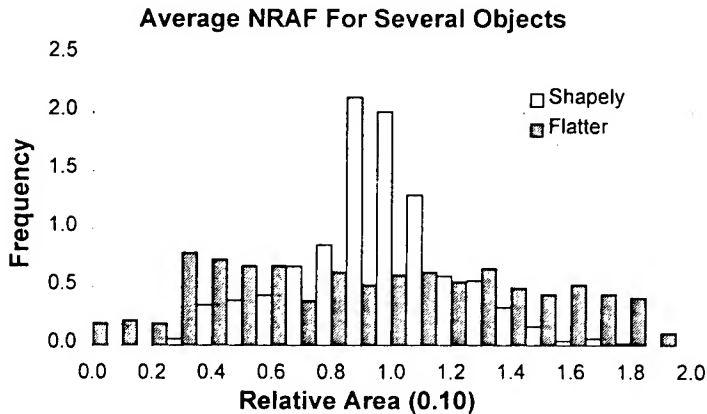


Figure 13: NRAF for "Shapely" and "Flatter" objects

The proposed "Shape Factor" based on the NRAF is the standard deviation of the frequency values. The more spherical an object becomes the lower the standard deviation is since the object has the same cross section from every orientation. Conversely the more like a flat plate the object becomes the larger the standard deviation becomes. This also agrees with the "Shape Factor" based on the characteristic dimensions for the pieces and visual observations. The characteristic dimension shape factor is based on the difference ratios between the characteristic dimensions. The difference ratios are defined as: $AC_{diff} = (A-C)/A$; $BC_{diff} = (B-C)/B$. A, B, and C are the 3 dimensions measured for the piece, from longest to smallest. As these ratios are defined, it is obvious that a sphere

will have difference ratios always equal to zero and a flat plate will have AC and BC difference ratios approaching 1 since the thickness of the plate is assumed to be small. The two methods for determining the qualitative shape are compared in Figure 14. The grouping of the objects from flatter to more shapely can also be seen in Figure 15, which plots the B/C and A/C difference ratios. When these two ratios are multiplied by one another, the two shape types are spread out well on a linear scale. This multiplication of the A/C and B/C difference ratios appears to be a good method to discriminate between the apparent shape of debris which corresponds well to the NRAF of the actual debris piece. However, the characteristic dimensions are only useful for ground based fragments, as the on-orbit fragments are not easily measured.

The characteristic dimensions and the NRAF distribution for the debris pieces are included in the appendix.

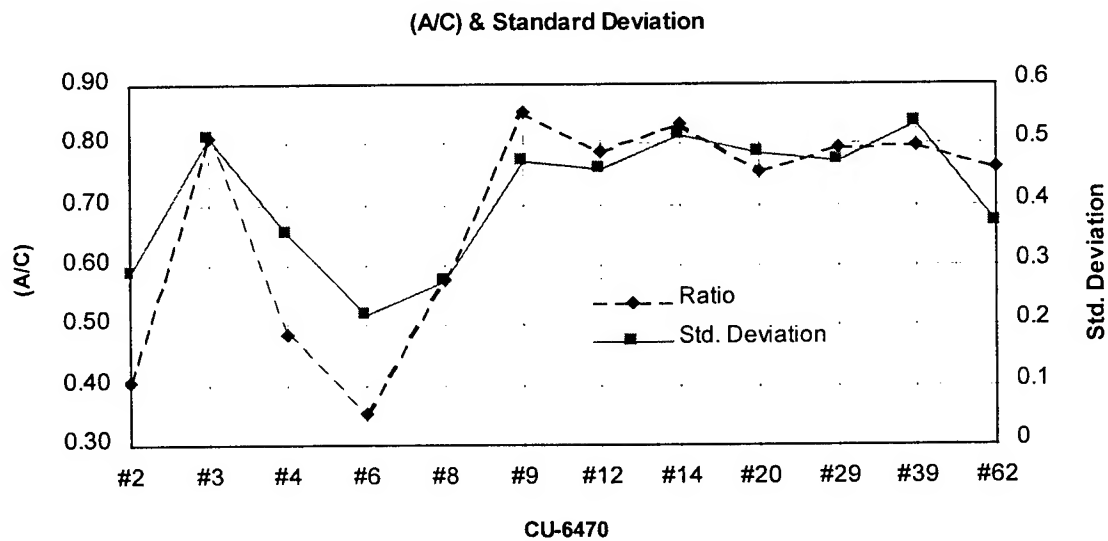


Figure 14: Comparison of shape factor parameters for CU-6470 pieces

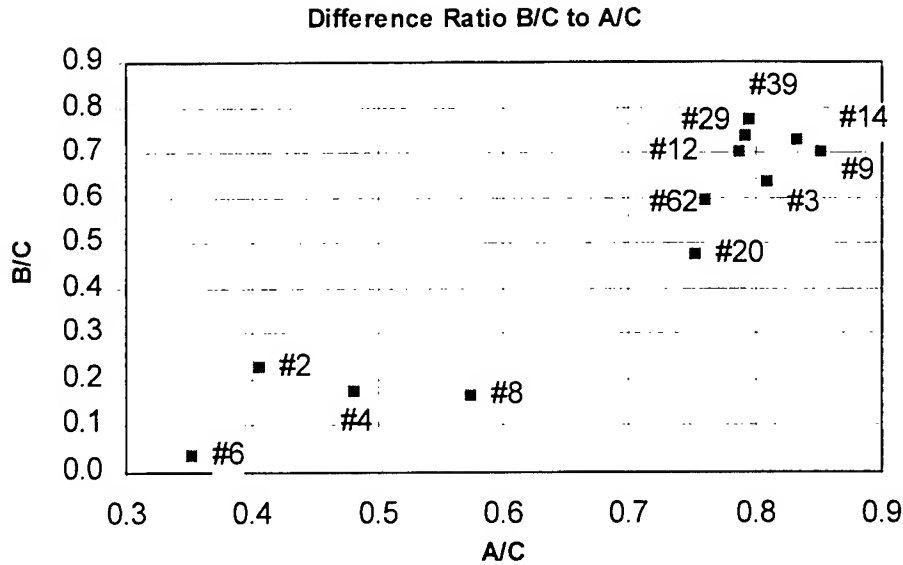


Figure 15: Difference ratio parameters for CU-6470 Pieces

Summary / Conclusions

The purposes of this research have been to examine methods for determining the cross sectional area of debris objects and analyzing the obtained data. For laboratory pieces, the area can be measured using several different techniques. A digital camera is used to image the debris piece and a known reference object together at a large number of orientations. The area of the object at each orientation can then be estimated by analyzing the digital images, or by using a planimeter. This will give an average area as well as a distribution of areas. The main advantage of the image analysis method is that the area at each orientation can be determined fairly quickly and accurately.

The results show that there appears to be a relationship between average area and characteristic dimensions. Also the normalized relative area frequency distribution (NRAF) as well as object aspect ratios may describe the shape of an object. Both of these results could lead to improvements in the modeling of debris fragments and the debris environment. Shape and area especially affect decay rates, penetration analysis, and reduction of observational data. Further data and study is required to clarify these observations.

Acknowledgements

This work was sponsored by the Air Force Office of Scientific Research (AFOSR), Bolling AFB, DC, as part of the Summer Faculty Research Program and the Summer Research Extension Program. Special thanks are due to the Space Debris Program Office at the Air Force Research Laboratory, Kirtland AFB. Also to Jonathan Rustick for countless hours working on this project and making sure everything was correct.

References

1. Grissom, W., and Myers, G., "History of On-Orbit Satellite Fragmentations," Tenth Edition, Teledyne Brown Engineering, July 1996.
2. Bess, T.D., "Size Distribution of Fragment Debris Produced by Simulated Meteoroid Impact of Spacecraft Wall," NASA SP-379, pp. 575-587, 1975.
3. Kessler, D.J. and Cour-Palais, B.G., "Collision Frequency of Artificial Satellites: The Creation of a Debris Belt," *Journal of Geophysical Research*, Vol. 83, No. A6, June 1, 1978.
4. Gravseth, I.J., Maclay, T.D., and Culp, R.D., "Mass-Diameter and Characteristic-Length Ratio Functions for Orbital Debris," *Journal of Spacecraft and Rockets*, Vol. 33, No. 3, pp. 433-437, May-June 1996.
5. Gravseth, I.J., Maclay, T.D., and Culp, R.D., "A Mass-Diameter Function for the Entire Size Regime of Orbital Debris," in *Space Environmental, Legal, and Safety Issues*, Timothy D. Maclay, Editor, Proc. SPIE 2483, 21--30, 1995.
6. Maclay, T.D., Hinga, M., and Madler, R., "Analysis of Shot CU-6470 Fragments," Colorado Center for Astrodynamics Research Internal Report No. SD-89-02T, University of Colorado, July, 1989.
7. Anz-Meador, P.D., Matney, M.J., and Kessler, D.J., "Physical Properties of Orbital Debris and Orbital Debris Clouds," *Advances in Space Research*, Vol. 16, No. 11, pp. 113-117, 1995.
8. Anz-Meador, P.D., Rast, R.H., and Potter, A.E., Jr., "Apparent Densities of Orbital Debris," *Advances in Space Research*, Vol. 13, No. 8, pp. 153-156, 1993.
9. Badhwar, G.D., and Anz-Meador, P.D., "Determination of the Area and Mass Distribution of Orbital Debris Fragments," *Earth, Moon, and Planets*, Vol. 45, pp. 29-51, 1989.
10. Dickey, M.R., and Culp, R.D., "Determining Characteristic Mass for Low-Earth-Orbiting Debris Objects," *Journal of Spacecraft and Rockets*, Vol. 26, No.6, pp. 460--464, 1989.
11. Madler, R.A., "Estimating the Area of Artificial Space Debris," Final report for the 1996 AFOSR Summer Faculty Research Program, August 1996.
12. Madler, R.A., Jorgensen, K., Spencer, D.B., and Culp, R.D., "Estimating the Area of Artificial Space Debris," in *Proceedings of the 2nd European Space Debris Conference, ESOC, Darmstadt, Germany, 17-19 March, 1997*, W. Flury, Editor, ESA SP-393, pp. 297-302, May 1997.
13. Chobotov, V.A., Spencer, D.B., Schmitt, D.L., Gupta, R.P., and Hopkins, R.G., "Dynamics of Debris Motion and the Collision Hazard to Spacecraft Resulting from an Orbital Breakup," Aerospace Report No. TR-0086A(2430-02)-1, January 1988.
14. Sridharan, R., Beavers, W., Lambour, R., Gaposchkin, E.M., Kansky, J., and Stansbery, E., "Remote Sensing and Characterization of Anomalous Debris," in *Proceedings of the 2nd European Space Debris Conference, ESOC, Darmstadt, Germany, 17-19 March, 1997*, W. Flury, Editor, ESA SP-393, pp. 261-269, May 1997.

Appendix

- Characteristic dimensions, area and shape factors for the CU-6470 debris
- Normalized relative area frequency (NRAF) distributions for the CU-6470 debris.

A Look At Characteristic Dimensions &
Dimension Fractions

Dimensions in cm
A/B = (A-B)/A

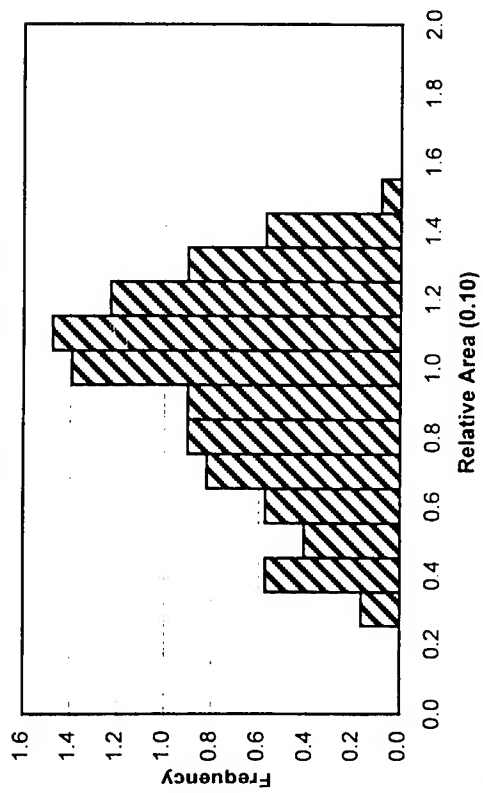
CU-6470 Debris	difference ratios			straight ratios			Difference Straight Ratio	
	A	B	C	Average	A/B	A/C	B/C	C/B
CU-6470 #2	15.900	12.103	9.427	12.477	0.239	0.407	0.221	0.761
CU-6470 #3	17.230	8.817	3.253	9.767	0.488	0.811	0.631	0.512
CU-6470 #4	10.107	6.285	5.223	7.205	0.378	0.483	0.169	0.622
CU-6470 #6	7.323	4.889	4.729	5.647	0.332	0.354	0.033	0.668
CU-6470 #8	10.720	5.423	4.548	6.897	0.494	0.576	0.161	0.506
CU-6470 #9	10.050	4.790	1.465	5.435	0.523	0.854	0.694	0.477
CU-6470 #12	8.181	5.671	1.730	5.194	0.307	0.789	0.695	0.693
CU-6470 #14	6.950	4.150	1.150	4.083	0.403	0.835	0.723	0.597
CU-6470 #20	6.557	3.033	1.609	3.733	0.537	0.755	0.470	0.463
CU-6470 #29	4.919	3.757	1.011	3.229	0.236	0.794	0.731	0.764
CU-6470 #39	3.772	3.232	0.761	2.588	0.143	0.798	0.765	0.857
CU-6470 #62	3.461	2.002	0.821	2.095	0.422	0.763	0.590	0.578

Area	SF	SF Ratio
57.1708	0.09	0.462
35.1175	0.512	0.07
18.8175	0.082	0.429
14.692	0.012	0.625
17.6047	0.093	0.356
17.36	0.593	0.045
9.82156	0.548	0.065
9.82342	0.604	0.046
7.31193	0.355	0.13
4.59018	0.58	0.055
3.48328	0.61	0.048
2.48075	0.45	0.097

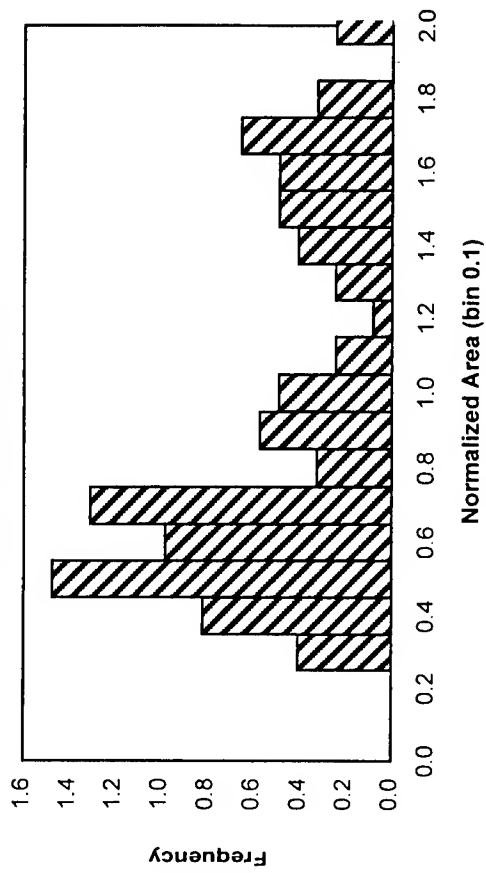
Characteristic Shapes - Actual				difference ratios				straight ratios			
Shape	A	B	C	Average	A/B	A/C	B/C	B/A	C/A	C/B	
Sphere	1.484	1.484	1.484	1.484	0.000	0.000	0.000	1.000	1.000	1.000	
Cube	1.813	1.375	1.125	1.438	0.241	0.379	0.182	0.759	0.621	0.818	
Rod	4.000	0.313	0.313	1.542	0.922	0.922	0.000	0.078	0.078	1.000	
Cylinder	2.000	1.000	1.000	1.333	0.500	0.500	0.000	0.500	0.500	1.000	
Flat Plate	5.657	5.657	0.063	3.792	0.000	0.989	0.989	1.000	0.011	0.011	

Area	SF	SF	SF
1.740	0	0	1
3.316	0.069	0.508	0.508
1.740	0	0.078	0.078
1.740	0	0.5	0.5
7.231	0.978	0	0

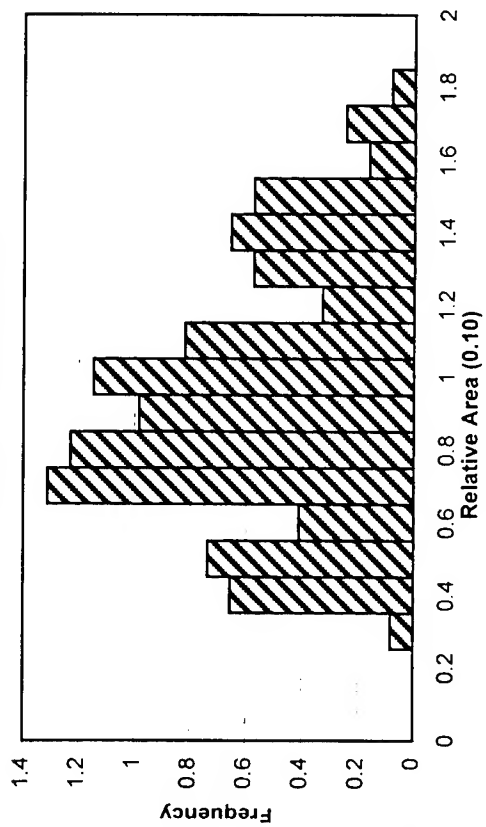
NRAF For CU-6470 #2



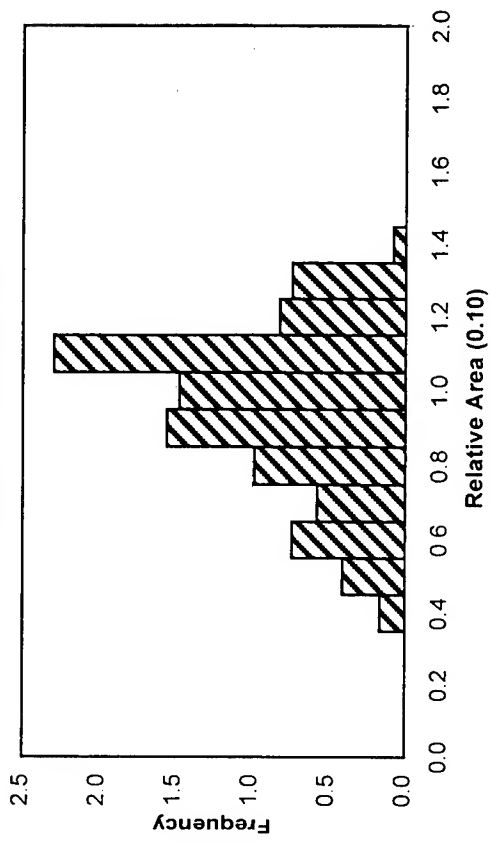
NRAF For CU-6470 #3



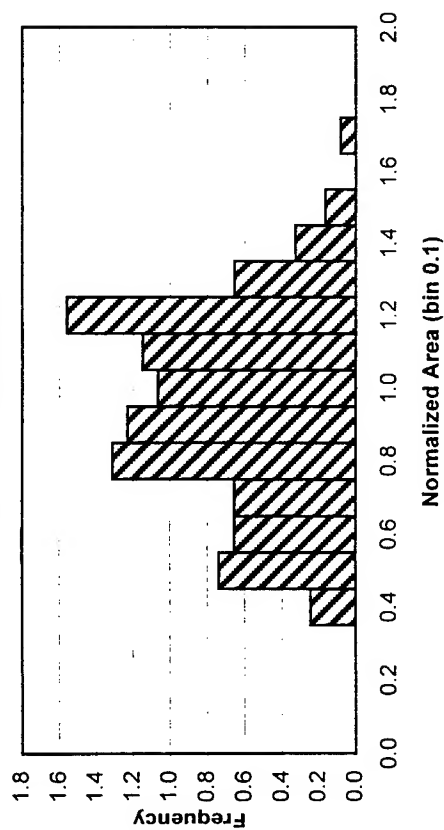
NRAF For CU-6470 #4



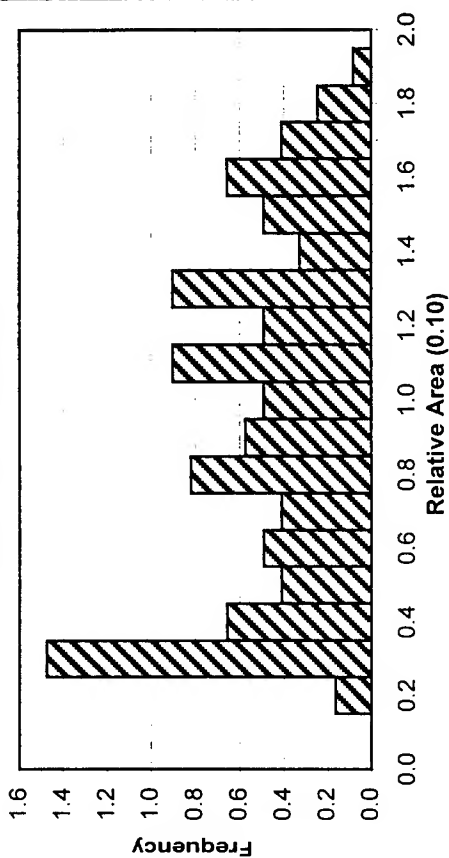
NRAF For CU-6470 #6



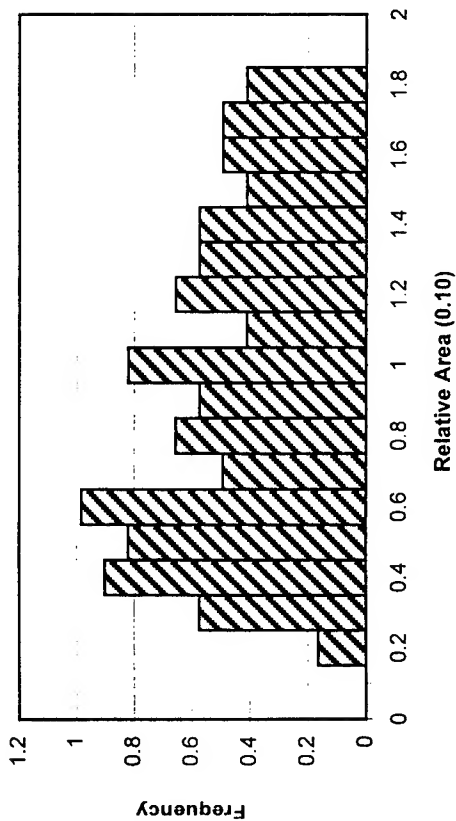
NRAF For CU-6470 #8



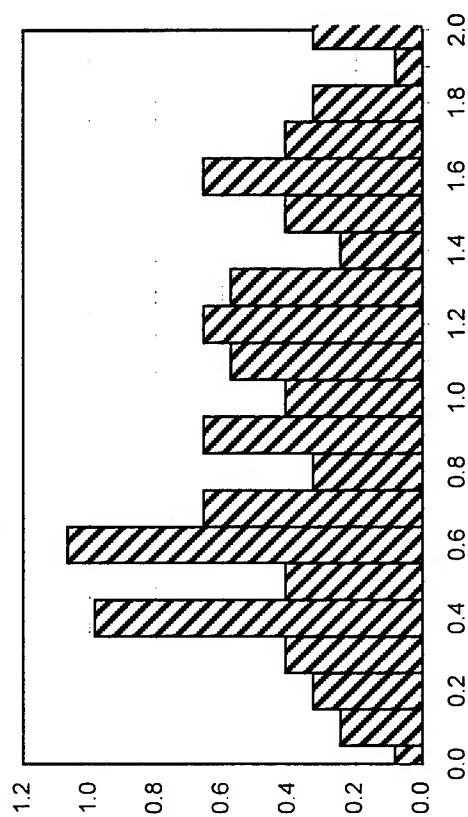
NRAF For CU-6470 #9

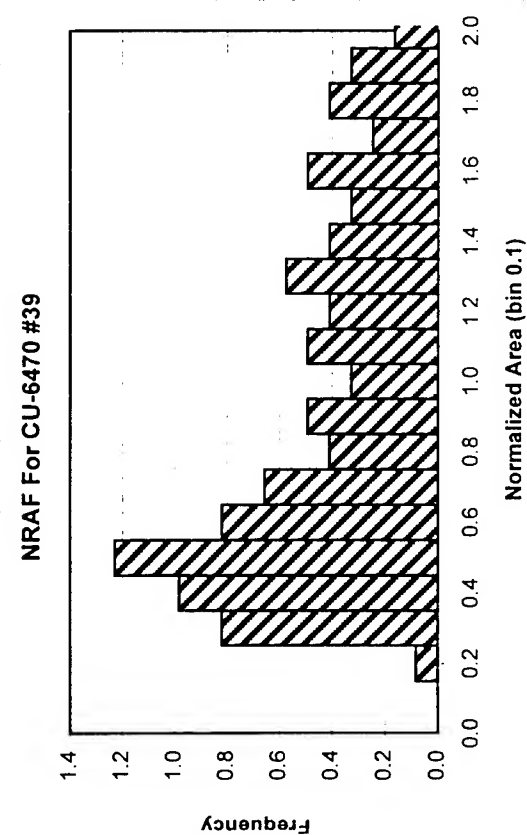
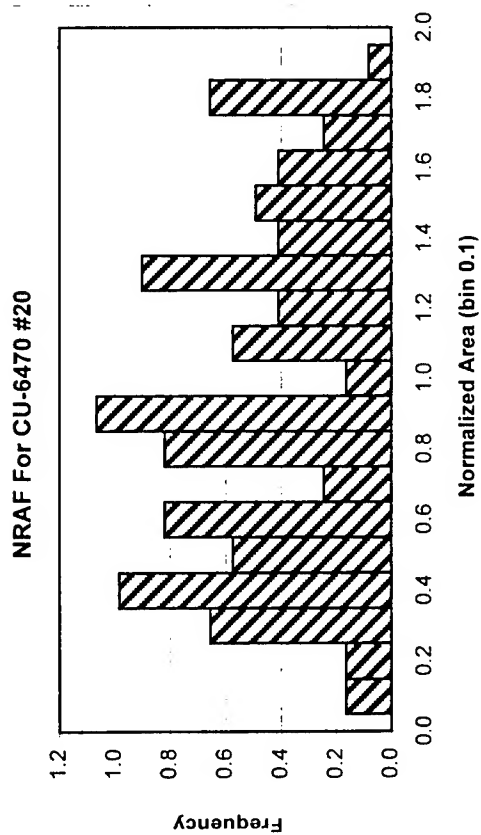
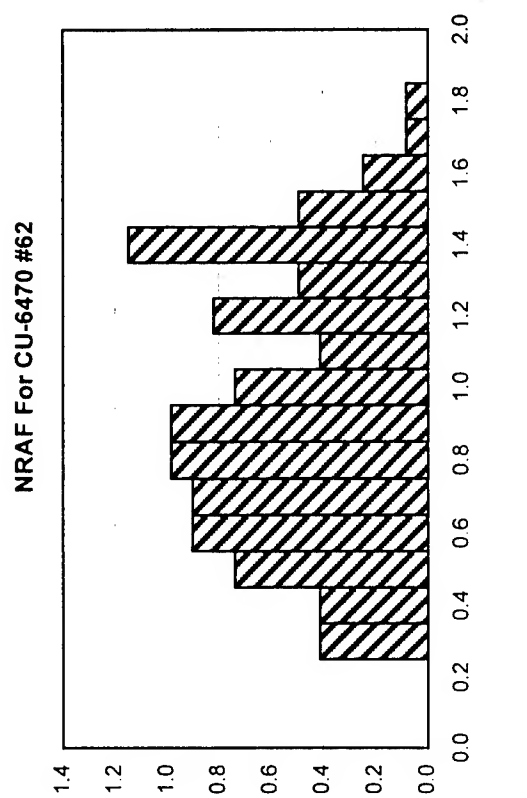
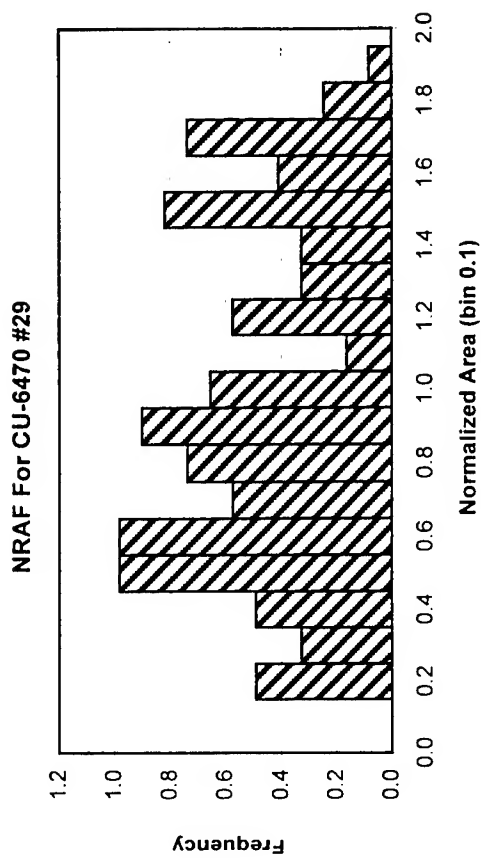


NRAF For CU-6470 #12



NRAF For CU-6470 #14





Carlos Ordonez
Report not available at time of publication.

WIDE SWATH, HIGH RESOLUTION, UNAMBIGUOUS
SYNTHETIC APERTURE RADAR (SAR) IMAGING
USING DIGITAL BEAMFORMING ARRAYS

James M. Stiles
Principal Investigator
Radar Systems and Remote Sensing Laboratory

The University of Kansas
Center for Research, Inc.
2291 Irving Hill Road
Lawrence, KS 66045

Final Report for:
Summer Research Extension Program
Phillips Laboratory

Sponsored by:
Air Force Office of Scientific Research
Bolling Air Force Base, DC

and

Phillips Laboratory

30 April 1998

WIDE SWATH, HIGH RESOLUTION, UNAMBIGUOUS
SYNTHETIC APERTURE RADAR (SAR) IMAGING
USING DIGITAL BEAMFORMING ARRAYS

James M. Stiles

Principal Investigator

Radar Systems and Remote Sensing Laboratory
The University of Kansas Center for Research, Inc.

ABSTRACT

The current performance issues related to a single receiver Synthetic Aperture Radar (SAR) were studied and illustrated. Specifically, the tradeoffs between swath, resolution and ambiguity in both the across-track and along-track directions were considered and documented. To improve upon current performance, it is proposed that the SAR be modeled in a multiple receiver environment. To physically illustrate the current situation and proposed solution, a SAR simulator was constructed using the C programming language. A square image was used to represent a target area. A single receiver SAR environment was developed and the data obtained clearly demonstrated the shortcomings of the present system. Subsequently, a multiple receiver SAR environment was created and the data collected has proven that a multiple receiver SAR environment produces higher performance with respect to swath width, resolution and ambiguity. Specifically, it has been shown that in a multiple receiver SAR environment, it is now possible to obtain wide swath, high resolution, and unambiguous SAR images within a wide range of pulse repetition frequencies.

**WIDE SWATH, HIGH RESOLUTION, UNAMBIGUOUS
SYNTHETIC APERTURE RADAR (SAR) IMAGING
USING DIGITAL BEAMFORMING ARRAYS**

James M. Stiles

1 INTRODUCTION

1.1 Overview

Synthetic Aperture Radar [1] is a powerful surveillance tool that can perform a multitude of functions in an all-weather day and night situation. In the military area, SAR may be used as a ground surveillance system to monitor troop and equipment activity. In the civilian area, SAR is a popular choice for weather monitoring, ocean surveillance and deforestation assessment.

1.2 SAR Imaging Performance

There are two critical criteria that a SAR needs to fulfill in order to perform optimally. Firstly, it must be able to map a wide spatial area in order to locate all objects of interest. In addition, it must also be able to exhibit fine resolution so as to specifically identify particular objects on the ground. Unfortunately, these two criteria are not easily achieved at the same time because of a tradeoff that is currently inherent in standard SAR sensors: observations of high spatial resolution are achieved unambiguously only when the width of the observed area is limited. Given that the converse of the previous statement is also true, it is now clear that this limitation could seriously inhibit the ability of a standard SAR sensor to produce unambiguous, wide swath, and high resolution images.

1.3 Ongoing Research

There has been much research performed in this area to attempt to limit the impact of the above restriction. Possible techniques for obtaining wide swath SAR images are presented in [2] and [3]. These references primarily focus on techniques now referred to as Multiple Elevation Beam (MEB) and Multiple Azimuth Beam (MAB). Whilst these techniques are effective, they each possess shortcomings. With MEB SAR, we are unable to obtain a continuous swath in the across-track direction due to the fact that the sensor is unable to receive whilst transmitting. With MAB SAR, there remains unresolved ambiguities in the doppler direction due to overlap of the sidelobe beams with that of the mainlobe. Yet another technique [4] involving the use of a broader elevation-plane beamwidth appears to be computational intensive. Finally, efficient filtering methods [5] to improve upon the resolution of SAR images have also been offered, but (as they use a variation of MAB) assume that ambiguities have been resolved. In addition, in all the cases mentioned above, techniques and theories presented have not been physically illustrated with a SAR imaging simulator.

1.4 Aim

The aim of this project is to discuss and validate the concepts leading to the development of a SAR model that utilizes the concept of multiple receive apertures and digital beamforming techniques [6,7] to produce unambiguous, wide swath, and high resolution SAR images.

2 DISCUSSION OF PROBLEM

2.1 Current Situation

Figure 2.1 shows the basic geometry of the SAR model. An airborne SAR traveling at a speed of v , and at a height h above the ground, will image over a time T a total area of $R_s v T$, where R_s is the ground swath coverage in the direction of range.

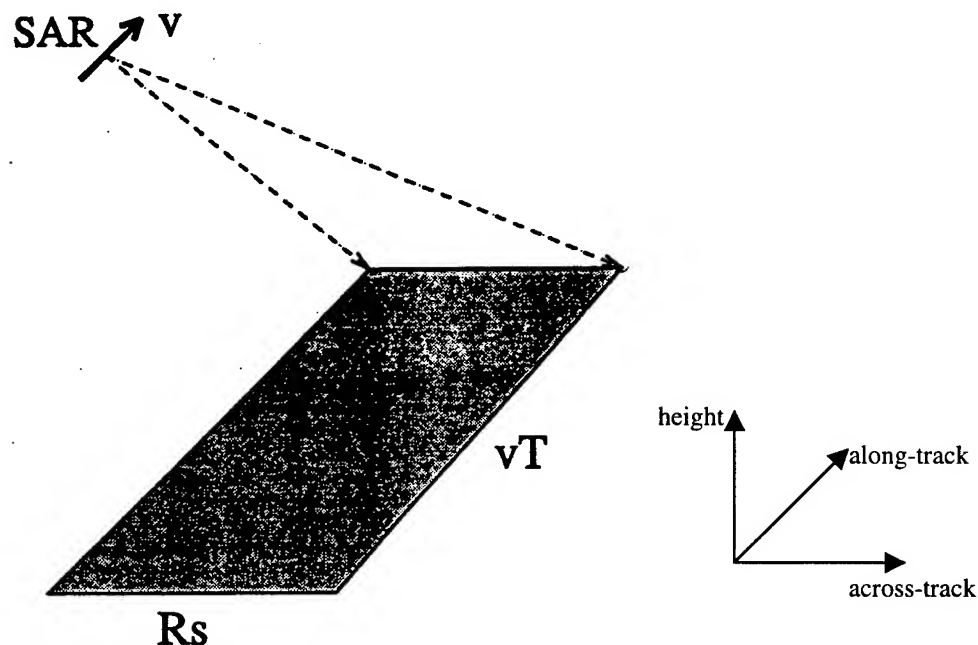


Figure 2.1: Basic Geometry of the SAR Model

We shall say that this imaged area, A , has an along-track length of l_x and an across-track length of l_y . Therefore,

$$A = l_x l_y = R_s v T. \quad (2.1)$$

A standard SAR sensor with a single receiver of bandwidth B will amass a total of BT independent samples over an observation time of T seconds. With this data, an unambiguous image of BT pixels may now be constructed.

The SAR sensor must not illuminate more than BT resolution cells if we wish to avoid ambiguity. If there are more than BT pixels illuminated, then the scattered energy from the extra area will appear in pixels of the imaged area, thus causing ambiguity. We are at liberty to develop a large image of moderate resolution, or a smaller image of high resolution. But in both cases, we remain constrained by the time-bandwidth product so long as we wish to produce an unambiguous image.

To avoid ambiguities, the pulse repetition frequency (prf) has to be carefully chosen. We require a low pulse repetition frequency to avoid range ambiguities. At the same time, a high pulse repetition frequency is required to eliminate ambiguity in the doppler direction. If the SAR antenna beamwidth illuminates more than BT resolution cells over an observation time T , then no value of the pulse repetition frequency can be found to produce an unambiguous image.

2.2 Proposed Solution

If, however, we were now to implement N receive apertures at the antenna, then the total number of independent samples available would increase to NBT . This now enables us to obtain an image with either greater resolution or larger size. As an example, let us consider the implementation of a three receive aperture antenna array. A graphical illustration of this is shown in Figure 2.2. We observe the existence of a low transmit pulse repetition frequency to accommodate a wide swath width. This results in the synthesized aperture being inadequately sampled. However, the spatially displaced receive apertures now provide the

additional samples and, in essence, enable the synthesized receive aperture to now exhibit spatial samples of a SAR with N times the pulse repetition frequency.

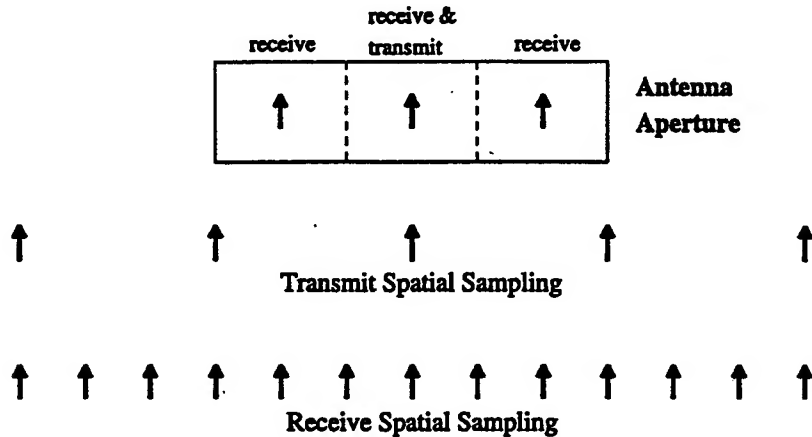


Figure 2.2: Spatial Sampling of the SAR Multi-Aperture Model

Since the single transmit element shares an aperture with the center receive element, we can now say that the along-track illumination pattern of each of the receive elements and the single transmit element are identical and will have a beamwidth three times larger than the original single receive aperture. When added correctly, then the azimuthal response of these three sub apertures will be equivalent to that of a single larger receive aperture. This now provides us with a beamwidth narrow enough to eliminate along-track ambiguity.

The three element receiver is essentially implemented as a phased array. Since each element is individually and coherently detected, digital beamforming may now be used in the processing of data. Because of the broader beamwidth of each sub aperture (explained above), a single target may be observed long enough to obtain a fine along-track resolution. At the same time, the coherent adding of the receiver channels will now ensure that

there will be a sufficiently narrow beam in the doppler direction to eliminate along-track ambiguities.

2.3 Multiple Receiver Antenna Design

The geometry of the radar antenna with respect to the object coordinate axes is shown as Figure 2.3. We should note here that the radar antenna axes do not have the same orientation as the object coordinate axes. The radar antenna is tilted towards the ground such that the normal axis out of the plane of the radar antenna, z' , makes an angle θ with the z direction of the object coordinate axis.

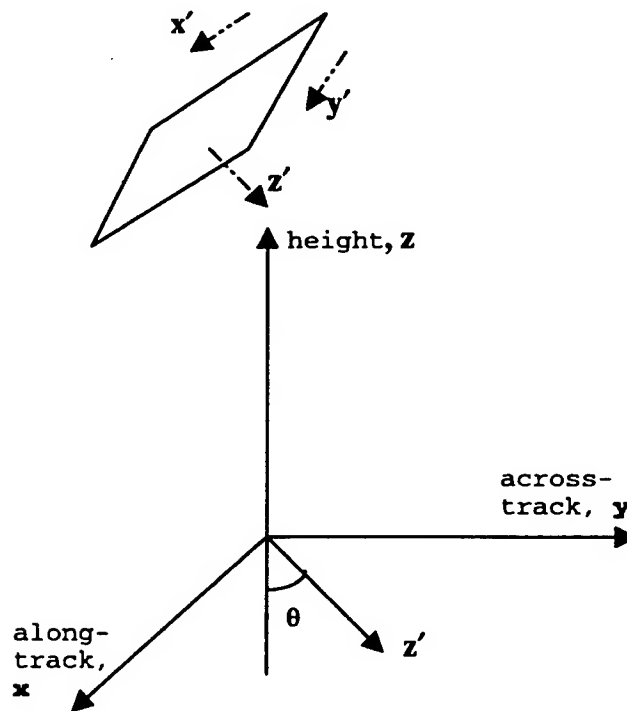


Figure 2.3: Radar Antenna Coordinate Geometry

Specifically, the relationships between the radar antenna coordinate axes and the object coordinate axes may be stated as follows:

$$\bar{x}' = \bar{x}, \quad (2.2)$$

$$\bar{y}' = (-\cos \theta)\bar{y} - (\sin \theta)\bar{z}, \quad (2.3)$$

and $\bar{z}' = (\sin \theta)\bar{y} - (\cos \theta)\bar{z}. \quad (2.4)$

The multiple receive aperture concept was illustrated in Figure 2.2 for a three receive aperture system. In this project, the simulation will ultimately move towards a nine receive aperture model. In that case, a possible design could be that shown in Figure 2.4.

We notice here that the nine receive apertures are laid out in a three by three orientation. We should also recognize that it would be also possible to orientate the apertures in a nine by one or a one by nine orientation as well. The decision on the orientation of the apertures will depend on the selection of the pulse repetition frequency. A choice of a high pulse repetition frequency would require us to orientate the apertures in a one by nine orientation (in the across-track direction) so as to eliminate ambiguity in the direction of range. Similarly, a low pulse repetition frequency selection will require that the apertures be lined up in a nine by one orientation (in the along-track direction) to eliminate ambiguity in the doppler direction.

It is important to note here that all elements in the array are of the same size, i.e. they each have a length L_x and a width L_y . The single transmitter is also located at the center of the array. The position vector \mathbf{r}'_r represents the distance and

direction from the center of the single transmit element to the center of any of the multiple receive elements. Whereas the conventional approach has been to design a single transmitter-receiver unit, we now instead propose implementing an antenna array that maintains a single transmitter but, in addition, possesses multiple receive elements oriented in a chosen manner.

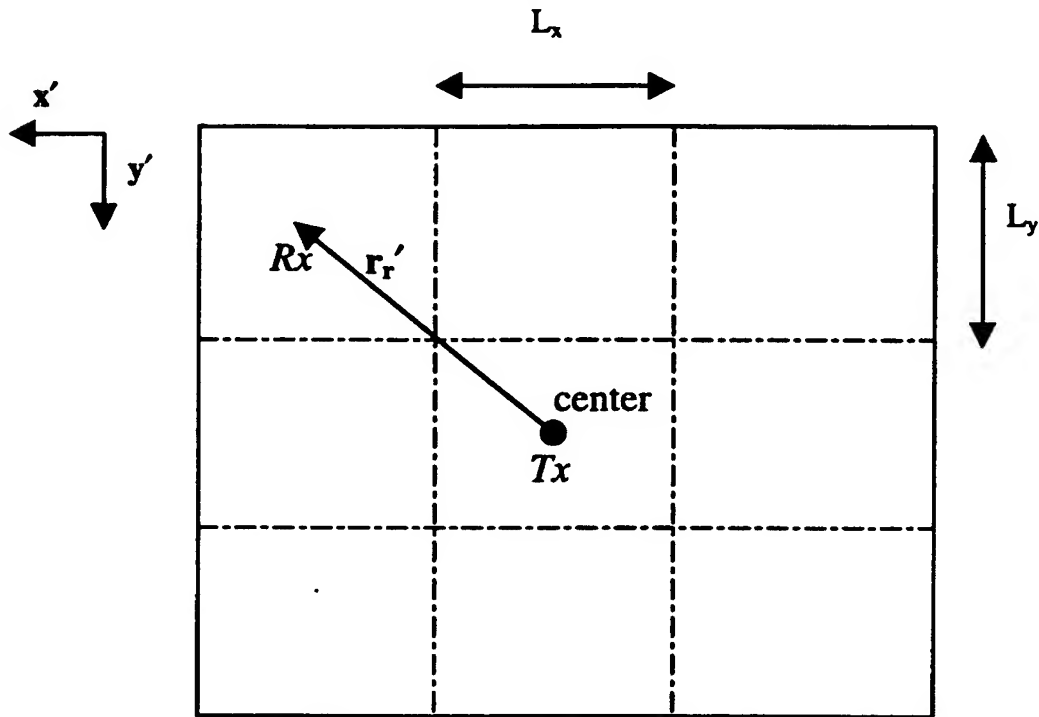


Figure 2.4: Nine Receive Element SAR Antenna Design

Once again, we note that the x' axis corresponds to the along-track direction and the projection of the y' axis corresponds to the across-track direction. This entire antenna is tilted to face the ground in such a manner that its normal will make an angle of θ with the height axis of the conventional axes.

3 SOLUTION METHODOLOGY

3.1 Parameter Design

Given that the SAR has an operating wavelength λ , its along-track pixel resolution can be determined from [8] to be

$$\Delta x = \frac{\lambda R}{2vT}. \quad (3.1)$$

Since the slant range R is defined as

$$R = \frac{h}{\cos \theta}, \quad (3.2)$$

equation (3.1) may now be written as

$$\Delta x = \frac{\lambda h}{2vT \cos \theta}. \quad (3.3)$$

Given that c is the speed of light, the across-track pixel resolution of the SAR may also be found from [8] to be

$$\Delta y = \frac{c}{2B \sin \theta}. \quad (3.4)$$

We set a standard requiring square pixels. Therefore

$$\Delta x = \Delta y. \quad (3.5)$$

Subsequently, by equating and rearranging terms in equations (3.3) and (3.4), we can thus arrive at

$$\frac{B}{T} = \frac{cv \cot \theta}{h\lambda}. \quad (3.6)$$

Making the mathematical assumption that

$$\cot \theta \approx 1, \quad (3.7)$$

and using the relationship between λ and the radar frequency, f , we can simplify the time-bandwidth ratio in equation (3.6) to be

$$\frac{B}{T} = \frac{vf}{h}. \quad (3.8)$$

Based on typical radar design parameters obtained from [9], we set the radar height, speed, operating frequency and antenna tilt angle to be:

$$\text{Radar Height: } h = 183\text{km} , \quad (3.9)$$

$$\text{Radar Speed: } v = 7.8\text{km/s} , \quad (3.10)$$

$$\text{Radar Frequency: } f = 10\text{GHz} , \quad (3.11)$$

$$\text{and Tilt Angle: } \theta = 45^\circ . \quad (3.12)$$

Using the above values, we can next numerically determine the time-bandwidth ratio in equation (3.8) to be

$$\frac{B}{T} = 4.26 \times 10^8 \text{s}^{-2} . \quad (3.13)$$

We select a square image containing 256 pixels in both length and width. If our aim is to reconstruct this image unambiguously with nine apertures, then

$$9BT \geq 256 \times 256 = 65536 . \quad (3.14)$$

This implies that

$$BT \geq 7281 . \quad (3.15)$$

Since equation (3.15) merely stipulates a lower bound for the time-bandwidth product, we are able to specify a higher value as well. Let us say that

$$BT = 10650 . \quad (3.16)$$

Solving equations (3.13) and (3.16) simultaneously, we can determine that

$$B = 2.13\text{MHz} , \quad (3.17)$$

and also that

$$T = 5\text{ms} . \quad (3.18)$$

With these values obtained we can confirm that

$$\Delta x \approx \Delta y \approx 100\text{m} . \quad (3.19)$$

This is now in accordance with equation (3.5).

To eliminate range ambiguities, we can determine from [8] that the prf is constrained by:

$$f_{\text{prf}} \leq \frac{c}{2l_y \sin \theta} . \quad (3.20)$$

To eliminate doppler ambiguities, however, we also require from [8] that

$$f_{\text{prf}} \geq \frac{2vl_x}{\lambda R} . \quad (3.21)$$

Equations (3.20) and (3.21) clearly illustrate once again the current difficulty faced in reducing ambiguity in both the range and doppler directions.

Rearranging (3.20) and (3.21), we can arrive at

$$l_y \leq \frac{c}{2f_{\text{prf}} \sin \theta} , \quad (3.22)$$

and

$$l_x \leq \frac{f_{\text{prf}} \lambda R}{2v} . \quad (3.23)$$

The maximum area may now be determined by setting the values of l_x and l_y to their individual maximum values. Therefore, the maximum area may be found by taking the product of equations (3.22) and (3.23) at the maximum values of l_x and l_y . Specifically,

$$l_x l_y = \frac{c \lambda R}{4v \sin \theta} . \quad (3.24)$$

Substituting (3.2) into (3.24), we can obtain

$$l_x l_y = \frac{c\lambda h}{4v \sin \theta \cos \theta} . \quad (3.25)$$

Replacing (3.25) with its numerical values,

$$l_x l_y = 105.6 \times 10^6 \text{m}^2 . \quad (3.26)$$

Since the image is square,

$$l_x \approx l_y \approx 10.27 \text{km} . \quad (3.27)$$

In our proposed solution design, we now specify the presence of nine receive apertures instead of just one. Therefore, we now expect our maximum area to be nine times larger. Given that the pixel resolution in both the range and doppler directions is approximately 100m, we may now set the pixel length in both range and doppler directions to be, say, 105m. Therefore, the new image length and width is now

$$l_x \approx l_y \approx 26.88 \text{km} . \quad (3.28)$$

Finally, we are now able to return to equation (3.20) and calculate that in order to eliminate range ambiguities,

$$f_{\text{prf}} \leq 7891 \text{Hz} . \quad (3.29)$$

Once again, as equation (3.29) is merely an upper bound, we can specify that in order to eliminate range ambiguities,

$$f_{\text{prf}} = 7 \text{KHz} . \quad (3.30)$$

Similarly, we are now also able to return to equation (3.21) and calculate that in order to eliminate doppler ambiguities,

$$f_{\text{prf}} \geq 54009 \text{Hz} . \quad (3.31)$$

As equation (3.31) also stipulates a lower bound, we can next say that in order to eliminate doppler ambiguities,

$$f_{\text{prf}} = 60 \text{KHz} . \quad (3.32)$$

The along-track aperture length may now be theoretically calculated as

$$L_x = \frac{\lambda h}{l_x \cos \theta} \approx 29\text{cm} . \quad (3.33)$$

Similarly, the across-track aperture width may now be theoretically found to be

$$L_y = \frac{\lambda h}{l_y \cos^2 \theta} \approx 41\text{cm} . \quad (3.34)$$

However, an alternate design method could also be to find the values of L_x and L_y such that the nearest point of ambiguity in both the range and doppler directions lies within the location of the first null of the radar antenna pattern. Using this method, we find that

$$L_x = 25.5\text{cm} , \quad (3.35)$$

and also that

$$L_y = 37.1\text{cm} . \quad (3.36)$$

This concludes the parameter design phase of the simulation. At this point, we have all necessary design parameters to simulate several different situations.

We notice that, as expected, there are conflicting requirements for the choice of a single radar pulse repetition frequency. We are required to select a value of 60KHz for the pulse repetition frequency if we wish to eliminate ambiguities in the doppler direction. But, we are also required to select a value of 7KHz for the pulse repetition frequency if we wish to eliminate ambiguities in range. This conflicting dependency on the pulse repetition frequency is the problem that we anticipate the multiple receive aperture SAR model to be able to resolve.

3.2 A Numerical Example

With the values obtained, it is now appropriate to develop a numerical example to physically illustrate the present problem and the proposed solution.

It should be noted here that the design methodology in the previous section centers on a radar with unfocused apertures, whereas in reality the SAR is often operated with fully focused apertures. This was done only to reduce computation time in the simulation. The problem of obtaining wide swath, unambiguous, high resolution radar images remains the same, regardless of the type of aperture used. To prove its validity, the following numerical example will use the derived values to illustrate the defined problem in the case of a focused SAR.

In the case of a focused SAR, the along-track pixel resolution is defined as

$$\Delta x = \frac{l}{2}, \quad (3.37)$$

where l is the length of the antenna.

Using the value for l found in (3.35) we can say that

$$\Delta x = 0.1275\text{m}. \quad (3.38)$$

Based next on the assumption of square cell resolution,

$$\Delta y = \Delta x = 0.1275\text{m}. \quad (3.39)$$

Returning to equation (3.4), we can find the bandwidth to be

$$B = 1.67 \times 10^9 \text{Hz}. \quad (3.40)$$

Similarly, we may next return to equation (3.1) and determine the new observation time to be

$$T = 3.9\text{s}. \quad (3.41)$$

We can see now that a fully focused SAR operating in our defined environment would actually have a bandwidth of 1.67GHz and a (longer) observation time of 3.9s. This will only result in a larger time-bandwidth product than that calculated earlier. The qualitative treatment of the problem from this point on remains the same whether one is dealing with an unfocused aperture or a focused one.

Assuming the physical aperture length of 25.5cm, equation (3.21) will require that in order to eliminate doppler ambiguities,

$$f_{prf} \geq 61176\text{Hz} . \quad (3.42)$$

However, since the maximum unambiguous swath width is

$$R_s = \frac{c}{2f_{prf} \sin \theta} , \quad (3.43)$$

we can see that this choice of pulse repetition frequency would seriously limit the unambiguous swath width to be

$$R_s \approx 3500\text{m} . \quad (3.44)$$

On the other hand, we note that the approximate image area may be determined to be

$$A = R_s vT = 1.05 \times 10^8 \text{m}^2 . \quad (3.45)$$

Since we also know that

$$\frac{A}{\Delta x \Delta y} \leq BT , \quad (3.46)$$

we can determine the maximum unambiguous swath width to be

$$R_s \approx 3500\text{m} . \quad (3.47)$$

It is clear now that we have arrived at the same value of maximum unambiguous swath width using two different approaches.

We can now see that it is possible to obtain more time-bandwidth samples by simply increasing the number of antenna elements. If we now had N elements, the total number of time bandwidth samples would now have increased by a factor of N to NBT .

Let us now specify a new swath width requirement of three times the value found in equations (3.44) and (3.47). That is, we now want the swath width to be

$$R_s = 10500\text{m} . \quad (3.48)$$

To eliminate range ambiguity at this new swath width, equation (3.20) will require that the new pulse repetition frequency be reduced by a factor of three. Specifically, we now require

$$f_{\text{prf}} \leq 20203\text{Hz} . \quad (3.49)$$

Obviously, this value of pulse repetition frequency does not agree with that defined earlier in equation (3.42), and will cause ambiguity in the doppler direction unless the antenna length is altered. Now, to satisfy equation (3.49), we require that the new antenna length be

$$L_x = 25.5\text{cm} \times 3 = 76.5\text{cm} . \quad (3.50)$$

Finally, returning to equation (3.37), this new aperture length would result in degradation of the along-track pixel resolution. Now,

$$\Delta x = 0.1275\text{m} \times 3 = 0.3825\text{m} . \quad (3.51)$$

It is clear that we have now traded swath width for resolution. This is the current problem we face.

If, however, we instead implemented the receive antenna as three individual apertures each of length 25.5cm, then the number of time-bandwidth samples increases by three times to 3BT instead of just BT. More importantly, we can see from equations (3.37) and (3.43) that we can now achieve the enlarged swath width of 10500m whilst maintaining the (original) superior pixel resolution of 0.1275m because we do not alter the physical length of each aperture. Rather, we have instead employed the use of multiple receive apertures to provide us this increase in overall antenna length.

Because the transmit antenna aperture occupies the same location as the center receive antenna aperture, the illumination patterns in the along-track direction of the single transmit aperture and the three receive apertures are identical. In addition, each is also three times as broad as the original enlarged aperture of length 76.5cm. From this broader beamwidth of each sub aperture, a single target can be observed long enough to achieve a fine along-track resolution. At the same time, this beamwidth is narrow enough to attenuate ambiguities in the along-track direction.

From this, it is evident that the use of multiple receive apertures has now allowed us to potentially obtain wide swath, high resolution, and unambiguous radar images. It is now an appropriate time to move towards a computer simulation environment and put our proposed theoretical solution to a practical test in order to determine how effective this design is.

3.3 Test Matrix

Following the completion of the parameter design, a test matrix was developed to list the situations to be addressed. This test matrix is listed as Table 3.1 and shows the different input parameters necessary to attain a particular test environment.

Situation	f_{prt} (KHz)	L_x (cm)	L_y (cm)	Apertures
1	7	25.5	37.1	1
2	7	25.5 * 9	37.1	1
3	60	25.5	37.1	1
4	60	25.5	37.1 * 9	1
5	20.5	25.5	37.1	1
6	20.5	25.5 * 3	37.1	1
7	20.5	25.5	37.1 * 3	1
8	20.5	25.5 * 3	37.1 * 3	1
9	20.5	25.5 by 3	37.1	3
10	20.5	25.5	37.1 by 3	3
11	7	25.5 by 3	37.1 by 3	9
12	7	25.5 by 9	37.1	9
13	60	25.5 by 3	37.1 by 3	9
14	60	25.5	37.1 by 9	9
15	20.5	25.5 by 3	37.1 by 3	9

Table 3.1: Test Matrix for Simulation

As is evident, the first eight situations in this test matrix will reflect the problems present in a single receive aperture SAR environment. The pulse repetition frequency and aperture size will be varied to test a variety of situations with the intention of proving that, whilst it is possible to obtain an image that has high resolution, wide swath, or low ambiguity, it is not presently possible to have all these traits present in a single image.

In the single receive aperture SAR environment, the physical length and width of the receive aperture is altered to reflect the particular test situation. For example, in Situation 8, the physical aperture length and width is three times as large because

the pulse repetition frequency in that instance is less than each extreme by a factor of three. There will be further analysis of each test situation in the following section.

The final seven situations will represent the transition to a considerably more efficient multiple receive aperture SAR environment. Here, the pulse repetition frequency will be varied together with the number of apertures with the intention of obtaining a single image that possesses wide swath, high resolution and low ambiguity.

In the multiple receive aperture SAR environment, we notice that there is no longer a physical change in the size of each aperture. All receive apertures (as well as the single transmit aperture) are of the same size. In the multiple receive aperture SAR environment, several of these receive apertures are placed in a suitable orientation depending on the test situation. For example, in Situation 12, there are nine receive apertures placed in the along-track direction due to the presence of a pulse repetition frequency that only eliminates ambiguity in the across-track direction. Once again, further analysis of each situation will be provided in the following section.

The pulse repetition frequency (f_{prt}) is varied between three values. A value of 60KHz reflects a situation in which doppler ambiguities will be eliminated. A value of 7KHz reflects the situation where we wish for range ambiguities to be eliminated. A value of 20.5KHz was also chosen as it is less than each of the other two test frequencies by a constant factor of three. This would represent a position of "compromise" between the complete elimination of range and doppler ambiguities in the test environment.

3.4 Test Image

Figure 3.1 shows the test image used for the simulation. This picture has (for decades) been an extremely popular choice of input in image processing research. It was first used by researchers at the University of Southern California in the 1970s and has since become a de facto standard for performance comparisons. The image consists of 65536 pixels oriented in a 256 by 256 manner. The intensity of each pixel ranges from zero (pure black) to 255 (pure white). The along-track direction would be equivalent to viewing this image from east to west (or left to right) and the across-track direction would be equivalent to viewing this image from north to south (or top to bottom).



Figure 3.1: Test Image used as Target Area

4 RESULTS

4.1 Situation 1

In this situation, the pulse repetition frequency is set at 7KHz whilst the single receive aperture has a length of 25.5cm in the along-track direction and a width of 37.1cm in the across-track direction. The receiver response is shown as Figure 4.1. The pulse repetition frequency setting is sufficient to eliminate range ambiguities, but not doppler ambiguities. The aperture size settings result in a wide swath that illuminates the entire input image area. However, the broad illumination beamwidth now detects points of ambiguity in the doppler direction. This is the reason why we observe repetitions of the input image in the along-track direction. The result is an image that possesses wide swath but poor resolution and high ambiguity in the along-track direction.

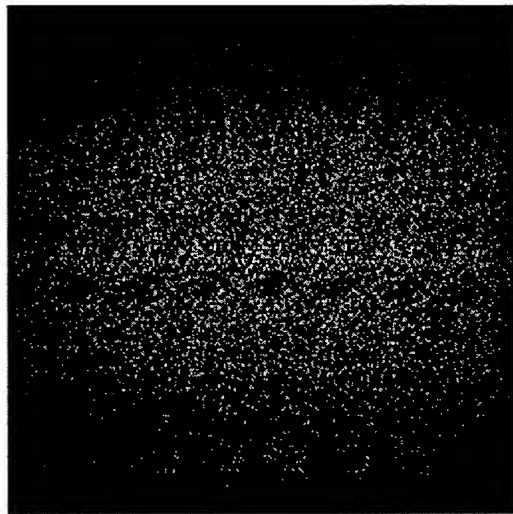


Figure 4.1: Radar Receiver Response for Situation 1

4.2 Situation 2

The poor resolution observed in Figure 4.1 is a result of the wide beamwidth illuminating areas of ambiguity in doppler. A possible solution would be to alter this beamwidth with the intention of improving resolution and lowering ambiguity. Thus in Situation 2, the pulse repetition frequency is maintained at 7KHz. However, to counter the effects of ambiguity in the along-track direction, the along-track aperture length of the single receiver will now be made nine times larger than the original value of 25.5cm. The across track aperture width remains at 37.1cm. This translates into a narrow illumination area in the along-track direction. In the results shown in Figure 4.2, we observe a thin illumination area in the doppler direction that is now able to eliminate the ambiguities present in the along-track direction. The result is an unambiguous image with high resolution but now with a narrow along-track illumination width.

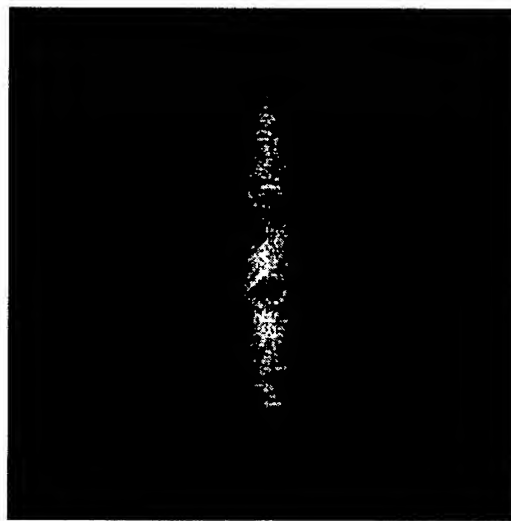


Figure 4.2: Radar Receiver Response for Situation 2

4.3 Situation 3

Figure 4.3 shows the radar receiver response for Situation 3. In this situation, the pulse repetition frequency is now set at a level of 60KHz. This satisfies the requirement for non-ambiguity in the along-track direction, but does not eliminate ambiguity in the across-track direction. The single receiver aperture size is once again set at 25.5cm in the along-track direction and 37.1cm in the across-track direction. This will result in a wide swath width, but our concern here is that this wide swath will now detect ambiguity in the across-track direction. As expected, Figure 4.3 now shows repetitions of the input image area in the across-track direction. The result here is an image with wide swath but poor resolution and high ambiguity in the across-track direction.

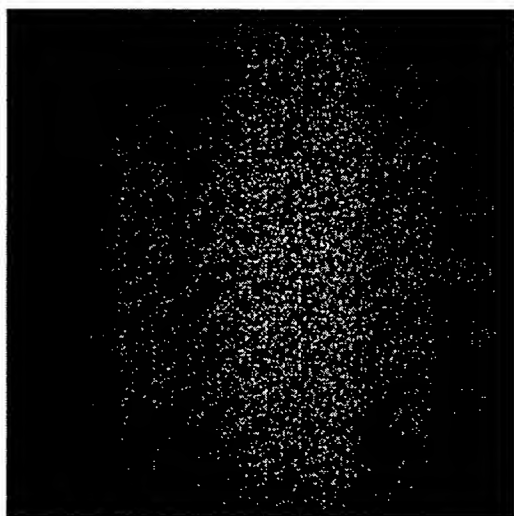


Figure 4.3: Radar Receiver Response for Situation 3

4.4 Situation 4

We observe once again that the poor resolution in Figure 4.3 is a result of the wide swath width detecting points of ambiguity in range. A possible solution to improve resolution would be to narrow the swath width. Therefore, in this situation the single receive aperture has an along-track length of 25.5cm but an across-track width of nine times the original value of 37.1cm. The pulse repetition frequency is maintained at 60KHz. Figure 4.4 shows the results obtained for this situation. We observe that there is now a narrow strip in the across-track direction that is able to eliminate all the ambiguities in the direction of range. However, this has come at the expense of narrow coverage in the across-track direction. The result we obtain here is an unambiguous image that has high resolution but now with a narrow swath width.



Figure 4.4: Radar Receiver Response for Situation 4

4.5 Situation 5

Next, the pulse repetition frequency was set at a value of 20.5KHz. This is a factor of three away from either 7KHz or 60KHz. The single receive aperture is also set at its original value of 25.5cm in the along-track direction and 37.1cm in the across-track direction. With this aperture size, we expect the entire image area to be illuminated. Figure 4.5 shows the results obtained in this situation. With the pulse repetition frequency set at a factor of three away from either extreme, we would thus expect three times less ambiguity in both range and doppler directions. In Figure 4.5, we are able to notice more of the original image than we did in Figures 4.1 and 4.3. We are also able to observe the distinct ambiguous positions in either direction. Thus this situation returns an image with poor resolution and moderate ambiguity.

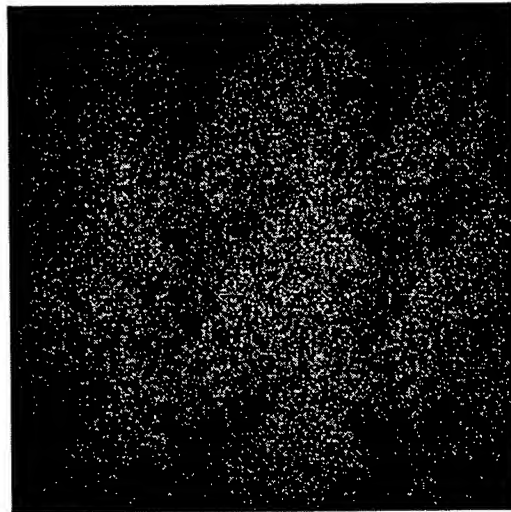


Figure 4.5: Radar Receiver Response for Situation 5

4.6 Situation 6

In the next test situation, the pulse repetition frequency was maintained at the intermediate value of 20.5KHz. This would again lead us to expect our resultant image to have less ambiguity in both directions. However, in this instance, we alter the value of the along-track aperture length to now read as three times its original value of 25.5cm. The across-track aperture length remains at 37.1cm. From this, we would expect a slightly wider illumination beamwidth than we did in Figure 4.2. Figure 4.6 shows the results obtained. We see that by increasing the along-track aperture length, we have eliminated a considerable amount of ambiguity. However, ambiguity remains in the across-track direction due to the fact that a pulse repetition frequency of 20.5KHz is still too low.

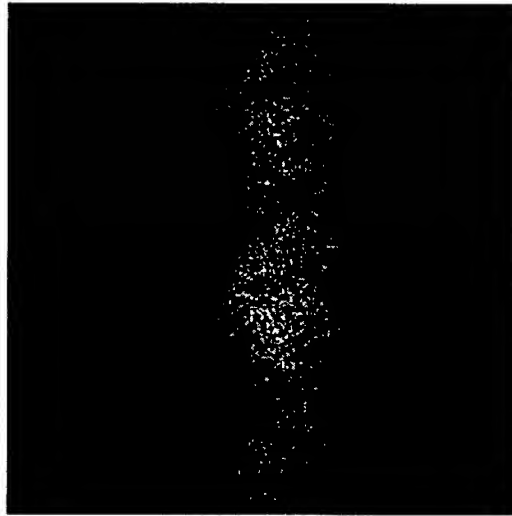


Figure 4.6: Radar Receiver Response for Situation 6

4.7 Situation 7

In Situation 7, it is the across-track aperture width that is now altered to read as three times its original value of 37.1cm. The along-track aperture length returns to its original value of 25.5cm. Therefore, we expect a swath width that is slightly wider than that of Figure 4.4. We maintain the pulse repetition frequency at the intermediate value of 20.5KHz. Once again, this leads us to expect a factor of three reduction in ambiguity. Figure 4.7 shows the results obtained for this situation. As expected, we have eliminated all the ambiguity in the across-track direction by enlarging the across-track aperture width. However, a pulse repetition frequency of 20.5KHz is not sufficiently high enough to eliminate all the along-track ambiguity within the illumination area. We are left with an ambiguous image that has limited swath coverage.

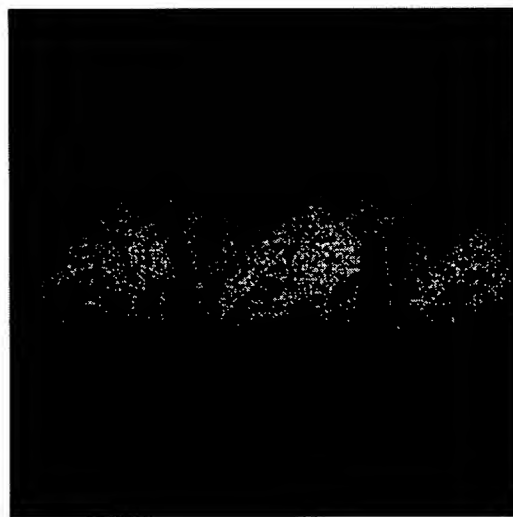


Figure 4.7: Radar Receiver Response for Situation 7

4.8 Situation 8

In the final single receive aperture test situation, we aim for some sort of compromise between ambiguity, resolution and swath width. Here, we maintain the pulse repetition frequency at the intermediate level of 20.5KHz. We alter the along-track aperture length to be three times its original value of 25.5cm and the across-track aperture width to be three times its original value of 37.1cm. The intermediate pulse repetition frequency will reduce the ambiguity by a factor of three in each direction. In addition, the larger aperture lengths in both directions will also be able to reduce ambiguity by a further factor of three in both directions. Thus, in this instance we would expect an unambiguous image. Figure 4.8 shows the results obtained in this situation. We observe that our unambiguous image prediction was true. However, this has now come at the expense of a narrow swath width (in range) and a narrow illumination beamwidth (in doppler).



Figure 4.8: Radar Receiver Response for Situation 8

4.9 Situation 9

This situation marks the transition to a multiple receive aperture SAR environment. From this situation onward, all receive apertures have a fixed length of 25.5cm in the along-track direction and 37.1cm in the across-track direction. Here, we design three receive apertures lined up in the along-track direction. The pulse repetition frequency is maintained at the intermediate value of 20.5KHz. The result for this situation is shown as Figure 4.9. We see a marked improvement now in the performance as compared to Figure 4.6. The additional apertures in the along-track direction have allowed for a wider illumination beamwidth in Figure 4.9 without any further increase in ambiguity from Figure 4.6. This was previously unachievable in the single receive aperture environment. However, whilst this is an improvement over the single aperture environment, the existing across-track ambiguity is clearly undesirable.



Figure 4.9: Radar Receiver Response for Situation 9

4.10 Situation 10

In this situation, the pulse repetition frequency is maintained at 20.5KHz. The three receive aperture design is also maintained, but these apertures are now laid out in the across-track direction. The result for this situation is shown as Figure 4.10. Here, we also notice a marked improvement in performance as compared to Figure 4.7. Whilst the ambiguity in the along-track direction remains the same, the three receive apertures in the across-track direction have allowed for a wider swath width to be present in the image. This, once again, was an unachievable goal in the single receive aperture environment. However, the remaining ambiguity is undesirable and clearly indicates that three apertures is an insufficient number to return an unambiguous image.



Figure 4.10: Radar Receiver Response for Situation 10

4.11 Situation 11

This situation marks the beginning of the nine receive aperture design phase. Here, we start once again by returning to a pulse repetition frequency of 7KHz that will eliminate range ambiguities but not ambiguities in the doppler direction. We also design the multiple receive aperture unit such that there are three apertures in the across-track direction and three in the along-track direction. With three apertures present, we expect the ambiguity in the along-track direction to be reduced by a factor of three. Figure 4.11 shows the results achieved for this situation. This result is a significant improvement over Figure 4.1. However, because the apertures are not oriented in the right manner, there remains ambiguity in the along-track direction. With a low pulse repetition frequency, all ambiguity in the across-track direction is eliminated and it is pointless to place additional apertures in the direction of range.

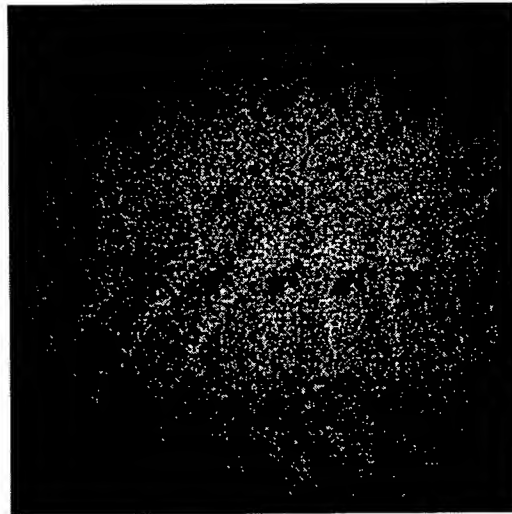


Figure 4.11: Radar Receiver Response for Situation 11

4.12 Situation 12

In this situation, we work to improve the result achieved in Figure 4.11. From the results achieved in Situation 11, it is clear that with a pulse repetition frequency of 7KHz, there is no longer a need for additional apertures in the across-track direction. A more appropriate design would be to maintain the nine aperture design but orientate the apertures in such a manner that there are nine apertures in the along-track direction. With a low pulse repetition frequency, the along-track direction is where ambiguity exists and, thus, needs to be removed. Figure 4.12 shows the results obtained in this situation. Finally, we have arrived at a satisfying result. We observe now a resultant unambiguous image that possesses high resolution and wide swath. A multiple receive aperture SAR environment coupled with proper orientation of apertures has allowed us to achieve this satisfying result.



Figure 4.12: Radar Receiver Response for Situation 12

4.13 Situation 13

We now refocus our attention on a pulse repetition frequency of 60KHz. This value will eliminate ambiguity in the along-track direction but not in the across-track direction. We return to our nine aperture receiver design with three apertures aligned in the across-track direction and three aligned in the along-track direction. From our results obtained in Situation 11, we can predict that this may not be the best receiver orientation to give us optimum performance. Figure 4.13 shows the result obtained for this situation. Although the multiple receivers have provided us with a wide swath, there still exists ambiguity in the across-track direction due to incorrect receiver orientation. It seems pointless here to add receivers in the along-track direction when our choice of pulse repetition frequency will already ensure that no ambiguity is present in the doppler direction. The three receive apertures in the across-track direction are only sufficient to reduce ambiguity by a factor of three.

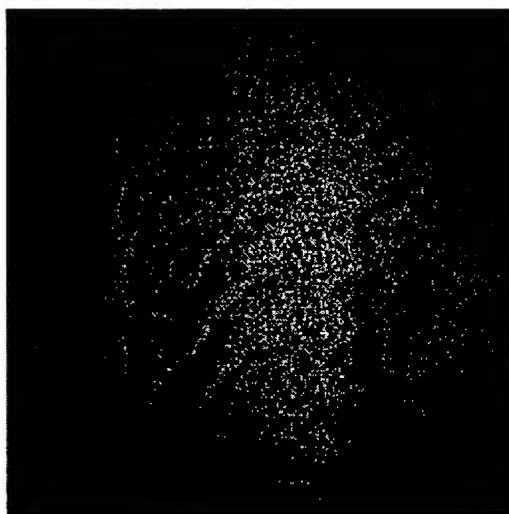


Figure 4.13: Radar Receiver Response for Situation 13

4.14 Situation 14

We now attempt to improve upon our results achieved in Figure 4.13. It is clear that our receiver design in Situation 13 was incorrect. A choice of 60KHz as the pulse repetition frequency effectively eliminates doppler ambiguities. There is no longer a need to place additional receivers in the along-track direction. Rather, it would seem that the nine receivers should all be placed in the across-track direction. This would provide the desired ambiguity reduction factor of nine in the across-track direction. Figure 4.14 shows the another extremely satisfying result obtained. We have once again managed to obtain an unambiguous image that possesses high resolution and wide swath width. The result obtained in Figure 4.14 is identical to that obtained in Figure 4.12. This point of note will be extremely useful once the results for the following section are finally obtained.



Figure 4.14: Radar Receiver Response for Situation 14

4.15 Situation 15

Finally, we return to a pulse repetition frequency of 20.5KHz. With experience from previous situations, we know that this choice of pulse repetition frequency reduces ambiguity in both along-track and across-track directions by a factor of three. We are now able to predict that our multiple receive aperture design must reduce the ambiguity by a further factor of three before we are able to obtain an unambiguous image. Thus, there must be three apertures in the across-track direction and three apertures in the along-track direction of the receiver. The results for this situation are shown as Figure 4.15. We have an unambiguous image that has high resolution and wide swath. Also, whilst they were all generated based on different pulse repetition frequencies, Figures 4.12, 4.14, and 4.15 are identical. The multiple receive aperture SAR environment has managed to relinquish the dependence of its receiver response on the pulse repetition frequency.



Figure 4.15: Radar Receiver Response for Situation 15

5 CONCLUSION

This project has documented in detail the performance benefits of a multiple receiver SAR in contrast to a single receiver one. In particular, it has been shown that the single receiver SAR environment constantly faces a tradeoff involving ambiguity, resolution, and swath width. A high pulse repetition frequency is necessary in order to eliminate ambiguity in the along-track direction. However, we also require a low pulse repetition frequency to eliminate ambiguity in the across-track direction. Compensation to this ambiguity may be made in either direction by reducing the illumination area. However, this later results in a narrow swath width. As a result, it is impossible (in the single receiver SAR environment) to completely eliminate ambiguity in both the along-track and across-track directions whilst maintaining wide swath width and high resolution.

The multiple receiver SAR environment has alleviated this problem because the restriction imposed by the time-bandwidth product is now lifted. We are now able to obtain a sufficient number of independent samples in order to generate an unambiguous result. This model has now relieved the dependence of the receiver response on the pulse repetition frequency. An unambiguous, wide swath, high resolution image may be now generated independent of the choice of pulse repetition frequency.

A SAR simulator was built to generate test images that reflect performance in a single and multiple receiver test environment. It was proven that when multiple receivers are employed in a SAR, it is possible to generate a high resolution, wide swath, and unambiguous SAR image.

6 RECOMMENDATIONS AND FUTURE WORK

Moving target indication (MTI) is another area of SAR data processing where there is currently a considerable amount of ongoing research. In conventional SAR imaging, it is the ground - and any stationary object on it - that is the target. However, the doppler shift that a moving target generates now competes with the SAR's doppler shift generation. It is this reason that makes moving targets difficult to resolve in SAR imaging. Whilst there have been new methods such as reflectivity displacement [10] and radial velocity band filtering [11] that have been offered as possible partial solutions to this problem, there undoubtedly remains much work to be done in the area of SAR moving target indication.

In the course of software development for the multiple receive element SAR simulator, it was ensured that functionality for future testing of this model on moving targets was also included. In essence, a velocity vector that defines each point in the imaged area has been included as part of the model. As this project focused on obtaining wide swath, high resolution, unambiguous images, this vector was simply defined as null for present purposes. Furthermore, this velocity vector has been designed with three dimensional coordinates. This implies that the model is suitable for research into both ground moving target indication (GMTI) and airborne moving target indication (AMTI). With straightforward modifications and the simple introduction of a ground or airborne velocity, the multiple receive element SAR simulator constructed may easily now be used in a variety of situations for future research on SAR-MTI.

REFERENCES

- [1] N. Levanon, *Radar Principles*, John Wiley & Sons Inc., 1988.
- [2] A. Currie, & M.A. Brown, "Wide-Swath SAR", *IEE Proceedings - F*, Vol. 139, No. 2, April 1992, pp. 122-135.
- [3] A. Currie, & C.D. Hall, "A Synthetic Aperture Radar Technique for the Simultaneous Provision of High-Resolution Wide-Swath Coverage", *Proceedings Military Microwaves '90*, Microwaves Exhibitions and Publishers Ltd., July 1990, pp. 539-544.
- [4] H.D. Griffiths, & P. Mancini, "Ambiguity Suppression in SARs using Adaptive Array Techniques", *Proceedings of IGARSS 1991 Symposium*, 1991, pp. 1015-1018.
- [5] S. Barbarossa, & A. Farina, "Space-Time-Frequency Processing of Synthetic Aperture Radar Signals", *IEEE Transactions on Aerospace and Electronic Systems*, Vol. 30, No. 2, April 1994, pp. 341-358.
- [6] H. Steyskal, "Digital Beamforming Antennas: An Introduction", *Microwave Journal*, January 1987, pp. 107-124.
- [7] H. Steyskal, & J.F. Rose, "Digital Beamforming for Radar Systems", *Microwave Journal*, January 1989, pp. 121-136.
- [8] F.T. Ulaby, A.K. Fung, & R.K. Moore, *Microwave Remote Sensing, Active and Passive*, Vol. 2: *Radar Remote Sensing and Surface Scattering and Emission Theory*, Artech House Inc., 1982.
- [9] M.I. Skolnik, *Radar Handbook*, McGraw Hill Inc., 1990.
- [10] J.R. Moreira, & W. Keydel, "A New MTI-SAR Approach using the Reflectivity Displacement Method", *IEEE Transactions on Geoscience and Remote Sensing*, Vol. 33, No. 5, September 1995, pp. 1238-1244.
- [11] A. Freeman, & A. Currie, "Synthetic Aperture Radar (SAR) Images of Moving Targets", *The GEC Journal of Research*, Vol. 5, No. 2, 1987, pp.106-115.

Charles Swenson
Report not available at time of publication.

**DEVELOPMENT OF ALGORITHMS FOR LINEAR AND NONLINEAR
RETRIEVAL PROBLEMS IN ATMOSPHERIC REMOTE SENSING**

**Miguel Vélez-Reyes
Associate Professor
Electrical and Computer Engineering Department**

**University of Puerto Rico
Mayagüez Campus
P.O. Box 9042
Mayagüez, PR 00681-9042**

**Final Report for:
Summer Research Extension Program
Phillips Laboratory**

**Sponsored by:
Air Force Office of Scientific Research
Boiling Air Force Base, DC**

and

**Phillips Laboratory
Hanscom Air Force Base**

June 1998

DEVELOPMENT OF ALGORITHMS FOR LINEAR AND NONLINEAR RETRIEVAL PROBLEMS IN ATMOSPHERIC REMOTE SENSING

Miguel Velez-Reyes
Associate Professor
Electrical and Computer Engineering Department
University of Puerto Rico Mayagüez Campus

Abstract

Infrared and microwave passive remote sensing of the atmosphere is used to determine the earth atmospheric state and surface properties. Radiance measured by the radiometers can be used to estimate atmospheric parameters such as temperature and water vapor content. These quantities are of primary importance for applications in meteorology, oceanography, and geophysical sciences. The retrieval or estimation of vertical profiles of temperature and trace-gas concentrations is called atmospheric sounding. Depending on the frequency range in the electromagnetic spectrum being measured by the radiometer and the atmospheric quantities to be estimated, the retrieval or inverse problem of determining atmospheric parameters from radiance measurements might be linear or nonlinear. In many applications, the retrieval problem requires the inversion of a Fredholm integral equation of the first kind, making this an ill-posed problem. The numerical solution of the retrieval problem requires the transformation of the continuous problem into a discrete problem. The ill-posedness of the continuous problem translates into ill-conditioning or ill-posedness of the discrete problem. Another difficulty associated with the retrieval problems is that they are underconstrained because only a few radiance intensities are being measured by the sensor while the quantities of interest are estimated at a higher vertical resolution (more unknowns). To further constraint the problem and deal with the ill-posedness, prior information is incorporated into the problem to convert the ill-posed problem into a well-posed one.

In this project, we developed an algorithm for nonlinear retrieval problems in atmospheric remote sensing based on the Gauss-Newton method to solve nonlinear least square problems. Regularization was applied to the underdetermined linear least-squares problem of computing the search direction using Tikhonov and TSVD regularization methods for linear inverse problems. The method was applied to the nonlinear problem of atmospheric temperature retrieval from HIRS/2 and MSU radiometry. A set of MATLAB macros implementing the algorithms was developed. Simulation studies were performed to understand the performance of the proposed method. Three key factors affect the performance of the retrieved profile: (1) the initial guess, (2) the updating criterion for the regularization parameter, and (3) the stopping criterion. The implementations of the retrieval algorithm produced similar results for both Tikhonov and TSVD regularization. The root mean square (RMS) error for the estimated temperature profiles varied from 0.9964 °K to 4.0728 °K for the noiseless case.

DEVELOPMENT OF ALGORITHMS FOR LINEAR AND NONLINEAR RETRIEVAL PROBLEMS IN ATMOSPHERIC REMOTE SENSING

Miguel Velez-Reyes

1. Introduction

Infrared and microwave passive remote sensing of the atmosphere is used to determine the earth atmospheric state and surface properties. Radiance measured by the radiometers can be used to estimate atmospheric parameters such as temperature and water vapor content. These quantities are of primary importance for applications in meteorology, oceanography, and geophysical sciences. The retrieval or estimation of vertical profiles of temperature and trace-gas concentrations is called atmospheric sounding.

Early satellite vertical sounding programs were justified on the basis of their potential for improving large-scale numerical weather forecasts for periods greater than one day over continents, as a result of improved observation over oceans. More recently, it has been recognized that satellite soundings can also play a key role in supplying the observations needed for small-scale intense weather prediction. Vertical soundings achieved from satellites have a positive impact on numerical weather prediction (NWP) analyses/forecast in the Southern Hemisphere. It was also demonstrated that they had, on average, a positive impact when used in data-sparse areas of the Northern Hemisphere (Eyre et al., 1993).

Depending on the frequency range in the electromagnetic spectrum being measured by the radiometer and the atmospheric quantities to be estimated, the retrieval or inverse problem of determining atmospheric parameters from radiance measurements might be linear or nonlinear. In many applications, the retrieval problem requires the inversion of a Fredholm integral equation of the first kind, making this an ill-posed problem (Hansen, 1998). The numerical solution of the retrieval problem requires the transformation of the continuous problem into a discrete problem. The ill-posedness of the continuous problem translates into ill-conditioning or ill-posedness of the discrete problem. Another difficulty associated with the retrieval problems is that they are underconstrained because only a few radiance intensities are being measured by the sensor while the quantities of interest are estimated at a higher vertical resolution (more unknowns). To further constraint the problem and deal with the ill-posedness, prior information is incorporated into the problem to convert the ill-posed problem into a well-posed one (Hansen, 1998).

This report presents the work supported by AFOSR 1996 Summer Research Extension Program Subcontract 97-0868. This research project develops and validates algorithms for nonlinear retrievals. Simulation results are presented for atmospheric temperature retrievals based on radiometry from the High Resolution Infrared Radiation Sounder/2 (HIRS/2) and the Microwave Sounding Unit (MSU) in the TIROS Operational Vertical Sounder (TOVS). Algorithms are based on the Gauss-Newton (GN) method for nonlinear least squares, and the Tikhonov and Truncated Singular Value Decomposition (TSVD) regularization methods for linear inverse problems described by Hansen (1996) and Eriksson (1996). In our work, we used the Goddard Laboratory for Atmospheres (GLA) TOVS radiative transfer code provided by the Goddard Data Assimilation Office (Sienkiewicz, 1996). A set

of MATLABTM functions has been developed for the retrieval algorithms. The algorithms are validated by means of simulations.

2. Radiative Transfer Theory for Forward Radiance

Radiative transfer theory describes the intensity of radiation propagating in a general class of media that absorbs, emits, transmits, and scatters the radiation (Lenoble, 1993). The general form of the radiative transfer equation (RTE) for a plane-parallel atmosphere is given by

$$\frac{dR_v(\theta)}{d\theta} = -\sigma(p)R_v(\theta) + S_v(\theta), \quad (1)$$

where $R_v(\theta)$ is the radiance that flows at each point in the medium per unit area, per unit of solid angle, at a given frequency ν and zenith angle θ ; $\sigma(p)$ is the extinction coefficient at pressure level p ; and $S_v(\theta)$ is a source term at zenith angle θ . These last two quantities describe the loss/gain of radiant intensity into the given direction.

In the general case, scattering into and from other directions can lead to both gains and losses to the intensity and are taken care by the terms $\sigma(p)$ and $S_v(\theta)$. For the infrared and microwave regions of the spectrum, the scattering term is usually neglected (Janssen, 1993). If scattering is neglected, the only source term to consider is that due to local emission and the extinction coefficient reduces to the absorption coefficient $\sigma_a(p)$. The emission follows Kirchoff's law at the local temperature, and the source term reduces to

$$S_v(\theta) = \sigma_a(p)B_v(T(p))$$

where $B_v(T)$ is the Planck function:

$$B_v(T) = \frac{2h\nu^3}{c^2} \frac{1}{e^{h\nu/kT} - 1}, \quad (2)$$

and $h = 6.625 \times 10^{-34}$ Js is Planck's constant, $c = 2.988 \times 10^8$ m/s is the speed of light, and $k = 1.381 \times 10^{-23}$ J/K. Equation (1) then becomes

$$\frac{dR_v(\theta)}{d\theta} = -\sigma_a(p)[R_v - B_v(T(p))]$$

This is a linear non-homogeneous first-order differential equation with solution

$$R_v(\theta) = R_v(p_s, \theta)\tau_v(p_s, \theta) + \int_{p_s}^0 B_v[T(p)] \frac{\partial \tau_v(p, \theta)}{\partial p} dp + R'_v(\theta), \quad (3)$$

where p_s is the surface pressure, and $R_v(p_s, \theta)$ is the surface boundary condition. The term $\tau_v(p, \theta)$ is the transmittance from pressure p to the top of the atmosphere at zenith angle θ , defined as

$$\tau_v(p, \theta) = \exp \left[- \int_0^p \sigma_a(P) \sec(\theta) dP \right]$$

$R'_v(\theta)$ is the contribution from radiance reflected from the surface. Equation (3) is the basic radiative transfer equation for radiation emitted at the top of the atmosphere at a single frequency ν .

Given a radiance observation R_v , it is convenient to think in terms of the quantity T_b , the brightness temperature of the observation. This is the temperature a blackbody would have if it gave off the same radiance at frequency ν . There is a unique relationship between R_v and T_b given by

$$T_b = B^{-1}[R_v] = \frac{h\nu / k}{\ln \left[\left((2h\nu^3 / c^2) / R_v \right) + 1 \right]}, \quad (4)$$

where R_v is given by (3) (Susskind et al., 1984). In the microwave region of the spectrum,

$$h\nu \ll kT$$

which results in (2) taking the form

$$B_v(T) = \frac{2\nu^2 kT}{c^2} = \frac{2kT}{\lambda^2}$$

where λ is wavelength. This is known as the Raleigh-Jeans approximation (Lenoble, 1993). From this expression it is clear that in the microwave region, the energy emitted is proportional to the physical temperature T . In terms of brightness temperature T_{bv} , (3) takes the form

$$T_{bv} = T_{bv}(p_s, \theta) \tau_v(p_s, \theta) + \int_{p_s}^0 B[T(p)] \frac{\partial \tau_v(p, \theta)}{\partial p} dp + T'_{bv}(\theta)$$

In the context of our experiment with HIRS/2 and MSU instruments, each channel represents an observation taken over a range of frequencies,

$$R_i(\theta) = \int_{\nu} \phi_i(\nu) R_\nu(\theta) d\nu$$

where $\phi_i(\nu)$ is the filter response function for satellite channel i (Sienkiewicz, 1996). Equation (3) can be rewritten as

$$R_i(\theta) = R_i(p_s, \theta) \tau_i(p_s, \theta) + \int_{p_s}^0 B_i[T(p)] \frac{\partial \tau_i(p, \theta)}{\partial p} dp + R'_i(\theta)$$

where now $B_i(T) = B_{\nu_i}(T)$, $\epsilon_i(\theta) = \epsilon_{\nu_i}(\theta)$ are evaluated at a prescribed central channel frequency ν_i and the transmittance τ_i is a modeled transmittance fitted to channel-averaged transmittances obtained from line-by-line calculations. Although the Planck function $B_{\nu_i}(T)$ changes with frequency ν it is assumed that the width of the channel response function ϕ is small enough that the Planck function at the central frequency ν_i can be used without modification (Sienkiewicz, 1996).

2.1 Radiative Transfer Theory for Reflected Radiance

Let us take a look now at $R'_i(\theta)$, the contribution from the reflected radiance. Susskind, et al. (1984) define it as

$$R'_i(\theta) = (1 - \varepsilon_i) R_i \downarrow \tau_i(p_s, \theta) + \rho_i H_i \tau_{iS}(\theta, \theta_S) \quad (5)$$

where $R_i \downarrow$ is the effective downward flux of radiation from atmospheric emission for channel i , ρ_i is the bi-directional reflectance of the surface to the satellite of solar radiation from the sun with zenith angle θ_S , H_i is the solar radiation at the top of the atmosphere, and $\tau_{iS}(\theta, \theta_S)$ is the atmospheric transmittance along the entire path of incident and reflected solar radiation. It is important to notice that the first term in the right-hand side of (5) represents the contribution of downwelling atmospheric radiation, and the second term represents the contribution of reflected solar radiation. Hence, these quantities account for the upper boundary conditions.

For the first term $R_i \downarrow$, there are several ways to calculate it, depending on the channel it is computed for. According to (Susskind et al., 1984), for HIRS IR channels 8, 10, 18, and 19 where the atmosphere is optically thin, the effective downward flux $R_i \downarrow$ is calculated as:

$$R_i \downarrow = 2 \cos(\theta) \int_0^{\tau_i(p_s)} B_i(T) d\tau \quad (6)$$

For the other HIRS channels, the effective downward flux $R_i \downarrow$ is modeled according to (Kornfield and Susskind, 1977):

$$R_i \downarrow = F_i B_i(T_s) (1 - \tau_i(p_s, \theta)) \quad (7)$$

where T_s is the surface air temperature and F_i is a channel-dependent constant.

Finally, for the MSU microwave channels, the downward flux $R_i \downarrow$ is calculated as:

$$R_i \downarrow = T_{BB} \tau_i(p_s, \theta) + \tau_i(p_s, \theta) \int_{p_s}^0 T(p) \frac{\partial}{\partial p} \left[\frac{1}{\tau_i(p, \theta)} \right] dp \quad (8)$$

where T_{BB} is the background radiation equal to 2.5° K.

2.2 Representation in Finite-Difference Form

To numerically solve the equation of radiative transfer, we used the Goddard Laboratory for Atmospheres (GLA) TOVS rapid algorithm for forward radiance and Jacobian calculation (Sienkiewicz, 1996). The algorithm consists of a set of Fortran modules for the computation of the forward radiance as stated in (3), and the corresponding Jacobian (derivative with respect to input parameters).

The approach followed in the modules was to develop a finite-difference forward model representation, and then perform derivative operations on this model to obtain the Jacobians for temperature. The set of brightness temperatures $T_b(\nu)$ is also computed by means of (4).

The forward radiance calculation from (3) can be written in finite-difference form as

$$R_i(\theta) = R_{i,s}(\theta)\tau_{i,N}(\theta) + \sum_{l=1}^N B_i(\bar{T}_l) \left(\tau_{i,l-1}(\theta) - \tau_{i,l}(\theta) \right) + R'_i(\theta)$$

where the subscript i indicates quantities corresponding to channel i , \bar{T}_l is the mean layer temperature at the atmospheric level or height l , and N is the total number of layers. Note that for microwave channels we use \bar{T}_l instead of $B_i(\bar{T}_l)$. In our problem, $i = 1, 2, \dots, 22$ and $N = 29$ levels.

Equation (5) for the reflected radiance is expressed in finite-difference form as

$$R'_i(\theta) = (1 - \varepsilon_i) R_i \downarrow \tau_{i,N}(\theta) + \rho_i H_i \tau_{iS}(\theta_{EFF})$$

where the effective solar zenith angle is $\theta_{EFF} = \sec^{-1}(\sec(\varphi) + \sec(\theta))$ and φ is the solar zenith angle. For channels where the atmosphere is optically thin (HIRS IR channels 8, 10, 18, and 19), (6) is approximated as

$$R_i \downarrow = 2 \cos \theta \sum_{l=1}^N B_i(\bar{T}_l) (\tau_{i,l-1}(\theta) - \tau_{i,l}(\theta))$$

Similarly, for the other IR channels (7) is approximated as

$$R_i \downarrow = F_i B_i(T_s) (1 - \tau_{iN}(\theta))$$

where T_s is the surface air temperature. For the microwave channels, the finite-difference representation of (8) is given as

$$R_i \downarrow = T_{BB} \tau_{i,N}(\theta) + \tau_{i,N}(\theta) \sum_{l=1}^N \bar{T}_l \left(\frac{1}{\tau_{i,l}(\theta)} - \frac{1}{\tau_{i,l-1}(\theta)} \right)$$

The total transmittance between satellite level and a level l , is the product of effective layer transmittances for all layers between satellite level and the level l . These effective layer transmittances are modeled as the product of terms representing absorption due to atmospheric gases having a fixed mixing ratio, absorption due to ozone, and absorption due to water vapor. Coefficients for these terms are obtained by fitting transmittances obtained from line-by-line calculations. Several sets containing the transmittance line-by-line calculations are precomputed and included with the GLA TOVS. A detailed description of the algorithm used for transmittance calculation can be found in (Sienkiewicz, 1996).

The calculation of the temperature Jacobian $J(T)$, or derivative of brightness temperature with respect to temperature is accomplished through operation of the finite-difference representation of the forward problem. The

expressions needed for the Jacobian calculation can be derived by repeated applications of the chain rule for derivatives. Recall from (4) that $T_b = B^{-1}[R_v]$. Thus, the derivative with respect to temperature T is given as

$$J_i = \frac{\partial T_{b,i}}{\partial \bar{T}_m} = \frac{\partial T_{b,i}}{\partial R_i} \frac{\partial R_i}{\partial \bar{T}_m} = \frac{\partial T_{b,i}}{\partial R_i} \left[R_{i,s}(\theta) \frac{\partial \tau_{i,N}(\theta)}{\partial \bar{T}_m} + \frac{\partial B_i(\bar{T}_m)}{\partial \bar{T}_m} (\tau_{i,m-1}(\theta) - \tau_{i,m}(\theta)) \right. \\ \left. + \sum_{l=1}^N B_i(\bar{T}_l) \frac{\partial}{\partial \bar{T}_m} (\tau_{i,l-1}(\theta) - \tau_{i,l}(\theta)) + \frac{\partial R'_i}{\partial \bar{T}_l} \right] \quad (9)$$

where $\bar{T}_m = 0.5(T_{m-1} + T_m)$ is the mean layer temperature.

As we can see from (9), the Jacobian plays a crucial role in the implementation of the temperature retrieval algorithms, since it provides the sensitivity weighting functions, which relate the change in brightness temperature to the change in atmospheric temperature profile. As we will see in future Sections, the sensitivity functions will be needed to solve our inversion problem. The weighting functions for the HIRS/2 and MSU channels used in our retrieval problems are shown in Figure 1, for the 1976 US Standard atmosphere model.

3. Ill-Posedness of Temperature Retrievals

If the atmosphere strongly absorbs, most of the contribution to the measured brightness temperature will come from the atmosphere itself. Assuming that the surface temperature contribution $T_{bv}(p_s, \theta) \tau_v(p_s, \theta)$ and the term due to the reflected radiance $T'_{bv}(\theta)$ are known, (3.11) can be written as

$$T_{bv} - (T_{bv}(p_s, \theta) \tau_v(p_s, \theta) + T'_{bv}(\theta)) = \int_{p_s}^0 B[T(p)] \frac{\partial \tau_v(p, \theta)}{\partial p} dp$$

or as

$$\tilde{T}_{bv} = \int_{p_s}^0 K(v, p) B[T(p)] dp \quad (10)$$

where $\tilde{T}_{bv} = T_{bv} - (T_{bv}(p_s, \theta) \tau_v(p_s, \theta) + T'_{bv}(\theta))$ and $K(v, p) = \frac{\partial \tau_v(p, \theta)}{\partial p}$.

Equation (10) is a Fredholm integral equation of the first kind,

$$g(x) = \int_a^b K(x, s) u(s) ds$$

The inversion of the Fredholm integral in (4.3) is an ill-posed problem (Groetsch, 1984 and Tikhonov, 1977). The following definition is taken from Hadamard (Groetsch, 1984 and Tikhonov, 1977).

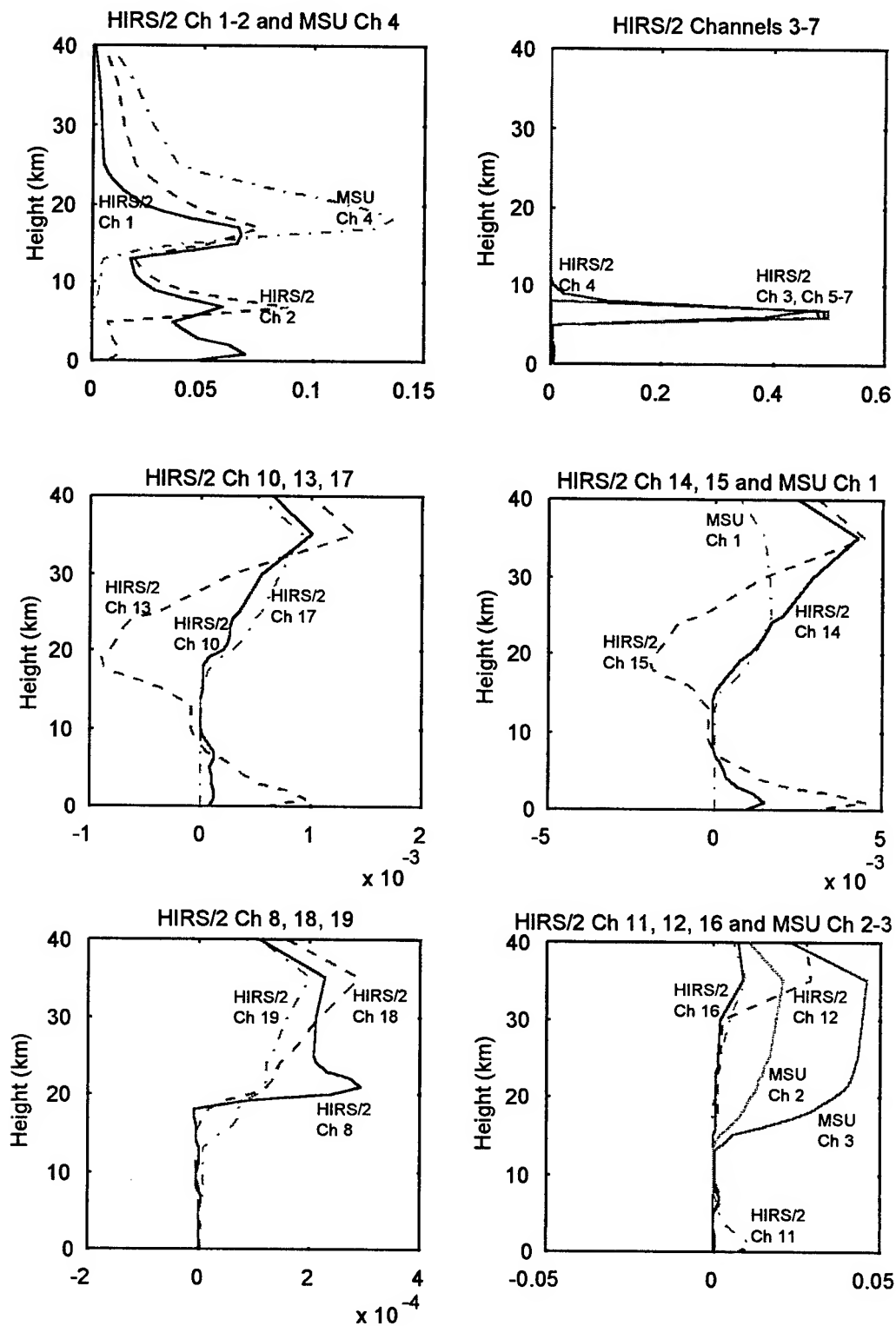


Figure 1: Weighting functions for HIRS/2 and MSU channels.

Definition 1: Well-Posed Problem: A problem is given by a datum g and a solution u , and it is Well-Posed (in the sense of Hadamard) when:

1. For each datum g in a class of functions Y there exists a solution u in a prescribed class X (existence).
2. The solution u is unique in X (uniqueness).
3. The dependence of u upon g is continuous.

An Ill-Posed problem is a problem that is not well-posed (i.e. it fails at least one condition stated above).

This is not a precise mathematical definition. To make it precise for a particular problem, the notion of a solution and the admissible data have to be specified. Also, the topology used for measuring continuity needs to be established. These specifications have to be such that they are appropriate for the particular problem (Engle, 1996).

The finite-difference representation of (10) is stated as

$$\tilde{T}_{bi} = \sum_{l=1}^N K(i, l) B[T_l], \quad (11)$$

where $\tilde{T}_{bi} = T_{bi} - (T_{bi,s}(\theta)\tau_{i,N}(\theta) + T'_{bi}(\theta))$ and $K(i, l) = (\tau_{i,j-1}(\theta) - \tau_{i,j}(\theta))$. This leads to the nonlinear model

$$\mathbf{T}_b = \mathbf{f}(\mathbf{T}) + \mathbf{e}$$

where \mathbf{T} is the temperature profile to be retrieved, $\mathbf{f}: \mathfrak{R}^n \rightarrow \mathfrak{R}^m$ is a nonlinear vector function that maps the desired parameters to the measurement space, and \mathbf{e} is an error term associated with measurement noise and the truncation error arising from the discretization of the integral in (10). This problem also suffers from inherited ill-conditioning and is underdetermined since in most retrieval problems of interest $m < n$.

4. Regularization of the Discrete Problem

The retrieval problem introduced in (11), has two major difficulties associated with it:

- ill-conditioning due to the ill-posedness of inverting the associated integral equation (10), and
- multiple solutions because of trying to estimate temperature profiles with more atmospheric levels, 29, than measurements available, 22.

To overcome these difficulties, we can use the so-called regularization methods. Regularization theory (Tikhonov, 1977) transforms an ill-posed problem into a well-posed one, using *a priori* knowledge on the nature of the solution. It is necessary to incorporate further information about the desired solution in order to stabilize the problem and to single out a useful and stable solution (Hansen, 1998). This is the purpose of regularization.

There are various methods to achieve regularization of ill-posed problems. In our algorithm, we first linearize the nonlinear retrieval problem and then regularize the resulting linear problem. Next, we will present the two methods we used to regularize the linearized problem. These are the Tikhonov method and the Truncated Singular Value Decomposition (TSVD) method.

4.1 Tikhonov regularization

The most common and well-known form of regularization is the one known as Tikhonov regularization (Tikhonov, 1977). To explain the method, consider the underdetermined linear least-squares problem

$$\min_{\mathbf{x}} \|\mathbf{Ax} - \mathbf{b}\|_2^2, \quad \mathbf{A} \in \mathbb{R}^{m \times n}, \quad m < n. \quad (12)$$

One way to regularize (12) is by computing the estimate, $\hat{\mathbf{x}}$, as the solution to the optimization problem

$$\hat{\mathbf{x}}_{\lambda_{TIKH}} = \arg \min_{\mathbf{x} \in \mathbb{R}^n} \left\{ \|\mathbf{Ax} - \mathbf{b}\|_2^2 + \lambda_{TIKH}^2 \|L(\mathbf{x} - \mathbf{x}_0)\|_2^2 \right\}, \quad (13)$$

or equivalently

$$\hat{\mathbf{x}}_{\lambda_{TIKH}} = \arg \min_{\mathbf{x} \in \mathbb{R}^n} \left\| \begin{pmatrix} \mathbf{A} \\ \lambda_{TIKH} L \end{pmatrix} \mathbf{x} - \begin{pmatrix} \mathbf{b} \\ \lambda_{TIKH} L \mathbf{x}_0 \end{pmatrix} \right\|_2^2$$

where $\|\cdot\|_2$ is the ℓ_2 norm¹, \mathbf{x}_0 is an initial estimate of the solution, and λ_{TIKH} is the regularization parameter for the Tikhonov method. In many instances, the matrix L is typically either the identity matrix I_n , as in our case, or an approximation to some derivative operator (Hansen, 1992).

A key issue in this method is the selection of the regularization parameter λ_{TIKH} . This parameter controls the weight given to minimization of the side constraint, $\|\mathbf{x} - \mathbf{x}_0\|_2$, relative to minimization of the residual norm, $\|\mathbf{Ax} - \mathbf{b}\|_2$. A large λ_{TIKH} (i.e., a large amount of regularization) favors a solution close to the initial guess at the cost of a large residual norm. Conversely, a small λ_{TIKH} (i.e., a small amount of regularization) favors a small residual norm at the cost of a high side constraint. An optimal value of λ_{TIKH} balances the two terms. This is further discussed in (Hansen, 1998).

In our algorithm, the selection of the Tikhonov regularization parameter λ was based on the L-curve method. The L-curve is a plot in log-log scale, for all valid regularization parameters, $\|\mathbf{x} - \mathbf{x}_0\|_2$, which indicates the discrepancy from the initial guess, versus the corresponding prediction error $\|\mathbf{Ax} - \mathbf{b}\|_2$. The curve displays the compromise between minimization of these two quantities (Hansen, 1998). Figure 2, adapted from (Hansen, 1992), shows the generic form of the L-curve. The horizontal part of the curve corresponds to solutions where the regularization error dominates, i.e., where so much regularization is applied, and the solution stays very smooth. For this case $\|\mathbf{x} - \mathbf{x}_0\|_2$ changes very little with λ_{TIKH} . The vertical part of the curve corresponds to

¹ The ℓ_2 norm is given by $\|\mathbf{x}\|_2 = \sqrt{\mathbf{x}^T \mathbf{x}}$.

solutions that are dominated by the prediction error, and the residual norm does not change much. In general, the optimal regularization parameter is very close to the L-curve's corner. Thus, by locating the corner of the curve, an approximation to the optimal regularization parameter can be computed (Hansen, 1996). The MATLAB Regularization Toolbox (Hansen, 1992) has a routine to compute this parameter.

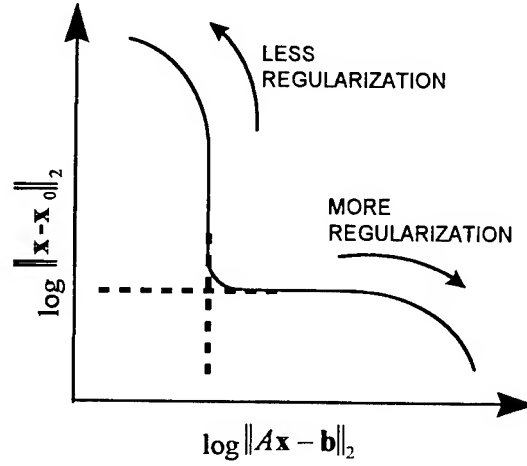


Figure 2: Generic form of the L-curve.

4.1.1 Truncated Singular Value Decomposition

Before we describe the Truncated Singular Value Decomposition (TSVD) regularization method, it is convenient to introduce the definition of singular value decomposition (SVD). The SVD is one of the best numerical tools for analysis of discrete ill-posed least-squares problems like (12), since it reveals all the difficulties associated with the ill-conditioning and rank deficiency of the matrix A . The use of SVD is the most reliable way to determine the rank and nearness to rank-deficiency of A (Datta, 1995). The following definition of the SVD has been modified to fit our problem.

Definition 4.2 Singular Value Decomposition: Let $A \in \mathbb{R}^{m \times n}$ be a rectangular matrix with $m \leq n$. Then the SVD of A is a decomposition of the form

$$A = V \Sigma U^T = \sum_{i=1}^m \mathbf{v}_i \sigma_i \mathbf{u}_i^T, \quad (14)$$

where $U = (\mathbf{u}_1, \dots, \mathbf{u}_m)$ and $V = (\mathbf{v}_1, \dots, \mathbf{v}_m)$ are matrices with orthonormal columns, $U^T U = V^T V = I_m$, and where $\Sigma = \text{diag}(\sigma_1, \dots, \sigma_m)$ has non-negative diagonal elements appearing in non-increasing order such that

$$\sigma_1 \geq \dots \geq \sigma_m \geq 0$$

The numbers σ_i are the singular values of A while the vectors \mathbf{u}_i and \mathbf{v}_i are the left and right singular vectors of A , respectively.

In terms of the SVD of A , the minimum norm least-squares solution of (12) is given as

$$\mathbf{x} = \sum_{i=1}^m \frac{\mathbf{v}_i^T \mathbf{b}}{\sigma_i} \mathbf{u}_i \quad (15)$$

The approach of TSVD is to derive a new problem with a well-conditioned rank deficient coefficient matrix. Using the SVD of A , we obtain the closest rank- k approximation A_k to A (measured in the 2-norm) by truncating the SVD expansion in (14) at k . Thus, A_k is given by

$$A_k = \sum_{i=1}^k \mathbf{v}_i \sigma_i \mathbf{u}_i^T, \quad k \leq m$$

where k is the TSVD regularization parameter λ_{TSVD} . When A is replaced by $A_k = A_{\lambda_{TSVD}}$ then we obtain a least square problem $\min_{\mathbf{x}} \|A_{\lambda_{TSVD}} \mathbf{x} - \mathbf{b}\|_2$. The truncated SVD solution (i.e., the minimum-norm solution $\mathbf{x}_{\lambda_{TSVD}}$ to this problem) is given by

$$\mathbf{x}_{\lambda_{TSVD}} = A_{\lambda_{TSVD}}^T \left(A_{\lambda_{TSVD}} A_{\lambda_{TSVD}}^T \right)^{-1} \mathbf{b} = \sum_{i=1}^{\lambda_{TSVD}} \frac{\mathbf{v}_i^T \mathbf{b}}{\sigma_i} \mathbf{u}_i, \quad (16)$$

and the complete method is referred to as the truncated SVD (TSVD) (Hansen, 1996). For all cases where $k < m$, (16) will be a truncated version of the minimum norm least-squares solution in (15).

5. The Discrete Picard Condition and Filter Factors

In this section, we introduce the discrete Picard condition, and the concept of filter factors. The latter play an important role in connection with regularization of discrete ill-posed problems (Hansen, 1996).

Let us refer to the Fredholm integral in (10) and its finite-difference form of (11), both repeated here for convenience:

$$\tilde{T}_{bv} = \int_{p_r}^0 K(v, p) B[T(p)] dp$$

and

$$\tilde{T}_{bi} = \sum_{j=1}^N K(i, j) B[T_j]$$

We can express the kernel K , of size 22×29 and rank 22, by its SVD expansion as

$$K = \sum_{i=1}^{22} \sigma_i \mathbf{v}_i \mathbf{u}_i^T$$

It is reasonable to think that the behavior of the singular values σ_i and the singular functions u_i and v_i is strongly connected with the properties of K . It is useful to note the following. (Hansen, 1996):

- The smoother the kernel, the faster the singular values decay to zero (where the number of continuous partial derivatives measures smoothness of the kernel).
- The smaller the singular values, the more oscillations (or zero-crossings) in the singular functions.

The decay rate of the singular values is so fundamental for the behavior of ill-posed problems, that some have proposed it as a tool to characterize the degree of ill-posedness. The mathematical formulation used to guarantee that there exist a square integrable solution $T(p)$ with finite L_2 norm in (16), based on an existing SVD of the kernel K is given by the Picard condition, (Hansen, 1996).

For discrete ill-posed problems, there is also a discrete Picard condition. Consider the discrete ill-posed problem (12). Let $\mathbf{b} = \bar{\mathbf{b}} + \mathbf{e}$, where \mathbf{e} is an error term due to measurement errors, approximation errors, and rounding errors, and $\bar{\mathbf{b}}$ is the unperturbed right-hand side. The discrete Picard condition provides the mathematical formulation needed to assure that we compute a regularized solution \mathbf{x}_λ from the given right-hand side \mathbf{b} such that \mathbf{x}_λ approximates the exact solution $\bar{\mathbf{x}}$ (Hansen, 1992).

Definition 4.3 Discrete Picard Condition: *The unperturbed right-hand side $\bar{\mathbf{b}}$ in a discrete ill-posed problem with regularization matrix L satisfies the Discrete Picard Condition if the Fourier coefficients $|\mathbf{v}_i^T \bar{\mathbf{b}}|$, on the average, decay to zero faster than the singular values σ_i . It can be shown that if (16) satisfies the Picard condition for the continuous case, then the discrete ill-posed problem obtained by discretization of the integral equation satisfies the discrete Picard condition (Hansen, 1992).*

Now consider again the standard solution given in (15). If the Fourier coefficients $|\mathbf{v}_i^T \mathbf{b}|$ in the numerator do not decay as fast as the singular values, the solution \mathbf{x} will be dominated by terms in the sum corresponding to the smallest singular values σ_i in the denominator. Thus, the solution \mathbf{x} will have many sign changes and will appear completely random. Regularization methods attempt to filter out this effects, or at least reduce them to some degree. Thus, in terms of SVD our desired regularized solution can stated as

$$\mathbf{x}_\lambda = \sum_{i=1}^m f_i \frac{\mathbf{v}_i^T \mathbf{b}}{\sigma_i} \mathbf{u}_i$$

where f_i are called the filter factors (Hansen, 1998). They have the property that as σ_i decreases, the corresponding f_i tend to zero such that the contribution of the smallest σ_i to the solution is filtered out.

There are various ways of computing the filter factors. In fact, different regularization methods can be defined as different ways to determine filter factors (Hansen, 1996). For Tikhonov regularization the filter factors are given by

$$f_i = \frac{\sigma_i^2}{\sigma_i^2 + \lambda_{\text{TIKH}}^2}$$

and for TSVD by

$$f_i = \begin{cases} 1 & \text{for } i \leq \lambda_{\text{TSVD}} \\ 0 & \text{otherwise} \end{cases}$$

6. Gauss-Newton Retrieval Algorithm

In this section, we explain the retrieval algorithms developed in this research based on the Gauss-Newton algorithm. We derive the Gauss-Newton formulation for our problem of interest, and explain how regularization is incorporated into the algorithm. A description of the developed set of Matlab[®] functions is included along with diagrams that show how these functions interact. Our approach is mostly based in a regularization method developed by (Eriksson, 1996). However some modifications were incorporated to make it work for our application. Finally, we provide a brief introduction to the GLA TOVS code for forward radiance and Jacobian computation (Sienkiewicz, 1996).

6.1 Gauss-Newton Algorithm

The Gauss-Newton method for nonlinear least square problems can be summarized as follows

Algorithm 1: GN algorithm for nonlinear least squares

Given an initial guess $\mathbf{T}^{(0)}$, and set $a = 0$. Iterate until convergence is achieved:

1. Update the estimate according to

$$\hat{\mathbf{T}}^{(a+1)} = \hat{\mathbf{T}}^{(a)} + \gamma^{(a)} \delta^{(a)}$$

where the search direction $\delta^{(a)}$ is computed by solving the least-squares problem

$$\delta^{(a)} = \arg \min_{\delta} \left\| \mathbf{J}(\hat{\mathbf{T}}^{(a)}) \delta - \left(\mathbf{T}_b - \mathbf{f}(\hat{\mathbf{T}}^{(a)}) \right) \right\|_2^2 \quad (17)$$

$\gamma^{(a)}$ is selected so that the cost function is sufficiently decreased, $\hat{\mathbf{T}}^{(a)}$ is the estimate at the iteration a , and $\mathbf{J}(\mathbf{T})$ is the Jacobian of \mathbf{f} evaluated at \mathbf{T} .

2. If the convergence criterion is satisfied, then stop, else, set $a=a+1$ and go back to 1.

Notice that the computation of the search direction in (17) is based on the linearization of the original nonlinear problem. The linear least square problem (17) is an underdetermined problems and is here where regularization techniques for linear discrete problems are applied. This approach is based on (Eriksson, 1996).

6.2 Retrieval Using Gauss-Newton Algorithm with Tikhonov Regularization

As discussed in Chapter 4, the linear least-squares problem in (17) is an underdetermined problem. Therefore, the regularization algorithms derived are used to regularize the linear problem using different techniques. A regularized version of Algorithm 5.1, including Tikhonov regularization can be summarized as follows

Algorithm 2: Regularization algorithm based on GN and Tikhonov regularization

Given an initial temperature profile $\mathbf{T}^{(0)}$, a center c , an initial regularization parameter $\lambda^{(0)}$ and with $a = 0$, iterate until convergence is achieved:

1. Compute $\mathbf{r}(\hat{\mathbf{T}}^{(a)}) = \mathbf{T}_b - \mathbf{f}(\hat{\mathbf{T}}^{(a)})$, $\mathbf{J}(\hat{\mathbf{T}}^{(a)})$, and the SVD of \mathbf{J} .
2. Do a convergence test. If the following criteria is fulfilled then stop the iterations:

$$\text{for } \mathbf{h}^{(a)} = \left\| \mathbf{J}^{(a)} \delta + \mathbf{r}^{(a)} \right\|_2,$$

$$\frac{|\mathbf{h}^{(a-1)} - \mathbf{h}^{(a)}|}{1 + |\mathbf{h}^{(a)}|} \leq \varepsilon$$

3. Compute the Tikhonov regularization parameter λ_{TIKH} using the L-curve method (Hansen, 1998)
4. If

$$\left\| \left(\mathbf{J}^{(a)} \right)^T \mathbf{r}^{(a)} + \left(\lambda_{\text{TIKH}}^{(a)} \right)^2 \left(\hat{\mathbf{T}}^{(a)} - c \right) \right\|_2 \leq \lambda_{\text{TIKH}}^{(a)} \gamma \quad (18)$$

and $\lambda_{\text{TIKH}} < \lambda_{\text{TIKH}}^{(a)}$, then $\lambda_{\text{TIKH}}^{(a+1)} = \lambda_{\text{TIKH}}$; else $\lambda_{\text{TIKH}}^{(a+1)} = \lambda_{\text{TIKH}}^{(a)}$. Use $\gamma = 100$.

5. Compute the search direction $\delta^{(a)}$ solving the Tikhonov regularized minimization problem

$$\delta_{\text{TIKH}}^{(a)} = \arg \min \left\{ \left\| \begin{pmatrix} \mathbf{J}^{(a)} \\ \lambda_{\text{TIKH}} \mathbf{I}_m \end{pmatrix} \delta - \begin{pmatrix} \mathbf{r}^{(a)} \\ \lambda_{\text{TIKH}} (\hat{\mathbf{T}}^{(a)} - c) \end{pmatrix} \right\|_2 \right\}$$

using the SVD decomposition of $\mathbf{J}^{(a)}$, where $\mathbf{r}^{(a)} = \mathbf{T}_b - \mathbf{f}(\hat{\mathbf{T}}^{(a)})$, $\mathbf{J}^{(a)} = \mathbf{J}(\hat{\mathbf{T}}^{(a)})$, and

$\hat{\mathbf{T}}^{(a)}$ is the estimate of \mathbf{T} at iteration a .

6. Determine the step-length $\alpha^{(a)}$ so that the objective function is sufficiently reduced, using the Armijo rule (Bertsekas, 1995).
7. Update the estimate according to

$$\hat{\mathbf{T}}^{(a+1)} = \hat{\mathbf{T}}^{(a)} + \alpha^{(a)} \delta_{\lambda_{TIKH}}^{(a)}$$

8. Set $a = a+1$ and go back to step 1.

Initialization plays an important role in optimization algorithms. In general, the final estimate $\hat{\mathbf{T}}_\lambda$ is highly dependent of the initial profile. The selection of the initial guess $\hat{\mathbf{T}}^{(0)}$ was primarily based on the location of the tropopause height. This would allow us to study whether the algorithm is capable of determining tropopause height when fed with initial guesses that have the tropopause height far from the actual height. The capability of determining this peak is a very useful feature of the retrieval algorithm since most important weather features are located at this region of the atmosphere (Trenberth, 1992).

Another parameter that must be chosen carefully is the center c . We want to make c as close as possible to the initial temperature profile $\hat{\mathbf{T}}^{(0)}$. In our problem, we set $c = \mathbf{T}^{(0)} - 0.25$. The brightness temperatures \mathbf{T}_b , and the Jacobian $\mathbf{J}(\hat{\mathbf{T}}^{(a)})$ were computed using the GLA TOVS rapid algorithm.

The criteria in step 4 of the algorithm is essential to achieve convergence (Eriksson, 1996). To assure convergence, the gradient of

$$\frac{1}{2} \left\| \begin{pmatrix} \mathbf{r}(\hat{\mathbf{T}}^{(a)}) \\ \lambda_{TIKH}^{(a)} (\hat{\mathbf{T}}^{(a)} - c) \end{pmatrix} \right\|^2$$

at $\hat{\mathbf{T}}^{(a)}$ for the regularization parameter $\lambda_{TIKH}^{(a)}$ has to be sufficiently small in comparison with $\lambda_{TIKH}^{(a)}$ when we change to a smaller $\lambda_{TIKH}^{(a+1)}$ value. We also require a decreasing sequence of λ_{TIKH} values. Proof of the validity of this criterion in (18) is provided in page 89 of (Eriksson, 1996).

Finally, the step-length computation in step 6 of the algorithm is done using Armijo rule (Bertsekas, 1995).

This rule is essentially a successive reduction rule. An initial step-length $\alpha^{(a)}$ is chosen, and if the corresponding vector $\hat{\mathbf{T}}^{(a+1)} = \hat{\mathbf{T}}^{(a)} + \alpha^{(a)} \delta^{(a)}$ does not yield a reduction of the residual norm function $\mathbf{g}(\hat{\mathbf{T}}^{(a)}) = \|\mathbf{J}^{(a)} \delta^{(a)} + \mathbf{r}^{(a)}\|_2$, i.e., $\mathbf{g}(\hat{\mathbf{T}}^{(a)} + \alpha^{(a)} \delta^{(a)}) \geq \mathbf{g}(\hat{\mathbf{T}}^{(a)})$, the step-length is reduced by a certain factor until the value of the residual norm is improved. The Armijo rule reduces the possibility of convergence to a local minimum by adding the following constraint to the reduction of $\alpha^{(a)}$ (Bertsekas, 1995),

$$\mathbf{g}(\hat{\mathbf{T}}^{(a)}) - \mathbf{g}(\hat{\mathbf{T}}^{(a)} + \beta^m s \delta^{(a)}) \geq -\sigma \beta^m s \nabla \mathbf{g}(\hat{\mathbf{T}}^{(a)})' \delta^{(a)}. \quad (5.22)$$

The step-lengths $\beta^m s$, $m = 0, 1, \dots$, are tried successively until the above inequality is satisfied for $m = m_a$.

Usually, $\sigma \in [10^{-5}, 10^{-1}]$, $\beta \in [1/2, 1/10]$, and $s = 1$.

A very important part of this iterative process is the computation of new brightness temperatures and a new Jacobian for each iteration. The new estimated temperature profile is used as new input to the radiative transfer code, to compute the corresponding outputs.

6.2.1 Retrieval Using Gauss-Newton Algorithm with TSVD Regularization

This algorithm differs from Algorithm 5.2 in the way that steps 3 through 5 are computed. The complete algorithm is outlined next

Algorithm 3: Regularization algorithm based on GN and TSVD regularization

Given an initial temperature profile $\mathbf{T}^{(0)}$, a center c , and with $a = 0$, iterate until convergence is achieved:

1. Compute $\mathbf{r}(\hat{\mathbf{T}}^{(a)}) = \mathbf{T}_b - \mathbf{f}(\hat{\mathbf{T}}^{(a)})$, $\mathbf{J}(\hat{\mathbf{T}}^{(a)})$, and the SVD of \mathbf{J} .
2. Do a convergence test. If the following criteria is fulfilled then stop the iterations: for

$$\mathbf{h}^{(a)} = \left\| \mathbf{J}^{(a)} \delta + \mathbf{r}^{(a)} \right\|_2,$$

$$\frac{|\mathbf{h}^{(a-1)} - \mathbf{h}^{(a)}|}{1 + |\mathbf{h}^{(a)}|} \leq \varepsilon$$

3. Compute the regularization parameter $\lambda_{TSVD}^{(a)}$ using the following criterion:

- a. Let $\lambda_{TSVD}^{(0)} = 3$, $\lambda_{TSVD}^{(1)} = 7$.

- b. For $a > 1$: If $\lambda_{TSVD}^{(a)} = \lambda_{TSVD,MAX}^{(a)}$ then $\lambda_{TSVD}^{(a+1)} = \lambda_{TSVD}^{(a)}$, else,

- c. Let $s^{(a)} = \left\| \left(\mathbf{J}^{(a)} \right)^T \mathbf{r}^{(a)} + \left(\lambda_{TSVD}^{(a)} \right)^2 \left(\hat{\mathbf{T}}^{(a)} - c \right) \right\|_2$, $t^{(a)} = \left\| \hat{\mathbf{T}}^{(a)} - \hat{\mathbf{T}}^{(a-1)} \right\|_2$,

$$w^{(a)} = \left\| \left(\mathbf{J}^{(a)} \right)^T \mathbf{r}^{(a)} \right\|_2. \text{ If } s^{(a)} - s^{(a-1)} \geq \gamma, \text{ and } w^{(a)} \leq w^{(a-1)}, \text{ and } t^{(a)} \geq \omega,$$

$$\text{then } \lambda_{TSVD}^{(a+1)} = \lambda_{TSVD}^{(a)} + 1, \text{ else}$$

- d. If $t^{(a)} < \omega$, then $\lambda_{TSVD}^{(a+1)} = \lambda_{TSVD}^{(a)} + 2$, else

- e. If $w^{(a)} > w^{(a-1)}$ or $s^{(a)} - s^{(a-1)} < \gamma$, then $\lambda_{TSVD}^{(a+1)} = \lambda_{TSVD}^{(a)} + 4$, else,

$$f. \quad \lambda_{TSVD}^{(a+1)} = \lambda_{TSVD}^{(a)} + 1.$$

4. Compute the search direction $\delta^{(a)}$ as follows

$$J_{\lambda_{TSVD}}^{(a)} = \sum_{i=1}^{\lambda_{TSVD}} \mathbf{v}_i \sigma_i^T \mathbf{u}_i^T, \quad \lambda_{TSVD} \leq 22$$

and

$$\delta_{\lambda_{TSVD}}^{(a)} = J_{\lambda_{TSVD}}^T \left(J_{\lambda_{TSVD}} J_{\lambda_{TSVD}}^T \right)^{-1} \mathbf{r}^{(a)} = \sum_{i=1}^{\lambda_{TSVD}} \frac{\mathbf{v}_i^T \mathbf{r}^{(a)}}{\sigma_i} \mathbf{u}_i$$

5. Determine the step-length $\alpha^{(a)}$ so that the objective function is sufficiently reduced, using the Armijo rule (Bertsekas, 1995).
6. Update the estimate according to

$$\hat{\mathbf{T}}^{(a+1)} = \hat{\mathbf{T}}^{(a)} + \alpha^{(a)} \delta^{(a)}$$

7. Set $a = a+1$ and go back to step 1.

From the definition of TSVD we know that $\lambda_{TSVD}^{(a+1)}$ is a positive integer and that $1 \leq \lambda_{TSVD}^{(a+1)} \leq m$, where

m is equal to the number of singular values of the SVD of \mathbf{J} . Thus, if any computed $\lambda_{TSVD}^{(a+1)}$ is greater than the maximum permissible value m , it will be assigned the maximum value. Also, we used $\gamma=1000$, and $\omega=4$. Much care must be taken when computing the regularized solution for the TSVD subproblem (Eriksson, 1996). The derivation of a regularization parameter update criterion that assures global convergence of the solution is not a simple task. The criterion outlined in step 3 of Algorithm 5.3 was defined by studying carefully the nature of our problem. The main characteristic of this criterion is that the regularization parameter λ_{TSVD} always increases (reducing the applied regularization). We know from the theory that enough regularization must be applied at the beginning of iterations, and then it should be gradually decreased. But it is very difficult to know how fast or how slow this should be done, or how much regularization must be applied at the beginning. Allowing the regularization parameter to decrease too fast will result in convergence towards a local minimum with a large residual norm (Eriksson, 1996).

6.3 GLA TOVS Forward Radiance and Jacobian Computations

In order to implement the retrieval algorithm, the forward radiative transfer calculation was needed. This would provide us with the brightness temperatures $\mathbf{T}_b = \mathbf{f}(\hat{\mathbf{T}}^{(a)})$ as a function of the estimated profile, as well as the Jacobian $\mathbf{J}(\hat{\mathbf{T}}^{(a)})$. This computation is performed at least once on each iteration.

We solved the RTE in (3) using the Goddard Laboratory for Atmospheres (GLA) TOVS Rapid Algorithm for Forward Radiance and Jacobian Computations Version 1.0. This is a Fortran code developed at the Data Assimilation Office of the Goddard Laboratory for Atmospheres, and the General Sciences Corporation in Laurel, Maryland (Sienkiewicz, 1996). The code allows the computation of forward radiance, brightness temperature, and brightness temperature Jacobian for simulations of the TOVS HIRS/2 and MSU radiometers. A detailed description can be found in (Sienkiewicz, 1996).

6.4 Description of the MATLAB® Code

The developed algorithms were implemented as MATLAB® functions. We divided the code into eight basic functions that allowed the debugging and documentation to be easier and clearer. The main functions used in the implementation of the algorithm are described in Table 1. Table 2 describes auxiliary routines to the main functions. The diagram in Figure 3 shows the function interaction, along with the most important input and output parameters for the main functions. The square box contains the program's output parameters.

Table 1: Main functions for the GN-based regularization algorithm.

Function	Description
gn_regu	Main program. Other functions are called from this routine. When execution is completed this function returns output parameters of interest.
J_f_init	Computes initial values for brightness temperature and Jacobian matrix. Also returns initial guess for temperature profile.
win_draw	Opens a window and generates plots of important quantities. A call is made to function picard *.
tikho_l	Computes the regularization parameter for the Tikhonov subproblem. A selection criteria is applied to assure global convergence. A call is made to function l_curve *.
tikho	Computes the Tikhonov regularized solution of the search direction.
tsvd_l	Computes the regularization parameter for the TSVD subproblem. A selection criteria is applied to assure global convergence. A call is made to function l_curve *.
tsvd_reg	Returns the TSVD regularized solution of the search direction. A call is made to function tsvd *.
update	Computes the updated temperature profile for each iteration. Implements the Armijo criterion for the computation of the step-length.

* Functions from P.C. Hansen's Regularization Tools

Table 2: Auxiliary functions for the GN-based regularization algorithm.

Function	Description
inpar	Generates needed atmospheric profiles used to run the GLA TOVS simulation.
atm_prof	Data file loaded by function inpar to read part of the needed atmospheric profiles.
profiles	Generates a vector with the chosen initial guess of the temperature profile.
picard *	Facilitates the visual inspection of the Picard condition.
l_curve *	Plots the L-curve and finds its corner.
l_corner *	Auxiliary function to function l_curve.
lcfun *	Auxiliary function to l_corner.
tsvd *	Computes the TSVD regularized solution of the search direction.

* Functions from P.C. Hansen's Regularization Tools

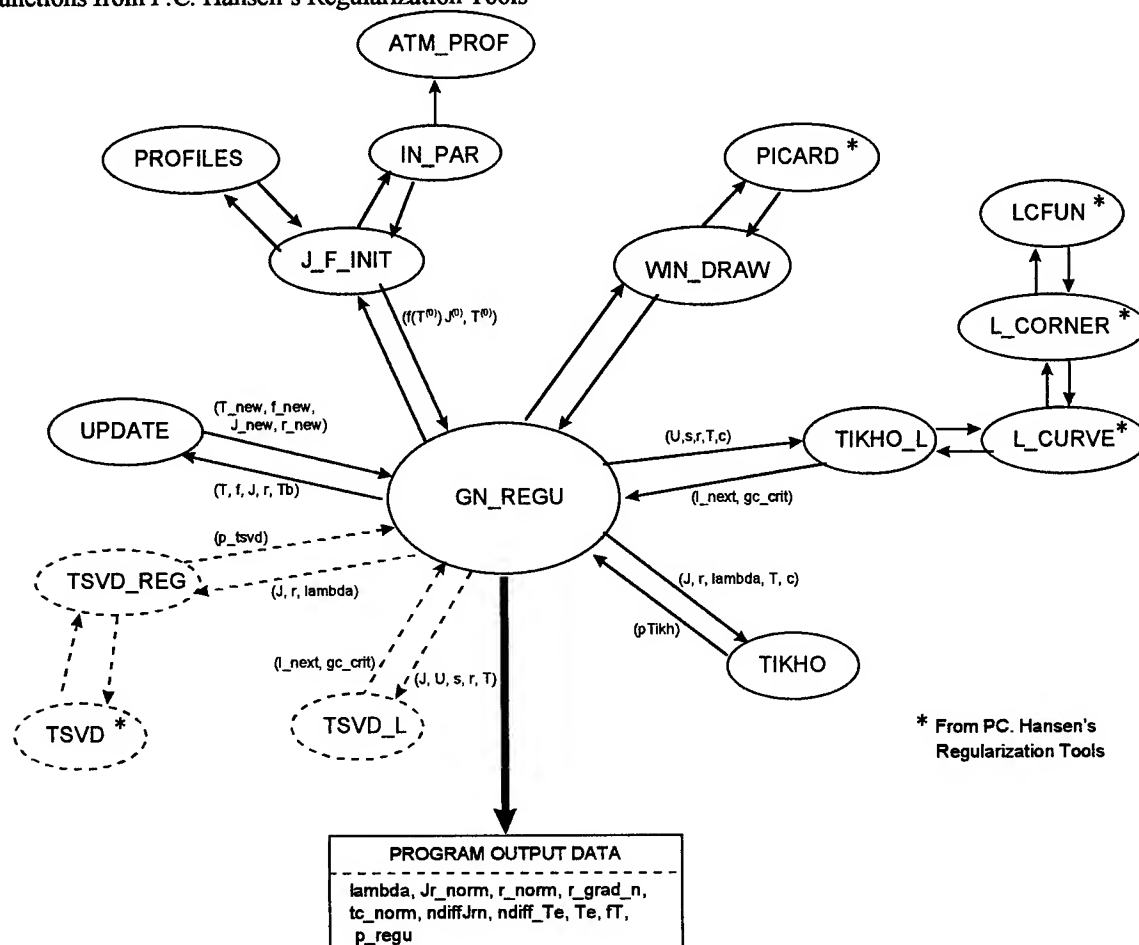


Figure 3: Function interaction for the GN-based regularization algorithm.

7. Simulation Results

In this section, we present and discuss the simulation results for the temperature retrievals. The section is divided into four main sections. In Section 7.1, we present the results of retrievals using Tikhonov regularization. The results for retrievals using TSVD regularization are included in Section 7.2. Similarly, in Section 7.3, we show some results of retrievals in the presence of noise. Finally, in Section 7.4, we establish a comparison between the two regularization methods for both noiseless and noisy cases, and discuss the main differences of the generated results.

7.1 Retrieval Using Tikhonov Regularization

Algorithm 2 was used to solve five different retrieval problems, each with a different temperature initial value $\hat{T}^{(0)}$. The first retrieval corresponds to a tropopause initial guess at 5 km. The real temperature profile used in all the retrievals is shown in Figure 4. All cases are noiseless.

Some important output parameters for the 5km simulation are included in Table 3. The first column of the table contains the regularization parameter computed for each iteration a . The linearization residual norm for the problem is included in column number two and shown in Figure 5. The residual norm for this case is shown in Figure 5. The residual norm of the nonlinear least-squares problem is included in column number four of Table 3.

Table 3: Output parameters for retrieval using Tikhonov regularization with 5 km tropopause initial guess.

a	$\lambda^{(a)}$	$\mathbf{h}^{(a)} = \ \mathbf{J}^{(a)}\delta + \mathbf{r}^{(a)}\ $	$\ \mathbf{r}^{(a)}\ _2$	$\ \mathbf{J}^{(a)^T} \mathbf{r}^{(a)}\ _2$	$\ \hat{\mathbf{T}}^{(a)} - \mathbf{c}\ _2$	$\frac{ \mathbf{h}^{(a-1)} - \mathbf{h}^{(a)} }{1 + \mathbf{h}^{(a)} }$	$\frac{\ \hat{\mathbf{T}}^{(a)} - \hat{\mathbf{T}}^{(a-1)}\ _2}{1 + \ \hat{\mathbf{T}}^{(a)}\ _2}$
0	1.0000e-02	1.5128e+02	7.5648e+01	1.1128e+02	1.3463e+00	-	-
1	1.0000e-02	7.5916e+01	2.0702e+00	8.1140e-01	8.5400e+01	9.7989e-01	6.7164e-02
2	7.9937e-05	1.4695e+00	8.4000e-01	2.3128e-01	1.0899e+02	3.0146e+1	5.4517e-02
3	7.9937e-05	7.7154e-01	7.5103e-02	1.6469e-02	1.0121e+02	3.9401e-01	1.9640e-02
4	7.9937e-05	5.8276e-02	1.7215e-02	3.3725e-03	1.0095e+02	6.7399e-01	7.4457e-03
5	9.0892e-07	2.7655e-02	4.2862e-02	1.0409e-02	1.0313e+02	2.9797e-02	1.5847e-02
6	9.0892e-07	2.3661e-02	3.7977e-02	7.9431e-03	1.0336e+02	3.9009e-03	1.1890e-02
7	9.0892e-07	1.0118e-02	2.8880e-02	5.7166e-03	1.0367e+02	1.3407e-02	1.2258e-02
8	9.0892e-07	8.1872e-03	3.3534e-02	6.3896e-03	1.0351e+02	1.9156e-03	1.3228e-02
9	9.0892e-07	1.9293e-02	1.4529e-02	3.0001e-03	1.0249e+02	1.0896e-02	9.4883e-03
10	9.0892e-07	2.5358e-02	2.2100e-02	4.3831e-03	1.0320e+02	5.9146e-03	1.0161e-02
11	9.0892e-07	9.4799e-03	3.1526e-02	6.0202e-03	1.0332e+02	1.5729e-02	1.3742e-02
12	9.0892e-07	3.0102e-02	6.1365e-02	1.2061e-02	1.0369e+02	2.0020e-02	1.5602e-02
13	9.0892e-07	1.5682e-02	5.8453e-02	1.3620e-02	1.0362e+02	1.4197e-02	1.0736e-02
14	9.0892e-07	3.7900e-02	2.0979e-02	4.4723e-03	1.0286e+02	2.1406e-02	8.3572e-03

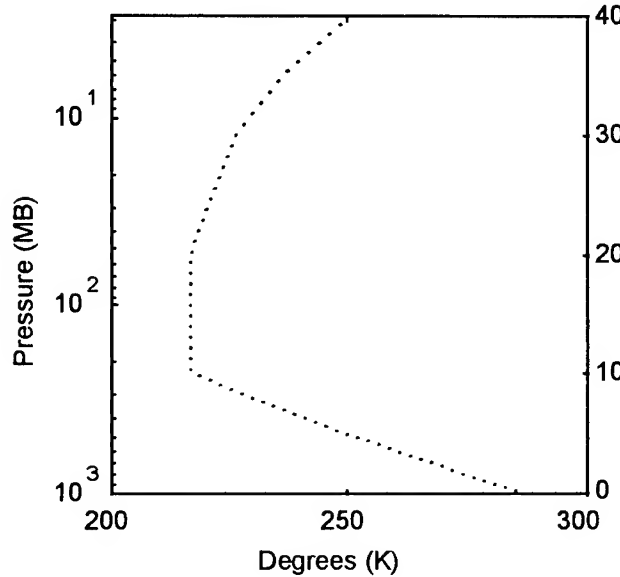


Figure 4: Real temperature profile used for the retrievals.

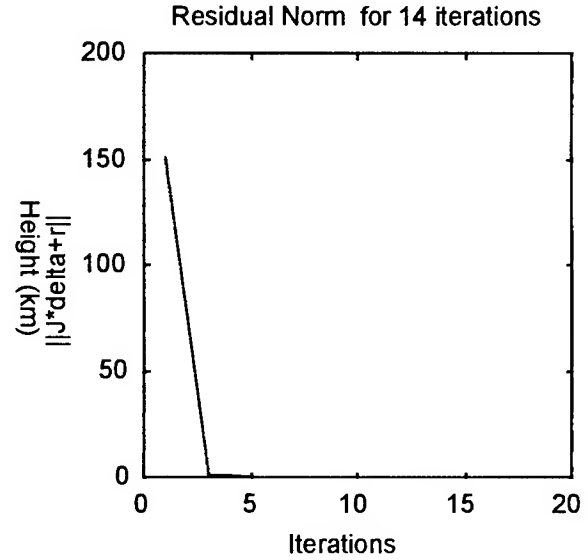


Figure 5: Residual norm for Tikhonov regularization with 5 km tropopause initial guess.

We expect this quantity to decrease towards zero as the estimated temperature profile approaches the real profile. The gradient of this quantity is contained in the next column. Column number six provides a quantitative measure of how the updated temperature estimate deviates from the center \mathbf{c} . Since the center was assigned very

close to the temperature initial guess, this is the only parameter that we expect to increase with the number of iterations. Finally, the last two columns of the table contain the quantities used in the algorithm stopping rule. The convergence criteria was satisfied when the following condition prevailed,

$$\frac{|\mathbf{h}^{(a-1)} - \mathbf{h}^{(a)}|}{1 + |\mathbf{h}^{(a)}|} < 10^{-3} \quad (19)$$

where $\mathbf{h}^{(a)} = \|\mathbf{J}^{(a)}\delta + \mathbf{r}^{(a)}\|_2$.

For this tropopause initial guess, the solution began diverging before (19) was satisfied. Figure 6 shows the estimated profile for fourteen iterations. Here, the dotted line is the real profile, the dashed line is the initial guess, and the solid line represents the estimated profile. The best approximation possible was achieved after four iterations, as shown in Figure 7.

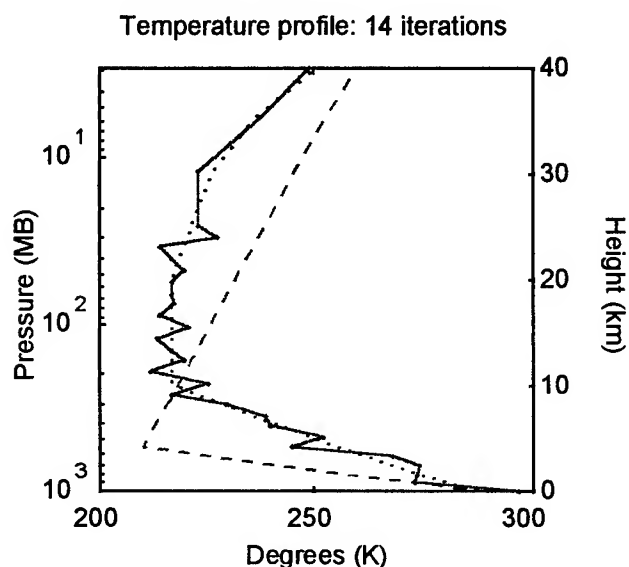


Figure 6: Estimated temperature profile for Tikhonov regularization with 5 km tropopause initial guess.

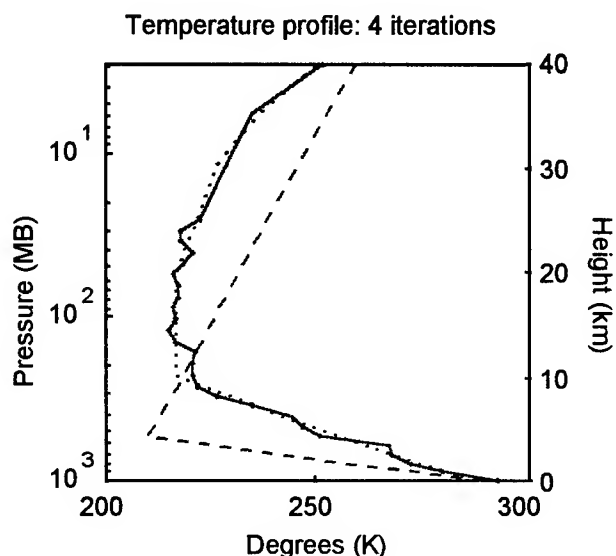


Figure 7: Estimated temperature profile for Tikhonov regularization with 5 km tropopause initial guess: best approximation.

The second case of the retrievals corresponds to a tropopause initial guess at 10 km. The corresponding output data is shown in Table 4. The stopping criterion was satisfied after seven iterations. The estimated profile is shown in Figure 8. It is clear from that figure that an initial guess with a 10 km tropopause yields a better solution than the 5 km case.

A tool that aids in the analysis of the solution to the problem of interest is the discrete Picard Condition. To help visualize how the satisfaction of the Picard condition relates to the solution of the problem, the plot of Figure 9 is generated using the `picard.m` function from Regularization Tools (Hansen, 1996). The picard plot in the first part of the figure corresponds to the Jacobian determined as a function of the initial guess of the temperature profile.

Here, we see that the Fourier coefficients $|\mathbf{v}_i^T \mathbf{b}|$ do not decay as fast as the singular values σ_i , and hence the discrete Picard condition is not satisfied. The initial temperature profile is far from the real value. In the second part of the figure, we show the Picard plot for the Jacobian corresponding to the final temperature profile estimate after seven iterations. As required by the Picard condition, the Fourier coefficients, on the average, decay faster than the corresponding singular values, and clearly from Figure 9, we can say that the estimated profile approximates the real profile. The accuracy of the estimated profiles is evaluated in Section 7.4. Because of limitations in space, we will not include Picard plots for every experimental case. However, the capability to generate these plots is incorporated into the algorithm, and we recommend their use as an analysis tool.

Table 4: Output parameters for retrieval using Tikhonov regularization with 10 km tropopause initial guess.

a	$\lambda^{(a)}$	$\mathbf{h}^{(a)} = \ \mathbf{J}^{(a)} \delta + \mathbf{r}^{(a)}\ $	$\ \mathbf{r}^{(a)}\ _2$	$\ (\mathbf{J}^{(a)})^T \mathbf{r}^{(a)}\ _2$	$\ \hat{\mathbf{T}}^{(a)} - \mathbf{c}\ _2$	$\frac{\ \mathbf{h}^{(a-1)} - \mathbf{h}^{(a)}\ }{1 + \ \mathbf{h}^{(a)}\ }$	$\frac{\ \hat{\mathbf{T}}^{(a)} - \hat{\mathbf{T}}^{(a-1)}\ _2}{1 + \ \hat{\mathbf{T}}^{(a)}\ _2}$
0	1.0000e-02	4.2226e+01	2.1118e+01	2.8080e+01	1.3463e+00	-	-
1	1.0000e-02	2.1061e+01	5.0422e-01	1.5695e-01	4.4359e+01	9.5941e-01	3.5229e-02
2	3.8815e-05	4.4081e-01	1.5180e-01	3.0271e-02	4.9344e+01	1.4311e+01	1.6002e-02
3	3.8815e-05	1.2543e-01	2.6442e-02	4.7559e-03	4.7391e+01	2.8023e-01	8.0636e-03
4	3.8815e-05	2.1706e-02	4.8564e-03	9.8002e-04	4.7026e+01	1.0152e-01	3.3632e-03
5	3.8815e-05	4.0675e-03	8.0563e-04	1.7120e-04	4.6980e+01	1.7567e-02	1.2373e-03
6	3.8815e-05	7.7232e-04	9.9696e-05	2.2121e-05	4.6975e+01	3.2926e-03	3.3741e-04
7	1.1694e-06	1.8579e-04	1.0971e-04	3.8968e-05	4.6975e+01	5.8642e-04	2.0819e-05

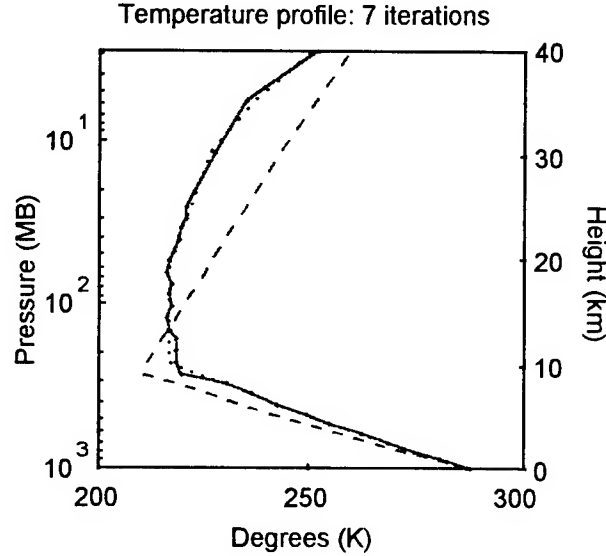


Figure 8: Estimated temperature profile for Tikhonov regularization with 10 km tropopause initial guess.

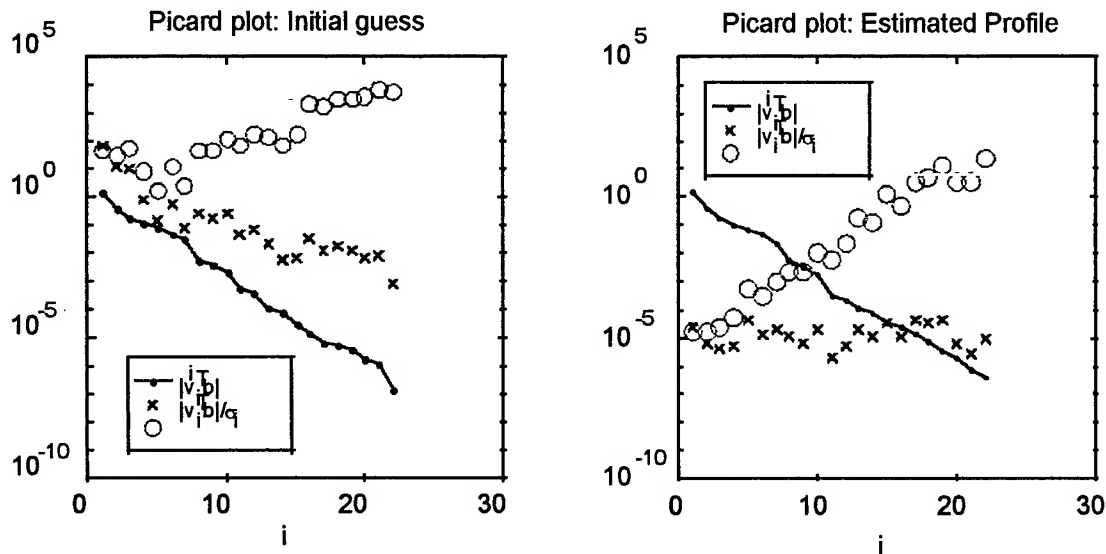


Figure 9: Picard plots for Tikhonov regularization with 10 km tropopause initial guess.

The third retrieval corresponds to a tropopause initial guess at 15 km. Table 5 contains the output parameters for this case. Similarly, Figure 10 shows the estimated profile. For this case the stopping criteria was satisfied after 9 iterations. When supplied with a 20 km tropopause initial guess, the results obtained were those of Table 6. In this case, the program stopped after 10 iterations. Figure 11 shows the estimated profile.

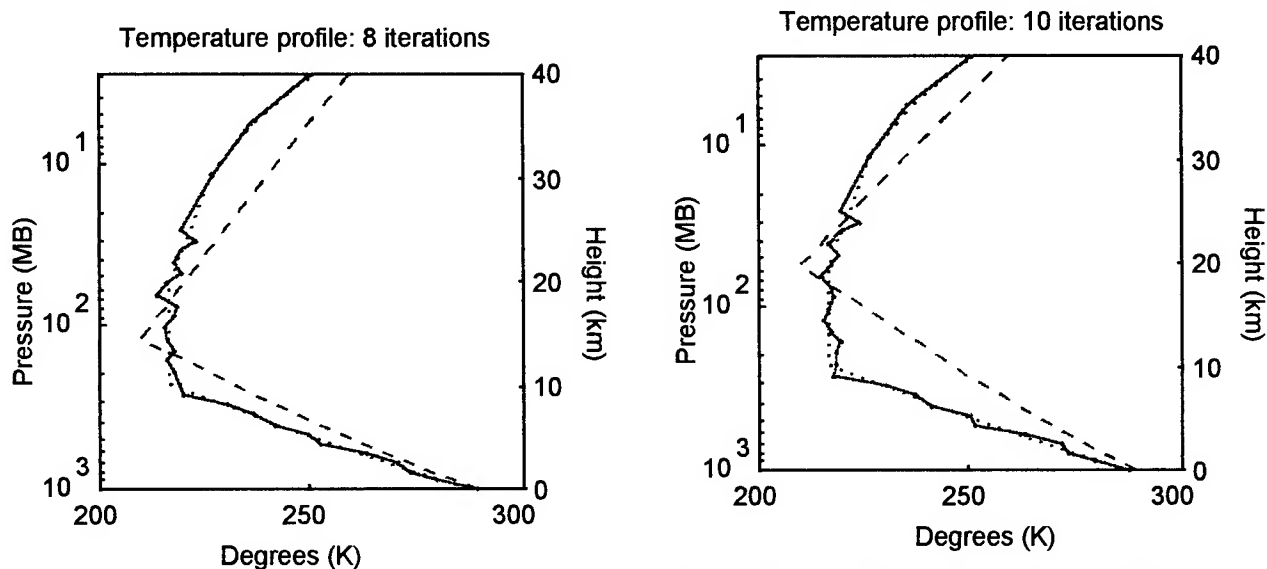


Figure 10: Estimated temperature profile for Tikhonov regularization with 15 km tropopause initial guess.

Figure 11: Estimated temperature profile for Tikhonov regularization with 20 km tropopause initial guess.

The last retrieval using Tikhonov regularization was performed using a 25 km tropopause initial guess. The results for this case are presented in Table 7. The corresponding estimated profile after 10 iterations is shown in Figure 12.

Table 5: Output parameters for retrieval using Tikhonov regularization with 15km tropopause initial guess.

a	$\lambda^{(a)}$	$\mathbf{h}^{(a)} = \ \mathbf{J}^{(a)}\delta + \mathbf{r}^{(a)}\ $	$\ \mathbf{r}^{(a)}\ _2$	$\left\ \left(\mathbf{J}^{(a)} \right)^T \mathbf{r}^{(a)} \right\ _2$	$\ \hat{\mathbf{T}}^{(a)} - \mathbf{c}\ _2$	$\frac{ \mathbf{h}^{(a-1)} - \mathbf{h}^{(a)} }{1 + \mathbf{h}^{(a)} }$	$\frac{\ \hat{\mathbf{T}}^{(a)} - \hat{\mathbf{T}}^{(a-1)}\ _2}{1 + \ \hat{\mathbf{T}}^{(a)}\ _2}$
0	1.0000e-02	4.4338e+01	2.2172e+01	3.2706e+01	1.3463e+00	-	-
1	1.0000e-02	2.2103e+01	2.4266e-01	5.4085e-02	3.4050e+01	9.6240e-01	2.7562e-02
2	4.0903e-06	1.5934e-01	2.4385e-01	4.7658e-02	5.8713e+01	1.8928e+01	3.6395e-02
3	4.0903e-06	1.6728e-01	7.6312e-02	1.5113e-02	4.7665e+01	6.7999e-03	2.1774e-02
4	4.0903e-06	5.3420e-02	2.6772e-02	4.3906e-03	4.3631e+01	1.0808e-01	1.1835e-02
5	4.0903e-06	1.7160e-02	9.5885e-03	1.6597e-03	4.3748e+01	3.5648e-02	8.0279e-03
6	4.0903e-06	4.6287e-03	5.2597e-03	1.1311e-03	4.3419e+01	1.2474e-02	4.3699e-03
7	4.0903e-06	8.0716e-03	1.3294e-02	2.7206e-03	4.3624e+01	3.4154e-03	7.2661e-03
8	4.0903e-06	8.5155e-03	4.9101e-03	9.5726e-04	4.2841e+01	4.4008e-04	4.9109e-03

Table 6: Output parameters for retrieval using Tikhonov regularization with 20 km tropopause initial guess.

a	$\lambda^{(a)}$	$\mathbf{h}^{(a)} = \ \mathbf{J}^{(a)}\delta + \mathbf{r}^{(a)}\ $	$\ \mathbf{r}^{(a)}\ _2$	$\left\ \left(\mathbf{J}^{(a)} \right)^T \mathbf{r}^{(a)} \right\ _2$	$\ \hat{\mathbf{T}}^{(a)} - \mathbf{c}\ _2$	$\frac{ \mathbf{h}^{(a-1)} - \mathbf{h}^{(a)} }{1 + \mathbf{h}^{(a)} }$	$\frac{\ \hat{\mathbf{T}}^{(a)} - \hat{\mathbf{T}}^{(a-1)}\ _2}{1 + \ \hat{\mathbf{T}}^{(a)}\ _2}$
0	1.0000e-02	8.6739e+01	4.3375e+01	6.3532e+01	1.3463e+00	-	-
1	1.0000e-02	4.3067e+01	1.0461e+00	2.2464e-01	6.5380e+01	9.9105e-01	5.1919e-02
2	3.7717e-06	4.4046e-01	6.6258e-01	1.3638e-01	9.6768e+01	2.9592e+01	5.3492e-02
3	3.7717e-06	4.4975e-01	2.1518e-01	4.4549e-02	8.3238e+01	6.4078e-03	3.5618e-02
4	3.7717e-06	1.5941e-01	5.6169e-02	1.2543e-02	7.7257e+01	2.5041e-01	1.6692e-02
5	3.7717e-06	3.5981e-02	2.0293e-02	4.5729e-03	7.6317e+01	1.1915e-01	7.6006e-03
6	3.7717e-06	5.7805e-03	1.5202e-02	3.6431e-03	7.6021e+01	3.0027e-02	5.3164e-03
7	3.7717e-06	8.2948e-03	6.9396e-03	1.5394e-03	7.5720e+01	2.4936e-03	4.6388e-03
8	3.7717e-06	4.7153e-03	3.0553e-03	6.0177e-04	7.5927e+01	3.5627e-03	4.2121e-03
9	3.7717e-06	2.4319e-03	5.4037e-03	1.1208e-03	7.5766e+01	2.2778e-03	5.7811e-03
10	3.7717e-06	2.6699e-03	2.9609e-03	5.6244e-04	7.5945e+01	2.3730e-04	4.0803e-03

Table 7: Output parameters for retrieval using Tikhonov regularization with 25 km tropopause initial guess.

a	$\lambda^{(a)}$	$\mathbf{h}^{(a)} = \ \mathbf{J}^{(a)}\delta + \mathbf{r}^{(a)}\ $	$\ \mathbf{r}^{(a)}\ _2$	$\left\ \left(\mathbf{J}^{(a)} \right)^T \mathbf{r}^{(a)} \right\ _2$	$\ \hat{\mathbf{T}}^{(a)} - \mathbf{c}\ _2$	$\frac{ \mathbf{h}^{(a-1)} - \mathbf{h}^{(a)} }{1 + \mathbf{h}^{(a)} }$	$\frac{\ \hat{\mathbf{T}}^{(a)} - \hat{\mathbf{T}}^{(a-1)}\ _2}{1 + \ \hat{\mathbf{T}}^{(a)}\ _2}$
0	1.0000e-02	1.1817e+02	5.9096e+01	8.2997e+01	1.3463e+00	-	-
1	1.0000e-02	5.8640e+01	2.2192e+00	4.6781e-01	1.0198e+02	9.9812e-01	8.0371e-02
2	5.5396e-06	1.3951e+00	9.8412e-01	2.3775e-01	1.3158e+02	2.3901e+01	7.0519e-02
3	5.5396e-06	6.8312e-01	3.0357e-01	6.9716e-02	1.1111e+02	4.2301e-01	4.4742e-02
4	5.5396e-06	2.2667e-01	7.6553e-02	1.8022e-02	1.0705e+02	3.7210e-01	2.0527e-02
5	5.5396e-06	6.0459e-02	1.6753e-02	3.5891e-03	1.0603e+02	1.5674e-01	9.3821e-03
6	5.5396e-06	1.3027e-02	3.7551e-03	7.4902e-04	1.0615e+02	4.6822e-02	4.3188e-03
7	5.5396e-06	1.8064e-03	2.2539e-03	5.7278e-04	1.0627e+02	1.1201e-02	3.3753e-03
8	5.5396e-06	1.5136e-03	2.9407e-03	6.3748e-04	1.0601e+02	2.9242e-04	3.2775e-03

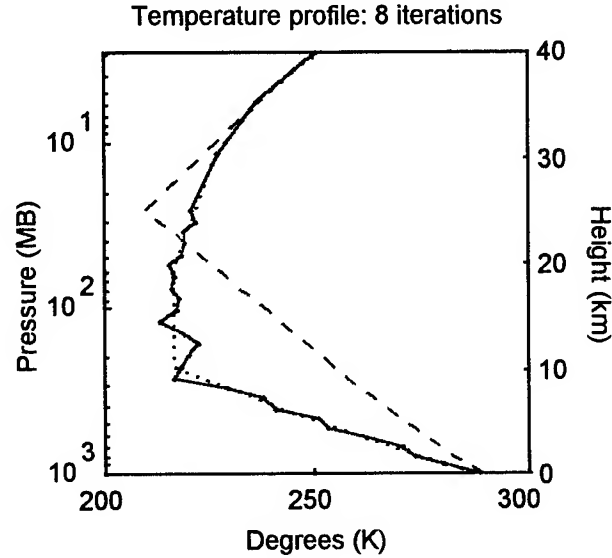


Figure 12: Estimated temperature profile for Tikhonov regularization with 25 km tropopause initial guess.

7.2 Retrieval Using TSVD Regularization

Algorithm 3 was used to solve the same retrieval problems as with Tikhonov regularization, i.e., using the same initial temperature profiles. For the 5 km tropopause initial guess, the output parameters of Table 8 were generated. The stopping criterion in column seven was satisfied after eight iterations. The estimated profile is shown in Figure 13.

The second case corresponds to a 10 km tropopause initial guess. The corresponding output data and estimated profile are those in Table 9 and Figure 14, respectively. There were a total of seven iterations before the program stopped.

Table 8: Output parameters for retrieval using TSVD regularization with 5 km tropopause initial guess.

a	$\lambda^{(a)}$	$\mathbf{h}^{(a)} = \mathbf{J}^{(a)} \delta + \mathbf{r}^{(a)}$	$\ \mathbf{r}^{(a)}\ _2$	$\ \mathbf{J}^{(a)T} \mathbf{r}^{(a)}\ _2$	$\ \hat{\mathbf{T}}^{(a)} - \mathbf{c}\ _2$	$\frac{\ \mathbf{h}^{(a-1)} - \mathbf{h}^{(a)}\ _2}{1 + \ \mathbf{h}^{(a)}\ _2}$	$\frac{\ \hat{\mathbf{T}}^{(a)} - \hat{\mathbf{T}}^{(a-1)}\ _2}{1 + \ \hat{\mathbf{T}}^{(a)}\ _2}$
0	3	1.5128e+02	7.5648e+01	1.1128e+02	1.3463e+00	-	-
1	7	7.5946e+01	2.1081e+00	8.3363e-01	8.4629e+01	9.7909e-01	6.6598e-02
2	8	1.9049e+00	2.5056e-01	6.5009e-02	9.0127e+01	2.5489e+01	2.8681e-02
3	9	1.0692e-01	1.9285e-01	4.5707e-02	9.8383e+01	1.6243e+00	2.1091e-02
4	10	8.0371e-02	1.9888e-01	3.6400e-02	9.9865e+01	2.4575e-02	1.7467e-02
5	11	1.7357e-01	2.4854e-02	5.1014e-03	1.0182e+02	7.9415e-02	7.1890e-03
6	12	2.4444e-02	1.5807e-03	7.9438e-05	1.0195e+02	1.4557e-01	1.0511e-03
7	14	2.9849e-03	1.5117e-03	6.7952e-05	1.0193e+02	2.1395e-02	3.0501e-04
8	16	2.9505e-03	1.5096e-03	9.6279e-05	1.0192e+02	3.4277e-05	1.0760e-04

Table 9: Output parameters for retrieval using TSVD regularization with 10 km tropopause initial guess.

a	$\lambda^{(a)}$	$\mathbf{h}^{(a)} = \ \mathbf{J}^{(a)}\delta + \mathbf{r}^{(a)}\ $	$\ \mathbf{r}^{(a)}\ _2$	$\ \mathbf{J}^{(a)^T} \mathbf{r}^{(a)}\ _2$	$\ \hat{\mathbf{T}}^{(a)} - \mathbf{c}\ _2$	$\frac{\ \mathbf{h}^{(a-1)} - \mathbf{h}^{(a)}\ }{1 + \ \mathbf{h}^{(a)}\ }$	$\frac{\ \hat{\mathbf{T}}^{(a)} - \hat{\mathbf{T}}^{(a-1)}\ _2}{1 + \ \hat{\mathbf{T}}^{(a)}\ _2}$
0	3	4.2151e+01	2.1118e+01	2.8080e+01	1.3463e+00	-	-
1	7	2.1070e+01	5.0748e-01	1.5552e-01	4.4161e+01	9.5521e-01	3.5071e-02
2	8	5.0114e-01	4.3163e-02	1.0188e-03	4.4633e+01	1.3702e+01	4.5050e-03
3	9	6.6883e-02	5.5095e-02	1.1095e-02	4.6473e+01	4.0703e-01	9.7473e-03
4	13	4.1516e-02	1.4391e-02	2.8421e-03	4.7006e+01	2.4356e-02	5.6180e-03
5	14	1.3429e-02	1.0537e-03	2.5637e-04	4.6977e+01	2.7714e-02	1.4779e-03
6	16	6.1013e-04	5.1023e-04	9.5322e-05	4.6990e+01	1.2811e-02	1.2513e-03
7	18	4.2216e-04	5.3989e-04	9.9192e-05	4.6990e+01	1.8789e-04	3.1702e-04

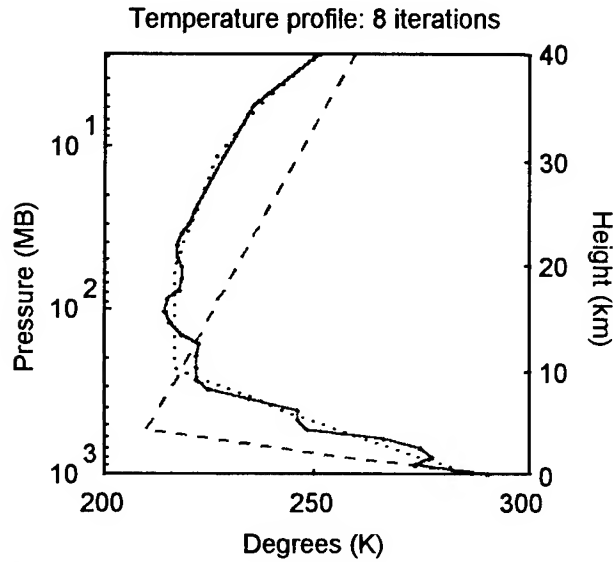


Figure 13: Estimated temperature profile for TSVD regularization with 5 km tropopause initial guess.

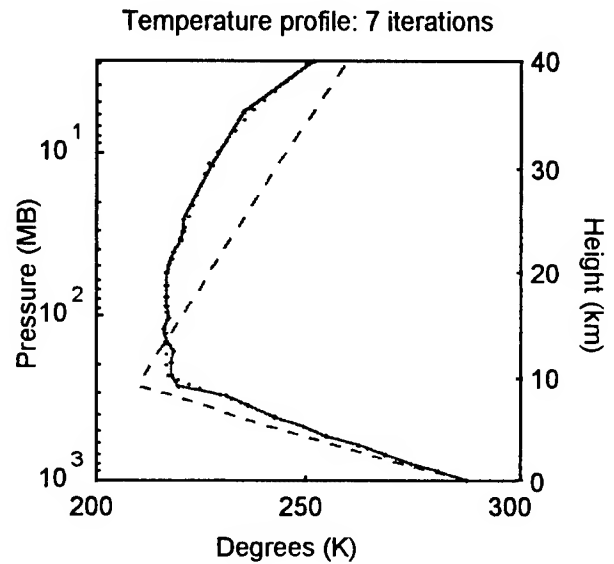


Figure 14: Estimated temperature profile for TSVD regularization with 10 km tropopause initial guess.

Table 10: Output parameters for retrieval using TSVD regularization with 15 km tropopause initial guess.

a	$\lambda^{(a)}$	$\mathbf{h}^{(a)} = \ \mathbf{J}^{(a)}\delta + \mathbf{r}^{(a)}\ $	$\ \mathbf{r}^{(a)}\ _2$	$\ \mathbf{J}^{(a)^T} \mathbf{r}^{(a)}\ _2$	$\ \hat{\mathbf{T}}^{(a)} - \mathbf{c}\ _2$	$\frac{\ \mathbf{h}^{(a-1)} - \mathbf{h}^{(a)}\ }{1 + \ \mathbf{h}^{(a)}\ }$	$\frac{\ \hat{\mathbf{T}}^{(a)} - \hat{\mathbf{T}}^{(a-1)}\ _2}{1 + \ \hat{\mathbf{T}}^{(a)}\ _2}$
0	3	4.4139e+01	2.2172e+01	3.2706e+01	1.3463e+00	-	-
1	7	2.2103e+01	2.2531e-01	5.1662e-02	3.4381e+01	9.5384e-01	2.7807e-02
2	8	2.0381e-01	4.8542e-02	6.2174e-03	3.6884e+01	1.8191e+01	7.7194e-03
3	9	4.7788e-02	5.3115e-02	9.4329e-03	3.9692e+01	1.4890e-01	1.0630e-02
4	13	2.2475e-02	4.2016e-02	8.0004e-03	4.1131e+01	2.4756e-02	8.7966e-03
5	14	3.5571e-02	6.5137e-03	1.3191e-03	4.1411e+01	1.2646e-02	3.6844e-03
6	16	6.3035e-03	7.4370e-03	2.5381e-03	4.2060e+01	2.9085e-02	5.5310e-03
7	20	1.2986e-02	7.2804e-03	2.4693e-03	4.2074e+01	6.5967e-03	6.4503e-04
8	22	1.1783e-02	6.9671e-03	2.3180e-03	4.2124e+01	1.1893e-03	1.1178e-03
9	22	1.0937e-02	7.3184e-03	2.2747e-03	4.2448e+01	8.3638e-04	3.4538e-03

For the 15 km tropopause initial guess, results are included in Table 10 and Figure 15. For this case, nine iterations were needed before the stopping criterion was satisfied. The next simulation presented corresponds to a tropopause initial guess at 20 km. For this case, the stopping rule was satisfied after the eighth iterations. Table 11 contains the output parameters for this case. The estimated profile can be seen in Figure 19.

Table 11: Output parameters for retrieval using TSVD regularization with 20 km tropopause initial guess.

a	$\lambda^{(a)}$	$\mathbf{h}^{(a)} = \mathbf{J}^{(a)} \delta + \mathbf{r}^{(a)}$	$\ \mathbf{r}^{(a)}\ _2$	$\ \mathbf{J}^{(a)^T} \mathbf{r}^{(a)}\ _2$	$\ \hat{\mathbf{T}}^{(a)} - \mathbf{c}\ _2$	$\frac{\ \mathbf{h}^{(a-1)} - \mathbf{h}^{(a)}\ _2}{1 + \ \mathbf{h}^{(a)}\ _2}$	$\frac{\ \hat{\mathbf{T}}^{(a)} - \hat{\mathbf{T}}^{(a-1)}\ _2}{1 + \ \hat{\mathbf{T}}^{(a)}\ _2}$
0	3	8.6698e+01	4.3375e+01	6.3532e+01	1.3463e+00	-	-
1	7	4.3085e+01	9.7295e-01	2.1238e-01	6.4713e+01	9.8930e-01	5.1368e-02
2	8	9.4577e-01	5.5869e-02	8.1417e-03	7.1524e+01	2.1657e+01	9.3532e-03
3	9	5.9868e-02	6.5188e-02	1.1613e-02	7.2517e+01	8.3587e-01	1.2733e-02
4	13	2.8183e-02	5.1013e-02	9.8628e-03	7.3321e+01	3.0817e-02	1.0274e-02
5	14	3.1125e-02	1.9630e-02	3.8637e-03	7.3841e+01	2.8538e-03	5.6148e-03
6	15	1.0046e-02	1.0861e-02	2.4072e-03	7.4350e+01	2.0870e-02	5.5236e-03
7	16	5.6516e-03	6.7127e-03	2.1867e-03	7.5150e+01	4.3694e-03	5.0050e-03
8	17	4.9841e-03	1.8566e-03	4.0340e-04	7.5435e+01	6.6426e-04	3.3368e-03

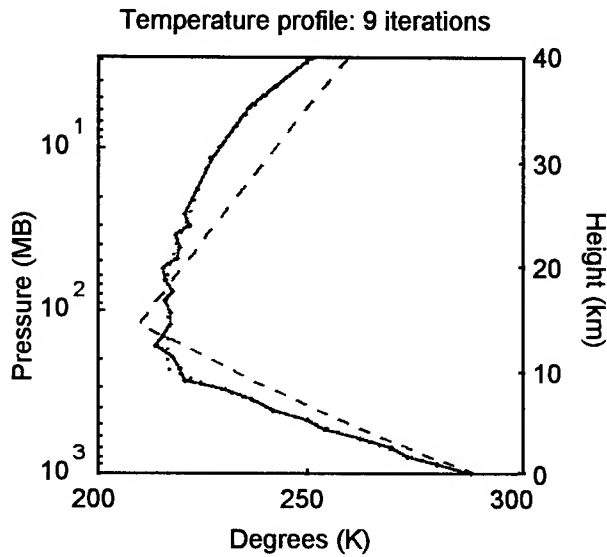


Figure 15: Estimated temperature profile for TSVD regularization with 15 km tropopause initial guess.

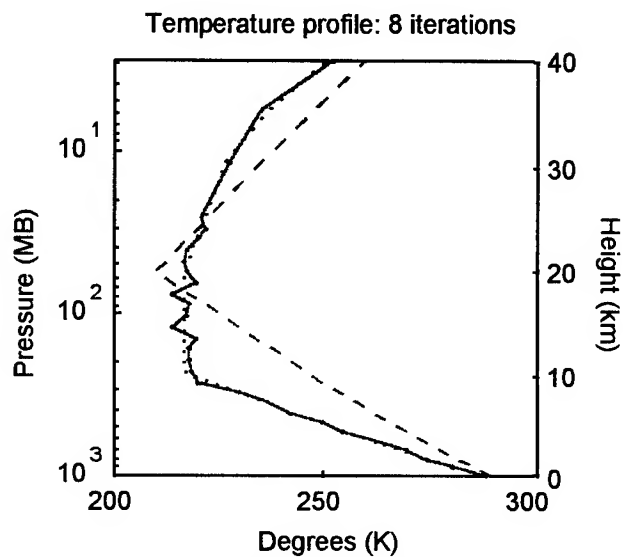


Figure 16: Estimated temperature profile for TSVD regularization with 20 km tropopause initial guess.

The last retrieval case corresponds to a 25 km tropopause initial guess. By looking at the output data in Table 12, we notice that the solution for this case began diverging after iteration number eight. The estimated profile in Figure 17 corresponds to 14 iterations. The best approximation possible corresponds to the eighth iteration and is shown in Figure 18.

Table 12: Output parameters for retrieval using TSVD regularization with 25 km tropopause initial guess.

a	$\lambda^{(a)}$	$\mathbf{h}^{(a)} = \frac{\mathbf{J}^{(a)} \delta + \mathbf{r}^{(a)}}{\ \mathbf{r}^{(a)}\ }$	$\ \mathbf{r}^{(a)}\ _2$	$\ \mathbf{J}^{(a)T} \mathbf{r}^{(a)}\ _2$	$\ \hat{\mathbf{T}}^{(a)} - \mathbf{c}\ _2$	$\frac{\ \mathbf{h}^{(a-1)} - \mathbf{h}^{(a)}\ }{1 + \ \mathbf{h}^{(a)}\ }$	$\frac{\ \hat{\mathbf{T}}^{(a)} - \hat{\mathbf{T}}^{(a-1)}\ _2}{1 + \ \hat{\mathbf{T}}^{(a)}\ _2}$
0	3	3.0000e+00	5.9096e+01	8.2997e+01	1.3463e+00	-	-
1	7	7.0000e+00	2.3071e+00	5.1721e-01	9.4097e+01	9.9159e-01	7.4034e-02
2	8	8.0000e+00	1.6798e-01	2.2658e-02	1.0034e+02	1.7727e+01	1.8078e-02
3	9	9.0000e+00	1.6187e-01	3.7741e-02	1.0226e+02	1.8306e+00	1.9883e-02
4	13	1.3000e+01	6.9324e-02	1.3771e-02	1.0318e+02	1.0819e-02	1.0429e-02
5	14	1.4000e+01	4.7905e-02	9.6947e-03	1.0401e+02	9.1401e-02	7.6560e-03
6	15	1.5000e+01	1.8327e-02	4.1013e-03	1.0475e+02	9.7661e-03	7.3739e-03
7	16	1.6000e+01	1.2303e-02	4.2865e-03	1.0589e+02	2.4109e-02	6.8166e-03
8	20	2.0000e+01	1.1624e-02	3.7980e-03	1.0599e+02	9.5003e-03	2.1652e-03
9	22	2.2000e+01	1.1980e-02	3.7617e-03	1.0606e+02	2.3413e-03	2.6360e-03
10	22	2.2000e+01	1.1846e-02	3.6780e-03	1.0615e+02	4.6390e-03	1.1528e-03
11	22	2.2000e+01	1.2086e-02	3.5771e-03	1.0625e+02	2.6560e-03	3.5291e-03
12	22	2.2000e+01	1.2301e-02	3.5823e-03	1.0638e+02	6.0531e-03	2.6600e-03
13	22	2.2000e+01	1.3061e-02	3.6439e-03	1.0692e+02	2.9468e-03	4.3784e-03
14	22	2.2000e+01	1.6494e-02	4.0111e-03	1.0808e+02	2.8906e-03	9.2406e-03
15	22	2.2000e+01	1.6609e-02	3.9007e-03	1.0795e+02	6.2099e-03	3.4094e-03

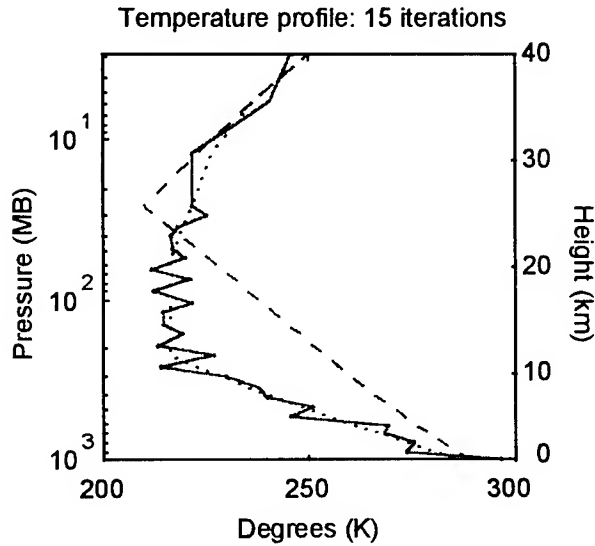


Figure 17: Estimated temperature profile for TSVD regularization with 25 km tropopause initial guess.

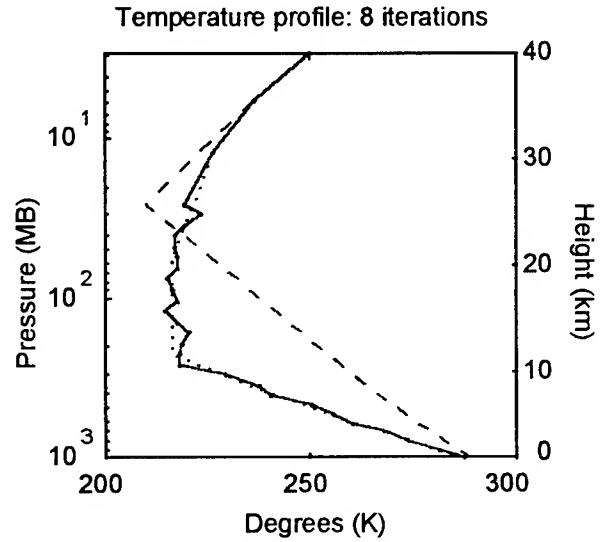


Figure 18: Estimated temperature profile for TSVD regularization with 25 km tropopause initial guess: best approximation.

7.3 Retrievals with the Addition of Noise

The purpose of this Section is to show how the retrievals are affected when we add a noise vector to the brightness temperatures \mathbf{T}_b . We define the measured brightness temperature, \mathbf{T}_b , as

$$\mathbf{T}_b = \bar{\mathbf{T}}_b + \mathbf{e}_m$$

where \bar{T}_b is the actual brightness temperature. The noise vector \mathbf{e}_m was white Gaussian noise with variance equal to the noise equivalent temperature difference (NE Δ T) for HIRS and MSU.

We performed two test retrievals for each regularization method, for tropopause initial guesses at 10 km and 15 km, respectively. The estimated profiles for the first test case are shown in Figures 19 and 20. We can appreciate from these figures that the results are very inaccurate. The stopping criteria was satisfied after a certain number of iterations, but convergence was far from being achieved. The small relative change in the residual norm \mathbf{h} may indicate that the algorithm is traversing a region in which the surface is fairly flat (Seber and Wild, 1989). This become apparent if look at Table 13 for Tikhonov regularization. We can see from the third column, that the residual norm \mathbf{h} remains high in comparison with previous retrievals, where the order of magnitude was as low as 10^{-3} . Also, small relative changes in the estimated profile indicate that the algorithm is taking short steps. Table 13 shows the output parameters for the Tikhonov regularization.

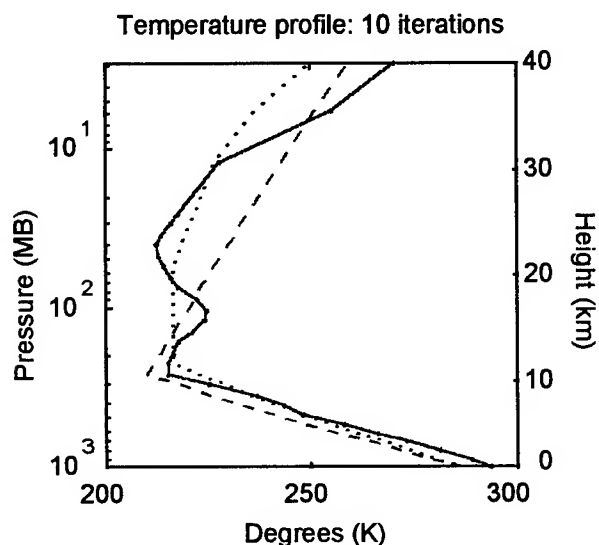


Figure 19: Estimated temperature profile for noisy Tikhonov regularization with 10 km tropopause initial guess.

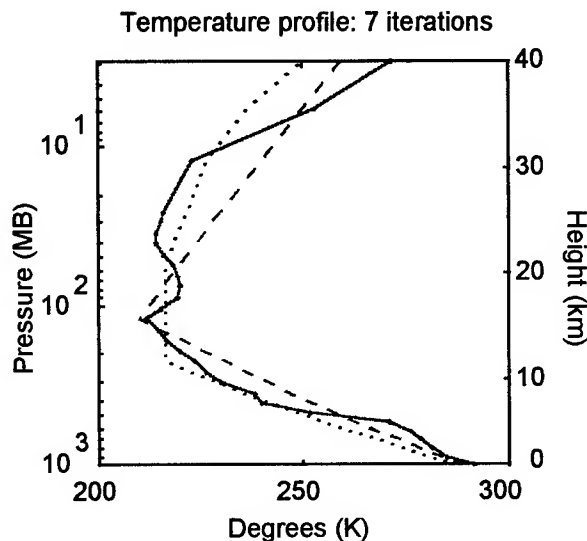


Figure 20: Estimated temperature profile for noisy TSVD regularization with 10 km tropopause initial guess.

Profiles for the second test case are shown in Figures 21 and 22. As shown in the figures, results are very similar to those of the previous case. An interesting fact is that after the third or fourth iteration the profile did not change significantly. In fact, if we stopped the program after the fifth iteration, we could not visually notice any difference in the estimates. This could mean that the regularization criterion incorporated into the algorithm is not appropriate for the noisy problem. In the following section, we discuss some important facts regarding the selection of the regularization parameter.

Table 13: Output parameters for noisy retrieval using Tikhonov regularization with 10 km tropopause initial guess.

a	$\lambda^{(a)}$	$\mathbf{h}^{(a)} = \frac{\ \mathbf{J}^{(a)}\delta + \mathbf{r}^{(a)}\ }{\ \mathbf{r}^{(a)}\ }$	$\ \mathbf{r}^{(a)}\ _2$	$\ \left(\mathbf{J}^{(a)}\right)^T \mathbf{r}^{(a)}\ _2$	$\ \hat{\mathbf{T}}^{(a)} - \mathbf{c}\ _2$	$\frac{\ \mathbf{h}^{(a-1)} - \mathbf{h}^{(a)}\ }{1 + \ \mathbf{h}^{(a)}\ }$	$\frac{\ \hat{\mathbf{T}}^{(a)} - \hat{\mathbf{T}}^{(a-1)}\ _2}{1 + \ \hat{\mathbf{T}}^{(a)}\ _2}$
0	1.0000e-02	4.3464e+01	2.1744e+01	2.9234e+01	1.3463e+00	-	-
1	1.0000e-02	2.1765e+01	8.3060e-01	1.4553e-01	5.5176e+01	9.5320e-01	4.3034e-02
2	5.5032e-06	1.5298e+00	8.3060e-01	1.4552e-01	5.5177e+01	7.9986e+00	1.4583e-04
3	5.5032e-06	1.6271e+00	8.3059e-01	1.4552e-01	5.5178e+01	3.7048e-02	1.5493e-04
4	5.5032e-06	1.4673e+00	8.3057e-01	1.4552e-01	5.5179e+01	6.4776e-02	8.3771e-05
5	5.5032e-06	1.4822e+00	8.3058e-01	1.4551e-01	5.5180e+01	5.9881e-03	8.7758e-05
6	5.5032e-06	1.5079e+00	8.3055e-01	1.4551e-01	5.5182e+01	1.0249e-02	9.2822e-05
7	5.5032e-06	1.5447e+00	8.3057e-01	1.4552e-01	5.5184e+01	1.4468e-02	9.8604e-05
8	5.5032e-06	1.5975e+00	8.3054e-01	1.4552e-01	5.5186e+01	2.0321e-02	1.0565e-04
9	5.5032e-06	1.4605e+00	8.3056e-01	1.4552e-01	5.5188e+01	5.5678e-02	5.6948e-05
10	5.5032e-06	1.4583e+00	8.3056e-01	1.4552e-01	5.5189e+01	8.6755e-04	5.9344e-05

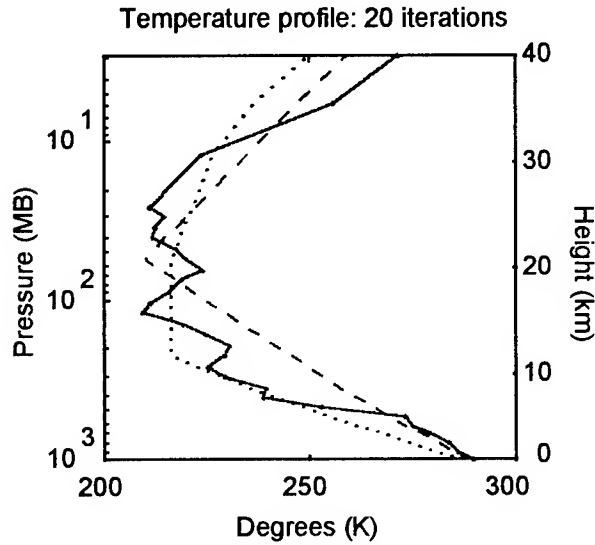


Figure 21: Estimated temperature profile for noisy Tikhonov regularization with 20 km tropopause initial guess.

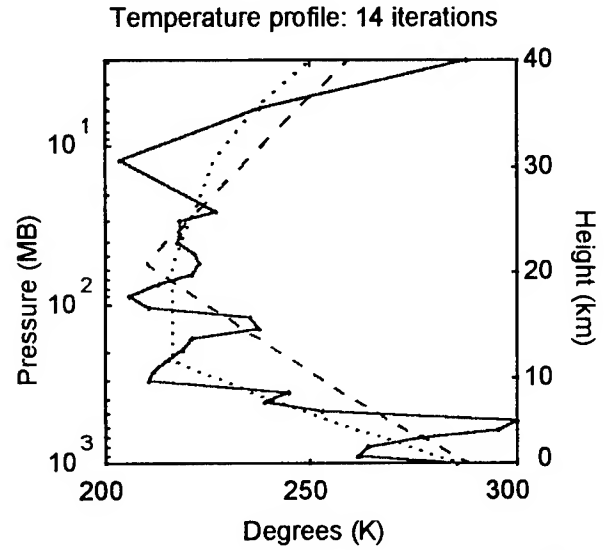


Figure 22: Estimated temperature profile for noisy TSVD regularization with 20 km tropopause initial guess.

7.4 Comparisons of the Retrievals

In this section, we will compare the accuracy of the estimated temperature profiles for Tikhonov regularization and TSVD regularization. We will also compare the retrievals with the addition of noise. Finally, we will discuss the main factors that influence the results of the retrievals.

To evaluate the accuracy of the estimated profiles, we used the root mean square (RMS) error metric. The RMS error can be computed as:

$$\text{RMS error} = \sqrt{\frac{1}{N} \sum_{i=1}^N \|\mathbf{T}_i - \hat{\mathbf{T}}_i\|_2^2}$$

where $N = 29$ is the total number of atmospheric layers, T_i are the elements of the real profile vector, and \hat{T}_i are elements of the estimated profile. The RMS errors of the estimated temperature profile for all the retrievals presented here are included in Table 14.

Table 14: Root Mean Square (RMS) error of estimated temperature profiles.

Tropopause initial guess (km)	RMS Error			
	Tikhonov (noiseless)	Tikhonov (noisy)	TSVD (noiseless)	TSVD (noisy)
5	4.0728*, 2.5171**	-	3.5182	-
10	0.9964	6.9729	1.0193	14.8480
15	1.5808	7.6453	1.2803	10.0670
20	1.9759	-	1.5111	-
25	2.1807	-	3.7580*, 1.6970**	-

* obtained for last iteration, ** best approximation obtained

Based on the RMS errors of Table 14, the best approximations were obtained for retrievals with a tropopause initial guess at 10 km. This is also what we concluded just by looking at the figures of the estimated profiles. This is not an unexpected outcome, since this initial guess was the closest to the real profile. For the real temperature profile, the tropopause is at approximately 12 km. The information in Table 14 also shows that the RMS error increases as the tropopause initial guess deviates from the real value. Therefore, the accuracy of the retrievals is dependent on the initial guess.

The accuracy of the estimated profiles also depends on the regularization parameter λ . Unfortunately, while this parameter is as important for the accuracy of the retrievals as the initial guess, its computation is not as easy. The selection criteria that we used for the computation of λ provided good regularization for most cases. Moreover, this criteria showed to be inadequate for several of the retrieval cases. Let us take as an example the first retrieval case, using Tikhonov regularization with a tropopause initial guess at 5 km, shown in Figure 5. For the λ selection criteria implemented in our algorithm, the problem did not yield an acceptable solution after 14 iterations. It started approximating the exact solution, but then started diverging in the fifth iteration. We could think at first that we selected a bad initial guess, or that our algorithm is just too sensitive to the initial guess. But if we modify our criteria for the selection of the regularization parameter, and start with $\lambda^{(0)} = 0.1$ instead of 0.01 we will obtain the profile shown in Figure 23. The RMS error was improved from 4.0728 to 2.3333. The stopping criterion for this case was satisfied after 8 iterations. Table 15 shows the output data for this case. Similarly, for the retrieval using TSVD regularization and the 25 km tropopause initial guess, a modification of the regularization parameter returned the improved estimated profile of Figure 24. Table 16 contains the sequence of values for λ , and the returned output data. The RMS error for this case improved from 3.7580 to 1.6137.

The results shown in Figures 23 and 24 are very important since they show the crucial role of the regularization parameter in the retrieval problem. The simple fact that we let λ to increase from one iteration to the other, will prevent the solution from achieving convergence. To show this, let us consider Figure 25. This figure corresponds to a problem solved with a previously implemented algorithm. This algorithm was a result of our

first attempts to solve our retrieval problem. It was implemented using a different criteria for the selection of λ . The criteria used was very simple; for each iteration a choose a $\lambda^{(a)}$ that optimally balances the solution norm and the residual norm only using the L-curve method. While this criteria is very useful, it has a major drawback when used alone. The value of λ is allowed to increase from one iteration to the next. Figure 26 shows the sequence of values for the regularization parameter. Here, we can appreciate the oscillations in the value assigned for each iteration.

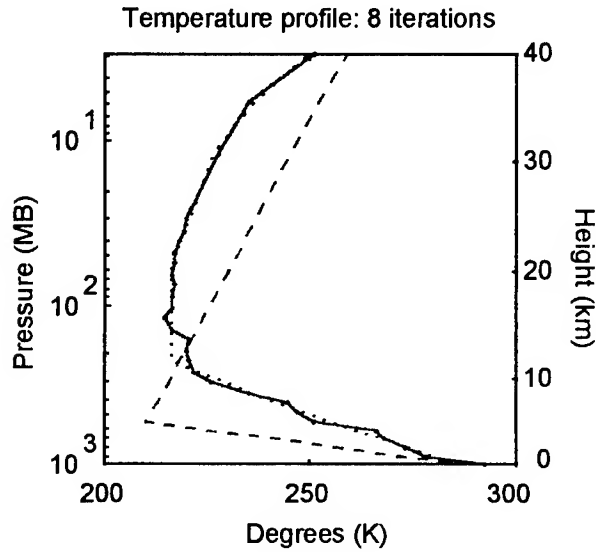


Figure 23: Temperature retrieval for Tikhonov regularization with 5 km tropopause initial guess and modified regularization parameter.

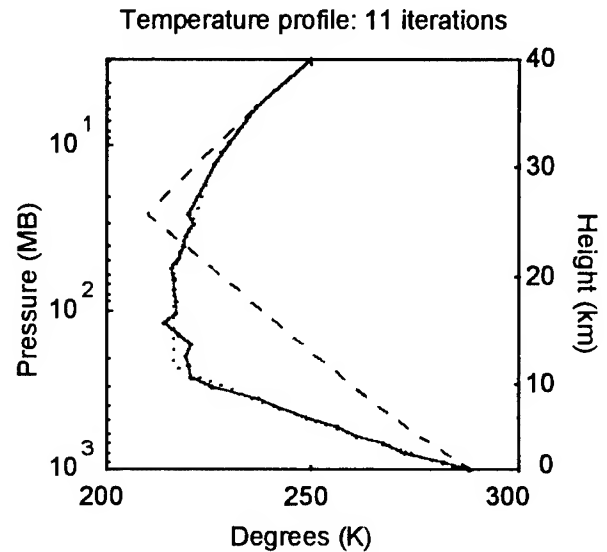


Figure 24: Temperature retrieval for TSVD regularization with 25 km tropopause initial guess and modified regularization parameter.

Table 15: Output parameters for retrieval using Tikhonov regularization with 5 km tropopause initial guess and modified regularization parameter.

a	$\lambda^{(a)}$	$\mathbf{h}^{(a)} = \ \mathbf{J}^{(a)}\delta + \mathbf{r}^{(a)}\ $	$\ \mathbf{r}^{(a)}\ _2$	$\left\ \left(\mathbf{J}^{(a)} \right)^T \mathbf{r}^{(a)} \right\ _2$	$\ \hat{\mathbf{T}}^{(a)} - \mathbf{c}\ _2$	$\frac{ \mathbf{h}^{(a-1)} - \mathbf{h}^{(a)} }{1 + \mathbf{h}^{(a)} }$	$\frac{\ \hat{\mathbf{T}}^{(a)} - \hat{\mathbf{T}}^{(a-1)}\ _2}{1 + \ \hat{\mathbf{T}}^{(a)}\ _2}$
0	1.0000e-02	1.5128e+02	7.5648e+01	1.1128e+02	1.3463e+00	-	-
1	1.0000e-02	7.5916e+01	2.0702e+00	8.1140e-01	8.5400e+01	9.7989e-01	6.7164e-02
2	1.0000e-02	1.9247e+00	2.6029e-01	3.4056e-02	8.4792e+01	2.5298e+01	2.2973e-02
3	8.3729e-05	4.3614e-01	5.2589e-01	1.6853e-01	1.0553e+02	1.0365e+00	4.5213e-02
4	8.3729e-05	4.8317e-01	4.5579e-02	1.1953e-02	1.0081e+02	3.1706e-02	1.8099e-02
5	8.3729e-05	3.7959e-02	8.7107e-03	1.8436e-03	1.0092e+02	4.2893e-01	5.1452e-03
6	8.3729e-05	8.3421e-03	5.1052e-04	7.1808e-05	1.0100e+02	2.9372e-02	1.2623e-03
7	8.3729e-05	4.6665e-04	3.1796e-04	9.0537e-06	1.0100e+02	7.8718e-03	1.9518e-04
8	5.3775e-07	6.3381e-04	3.1415e-04	5.7922e-06	1.0100e+02	1.6705e-04	1.0511e-05

For the retrievals with the addition of noise, it was not possible to achieve convergence with the selected regularization parameters. Unlike in other cases, the various sequences tried were not successful at regularizing the problem adequately. Moreover, we cannot assure without studying the problem further that a modified regularization parameter alone will solve the noisy problem.

Table 16: Output parameters for retrieval using TSVD regularization with 25 km tropopause initial guess and modified regularization parameter.

a	$\lambda^{(a)}$	$\mathbf{h}^{(a)} = \ \mathbf{J}^{(a)}\delta + \mathbf{r}^{(a)}\ $	$\ \mathbf{r}^{(a)}\ _2$	$\ \mathbf{J}^{(a)^T} \mathbf{r}^{(a)}\ _2$	$\ \hat{\mathbf{T}}^{(a)} - \mathbf{c}\ _2$	$\frac{\ \mathbf{h}^{(a-1)} - \mathbf{h}^{(a)}\ }{1 + \ \mathbf{h}^{(a)}\ }$	$\frac{\ \hat{\mathbf{T}}^{(a)} - \hat{\mathbf{T}}^{(a-1)}\ _2}{1 + \ \hat{\mathbf{T}}^{(a)}\ _2}$
0	3	1.1813e+02	5.9096e+01	8.2997e+01	1.3463e+00	-	-
1	3	5.8871e+01	2.2342e+00	3.4294e-01	8.7470e+01	9.8982e-01	6.9435e-02
2	7	2.0914e+00	3.9102e-01	1.2501e-01	9.9069e+01	1.8367e+01	3.0033e-02
3	8	3.6311e-01	6.3232e-02	6.9684e-03	1.0057e+02	1.2679e+00	7.4709e-03
4	9	7.6942e-02	8.7632e-02	2.1264e-02	1.0231e+02	2.6572e-01	1.6747e-02
5	10	7.4146e-02	1.7880e-02	2.7300e-03	1.0278e+02	2.6034e-03	6.1012e-03
6	12	1.7040e-02	3.2845e-02	6.5873e-03	1.0325e+02	5.6148e-02	6.7660e-03
7	12	2.6887e-02	6.0787e-03	1.1864e-03	1.0357e+02	9.5888e-03	3.1218e-03
8	13	6.5282e-03	6.7191e-03	1.3494e-03	1.0367e+02	2.0227e-02	2.2409e-03
9	14	9.5719e-03	9.6549e-03	1.9501e-03	1.0402e+02	3.0148e-03	3.2054e-03
10	15	1.2225e-02	1.8515e-02	4.9941e-03	1.0472e+02	2.6215e-03	7.5048e-03
11	15	1.3038e-02	6.7517e-03	1.3980e-03	1.0524e+02	8.0244e-04	4.3044e-03

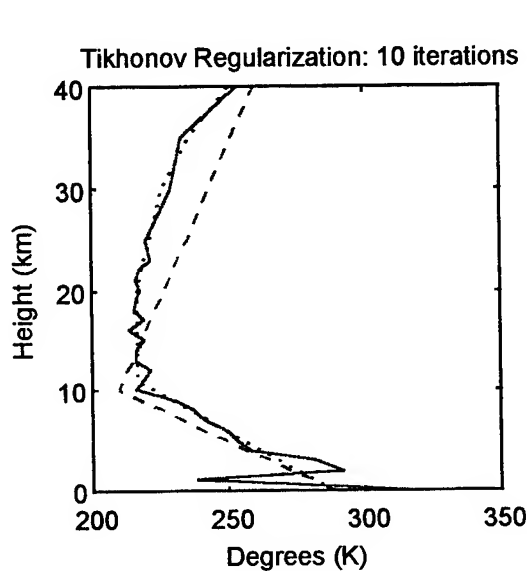


Figure 25: Retrieval using only the L-curve for the selection of the regularization parameter.

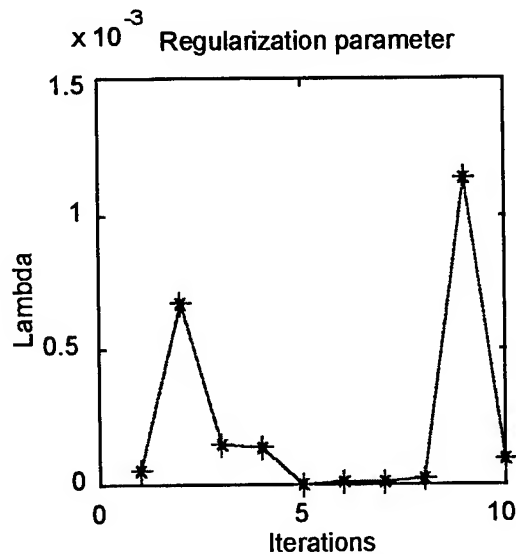


Figure 26: Regularization parameter selected using only the L-curve.

8. Conclusions

In this project, we developed an algorithm for nonlinear retrieval problems in atmospheric remote sensing based on the Gauss-Newton method to solve nonlinear least square problems. Regularization was applied to the underdetermined linear least-squares problem of computing the search direction using Tikhonov and TSVD regularization methods for linear inverse problems. The method was applied to the nonlinear problem of atmospheric temperature retrieval from HIRS/2 and MSU radiometry. A set of MATLAB macros implementing the algorithms was developed.

Simulation studies were performed to understand the performance of the proposed method. Simulations and Jacobian calculations were made using GLA TOVS fast radiative transfer code from NASA Goddard Space Flight

Center. Three key factors affect the performance of the retrieved profile: (1) the initial guess, (2) the updating criterion for the regularization parameter, and (3) the stopping criterion. In our simulation studies, temperature profiles with 5 km, 10 km, 15 km, 20 km, and 25 km tropopause initial guesses were used. The best performance was achieved with those profiles close to the actual profile. The implementations of the retrieval algorithm produced similar results for both Tikhonov and TSVD regularization. The root mean square (RMS) error for the estimated temperature profiles varied from 0.9964 to 4.0728 for the noiseless case. Most of the noiseless cases studied, produced a solution in less than 10 iterations.

We saw that the regularization parameter for both methods should be a nonincreasing sequence. That condition guarantees that regularization is reduced as the algorithm progresses. A good stopping criterion will guarantee that the algorithm will stop before the profile estimate start to behave erratically. In our simulations, we saw that when these conditions are not met the algorithm could stay close to the initial guess or could produce a useless highly oscillatory solution. The criteria implemented in the algorithms worked in most of the examples presented. However, we showed with a couple of examples that we were capable of obtaining better estimates if the algorithm was stopped earlier or by changing some parameters in the regularization parameter update.

We worked out some simulations with white Gaussian noise added to the simulated brightness temperature. The results were unsatisfactory. The retrievals for noisy cases produced RMS errors considerably high from 6.9729°K to 14.8480°K. The criteria for selecting the regularization parameter in the noiseless case seemed to be inappropriate for the noisy case. In most of the noisy cases studied, the solution was fixed at a value after the first four or five iterations. This point out to the need of better modeling of the sensor noise process and the need of evaluating the performance of the stopping and regularization criteria under these circumstances. This is a subject for future work.

The objectives and goals of the original proposal were quite ambitious for one year. We proposed to work with simulations of the DMSP SSM/T1 & 2 sensor. Although, we were capable of obtaining radiative transfer code to simulate the measured brightness temperature, no code was found that would provide us with the Jacobian (sensitivity functions) needed by the algorithm. We did not have time to perform the experimental validation of the proposed algorithm. We are in search of a validated data set from TOVS and DMSP for this purpose. Initial talks with researchers at the GSFC Data Assimilation Office have been going on to obtain a validated data set for TOVS. Mr. Vincent Falcone will provide the data set from AF Phillips Laboratory.

9. Future Work

The proposed algorithms need to be validated using experimental data and their performance compared to standard retrieval algorithms already in use at the field.

Future work needs to investigating different criteria for the computation of the regularization parameter λ . New and improved criteria could be developed that adjust according to other important parameters, such as the residual norm, the gradient or relative changes in the estimated profiles, just to mention a few. Also, the retrievals

for the noisy cases should be investigated further, in order to determine what modifications to the regularization update criterion are needed to obtain an accurate retrieval.

In this project, we looked at the development of regularization algorithms that regularize a linearization of the nonlinear retrieval problem. Algorithms that look at the regularization of the original nonlinear problem are of interest and might result in more accurate retrievals.

10. References

- [1] Bertsekas, D. P. 1995. **Nonlinear Programming**. Athena Scientific, Belmont, Massachusetts, 646 pp.
- [2] Datta, B. N. 1995. **Numerical linear algebra and applications**. Brooks/Cole Publishing Company, Pacific Grove, California, 680 pp.
- [3] Engle, H. W., M. Hanke, and A. Neubauer. **Regularization of inverse problems**. Kluwer Academic Publishers, Dordrecht, The Netherlands, 321 pp.
- [4] Eriksson, J. 1996. **Optimization and regularization of nonlinear least squares problems**. Ph.D. Thesis, Department of Computing Science, Umea University, Sweden.
- [5] Eyre, J. R. 1989. "Inversion of cloudy satellite sounding radiance by nonlinear optimal estimation: Theory and simulation for TOVS." **Q. J. Roy. Met. Soc.** 115 (489): 1001-1025.
- [6] Eyre, J. R., G. A. Kelly, A. P. McNally, E. Anderson, and A. Persson. 1993. "Assimilation of TOVS radiance information through one-dimensional variational analysis." **Q. J. Roy. Met. Soc.** 119: 1427-1463.
- [7] Groetsch, C. W. 1984. **The theory of Tikhonov regularization for Fredholm equations of the first kind**. Pitman Publishing, Inc.
- [8] Hansen, P. C. 1992. **Regularization tools: A MATLAB package for analysis and solution of discrete ill-posed problems**. Technical Report. Technical University of Denmark, Lyngby, Denmark.
- [9] Hansen, P. C. 1996. **Rank-deficient and discrete ill-posed problems**. Doctoral Dissertation. Technical University of Denmark, Lyngby, Denmark.
- [10] Hansen, P. C. 1998. **Rank-deficient and discrete ill-posed problems: Numerical aspects of linear inversion**. SIAM, Philadelphia, Pennsylvania, 247 pp.
- [11] Janssen, M. A. 1993. **Atmospheric remote sensing by microwave radiometry**. John Wiley & Sons, New York, New York.
- [12] Kidder, S. Q., and T. H. Vonder Haar. 1995. **Satellite meteorology: An introduction**. Academic Press, San Diego, California, 466 pp.
- [13] Kidwell, K. B. 1995. **NOAA polar orbiter data users guide**. NASA, Washington, D.C.
- [14] Kornfield, J., and J. Susskind. 1977. "On the effect of surface emissivity on temperature retrievals." **Mon. Wea. Rev.** 105: 1605-1608.
- [15] Lenoble, J. 1993. **Atmospheric radiative transfer**. A. Deepak Publishing, Hampton, Virginia, 532 pp.
- [16] Seber, G. A. F., and C. J. Wild. 1989. **Nonlinear regression**. John Wiley & Sons, New York, New York, 768 pp.
- [17] Sienkiewicz, M. 1996. **The GLA TOVS rapid algorithm forward radiance modules and Jacobian version 1.0**. Goddard Space Flight Center, Greenbelt, Maryland.
- [18] Smith, W. L., H. M. Woolf, and H.E. Fleming. 1972. "Retrieval of atmospheric temperature profiles from satellite measurements for dynamic forecasting." **J. App. Met.** 11: 113-122.

- [19] Susskind, J., J. Rosenfield, and D. Reuter. 1984. "Remote sensing of weather and climate parameters from HIRS2/MSU on TIROS-N." **J.Geo. Re.** 89 (3): 4677-4697.
- [20] The Math Works. 1996. **MATLAB® external interface guide**. The Math Works, Inc., Natick, Massachusetts, 104 pp.
- [21] Thompson, O. E. 1992. "Regularizing the satellite temperature-retrieval problem through singular-value decomposition of the radiative transfer physics." **Mo. We. Rev.** 120: 2314-2328.
- [22] Tikhonov, A. N. 1977. **Solution of ill-posed problems**. John Wiley & Sons, New York, New York.
- [23] Trenberth, K. E., editor. **Climate system modeling**. Cambridge Press, 1992.
- [24] Vélez, M. 1998. "Atmospheric retrievals using regularization methods." **Proceedings of the IEEE international geoscience and remote sensing symposium**. Seattle, Washington.

Experimental Investigation of Impinging Jets

David Holtzclaw, Graduate Student
Zhanhua Ma, Graduate Student
San-Mou Jeng, Associate Professor
Aerospace Engineering and Engineering Mechanics

Mail Location 70
University of Cincinnati
Cincinnati, OH 45221-0070

Final Report for:
Summer Research Extension Program

Sponsored by:
Air force Office of Scientific Research
Bolling Air Force Base, DC

and

Phillips Laboratory

December 1997

Experimental Investigation of Impinging Jets

Zhanhua Ma, Graduate Student
David Holtzclaw, Graduate Student
San-Mou Jeng, Associate Professor
Aerospace Engineering and Engineering Mechanics
University of Cincinnati, OH 45221-0070

Abstract

An experimental study of the spray characteristics of impinging water jets was conducted. The Phase Doppler particle analyzer (PDPA) and video photography were used to measure droplet size and velocity distributions and liquid sheet behavior. Two impinging angles, 60 and 90 degrees, were investigated. The injection speed is varied from 4 to 13 m/s, or Reynolds number from 4,600 to 15,000. Detailed distribution of droplet diameter and velocity for three injection speeds (7.6, 9.0 and 11.3 m/s) are reported. The droplet size measurements indicate that 90 degree impinging angles provide finer atomization than that of 60 degree at the same Reynolds number. The better atomization were also measured as Reynolds number increases for both impinging angles. The droplet size measurements indicate that the Sauter mean diameter (SMD) increases as the azimuthal angle increases. This trend is a reversal of the existing atomization models. The droplet velocity distributions were found either normal or bi-modal depending on measuring locations. The instantaneous sizes and shapes of liquid sheet were measured. The liquid sheet instability wave was clearly observed which propagated upstream to the injector. The spray photographs also indicated that the sprays generated by 90 degree injector have wider spray angles and are more three-dimensional compared than those of 60 degree injector.

$$f(\theta, \varphi) = [(1 - \cos \theta \cdot \cos \varphi)^2 / \sin^3 \theta].$$

And d_0 is the initial jet diameter, W_e is the Weber number based on the injection speed and diameter, 2θ and φ are the impinging angle and the azimuthal angle from the z axis, respectively. This model predicts that the Sauter mean diameter (SMD) of droplets decreases with the increase of the injection speed and the impingement angle. For a given injector configuration and flow rate, the droplet size decreases as the azimuthal angle increases.

In this experimental study, the Phase Doppler particle analyzer (PDPA) and video photography were used to measure droplet size and velocity distributions and liquid sheet behavior. Two impinging angles (60 and 90 degrees) with water injection speed from 4 to 13 m/s were investigated. Detailed distribution of droplet diameter and velocity at three injection speeds (7.6, 9.0 and 11.3 m/s) are reported and compared to the trend predicted by existing atomization model⁶. The size, shape and instability of liquid sheets were measured by the instantaneous photography.

Experimental setup

Two-jet impinging jet injectors, depicted in Figure 1, are used in this study. These injectors are made up of two capillary stainless steel tubes with 1mm inner diameter and 100 mm length. The exit orifices were either 50 mm or 80mm apart and the impinging angles (2θ) are either 60 or 90 degree. The injector is mounted downward on a three-dimensional traversing system in order to have spatially resolved droplet size measurements. A water-proof tank (3 x 3 x 2 ft) locates about 2 ft downstream of the injector was used to collect and drain the test liquid. A 40-galon water tank pressurized by a gaseous nitrogen k-bottle is used to steadily supply the test fluids. The nitrogen pressure, injector pressure, was precisely regulated, and the water flow rate was calibrated using a gradual cylinder and a stop watch. The flow rate was constantly monitored during the tests.

Two optical instruments were used in this study. Two component PDPA was used for simultaneous measurements of droplet diameter and velocity. The current PDPA setup can measure the droplet size up to 200 μm and the velocity up to 100 m/s. The data reported in this study are based on 1,000 droplet samples. The liquid sheet behavior was investigated by a 30 frame per second S-VHS video system. The back-lighted video were taken using a stroboscope with the pulse length duration about 1 μs .

Results and Discussions

Figure 2 shows the water injection speed as a function of the injection pressure. In the current test article, the injector length (100 mm) to diameter (1 mm) ratio is 100. The injection pressure shows a

linear relationship with the injection speed which indicates that the majority of the pressure loss is due to the friction loss within the injector body. The Reynolds number, based on the injector diameter and injection speed, is from 4,600(10 psid) to 15,000(80 psid) . The flow conditions in this study are turbulent, and the injection pressure loss is found to be consistent with the estimated friction loss of fully developed turbulent pipe flow. Although the velocity profile of the liquid at the nozzle orifice was not measured in this study, It should be same as the fully developed turbulent pipe flow at the same Reynolds number.

The stroboscope back-lighted instantaneous photographs of spray are shown in Figures 3-7. The field of view of these photographs is roughly 34x44mm. The front view shows the formation of the spray in the perpendicular direction to the plane of impinging jets. At 10 psid, the liquid sheet is still intact although the instability wave within this liquid sheet is evident, and the droplets were formed at the edge of the sheet. The edge of liquid sheet rolls up due to the surface tension force. The droplets are confined to the centerline for the 60 degree injector while the droplets begin to disperse in the y direction for the 90 degree injector. The instability wave of liquid sheet was found to propagate back to the injectors for both cases. The variations of the liquid jet diameter were clearly captured in the photos. These variations are regular and have the fixed spatial frequencies. The higher spatial frequency is observed for the 90 degree injector.

Some general conclusions are reached from the photos illustrated in Figures 3-7. The higher injection speed generates better atomized spray and has the the liquid sheet break-up location closer to the impingement point. The ligaments were formed from the liquid sheet with some dominated frequencies. When the injection speed increases, this frequency is higher and the ligament size is smaller. In all test conditions except the 10 psid case, the ligaments and droplets propagates outward from the impingement point. The 90 degree injector atomizes the liquid better than that of 60 degree injector at the same flow rate. The 90 degree sprays disperse wider in the y-direction (see side view of photos) than the 60 degree sprays.

The sprays contain ligaments and non-spherical droplets near the impingement point as shown in the figures. The PDPA was used to measure the droplet size and velocity distribution at locations as close to the sprays as possible. These measurements were made along a rectangular box (60x30 mm and 80x30 mm for the 90 and 60 degree injectors, respectively) where validation rate of PDPA is greater than 80%. The velocity vectors of the measurements at three flow rate (35, 46 and 66 psid) are shown in Figures 8 and 9. From the directions of droplet velocity vectors, it is clear that droplets at all measuring points originates from the impingement point. The droplet dispersion can be neglected between the impingement point and the measurement locations. These velocity measurements are

consistent with the flow visualization shown in Figures 3-7. The contours of "continuous" liquid sheet, based on the video recording tapes, are also depicted in these figures. As the flow rate increase, the liquid sheet is wider. Generally speaking, the liquid sheets generated from the 90 degree injector are wider.

The droplet size measurements along the rectangle box as depicted in the Figures 8 and 9 were converted to the polar coordinate. The impingement point is the origin. The Sauter Mean Diameter (SMD) as a function of the azimuthal angle is presented in Figures 10 and 11. The droplet size decreases as the injection speed increases for both impinging angles. The 90 degree injector produces better atomization than that of the 60 degree injector.

The existing atomization models predict the droplet size decreases as the azimuthal angle from the vertical axis increases. However, the SMD measurements conducted in this study shows the reverse trend. Kang et al⁹. recently conducted the droplet size measurements on the similar sprays using holographic method. The locations of their measurements are around the edge of the liquid sheet and are not limited to the spherical droplets. Although their data are scattered as a function of the azimuthal angle, they do show the trend consistent to the SMD measurements conducted in this study: the SMD increases as the azimuthal angle increases. They also compared their experimental results with three different models, and all models predicted the reverse trend of the droplet size as a function of the azimuthal angle. Experimental results from the this study and Kang et al⁹. suggests that the existing models to predict the atomization process of the impinging injectors should be re-examined.

Droplet size and velocity distribution at four locations (40, 45, 50 and 50mm downstream of the impingement point) along the centerline of the 90 degree injector is shown in Figure 12. All droplet size distributions can be fitted with log-normal distributions with confidence. However, the trend of the axial velocity distributions is interesting. Near the liquid sheet (40mm), it is a bi-modal distribution with the higher droplet population density in the high velocity group, then the higher droplet population density switches to the lower speed group, and finally (65mm) it becomes a normal distribution. To further examine this trend, the correlation between the droplet size and axial velocity are shown in Figure 13. It is clear that two groups of droplet were formed from the liquid sheet. The group containing large droplets moves outward at the higher velocity. As this group of droplets moves downstream, secondary atomization may occurs on the larger droplets. This reduces the droplet population density of this group compared to that of the other group (traveling at lower velocity). At far downstream, these two groups of droplets merge into a single group. These droplet size and velocity distribution measurements indicate that the atomization mechanisms of the impinging jets may be far more complicated than the mechanisms postulated in the existing models. Two physical mechanisms may

co-exist to generate two different groups of the droplets. Further study to explore these physical mechanisms are recommended.

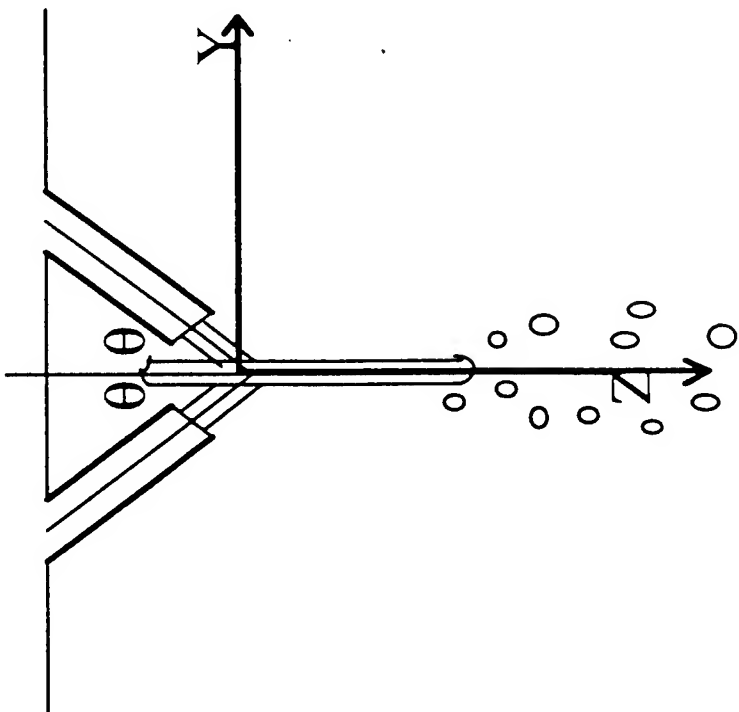
Conclusions

Impinging jets with two impinging angles (60 and 90 degrees) were investigated in this study. The liquid sheet instability wave was clearly observed and can propagate upstream to the injector. The higher injection speed generates better atomized spray and has the liquid sheet break-up location closer to the impingement point. When the injection speed increases, this ligament size becomes smaller. The droplet size measurements by PDPA indicate that the droplet size decreases as the injection speed increases for both impinging angles. The 90 degree injector atomizes better than the 60 degree injector. However, the measured droplet size increases as the azimuthal angle increases. This behavior is not consistent with predictions from the existing models. Two distinct groups of droplets, traveling at different velocities, were found near the liquid sheet. It is clear that existing models in the literature have to be improved in order to predict the atomization process of the impinging jets.

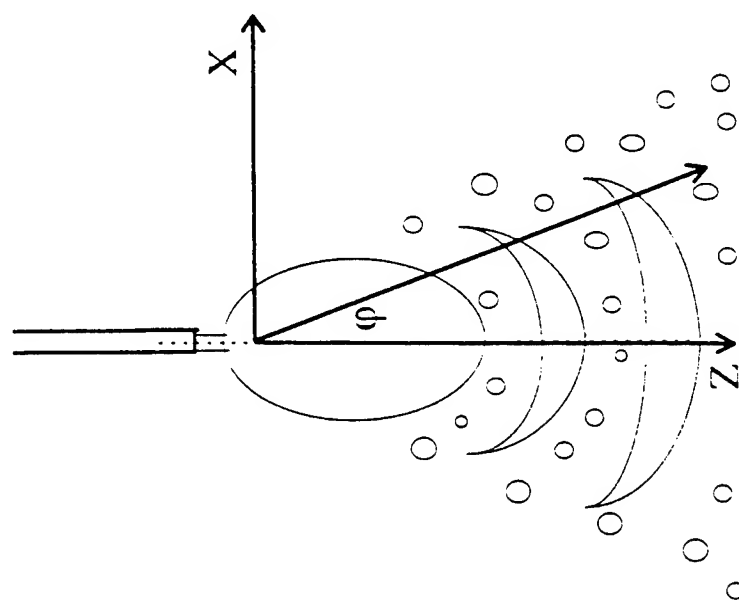
Reference

1. Rupe, J. H., Propulsion Laboratory Progress Report 20-209, California Institute of Technology, Pasadena, CA., 1956.
2. Heidmann, M. F., Priem, R. J., and Humphrey, J. C., "A Study of Sprays Formed by Two impinging Jets," NACA TN 3835, 1957.
3. Foster, H. H., and Heidmann, M. F., "Spatial Characteristics of a Water Spray Formed by Two Impinging Jets at Several Jet Velocities in Quiescent Air," NASA TN D-301, 1960.
4. Heidmann, M. F., and Foster, H. H., "Effect of Impingement Angle on Drop Size Distribution and Spray Pattern of Two Impinging Water Jets," NASA TN D-872, 1961.
5. Dombrowski, N., and Hooper, P. C., "A Study of the Sprays Formed by Impinging Jets in Laminar and Turbulent Flow," *Journal of Fluid Mechanics*, Vol. 18, 1963, p.392.
6. Dombrowski, N., and Johns, W. R., "The Aerodynamic Instability and Disintegration of Viscous Liquid Sheets," *Chemical Engineering Science*, Vol. 18, 1963, p. 203.
7. Anderson, W. E., Ryan, H. M., Pal, S., and Santoro, R. J., "Fundamental Studies of Impinging Liquid Jets," AIAA Paper 92-0458, 1992.

8. Ryan, H. M., Anderson, W. E., Pal, S., and Santoro, R. J., "Atomization Characteristics of Impinging Liquid Jets," *Journal of Propulsion and Power*, vol. 11, no. 1, 1995, p. 135.
9. Kang, B., Poulikakos, D., and Shen, Y., "Holography measurements on Impinging Liquid Jet Atomization: Testing of Theory Predictions," *Atomization and Spray*, vol. 5, p. 387, 1995.
10. Kang, B. and Poulikakos, D., "Holography Experiments in a Dense High-Speed Impinging Jet Spray", *Journal of Propulsion and Power*, vol. 12, no.2, 1996, p. 348.
11. Couto, H. S. and Bastos-Netto, D., "Modeling Droplet Size Distribution from Impinging Jets", *J. of Propulsion and Power*, vol. 7, no. 4, 1991, p. 654.
12. Couto, H. S. , Bastos-Netto, D. and Migueis, C. E., "Modeling the Initial Droplet Size Distribution Function in the Spray Formed by Impinging Jets," *J. of Propulsion and Power*, vol. 8, no. 3, 1992, p.725.



Side View



Front View

Figure 1 Schematic Diagram of a Spray Formed by Two Impinging Jets

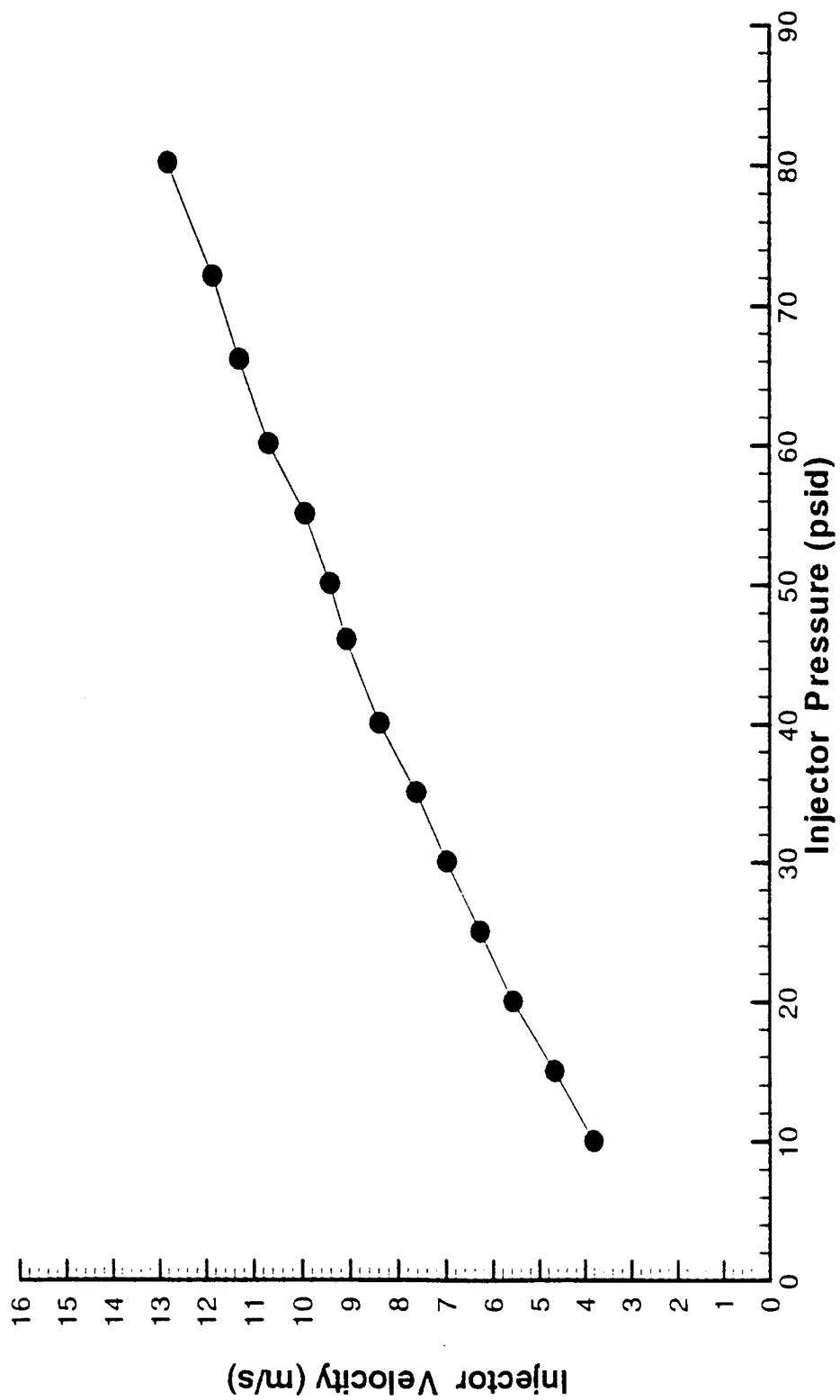
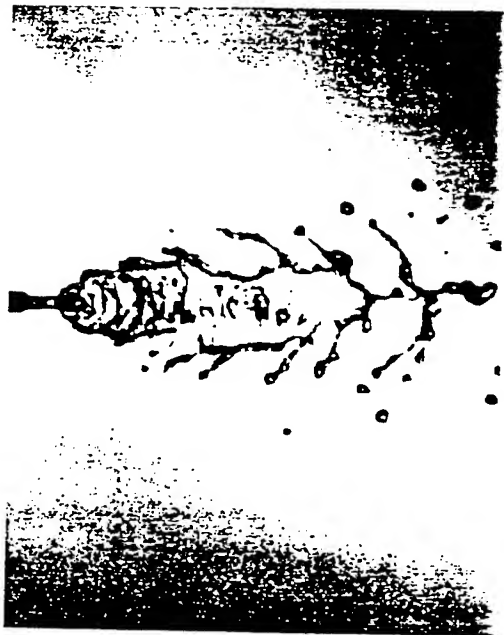
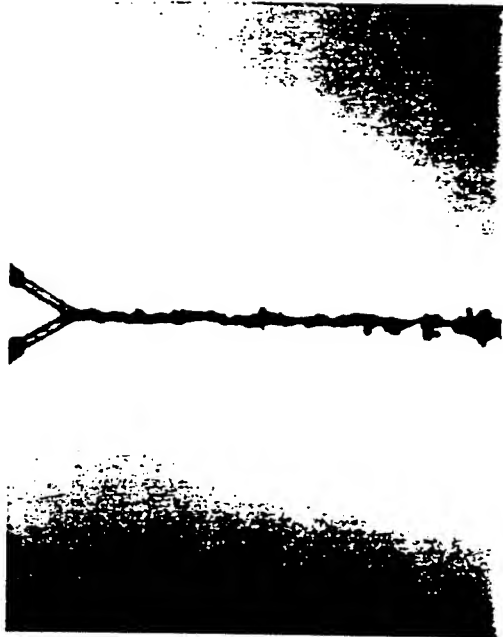


Figure 2 Injection Speed as a Function of Injection Pressure



Front View

Impinging Angle = 60°, Pressure = 10 psi



Side View



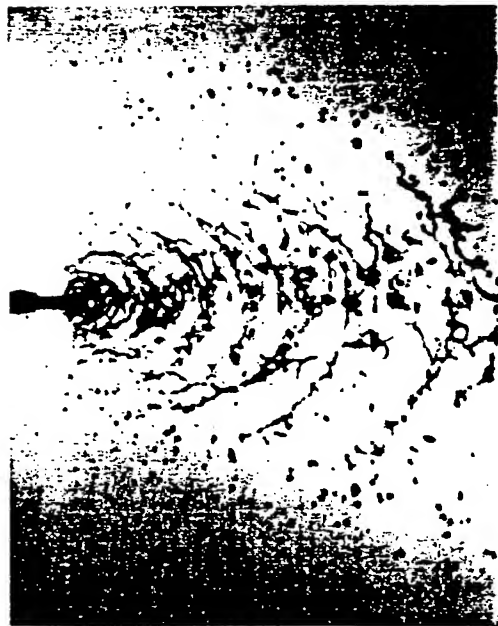
Front View

Impinging Angle = 90°, Pressure = 10 psi



Side View

Figure 3 Photograph of Spray Formed by Two Impinging Jets: 10 psid



Front View

Impinging Angle=60°, Pressure=35 psi



Side View



Front View

Impinging Angle=90°, Pressure=35 psi



Side View

Figure 4 Photograph of Spray Formed by Two Impinging Jets: 35 psid

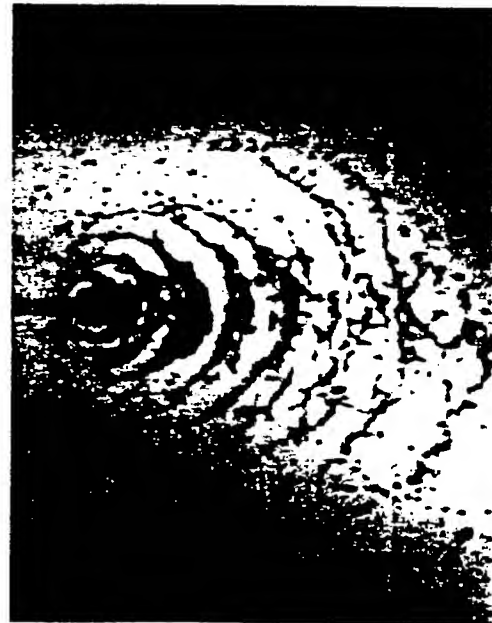


Front View

Impinging Angle=60°, Pressure=46 psi



Side View



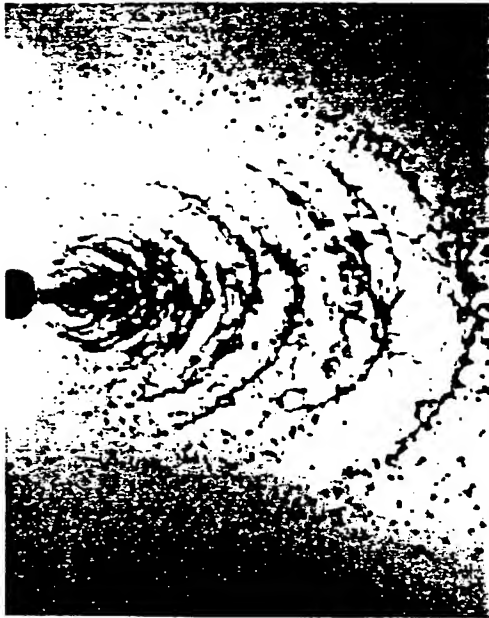
Front View

Impinging Angle=90°, Pressure=46 psi



Side View

Figure 5 Photograph of Spray Formed by Two Impinging Jets: 46 psid



Front View

Impinging Angle: 60°, Pressure: 66 psi



Side View



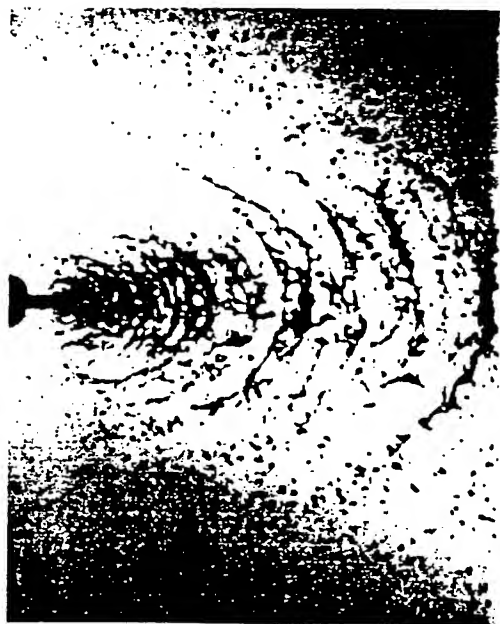
Front View

Impinging Angle: 90°, Pressure: 66 psi



Side View

Figure 6 Photograph of Spray Formed by Two Impinging Jets: 66 psid



Front View

Impinging Angle=60°, Pressure=80 psi



Side View



Front View

Impinging Angle=90°, Pressure=80 psi



Side View

Figure 7 Photograph of Spray Formed by Two Impinging Jets: 88 psid

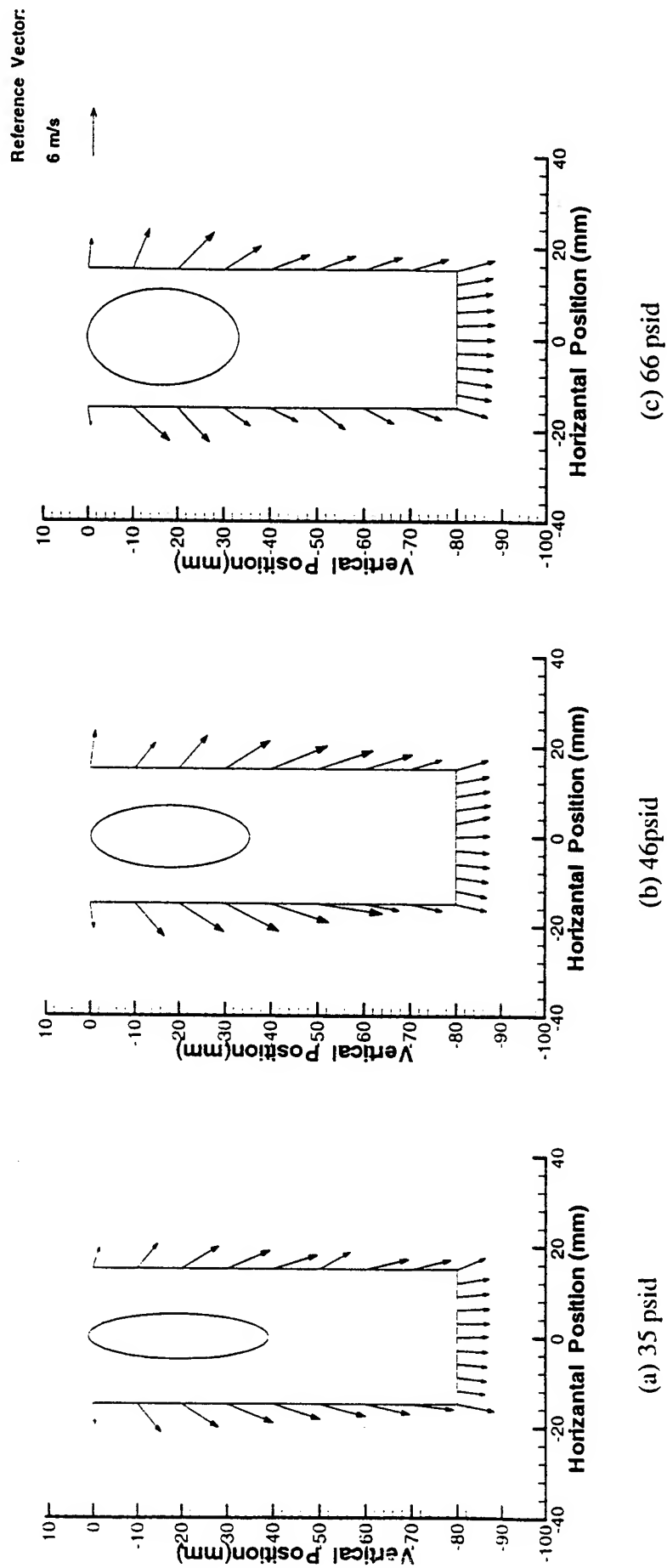


Figure 8 Droplet Velocity Vector Plot: 60° Impinging angle

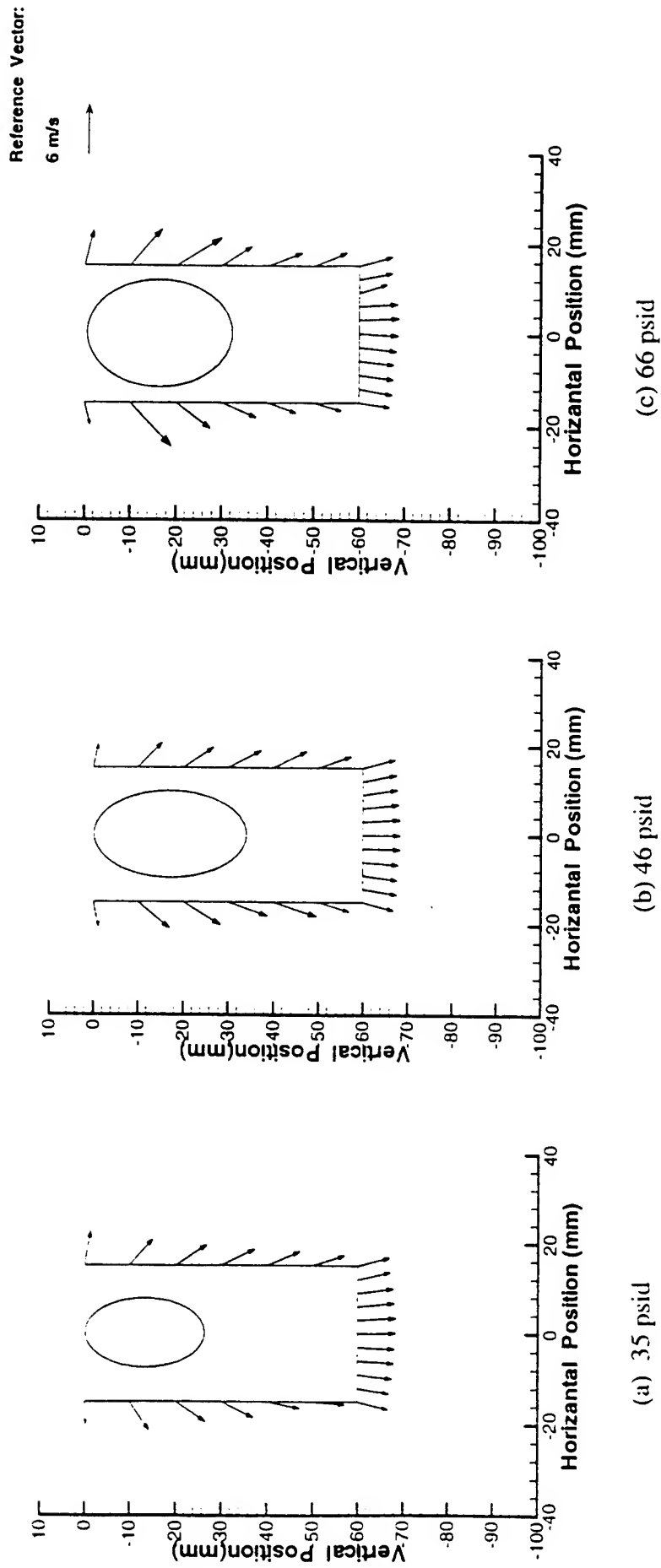


Figure 9 Droplet Velocity Vector Plot: 90° Impinging angle

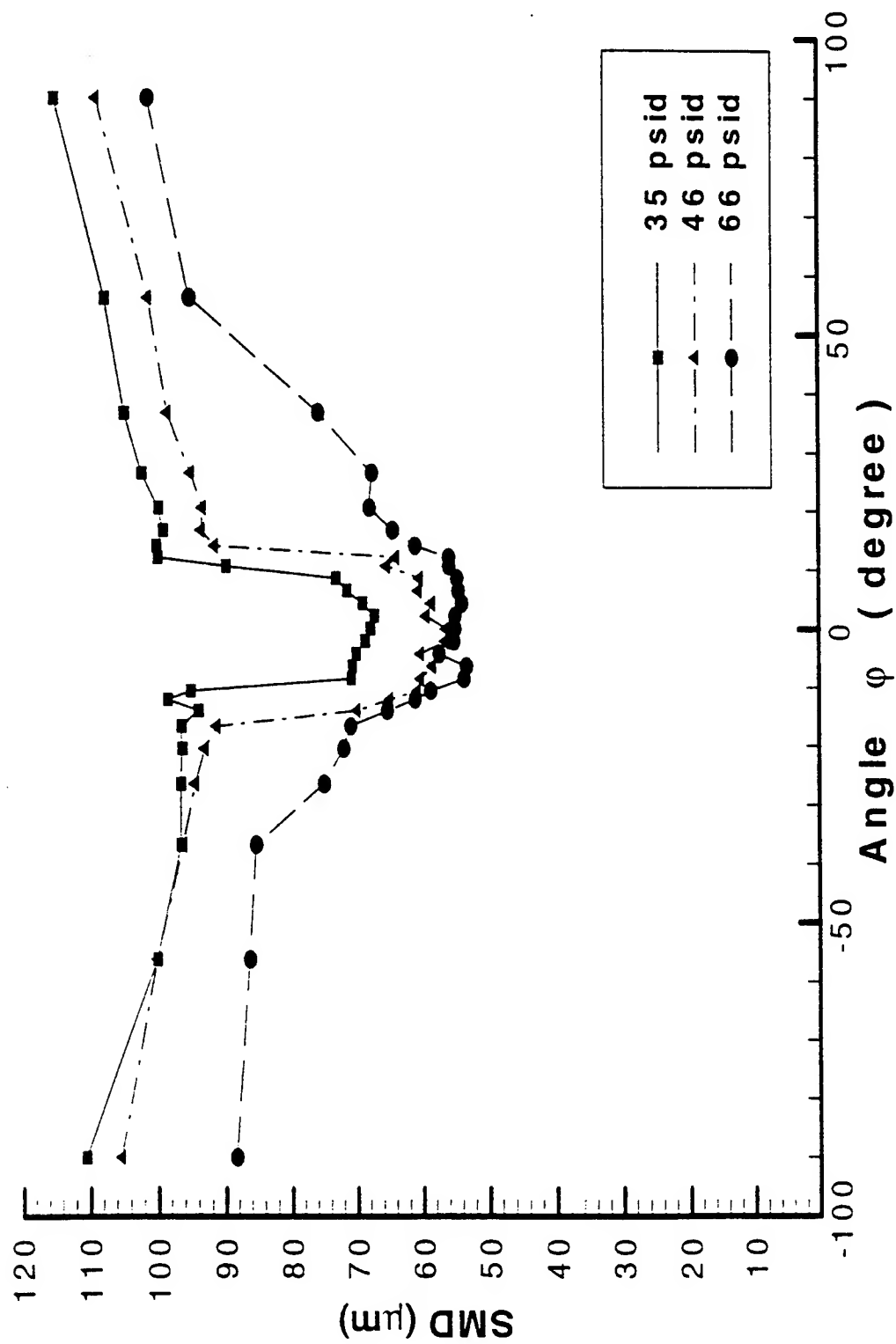


Figure 10 Sauter Mean Diameter (SMD) as a function angle: 60° Impinging angle

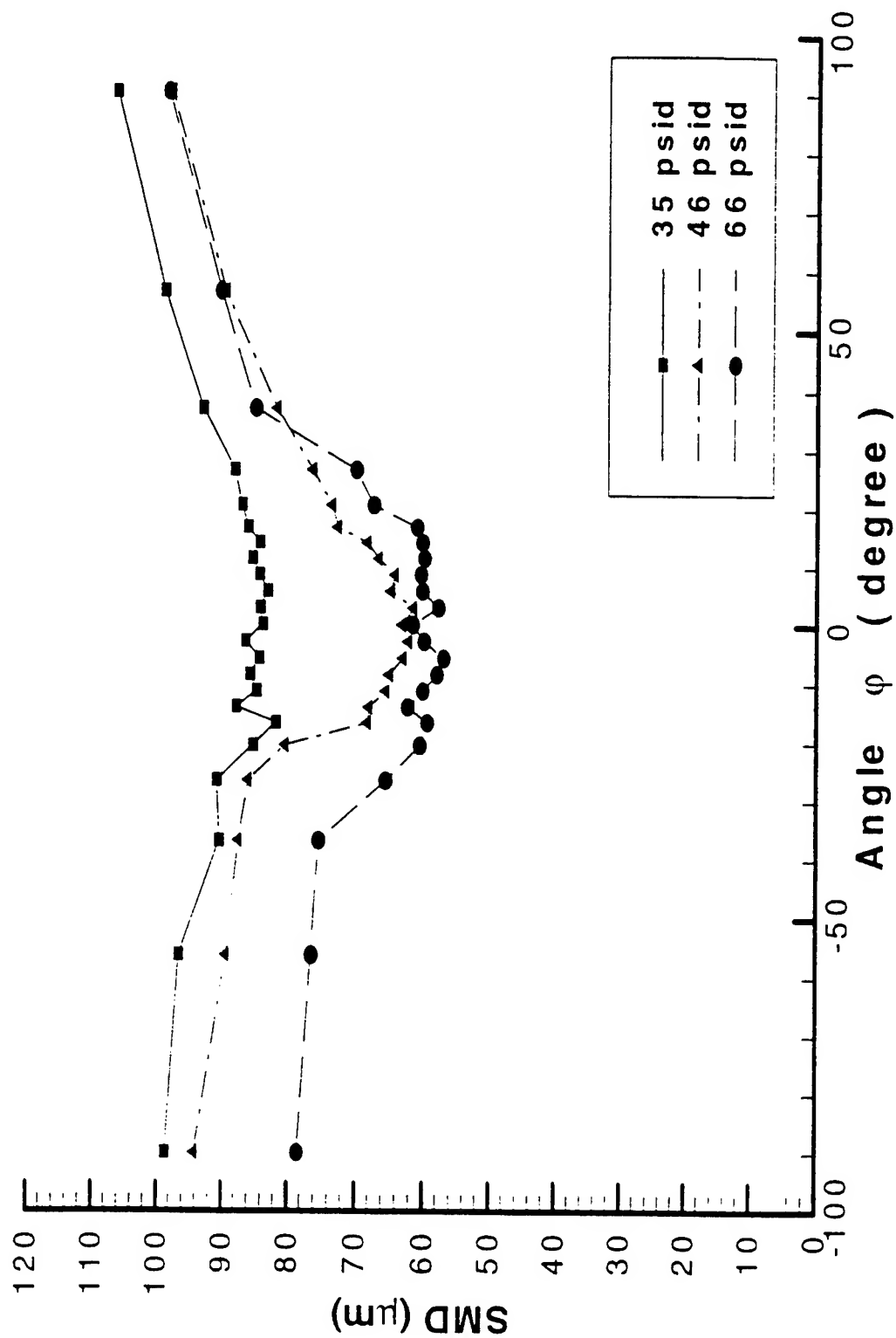


Figure 11 Sauter Mean Diameter (SMD) as a function angle: 90° Impinging angle

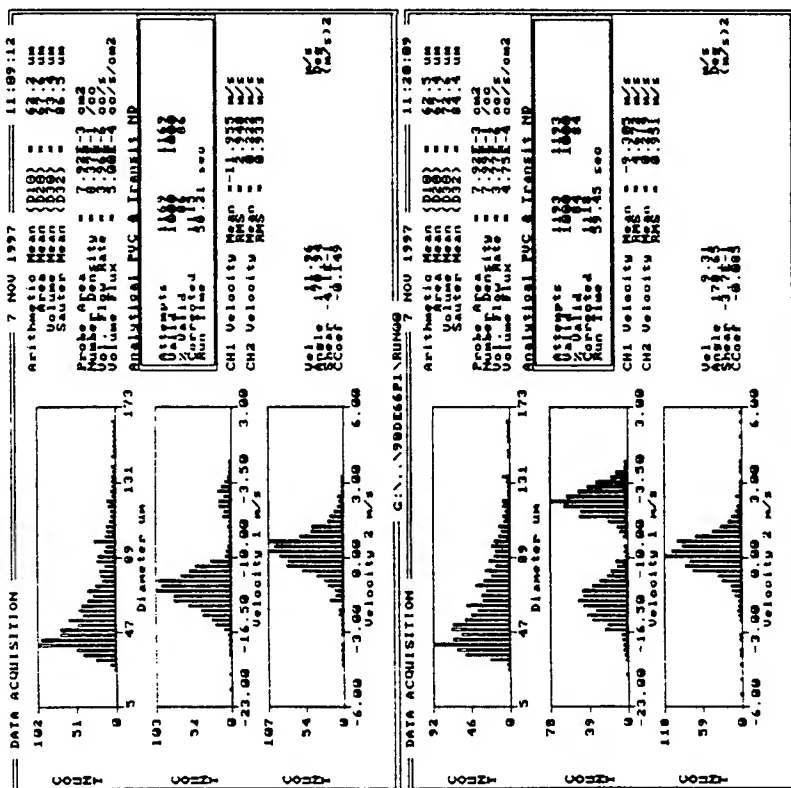
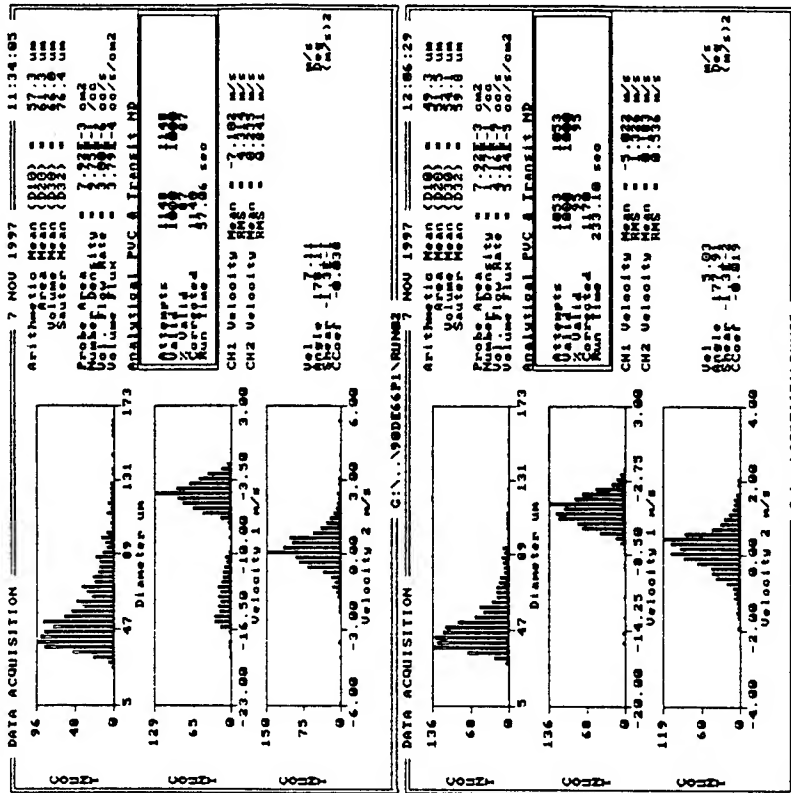


Figure 12 Distribution of Droplet Size and Velocity

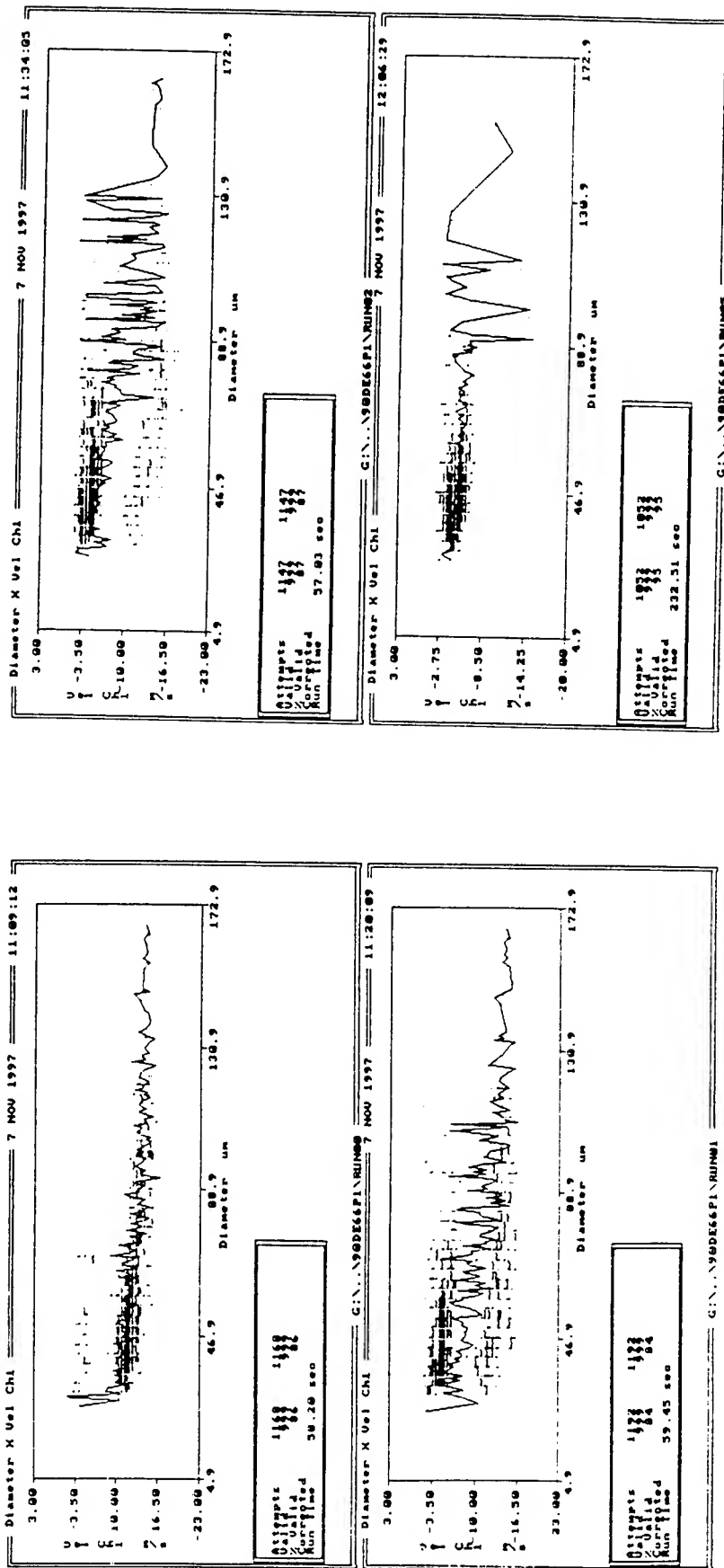


Figure 13 Correlation between Droplet Size and velocity

Jeffrey W. Nicholson
Report not available at time of publication.